ADVANCED PET, SPECT, MR AND OPTICAL IMAGING IN CLINICAL AND PRE-CLINICAL RESEARCH OF NEUROPSYCHIATRIC DISORDERS

EDITED BY: Boldizsar Czeh, Zsigmond Tamás Kincses, Szilvia Anett Nagy and Nicola Toschi

PUBLISHED IN: Frontiers in Psychiatry, Frontiers in Neuroscience and Frontiers in Neurology

frontiers Research Topics

ISSN 1664-8714
ISBN 978-2-88974-339-1
DOI 10.3389/978-2-88974-339-1

About Frontiers

Frontiers is more than just an open-access publisher of scholarly articles: it is a pioneering approach to the world of academia, radically improving the way scholarly research is managed. The grand vision of Frontiers is a world where all people have an equal opportunity to seek, share and generate knowledge. Frontiers provides immediate and permanent online open access to all its publications, but this alone is not enough to realize our grand goals.

Frontiers Journal Series

The Frontiers Journal Series is a multi-tier and interdisciplinary set of open-access, online journals, promising a paradigm shift from the current review, selection and dissemination processes in academic publishing. All Frontiers journals are driven by researchers for researchers; therefore, they constitute a service to the scholarly community. At the same time, the Frontiers Journal Series operates on a revolutionary invention, the tiered publishing system, initially addressing specific communities of scholars, and gradually climbing up to broader public understanding, thus serving the interests of the lay society, too.

Dedication to Quality

Each Frontiers article is a landmark of the highest quality, thanks to genuinely collaborative interactions between authors and review editors, who include some of the world's best academicians. Research must be certified by peers before entering a stream of knowledge that may eventually reach the public - and shape society; therefore, Frontiers only applies the most rigorous and unbiased reviews.
Frontiers revolutionizes research publishing by freely delivering the most outstanding research, evaluated with no bias from both the academic and social point of view. By applying the most advanced information technologies, Frontiers is catapulting scholarly publishing into a new generation.

What are Frontiers Research Topics?

Frontiers Research Topics are very popular trademarks of the Frontiers Journals Series: they are collections of at least ten articles, all centered on a particular subject. With their unique mix of varied contributions from Original Research to Review Articles, Frontiers Research Topics unify the most influential researchers, the latest key findings and historical advances in a hot research area! Find out more on how to host your own Frontiers Research Topic or contribute to one as an author by contacting the Frontiers Editorial Office: frontiersin.org/about/contact

ADVANCED PET, SPECT, MR AND OPTICAL IMAGING IN CLINICAL AND PRE-CLINICAL RESEARCH OF NEUROPSYCHIATRIC DISORDERS

Topic Editors:
Boldizsar Czeh, University of Pécs, Hungary
Zsigmond Tamás Kincses, University of Szeged, Hungary
Szilvia Anett Nagy, University of Pécs, Hungary
Nicola Toschi, University of Rome Tor Vergata, Italy

Citation: Czeh, B., Kincses, Z. T., Nagy, S. A., Toschi, N., eds. (2022). Advanced PET, SPECT, MR and Optical Imaging in Clinical and Pre-Clinical Research of Neuropsychiatric Disorders. Lausanne: Frontiers Media SA.
doi: 10.3389/978-2-88974-339-1

Table of Contents

frontiers in Neurology

ORIGINAL RESEARCH
published: 28 April 2020
doi: 10.3389/fneur.2020.00272

Altered Resting-State Functional Connectivity of Multiple Networks and Disrupted Correlation With Executive Function in Major Depressive Disorder

*Yujie Liu[1,2], Yaoping Chen[1], Xinyu Liang[1], Danian Li[3], Yanting Zheng[1,2], Hanyue Zhang[1], Ying Cui[4], Jingxian Chen[5], Jiarui Liu[6] and Shijun Qiu[2]**

[1] First Clinical Medical College, Guangzhou University of Chinese Medicine, Guangzhou, China, [2] Department of Radiology, The First Affiliated Hospital of Guangzhou University of Chinese Medicine, Guangzhou, China, [3] Cerebropathy Center, The First Affiliated Hospital of Guangzhou University of Chinese Medicine, Guangzhou, China, [4] Cerebropathy Center, The Third Affiliated Hospital of Guangzhou Medical University, Guangzhou, China, [5] Department of Radiology, Shunde Hospital of Southern Medical University, Shunde, China, [6] Department of Radiology, Zhuhai Hospital of Southern Medical University, Zhuhai, China

OPEN ACCESS

Edited by:
Boldizsar Czeh,
University of Pécs, Hungary

Reviewed by:
Feng Liu,
Tianjin Medical University General Hospital, China
Long Jiang Zhang,
Medical School of Nanjing Univeristy, Nanjing, China

***Correspondence:**
Shijun Qiu
qiu-sj@163.com

Specialty section:
This article was submitted to Applied Neuroimaging, a section of the journal Frontiers in Neurology

Received: 14 January 2020
Accepted: 24 March 2020
Published: 28 April 2020

Citation:
Liu Y, Chen Y, Liang X, Li D, Zheng Y, Zhang H, Cui Y, Chen J, Liu J and Qiu S (2020) Altered Resting-State Functional Connectivity of Multiple Networks and Disrupted Correlation With Executive Function in Major Depressive Disorder. Front. Neurol. 11:272. doi: 10.3389/fneur.2020.00272

Background: Major depressive disorder (MDD) is one of the most common and costly psychiatric disorders. In addition to significant changes in mood, MDD patients face an increased risk of developing cognitive dysfunction. It is important to gain an improved understanding of cognitive impairments and find a biomarker for cognitive impairment diagnosis in MDD.

Methods: One hundred MDD patients and 100 normal controls (NCs) completed resting-state fMRI (rs-fMRI) scan, in which 34 MDD patients and 34 NCs had scores in multiple cognitive domains (executive function, verbal fluency, and processing speed). Twenty-seven regions of interest from the default mode network (DMN), central executive network (CEN), salience network (SN), and limbic system (LS) were selected as seeds for functional connectivity (FC) analyses with the voxels in the whole brain. Finally, partial correlations were conducted for cognitive domain scores and FCs with significant differences between the MDD and NC groups.

Results: Significant FC differences between groups were identified among the seeds and clusters in the DMN, CEN, LS, visual network, somatomotor network, ventral attention network, and dorsal attention network. In the MDD patients, the magnitude of the Stroop interference effect was positively correlated with the illness duration, and the illness duration was negatively correlated with the FC between the right ventral hippocampal gyrus and the left inferior frontal gyrus. However, the correlation between the Stroop interference effect and the FC of the right anterior prefrontal cortex with the left cerebellum_4_5 was disrupted in these patients.

Conclusions: The MDD patients have altered FCs among multiple brain networks and a disrupted correlation between the FC of prefrontal cortex and executive function. The disrupted correlation could present before the symptoms develop and may be the core process in the development of executive function impairment.

Keywords: major depressive disorder, functional connectivity, resting state, fMRI, neuropsychological test, executive function

INTRODUCTION

Major depressive disorder (MDD) is one of the most common and costly psychiatric disorders (1). This condition has been ranked as one of the top 10 leading causes of disability among 191 countries (2) and is the second leading cause of disability worldwide, affecting 4.7% of the global population (3). MDD patients suffer significant changes in mood, characterized by sadness along with various other symptoms, such as fatigue, altered appetite, and/or sleep (4). Moreover, cognitive impairments are commonly detected in MDD patients (5–7). In a recent study, cognitive impairments related to MDD were grouped into four cognitive domains: (i) verbal learning and memory, (ii) visuospatial learning and memory, (iii) executive function (EF)/attention, and (iv) psychomotor speed; 8.9–37.5% of MDD patients were impaired in two or more cognitive domains (8). High rates of persisting cognitive impairments were also found in MDD patients that nearly 60% of MDD patients remained cognitively impaired at 6-month follow-up (9). There are data suggesting that proper medical treatment may lead to improved cognitive functioning (10–12), while worse treatment outcomes and higher rates of recurrence are associated with poorer cognition (13). In light of these findings, it is important to gain an improved understanding of cognitive impairments in MDD and find a potential biomarker for cognitive impairment diagnosis in MDD, which could be of great clinical importance in terms of allowing early, accurate diagnosis and reducing the chances of chronic relapse and recurrence (5).

Resting-state functional MRI (rs-fMRI) has been widely used to investigate the neural mechanisms of brain dysfunctions (14) and to explore potential imaging biomarkers in various diseases (e.g., MDD, social anxiety disorder, and Alzheimer's disease) (15–17). By measuring fluctuations in blood-oxygen-level-dependent (BOLD) signals, rs-fMRI can be used to assess brain functional connectivity (FC). Researchers have indicated that cognitive impairments in MDD are related to significant FC changes within and between several brain networks, such as the default mode network (DMN), central executive network (CEN), salience network (SN), and limbic system (LS) (18–23). For example, the fronto-limbic system, a key network for emotional regulation and memory, is potentially linked to cognitive impairment in unmedicated MDD patients (24). The alterations in the large-scale brain FC network in MDD may demonstrate the depressive biases toward internal thoughts at the cost of engaging with the external world, resulting in lapses in cognitive problems (15, 25).

However, limitations exist in the previous studies. First, most studies that used seed-based methods to examine the whole-brain voxel-wise FC alteration in MDD only chose seeds from a single network, but seeds from multiple cognition-related networks would be more helpful in detecting the cognitive impairments. Second, the sample size in the previous studies is relatively small, and the majority of the patients in the study have a treatment history. In this scenario, the medication effect cannot be distinguished from those associated with the disease itself. Therefore, a larger sample composed purely of first-episode and drug-naïve MDD patients may eliminate possible confounding factors such as different episodes and medication use and achieve a more reliable result. In our previous study (26), we applied spectral dynamic causal modeling to estimate the effective connectivity of a large-scale network consisting of 27 ROIs (from the DMN, CEN, SN, and LS) in the 100 MDD patients and 100 NCs, and found that reduced excitatory and increased inhibitory connections coexisted within the DMN, underlying disrupted self-recognition and emotional control in MDD. We also proposed a new dynamic FC-based metric, high-order FC (27), to measure the temporal synchronization of long-range FC dynamics; we found that high-order FC significantly improved MDD diagnostic accuracy compared to conventional FC (28). Since the above studies did not analyze cognitive performance in MDD patients, we will do so in this paper.

In this study, we hypothesized that the FC alterations of four likely involved resting-state networks (DMN, CEN, SN, and LS) were associated with the cognitive impairments in first-episode and drug-naïve MDD patients. We applied a seed-based method to examine the whole-brain voxel-wise FC of 27 predefined seeds from DMN, CEN, SN, and LS based on rs-fMRI data collected from a relatively large sample size, including 100 first-episode and drug-naïve MDD and 100 normal controls (NCs). We also correlated the significantly altered FC with scores on a battery of neuropsychological tests that covered cognitive domains including executive function, verbal fluency, and processing speed in 34 MDD patients and 34 NCs. The results showed that MDD patients possessed altered FCs in multiple brain networks and a disrupted correlation between the FC of prefrontal cortex and executive function. The disrupted correlation could present before the symptoms develop and may be the core process in the development of executive function impairment.

METHODS AND MATERIALS

Participants

A total of 119 first-episode, treatment-naïve MDD patients and 109 NCs from two datasets were used in this study. MDD patients were recruited from the psychological counseling outpatient

clinic of the First Affiliated Hospital of Guangzhou University of Chinese Medicine from August 2015 to June 2018. The diagnosis of treatment-naïve, first-episode depression was made by two attending psychiatrists, each of whom had more than 10 years of experience with the Diagnostic and Statistical Manual of Mental Disorders (DSM)-5 (29); the Structured Clinical Interview for the DSM (SCID) was used to assess whether the diagnostic criteria were met (30). The 17-item Hamilton Depression Rating Scale (HDRS-17) (31) was also used to evaluate the severity of depression (32). Each patient self-reported a rough estimate of illness duration. The other inclusion criteria for MDD patients were as follows: (1) aged between 18 and 55 years old, (2) HDRS-17 score > 17, (3) right-handed native Chinese speaker, and (4) free of any history of neurological illness or any other psychiatric disorder according to the DSM-5. Exclusion criteria included (1) a history of any significant illness, (2) alcohol abuse [a total score ≥ 8 on the Alcohol Use Disorders Identification Test (33)], and (3) contraindications to MRI scans. The NCs were all volunteers who were physically healthy based on their self-reported medical history and mentally healthy according to the Mini-International Neuropsychiatric Interview (MINI) (34) as applied by two psychologists. Besides, the HDRS-17 score of NCs was <7. This study was conducted in accordance with the Declaration of Helsinki. All participants provided written informed consent, and the study was approved by the Ethics Committee of the First Affiliated Hospital of Guangzhou University of Chinese Medicine, Guangzhou, China.

Clinical Assessment and Neuropsychological Testing

Participants in the second dataset (37 MDD patients and 37 NCs) were assessed by a battery of neuropsychological tests that covered cognitive domains including executive function, verbal fluency, and processing speed. The tests were administered by a trained psychometric technician supervised by a clinical neuropsychologist.

First, participants were subjected to a Stroop Color-Word Test (SCWT) (35), as research has consistently found inhibitory control impaired in MDD (36), and we hypothesized that the FC changes were associated with this cognitive impairment. The SCWT included three parts. Two of them represent the "congruous condition" in which participants were required to read out the name of a color written in black (W) and name different color patches (C). Conversely, in the third part, named color-word (CW) condition or incongruent condition, color-words were printed in an inconsistent color ink (i.e., the word "blue" printed in yellow) and participants were required to name the color of the ink instead of reading the word itself. The difficulty in inhibiting reading the word was called the Stroop interference effect (SIE) (35). Speed and accuracy scores were recorded for calculation of the SIE (SIE_time and SIE_accuracy) to evaluate inhibitory control ability (37). The calculation method has been detailed in (38).

Verbal fluency test (VFT) is used to measure the ability to generate words in a limited period of time, either from given semantic categories (as in the semantic VFT) or starting with certain letters (as in the phonemic VFT) (39). In this study, we gave the participants 1 min to name as many words from the category of "animals" or items starting with a certain Chinese word (Fa) as possible. The dependent measure reported was the number of words generated.

Participants were also assessed by the most reported processing speed task, the Symbol Digit Modalities Test (SDMT). The dependent measure was the number of items correctly completed within 90 s.

Statistical analyses were performed using IBM SPSS Statistics version 23.0 (Chicago, IL, USA). Age and education level were compared using two-sample *t*-tests, gender was compared using a chi-squared test, and SCWT (SIE_time and SIE_accuracy), VFT (semantic VFT and phonemic VFT), and SDMT scores between MDD patients and NCs were compared by using linear regression analyses (age, gender, and education level as covariates).

Image Acquisition

All MRI data were acquired using a 3.0-T GE Signa HDxt scanner with an 8-channel head-coil within 3 days of diagnosis. The participants were instructed to close their eyes and refrain from thinking anything in particular. Two radiologists made consensus decisions that all participants were free of visible brain abnormalities or any form of lesions based on thick-slice axial T1- and T2-weighted images as well as T2-weighted fluid-attenuated inversion recovery (T2-FLAIR) images. In order to increase sample size, this study included two image datasets, which were acquired during two different periods but had largely the same parameters, including TR/TE = 2000/30 ms, flip angle = 90°, matrix size = 64 × 64, and slice spacing = 1.0 mm for rs-fMRI and slice thickness = 1 mm, no slice gap, matrix size = 256 × 256, field of view (FOV) = 256 × 256 mm^2 for three-dimensional T1-weighted images (3D-T1WI). The different parameters are as follows. For the first dataset [82 MDD patients and 72 NCs, also used in (28)], the parameters included FOV = 240 × 240 mm^2, slice thickness = 4 mm, slice number = 33, and scanning time = 8′20″ (250 volumes) for rs-fMRI and TR/TE = 10.4/4.3 ms, FA = 15°, and 156 slices for 3D-T1WI. For the second dataset (37 MDD patients and 37 NCs), the parameters included FOV = 220 × 220 mm^2, slice thickness = 3 mm, slice number = 36, scanning time = 6′10″ (185 volumes) for rs-fMRI and TR/TE = 6.9/1.5 ms, FA = 12°, and 188 slices for 3D-T1WI. Compared to the first dataset, the second dataset has a slightly increased spatial resolution for rs-fMRI (we used the same number of volumes for each of the two datasets). The effect of different datasets was removed in the statistical analysis later.

Image Preprocessing

Image preprocessing was performed using SPM12 (www.fil.ion.ucl.ac.uk/spm) and DPARSF version 2.3 (http://rfmri.org/DPARSF). For each rs-fMRI scan, 180 volumes remained for further analyses. The remaining images were corrected for acquisition time intervals between slices and head motion between volumes. Data from 19 MDD patients and 10 NC were discarded because their maximum cumulative head motion exceeded 2 mm in translation or 2° in rotation along any direction, or the mean framewise displacement (FD) exceeded

0.2 mm (40). Next, 3D-T1WI data were coregistered to the rs-fMRI data of the same subject and further segmented using unified segment (http://www.fil.ion.ucl.ac.uk/spm) and registered to the standard Montreal Neurological Institutes (MNI) space using diffeomorphic anatomical registration through exponentiated Lie algebra (DARTEL). The rs-fMRI data were then warped to MNI space according to the generated deformation field and smoothed with a Gaussian kernel of 6 mm full width at half maximum (FWHM). Several nuisance signals, including the Friston-24 head motion parameters and mean signals from cerebrospinal fluid and white matter, were regressed out from the rs-fMRI data. Then, linear detrending and bandpass filtering (0.01–0.08 Hz) were performed to reduce low-frequency drift and high-frequency noise.

FC Analysis

We specified 27 predefined ROIs (see the detailed ROI definition in **Table 1**) from DMN, CEN, SN, and LS based on their vital role in MDD neuropathology (22, 23, 41). The coordinates of the ROIs from the DMN, CEN, and SN were adopted from Raichle (42), and those from the LS were taken from Drysdale et al. (41).

Using DPARSF version 2.3 (http://rfmri.org/DPARSF), we computed Pearson correlation coefficients between the mean time series of each ROI (each ROI was a sphere centering at the above coordinates with a radius of 5 mm) and that of each voxel of the whole brain. Then, a Fisher r-to-z transformation was used to convert the correlation coefficient to z values to improve normality. Finally, we obtained z-FC maps of each individual for further analysis. Next, we used SPM 12 (www.fil.ion.ucl.ac.uk/spm) to perform two-sample t-tests (gender, age, education, and center as covariates) to determine areas with significantly different FCs to the ROIs between MDD patients and NCs. We used $P < 0.001$ for the cluster-forming threshold and implemented a familywise error (FWE) correction approach at the cluster level. All results survived whole-brain cluster correction ($P_{\mathrm{FWE}} < 0.05$).

Correlation Between FC and Clinical Scores

The correlations between significantly different FCs and clinical scores (illness duration, HDRS-17 scores, SIE_time, SIE_accuracy, semantic VFT, phonemic VFT, and SDMT scores) were calculated using partial correlation analysis. $P < 0.05$ after Bonferroni correction was considered significant. Age, gender, and education were included as covariates in the correlation analyses of cognitive scores.

RESULTS

Demographic and Clinical Characteristics

A total of 100 MDD patients (66 females, 34 males; mean age: 29.46 years) and 100 NCs (59 females, 41 males; mean age: 29.59 years) entered the following analysis, where 34 MDD patients (25 females, 9 males; mean age: 29.41 years) and 34 NCs (24 females, 10 males; mean age: 30.09 years) with neuropsychological test scores were included in the correlation analysis. No significant differences in age, gender, and education were found between the 100 MDD patients and the 100 NCs. The demographic and clinical data of 100 MDD patients and 100 NCs are summarized in **Table 2**.

TABLE 1 | Names and MNI coordinates of 27 ROIs from four networks.

	Seed	MNI coordinates (mm)		Seed	MNI coordinates (mm)
Default mode network			**Salience network**		
1	Posterior cingulate cortex/precuneus	0 −52 7	15	Dorsal anterior cingulate cortex	0 21 36
2	Medial prefrontal cortex	−1 54 27	16	L-anterior prefrontal cortex	−35 45 30
3	L-lateral parietal cortex	−46 −66 30	17	R-anterior prefrontal cortex	32 45 30
4	R-lateral parietal cortex	49 −63 33	18	L-insula	−41 3 6
5	L-inferior temporal gyrus	−61 −24 −9	19	R-insula	41 3 6
6	R-inferior temporal gyrus	58 −24 −9	20	L-lateral parietal cortex	−62 −45 30
7	Medial dorsal thalamus	0 −12 9	21	R-lateral parietal cortex	62 −45 30
8	L-posterior cerebellum	−25 −81 −33	**Limbic system**		
9	R-posterior cerebellum	25 −81 −33	22	L-subgenual anterior cingulate cortex	−4 15 −11
Central executive network			23	R-subgenual anterior cingulate cortex	4 15 −11
10	Dorsal medial prefrontal cortex	0 24 46	24	L-amygdala	−19 −2 −21
11	L-anterior prefrontal cortex	−44 45 0	25	R-amygdala	19 −2 −21
12	R-anterior prefrontal cortex	44 45 0	26	L-ventral hippocampus	−27 −15 −18
13	L-superior parietal lobule	−50 −51 45	27	R-ventral hippocampus	27 −15 −18
14	R-superior parietal lobule	50 −51 45			

R, Right; L, left.

TABLE 2 | Demographic and clinical characteristics of participants.

Characteristics	MDD ($N = 100$)	NC ($N = 100$)	t/χ^2	*P*-value
Age (years)	29.46 ± 9.34§	29.59 ± 10.33	−0.09	0.93†
Gender (F/M)	66/34	59/41	1.05	0.31‡
Education (years)	12.46 ± 3.22§	12.88 ± 2.77	−0.09	0.32†
Illness duration (months)	8.64 ± 10.86§	NA	NA	NA
HDRS-17	22.15 ± 3.18§	NA	NA	NA

MDD, major depressive disorder; NC, normal control; HDRS-17, 17-item hamilton depression rating scale.
§*Mean ± standard deviation.*
†*The P-values were obtained through a two-sample t-test.*
‡*The P-value was obtained through a chi-squared test.*

TABLE 3 | Demographic and clinical characteristics of the participants with neuropsychological tests.

Characteristics	MDD ($n = 34$)	NC ($n = 34$)	t/χ^2	*P*-value
Age (years)	29.41 ± 8.27§	30.09 ± 10.88§	−0.29	0.77†
Gender (F/M)	25/9	24/10	0.07	0.787‡
Education (years)	13.00 ± 3.44§	13.68 ± 3.07§	−0.86	0.395†
Illness duration (months)	7.81 ± 8.46§	NA	NA	NA
HDRS-17	21.85 ± 2.25§	NA	NA	NA
SIE_time	1.17 ± 0.37§	1.10 ± 0.32§	−0.95	0.35¶
SIE_accuracy	−0.05 ± 0.06§	−0.03 ± 0.04§	1.57	0.12¶
Semantic VFT	18.15 ± 5.77§	21.47 ± 4.82§	2.44	0.02¶
Phonemic VFT	8.15 ± 4.34§	9.91 ± 3.98§	1.86	0.07¶
SDMT	53.21 ± 12.28§	62.03 ± 14.12§	3.40	0.00¶

MDD, major depressive disorder; NC, normal control; HDRS-17, 17-item hamilton depression rating scale; CTQ, childhood trauma questionnaire; SIE_time, interference effect of time during the Stroop test; SIE_accuracy, interference effect of accuracy during the Stroop test.
§*Mean ± standard deviation (SD).*
†*The P-values were obtained by two-sample t-tests.*
‡*The P-value was obtained by a chi-squared test.*
¶*The P-values were obtained by linear regression analyses. Age, gender, and education level were included as covariates.*

No significant difference was found between the 34 MDD patients and the 34 NCs in terms of age, gender, education, SIE_time, SIE_accuracy or phonemic VFT scores, but the MDD patients had significantly lower semantic VFT and SDMT scores than the NCs ($P < 0.05$). See details in **Table 3**.

MDD-Related FC Alterations

Significant differences were found in the FC of seven ROIs between MDD and NCs. As shown in **Table 4** and **Figure 1**, MDD patients had higher FC than NCs between the following ROI and clusters: (A) the posterior cingulate cortex/precuneus and the right paracentral gyrus, (B) the left inferior temporal gyrus and the right cuneus, (C) the right anterior prefrontal cortex and the left cerebellum_4_5 (part extend to right cerebellum_4_5), (D) the right anterior PFC and the right middle frontal gyrus, (E) the right amygdala and the left inferior frontal gyrus (triangular part), (F) the right amygdala and the left rolandic operculum, (G) the left ventral hippocampus and the right inferior frontal gyrus (opercular part), (H) the left ventral hippocampus and the left inferior frontal gyrus (opercular part), (I) the left ventral hippocampus and the left inferior frontal gyrus (orbital part), (J) the right ventral hippocampus and the right inferior frontal gyrus (opercular part), and (K) the right ventral hippocampus and the left inferior frontal gyrus (opercular part). Additionally, lower FC was also observed between the left posterior cerebellum and the left postcentral gyrus (L).

Correlations Between Altered FC and Clinical Scores

For all 100 MDD patients, FC between the right ventral hippocampus in the LS and the left inferior frontal gyrus in the CEN was negatively correlated with illness duration ($r = -0.25$, $P_{\text{corrected}} = 0.01$). In the 34 MDD patients and 34 NCs with neuropsychological test scores, the SIE_accuracy score was correlated with illness duration in the MDD group ($r = 0.44$, $P_{\text{corrected}} = 0.03$). Although there was no difference in SIE_time or SIE_accuracy scores between the two groups, we still found that the SIE_accuracy score was positively correlated with the FC between the right anterior prefrontal cortex in the CEN and the left cerebellum_4_5 in the visual network ($r = 0.43$, $P_{\text{corrected}} = 0.03$) in the NCs but not the MDD patients (**Figure 2**). In addition, there were significant differences in semantic VFT and SCWT scores between the two groups. However, no correlation was found between FCs and HRDS-17, semantic VFT, phonemic VFT, or SDMT scores.

DISCUSSION

In this study, we analyzed the FC differences of 27 seeds from the DMN, CEN, SN, and LS with the voxels of the whole brain between 100 first-episode, drug-naïve MDD patients and 100 NCs. We also correlated the significantly altered FC with scores on a battery of neuropsychological tests that covered cognitive domains including executive function, verbal fluency, and processing speed in 34 MDD patients and 34 NCs. The result showed that significant FC differences between groups were identified among the seeds and clusters in the DMN, CEN, LS, visual network, somatomotor network, ventral attention network, and dorsal attention network. In the MDD patients, the magnitude of the Stroop interference effect was positively correlated with the illness duration, and the illness duration was negatively correlated with the FC between the right ventral hippocampal gyrus and the left inferior frontal gyrus. However, the correlation between the Stroop interference effect and the FC of the right anterior prefrontal cortex with the left cerebellum_4_5 was disrupted in the MDD patients. Our findings offer a novel insight into the pathophysiological mechanisms of executive function in MDD.

MDD-Related FC Alterations

The DMN, CEN, SN, and LS support emotion regulation and higher cognitive functions in MDD (43). In this study, we observed several discriminative brain regions contributing to MDD-related FC alterations, including the posterior cingulate cortex, left inferior temporal gyrus and left posterior cerebellum in the DMN, the right anterior prefrontal cortex in the CEN,

TABLE 4 | MDD-related FC alterations.

FC number	Seed	Brain region	MNI coordinates (mm)	Cluster size	Peak *T*
MDD > NC	**Default mode network**				
A	Posterior cingulate cortex/precuneus	R-paracentral gyrus	12 −24 69	73	4.94
B	L-inferior temporal gyrus	R-cuneus	21 −69 24	72	4.06
	Central executive network				
C	R-anterior prefrontal gyrus	L-cerebellum_4_5	−3 −45 0	118	4.72
D		R middle frontal gyrus	27 45 33	50	4.35
	Limbic system				
E	R-amygdala	L-inferior frontal gyrus, triangular part	−33 30 18	90	4.80
F		L-rolandic operculum	−45 −3 21	97	4.45
G	L-ventral hippocampus	R-inferior frontal gyrus, opercular part	54 9 21	47	4.45
H		L-inferior frontal gyrus, opercular part	−48 6 24	60	4.31
I		L-inferior frontal gyrus, orbital part	−36 24 −3	44	4.08
J	R-ventral hippocampus	R-inferior frontal gyrus, opercular part	51 6 21	47	4.24
K		L-inferior frontal gyrus, opercular part	−54 9 27	59	3.80
NC > MDD	**Default mode network**				
L	L-posterior cerebellum	L-precentral gyrus	−33 −24 66	54	−4.35

R, right; L, left.

and the right amygdala and bilateral ventral hippocampus in the LS. The DMN provides the neural substrate for depressive rumination and is the network that receives the most attention in clinical MDD imaging research (44, 45). In our study, the results showed that MDD patients had altered FC between the DMN and the somatomotor network—we reported the novel finding of increased FC between the posterior cingulate cortex and the right paracentral gyrus, while decreased FC between the left posterior cerebellum and left precentral gyrus in MDD patients. The posterior cingulate cortex plays a pivotal role in the DMN (46), and from the current body of research, it has been demonstrated to have increased engagement in MDD and predicts disease severity (47, 48). The left posterior cerebellum (crus II) is believed to be coupled with the DMN, showing a possible role in memory and planning processing (49). Also, according to our previous study, crus II may be a promising biomarker for MDD diagnosis (28). The paracentral gyrus and precentral gyrus belong to the somatomotor network. They are not simply motor structures but also involved in more "cognitive" processes, including response inhibition, action sequencing,working memory, speech and language processing (50–52). Previous studies have reported the altered FC between the DMN and somatomotor network. Bessette et al. (53) found that the remitted MDD patients had weaker connectivity between the DMN seed (right hippocampus) and the SMN seed (right paracentral lobule). These altered FCs between the DMN and SMN may reflect ongoing rumination and underlie deficits in cognitive control. Besides, in MDD patients, altered FC was also found between the DMN and the visual network. Our result showed an increased FC between the left inferior temporal gyrus and the right cuneus, suggesting abnormal processing in the DMN and visual network in MDD. This was contradicting to the results of other studies; they found reduced FC between these two networks in MDD patients (45). However, most of these results were contributed by recurrent MDD patients, not by first-episode and drug-naïve patients, which need to be confirmed by more future studies.

Multiple MDD studies have focused on other typically impaired brain networks such as CEN and LS because of their roles in emotion processing, executive functioning and antidepressant action (21). Our results also indicated that the fronto-limbic system has altered in the first-episode and drug-naïve MDD patients. We found increased FC of the right amygdala with the left inferior frontal gyrus and the left rolandic operculum, and increased FC of bilateral ventral hippocampus with the bilateral inferior frontal gyrus. The amygdala and hippocampus are the core regions in the LS and have widespread connections to diverse cortical areas, such as the frontal cortex, which is the region known to constitute the neuroanatomical network of cognitive function (54). In addition, increased FC of CEN with ventral attention network and visual network, and increased FC of LS with dorsal attention network may reflect altered or biased salience monitoring.

Relationship Between Altered FC and Clinical Scores

SCWT is a famous test for measuring the executive function, especially inhibition (55). In the SCWT, the difficulty in inhibiting reading the word in the incongruent condition was called the SIE (35). Traditionally, MDD patients had higher SIE score than the NCs, indicating poor executive function in MDD (36). An event-related fMRI study concluded that higher SIE was correlated with reduced activation in the dorsal anterior cingulate cortex and the left dorsolateral prefrontal cortex (56). In our study, no difference of SIE was found between the MDD patients and the NCs, which is in accordance with the result of Wagner et al. (57), but the correlation between the SIE and the FC of the right anterior prefrontal

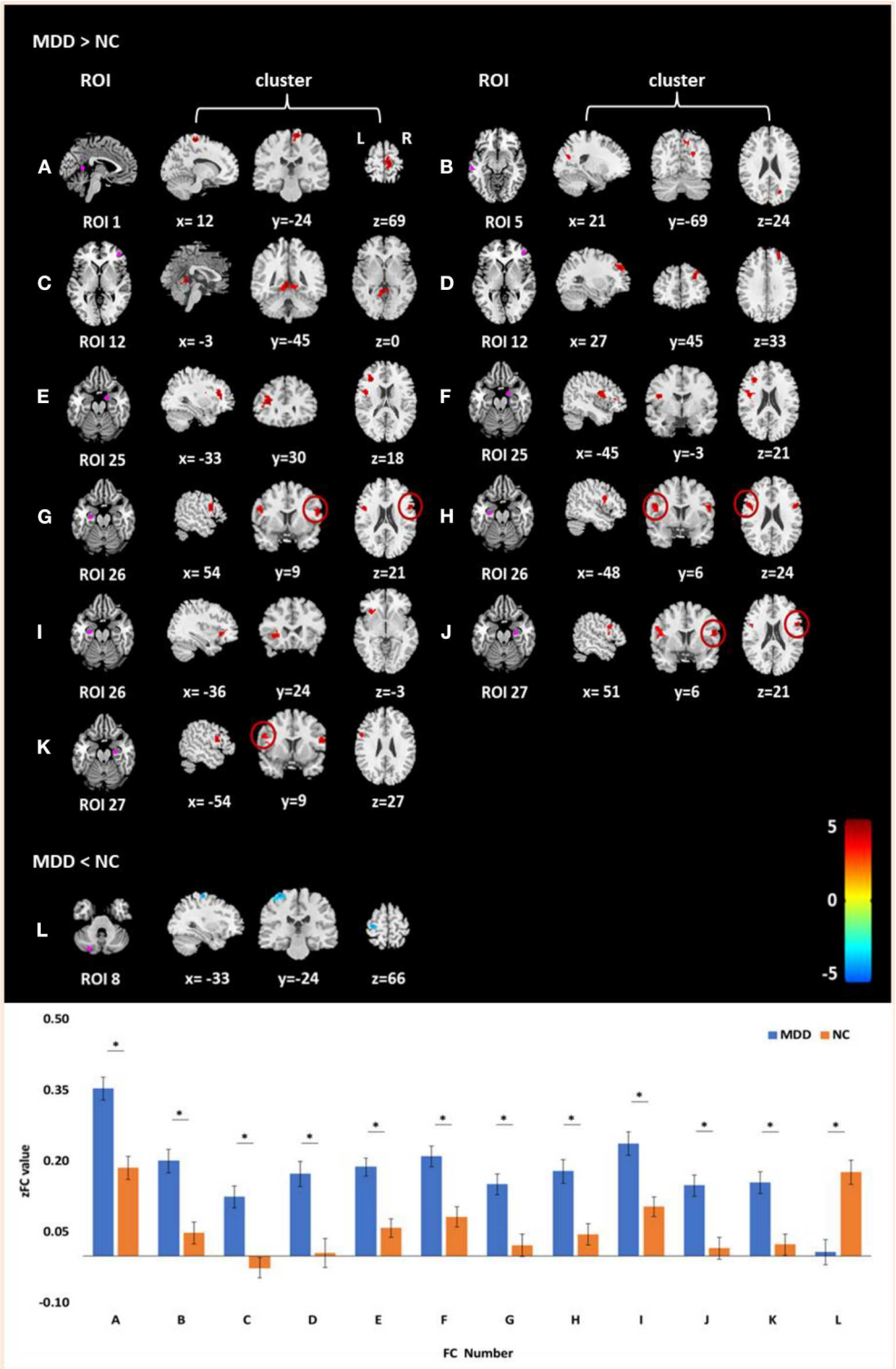

FIGURE 1 | Clusters of between-group differences of FC with age, gender, education level, and center adjusted ($P < 0.05$, FWE corrected). Compared to the NCs, significantly increased FCs in MDD patients were found between **(A)** the posterior cingulate cortex/precuneus and the right paracentral gyrus; **(B)** the left inferior temporal gyrus and the right cuneus; **(C)** the right anterior prefrontal cortex and the left cerebellum_4_5 (part extend to right cerebellum_4_5); **(D)** the right anterior PFC and the right middle frontal gyrus; **(E)** the right amygdala and the left inferior frontal gyrus (triangular part); **(F)** the right amygdala and the left rolandic operculum; **(G)** the left ventral hippocampus and the right inferior frontal gyrus (opercular part); **(H)** the left ventral hippocampus and the left inferior frontal gyrus (opercular part); **(I)**

(Continued)

FIGURE 1 | the left ventral hippocampus and the left inferior frontal gyrus (orbital part); **(J)** the right ventral hippocampus and the right inferior frontal gyrus (opercular part); and **(K)** the right ventral hippocampus and the left inferior frontal gyrus (opercular part). Decreased FC in MDD patients was found between the left posterior cerebellum and the left postcentral gyrus **(L)**. Color scale denotes the *t* values; *x*, *y*, *z*, Montreal Neurological Institutes coordinates; L, left; R, right. The bar graph shows the *z* value of the above FCs (means and SD; * indicates $P < 0.05$, FWE corrected).

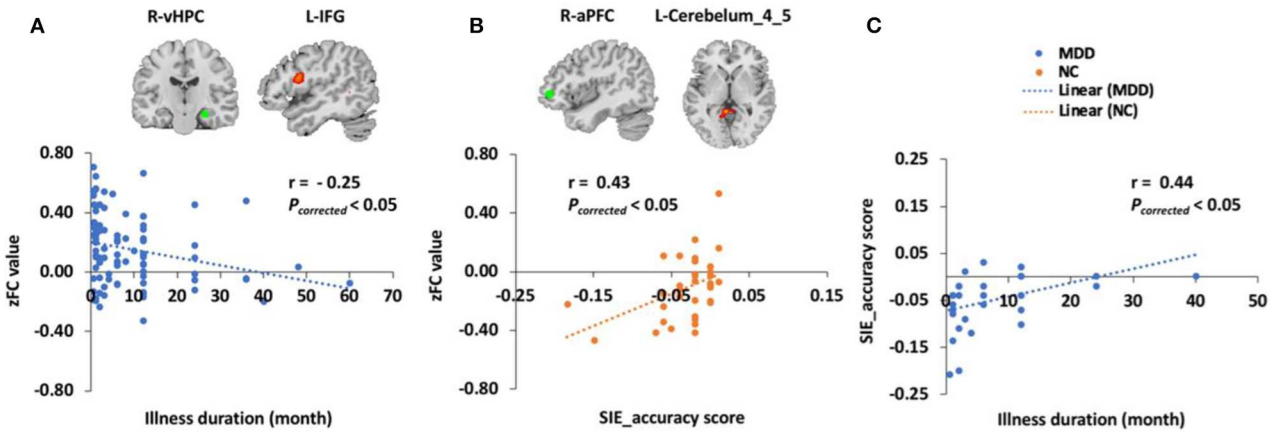

FIGURE 2 | Correlations between altered FC and clinical scores. **(A)** The *z* score of the FC (zFC) between the right ventral hippocampus (R-vHPC) and the left inferior frontal gyrus (L-IFG) was negatively correlated with illness duration ($r = -0.25$, $P_{corrected} < 0.01$) in 100 MDD patients. **(B)** The zFC between the right anterior prefrontal cortex (R-aPFC) and the left cerebellum_4_5 (L-cerebellum_4_5) was positively correlated with the SIE_accuracy score ($r = 0.43$, $P_{corrected} < 0.05$) in the 34 NCs. **(C)** The SIE_accuracy score was correlated with illness duration in the 34 MDD patients ($r = 0.44$, $P_{corrected} < 0.05$).

cortex with the left cerebellum_4_5 (part extend to the right cerebellum_4_5) was disrupted in the patients. The disrupted correlation indicates that the altered FC may present before symptoms develop, suggesting that it is the core process in the development of executive function impairment rather than being produced by the symptoms. In addition, we found that in the MDD patients, the SIE accuracy was related to the illness duration. However, the inconsistency of the above studies highlighted the importance of replicating the results of previous studies (58). Besides, we found that the longer illness duration in MDD was correlated with decreased FC between the right ventral hippocampus and the left inferior frontal gyrus in the MDD patients, supporting the notion that the fronto-limbic system is the key network in MDD (21). Collectively, our observation may indicate that altered FC of seeds in the CEN and LS could be associated with illness duration and executive function impairment via wide-ranging connections to cortical and subcortical brain regions.

In our study, MDD patients produced significantly fewer words than NCs in the semantic VFT but not in the phonemic VFT. Some previous studies indicated that MDD patients had worse performance than NCs in both the semantic and phonemic VFT, but with a significantly larger effect size for semantic fluency (59–61). Our study also showed that the SDMT score was significantly lower in MDD patients than in NCs, indicating a slower processing speed of MDD patients (62–64). We may need other metrics from fMRI to study the above cognitive impairments since no correlation was found between the altered FCs and VFT or SDMT scores in the present study.

Limitations

Our study had some limitations. First, we did not compute the sample size formula before the experiment. Although the sample size of MDD patients in our study was larger than those of most MDD studies, it is still insufficient, especially the number of MDD patients with available cognitive domain scores. The very small sample size will reduce the statistical power and the reproducibility of a study (65). We will do sample size calculation and continue to recruit more MDD patients with cognitive scores in further work. Second, we did not divide the MDD patients into mild, moderate, and severe depression subgroups. As we know, more subgroups of MDD subjects based on the disease severity could lead to more meaningful findings, as the depression severity may also be correlated to a different degree of cognitive impairments. However, in our study, only moderate and severe subgroups could be identified from the patient group. Besides, creating different subgroups will cause small sample size in each subgroup, which could negatively affect the result of our study. We will recruit mild depression patients in further work and separately investigate different subgroups. Besides, we only recruited only first-episode, drug-naïve MDD patients. Selecting this group of MDD patients eliminates possible confounding factors such as illness duration and medication use (66). However, different MDD subtypes could have different neurobiological mechanisms and should be investigated separately in the future (67). Third, we used only one imaging modality, but other modalities also provide valuable diagnostic information and could be used jointly with our protocol in order to improve diagnosis. In addition, conventional FC is commonly used in

fMRI studies, but if we wish to further our understanding of its biological meaning, other advanced methods, such as dynamic FC and high-order FC, should be applied to our future MDD study.

CONCLUSIONS

The MDD patients have altered FCs among multiple brain networks and a disrupted correlation between the FC of prefrontal cortex and executive function. The disrupted correlation could present before the symptoms develop and may be the core process in the development of executive function impairment. This study offers a novel insight into the pathophysiological mechanisms of executive function impairment in MDD.

DATA AVAILABILITY STATEMENT

The datasets generated for this study are available on request to the corresponding author.

ETHICS STATEMENT

The studies involving human participants were reviewed and approved by The First Affiliated Hospital of Guangzhou University of Chinese Medicine. The patients/participants provided their written informed consent to participate in this study.

AUTHOR CONTRIBUTIONS

YL, YCh, XL, and SQ contributed to conception and design of the study. DL, YZ, HZ, YCu, JC, and JL organized the data. YL performed the data analysis and drafted the manuscript. All authors revised the manuscript, and read and approved the submitted version.

ACKNOWLEDGMENTS

YL, YCh, XL, YZ, HZ, and SQ were supported by the National Natural Science Foundation of China—Major International (Regional) Joint Research Project (81920108019), Major Project (91649117), and General Project (81771344, and 81471251), Innovation and Strong School Project of Education Department of Guangdong Province (2014GKXM034), and Science and Technology Plan Project of Guangzhou (2018-1002-SF-0442). YL was also supported by China Scholarship Council (201708440259) and Excellent Doctoral and PhD Thesis Research Papers Project of Guangzhou University of Chinese Medicine (A1-AFD018181A55). DL was supported by Tranditional Chineses Medicine Bureau of Guangdong Province (20202059).

REFERENCES

1. Kessler RC, Berglund P, Demler O, Jin R, Koretz D, Merikangas KR, et al. The epidemiology of major depressive disorder: results from the national comorbidity survey replication (NCS-R). *JAMA.* (2003) 289:3095–105. doi: 10.1001/jama.289.23.3095
2. Disease GBD, Injury I, Prevalence C. Global, regional, and national incidence, prevalence, and years lived with disability for 328 diseases and injuries for 195 countries, 1990-2016: a systematic anCalysis for the global burden of disease study 2016. *Lancet.* (2017) 390:1211–59. doi: 10.1016/S0140-6736(17)32154-2
3. Ferrari AJ, Charlson FJ, Norman RE, Flaxman AD, Patten SB, Vos T, et al. The epidemiological modelling of major depressive disorder: application for the global burden of disease study 2010. (2013) 8:e69637. doi: 10.1371/journal.pone.0069637
4. Kennedy SH. Core symptoms of major depressive disorder: relevance to diagnosis and treatment. *Dialogues Clin Neurosci.* (2008) 10:271–7. Available online at: https://www.dialogues-cns.org/wp-content/uploads/issues/10/DialoguesClinNeurosci-10-271.pdf
5. Gotlib IH, Joormann J. Cognition and depression: current status and future directions. *Ann Rev Clin Psychol.* (2010) 6:285–312. doi: 10.1146/annurev.clinpsy.121208.131305
6. McIntyre RS, Cha DS, Soczynska JK, Woldeyohannes HO, Gallaugher LA, Kudlow P, et al. Cognitive deficits and functional outcomes in major depressive disorder: determinants, substrates, and treatment interventions. *Depress Anxiety.* (2013) 30:515–27. doi: 10.1002/da.22063
7. Roca M, Vives M, Lopez-Navarro E, Garcia-Campayo J, Gili M. Cognitive impairments and depression: a critical review. *Actas Esp Psiquiatr.* (2015) 43:187–93. Available online at: https://www.actaspsiquiatria.es/repositorio/17/97/ENG/17-97-ENG-187-93-556584.pdf
8. Douglas KM, Gallagher P, Robinson LJ, Carter JD, McIntosh VV, Frampton CM, et al. Prevalence of cognitive impairment in major depression and bipolar disorder. *Bipolar Disord.* (2018) 20:260–74. doi: 10.1111/bdi.12602
9. Jaeger J, Berns S, Uzelac S, Davis-Conway S. Neurocognitive deficits and disability in major depressive disorder. *Psychiatry Res.* (2006) 145:39–48. doi: 10.1016/j.psychres.2005.11.011
10. Lee RS, Hermens DF, Porter MA, Redoblado-Hodge MA. A meta-analysis of cognitive deficits in first-episode major depressive disorder. *J Affect Disord.* (2012) 140:113–24. doi: 10.1016/j.jad.2011.10.023
11. Simon SS, Cordas TA, Bottino CM. Cognitive behavioral therapies in older adults with depression and cognitive deficits: a systematic review. *Int J Geriatr Psychiatry.* (2015) 30:223–33. doi: 10.1002/gps.4239
12. Duan Y, Wei J, Geng W, Jiang J, Zhao X, Li T, et al. The effect of short-term use of benzodiazepines on cognitive function of major depressive disorder patients being treated with antidepressants. *J Affect Disord.* (2019) 256:1–7. doi: 10.1016/j.jad.2019.05.059
13. McDermott LM, Ebmeier KP. A meta-analysis of depression severity and cognitive function. *J Affect Disord.* (2009) 119:1–8. doi: 10.1016/j.jad.2009.04.022
14. Lee MH, Smyser CD, Shimony JS. Resting-state fMRI: a review of methods and clinical applications. *AJNR Am J Neuroradiol.* (2013) 34:1866–72. doi: 10.3174/ajnr.A3263
15. Kaiser RH, Andrews-Hanna JR, Wager TD, Pizzagalli DA. Large-Scale network dysfunction in major depressive disorder: a meta-analysis of resting-state functional connectivity. *JAMA Psychiatry.* (2015) 72:603–11. doi: 10.1001/jamapsychiatry.2015.0071
16. Liu F, Guo W, Fouche JP, Wang Y, Wang W, Ding J, et al. Multivariate classification of social anxiety disorder using whole brain functional connectivity. *Brain Struct Funct.* (2015) 220:101–15. doi: 10.1007/s00429-013-0641-4
17. Li HJ, Hou XH, Liu HH, Yue CL, He Y, Zuo XN. Toward systems neuroscience in mild cognitive impairment and Alzheimer's disease: a meta-analysis of 75 fMRI studies. *Hum Brain Mapp.* (2015) 36:1217–32. doi: 10.1002/hbm.22689
18. Albert KM, Potter GG, Boyd BD, Kang H, Taylor WD. Brain network functional connectivity and cognitive performance

in major depressive disorder. *J Psychiatr Res.* (2019) 110:51–6. doi: 10.1016/j.jpsychires.2018.11.020
19. Figueroa CA, Mocking RJT, van Wingen G, Martens S, Ruhe HG, Schene AH. Aberrant default-mode network-hippocampus connectivity after sad memory-recall in remitted-depression. *Soc Cogn Affect Neurosci.* (2017) 12:1803–13. doi: 10.1093/scan/nsx108
20. Yin Y, Hou Z, Wang X, Sui Y, Yuan Y. Association between altered resting-state cortico-cerebellar functional connectivity networks and mood/cognition dysfunction in late-onset depression. *J Neural Transm.* (2015) 122:887–96. doi: 10.1007/s00702-014-1347-3
21. Dutta A, McKie S, Deakin JF. Resting state networks in major depressive disorder. *Psychiatry Res.* (2014) 224:139–51. doi: 10.1016/j.pscychresns.2014.10.003
22. Brakowski J, Spinelli S, Dorig N, Bosch OG, Manoliu A, Holtforth MG, et al. Resting state brain network function in major depression - Depression symptomatology, antidepressant treatment effects, future research. *J Psychiatr Res.* (2017) 92:147–59. doi: 10.1016/j.jpsychires.2017.04.007
23. Culpepper L. Neuroanatomy and physiology of cognition. *J Clin Psychiatry.* (2015) 76:e900. doi: 10.4088/JCP.13086tx3c
24. Clark L, Chamberlain SR, Sahakian BJ. Neurocognitive mechanisms in depression: implications for treatment. *Ann Rev Neurosci.* (2009) 32:57–74. doi: 10.1146/annurev.neuro.31.060407.125618
25. Menon V. Large-scale brain networks and psychopathology: a unifying triple network model. *Trends Cogn Sci.* (2011) 15:483–506. doi: 10.1016/j.tics.2011.08.003
26. Li G, Liu Y, Zheng Y, Li D, Liang X, Chen Y, et al. Large-scale dynamic causal modeling of major depressive disorder based on resting-state functional magnetic resonance imaging. *Hum Brain Mapp.* (2019) 41:865–81. doi: 10.1002/hbm.24845
27. Chen X, Zhang H, Gao Y, Wee CY, Li G, Shen D. High-order resting-state functional connectivity network for MCI classification. *Human Brain Mapp.* (2016) 37:3282–96. doi: 10.1002/hbm.23240
28. Zheng Y, Chen X, Li D, Liu Y, Tan X, Liang Y, et al. Treatment-naive first episode depression classification based on high-order brain functional network. *J Affect Disord.* (2019) 256:33–41. doi: 10.1016/j.jad.2019.05.067
29. Association AP. *Diagnostic and Statistical Manual of Mental Disorders (DSM-5®)*. Arlington, VA: American Psychiatric Pub (2013).
30. Qiu L, Xia M, Cheng B, Yuan L, Kuang W, Bi F, et al. Abnormal dynamic functional connectivity of amygdalar subregions in untreated patients with first-episode major depressive disorder. *J Psychiatry Neurosci.* (2018) 43:262–72. doi: 10.1503/jpn.170112
31. Hamilton M. Development of a rating scale for primary depressive illness. *Br J Soc Clin Psychol.* (1967) 6:278–96. doi: 10.1111/j.2044-8260.1967.tb00530.x
32. Guo W, Liu F, Xiao C, Zhang Z, Liu J, Yu M, et al. Decreased insular connectivity in drug-naive major depressive disorder at rest. *J Affect Disord.* (2015) 179:31–7. doi: 10.1016/j.jad.2015.03.028
33. Saunders JB, Aasland OG, Babor TF, de la Fuente JR, Grant M. Development of the alcohol use disorders identification test (AUDIT): WHO collaborative project on early detection of persons with harmful alcohol consumption–II. *Addiction.* (1993) 88:791–804. doi: 10.1111/j.1360-0443.1993.tb02093.x
34. Sheehan DV, Lecrubier Y, Sheehan KH, Amorim P, Janavs J, Weiller E, et al. The mini-international neuropsychiatric interview (M.I.N.I.): the development and validation of a structured diagnostic psychiatric interview for DSM-IV and ICD-10. *J Clin Psychiatry.* (1998) 59(Suppl. 20):22–33; quiz 4–57.
35. Stroop JR. Studies of interference in serial verbal reactions. *J Exp Psychol.* (1935) 18:643–62. doi: 10.1037/h0054651
36. Snyder HR. Major depressive disorder is associated with broad impairments on neuropsychological measures of executive function: a meta-analysis and review. *Psychol Bull.* (2013) 139:81–132. doi: 10.1037/a0028727
37. Houx PJ, Jolles J, Vreeling FW. Stroop interference: aging effects assessed with the Stroop Color-Word Test. *Exp Aging Res.* (1993) 19:209–24. doi: 10.1080/03610739308253934
38. Golden CJ, Freshwater SM. (2002). *The Stroop Color and Word Test: A Manual for Clinical and Experimental Uses.* Chicago, IL: Stoelting.
39. Troyer AK, Moscovitch M, Winocur GJ. Clustering and switching as two components of verbal fluency: evidence from younger and older healthy adults. *Neuropsychology.* (1997) 11:138–46. doi: 10.1037/0894-4105.11.1.138
40. Jenkinson M, Bannister P, Brady M, Smith S. Improved optimization for the robust and accurate linear registration and motion correction of brain images. *Neuroimage.* (2002) 17:825–41. doi: 10.1006/nimg.2002.1132
41. Drysdale AT, Grosenick L, Downar J, Dunlop K, Mansouri F, Meng Y, et al. Resting-state connectivity biomarkers define neurophysiological subtypes of depression. *Nat Med.* (2017) 23:28–38. doi: 10.1038/nm.4246
42. Raichle ME. The restless brain. *Brain Connect.* (2011) 1:3–12. doi: 10.1089/brain.2011.0019
43. Mulders PC, van Eijndhoven PF, Schene AH, Beckmann CF, Tendolkar I. Resting-state functional connectivity in major depressive disorder: a review. *Neurosci Biobehav Rev.* (2015) 56:330–44. doi: 10.1016/j.neubiorev.2015.07.014
44. Hamilton JP, Farmer M, Fogelman P, Gotlib IH. Depressive rumination, the default-mode network, and the dark matter of clinical neuroscience. *Biol Psychiatry.* (2015) 78:224–30. doi: 10.1016/j.biopsych.2015.02.020
45. Yan CG, Chen X, Li L, Castellanos FX, Bai TJ, Bo QJ, et al. Reduced default mode network functional connectivity in patients with recurrent major depressive disorder. *Proc Natl Acad Sci USA.* (2019) 116:9078–83. doi: 10.1073/pnas.1900390116
46. Fransson P, Marrelec G. The precuneus/posterior cingulate cortex plays a pivotal role in the default mode network: evidence from a partial correlation network analysis. *Neuroimage.* (2008) 42:1178–84. doi: 10.1016/j.neuroimage.2008.05.059
47. Wang L, Hermens DF, Hickie IB, Lagopoulos J. A systematic review of resting-state functional-MRI studies in major depression. *J Affect Disord.* (2012) 142:6–12. doi: 10.1016/j.jad.2012.04.013
48. Sambataro F, Wolf ND, Pennuto M, Vasic N, Wolf RC. Revisiting default mode network function in major depression: evidence for disrupted subsystem connectivity. *Psychol Med.* (2014) 44:2041–51. doi: 10.1017/S0033291713002596
49. Buckner RL, Krienen FM, Castellanos A, Diaz JC, Yeo BT. The organization of the human cerebellum estimated by intrinsic functional connectivity. *J Neurophysiol.* (2011) 106:2322–45. doi: 10.1152/jn.00339.2011
50. Cona G, Semenza C. Supplementary motor area as key structure for domain-general sequence processing: a unified account. *Neurosci Biobehav Rev.* (2017) 72:28–42. doi: 10.1016/j.neubiorev.2016.10.033
51. Hertrich I, Dietrich S, Ackermann H. The role of the supplementary motor area for speech and language processing. *Neurosci Biobehav Rev.* (2016) 68:602–10. doi: 10.1016/j.neubiorev.2016.06.030
52. Welniarz Q, Gallea C, Lamy JC, Meneret A, Popa T, Valabregue R, et al. The supplementary motor area modulates interhemispheric interactions during movement preparation. *Hum Brain Mapp.* (2019) 40:2125–42. doi: 10.1002/hbm.24512
53. Bessette KL, Jenkins LM, Skerrett KA, Gowins JR, DelDonno SR, Zubieta JK, et al. Reliability, convergent validity and time invariance of default mode network deviations in early adult major depressive disorder. *Front Psychiatry.* (2018) 9:244. doi: 10.3389/fpsyt.2018.00244
54. Dolcos F, Wang L, Mather M. Current research and emerging directions in emotion-cognition interactions. *Front Integr Neurosci.* (2014) 8:83. doi: 10.3389/fnint.2014.00083
55. Gohier B, Ferracci L, Surguladze SA, Lawrence E, El Hage W, Kefi MZ, et al. Cognitive inhibition and working memory in unipolar depression. (2009) 116:100–5. doi: 10.1016/j.jad.2008.10.028
56. Holmes AJ, Pizzagalli DA. Response conflict and frontocingulate dysfunction in unmedicated participants with major depression. *Neuropsychologia.* (2008) 46:2904–13. doi: 10.1016/j.neuropsychologia.2008.05.028
57. Wagner G, Sinsel E, Sobanski T, Kohler S, Marinou V, Mentzel HJ, et al. Cortical inefficiency in patients with unipolar depression: an event-related FMRI study with the Stroop task. *Biol Psychiatry.* (2006) 59:958–65. doi: 10.1016/j.biopsych.2005.10.025
58. Muller VI, Cieslik EC, Serbanescu I, Laird AR, Fox PT, Eickhoff SB. Altered brain activity in unipolar depression revisited: meta-analyses of neuroimaging studies. *JAMA Psychiatry.* (2017) 74:47–55. doi: 10.1001/jamapsychiatry.2016.2783
59. Zakzanis KK, Leach L, Kaplan E. On the nature and pattern of neurocognitive function in major depressive disorder. *Neuropsychiatry Neuropsychol Behav Neurol.* (1998) 11:111–9. Available online at: https://psycnet.apa.org/record/1998-12692-001

60. Veiel HO. A preliminary profile of neuropsychological deficits associated with major depression. *J Clin Exp Neuropsychol.* (1997) 19:587–603. doi: 10.1080/01688639708403745
61. Christensen H, Griffiths K, Mackinnon A, Jacomb P. A quantitative review of cognitive deficits in depression and Alzheimer-type dementia. *J Int Neuropsychol Soc.* (1997) 3:631–51. doi: 10.1017/S1355617797006310
62. McIntyre RS, Harrison J, Loft H, Jacobson W, Olsen CK. The effects of vortioxetine on cognitive function in patients with major depressive disorder: a meta-analysis of three randomized controlled trials. *Int J Neuropsychopharmacol.* (2016) 19:pyw055. doi: 10.1093/ijnp/pyw055
63. Baune BT, Brignone M, Larsen KG. A network meta-analysis comparing effects of various antidepressant classes on the digit symbol substitution test (DSST) as a measure of cognitive dysfunction in patients with major depressive disorder. *Int J Neuropsychopharmacol.* (2018) 21:97–107. doi: 10.1093/ijnp/pyx070
64. Shimada H, Park H, Makizako H, Doi T, Lee S, Suzuki T. Depressive symptoms and cognitive performance in older adults. *J Psychiatr Res.* (2014) 57:149–56. doi: 10.1016/j.jpsychires.2014.06.004
65. Chen X, Lu B, Yan CG. Reproducibility of R-fMRI metrics on the impact of different strategies for multiple comparison correction and sample sizes. *Hum Brain Mapp.* (2018) 39:300–18. doi: 10.1002/hbm.23843
66. Brookhart MA, Sturmer T, Glynn RJ, Rassen J, Schneeweiss S. Confounding control in healthcare database research: challenges and potential approaches. *Med Care.* (2010) 48(Suppl. 6):S114–20. doi: 10.1097/MLR.0b013e3181dbebe3
67. Wager TD, Woo CW. Imaging biomarkers and biotypes for depression. *Nat Med.* (2017) 23:16–7. doi: 10.1038/nm.4264

Conflict of Interest: The authors declare that the research was conducted in the absence of any commercial or financial relationships that could be construed as a potential conflict of interest.

frontiers in Neuroscience

ORIGINAL RESEARCH
published: 03 June 2020
doi: 10.3389/fnins.2020.00474

Stress-Induced Microstructural Alterations Correlate With the Cognitive Performance of Rats: A Longitudinal *in vivo* Diffusion Tensor Imaging Study

Szilvia Anett Nagy[1,2,3,4,5†], *Anett Vranesics*[1,6,7†], *Zsófia Varga*[1], *Dávid Csabai*[1], *Nóra Bruszt*[8,9], *Zsolt Kristóf Bali*[8,10], *Gábor Perlaki*[2,3,4], *István Hernádi*[8,9,10,11], *Zoltán Berente*[6,7], *Attila Miseta*[5], *Tamás Dóczi*[2,3,4] *and Boldizsár Czéh*[1,5*]

[1] *Neurobiology of Stress Research Group, Szentágothai Research Centre, University of Pécs, Pécs, Hungary,* [2] *MTA-PTE, Clinical Neuroscience MR Research Group, Pécs, Hungary,* [3] *Department of Neurosurgery, Medical School, University of Pécs, Pécs, Hungary,* [4] *Pécs Diagnostic Centre, Pécs, Hungary,* [5] *Department of Laboratory Medicine, Medical School, University of Pécs, Pécs, Hungary,* [6] *Research Group for Experimental Diagnostic Imaging, Medical School, University of Pécs, Pécs, Hungary,* [7] *Department of Biochemistry and Medical Chemistry, Medical School, University of Pécs, Pécs, Hungary,* [8] *Translational Neuroscience Research Group, Centre for Neuroscience, Szentágothai Research Centre, University of Pécs, Pécs, Hungary,* [9] *Department of Physiology, Medical School, University of Pécs, Pécs, Hungary,* [10] *Grastyán Translational Research Centre, University of Pécs, Pécs, Hungary,* [11] *Department of Experimental Zoology and Neurobiology, Faculty of Sciences, University of Pécs, Pécs, Hungary*

OPEN ACCESS

Edited by:
Jennifer L. Robinson, Auburn University, United States

Reviewed by:
Dong-Hoon Lee, Yonsei University, South Korea
Elisabetta C. del Re, Harvard Medical School, United States

***Correspondence:**
Boldizsár Czéh
czeh.boldizsar@pte.hu

† *These authors have contributed equally to this work*

Specialty section:
This article was submitted to Brain Imaging Methods, a section of the journal Frontiers in Neuroscience

Received: *14 January 2020*
Accepted: *16 April 2020*
Published: *03 June 2020*

Citation:
Nagy SA, Vranesics A, Varga Z, Csabai D, Bruszt N, Bali ZK, Perlaki G, Hernádi I, Berente Z, Miseta A, Dóczi T and Czéh B (2020) Stress-Induced Microstructural Alterations Correlate With the Cognitive Performance of Rats: A Longitudinal in vivo Diffusion Tensor Imaging Study. Front. Neurosci. 14:474. doi: 10.3389/fnins.2020.00474

Background: Stress-induced cellular changes in limbic brain structures contribute to the development of various psychopathologies. *In vivo* detection of these microstructural changes may help us to develop objective biomarkers for psychiatric disorders. Diffusion tensor imaging (DTI) is an advanced neuroimaging technique that enables the non-invasive examination of white matter integrity and provides insights into the microstructure of pathways connecting brain areas.

Objective: Our aim was to examine the temporal dynamics of stress-induced structural changes with repeated *in vivo* DTI scans and correlate them with behavioral alterations.

Methods: Out of 32 young adult male rats, 16 were exposed to daily immobilization stress for 3 weeks. Four DTI measurements were done: one before the stress exposure (*baseline*), two scans during the stress (*acute* and *chronic* phases), and a last one 2 weeks after the end of the stress protocol (*recovery*). We used a 4.7T small-animal MRI system and examined 18 gray and white matter structures calculating the following parameters: fractional anisotropy (FA), mean diffusivity (MD), axial diffusivity (AD), and radial diffusivity (RD). T2-weighted images were used for volumetry. Cognitive performance and anxiety levels of the animals were assessed in the Morris water maze, novel object recognition, open field, and elevated plus maze tests.

Results: Reduced FA and increased MD and RD values were found in the corpus callosum and external capsule of stressed rats. Stress increased RD in the anterior commissure and reduced MD and RD in the amygdala. We observed time-dependent changes in several DTI parameters as the rats matured, but we found no evidence of

stress-induced volumetric alterations in the brains. Stressed rats displayed cognitive impairments and we found numerous correlations between the cognitive performance of the animals and between various DTI metrics of the inferior colliculus, corpus callosum, anterior commissure, and amygdala.

Conclusions: Our data provide further support to the translational value of DTI studies and suggest that chronic stress exposure results in similar white matter microstructural alterations that have been documented in stress-related psychiatric disorders. These DTI findings imply microstructural abnormalities in the brain, which may underlie the cognitive deficits that are often present in stress-related mental disorders.

Keywords: chronic stress, magnetic resonance imaging, DTI, fractional anisotropy, mean diffusivity, radial diffusivity, Morris water maze, novel object recognition test

INTRODUCTION

Stress is an important element of our everyday life as all living organisms need to overcome external and internal challenges to succeed in life. However, when stress is too severe, or when it becomes chronic, then it may lead to the development of various somatic and mental disorders (McEwen, 1998; Kendler et al., 1999; Chandola et al., 2006; Dube et al., 2009; Lanius et al., 2010; Steptoe and Kivimaki, 2012). It is well-documented that chronic stress can induce morphological and functional changes of specific limbic brain areas, and these alterations are believed to contribute to the development of various psychopathologies (Pittenger and Duman, 2008; MacQueen and Frodl, 2011; Popoli et al., 2011). Numerous postmortem histopathological studies have documented that stress can modify the dendritic architecture of pyramidal neurons, inhibits adult hippocampal neurogenesis, and affects glial cells, as well as GABAergic interneurons (Lucassen et al., 2014; McEwen et al., 2015, 2016; Fogaca and Duman, 2019). These neuroanatomical alterations contribute to the disturbed functioning of synaptic contacts (Popoli et al., 2011), which in turn leads to disrupted structural and functional connectivity of neuronal networks and eventually results in impaired emotional and cognitive functioning (de Kloet et al., 1999; Evans and Schamberg, 2009; Kim et al., 2013; Sousa, 2016; Duman et al., 2019).

The rapid methodological developments in magnetic resonance imaging (MRI) allows us to investigate the stress-induced structural changes directly in living organisms. This opportunity inspired numerous research groups to examine the impact of chronic stress on brain activity and morphology in living animals. Henckens and co-workers were the first to carry out a detailed investigation of the consequences of 10 days of repeated immobilization stress on the structural integrity and functional connectivity patterns in the rodent brain, using high-resolution structural MRI, diffusion kurtosis imaging, and resting-state functional MRI (Henckens et al., 2015). They reported that chronic stress exposure can alter large-scale functional connectivity networks by increasing connectivity in the somatosensory, visual, and default mode networks, but it does not induce any major changes in gray matter volumes of the rat brain (Henckens et al., 2015). Later studies, however, found hippocampal atrophy in rats subjected to a 4-weeks chronic unpredictable mild stress paradigm (Li et al., 2017). More recently, a longitudinal neuroimaging study examined the effects of chronic unpredictable stress on the structure and functional connectome of the rat brain in stress-susceptible and stress-resilient animals (Magalhaes et al., 2018). They found stress-induced structural atrophy of several limbic and non-limbic brain areas, which was associated with increased functional connectivity in a network formed by these specific regions (Magalhaes et al., 2018).

Overall, these MRI studies confirm and further extend the earlier histopathological findings documenting disrupted connectivity between key limbic structures that are known to regulate the stress response. Diffusion tensor imaging (DTI) is an MRI-based neuroimaging technique, which enables the examination of white (and gray) matter integrity and provides insights into the microstructure of pathways connecting different brain areas. The typical readouts of DTI studies are mean diffusivity (MD) and fractional anisotropy (FA), which represent the overall diffusion regardless of directionality (i.e., the degree to which tissue organization limits the diffusion of water molecules) and the degree of diffusion anisotropy (i.e., directionality of diffusion related to tract integrity and the alignment of neuronal fibers), respectively. Other DTI-related parameters, such as axial diffusivity (AD) and radial diffusivity (RD), indicate axonal, and myelin microstructural changes. Therefore, developmental alterations (e.g., myelination), fiber organization, as well as structural integrity of the white matter can be detected by DTI (Yoshida et al., 2013). More recently, advanced diffusion-weighted imaging techniques were developed, such as high angular resolution diffusion (including diffusion spectrum and q-ball imaging) and diffusion kurtosis imaging to model diffusion signal more precisely (Tuch, 2004; Wedeen et al., 2005; Jensen and Helpern, 2010). However, these advanced methods typically

Abbreviations: AC, anterior commissure; AD, axial diffusivity; BG, basal ganglia; CC, corpus callosum; DI, discrimination index; DTI, diffusion tensor imaging; EC, external capsule; EPM, elevated plus maze test; FA, fractional anisotropy; HI, habituation index; IC, inferior colliculus; MD, mean diffusivity; MDD, major depressive disorder; MR, magnetic resonance; MRI, magnetic resonance imaging; MWM, Morris water maze; NOR, novel object recognition test; OFT, open field test; RD, radial diffusivity; ROI, regions of interest.

require substantial increase in image acquisition time compared to DTI and therefore cannot be properly applied for *in vivo* animal studies. Consequently, DTI is by far the most commonly used method to characterize the microstructural changes affecting white and gray matter areas.

So far, only a handful of studies have used diffusion MRI to examine structural alterations in the brains of experimental animals exposed to chronic stress, and the outcome of these studies are inconsistent. Delgado y Palacios and co-workers were the first to report on subtle substructural changes in the hippocampus of chronically stressed rats using *in vivo* diffusion kurtosis imaging (Delgado y Palacios et al., 2011). Later, the same research group investigated diffusion properties in the prefrontal cortex, caudate putamen, and amygdala and found that mean kurtosis in the striatum was significantly different between the stress-susceptible and stress-resilient animals (Delgado y Palacios et al., 2014). Parallel to these findings, Vestergaard-Poulsen et al. conducted a high-field (16.4 T) diffusion-weighted MRI in combination with quantitative biophysical modeling of the hippocampal dendritic loss using rats subjected to 3 weeks of restraint stress and found that diffusion-weighted MRI data could sensitively detect regional dendritic loss (Vestergaard-Poulsen et al., 2011). Another research group found significant changes in MD, FA, AD, and RD values in numerous brain areas suggesting demyelination and axonal damage (Hemanth Kumar et al., 2014). Yet, another research group found no evidence for white matter microstructural changes in rats exposed to 10 days of repeated immobilization stress (Henckens et al., 2015). Another study using a tract-based spatial statistics analysis approach reported that stress can increase FA and reduced MD and RD in several white matter bundles of the brain after 2 weeks of repeated inescapable stress (Magalhaes et al., 2017). Others reported increased FA in the hypothalamus and hippocampal CA3 in stress-susceptible mice after 10 days of social defeat stress (Anacker et al., 2016). *Ex-vivo* diffusion MRI and diffusion kurtosis imaging studies documented specific microstructural changes in the hippocampus, amygdala, and several cortical areas of rats exposed to chronic stress (Khan et al., 2016a,b, 2018). These findings have been confirmed by a recent *in vivo* imaging experiment (Liu X. et al., 2018).

To address these discrepancies, we designed an experiment to examine the temporal dynamics of the stress response using repeated DTI measurements of rats subjected to 3 weeks of daily restraint stress. Our hypothesis was that we should observe different microstructural parameters before, during, and after the stress exposure and that the DTI results should be able to differentiate between the *acute* and *chronic* phases of the stress response. We used a chronic stress paradigm, which is known to be stressful for rodents and reliably induce structural changes in the hippocampus and prefrontal cortex including dendritic atrophy of pyramidal cells and reduced neurogenesis in the adult dentate gyrus (Cook and Wellman, 2004; Radley et al., 2004; McLaughlin et al., 2007; Perez-Cruz et al., 2009a,b; Veena et al., 2009). We carried out repeated DTI measurements at four time points: once before the stress, twice during the stress procedures, and a last one after a recovery period of 2 weeks (**Figure 1**). In addition, through behavioral profiling, we extensively assessed the effects of chronic stress on the animals' cognitive capacity and anxiety levels as numerous studies have documented that these behavioral outcomes are influenced by chronic stress exposure (Katz et al., 1981; Baker and Kim, 2002; Bowman et al., 2003; Gouirand and Matuszewich, 2005; Rygula et al., 2005; Bondi et al., 2008). The cognitive performance of the animals was assessed in the Morris water maze and novel object recognition tests and we conducted elevated plus maze and open field tests to assess anxiety levels. Our hypothesis was that stress should influence the behavior and that the DTI results should correlate with the behavioral performance of the animals.

MATERIALS AND METHODS

Ethics

All animal procedures were carried out in accordance with the guidelines of Decree No. 40/2013 (II. 14) of the Hungarian Government and the EU Directive 2010/63/EU. The experiments were approved by the Hungarian Ethical Committee on Animal Research according to the Ethical Codex of Animal Experiments (License No. BA02/2000-12/2015). Throughout the entire experiment, adequate measures were taken to minimize pain, or discomfort for the experimental animals.

Animals

Thirty-two young male Sprague–Dawley rats (Charles River Laboratories, Sulzfeld, Germany) aged 4 weeks (50–80 *g*) upon arrival were group housed in plastic cages (378 × 217 × 180 mm, equipped with feeder and bottle container) under standard animal room conditions (temperature 22–24°C; humidity 45–55%; 12 h light/dark cycle; milled chow and water *ad-libitum*).

Experimental Design

The experimental design and the timeline of the procedures are depicted in **Figure 1**. First, the animals were allowed to habituate to the new housing conditions for 4 weeks. During this habituation period and throughout the entire experiment, all animals were handled daily. After the 4-weeks habituation period, when animals were 8 weeks old young adults, they were randomly selected and divided into two groups: the control group ($n = 16$) contained animals that were left completely undisturbed, while the stress group ($n = 16$) received daily restraint stress for 21 days (**Figure 1A**). MRI measurements were performed at four time points: the first scan was done before the stress procedure (*baseline* measurements), the second scan was carried out 7 days after the beginning of the stress exposure (*acute* stress effect), the 3rd scan was done at the end of the 3-weeks stress protocol (*chronic* stress effect), and the last scan was done 2 weeks after the end of stress procedures (*recovery* period) (**Figure 1B**).

Restraint Stress Procedures

Restraint stress protocol was used since it has been demonstrated that this is stressful for rodents and results in pronounced structural changes in the hippocampus and prefrontal cortex including dendritic atrophy and reduced neurogenesis in the adult dentate gyrus (Cook and Wellman, 2004; Radley et al.,

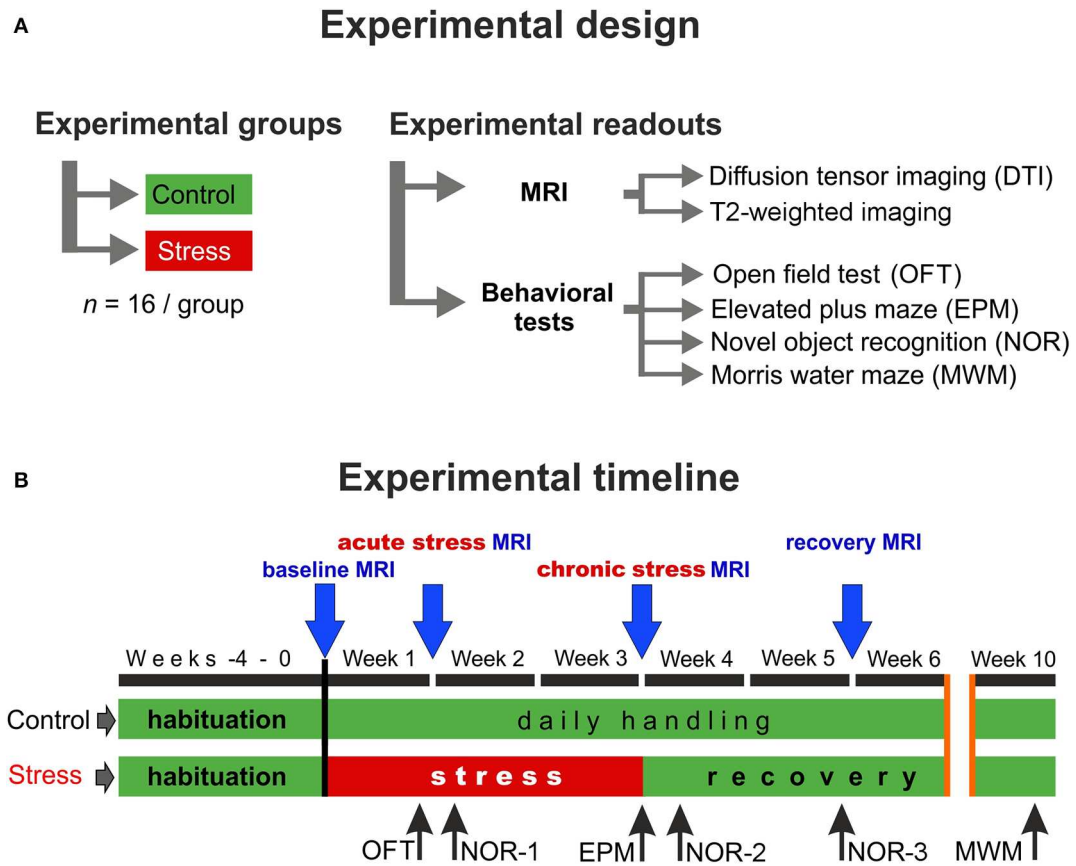

FIGURE 1 | Experimental design and the timeline of the procedures. **(A)** In this study, two groups of young adult male Sprague–Dawley rats were used ($n = 16$ controls and $n = 16$ stressed animals). We did repeated *in vivo* MR imaging and detailed behavioral profiling to assess the effects of chronic stress. **(B)** MRI measurements were performed on four occasions: first before the stress (*baseline*), second during the 1st week of the stress exposure (*acute* stress effect), the third one on the last week of the stress (*chronic* stress effect), and the last one after 2 weeks of recovery period (*recovery* effect). We used various behavioral tests to assess the emotional and cognitive status of the animals. Blue arrows indicate the timing of MRI scans and the black arrows specify the behavioral tests.

2004; McLaughlin et al., 2007; Perez-Cruz et al., 2009a,b; Veena et al., 2009). During the restraint stress protocol, the animals were immobilized daily for 6 h, between 07:00 a.m. and 1:00 p.m. using well-ventilated acrylic tubes (Harvard Apparatus, USA) in accordance with our previous protocol (Perez-Cruz et al., 2009a,b). Control rats were kept in a different room and were not subjected to any kind of stress except daily handling.

In vivo MRI

All acquisitions were performed using a 4.7T small-animal MRI system running Paravision 6.0.1 (Pharmascan 47/16 US; Bruker BioSpin MRI GmbH, Ettlingen, Germany) with a gradient strength of 380 mT/m and a slew rate of 3,420 T/m/s, a circularly polarized hydrogen transmit only volume coil (outer/inner diameter = 89/72 mm), and a circularly polarized hydrogen receive only surface coil anatomically shaped for rat brain. MRI measurements were performed under inhalation anesthesia using 1.8–2.5% (3% for induction) isoflurane (Forane; Abbvie, Budapest) in 1:2 mixture of O_2/N_2O, administered via a nosecone. Each rat was placed in prone position on a heated water pad to maintain rectal temperature at ∼37°C, while a head holder with ear and bite bars were used to prevent head motion. Respiration was monitored using a pressure sensor placed below the abdomen (SA Instruments, Inc., Stony Brook, NY, USA) and was stable at the range of 50–60 breaths/min under anesthesia.

After a gradient-echo localizer scan in three directions, the imaging protocol included fat-suppressed T2-weighted two dimensional fast-spin echo imaging (2D RARE) in axial, sagittal and coronal planes. Axial T2-weighted images were used for volumetric purposes with the following parameters: TR = 2,429 ms; TE = 36 ms; echo spacing = 12 ms; echo train length = 8; field of view (FOV) = 35 × 35 mm^2; matrix = 256 × 256; slice thickness = 0.7 mm; interslice gap = 0.3 mm.

In order to optimize B0 field homogeneity, DTI was performed after field map-based shimming using Bruker MAPSHIM protocol. Fat-suppressed DTI data were obtained using a four-shot segmented spin-echo echo planar imaging sequence with 30 diffusion gradient directions sampled on a half sphere (TR = 2,000 ms; TE = 31.35 ms; *b*-value = 1,000 s/mm^2, five reference images with no diffusion gradients applied; diffusion gradient's duration and separation = 4.3 and 10.5 ms, respectively, number of averages = 2; 15 axial slices; FOV = 30 ×

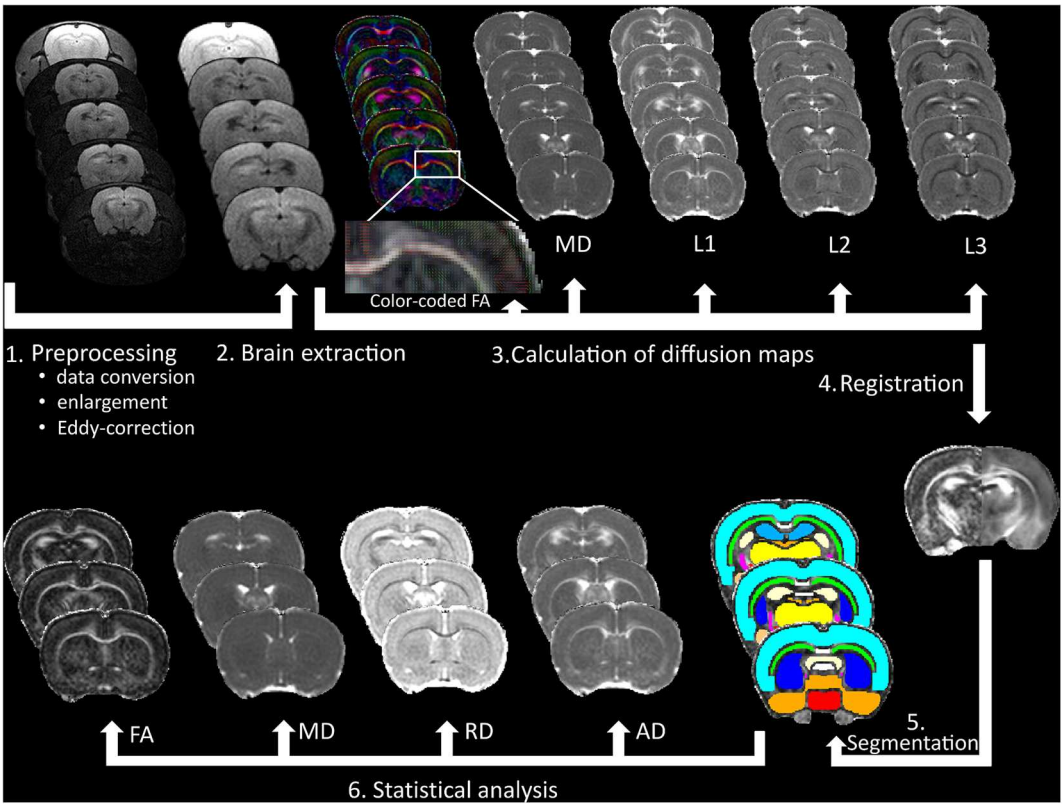

FIGURE 2 | Data processing of the DTI measurements. After pre-processing of the raw data, (1) brain extraction was made to calculate fractional anisotropy (FA), mean diffusivity (MD), first (L1), second (L2), and third (L3) eigenvalues and (2) to improve registration accuracy to a rat brain atlas (3), which was used for gray and white matter segmentation (4–5). Finally, FA, MD, radial diffusivity (RD), and axial diffusivity (AD) were calculated, and statistical analyses were made in 18 bilateral brain areas (6).

30 mm^2; matrix = 240 × 240; slice thickness = 1 mm; interslice gap = 0.2 mm).

Data Analysis of the MR Imaging

Preprocessing

After careful inspection of the acquired MR data, a few animals had to be excluded due to considerable motion artifacts. In total, 27 rats (n = 13 stressed and n = 14 controls) were used for diffusion analysis and 26 animals (n = 12 stressed and n = 14 controls) were involved in MR volumetry.

In order to analyze volumetric and diffusion-related alterations, MRI data were first converted from Bruker format to NIfTI using a Python script. The voxel size of the images was scaled up individually by the factor of 10 to better approximate human dimensions. Then, to improve image registration and segmentation, Brain Extraction Tool provided by FMRIB Software Library (FSL) was applied on the raw MRI data to eliminate non-brain tissues including skull, skin, fat, muscles, and other surrounding tissues (Smith, 2002). Here, the fractional intensity threshold was set to 0.65 and the coordinates (in voxels) for center of initial brain surface sphere were individually chosen to further improve brain extraction. Skull stripping errors were manually corrected when it was necessary by FSLview.

The CUDA implementation of FSL eddy (eddy_cuda7.0) was used to correct diffusion data for susceptibility-induced distortions, eddy currents, and subject motion, and to perform positive and negative outlier detection and replacement for slices with average intensity at least two standard deviations lower than expected (Andersson and Sotiropoulos, 2016; Andersson et al., 2016). Using FMRIB's diffusion toolbox (FDT v3.0, https://fsl.fmrib.ox.ac.uk/fsl/fslwiki/FDT), DTIFIT was applied to fit a single tensor model at each voxel of the preprocessed diffusion-weighted data and to calculate maps of FA, MD, eigenvalues ($L_{1,2,3}$), and eigenvectors ($V_{1,2,3}$).

Diffusion Analysis

To evaluate diffusion alterations, 18 gray and white matter structures were segmented based on a brain-extracted three-dimensional DTI rat brain atlas (Rumple et al., 2013) using the following steps:

(1) Brain-extracted FA image was registered to atlas space (seven degrees-of-freedom linear fit) using FMRIB's Linear Image Registration Tool (Jenkinson and Smith, 2001) and sinc interpolation.
(2) The inverse of the spatial transformation from diffusion space to atlas space was applied to align the 18 brain

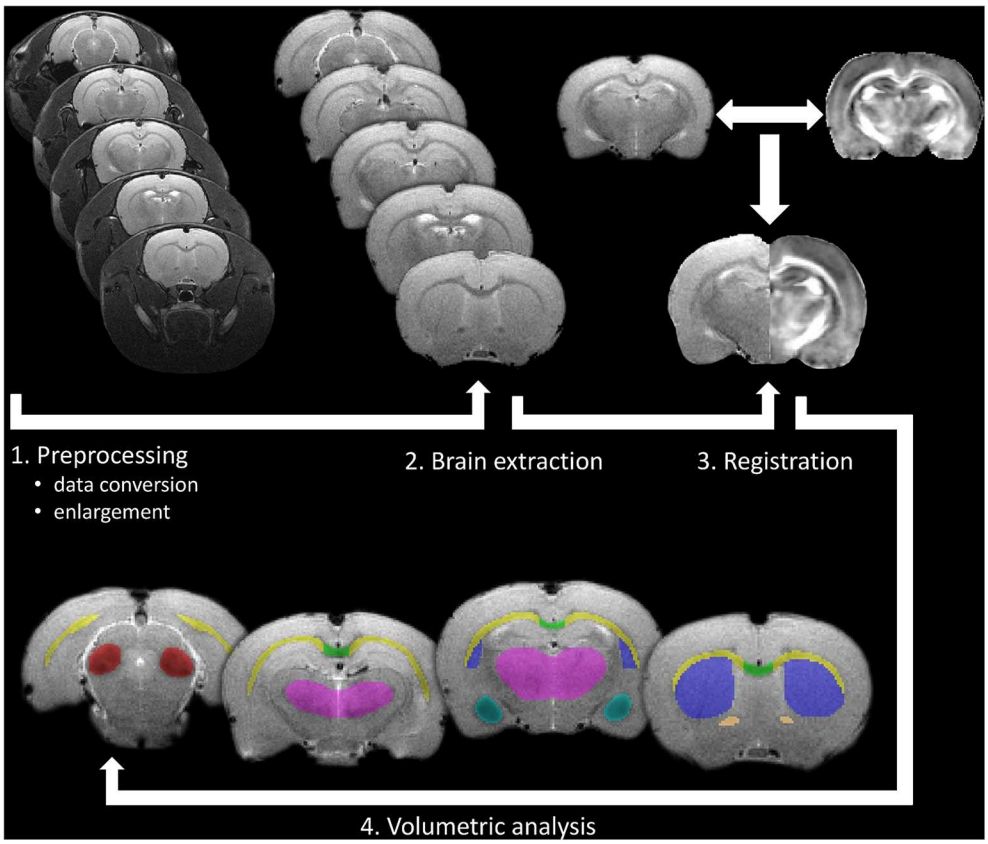

FIGURE 3 | Processing pipeline of the *in vivo* volumetric analysis. After pre-processing of the raw data as a first step, brain extraction was made to improve registration accuracy to a rat brain atlas (2 and 3), which was used for gray and white matter segmentation. Finally, volumetric analysis was performed on manually corrected brain areas using FSLstats (4).

masks to native diffusion space, where diffusion analyses were performed.

The native space masks were eroded using a 2D kernel of 3 × 3 × 1 voxels to avoid partial volume effects and to minimize possible impacts of misregistration. All segmentation outputs were visually inspected and corrected manually if necessary. Besides FA and MD, RD and AD were also calculated (using eigenvalues) and statistical analyses were performed for the following bilateral eroded gray and white matter regions of interest (ROIs): hippocampus, amygdala, neocortex, corpus callosum, corpus callosum genu, anterior commissure, external and internal capsule, inferior colliculus, fornix, fimbria, substantia nigra, hypothalamus, basal ganglia, thalamus, and central gray. We also included the rest of forebrain and midbrain as ROIs. Major steps of diffusion data processing are depicted in **Figure 2**.

MR Volumetry

Volumetric analysis was performed in gray and white matter structures, where diffusion abnormalities were found (amygdala, corpus callosum, anterior commissure, external capsule, inferior colliculus, basal ganglia, and thalamus). For MR volumetry, T2-weighted images were spatially registered into a rat brain DTI atlas (Rumple et al., 2013) space using seven degrees-of-freedom linear image registration. Then, the inverse of the transformation from T2 space to atlas space was applied to align the segmented brain masks to T2 space, where volumetric analyses were performed. After that, all segmentation outputs were visually inspected and corrected manually if necessary and the volume of each segmented brain area was calculated by FSLstats, a part of the FSL. Details of MR volumetry can be seen in **Figure 3**.

Behavioral Assessment

Open Field Test

Locomotor activity was measured using the open field test (OFT) in the *acute* phase of the stress protocol (Week 1, see **Figure 1**). The OFT arena was a black-colored plywood box with a size of 57.5 × 57.5 cm (length × width) surrounded by 39.5 cm high walls. The floor of the arena was divided with light gray painted lines to four by four equal squares. The four squares in the middle of the arena, which were not bordered by walls, were considered together as the center area of the arena. The rats were allowed to explore the OFT arena for 5 min. After each session, the box was thoroughly cleaned using 20 v/v% ethanol. The sessions were recorded using a high-speed video camera

(JVC super LoLux, JVC KENWOOD, Yokohama, Japan), and Ethovision XT10 software (Noldus, Wageningen, Netherlands). During the sessions, the number of line crossings and center area entries of the rats were registered.

Novel Object Recognition Test

Recognition memory performance of the animals was tested in the novel object recognition test (NOR) in three occasions: once during the stress procedures and twice during the *recovery* period (**Figure 1**). The same apparatus (box) was used in the NOR test as in the OFT with the same video tracking system. The NOR test consisted of two trials. In the 1st trial (acquisition), two identical objects were put in the arena, and the rats were allowed to explore them for 3 min. After either 30 min or 3 h retention time, a 2nd trial (recognition) was run with one object kept from the 1st trial (familiar object) and a novel object was introduced, which had never been seen by the animal before. Observation behavior of the animals in the second trial was recorded for 3 min. During the retention period, rats were not transferred back to the animal house but were kept in normal home cages in a dark room located next to the testing room. In both trials, time spent with the exploration of one and the other object was recorded. The animal was considered to explore a given object, when he sniffed the object or put his nose close to it while facing the object.

Three different object pairs were used. The object pairs were distributed randomly between animals and experimental sessions in a counterbalanced latin-square design. In the *acute* stress phase and shortly after the end of the stress protocol (Week 2 and 4, respectively, see **Figure 1**), the NOR test was run with 30 min retention time between the two trials, while in the stress *recovery* phase (Week 5), 3 h retention time was used.

In the 1st and the 2nd trials of each NOR test session, overall exploratory activity ($SumE_1$ and $SumE_2$, respectively) was measured by summing the exploration times for the two objects. In the 2nd trial, the time spent with the exploration of the novel (E_n) and the familiar (E_f) objects were compared by calculating a discrimination index (*DI*) using the following equation: $DI = (E_n - E_f)/(E_n + E_f)$. The DI was a positive number if the novel object was observed longer, while the DI was negative if the familiar object was observed longer, and the DI was around zero if the two objects were observed for an equally long time. Furthermore, a habituation index (HI) was also calculated using the following equation: $HI = (SumE_1/2) - (E_f^* SumE_1/SumE_2)$. The habituation index indicated the extent of decrease in the interest toward the familiar object in the 2nd trial of the NOR test. Only those rats were included in the statistical analysis, who observed both objects and observed them together for at least 5 s in the 2nd trial.

Elevated Plus Maze Test

Anxiety-like behavior was tested in the conventional elevated plus maze test (EPM) on the last day of the stress protocol (Week 3, see **Figure 1**). The EPM apparatus consisted of a central square (11.5 × 11.5 cm) and of four orthogonally situated and equally long arms (45 cm long and 11.5 cm wide) forming a symmetrical plus shape. Two arms had no walls (open arms) and two were enclosed by walls 37 cm in height. The maze stood on an about 100 cm high stand. Rats were placed in the center of the plus maze (i.e., where the four arms met), and they were allowed to explore the maze for 5 min. Time spent in the open arms was recorded during the experiments to assess anxiety-like behavior of the rats.

Morris Water Maze Test

Short- and long-term spatial memory of the rats was tested in the Morris water maze apparatus (MWM) 7 weeks after the end of the stress protocol (Week 10 on **Figure 1**). For the MWM test, we used a blue, circular pool, 180 cm in diameter and 90 cm in height (Ugo Basile, Gemonio, Italy). Four points around the circumference of the pool were designated as North, South, East, and West. On this basis, the area of the pool was divided into four virtual quadrants (NW, SW, SE, and NE). The maze was filled with room-temperature tap water up to the height of 30 cm, and the water was made opaque by mixing 200 g of milk powder and 30 ml of blue food coloring (E131) in it. The rats were trained in the MWM for four consecutive days with one training session per day and four trials per session for each animal on each day. On each trial, a hidden platform was placed in the center of one of the pool quadrants. In each trial, rats were put in the water and were allowed to search for the hidden platform for 120 s. The swimming time elapsed until finding the platform (i.e., sitting on it) was measured as escape latency. If the platform was not found, rats were transferred to the platform and the cutoff time (120 s) was recorded as escape latency. Platform locations were randomly and equally assigned to rats and remained the same for a given rat in every trial on the same day. The quadrant from where the animal started swimming was changed clockwise in the four consecutive trials on a given day. Experiments were recorded using a Basler GenI acA1300 GigE camera (Basler AG, Ahrensburg, Germany). Data were processed onto a computer, where Ethovision X10 software (Noldus, Wageningen, Netherlands) was used for video image recording and data analysis. Short-term learning curves were established by analyzing changes in escape latency from trial to trial on the 1st day of training. Furthermore, escape latency in individual trials were averaged day by day (DayAVG), and long-term learning curves were established by analyzing changes in average escape latency from day to day in the 4-days-long training course.

Statistical Analysis

Data analyses were performed using IBM SPSS Statistics for Windows, Version 23.0 (IBM Corp., Armonk, NY, USA).

Before using statistical tests, the homogeneity of variance was inspected by Levene's test, while the normality of data was assessed by Shapiro–Wilk statistics. Welch's correction was applied for data demonstrating unequal variances. Prior to the analysis of variance, the data were tested for normality, outliers, and sphericity to ensure the assumptions of repeated measures test. The assumptions of mixed design ANOVA were satisfied, as judged by testing for normality, outliers, homogeneity of variances, and sphericity.

One-way repeated measures ANOVA was performed for each group and structure separately to compare changes in diffusion and volumetric metrics among the time points.

A mixed design ANOVA was used to determine whether any change in MRI metrics is the result of the interaction between the type of group (control vs. stressed) and time. Short-term and long-term learning curves of control and stressed animals were also compared using a mixed design ANOVA, where main effects of TRAINING trials/days (repeated measures) and STRESS (between-subject) and TRAINING × STRESS interaction were tested.

Differences between stressed and control groups were assessed in each time point with independent samples *t*-test (MRI metrics, EPM, DI, and HI in the NOR) or Mann–Whitney *U*-test (OFT). In the NOR test, normal recognition memory performance of a rat was assessed by comparing the difference between the time spent with the novel and with the familiar object using paired *t*-test.

Finally, within-group correlations between MRI metrics and behavioral data were measured separately in the control and the stressed groups using Pearson's or Kendall's tests depending on the normality of the data. Behavioral data were analyzed in pairs with the corresponding (time-matched) MRI data. Thus, results of OFT and NOR-1 experiments were compared with the *acute* phase MRI data, results of EPM and NOR-2 experiments were compared with the *chronic* phase MRI data, and results of NOR-3 and MWM experiments were compared with the *recovery* phase MRI data.

Bonferroni correction was applied for one-way repeated measures and mixed design ANOVA to adjust for multiple comparisons. For one-way repeated measures ANOVA, a level of $p < 0.002$ ($p' = 0.05/18 \approx 0.002$) was defined significant in case of DTI metrics, while it was set $p < 0.007$ ($p' = 0.05/7 \approx 0.007$) in MR volumetry. Otherwise, results were considered significant at $p \leq 0.05$.

RESULTS

Stress-Induced Changes in White Matter Structures

As expected, the most pronounced stress-induced changes were observed in the white matter. Our MRI measurements revealed that stress significantly altered diffusion properties of the following white matter structures: corpus callosum (CC), external capsule (EC), and anterior commissure (AC).

Corpus Callosum

In control animals, the FA values significantly increased over time as the animals matured [$F_{(3, 36)} = 11.897$, $p = 0.000015$], but this developmental change was hindered in the stressed rats [$F_{(3, 36)} = 4.331$, $p = 0.010$] (**Figure 4A**). MD values decreased significantly over time in controls [$F_{(3, 39)} = 9.866$, $p = 0.000057$], and again this progressive change was not significant in the stressed group [$F_{(3, 36)} = 5.062$, $p = 0.005$] (**Figure 4B**). RD showed a remarkable decrease over time in both the control [$F_{(3, 39)} = 18.126$, $p < 0.0000001$] and stressed animals [$F_{(3, 36)} = 7.181$, $p = 0.000672$] (**Figure 4C**), while none of the groups showed time-related AD change. Significant between-group differences were found in FA [$F_{(1, 24)} = 4.584$, $p = 0.043$], MD [$F_{(1, 25)} = 8.382$, $p = 0.008$], and RD values [$F_{(1, 25)} = 8.555$, $p = 0.007$] without any group × time interaction. In the *chronic* stress period, FA values were significantly lower in stressed rats, but no differences were found in the *baseline*, *acute*, or *recovery* phases (**Table 1** and **Figure 4A**). In the *recovery* period, the MD and RD values were significantly higher in the stressed rats (**Table 1** and **Figures 4B,C**). The volume of CC did not show any change (**Table 1**).

External Capsule

FA values increased significantly in a time-dependent manner both in control [$F_{(3, 39)} = 13.871$, $p = 0.000003$] and stressed [$F_{(3, 36)} = 8.831$, $p = 0.000161$] rats, without a significant group × time interaction, while MD was decreased rapidly in control subjects only [$F_{(3, 39} = 10.368$, $p = 0.000038$] (**Figures 4D,E**). Here, the between-group difference was significant for FA [$F_{(1, 25)} = 5.109$, $p = 0.033$], but not for MD [$F_{(1, 25)} = 2.999$, $p = 0.096$]. In the *recovery* period, FA was significantly lower, and mean MD was higher in stressed rats (**Table 1** and **Figures 4D,E**). RD showed remarkable decrease over time both in control [$F_{(3, 39)} = 30.157$, $p < 0.0000001$] and in stressed animals [$F_{(3, 36)} = 9.261$, $p = 0.000113$] and we found a significant between-group difference [$F_{(1, 25)} = 9.127$, $p = 0.006$] and a group × time interaction [$F_{(3, 75)} = 2.996$, $p = 0.036$] (**Figure 4F**). In the *chronic* stress period and in the *recovery* phase, RD was significantly higher in stressed rats compared to controls (**Table 1** and **Figure 4F**). The volume of the EC increased significantly as the animals matured both in control [$F_{(3, 39)} = 11.405$, $p = 0.000017$] and in stressed [$F_{(3, 33)} = 15.108$, $p = 0.000002$] rats, and there was also a between-group difference [$F_{(1, 24)} = 5.477$, $p = 0.028$] without group × time interaction probably due to the initial difference in the *baseline* measurements ($p = 0.032$). This difference remained constant over the time (**Table 1**).

Anterior Commissure

AD was significantly increased in the stressed rats [$F_{(3, 33)} = 12.085$, $p = 0.000017$] (**Figure 4G**), but remained constant in the control group. We found a group × time interaction [$F_{(3, 69)} = 3.396$, $p = 0.023$] without a between-group difference. In the *baseline* period, AD was significantly higher in control rats compared to stressed animals, which most likely contributed to the group × time interaction (**Table 1** and **Figure 4G**). RD significantly decreased in controls [$F_{(3, 39)} = 13.655$, $p = 0.000003$], but not in stressed rats (**Figure 4H**) and we found a significant between-group difference [$F_{(1, 25)} = 4.800$, $p = 0.038$] as well. In the *chronic* phase, the RD was significantly higher in stressed rats, while no differences were found in the *baseline*, *acute*, or *recovery* phases (**Table 1** and **Figure 4H**). The volume of AC did not change.

Stress-Induced Changes in Gray Matter Structures

We could observe stress-induced microstructural alterations in a few gray matter areas as follows: amygdala, inferior colliculus (IC), thalamus, and the basal ganglia (BG).

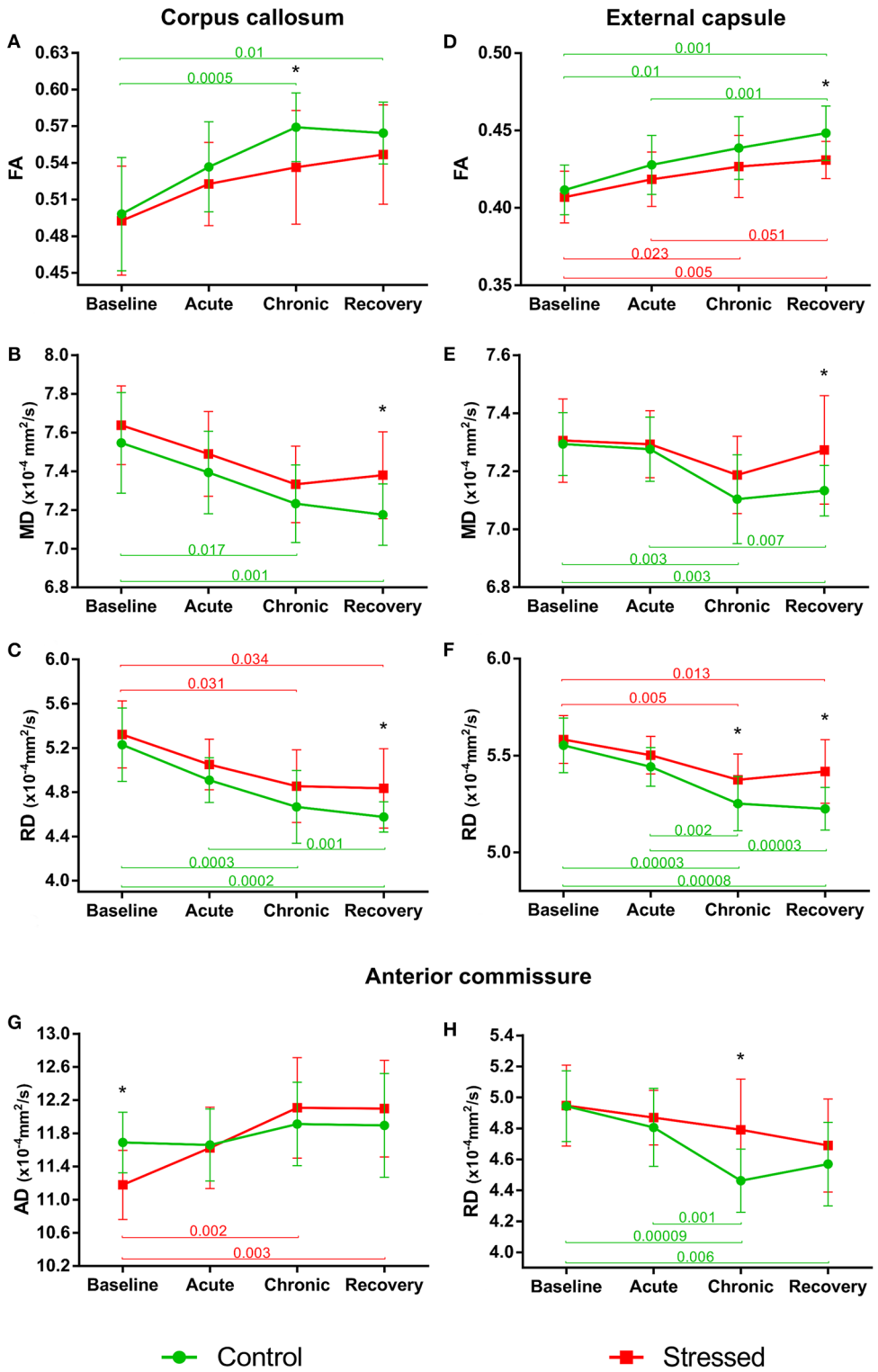

FIGURE 4 | Stress-induced changes of DTI metrics in white matter structures. Longitudinal within- and between-group differences of DTI metrics in the corpus callosum **(A–C)**, external capsule **(D–F)**, and anterior commissure **(G,H)**. Note that most values changed significantly over time as the animals matured. Data are means ± *SD*. Asterisks indicate significant differences between the control and stress groups at the given time point. FA, Fractional anisotropy; MD, Mean diffusivity; RD, Radial diffusivity; AD, Axial diffusivity.

TABLE 1 | Diffusion and volumetric data of white matter structures with between group differences at different time points.

MRI metrics	Brain structure	Group (*n*)	Baseline	*p*-value	Acute stress	*p*-value	Chronic stress	*p*-value	Recovery	*p*-value
FA	CC	Control (13)	0.50 ± 0.05	ns	0.54 ± 0.04	ns	0.57 ± 0.03	0.04[c]	0.56 ± 0.03	ns
		Stress (13)	0.50 ± 0.04		0.52 ± 0.03		0.54 ± 0.05		0.55 ± 0.04	
	EC	Control (14)	0.41 ± 0.02	ns	0.43 ± 0.02	ns	0.44 ± 0.02	ns	0.45 ± 0.02	0.007
		Stress (13)	0.41 ± 0.02		0.42 ± 0.02		0.43 ± 0.02		0.43 ± 0.01	
	AC	Control (14)	0.49 ± 0.03	ns	0.51 ± 0.03	ns	0.55 ± 0.03	ns	0.53 ± 0.03	ns
		Stress (13)	0.48 ± 0.03		0.50 ± 0.03		0.52 ± 0.04		0.53 ± 0.03	
MD[a]	CC	Control (14)	7.55 ± 0.26	ns	7.39 ± 0.21	ns	7.23 ± 0.20	ns	7.18 ± 0.16	0.011
		Stress (13)	7.64 ± 0.20		7.49 ± 0.22		7.33 ± 0.20		7.38 ± 0.22	
	EC	Control (14)	7.29 ± 0.11	ns	7.28 ± 0.11	ns	7.10 ± 0.15	ns	7.13 ± 0.09	0.024[d]
		Stress (13)	7.31 ± 0.14		7.29 ± 0.12		7.19 ± 0.13		7.27 ± 0.19	
	AC	Control (14)	7.16 ± 0.21	ns	7.11 ± 0.22	ns	6.97 ± 0.18	ns	7.02 ± 0.30	ns
		Stress (10)	7.03 ± 0.24		7.09 ± 0.17		7.08 ± 0.08		7.19 ± 0.31	
AD[a]	CC	Control (14)	12.18 ± 0.72	ns	12.36 ± 0.72	ns	12.36 ± 0.54	ns	12.38 ± 0.50	ns
		Stress (13)	12.27 ± 0.74		12.37 ± 0.71		12.29 ± 0.56		12.47 ± 0.47	
	EC	Control (14)	10.77 ± 0.18	ns	10.95 ± 0.30	ns	10.81 ± 0.34	ns	10.95 ± 0.20	ns
		Stress (13)	10.75 ± 0.30		10.88 ± 0.30		10.81 ± 0.32		10.99 ± 0.28	
	AC	Control (13)	11.69 ± 0.37	0.003	11.66 ± 0.43	ns	11.91 ± 0.50	ns	11.90 ± 0.62	ns
		Stress (12)	11.18 ± 0.42		11.63 ± 0.49		12.11 ± 0.61		12.10 ± 0.58	
RD[a]	CC	Control (14)	5.23 ± 0.33	ns	4.91 ± 0.20	ns	4.67 ± 0.33	ns	4.58 ± 0.14	0.019
		Stress (13)	5.32 ± 0.30		5.05 ± 0.23		4.86 ± 0.33		4.84 ± 0.36	
	EC	Control (14)	5.55 ± 0.14	ns	5.44 ± 0.10	ns	5.25 ± 0.14	0.027	5.23 ± 0.11	0.001
		Stress (13)	5.58 ± 0.12		5.50 ± 0.10		5.37 ± 0.13		5.42 ± 0.16	
	AC	Control (14)	4.94 ± 0.23	ns	4.81 ± 0.25	ns	4.46 ± 0.20	0.004	4.57 ± 0.27	ns
		Stress (13)	4.95 ± 0.26		4.87 ± 0.18		4.79 ± 0.33		4.69 ± 0.30	
Volume[b]	CC	Control (14)	5.24 ± 0.59	ns	5.25 ± 0.51	ns	5.42 ± 0.54	ns	5.62 ± 0.42	ns
		Stress (12)	5.18 ± 0.57		5.30 ± 0.65		5.79 ± 0.64		5.79 ± 0.69	
	EC	Control (14)	50.88 ± 5.12	0.032	53.76 ± 4.55	0.032	55.34 ± 6.67	0.062	55.83 ± 5.30	0.032
		Stress (12)	55.46 ± 5.09		58.41 ± 5.90		59.98 ± 5.19		61.30 ± 6.96	
	AC	Control (14)	3.35 ± 0.87	ns	3.07 ± 0.86	ns	3.83 ± 0.95	ns[c]	3.50 ± 0.84	ns
		Stress (11)	3.16 ± 0.84		3.02 ± 0.56		3.66 ± 0.89		3.03 ± 0.49	

A few subjects were excluded from the analysis when assumptions like no significant outliers or normality were not met.
CC, corpus callosum; EC, external capsule; AC, anterior commissure.
[a]*Values are expressed in units of* $\times 10^{-4}$ mm^2/s.
[b]*Values are expressed in units of* mm^3 *without scaling.*
[c]*Welch-corrected p-values.*
[d]*Without or with marginally significant between-group difference assessed by mixed design ANOVA.*

Amygdala

Stress reduced MD and RD of the amygdala [$F_{(3, 30)} = 6.076$, $p = 0.002$ and $F_{(3, 30)} = 5.999$, $p = 0.002$, respectively], but these values remained constant in control rats. We found no between-group differences or group × time interaction (**Figures 5A,B**). The stress-induced decrease of AD was close to the level of significance [$F_{(3, 30)} = 4.703$, $p = 0.008$], while this value did not change in the controls (**Figure 5C**). We found no between-group differences or group × time interaction. Neither stress nor time affected FA or the volume of the amygdala (see data in the **Supplementary Table S1**).

Inferior Colliculus

As the animals developed, the FA values significantly increased in the control rats [$F_{(3, 39)} = 7.005$, $p = 0.0007$], but did not change in the stress group (**Figure 5D**). We found no between-group differences or group × time interaction. MD and RD values showed a nearly significant decrease in the stressed rats [$F_{(1.52, 18.25)} = 6.833$, $p = 0.010$ and $F_{(1.41, 16.86)} = 7.376$, $p = 0.009$ both with Greenhouse–Geisser correction], while no change was found in the controls (**Figures 5E,F**). None of the groups showed significant time-related volume change in the IC; however, there was a between-group difference [$F_{(1, 24)} = 5.866$, $p = 0.023$] without group × time interaction probably due to the initial difference at the *baseline* measurements ($p = 0.003$) (**Supplementary Table S1**).

Thalamus

FA values tended to increase both in the control [$F_{(3, 39)} = 4.198$, $p = 0.011$] and in the stress group over time [$F_{(3, 36)} = 3.295$, $p = 0.031$], but these changes could only approach the level

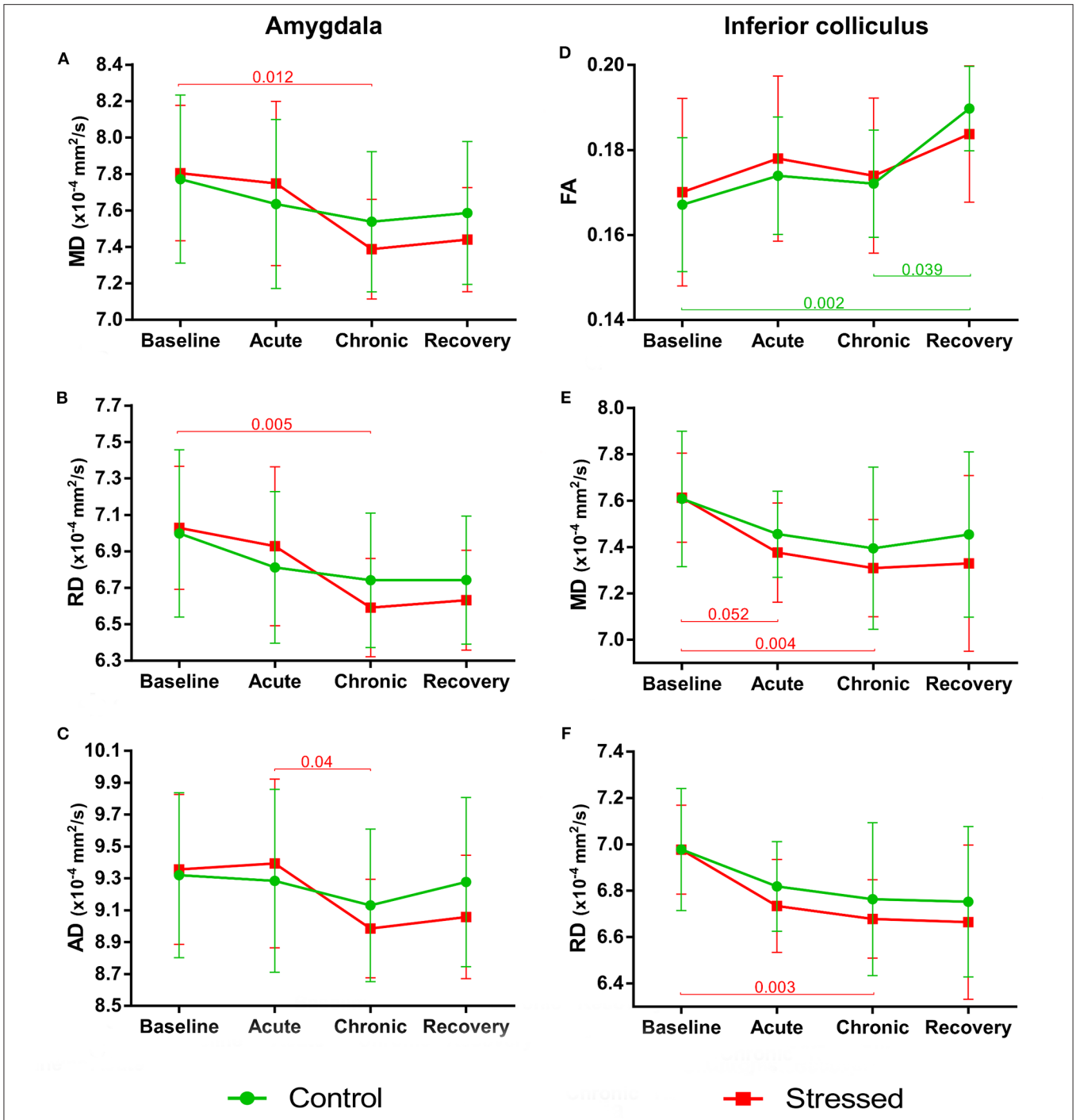

FIGURE 5 | Stress-induced changes of DTI metrics in gray matter areas I. Longitudinal within-group differences of DTI metrics in the amygdala **(A–C)** and inferior colliculus **(D–F)**. Note that most values changed significantly as the animals matured. Data are means ± *SD*. FA, Fractional anisotropy; MD, Mean diffusivity; RD, Radial diffusivity; AD, Axial diffusivity.

of significance (**Figure 6A**). A similar effect was found in MD, where a nearly significant decrease was observed in both the stressed [$F_{(3, 36)} = 3.321$, $p = 0.030$] and the control animals [$F_{(3, 39)} = 4.504$, $p = 0.008$] (**Figure 6B**). AD of thalamus was not altered in any way, but RD decreased significantly in control rats [$F_{(3, 39)} = 7.782$, $p = 0.0003$] over time, while it was only close to the level of significance in the stressed animals [$F_{(3, 36)} = 4.575$, $p = 0.008$] (**Figure 6C**). The volume of the thalamus

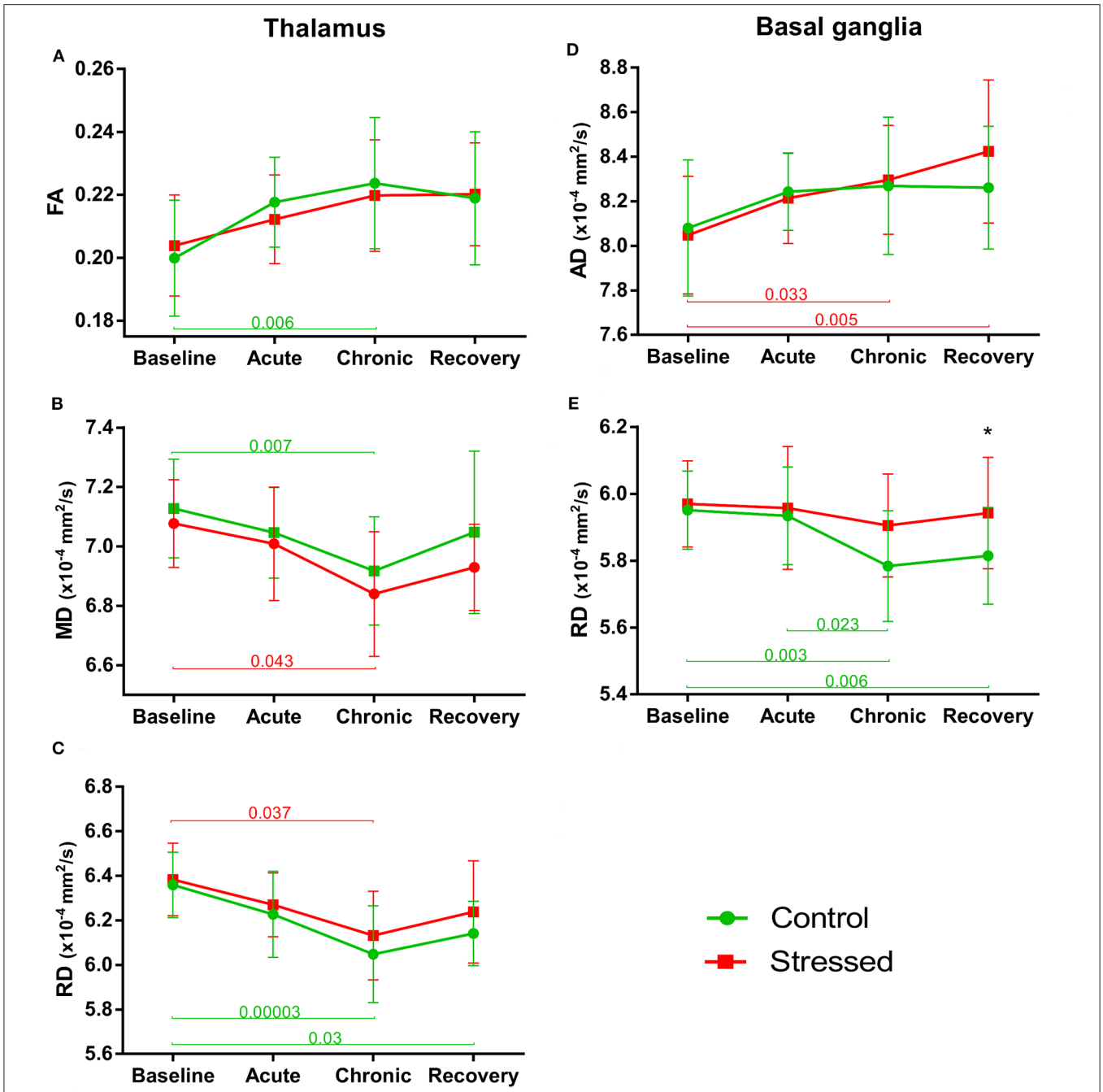

FIGURE 6 | Stress-induced changes of DTI metrics in gray matter areas II. Longitudinal within- and between-group differences of DTI metrics in the thalamus **(A–C)** and basal ganglia **(D,E)**. Note that most values changed significantly over time as the animals matured. Data are means ± *SD*. Asterisk shows significant between-subject differences per time point. FA, Fractional anisotropy; MD, Mean diffusivity; RD, Radial diffusivity; AD, Axial diffusivity.

did not change and none of the MRI metrics showed any group × time interactions or between group differences (see data in **Supplementary Table S1**).

Basal Ganglia

FA values gradually increased in both the stressed [$F_{(3, 36)} = 7.852$, $p = 0.00037$] and control [$F_{(3, 39)} = 7.292$, $p = 0.000537$] animals without any significant group × time interaction or between-group difference (**Supplementary Table S1**). MD did not change over time either in the control or in the stressed rats. AD was increased significantly in the stress group [$F_{(3, 36)} = 7.866$, $p = 0.00036$], but did not change in the controls (**Figure 6D**). Here, there was no significant group × time interaction and between-group difference. In contrast to that,

TABLE 2 | Correlations between MRI metrics and cognitive performance in the *acute* stress period.

Brain area	NOR-1 results	MRI metrics	Control	Stress
Amygdala	DI	Vol	$R = 0.303$	$R = 0.752^{*}$
	HI	Vol	$R = 0.339$	$R = 0.757^{*}$
Anterior commissure	DI	Vol	$R = 0.667^{**}$	$R = 0.244$
	HI	Vol	$R = 0.635^{*}$	$R = 0.097$
Corpus callosum	DI	MD	$R = -0.259$	$R = 0.750^{*}$
	HI	MD	$R = -0.173$	$R = 0.688^{*}$
Inferior colliculus	DI	AD	$R = 0.270$	$R = 0.711^{*}$
	DI	MD	$R = 0.306$	$R = 0.689^{*}$
	HI	MD	$R = 0.225$	$R = 0.743^{*}$
	HI	AD	$R = 0.213$	$R = 0.785^{**}$
	HI	RD	$R = 0.212$	$R = 0.636^{*}$

*NOR-1, novel object recognition test performed on the 10th day of the stress exposure; DI, discrimination index; HI, habituation index; AD, axial diffusivity; MD, mean diffusivity; RD, radial diffusivity; Vol, volume; R, Pearson's correlation coefficient; *p < 0.05; **p < 0.01.*

TABLE 3 | Correlations between MRI metrics and cognitive performance in the *chronic* stress period.

Brain area	NOR-2 results	MRI metrics	Control	Stress
Amygdala	DI	Vol	$R = -0.186$	$R = 0.665^{*}$
Anterior commissure	HI	FA	$R = 0.079$	$R = -0.614^{*}$
	HI	RD	$R = 0.063$	$R = 0.603^{*}$
Inferior colliculus	DI	FA	$R = -0.172$	$R = 0.666^{*}$
	DI	MD	$R = 0.028$	$R = 0.669^{*}$
	DI	AD	$R = -0.024$	$R = 0.733^{*}$
	HI	AD	$R = 0.160$	$R = 0.649^{*}$

*NOR-2, novel object recognition test performed few days after the end of the chronic stress exposure; DI, discrimination index; HI, habituation index; AD, axial diffusivity; FA, fractional anisotropy; MD, mean diffusivity; RD, radial diffusivity; Vol, volume; R, Pearson's correlation coefficient; *p < 0.05.*

RD significantly decreased in controls [$F_{(3, 39)} = 7.292$, $p = 0.000537$], but did not change over time in the stressed rats (**Figure 6E**). For RD values, we found nearly significant between-group difference [$F_{(1, 25)} = 3.339$, $p = 0.080$] without group × time interaction. In the *recovery* phase, the RD was higher in the stressed rats compared to the controls, while no alterations were found in the *baseline*, *acute*, or *chronic* phases (**Supplementary Table S1** and **Figure 6E**). The volume of BG showed significant time-dependent increase in both the stressed [$F_{(1,99,19,87)} = 7.665$, $p = 0.003$ with Greenhouse–Geisser correction and control rats [$F_{(3, 39)} = 4.898$, $p = 0.0055$] without group × time interaction and between-group differences (**Supplementary Table S1**).

Behavioral Assessment

Stress exposure had no influence on the cognitive performance, anxiety-like behavior, or locomotor activity of the animals during the *acute* and *chronic* stress periods. We performed an OFT and a NOR test at the end of the 1st week of the stress protocol (*acute stress* period, **Figure 1**), and an EPM test in the last day of the chronic stress procedures (*chronic stress* period, **Figure 1**). None of these tests yielded any difference between the control and stressed rats (for details, please see the **Supplementary Material**).

Stress-induced behavioral differences emerged only in the *recovery* period (**Figure 1**). In the NOR-3 test, we applied longer retention times—making the task more difficult for the animals—which probably contributed to the higher sensitivity for detecting a cognitive impairment in the stressed rats. In Week 5, stressed animals ($n = 15$) showed no discrimination behavior in the NOR-3 test after a 3-h retention period (observation of novel vs. familiar object: 9.8 ± 1.3 vs. 6.6 ± 0.9, $t = 1.895$, $p = 0.078$), while control animals ($n = 16$) spent significantly more time with the exploration of the novel object (10.5 ± 1.0 vs. 6.5 ± 0.5 s, $t = 3.270$, $p = 0.006$).

A similar difference was present between the control and stressed rats in the MWM, which was done 7 weeks after the end of the stress procedures. Stressed rats showed impaired short-term memory performance in the MWM as the mixed ANOVA indicated a significant main effect of STRESS on the escape latency on the 1st day of the training [$F_{(1, 30)} = 10.144$, $p = 0.003$; $n = 16$ for both groups]. Stressed animals could also learn the location of the platform during the 4 days of training; however, their escape latency was longer during the whole training procedure [main effect of STRESS: $F_{(1, 30)} = 4.945$, $p = 0.034$].

Correlation Analysis Between the MRI Data and Behavioral Performance

While stress resulted only in mild cognitive impairments, we found that numerous parameters of the cognitive performance showed significant correlations with the DTI and volumetric data (see **Tables 2**–**4**).

Acute Stress Period

We found significant correlations between specific parameters of the MRI data and results of the NOR-1 and OFT. DI and HI of the NOR-1 test correlated with the volume of the amygdala in the stressed rats and with the volume of the AC in the control animals (**Table 2**). DI and HI values of the NOR-1 test correlated with MD in the CC of the stressed rats and with AD, MD, and RD values of the IC in the stressed rats (**Table 2**).

We also found significant correlations between specific parameters of the DTI data and results of the OFT. Entries to the center area correlated with FA ($\tau = 0.486$, $p < 0.05$) and RD ($\tau = -0.509$, $p < 0.05$) values of the AC in the control rats.

Chronic Stress Period

We found significant correlations between specific parameters of the MRI data and results of the NOR-2 and EPM tests. DI of the NOR-2 test correlated with the volume of the amygdala in the stressed rats (**Table 3**). In the AC, FA and RD values correlated with the HI of the NOR-2 test of the stressed animals (**Table 3**).

TABLE 4 | Correlations between MRI metrics and cognitive performance in the *recovery* period.

Brain area	Behavioral task	Behavioral parameter	MRI metrics	Control	Stress
Amygdala	MWM	Day2 escape latency	MD	$\tau = 0.322$	$\tau = -0.474^*$
	MWM	Day2 escape latency	RD	$\tau = 0.429^*$	$\tau = -0.500^*$
Anterior commissure	NOR-3	HI	FA	$\tau = 0.103$	$\tau = 0.487^*$
	MWM	Trial2 escape latency	FA	$\tau = -0.501^*$	$\tau = -0.118$
	MWM	Trial3 escape latency	MD	$\tau = 0.478^*$	$\tau = -0.295$
	MWM	Trial3 escape latency	AD	$\tau = 0.454^*$	$\tau = -0.113$
	MWM	Day1 escape latency	AD	$\tau = 0.055$	$\tau = -0.460^*$
Basal ganglia	NOR-3	HI	MD	$\tau = 0.431^*$	$\tau = -0.051$
	MWM	Trial4 escape latency	Vol	$\tau = -0.035$	$\tau = -0.510^*$
	MWM	Day1 escape latency	Vol	$\tau = 0.033$	$\tau = -0.557^*$
	MWM	Day4 escape latency	Vol	$\tau = 0.331$	$\tau = -0.485^*$
	MWM	Day4 escape latency	FA	$\tau = 0.486^*$	$\tau = 0.103$
Corpus callosum	MWM	Trial2 escape latency	FA	$\tau = -0.426^*$	$\tau = -0.024$
	MWM	Trial3 escape latency	FA	$\tau = -0.408^*$	$\tau = 0.113$
	MWM	Trial3 escape latency	AD	$\tau = -0.478^*$	$\tau = -0.033$
	MWM	Day3 escape latency	MD	$\tau = 0.187$	$\tau = -0.458^*$
	MWM	Day3 escape latency	AD	$\tau = 0.275$	$\tau = -0.452^*$
	MWM	Day4 escape latency	AD	$\tau = -0.022$	$\tau = -0.555^{**}$
External capsule	MWM	Day1 escape latency	Vol	$\tau = -0.143$	$\tau = -0.522^*$
	MWM	Day1 escape latency	AD	$\tau = -0.253$	$\tau = -0.489^*$
	MWM	Day3 escape latency	MD	$\tau = 0.416^*$	$\tau = -0.231$
Inferior colliculus	MWM	Trial4 escape latency	FA	$\tau = 0.046$	$\tau = 0.496^*$
	MWM	Day1 escape latency	FA	$\tau = 0.033$	$\tau = 0.633^{**}$
	MWM	Day4 escape latency	FA	$\tau = -0.398^*$	$\tau = -0.077$
Thalamus	MWM	Day1 escape latency	RD	$\tau = 0.033$	$\tau = -0.449^*$
	MWM	Day2 escape latency	Vol	$\tau = -0.099$	$\tau = -0.688^{**}$
	MWM	Day4 escape latency	AD	$\tau = 0.000$	$\tau = -0.436^*$

NOR-3, novel object recognition test which was performed on the 2nd week of the recovery period; MWM, Morris water maze test, which was done on the 7th week of the recovery period; HI: habituation index; AD, axial diffusivity; FA, fractional anisotropy; MD, mean diffusivity; RD, radial diffusivity; Vol, volume; R, Pearson's correlation coefficient; τ, Kendall's tau coefficient.

$^*p < 0.05$; $^{**}p < 0.01$.

Furthermore, DI and HI values of the NOR-2 test correlated with AD, FA, and MD values in the IC of the stressed rats (**Table 3**).

Significant correlations between DTI data and behavior were found also in the EPM. In control rats, FA values of the AC correlated with the time spent in the open arms of the EPM ($R = -0.539$, $p < 0.05$).

Recovery Period

Surprisingly, most of the correlations between behavior and MRI data were found in the *recovery* period (**Table 4**). In this phase, we did a NOR test 2 weeks after the end of the stress (NOR-3) and a MWM test 7 weeks after the end of the stress (**Figure 1**). The HI of the NOR-3 test correlated with the FA value of the AC in stressed rats and with the MD value of the BG in the control animals (**Table 4**). Most of the correlations were found between the animal's performance in the MWM and between the MRI data (for details, see **Table 4**). In the amygdala, RD and MD values correlated with escape latencies of the control (RD, $\tau = 0.429$, $p < 0.05$) and stressed (MD, $\tau = -0.474$, $p < 0.05$; RD, $\tau = -0.500$, $p < 0.05$) rats. In the anterior commissure, the AD, FA, and MD values correlated with the cognitive performance of the control rats and with the AD value of the stressed rats (**Table 4**). The volume of the BG in the stressed animals correlated with escape latencies, whereas in controls, the FA value correlated with the escape latency (**Table 4**). In the corpus callosum, the AD and FA values correlated with escape latencies of the control rats and AD and MD values correlated with escape latencies of the stressed rats (**Table 4**). In the EC, the volume and AD of the stressed rats correlated with escape latency, whereas in the controls, the MD correlated with escape latency (**Table 4**). In the inferior colliculus, FA values correlated with escape latencies of both the control and stressed rats (**Table 4**). In the thalamus, the volume as well as AD and RD values of the stressed rats correlated with their escape latencies (**Table 4**).

DISCUSSION

Main Findings

Here, we report that chronic stress exposure results in pronounced microstructural changes in white matter structures

of rats such as the corpus callosum, anterior commissure, and external capsule. We observed modest microstructural alterations also in gray matter structures such as the amygdala, thalamus, inferior colliculus, and basal ganglia. These stress-induced microstructural differences developed gradually, and many of them were lasting and remained even after the end of the stress exposure. Since we used young adult rats, consequently most of the DTI parameters changed as the rats matured. In many cases, stress exposure hindered these developmental changes of DTI values. We found no effect of repeated restraint stress on the volume of the examined brain areas.

In the present experiment, the chronic stress exposure induced only modest cognitive impairments, but these changes were long-lasting, i.e., the cognitive performance was impaired even several weeks after the end of the stress protocol (in the *recovery* period). Notably, we found numerous correlations between the cognitive performance of the rats and the DTI metrics of the amygdala, anterior commissure, basal ganglia, corpus callosum, external capsule, inferior colliculus, and thalamus. To the best of our knowledge, we are the first to document correlations between cognitive capacities and stress-induced microstructural changes detected by DTI. Overall, these data extend and complement the earlier histopathological findings documenting multifaceted cellular alterations in the brains of chronically stressed animals. Importantly, our present data on the stress-induced reduction of FA and increased MD and RD values of white matter structures are in good harmony with the findings of recent meta-analyses revealing similar microstructural changes in stress-related psychiatric disorders (Kelly et al., 2018; Dennis et al., 2019; Favre et al., 2019; Koshiyama et al., 2019; van Velzen et al., 2019).

Stress-Induced Structural Changes Detected by *in vivo* DTI Measurements

A large body of evidence document stress-induced cellular alterations of neurons and glia in the brains of humans and animals (see, e.g., Lucassen et al., 2014; Lupien et al., 2018). Most of these data stem from postmortem investigations, but a growing number of neuroimaging data complement these findings. *In vivo* imaging experiments of chronically stressed animals reveals significant changes in large-scale functional connectivity networks (Henckens et al., 2015; Gass et al., 2016; Magalhaes et al., 2018, 2019), while proton MR spectroscopy documents altered brain metabolites and neurotransmitter levels (Czéh et al., 2001; Khan et al., 2018; Magalhaes et al., 2019). However, these findings are not without controversies. For example, some studies reported on stress-induced volume reductions of specific brain structures (Li et al., 2017; Magalhaes et al., 2018), whereas other experiments could not substantiate that (Henckens et al., 2015, and our present data). The available diffusion MRI findings are also ambiguous. For example, a recent study using tract-based spatial statistical analysis approach reported that stress can increase FA and reduce MD and RD in several white matter bundles after 2 weeks of repeated inescapable stress (Magalhaes et al., 2017). Another study also reported increased FA in the hypothalamus and hippocampal CA3 in stress-susceptible mice, which were subjected to 10 days of social defeat stress (Anacker et al., 2016). Yet, another research group found no evidence for white matter microstructural changes in rats exposed to 10 days of repeated immobilization stress (Henckens et al., 2015). A study investigating a genetic rat model of depression documented decreased FA in the CC and AC and increased MD in the CC (Zalsman et al., 2017). In our present experiment, we also found reduced FA and increased MD and RD values in several white matter structures indicating myelin destruction (Alexander et al., 2007). However, the between-group differences and the group × time interactions of DTI metrics were different in the various brain areas. Most likely, this was due to the fact that DTI metrics have a complex origin and show a regionally varying, non-linear change across a wide age range (Lebel et al., 2012; Mengler et al., 2014; Kulikova et al., 2015). In general, FA increases, while MD and RD decrease as white matter structures mature, but the temporal dynamics are inhomogeneous in the different pathways (Lebel et al., 2012; Kulikova et al., 2015), which could explain the variances in our data. Despite all that, our data suggest that the stress-induced microstructural changes are long-lasting and may remain detectable even weeks after the end of the stress procedures. This finding was supported by a recent study, which investigated the lasting effects of stress and found that it may take up to 8 weeks of recovery to normalize the stress-induced microstructural changes (Khan et al., 2018).

In our present experiment, the rats were 8 weeks old when we started to stress them, which means that they were at the age of late adolescence or young adulthood as defined by Tirelli and co-workers (Tirelli et al., 2003). At this age, the rat brain is almost completely matured. After the end of the 2nd month, brain areas do not change in their volume anymore, but there are still significant changes in myelination between the 2nd and 3rd months, which are also reflected by the significant reductions of MD and RD values of the whole brain (Mengler et al., 2014). There are significant regional differences, e.g., the neocortex appears to be fully matured by the age of 2 months, but there are still significant changes in neuron numbers of the striatum between the 2nd and 3rd months (Mengler et al., 2014). There is postmortem histological evidence that maturation of the axon fibers lasts even longer and myelination is still changing up to 6 months of age in rats (Mengler et al., 2014).

It is well-documented that during adolescence, individuals (both humans and experimental animals) are more susceptible to stress because during this age, stress exposure leads to more prolonged glucocorticoid exposure and appears to alter the development of emotional and cognitive systems, which may result in enduring mild deficits in learning and memory tasks or increased anxiety-like behavior (Spear, 2000; McCormick et al., 2010, 2017; Romeo et al., 2016). In the human brain, FA values continuously increase during childhood and adolescence and reach a peak between 20 and 42 years of age, while MD shows an opposite trend, decreasing first, reaching a minimum at 18–41 years, and then increasing later in life (Lebel et al., 2012). Numerous human DTI studies documented white matter abnormalities in individuals who experienced adverse life events during their childhood and adolescence.

Specifically, microstructural white matter changes were found in adolescents exposed to childhood maltreatment (Huang et al., 2012) or in young adults who witnessed domestic violence (Choi et al., 2012) or experienced parental verbal abuse (Choi et al., 2009) during their early age. Childhood maltreatment can result in reduced corpus callosum area (Teicher et al., 2004) and reduced FA values in the corpus callosum (Jackowski et al., 2008). Notably, a recent study that compared the timing of the adverse experiences found that stress seems to induce different types of changes in DTI metrics depending on the age when individuals experienced the stress (Jensen et al., 2018).

To the best of our current knowledge, the microstructural alterations and anisotropy of gray and white matter structures are the consequences of altered myelination, fiber density, neuronal morphology, and synaptogenesis (Evans, 2013; Jensen et al., 2018). There are very few studies that analyzed the stress-induced structural changes with both neuroimaging and conventional light microscopy techniques (but see Khan et al., 2019). At the same time, plenty of postmortem studies document stress-induced reductions of dendritic complexity of pyramidal cells in the hippocampus (Magarinos et al., 1996) and neocortex (Cook and Wellman, 2004; Radley et al., 2004), and reduced synapse numbers (Sandi et al., 2003; Hajszan et al., 2009; Maras et al., 2014; Csabai et al., 2018). Furthermore, stress affects not only neurons but also the level of myelination and oligodendrocytes (Czéh et al., 2007; Miyata et al., 2016; Yang et al., 2016; Lehmann et al., 2017; Liu J. et al., 2018) and can reduce fiber density as well (Kitayama et al., 1997; Csabai et al., 2018).

Overall, these *in vivo* MR measurements may help us develop objective biomarkers (Kelly et al., 2018; Koshiyama et al., 2019; Nugent et al., 2019; van Velzen et al., 2019) and predict treatment response in mental disorders (Crossley et al., 2017; Coenen et al., 2019; Davis et al., 2019).

Correlation Between the DTI Parameters and Cognitive Behavior

Several studies aimed to find correlations between stress-induced behavioral changes and MRI findings. Most of these studies analyzed the correlation between stress susceptibility and neuroimaging data. For example, Anacker et al. investigated the neurobiological mechanisms underlying stress susceptibility using structural MRI and DTI to determine neuroanatomic differences between stress-susceptible and stress-resilient mice (Anacker et al., 2016). They scanned the brains *ex vivo* and found that social avoidance correlated negatively with local volume of the cingulate cortex, nucleus accumbens, thalamus, raphe nuclei, and bed nucleus of the stria terminalis (Anacker et al., 2016). Furthermore, they found a positive correlation between social avoidance and the volume of the ventral tegmental area, habenula, periaqueductal gray, cerebellum, hypothalamus, and hippocampal CA3 (Anacker et al., 2016). They also observed increased FA in the hypothalamus and hippocampal CA3 and different structural covariance between brain regions in susceptible and resilient mice (Anacker et al., 2016). Others reported on a significantly lower FA in the right ventral hippocampus of the stress-susceptible mice prior to the chronic stress exposure, suggesting that pre-existing microstructural abnormalities may result in stress susceptibility (Liu X. et al., 2018). Another study documented substantial increase (45%) in the volume of the amygdala of a rat strain that is susceptible to the repeated stress procedure (F344 rats; Bourgin et al., 2015). More recently, Bonnefil et al. documented that region-specific myelin differences define the behavioral consequences of the chronic social defeat stress in mice (Bonnefil et al., 2019).

In our present study, we expected that stress would result in pronounced cognitive deficits and elevated anxiety-like behavior in the stressed animals. In contrast, we observed only mild cognitive impairments in the stressed rats, but we found numerous correlations between the DTI parameters and the cognitive performance of the animals. The most pronounced correlations were found between the DTI values of the amygdala, IC, AC, CC, EC, and between the behavioral performance in the NOR test. Surprisingly, in the present experiment, the MRI data recorded 2 weeks after the end of the stress correlated best with escape latencies in the MWM test, which was done 5 weeks after the MRI scans. Numerous reports document that learning can induce changes in structural neuroplasticity, which can be then measured with DTI (e.g., Blumenfeld-Katzir et al., 2011; Zatorre et al., 2012; Ding et al., 2013; Nasrallah et al., 2016; Hofstetter and Assaf, 2017; Huber et al., 2018). These studies suggest neuronal activity-dependent changes in myelination levels and the remodeling of the existing myelin sheath as an underlying cellular process behind the altered DTI metrics (Fields, 2015; Kaller et al., 2017). Our present data extend these findings and document that the stress-induced microstructural changes can also predict the alterations of cognitive performance.

Clinical Relevance

Stress is a major contributing factor to the development of various stress-related psychiatric disorders such as post-traumatic stress disorder (PTSD), depressive disorders, or schizophrenia. Since these disorders are common and impose severe socio-economic burden, substantial efforts have been devoted to mimic these conditions in experimental animals. Chronic stress models are typically regarded as valid models for major depressive disorder (MDD) (see, e.g., Willner, 1997; Czéh et al., 2016), and the translational value of neuroimaging has been well-demonstrated in earlier studies using chronic psychosocial stress protocols, which had led to alterations in brain volume, functional connectivity, and metabolite levels comparable to human depression (Czéh et al., 2001; Grandjean et al., 2016). At the same time, numerous clinical studies seek for neuroimaging biomarkers, which could help the objective diagnosis of stress-related psychiatric disorders. The ENIGMA Schizophrenia DTI Working Group analyzed the data of 2,359 healthy controls and 1,963 schizophrenia patients and found significant reductions of FA in schizophrenia patients, especially in the corpus callosum, but also in 20 out of 25 major white matter fasciculi (Kelly et al., 2018). They also found significantly higher MD and RD in the schizophrenia group (Kelly et al., 2018). These data have been confirmed more recently by another mega-analysis comparing white matter microstructural differences between healthy controls and sufferers of schizophrenia, bipolar disorder, autism spectrum disorder, and MDD (Koshiyama et al., 2019). These comparisons document significantly lower

FA and higher MD and AD values for most of the major white matter bundles in these disorders (Koshiyama et al., 2019). Another study, the ENIGMA MDD working group, examined white matter anisotropy and diffusivity in 1,305 MDD patients and 1,602 healthy controls and found subtle, but widespread alterations showing reduced FA in adult MDD patients compared to controls in 16 out of 25 white matter tracts (van Velzen et al., 2019). The largest difference was depicted in the corpus callosum and widespread higher RD values were also observed (van Velzen et al., 2019). Notably, in our present study, we also found lower FA and higher MD and RD values in the CC and EC of the stressed rats, which is in good harmony with these clinical findings. Similar data are available on PTSD patients: significantly lower FA values of the CC have been documented in traumatized individuals (Hu et al., 2016; O'Doherty et al., 2018; Siehl et al., 2018; Dennis et al., 2019), in maltreated children (Jackowski et al., 2008), or in adolescents after childhood sexual abuse (Rinne-Albers et al., 2016).

CONCLUSIONS

In conclusion, our data provide further support to the translational value of DTI studies and suggest that chronic stress exposure can result in similar white matter microstructural alterations, which have been documented in stress-related psychiatric disorders. Furthermore, we report here significant correlations between cognitive performance and stress-induced microstructural changes detected by DTI. Overall, the *in vivo* imaging findings complement the earlier postmortem histopathological data and suggest structural disconnectivity in stress-related pathologies.

DATA AVAILABILITY STATEMENT

All datasets generated for this study are included in the article/ **Supplementary Material**.

ETHICS STATEMENT

The animal study was reviewed and approved by the Hungarian Ethical Committee on Animal Research according to the Ethical Codex of Animal Experiments (License No. BA02/2000-12/2015).

AUTHOR CONTRIBUTIONS

BC and SN had the concept, designed the experiments, and drafted the manuscript. ZV and DC did the stress procedures. NB, ZBa, and IH did all the behavioral testing and analyzed the behavioral data. AV, SN, and GP did the MRI measurements and analyzed the MRI data. AM, TD, and ZBe provided supervision for the experimental procedures and contributed to the interpretation of the data. All authors contributed to the writing of the paper and revised it critically for important intellectual content and approved the final version to be published and agreed to be accountable for all aspects of the work in ensuring that questions related to the accuracy or integrity of any part of the work are appropriately investigated and resolved.

FUNDING

This work was financially supported by the following grant agencies: Hungarian Brain Research Program (KTIA_NAP_13-2-2014-0019 and 2017-1.2.1-NKP-2017-00002), EU Social Funds (EFOP-3.6.2-16-2017-00008 and EFOP-3.6.3-VEKOP-16-2017-00009), and Institutional Excellence Program for the Higher Education II within the framework of the 5th thematic program. Further financial support was received from the ÚNKP-19-4-PTE-126, ÚNKP-19-4-PTE-122 New National Excellence Program of the Ministry for Innovation and Technology, and János Bolyai Research Scholarship of the Hungarian Academy of Sciences (SN, GP). These grant agencies had no influence in study design; in the collection, analysis, and interpretation of data; in the writing of the report; and in the decision to submit the article for publication.

ACKNOWLEDGMENTS

The authors would like to thank Klára Lencse for her assistance in animal care and Sai Ambika Tadepalli for her assistance in behavioral testing. We would also like to show our gratitude to Michael Diedenhofen for his help in MRI data conversion.

SUPPLEMENTARY MATERIAL

The Supplementary Material for this article can be found online at: https://www.frontiersin.org/articles/10.3389/fnins.2020.00474/full#supplementary-material

REFERENCES

Alexander, A. L., Lee, J. E., Lazar, M., and Field, A. S. (2007). Diffusion tensor imaging of the brain. *Neurotherapeutics* 4, 316–329. doi: 10.1016/j.nurt.2007.05.011

Anacker, C., Scholz, J., O'Donnell, K. J., Allemang-Grand, R., Diorio, J., Bagot, R. C., et al. (2016). Neuroanatomic differences associated with stress susceptibility and resilience. *Biol. Psychiatry* 79, 840–849. doi: 10.1016/j.biopsych.2015.08.009

Andersson, J. L. R., Graham, M. S., Zsoldos, E., and Sotiropoulos, S. N. (2016). Incorporating outlier detection and replacement into a non-parametric framework for movement and distortion correction of diffusion MR images. *Neuroimage* 141, 556–572. doi: 10.1016/j.neuroimage.2016.06.058

Andersson, J. L. R., and Sotiropoulos, S. N. (2016). An integrated approach to correction for off-resonance effects and subject movement in diffusion MR imaging. *Neuroimage* 125, 1063–1078. doi: 10.1016/j.neuroimage.2015.10.019

Baker, K. B., and Kim, J. J. (2002). Effects of stress and hippocampal NMDA receptor antagonism on recognition memory in rats. *Learn. Mem.* 9, 58–65. doi: 10.1101/lm.46102

Blumenfeld-Katzir, T., Pasternak, O., Dagan, M., and Assaf, Y. (2011). Diffusion MRI of structural brain plasticity induced by a learning and memory task. *PLoS ONE* 6:e20678. doi: 10.1371/journal.pone.0020678

Bondi, C. O., Rodriguez, G., Gould, G. G., Frazer, A., and Morilak, D. A. (2008). Chronic unpredictable stress induces a cognitive deficit and anxiety-like behavior in rats that is prevented by chronic antidepressant drug treatment. *Neuropsychopharmacology* 33, 320–331. doi: 10.1038/sj.npp.1301410

Bonnefil, V., Dietz, K., Amatruda, M., Wentling, M., Aubry, A. V., Dupree, J. L., et al. (2019). Region-specific myelin differences define behavioral consequences of chronic social defeat stress in mice. *Elife* 8:e40855. doi: 10.7554/eLife.40855.014

Bourgin, J., Cachia, A., Boumezbeur, F., Djemai, B., Bottlaender, M., Duchesnay, E., et al. (2015). Hyper-responsivity to stress in rats is associated with a large increase in amygdala volume. A 7T MRI study. *Eur. Neuropsychopharmacol.* 25, 828–835. doi: 10.1016/j.euroneuro.2015.02.010

Bowman, R. E., Beck, K. D., and Luine, V. N. (2003). Chronic stress effects on memory: sex differences in performance and monoaminergic activity. *Horm. Behav.* 43, 48–59. doi: 10.1016/S0018-506X(02)00022-3

Chandola, T., Brunner, E., and Marmot, M. (2006). Chronic stress at work and the metabolic syndrome: prospective study. *BMJ* 332, 521–525. doi: 10.1136/bmj.38693.435301.80

Choi, J., Jeong, B., Polcari, A., Rohan, M. L., and Teicher, M. H. (2012). Reduced fractional anisotropy in the visual limbic pathway of young adults witnessing domestic violence in childhood. *Neuroimage* 59, 1071–1079. doi: 10.1016/j.neuroimage.2011.09.033

Choi, J., Jeong, B., Rohan, M. L., Polcari, A. M., and Teicher, M. H. (2009). Preliminary evidence for white matter tract abnormalities in young adults exposed to parental verbal abuse. *Biol. Psychiatry* 65, 227–234. doi: 10.1016/j.biopsych.2008.06.022

Coenen, V. A., Schlaepfer, T. E., Bewernick, B., Kilian, H., Kaller, C. P., Urbach, H., et al. (2019). Frontal white matter architecture predicts efficacy of deep brain stimulation in major depression. *Transl. Psychiatry* 9:197. doi: 10.1038/s41398-019-0540-4

Cook, S. C., and Wellman, C. L. (2004). Chronic stress alters dendritic morphology in rat medial prefrontal cortex. *J. Neurobiol.* 60, 236–248. doi: 10.1002/neu.20025

Crossley, N. A., Marques, T. R., Taylor, H., Chaddock, C., Dell'Acqua, F., Reinders, A. A., et al. (2017). Connectomic correlates of response to treatment in first-episode psychosis. *Brain* 140, 487–496. doi: 10.1093/brain/aww297

Csabai, D., Wiborg, O., and Czeh, B. (2018). Reduced synapse and axon numbers in the prefrontal cortex of rats subjected to a chronic stress model for depression. *Front. Cell. Neurosci.* 12:24. doi: 10.3389/fncel.2018.00024

Czéh, B., Fuchs, E., Wiborg, O., and Simon, M. (2016). Animal models of major depression and their clinical implications. *Prog. Neuropsychopharmacol. Biol. Psychiatry* 64, 293–310. doi: 10.1016/j.pnpbp.2015.04.004

Czéh, B., Michaelis, T., Watanabe, T., Frahm, J., de Biurrun, G., van Kampen, M., et al. (2001). Stress-induced changes in cerebral metabolites, hippocampal volume, and cell proliferation are prevented by antidepressant treatment with tianeptine. *Proc. Natl. Acad. Sci. U. S. A.* 98, 12796–12801. doi: 10.1073/pnas.211427898

Czéh, B., Muller-Keuker, J. I., Rygula, R., Abumaria, N., Hiemke, C., Domenici, E., et al. (2007). Chronic social stress inhibits cell proliferation in the adult medial prefrontal cortex: hemispheric asymmetry and reversal by fluoxetine treatment. *Neuropsychopharmacology* 32, 1490–1503. doi: 10.1038/sj.npp.1301275

Davis, A. D., Hassel, S., Arnott, S. R., Harris, J., Lam, R. W., Milev, R., et al. (2019). White matter indices of medication response in major depression: a diffusion tensor imaging study. *Biol. Psychiatry Cogn. Neurosci. Neuroimaging* 4, 913–924. doi: 10.1016/j.bpsc.2019.05.016

de Kloet, E. R., Oitzl, M. S., and Joels, M. (1999). Stress and cognition: are corticosteroids good or bad guys? *Trends Neurosci.* 22, 422–426. doi: 10.1016/S0166-2236(99)01438-1

Delgado y Palacios, R., Campo, A., Henningsen, K., Verhoye, M., Poot, D., Dijkstra, J., et al. (2011). Magnetic resonance imaging and spectroscopy reveal differential hippocampal changes in anhedonic and resilient subtypes of the chronic mild stress rat model. *Biol. Psychiatry* 70, 449–457. doi: 10.1016/j.biopsych.2011.05.014

Delgado y Palacios, R., Verhoye, M., Henningsen, K., Wiborg, O., and Van der Linden, A. (2014). Diffusion kurtosis imaging and high-resolution MRI demonstrate structural aberrations of caudate putamen and amygdala after chronic mild stress. *PLoS ONE* 9:e95077. doi: 10.1371/journal.pone.0095077

Dennis, E. L., Disner, S. G., Fani, N., Salminen, L. E., Logue, M., Clarke, E. K., et al. (2019). Altered white matter microstructural organization in posttraumatic stress disorder across 3047 adults: results from the PGC-ENIGMA PTSD consortium. *Mol. Psychiatry*. doi: 10.1038/s41380-019-0631-x. [Epub ahead of print].

Ding, A. Y., Li, Q., Zhou, I. Y., Ma, S. J., Tong, G., McAlonan, G. M., et al. (2013). MR diffusion tensor imaging detects rapid microstructural changes in amygdala and hippocampus following fear conditioning in mice. *PLoS ONE* 8:e51704. doi: 10.1371/journal.pone.0051704

Dube, S. R., Fairweather, D., Pearson, W. S., Felitti, V. J., Anda, R. F., and Croft, J. B. (2009). Cumulative childhood stress and autoimmune diseases in adults. *Psychosom. Med.* 71, 243–250. doi: 10.1097/PSY.0b013e3181907888

Duman, R. S., Sanacora, G., and Krystal, J. H. (2019). Altered connectivity in depression: GABA and glutamate neurotransmitter deficits and reversal by novel treatments. *Neuron* 102, 75–90. doi: 10.1016/j.neuron.2019.03.013

Evans, A. C. (2013). Networks of anatomical covariance. *Neuroimage* 80, 489–504. doi: 10.1016/j.neuroimage.2013.05.054

Evans, G. W., and Schamberg, M. A. (2009). Childhood poverty, chronic stress, and adult working memory. *Proc. Natl. Acad. Sci. U. S. A.* 106, 6545–6549. doi: 10.1073/pnas.0811910106

Favre, P., Pauling, M., Stout, J., Hozer, F., Sarrazin, S., Abé, C., et al. (2019). Widespread white matter microstructural abnormalities in bipolar disorder: evidence from mega- and meta-analyses across 3033 individuals. *Neuropsychopharmacology* 44, 2285–2293. doi: 10.1038/s41386-019-0485-6

Fields, R. D. (2015). A new mechanism of nervous system plasticity: activity-dependent myelination. *Nat. Rev. Neurosci.* 16, 756–767. doi: 10.1038/nrn4023

Fogaca, M. V., and Duman, R. S. (2019). Cortical GABAergic dysfunction in stress and depression: new insights for therapeutic interventions. *Front. Cell. Neurosci.* 13:87. doi: 10.3389/fncel.2019.00087

Gass, N., Becker, R., Schwarz, A. J., Weber-Fahr, W., Clemm von Hohenberg, C., Vollmayr, B., et al. (2016). Brain network reorganization differs in response to stress in rats genetically predisposed to depression and stress-resilient rats. *Transl. Psychiatry* 6:e970. doi: 10.1038/tp.2016.233

Gouirand, A. M., and Matuszewich, L. (2005). The effects of chronic unpredictable stress on male rats in the water maze. *Physiol. Behav.* 86, 21–31. doi: 10.1016/j.physbeh.2005.06.027

Grandjean, J., Azzinnari, D., Seuwen, A., Sigrist, H., Seifritz, E., Pryce, C. R., et al. (2016). Chronic psychosocial stress in mice leads to changes in brain functional connectivity and metabolite levels comparable to human depression. *Neuroimage* 142, 544–552. doi: 10.1016/j.neuroimage.2016.08.013

Hajszan, T., Dow, A., Warner-Schmidt, J. L., Szigeti-Buck, K., Sallam, N. L., Parducz, A., et al. (2009). Remodeling of hippocampal spine synapses in the rat learned helplessness model of depression. *Biol. Psychiatry* 65, 392–400. doi: 10.1016/j.biopsych.2008.09.031

Hemanth Kumar, B. S., Mishra, S. K., Trivedi, R., Singh, S., Rana, P., and Khushu, S. (2014). Demyelinating evidences in CMS rat model of depression: a DTI study at 7 T. *Neuroscience* 275, 12–21. doi: 10.1016/j.neuroscience.2014.05.037

Henckens, M. J., van der Marel, K., van der Toorn, A., Pillai, A. G., Fernandez, G., Dijkhuizen, R. M., et al. (2015). Stress-induced alterations in large-scale functional networks of the rodent brain. *Neuroimage* 105, 312–322. doi: 10.1016/j.neuroimage.2014.10.037

Hofstetter, S., and Assaf, Y. (2017). The rapid development of structural plasticity through short water maze training: a DTI study. *Neuroimage* 155, 202–208. doi: 10.1016/j.neuroimage.2017.04.056

Hu, H., Zhou, Y., Wang, Q., Su, S., Qiu, Y., Ge, J., et al. (2016). Association of abnormal white matter integrity in the acute phase of motor vehicle accidents with post-traumatic stress disorder. *J. Affect. Disord.* 190, 714–722. doi: 10.1016/j.jad.2015.09.044

Huang, H., Gundapuneedi, T., and Rao, U. (2012). White matter disruptions in adolescents exposed to childhood maltreatment and vulnerability to psychopathology. *Neuropsychopharmacology* 37, 2693–2701. doi: 10.1038/npp.2012.133

Huber, E., Donnelly, P. M., Rokem, A., and Yeatman, J. D. (2018). Rapid and widespread white matter plasticity during an intensive reading intervention. *Nat. Commun.* 9:2260. doi: 10.1038/s41467-018-04627-5

Jackowski, A. P., Douglas-Palumberi, H., Jackowski, M., Win, L., Schultz, R. T., Staib, L. W., et al. (2008). Corpus callosum in maltreated children with posttraumatic stress disorder: a diffusion tensor imaging study. *Psychiatry Res.* 162, 256–261. doi: 10.1016/j.pscychresns.2007.08.006

Jenkinson, M., and Smith, S. (2001). A global optimisation method for robust affine registration of brain images. *Med. Image. Anal.* 5, 143–156. doi: 10.1016/S1361-8415(01)00036-6

Jensen, J. H., and Helpern, J. A. (2010). MRI quantification of non-gaussian water diffusion by kurtosis analysis. *NMR Biomed.* 23, 698–710. doi: 10.1002/nbm.1518

Jensen, S. K. G., Pangelinan, M., Bjornholm, L., Klasnja, A., Leemans, A., Drakesmith, M., et al. (2018). Associations between prenatal, childhood, and adolescent stress and variations in white-matter properties in young men. *Neuroimage* 182, 389–397. doi: 10.1016/j.neuroimage.2017.10.033

Kaller, M. S., Lazari, A., Blanco-Duque, C., Sampaio-Baptista, C., and Johansen-Berg, H. (2017). Myelin plasticity and behaviour-connecting the dots. *Curr. Opin. Neurobiol.* 47, 86–92. doi: 10.1016/j.conb.2017.09.014

Katz, R. J., Roth, K. A., and Carroll, B. J. (1981). Acute and chronic stress effects on open field activity in the rat: implications for a model of depression. *Neurosci. Biobehav. Rev.* 5, 247–251. doi: 10.1016/0149-7634(81)90005-1

Kelly, S., Jahanshad, N., Zalesky, A., Kochunov, P., Agartz, I., Alloza, C., et al. (2018). Widespread white matter microstructural differences in schizophrenia across 4322 individuals: results from the ENIGMA schizophrenia DTI working group. *Mol. Psychiatry* 23, 1261–1269. doi: 10.1038/mp.2017.170

Kendler, K. S., Karkowski, L. M., and Prescott, C. A. (1999). Causal relationship between stressful life events and the onset of major depression. *Am. J. Psychiatry* 156, 837–841. doi: 10.1176/ajp.156.6.837

Khan, A. R., Chuhutin, A., Wiborg, O., Kroenke, C. D., Nyengaard, J. R., Hansen, B., et al. (2016a). Biophysical modeling of high field diffusion MRI demonstrates micro-structural aberration in chronic mild stress rat brain. *Neuroimage* 142, 421–430. doi: 10.1016/j.neuroimage.2016.07.001

Khan, A. R., Chuhutin, A., Wiborg, O., Kroenke, C. D., Nyengaard, J. R., Hansen, B., et al. (2016b). Summary of high field diffusion MRI and microscopy data demonstrate microstructural aberration in chronic mild stress rat brain. *Data Brief.* 8, 934–937. doi: 10.1016/j.dib.2016.06.061

Khan, A. R., Hansen, B., Danladi, J., Chuhutin, A., Wiborg, O., Nyengaard, J. R., et al. (2019). Neurite atrophy in dorsal hippocampus of rat indicates incomplete recovery of chronic mild stress induced depression. *NMR Biomed.* 32:e4057. doi: 10.1002/nbm.4057

Khan, A. R., Hansen, B., Wiborg, O., Kroenke, C. D., and Jespersen, S. N. (2018). Diffusion MRI and MR spectroscopy reveal microstructural and metabolic brain alterations in chronic mild stress exposed rats: a CMS recovery study. *Neuroimage* 167, 342–353. doi: 10.1016/j.neuroimage.2017.11.053

Kim, P., Evans, G. W., Angstadt, M., Ho, S. S., Sripada, C. S., Swain, J. E., et al. (2013). Effects of childhood poverty and chronic stress on emotion regulatory brain function in adulthood. *Proc. Natl. Acad. Sci. U. S. A.* 110, 18442–18447. doi: 10.1073/pnas.1308240110

Kitayama, I., Yaga, T., Kayahara, T., Nakano, K., Murase, S., Otani, M., et al. (1997). Long-term stress degenerates, but imipramine regenerates, noradrenergic axons in the rat cerebral cortex. *Biol. Psychiatry* 42, 687–696. doi: 10.1016/S0006-3223(96)00502-1

Koshiyama, D., Fukunaga, M., Okada, N., Morita, K., Nemoto, K., Usui, K., et al. (2019). White matter microstructural alterations across four major psychiatric disorders: mega-analysis study in 2937 individuals. *Mol. Psychiatry*. 25, 883–895. doi: 10.1038/s41380-019-0553-7

Kulikova, S., Hertz-Pannier, L., Dehaene-Lambertz, G., Buzmakov, A., Poupon, C., and Dubois, J. (2015). Multi-parametric evaluation of the white matter maturation. *Brain Struct. Funct.* 220, 3657–3672. doi: 10.1007/s00429-014-0881-y

Lanius, R. A., Vermetten, E., and Pain, C. (2010). *The Impact of Early Life Trauma on Health and Disease : the Hidden Epidemic. Cambridge, UK; New York: Cambridge University Press*. doi: 10.1017/CBO9780511777042

Lebel, C., Gee, M., Camicioli, R., Wieler, M., Martin, W., and Beaulieu, C. (2012). Diffusion tensor imaging of white matter tract evolution over the lifespan. *Neuroimage* 60, 340–352. doi: 10.1016/j.neuroimage.2011.11.094

Lehmann, M. L., Weigel, T. K., Elkahloun, A. G., and Herkenham, M. (2017). Chronic social defeat reduces myelination in the mouse medial prefrontal cortex. *Sci. Rep.* 7:46548. doi: 10.1038/srep46548

Li, Y., Zhu, X., Ju, S., Yan, J., Wang, D., Zhu, Y., et al. (2017). Detection of volume alterations in hippocampal subfields of rats under chronic unpredictable mild stress using 7T MRI: A follow-up study. *J. Magn. Reson. Imaging* 46, 1456–1463. doi: 10.1002/jmri.25667

Liu, J., Dietz, K., Hodes, G. E., Russo, S. J., and Casaccia, P. (2018). Widespread transcriptional alternations in oligodendrocytes in the adult mouse brain following chronic stress. *Dev. Neurobiol.* 78, 152–162. doi: 10.1002/dneu.22533

Liu, X., Yuan, J., Guang, Y., Wang, X., and Feng, Z. (2018). Longitudinal *in vivo* diffusion tensor imaging detects differential microstructural alterations in the hippocampus of chronic social defeat stress-susceptible and resilient mice. *Front. Neurosci.* 12:613. doi: 10.3389/fnins.2018.00613

Lucassen, P. J., Pruessner, J., Sousa, N., Almeida, O. F., Van Dam, A. M., Rajkowska, G., et al. (2014). Neuropathology of stress. *Acta Neuropathol.* 127, 109–135. doi: 10.1007/s00401-013-1223-5

Lupien, S. J., Juster, R. P., Raymond, C., and Marin, M. F. (2018). The effects of chronic stress on the human brain: from neurotoxicity, to vulnerability, to opportunity. *Front. Neuroendocrinol.* 49, 91–105. doi: 10.1016/j.yfrne.2018.02.001

MacQueen, G., and Frodl, T. (2011). The hippocampus in major depression: evidence for the convergence of the bench and bedside in psychiatric research? *Mol. Psychiatry* 16, 252–264. doi: 10.1038/mp.2010.80

Magalhaes, R., Barriere, D. A., Novais, A., Marques, F., Marques, P., Cerqueira, J., et al. (2018). The dynamics of stress: a longitudinal MRI study of rat brain structure and connectome. *Mol. Psychiatry* 23, 1998–2006. doi: 10.1038/mp.2017.244

Magalhaes, R., Bourgin, J., Boumezbeur, F., Marques, P., Bottlaender, M., Poupon, C., et al. (2017). White matter changes in microstructure associated with a maladaptive response to stress in rats. *Transl. Psychiatry* 7:e1009. doi: 10.1038/tp.2016.283

Magalhaes, R., Novais, A., Barriere, D. A., Marques, P., Marques, F., Sousa, J. C., et al. (2019). A resting-state functional MR imaging and spectroscopy study of the dorsal hippocampus in the chronic unpredictable stress rat model. *J. Neurosci.* 39, 3640–3650. doi: 10.1523/JNEUROSCI.2192-18.2019

Magarinos, A. M., McEwen, B. S., Flugge, G., and Fuchs, E. (1996). Chronic psychosocial stress causes apical dendritic atrophy of hippocampal CA3 pyramidal neurons in subordinate tree shrews. *J. Neurosci.* 16, 3534–3540. doi: 10.1523/JNEUROSCI.16-10-03534.1996

Maras, P. M., Molet, J., Chen, Y., Rice, C., Ji, S. G., Solodkin, A., et al. (2014). Preferential loss of dorsal-hippocampus synapses underlies memory impairments provoked by short, multimodal stress. *Mol. Psychiatry* 19, 811–822. doi: 10.1038/mp.2014.12

McCormick, C. M., Green, M. R., and Simone, J. J. (2017). Translational relevance of rodent models of hypothalamic-pituitary-adrenal function and stressors in adolescence. *Neurobiol. Stress* 6, 31–43. doi: 10.1016/j.ynstr.2016.08.003

McCormick, C. M., Mathews, I. Z., Thomas, C., and Waters, P. (2010). Investigations of HPA function and the enduring consequences of stressors in adolescence in animal models. *Brain Cogn.* 72, 73–85. doi: 10.1016/j.bandc.2009.06.003

McEwen, B. S. (1998). Stress, adaptation, and disease. *Allostasis and allostatic load. Ann. N. Y. Acad. Sci.* 840, 33–44. doi: 10.1111/j.1749-6632.1998.tb09546.x

McEwen, B. S., Bowles, N. P., Gray, J. D., Hill, M. N., Hunter, R. G., Karatsoreos, I. N., et al. (2015). Mechanisms of stress in the brain. *Nat. Neurosci.* 18, 1353–1363. doi: 10.1038/nn.4086

McEwen, B. S., Nasca, C., and Gray, J. D. (2016). Stress effects on neuronal structure: hippocampus, amygdala, and prefrontal cortex. *Neuropsychopharmacology* 41, 3–23. doi: 10.1038/npp.2015.171

McLaughlin, K. J., Gomez, J. L., Baran, S. E., and Conrad, C. D. (2007). The effects of chronic stress on hippocampal morphology and function: an evaluation of chronic restraint paradigms. *Brain Res.* 1161, 56–64. doi: 10.1016/j.brainres.2007.05.042

Mengler, L., Khmelinskii, A., Diedenhofen, M., Po, C., Staring, M., Lelieveldt, B. P., et al. (2014). Brain maturation of the adolescent rat cortex and striatum: changes in volume and myelination. *Neuroimage* 84, 35–44. doi: 10.1016/j.neuroimage.2013.08.034

Miyata, S., Taniguchi, M., Koyama, Y., Shimizu, S., Tanaka, T., Yasuno, F., et al. (2016). Association between chronic stress-induced structural abnormalities in Ranvier nodes and reduced oligodendrocyte activity in major depression. *Sci. Rep.* 6:23084. doi: 10.1038/srep23084

Nasrallah, F. A., To, X. V., Chen, D. Y., Routtenberg, A., and Chuang, K. H. (2016). Functional connectivity MRI tracks memory networks after maze learning in rodents. *Neuroimage* 127, 196–202. doi: 10.1016/j.neuroimage.2015.08.013

Nugent, A. C., Farmer, C., Evans, J. W., Snider, S. L., Banerjee, D., and Zarate, C. A. Jr. (2019). Multimodal imaging reveals a complex pattern of dysfunction in corticolimbic pathways in major depressive disorder. *Hum. Brain Mapp.* 40, 3940–3950. doi: 10.1002/hbm.24679

O'Doherty, D. C. M., Ryder, W., Paquola, C., Tickell, A., Chan, C., Hermens, D. F., et al. (2018). White matter integrity alterations in post-traumatic stress disorder. *Hum. Brain Mapp.* 39, 1327–1338. doi: 10.1002/hbm.23920

Perez-Cruz, C., Simon, M., Czeh, B., Flugge, G., and Fuchs, E. (2009a). Hemispheric differences in basilar dendrites and spines of pyramidal neurons in the rat prelimbic cortex: activity- and stress-induced changes. *Eur. J. Neurosci.* 29, 738–747. doi: 10.1111/j.1460-9568.2009.06622.x

Perez-Cruz, C., Simon, M., Flugge, G., Fuchs, E., and Czeh, B. (2009b). Diurnal rhythm and stress regulate dendritic architecture and spine density of pyramidal neurons in the rat infralimbic cortex. *Behav. Brain Res.* 205, 406–413. doi: 10.1016/j.bbr.2009.07.021

Pittenger, C., and Duman, R. S. (2008). Stress, depression, and neuroplasticity: a convergence of mechanisms. *Neuropsychopharmacology* 33, 88–109. doi: 10.1038/sj.npp.1301574

Popoli, M., Yan, Z., McEwen, B. S., and Sanacora, G. (2011). The stressed synapse: the impact of stress and glucocorticoids on glutamate transmission. *Nat. Rev. Neurosci.* 13, 22–37. doi: 10.1038/nrn3138

Radley, J. J., Sisti, H. M., Hao, J., Rocher, A. B., McCall, T., Hof, P. R., et al. (2004). Chronic behavioral stress induces apical dendritic reorganization in pyramidal neurons of the medial prefrontal cortex. *Neuroscience* 125, 1–6. doi: 10.1016/j.neuroscience.2004.01.006

Rinne-Albers, M. A., van der Werff, S. J., van Hoof, M. J., van Lang, N. D., Lamers-Winkelman, F., Rombouts, S. A., et al. (2016). Abnormalities of white matter integrity in the corpus callosum of adolescents with PTSD after childhood sexual abuse: a DTI study. *Eur. Child Adolesc. Psychiatry* 25, 869–878. doi: 10.1007/s00787-015-0805-2

Romeo, R. D., Patel, R., Pham, L., and So, V. M. (2016). Adolescence and the ontogeny of the hormonal stress response in male and female rats and mice. *Neurosci. Biobehav. Rev.* 70, 206–216. doi: 10.1016/j.neubiorev.2016.05.020

Rumple, A., McMurray, M., Johns, J., Lauder, J., Makam, P., Radcliffe, M., et al. (2013). 3-dimensional diffusion tensor imaging (DTI) atlas of the rat brain. *PLoS ONE* 8:e67334. doi: 10.1371/journal.pone.0067334

Rygula, R., Abumaria, N., Flugge, G., Fuchs, E., Ruther, E., and Havemann-Reinecke, U. (2005). Anhedonia and motivational deficits in rats: impact of chronic social stress. *Behav. Brain Res.* 162, 127–134. doi: 10.1016/j.bbr.2005.03.009

Sandi, C., Davies, H. A., Cordero, M. I., Rodriguez, J. J., Popov, V. I., and Stewart, M. G. (2003). Rapid reversal of stress induced loss of synapses in CA3 of rat hippocampus following water maze training. *Eur. J. Neurosci.* 17, 2447–2456. doi: 10.1046/j.1460-9568.2003.02675.x

Siehl, S., King, J. A., Burgess, N., Flor, H., and Nees, F. (2018). Structural white matter changes in adults and children with posttraumatic stress disorder: a systematic review and meta-analysis. *Neuroimage Clin.* 19, 581–598. doi: 10.1016/j.nicl.2018.05.013

Smith, S. M. (2002). Fast robust automated brain extraction. *Hum. Brain Mapp.* 17, 143–155. doi: 10.1002/hbm.10062

Sousa, N. (2016). The dynamics of the stress neuromatrix. *Mol. Psychiatry* 21, 302–312. doi: 10.1038/mp.2015.196

Spear, L. P. (2000). The adolescent brain and age-related behavioral manifestations. *Neurosci. Biobehav. Rev.* 24, 417–463. doi: 10.1016/S0149-7634(00)00014-2

Steptoe, A., and Kivimaki, M. (2012). Stress and cardiovascular disease. *Nat. Rev. Cardiol.* 9, 360–370. doi: 10.1038/nrcardio.2012.45

Teicher, M. H., Dumont, N. L., Ito, Y., Vaituzis, C., Giedd, J. N., and Andersen, S. L. (2004). Childhood neglect is associated with reduced corpus callosum area. *Biol. Psychiatry* 56, 80–85. doi: 10.1016/j.biopsych.2004.03.016

Tirelli, E., Laviola, G., and Adriani, W. (2003). Ontogenesis of behavioral sensitization and conditioned place preference induced by psychostimulants in laboratory rodents. *Neurosci. Biobehav. Rev.* 27, 163–178. doi: 10.1016/S0149-7634(03)00018-6

Tuch, D. S. (2004). Q-ball imaging. *Magn. Reson. Med.* 52, 1358–1372. doi: 10.1002/mrm.20279

van Velzen, L. S., Kelly, S., Isaev, D., Aleman, A., Aftanas, L. I., Bauer, J., et al. (2019). White matter disturbances in major depressive disorder: a coordinated analysis across 20 international cohorts in the ENIGMA MDD working group. *Mo.l Psychiatry* doi: 10.1038/s41380-019-0477-2. [Epub ahead of print].

Veena, J., Srikumar, B. N., Raju, T. R., and Shankaranarayana Rao, B. S. (2009). Exposure to enriched environment restores the survival and differentiation of new born cells in the hippocampus and ameliorates depressive symptoms in chronically stressed rats. *Neurosci. Lett.* 455, 178–182. doi: 10.1016/j.neulet.2009.03.059

Vestergaard-Poulsen, P., Wegener, G., Hansen, B., Bjarkam, C. R., Blackband, S. J., Nielsen, N. C., et al. (2011). Diffusion-weighted MRI and quantitative biophysical modeling of hippocampal neurite loss in chronic stress. *PLoS ONE* 6:e20653. doi: 10.1371/journal.pone.0020653

Wedeen, V. J., Hagmann, P., Tseng, W. Y., Reese, T. G., and Weisskoff, R. M. (2005). Mapping complex tissue architecture with diffusion spectrum magnetic resonance imaging. *Magn. Reson. Med.* 54, 1377–1386. doi: 10.1002/mrm.20642

Willner, P. (1997). Validity, reliability and utility of the chronic mild stress model of depression: a 10-year review and evaluation. *Psychopharmacology (Berl)* 134, 319–329. doi: 10.1007/s002130050456

Yang, Y., Zhang, Y., Luo, F., and Li, B. (2016). Chronic stress regulates $NG2^{+}$ cell maturation and myelination in the prefrontal cortex through induction of death receptor 6. *Exp. Neurol.* 277, 202–214. doi: 10.1016/j.expneurol.2016.01.003

Yoshida, S., Oishi, K., Faria, A. V., and Mori, S. (2013). Diffusion tensor imaging of normal brain development. *Pediatr. Radiol.* 43, 15–27. doi: 10.1007/s00247-012-2496-x

Zalsman, G., Weller, A., Shbiro, L., Barzilay, R., Gutman, A., Weizman, A., et al. (2017). Fibre tract analysis using diffusion tensor imaging reveals aberrant connectivity in a rat model of depression. *World J. Biol. Psychiatry* 18, 615–623. doi: 10.1080/15622975.2016.1190866

Zatorre, R. J., Fields, R. D., and Johansen-Berg, H. (2012). Plasticity in gray and white: neuroimaging changes in brain structure during learning. *Nat. Neurosci.* 15, 528–536. doi: 10.1038/nn.3045

Conflict of Interest: The authors declare that the research was conducted in the absence of any commercial or financial relationships that could be construed as a potential conflict of interest.

frontiers in Neuroscience

REVIEW
published: 14 July 2020
doi: 10.3389/fnins.2020.00682

Elucidating the Relationship Between Diabetes Mellitus and Parkinson's Disease Using ^{18}F-FP-(+)-DTBZ, a Positron-Emission Tomography Probe for Vesicular Monoamine Transporter 2

Yanyan Kong[1], Haicong Zhou[2], Hu Feng[2], Junyi Zhuang[2], Tieqiao Wen[2], Chencheng Zhang[3], Bomin Sun[3], Jiao Wang[2]* and Yihui Guan[1]**

[1] PET Center, Huashan Hospital, Fudan University, Shanghai, China, [2] Laboratory of Molecular Neural Biology, School of Life Sciences, Shanghai University, Shanghai, China, [3] Department of Neurosurgery, Ruijin Hospital, Shanghai Jiao Tong University School of Medicine, Shanghai, China

OPEN ACCESS

Edited by:
Nicola Toschi,
University of Rome Tor Vergata, Italy

Reviewed by:
Chengxiang Qiu,
University of Washington, United States
Delia Cabrera DeBuc,
University of Miami, United States

***Correspondence:**
Bomin Sun
sbm11224@rjh.com.cn
Jiao Wang
jo717@shu.edu.cn
Yihui Guan
guanyihui@hotmail.com

Specialty section:
This article was submitted to Brain Imaging Methods, a section of the journal Frontiers in Neuroscience

Received: 08 March 2020
Accepted: 03 June 2020
Published: 14 July 2020

Citation:
Kong Y, Zhou H, Feng H, Zhuang J, Wen T, Zhang C, Sun B, Wang J and Guan Y (2020) Elucidating the Relationship Between Diabetes Mellitus and Parkinson's Disease Using ^{18}F-FP-(+)-DTBZ, a Positron-Emission Tomography Probe for Vesicular Monoamine Transporter 2. Front. Neurosci. 14:682. doi: 10.3389/fnins.2020.00682

Diabetes mellitus (DM) and Parkinson's disease (PD) have been and will continue to be two common chronic diseases globally that are difficult to diagnose during the prodromal phase. Current molecular genetics, cell biological, and epidemiological evidences have shown the correlation between PD and DM. PD shares the same pathogenesis pathways and pathological factors with DM. In addition, β-cell reduction, which can cause hyperglycemia, is a striking feature of DM. Recent studies indicated that hyperglycemia is highly relevant to the pathologic changes in PD. However, further correlation between DM and PD remains to be investigated. Intriguingly, polycystic monoamine transporter 2 (VMAT2), which is co-expressed in dopaminergic neurons and β cells, is responsible for taking up dopamine into the presynaptic vesicles and can specifically bind to the β cells. Furthermore, we have summarized the specific molecular and diagnostic functions of VMAT2 for the two diseases reported in this review. Therefore, VMAT2 can be applied as a target probe for positron emission tomography (PET) imaging to detect β-cell and dopamine level changes, which can contribute to the diagnosis of DM and PD during the prodromal phase. Targeting VMAT2 with the molecular probe ^{18}F-FP-(+)-DTBZ can be an entry point for the β cell mass (BCM) changes in DM at the molecular level, to clarify the potential relationship between DM and PD. VMAT2 has promising clinical significance in investigating the pathogenesis, early diagnosis, and treatment evaluation of the two diseases.

Keywords: diabetes mellitus, β-cell mass, Parkinson's disease, dopamine, VMAT2

Abbreviations: ^{11}C-CFT, ^{11}C-methyl-N-2b-carbomethoxy-3b-(4-fluorophenyl) tropane; ^{11}C-DTBZ, ^{11}C-dihydrotetrabenazine; ^{11}C-DTBZ, ^{11}C-dihydrotetrabenazine; ^{11}C-RAC, ^{11}C-raclopride; ^{18}F-DOPA, L-3,4-dihydroxy-6-^{18}F-fluorophenylalanine; ^{18}F-FP-(+)-DTBZ, ^{18}F-fluoropropyl-(+)-dihydrotetrabenazine; AADC, L-aromatic amino acid decarboxylase; BCM, β cell mass; DA, dopamine; DAT, dopamine transporter; DM, diabetes mellitus; DTBZ, dihydrotetrabenazine; PD, Parkinson's disease; PET, positron-emission tomography; SUVR, standardized uptake value ratio; T1DM, type 1 DM; T2DM, type 2 DM; TH, tyrosine hydroxylase; VMAT2, vesicular monoamine transporter-2.

INTRODUCTION

Parkinson's disease (PD) is the most common progressive neurodegenerative disorder and is characterized by severe motor and non-motor symptoms including uncontrollable tremor, bradykinesia, rigidity, and sleep disturbances. More than 6 million individuals worldwide have PD (Armstrong and Okun, 2020). However, in the prodromal phase, diagnosis based on the clinical profiles is difficult. Diabetes mellitus (DM) is a metabolic disorder characterized by an absolute or relative deficiency of β cell mass (BCM), which manifests as persistent hyperglycemia (Jonietz, 2012; Cinti et al., 2016). DM can be largely classified into type I and type II. According to a 2019 epidemiological survey, the global prevalence of diabetes was an estimated 9.3% (463 million people) at publication, and it was predicted to rise to 10.2% (578 million) by 2030 and 10.9% (700 million) by 2045. The prevailing evidence points to diabetes accounting for a considerable global burden of chronic illness in aging societies (Saeedi et al., 2019; Sinclair et al., 2020).

Both PD and DM are highly prevalent. Previous research suggests that DM predisposes toward a Parkinson-like pathology and induces a more aggressive phenotype in patients already ill with PD (Pagano et al., 2018). In addition, studies have shown that these two diseases exhibit common pathogenic and pathological changes. Moreover, studies have demonstrated that hyperglycemia, which is caused by decreased BCM in DM patients, may lead to the occurrence of PD or aggravate PD symptoms.

The β-cell marker, vesicular monoamine transporter-2 (VMAT2), is closely linked to the occurrence of PD. Therefore, detecting progressive changes in BCM can both assist in the diagnosis of PD and clarify the pathogenesis of DM. Positron–emission tomography (PET) imaging using probes targeting VMAT2 has been applied to the diagnosis of PD and DM. Because of the low abundance of β cells, researchers use a notably sensitive tracer, an ^{18}F-labeled dihydrotetrabenazine derivative (^{18}F-FP-(+)-DTBZ), in their study (Wu et al., 2015). Researchers have used VMAT2 imaging with ^{18}F-FP-(+)-DTBZ to identify DM as a risk factor for PD. In summary, this probe may, in the future, reveal the pathogenesis of DM and permit the early diagnosis of PD.

MOLECULAR GENETICS, CELL BIOLOGY, AND EPIDEMIOLOGY: CORRELATION BETWEEN PD AND DM

Studies in molecular genetics, cell biology, and epidemiology have shown that the pathogeneses of PD and DM have common characteristics. Approximately 60% of patients with PD have impaired insulin signaling and impaired glucose tolerance (Santiago and Potashkin, 2014). Moreover, 62% of patients with PD and dementia have insulin resistance, and 30% of these patients also have impaired glucose tolerance (Bosco et al., 2012). PD is aggravated if the onset of comorbid DM is earlier than that of PD (Cereda et al., 2012). In the pathogenesis and progression of PD and DM, insulin and dopamine are regulated mutually, and hypoinsulinemia induced by streptozotocin can reduce the levels of dopamine transporter (DAT) and tyrosine hydroxylase (TH) transcription in the substantia nigra pars compacta (Lima et al., 2014). In addition, reduction of dopamine in the striatum can attenuate insulin signaling in the basal ganglia region. Pathways common to both diseases are mitochondrial dysfunction, endoplasmic reticulum stress, inflammatory response, vitamin D deficiency, and ubiquitin-protease/autophagy-lysosomal-system dysfunction (**Table 1**). Peroxisome proliferator-activated receptor gamma coactivator 1-alpha (PGC-1α) is a key regulator of the enzymes involved in the mitochondrial respiratory chain and of insulin resistance and plays an important role in the pathogenesis of both DM and PD. In addition, ATP-sensitive K^+ channels, AMP-activated protein kinases, glucagon-like peptide-1, and dipeptidyl peptidase enzyme 4 show common pathological changes in DM and PD. Hyperglycemia can cause disturbances in the energy metabolism in the brain, damage neurons through various injury mechanisms, and lead to abnormal expression of proteins in the striatum and hippocampus. Consequently, recent studies have focused on the relationship between PD and hyperglycemia. One study found that thioredoxin-interacting protein (TXNIP), an endogenous inhibitor of reactive oxygen species elimination, regulates Parkin/PINK1-mediated mitophagy in dopaminergic

TABLE 1 | Common pathogenesis pathways in Parkinson's disease (PD) and diabetes mellitus (DM).

Common pathways	Pathogenesis of PD	Pathogenesis of DM
Mitochondrial dysfunction (Bonnard et al., 2008; Parker et al., 2008)	Increased ROS production—damage to lipids, protein, and DNA. Endoplasmic reticulum stress.	Increased ROS production, lipid accumulation. Endoplasmic reticulum stress. Insulin resistance.
Autophagy (Webb et al., 2003; Cuervo et al., 2004; Matos et al., 2018)	α-Synuclein aggregation. Lipid accumulation	Inclusion bodies in the liver and pancreas
Inflammatory response (Allan and Rothwell, 2001; Chen et al., 2008; Sun et al., 2011)	Increased production of cytokines IL-1β and TNF-α. Anti-inflammatory treatments are neuroprotective.	Chronic inflammation increases risk of diabetes. Anti-inflammatory treatments improve insulin resistance.
Metabolism (Moroo et al., 1994; Ogama et al., 2018; Ter Horst et al., 2018; Wang et al., 2020)	60–80% of PD patients exhibit impaired glucose tolerance. Dopamine release is glucose sensitive Loss of insulin-receptor immunoreactivity in the substantia nigra.	Insulin resistance is associated with cognitive decline. Peripheral insulin resistance leads to ischemic cerebrovascular disease. Hyperglycemia is associated with neurodegeneration.
Vitamin D deficiency (Derex and Trouillas, 1997; Boucher et al., 2004; Evatt et al., 2008)	Reduced vitamin D levels increase the risk of PD. Vitamin D improves motor function in human PD	Reduced vitamin D levels increase the risk of diabetes. Vitamin D improves insulin resistance in diabetes.

neurons under high-glucose conditions (Su et al., 2020), which revealed the neuronal impact of mitochondrial dysfunction caused by hyperglycemia and hyperglycemia-induced oxidative stress. In addition, the preferential occurrence of nigrostriatal dopaminergic neurodegeneration in long-term hyperglycemia suggests that hyperglycemia causes premature aging of the central nervous system, fostering the development of age-related neurodegenerative diseases (Renaud et al., 2018). However, these studies did not sufficiently clarify the molecular link between hyperglycemia and PD. Further research on this topic will help elucidate the pathogenesis of PD, which is important for better clinical diagnosis, prevention, and treatment.

Both type 2 diabetes (T2DM) and PD are involved in the accumulation of misfolded proteins in amyloid aggregates. In diabetic patients, the accumulation of islet amyloid polypeptide (IAPP) in pancreatic cells can cause cell dysfunction. In patients with PD, α-synuclein eventually aggregates into the Lewy bodies (Wang and Raleigh, 2014; Bridi and Hirth, 2018). Researchers have found that IAPP and α-synuclein cross-interact in the two diseases, and IAPP in patients with T2DM can promote α-synuclein aggregation, which leads to the occurrence of PD (Horvath and Wittung-Stafshede, 2016). Another study showed that insulin-degrading enzymes (IDE) can bind to synuclein oligomers to prevent further aggregation. Moreover, insulin resistance can inhibit IDE and promote the formation of α-synuclein fibrils, which may enhance PD progression (Sharma et al., 2015).

1-Methyl-4-phenyl-1,2,3,6-tetrahydropyridine (MPTP) can lead to neuronal death by inhibiting the mitochondrial respiratory chain enzyme, which is a PD animal model inducer (Jing et al., 2017). In addition, studies have shown that mitochondrial dysfunction occurs in patients with DM and PD, and insulin resistance in diabetic mice can lead to mitochondrial destruction and dopaminergic neuron degeneration (Khang et al., 2015).

According to many case–control studies, longitudinal studies, and meta-analyses, DM is a risk factor for PD (some of these results are shown in **Table 2**). DM can accelerate the development and progression of PD, especially in young women aged between 8 and 12 years (Sun et al., 2012; Aviles-Olmos et al., 2013a; Ahn et al., 2015; Santiago et al., 2017; Pagano et al., 2018). Several studies in the late 1990s showed that, in the diabetic mouse, the levels of DAT in the V9 and V10 regions (Del Pino et al., 2017) and in the medial forebrain bundle of the midbrain (Petrisic et al., 1997) were decreased significantly. A positive correlation was established between insulin reduction in DM and decreases in the levels of DAT, VMAT (mainly VMAT2), and TH. Insulin regulates DAT and VMAT2 levels through the PI3K/AKT pathway, and insulin deficiency leads to DAT and VMAT2 dysfunction. Dopamine D2 receptors can also regulate DAT and VMAT2 expression through the ERK signaling pathway (Carvelli et al., 2002; Owens et al., 2012; Samandari et al., 2013; Bini et al., 2019).

There are also other molecular targets that tightly link PD and DM. For example, glucose-dependent insulin-promoting polypeptide (GIP) is not only an endogenous hormone of the incretin family but also a neurotrophic factor. It activates cell proliferation and protects the neurons by promoting cell repair and preventing apoptosis, which enhances the survival ability of β-cells in the pancreas and neurons in the brain (Maino et al., 2014; Altmann et al., 2016). Besides, the GIP receptor is a G protein-coupled receptor that belongs to the glucagon family and increases insulin secretion during the onset of hyperglycemia

TABLE 2 | Recent studies on the correlation between diabetes mellitus (DM) and Parkinson's disease (PD).

Study	Study design	Sample size	Main results
Hu et al., 2007 (Hu et al., 2007)	Cohort	PD: 633 Controls: 51,552	T2DM is associated with an increased risk of PD.
Moran and Graeber, 2008 (Moran and Graeber, 2008)	Meta-analysis	N/A	Shared biological pathways between PD, T2DM, cancer, and inflammation.
D'Amelio et al., 2009 (D'Amelio et al., 2009)	Case–control	PD: 318 Controls: 318	Inverse association between PD and DM preceding PD onset.
Palacios et al., 2011 (Palacios et al., 2011)	Case–control	PD: 1931 Controls: 9651	T2DM is associated with an increased risk of PD, especially younger-onset PD.
Xu et al., 2011 (Xu et al., 2011)	Cohort	DM: 21,611 Controls: 267,051	T2DM is associated with an increased risk of PD.
Bosco et al., 2012 (Bosco et al., 2012)	Case–control	PD+dementia: 53 PD: 57	Insulin resistance is associated with an increased risk of dementia in PD.
Sun et al., 2012 (Sun et al., 2012)	Case–control	DM: 603,416 Controls: 472,118	DM is associated with an increased risk of PD onset.
Wahlqvist et al., 2012 (Wahlqvist et al., 2012)	Case–control	DM: 64,166 Controls: 698,587	T2DM is associated with an increased risk of PD. Metformin-sulfonylurea therapy reduces the risk of PD.
Yue et al., 2016 (Yue et al., 2016)	Meta-analysis	Based studies: 7 Sample total: 1,761,632	Diabetes is associated with an ∼38% increase in the risk of PD.
De Pablo-Fernandez et al., 2017 (De Pablo-Fernandez et al., 2017)	Cohort	PD: 79 Controls: 4919	Diabetes duration might be an important factor in the association of PD and diabetes.
De Pablo-Fernandez et al., 2018 (De Pablo-Fernandez et al., 2018)	Cohort	DM: 2,017,115 Controls: 6,173,208	Significantly elevated rates of PD following T2DM.
Pagano et al., 2018 (Pagano et al., 2018)	Case–control	PD+DM: 25 PD without DM: 25 DM: 14 Controls: 14	DM may predispose toward a Parkinson-like pathology and, when present in patients with PD, can induce a more aggressive phenotype.

T2DM, type 2 diabetes mellitus.

(Park et al., 2013). In addition, studies have revealed that treatment with GIP analogs can increase the level of reduced TH in PD patients (Li et al., 2016).

Another incretin hormone, glucagon-like peptide-1 (GLP-1), which is functionally similar to GIP, also plays a role in DM and PD pathogenesis. The GLP-1 receptor agonists have been approved for the treatment of T2DM and have a good therapeutic effect on the clinical symptoms of PD including motor and cognitive dysfunctions. Their neuroprotective effect is shown in the protection of dopaminergic neurons in the substantia nigra, and they reduce the accumulation of synuclein proteins (Aviles-Olmos et al., 2013b; Ji et al., 2016). In addition, GLP-1 treatment reduces oxidative stress and lipid peroxidation and increases the level of brain-derived neurotrophic factor (BDNF), alleviating the symptoms of neuroinflammation in the brain (Li et al., 2017). Studies on the effects of GLP1 analogs on MPTP rodents have revealed that by inhibiting inflammation and excitatory cytokines and stimulating antioxidant enzymes, striatum dopamine levels can be improved and neuronal damage can be reduced (Elbassuoni and Ahmed, 2019).

After treatment with GLP1/GIP receptor agonists, TH in the brain increases and microglial activation decreases, promoting the production of dopamine and providing neuroprotection for dopaminergic neurons. These two peptides can be used as evidence for the connection between PD and DM.

Although these studies proved that DM is a risk factor for PD, the mechanistic basis of the relationship has not been fully elucidated. In addition, because a deficiency in BCM is the absolute or relative characteristic of DM, early, effective evaluation of BCM levels in patients with DM will be of great significance for the prevention, early diagnosis, and treatment of PD. VMAT2 is expressed in brain monoaminergic neurons, especially in the striatum, which is a regulator of monoaminergic neuronal function. Besides, VMAT2 is also a potential target for the assessment of BCM, and decreases in BCM level in the human pancreases correlate with decreases in insulin level in the blood (Anlauf et al., 2003; Fu et al., 2019). Jiang et al. (2020) found a decreased VMAT2 expression in the striatum due to the β-cell impairment in a type 1 DM (T1DM) rat model. Furthermore, VMAT2 expression in the striatum was also increased with the recovery of BCM and glucose levels in DM rats after streptozotocin injection treatment (Jiang et al., 2020). VMAT2 is, therefore, a key factor in connecting PD and DM.

Considering the correlation between DM and PD, researchers have employed a molecular imaging probe for VMAT2, the PET radioligand [18F]fluoropropyl-(+)-dihydrotetrabenazine (18F-FP-(+)-DTBZ or 18F-AV-133), as a molecular marker that can be used to objectively analyze dopamine and β cells.

VMAT2 FUNCTION AND ANATOMICAL DISTRIBUTION

VMAT2, a glycoprotein bound to secretory vesicle membranes and a constitutive protein in humans, is a subtype of the vesicle monoamine transporter (Stahl, 2018). A large number of studies have shown that VMAT2 is pivotal in the pathogenesis of PD (Ma et al., 2019; Shi et al., 2019), which is well known as a disease of dopamine deficiency. In endocrine islets, a large number of genes expressed by β cells have homologs in neural cells, one of which is VMAT2 (Harris et al., 2008). In 2003, Anlauf et al. (2003) determined the distribution of VMAT2 in human and monkey pancreas by immunohistochemistry and *in situ* hybridization. This was the first confirmation of VMAT2 localized in islet β cells. The monoamine neurotransmitters transported by VMAT2 are important paracrine and/or autocrine regulators of islet β cells and include dopamine, which inhibits insulin release via dopamine D2 receptors on β cells (Pecic et al., 2019). Recent studies have found that VMAT2 also mediates the release of the inhibitory neurotransmitter γ-aminobutyric acid (Tritsch et al., 2012), which plays a protective role by inhibiting β-cell apoptosis (Purwana et al., 2014). Exocytosis or endocytosis of the vesicles is important for the regulation of cellular signal transduction. Although glucose is an important factor in stimulating insulin secretion, VMAT2 also regulates glucose and insulin homeostasis (Raffo et al., 2008; Rodriguez-Diaz et al., 2011). Neuroendocrine cells accumulate biogenic amines and peptides, and the VMAT2 that they express serves to take up monoamines from the cytoplasm, which are then stored in the secretory vesicles for use in signaling (Bernstein et al., 2012). Accumulating evidence shows that VMAT2 is a contributor in PD progression (Ma et al., 2019; Shi et al., 2019). The accumulation of toxic α-synuclein in the prodromal phase of PD can impair VMAT2 activity, which eventually increases the cytosolic levels of dopamine (Bridi and Hirth, 2018). The metabolites of dopamine itself are cytotoxic; thus, an abnormal level of dopamine can exacerbate PD symptoms (Lotharius and Brundin, 2002). Moreover, disturbances of VMAT2 expression decrease neurogenesis in the olfactory nerve, causing hyposmia, which is another symptom of PD (Ma et al., 2019). It is known that the main histopathological change observed in PD is the selective degeneration of dopaminergic neurons in the substantia nigra pars compacta and of dopaminergic nerve endings in the striatum. A previous study identified a correlation between decreased striatal VMAT2 and multiple non-motor symptoms in patients with PD (Shi et al., 2019).

Furthermore, physiological effects of knocking out the VMAT2 mouse model were studied. Homozygous (VMAT2-/-) mice die within a few days after birth due to poor eating. The number of monoaminergic cells in the brain of knockout mice is lower than that of wild-type littermates (Fon et al., 1997). In addition, heterozygosity (VMAT2 +/−) shows low sensitization to dopamine agonist synaptic apomorphine, psychostimulant cocaine, and other neurotoxins (Wang et al., 1997). In VMAT2 knockout mice, disruption of vesicle trafficking leads to enhanced methamphetamine (METH)-induced dopaminergic neurotoxicity. METH produces greater dopamine consumption and metabolite content in the VMAT2 +/− striatum. DAT expression in the striatum of VAT2 +/− mice was further reduced, and the dopamine transporter content was lower than that of the wild type after treatment with METH (Fumagalli et al., 1999). Moreover, neurotoxin MPTP to heterozygotes' dopamine cells is more than two times lower than that in wild-type mice (Takahashi et al., 1997). These results suggest that monoamine

function, post-synaptic sensitization, and neurotoxin mechanism of action are linked to VMAT2 expression. In summary, VMAT2 may play an important role in the pathogenesis of PD.

T1DM is caused by the reductions in BCM due to an autoimmune reaction, resulting in an absolute deficiency of endogenous insulin secretion (Wilcox et al., 2016; Yu et al., 2019). T2DM stems from metabolic disorders and insulin resistance, and the toxic downstream effects of these metabolic disorders can further exacerbate BCM reduction by up to 60% (Ashcroft and Rorsman, 2012; Johnson and Olefsky, 2013; Derakhshan et al., 2015). Significant losses of BCM precede rises in blood glucose; therefore, an in-depth study of β-cell numbers can provide new clues to the pathology, early diagnosis, and treatment of DM. A non-invasive method for determining the residual BCM of patients with DM would be extremely useful. Great efforts have been devoted to improving the diagnostic accuracy of DM/BCM determination using highly β-cell-specific molecular imaging probes. Considering the necessity of tracking dynamic changes in BCM over time, PET imaging seems to be a feasible method for accessing BCM (Wei et al., 2019). Moreover, VMAT2 is one of the β-cell biomarkers, and the binding of VMAT2 with specific radioactive probe substances is well correlated with the amount of insulin secretion observed after a glucose challenge (Naganawa et al., 2018). Compared with the approach of directly determining insulin levels, determining VMAT2 as a proxy for BCM has the advantages of not being affected by insulin secretion, metabolism, inflammation, etc. (Freeby et al., 2012). In addition, multiple molecular probes are available for imaging β cells, including the voltage-dependent Ca^{2+} channel (VDCC), the glucose transporter (GLUT), the radiotracer ^{18}F-fluorodeoxyglucose (^{18}F-FDG), VMAT2, dihydrotetrabenazine (DTBZ), 5-hydroxytryptophan (5-HTP), and GPL-1 receptor (GLP-1R) (Wei et al., 2019). VMAT2 has high specific binding and a high density in β cells, which makes it a promising target for BCM imaging (Yang et al., 2017). Dopaminergic neuron damage in PD primarily begins with the nigrostriatal neurons, subsequently affecting the nigrostriatal pathway and finally the mesolimbic system. The striatum has the highest VMAT2 level (Hsiao et al., 2014). VMAT2 is located in the presynaptic neurons, which are responsible for storing and packing the neurotransmitter to regulate the cytoplasmic dopamine level (**Figure 1**; Hefti et al., 2010). Moreover, previous studies have delineated a strong correlation between the density of striatal VMAT2 and the non-motor symptoms of PD (Shi et al., 2019). Therefore, VMAT2 is promising as an imaging target for the diagnosis PD.

IMAGING THE MONOAMINERGIC SYSTEM: VMAT2

Role in PD Research

At present, the positron–emission molecular probes used in the diagnosis of PD mainly employ dopaminergic targets and are divided into presynaptic and post-synaptic imaging agents according to their binding targets. Targets on the presynaptic membrane include the following: (1) The dopamine transporter (DAT) of dopaminergic neurons, which transports DA from the synaptic gap back to the presynaptic compartment. Its signal is closely related to the number of dopaminergic neurons. Therefore, DAT imaging can assess the function of dopaminergic nerve endings. ^{11}C-methyl-N-2b-carbomethoxy-3b-(4-fluorophenyl)tropane (^{11}C-CFT) is a DAT radiotracer widely used in clinical practice. However, DAT is commonly downregulated in the early stages of disease, resulting in an overestimation of the amount of degeneration (Lee et al., 2000). (2) L-Aromatic amino acid decarboxylase (AADC) is one of the most important enzymes in dopamine synthesis, being responsible for converting levodopa into dopamine. The activity of AADC is measured by the tracer L-3,4-dihydroxy-6-^{18}F-fluorophenylalanine (^{18}F-DOPA) (Stormezand et al., 2020). (3) VMAT2 is responsible for taking up cytoplasmic dopamine into presynaptic vesicles. The main tracers used are ^{11}C-dihydrotetrabenazine (^{11}C-DTBZ) and ^{18}F-FP-(+)-DTBZ (Bohnen et al., 2006). Furthermore, post-synaptic dopamine receptors are mainly in the D1 family (D1 and D5) and D2 family (D2, D3, and D4). The main tracers used are ^{11}C-FLB 457, ^{18}F-fallypride, and ^{11}C-raclopride (^{11}C-RAC), which bind to D2 (Laruelle, 2000; Ray et al., 2012), and ^{11}C-PHNO, which binds to D3 (**Figure 2**; Payer et al., 2016).

The diagnostic imaging agent most used to assess DAT expression in cases of PD is ^{11}C-CFT, but its use is limited by the short half-life of ^{11}C (20 min). Recent studies have shown that, in the primate PD model, the changes in DAT and VMAT2 binding sites in the striatum of surviving substantia nigra neurons are similar, suggesting that targeting VMAT2 with the ^{18}F-labeled dihydrotetrabenazine derivative (^{18}F-FP-(+)-DTBZ) for imaging can provide results similar to those of the DAT imaging presently used to diagnose PD (Lin et al., 2014; Wood, 2014; Cho et al., 2019), but with the further advantage that ^{18}F-FP-(+)-DTBZ imaging can also be used to assess the severity of PD (Hsiao et al., 2014). Another advantage is that it is less affected by compensation or pharmacological regulation (Wilson and Kish, 1996).

^{18}F-FP-(+)-DTBZ in the Diagnosis of DM

^{11}C-Dihydrotetrabenazine (^{11}C-DTBZ) is a specific VMAT2 radioligand currently used in PD research and in clinical imaging of the brain for the diagnosis of PD (Lin et al., 2013). In rodents, a model of type-1 DM showed a good correlation between ^{11}C-DTBZ uptake in the pancreas and blood glucose homeostasis (Naganawa et al., 2016).

A limitation of PET technology in VMAT2 imaging is its low spatial resolution. Moreover, β cells account for a small proportion (1–2%) of the pancreas and are relatively dispersed. To overcome these challenges, it is necessary to further improve the signal-to-noise ratio of the images provided by the radiotracer. Therefore, the ^{18}F-labeled dihydrotetrabenazine derivative ^{18}F-FP-(+)-DTBZ (^{18}F-AV-133), which improves upon certain properties of ^{11}C-DTBZ, is preferred. Compared with ^{11}C-DTBZ, ^{18}F-FP-(+)-DTBZ has better affinity for VMAT2 and lower fat solubility, which translates into less non-specific binding (Wu et al., 2015). In addition, ^{18}F has a longer half-life than ^{11}C, making it suitable for a wider range of applications.

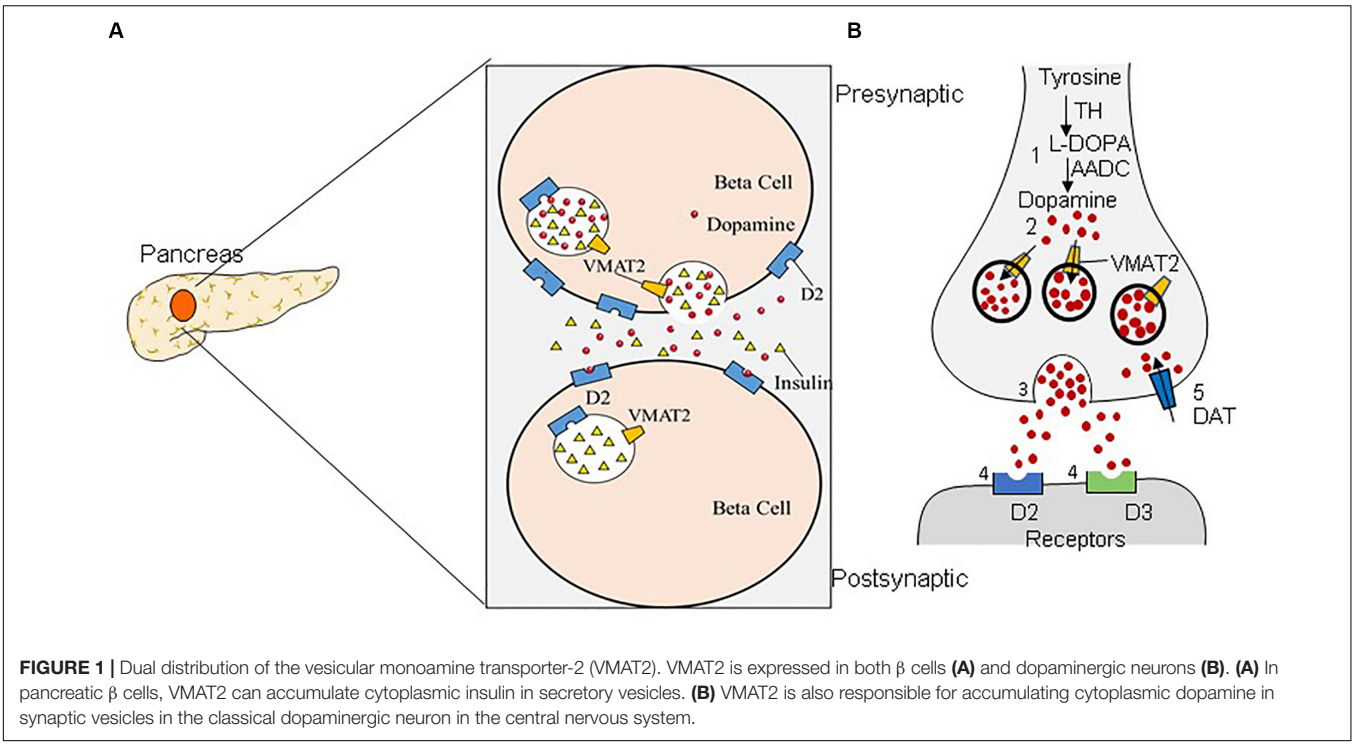

FIGURE 1 | Dual distribution of the vesicular monoamine transporter-2 (VMAT2). VMAT2 is expressed in both β cells **(A)** and dopaminergic neurons **(B)**. **(A)** In pancreatic β cells, VMAT2 can accumulate cytoplasmic insulin in secretory vesicles. **(B)** VMAT2 is also responsible for accumulating cytoplasmic dopamine in synaptic vesicles in the classical dopaminergic neuron in the central nervous system.

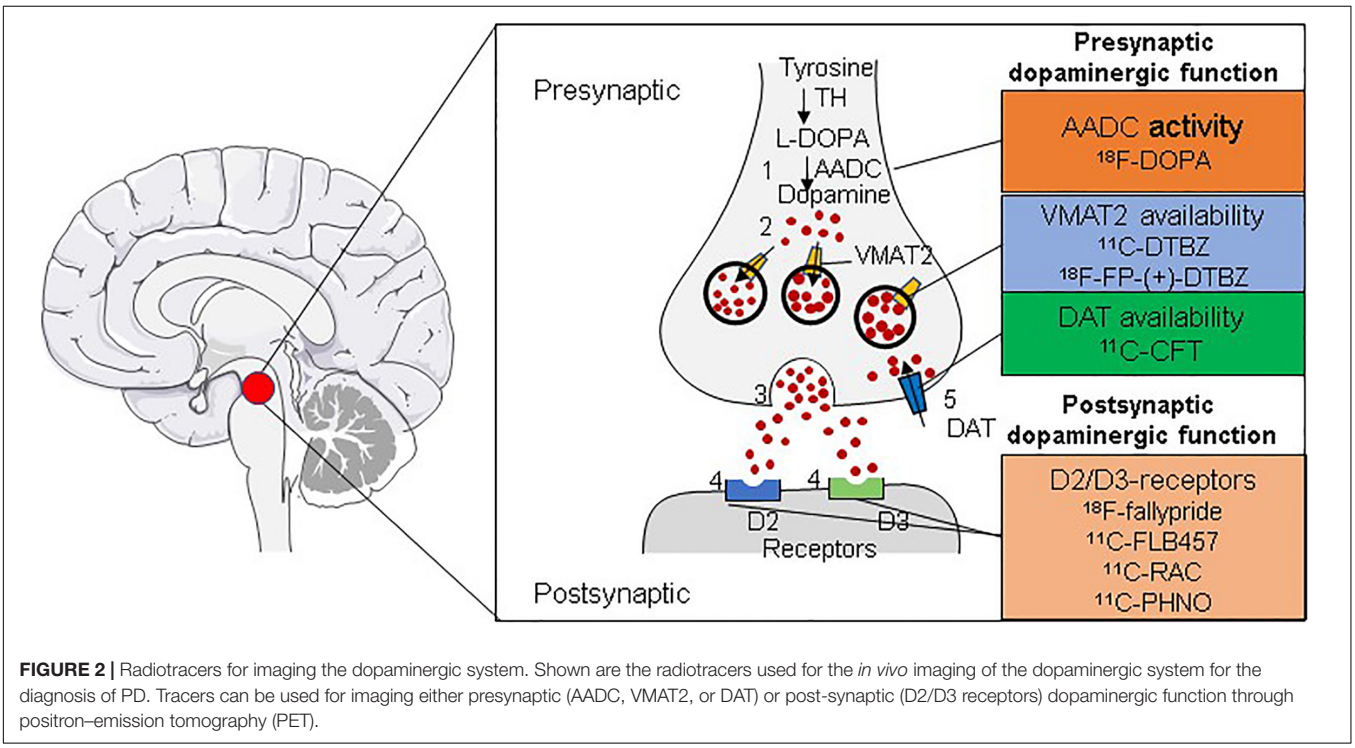

FIGURE 2 | Radiotracers for imaging the dopaminergic system. Shown are the radiotracers used for the *in vivo* imaging of the dopaminergic system for the diagnosis of PD. Tracers can be used for imaging either presynaptic (AADC, VMAT2, or DAT) or post-synaptic (D2/D3 receptors) dopaminergic function through positron–emission tomography (PET).

In the most recent primate experiments, the renal cortex, which contains no VMAT2, has been used as a control for non-specific binding in estimations of the specific binding ability of ^{18}F-FP-(+)-DTBZ to VMAT2. Recent experiments on sputum have confirmed that the probe's specific binding capacity to such samples can reach 85% of that in the striatum, and pancreatic BCM has been successfully reevaluated by PET scanning in humans (Naganawa et al., 2016). ^{18}F-FP-(+)-DTBZ can be both precise and accurate. A quantitative display of PET results, therefore, can be used as a non-invasive means to effectively quantify the BCM and thus the secretion of insulin, which has broad application in the diagnosis, treatment, and monitoring of

DM (Singhal et al., 2011). The ^{18}F-FP-(+)-DTBZ-standardized uptake value (SUV), the total volume of distribution, and the binding potential in the pancreas were shown to be reduced by 38, 20, and 40%, respectively, in patients with T1DM compared with those in healthy controls (Normandin et al., 2012). Moreover, the new procedure reduced the patient's exposure to radioactivity. In addition, the extent of tracer uptake correlated with the rate of insulin secretion. The PET Center of Huashan Hospital in China conducted a study in baboons on the use of ^{18}F-FP-(+)DTBZ for imaging the pancreas and reached similar conclusions (Naganawa et al., 2016).

VMAT2 Imaging Reveals a Correlation Between PD and DM

Using ^{18}F-FP-(+)DTBZ imaging of rat models of T1DM and T2DM, previous studies at the Huashan Hospital PET Center demonstrated that the uptake of ^{18}F-FP-(+)DTBZ in the striatum and the fasting blood glucose of the two groups were significantly negatively correlated. This indicates that BCM is closely related to VMAT2 expression in the brain. At the same time, T2DM caused a decrease in the expression of VMAT2 in the dopaminergic pathway in the brain. In addition, it was found that in the dopamine neurological abnormalities caused by T2DM, the abnormal expression of VMAT2 appeared earlier than that of DAT, and to a greater degree. These results suggest that DM and PD have a common pathogenesis.

Furthermore, imaging of the pancreas in patients with T1DM, patients with T2DM, and normal controls revealed that the uptake of ^{18}F-FP-(+)-DTBZ was significantly lower in T1DM and T2DM than in controls (**Figures 3**, **4**; Donglang et al., 2018; Jianfei et al., 2019). Quantification of ^{18}F-FP-(+)-DTBZ can be used to evaluate BCM in the pancreas of diabetic patients. ^{18}F-FP-(+)-DTBZ imaging in the caudate nucleus and putamen of patients with comorbid PD and T2DM showed that the standardized uptake value ratio (SUVR) of the caudate nucleus in the comorbid group was significantly lower than that of PD patients and normal controls. The SUVR was also lower in the putamen in the comorbid group than in PD patients. This result indicates that T2DM exacerbates the decline in VMAT2 expression in the caudate and putamen of the brain (**Figure 5**; Jiang et al., 2020). Previous clinical studies have also found that DM aggravates the symptoms of PD (Yue et al., 2016).

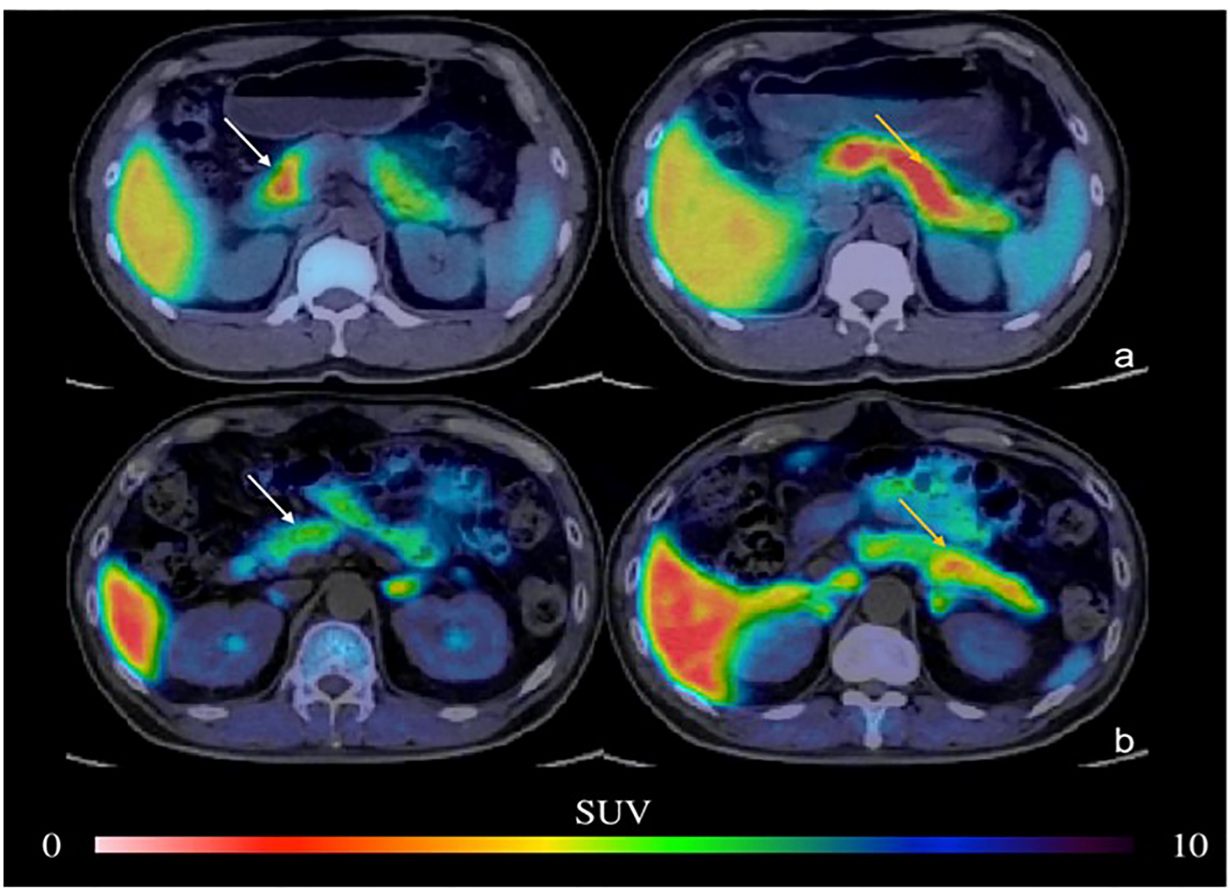

FIGURE 3 | PET imaging of the pancreas in type 2 DM (Donglang et al., 2018) (E-produced/adapted from Chin J Endocrinol Metab, used with permission) Representative PET imaging of the pancreatic head, body, and tail in the baboon in type 2 DM and in healthy controls. **(a)** Normal pancreas; **(b)** type 2 DM; white arrow, pancreatic head; yellow arrow, pancreatic body and tail; SUV, standardized uptake value.

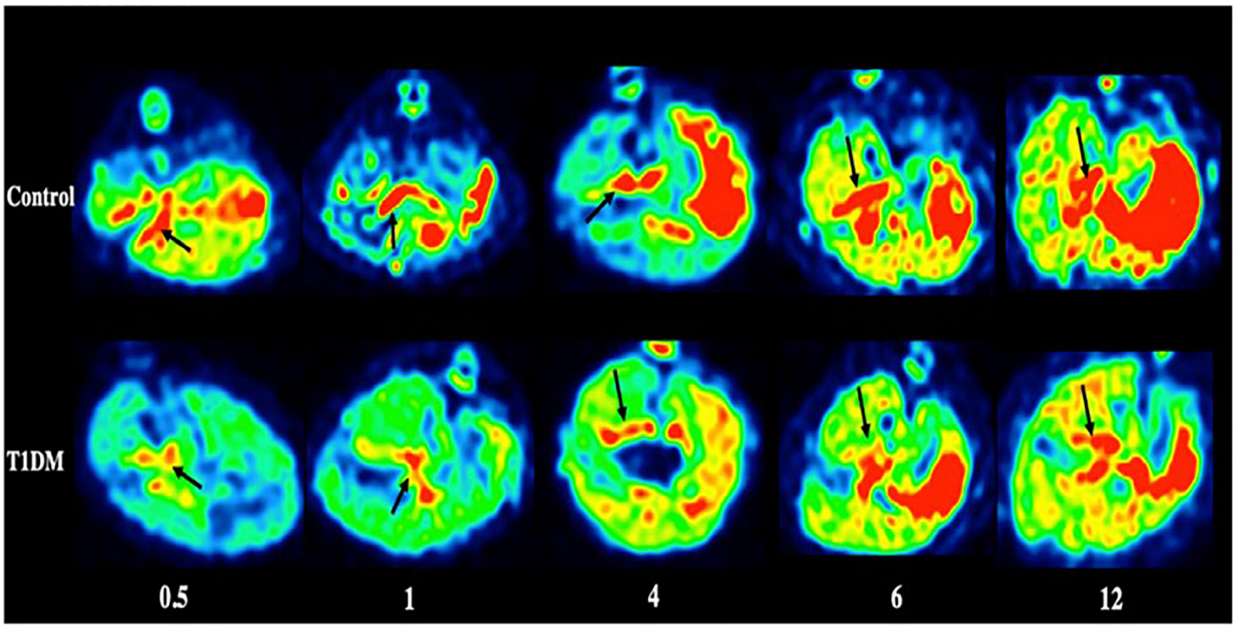

FIGURE 4 | PET imaging of the pancreas in type 1 DM (Jianfei et al., 2019) (E-produced/adapted from Chin J Endocrinol Metab, used with permission) Shown are representative ^{18}F-PF-(+)-DTBZ PET images of the pancreas (black arrows) of rats with type 1 diabetes mellitus (T1DM) and control rats, 0.5, 1, 4, 6, and 12 months after model induction.

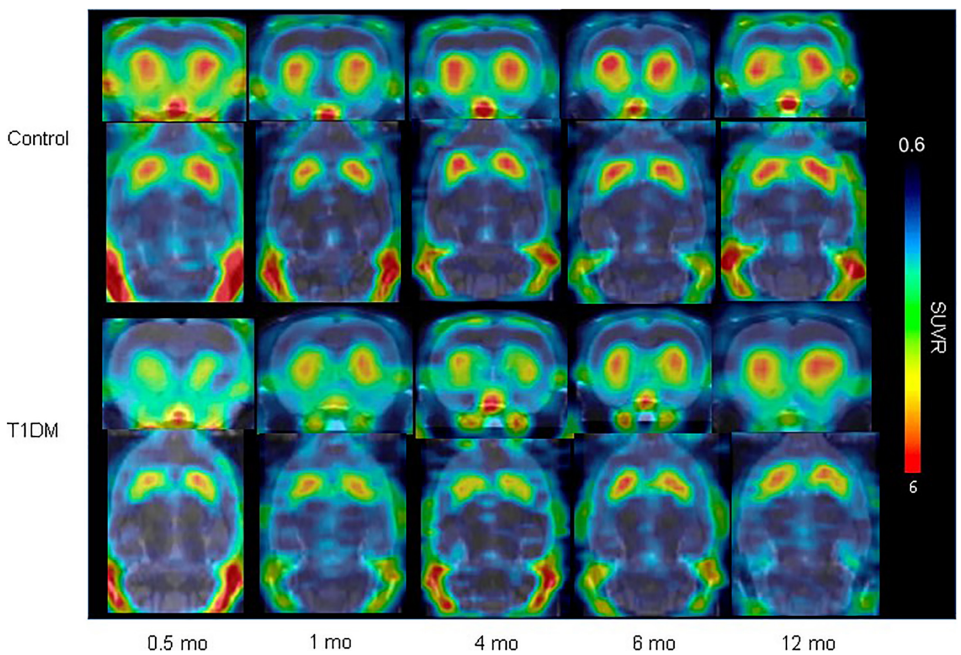

FIGURE 5 | VMAT2 expression in the striatum in type 1 DM (Jiang et al., 2020) (E-produced/adapted from Nuclear Medicine and Biology, used with permission) Shown is the decreased VMAT2 expression in the striatum in a rat model of T1DM, and in control rats, 0.5, 1, 4, 6, and 12 months after model induction, as imaged by ^{18}F-FP-(+)-DTBZ-PET/CT; SUVR, standardized uptake ratio.

As a protein that transports neurotransmitters, the distribution and expression of VMAT2 in human pancreas and its presence in sputum cells have clinical applications. The homology of the human, mouse, and rat VMAT2 amino acid sequences can be above 90% (German et al., 2015; Wu et al., 2016). Thus, studies based on diverse animal models suggest a correlation between BCM reduction and PD in humans (Jiang et al., 2020). In summary, diabetes is a demonstrated risk

factor for PD, and a correlation between DM and PD has been established by the above experiments.

FUTURE PERSPECTIVES

The physiological function of VMAT2 in islet β cells needs further study to determine the molecular mechanisms affecting BCM and insulin secretion and how VMAT2 participates in regulating the secretion of neurotransmitters. This information will provide new molecular therapeutic targets and an important theoretical basis for the early prediction, diagnosis, and treatment of DM. Future research should use PET scans to compare VMAT2 distributions among patients with T2DM, patients with obesity but without DM, and participants without DM. Undoubtedly, the advantages of using VMAT2 as a BCM marker will lead to useful information.

Positron emission tomography has shown prominent features compared with other molecular imaging approaches. PET can trace suspicious malignant lesions and provide functional imaging of those areas, which is useful for early diagnosis of diseases (Kang et al., 2004; Machtens et al., 2004). Although magnetic resonance imaging (MRI) has a higher resolution, the specificity of its related contrast agents for β cells is not as good as PET imaging. Moreover, the radiation exposure of PET imaging is much lower than that of CT scan. In addition, the evaluation of the BCM level has a significant effect through PET imaging (Wei et al., 2019; Yang et al., 2019). However, the high cost of PET has limited its promotion.

Molecular imaging allows qualitative and quantitative studies of biological processes *in vivo* at the cellular and molecular levels. The establishment of a functional imaging platform based on PET technology to observe physiological and pathological changes in the BCM can objectively, intuitively, and quantitatively reveal the key factors affecting insulin secretion and insulin resistance. Such a platform will advance our understanding of the pathogenesis of DM and the evaluation of the efficacy of experimental treatments, resulting in great clinical and social benefits.

CONCLUSION

Targeting VMAT2 with the molecular probe ^{18}F-FP-(+)-DTBZ provides an entry point for revealing the relationship between DM and PD. Interest in the use of imaging methods in research on BCM determination and DM has steadily increased because of their practicality, non-invasiveness, and safety. At present, radionuclide labeling remains the most sensitive imaging method for human β cells. This approach serves to clarify the role of BCM in the pathogenesis and progression of DM and has practical, clinical, and social value for the early diagnosis and treatment of DM.

AUTHOR CONTRIBUTIONS

YK conceived and designed the idea for the review. YK, HZ, HF, and JZ searched and reviewed the PD and DM literature and drafted the manuscript. YK, JW, and CZ further revised the manuscript. JW, YG, and BS reviewed and edited the manuscript. All authors read and approved the final manuscript.

FUNDING

This study was supported by the National Natural Science Foundation of China (Project Nos. 81571345 and 81701732), Shanghai Municipal Science and Technology Major Project (No. 2018SHZDZX01) and ZJLab, Shanghai Municipal Key Clinical Specialty (shslczdzk03402).

SUPPLEMENTARY MATERIAL

The Supplementary Material for this article can be found online at: https://www.frontiersin.org/articles/10.3389/fnins.2020.00682/full#supplementary-material

REFERENCES

Ahn, H. J., Yoo, W. K., Park, J., Ma, H. I., and Kim, Y. J. (2015). Cognitive dysfunction in drug-induced parkinsonism caused by prokinetics and antiemetics. *J. Korean Med. Sci.* 30, 1328–1333.

Allan, S. M., and Rothwell, N. J. (2001). Cytokines and acute neurodegeneration. *Nat. Rev. Neurosci.* 2, 734–744. doi: 10.1038/35094583

Altmann, V., Schumacher-Schuh, A. F., Rieck, M., Callegari-Jacques, S. M., Rieder, C. R., and Hutz, M. H. (2016). Val66Met BDNF polymorphism is associated with Parkinson's disease cognitive impairment. *Neurosci. Lett.* 615, 88–91. doi: 10.1016/j.neulet.2016.01.030

Anlauf, M., Eissele, R., Schafer, M. K., Eiden, L. E., Arnold, R., Pauser, U., et al. (2003). Expression of the two isoforms of the vesicular monoamine transporter (VMAT1 and VMAT2) in the endocrine pancreas and pancreatic endocrine tumors. *J. Histochem. Cytochem.* 51, 1027–1040. doi: 10.1177/002215540305100806

Armstrong, M. J., and Okun, M. S. (2020). Diagnosis and treatment of parkinson disease: a review. *JAMA* 323, 548–560.

Ashcroft, F. M., and Rorsman, P. (2012). Diabetes mellitus and the beta cell: the last ten years. *Cell* 148, 1160–1171. doi: 10.1016/j.cell.2012.02.010

Aviles-Olmos, I., Dickson, J., Kefalopoulou, Z., Djamshidian, A., Ell, P., Soderlund, T., et al. (2013a). Exenatide and the treatment of patients with Parkinson's disease. *J. Clin. Invest.* 123, 2730–2736.

Aviles-Olmos, I., Limousin, P., Lees, A., and Foltynie, T. (2013b). Parkinson's disease, insulin resistance and novel agents of neuroprotection. *Brain* 136(Pt 2), 374–384. doi: 10.1093/brain/aws009

Bernstein, A. I., Stout, K. A., and Miller, G. W. (2012). A fluorescent-based assay for live cell, spatially resolved assessment of vesicular monoamine transporter 2-mediated neurotransmitter transport. *J. Neurosci. Methods* 209, 357–366. doi: 10.1016/j.jneumeth.2012.06.002

Bini, J., Sanchez-Rangel, E., Gallezot, J. D., Naganawa, M., Nabulsi, N. B., Lim, K., et al. (2019). PET imaging of pancreatic dopamine D3/D2 receptor density with (11)C (+)-PHNO in Type-1 Diabetes Mellitus. *J. Nucl. Med.* 61, 570–576. doi: 10.2967/jnumed.119.234013

Bohnen, N. I., Albin, R. L., Koeppe, R. A., Wernette, K. A., Kilbourn, M. R., Minoshima, S., et al. (2006). Positron emission tomography of monoaminergic vesicular binding in aging and Parkinson disease. *J. Cereb. Blood Flow Metab.* 26, 1198–1212. doi: 10.1038/sj.jcbfm.9600276

Bonnard, C., Durand, A., Peyrol, S., Chanseaume, E., Chauvin, M. A., Morio, B., et al. (2008). Mitochondrial dysfunction results from oxidative stress in

the skeletal muscle of diet-induced insulin-resistant mice. *J. Clin. Invest.* 118, 789–800.

Bosco, D., Plastino, M., Cristiano, D., Colica, C., Ermio, C., De Bartolo, M., et al. (2012). Dementia is associated with insulin resistance in patients with Parkinson's disease. *J. Neurol. Sci.* 315, 39–43.

Boucher, B. J., John, W. G., and Noonan, K. (2004). Hypovitaminosis D is associated with insulin resistance and beta cell dysfunction. *Am. J. Clin. Nutr.* 80, 1666; author rely1666–1667.

Bridi, J. C., and Hirth, F. (2018). Mechanisms of α-Synuclein induced synaptopathy in Parkinson's disease. *Front. Neurosci.* 12:80. doi: 10.3389/fnins.2018.00080

Carvelli, L., Moron, J. A., Kahlig, K. M., Ferrer, J. V., Sen, N., Lechleiter, J. D., et al. (2002). PI 3-kinase regulation of dopamine uptake. *J. Neurochem.* 81, 859–869. doi: 10.1046/j.1471-4159.2002.00892.x

Cereda, E., Barichella, M., Cassani, E., Caccialanza, R., and Pezzoli, G. (2012). Clinical features of Parkinson disease when onset of diabetes came first: a case-control study. *Neurology* 78, 1507–1511. doi: 10.1212/wnl.0b013e3182553cc9

Chen, H., O'Reilly, E. J., Schwarzschild, M. A., and Ascherio, A. (2008). Peripheral inflammatory biomarkers and risk of Parkinson's disease. *Am. J. Epidemiol.* 167, 90–95. doi: 10.1093/aje/kwm260

Cho, S. S., Christopher, L., Koshimori, Y., Li, C., Lang, A. E., Houle, S., et al. (2019). Decreased pallidal vesicular monoamine transporter type 2 availability in Parkinson's disease: the contribution of the nigropallidal pathway. *Neurobiol. Dis.* 124, 176–182. doi: 10.1016/j.nbd.2018.11.022

Cinti, F., Bouchi, R., Kim-Muller, J. Y., Ohmura, Y., Sandoval, P. R., Masini, M., et al. (2016). Evidence of beta-Cell dedifferentiation in human type 2 diabetes. *J. Clin. Endocrinol. Metab.* 101, 1044–1054.

Cuervo, A. M., Stefanis, L., Fredenburg, R., Lansbury, P. T., and Sulzer, D. (2004). Impaired degradation of mutant alpha-synuclein by chaperone-mediated autophagy. *Science* 305, 1292–1295. doi: 10.1126/science.1101738

D'Amelio, M., Ragonese, P., Callari, G., Di Benedetto, N., Palmeri, B., Terruso, V., et al. (2009). Diabetes preceding Parkinson's disease onset. A case-control study. *Parkinson. Relat. Disord.* 15, 660–664. doi: 10.1016/j.parkreldis.2009.02.013

De Pablo-Fernandez, E., Goldacre, R., Pakpoor, J., Noyce, A. J., and Warner, T. T. (2018). Association between diabetes and subsequent Parkinson disease: a record-linkage cohort study. *Neurology* 91, e139–e142. doi: 10.1212/wnl.0000000000005771

De Pablo-Fernandez, E., Sierra-Hidalgo, F., Benito-Leon, J., and Bermejo-Pareja, F. (2017). Association between Parkinson's disease and diabetes: data from NEDICES study. *Acta Neurol. Scand.* 136, 732–736. doi: 10.1111/ane.12793

Del Pino, J., Moyano, P., Ruiz, M., Anadon, M. J., Diaz, M. J., Garcia, J. M., et al. (2017). Amitraz changes NE, DA and 5-HT biosynthesis and metabolism mediated by alterations in estradiol content in CNS of male rats. *Chemosphere* 181, 518–529. doi: 10.1016/j.chemosphere.2017.04.113

Derakhshan, A., Tohidi, M., Arshi, B., Khalili, D., Azizi, F., and Hadaegh, F. (2015). Relationship of hyperinsulinaemia, insulin resistance and beta-cell dysfunction with incident diabetes and pre-diabetes: the Tehran lipid and glucose study. *Diabet Med.* 32, 24–32. doi: 10.1111/dme.12560

Derex, L., and Trouillas, P. (1997). Reversible parkinsonism, hypophosphoremia, and hypocalcemia under vitamin D therapy. *Mov. Disord.* 12, 612–613. doi: 10.1002/mds.870120424

Donglang, J., Yanyan, K., Xiuhong, L., Ming, L., Weiyan, Z., and Fengchun, H. (2018). Evaluation of β-cell mass in type 2 diabetic patients with [18F]-FP-(+)-DTBZ, a vesicular monoamine transporter type 2 molecular probe. *Chin. J. Endocrinol. Metab.* 34, 638–642.

Elbassuoni, E. A., and Ahmed, R. F. (2019). Mechanism of the neuroprotective effect of GLP-1 in a rat model of Parkinson's with pre-existing diabetes. *Neurochem. Int.* 131:104583. doi: 10.1016/j.neuint.2019.104583

Evatt, M. L., Delong, M. R., Khazai, N., Rosen, A., Triche, S., et al. (2008). Prevalence of vitamin d insufficiency in patients with Parkinson disease and Alzheimer disease. *Arch. Neurol.* 65, 1348–1352.

Fon, E. A., Pothos, E. N., Sun, B. C., Killeen, N., Sulzer, D., and Edwards, R. H. (1997). Vesicular transport regulates monoamine storage and release but is not essential for amphetamine action. *Neuron* 19, 1271–1283. doi: 10.1016/s0896-6273(00)80418-3

Freeby, M., Ichise, M., and Harris, P. E. (2012). Vesicular monoamine transporter, type 2 (VMAT2) expression as it compares to insulin and pancreatic polypeptide in the head, body and tail of the human pancreas. *Islets* 4, 393–397. doi: 10.4161/isl.22995

Fu, J. F., Klyuzhin, I., McKenzie, J., Neilson, N., Shahinfard, E., Dinelle, K., et al. (2019). Joint pattern analysis applied to PET DAT and VMAT2 imaging reveals new insights into Parkinson's disease induced presynaptic alterations. *Neuroimage Clin.* 23:101856. doi: 10.1016/j.nicl.2019.101856

Fumagalli, F., Gainetdinov, R. R., Wang, Y. M., Valenzano, K. J., Miller, G. W., and Caron, M. G. (1999). Increased methamphetamine neurotoxicity in heterozygous vesicular monoamine transporter 2 knock-out mice. *J. Neurosci.* 19, 2424–2431. doi: 10.1523/jneurosci.19-07-02424.1999

German, C. L., Baladi, M. G., McFadden, L. M., Hanson, G. R., and Fleckenstein, A. E. (2015). Regulation of the dopamine and vesicular monoamine transporters: pharmacological targets and implications for disease. *Pharmacol. Rev.* 67, 1005–1024. doi: 10.1124/pr.114.010397

Harris, P. E., Ferrara, C., Barba, P., Polito, T., Freeby, M., et al. (2008). VMAT2 gene expression and function as it applies to imaging beta-cell mass. *J. Mol. Med.* 86, 5–16. doi: 10.1007/s00109-007-0242-x

Hefti, F. F., Kung, H. F., Kilbourn, M. R., Carpenter, A. P., Clark, C. M., and Skovronsky, D. M. (2010). 18F-AV-133: a selective VMAT2-binding radiopharmaceutical for PET imaging of dopaminergic neurons. *PET Clin.* 5, 75–82. doi: 10.1016/j.cpet.2010.02.001

Horvath, I., and Wittung-Stafshede, P. (2016). Cross-talk between amyloidogenic proteins in type-2 diabetes and Parkinson's disease. *Proc. Natl. Acad. Sci. U.S.A.* 113, 12473–12477. doi: 10.1073/pnas.1610371113

Hsiao, I. T., Weng, Y. H., Hsieh, C. J., Lin, W. Y., Wey, S. P., Kung, M. P., et al. (2014). Correlation of Parkinson disease severity and 18F-DTBZ positron emission tomography. *JAMA Neurol.* 71, 758–766.

Hu, G., Jousilahti, P., Bidel, S., Antikainen, R., and Tuomilehto, J. (2007). Type 2 diabetes and the risk of Parkinson's disease. *Diabetes Care* 30, 842–847.

Ji, C., Xue, G. F., Lijun, C., Feng, P., Li, D., Li, L., et al. (2016). A novel dual GLP-1 and GIP receptor agonist is neuroprotective in the MPTP mouse model of Parkinson's disease by increasing expression of BNDF. *Brain Res.* 1634, 1–11. doi: 10.1016/j.brainres.2015.09.035

Jianfei, X., Donglang, J., Shuhua, R., Qi, H., Fang, X., Yihui, G., et al. (2019). Quantification of β cell mass using18F-FP-(+)-DTBZ, a vesicular monoamine transporter type 2 radiotracer: a longitudinal study in type 1 diabetic rats. *Chin. J. Endocrinol. Metab.* 35, 494–498.

Jiang, D., Kong, Y., Ren, S., Cai, H., Zhang, Z., Huang, Z., et al. (2020). Decreased striatal vesicular monoamine transporter 2 (VMAT2) expression in a type 1 diabetic rat model: a longitudinal study using micro-PET/CT. *Nucl. Med. Biol.* 8, 89–95. doi: 10.1016/j.nucmedbio.2020.02.011

Jing, H., Wang, S., Wang, M., Fu, W., Zhang, C., and Xu, D. (2017). Isobavachalcone attenuates MPTP-induced Parkinson's disease in mice by inhibition of microglial activation through NF-κB pathway. *PLoS One* 12:e0169560. doi: 10.1371/journal.pone.0169560

Johnson, A. M., and Olefsky, J. M. (2013). The origins and drivers of insulin resistance. *Cell* 152, 673–684. doi: 10.1016/j.cell.2013.01.041

Jonietz, E. (2012). Pathology: cause and effect. *Nature* 485, S10–S11.

Kang, D. E., White, R. L. Jr., Zuger, J. H., Sasser, H. C., and Teigland, C. M. (2004). Clinical use of fluorodeoxyglucose F 18 positron emission tomography for detection of renal cell carcinoma. *J. Urol.* 171, 1806–1809. doi: 10.1097/01.ju.0000120241.50061.e4

Khang, R., Park, C., and Shin, J. H. (2015). Dysregulation of parkin in the substantia nigra of db/db and high-fat diet mice. *Neuroscience* 294, 182–192. doi: 10.1016/j.neuroscience.2015.03.017

Laruelle, M. (2000). Imaging synaptic neurotransmission with in vivo binding competition techniques: a critical review. *J. Cereb. Blood Flow Metab.* 20, 423–451. doi: 10.1097/00004647-200003000-00001

Lee, C. S., Samii, A., Sossi, V., Ruth, T. J., Schulzer, M., Holden, J. E., et al. (2000). In vivo positron emission tomographic evidence for compensatory changes in presynaptic dopaminergic nerve terminals in Parkinson's disease. *Ann. Neurol.* 47, 493–503. doi: 10.1002/1531-8249(200004)47:4<493::aid-ana13>3.0.co;2-4

Li, Y., Liu, W., Li, L., and Hölscher, C. (2016). Neuroprotective effects of a GIP analogue in the MPTP Parkinson's disease mouse model. *Neuropharmacology* 101, 255–263. doi: 10.1016/j.neuropharm.2015.10.002

Li, Y., Liu, W., Li, L., and Holscher, C. (2017). D-Ala2-GIP-glu-PAL is neuroprotective in a chronic Parkinson's disease mouse model and increases BNDF expression while reducing neuroinflammation and lipid peroxidation. *Eur. J. Pharmacol.* 797, 162–172. doi: 10.1016/j.ejphar.2016.11.050

Lima, M. M., Targa, A. D., Noseda, A. C., Rodrigues, L. S., Delattre, A. M., dos Santos, F. V., et al. (2014). Does Parkinson's disease and type-2 diabetes mellitus present common pathophysiological mechanisms and treatments? *CNS Neurol. Disord. Drug Targets* 13, 418–428. doi: 10.2174/18715273113126660155

Lin, K. J., Weng, Y. H., Hsieh, C. J., Lin, W. Y., Wey, S. P., Kung, M. P., et al. (2013). Brain imaging of vesicular monoamine transporter type 2 in healthy aging subjects by 18F-FP-(+)-DTBZ PET. *PLoS One* 8:e75952. doi: 10.1371/journal.pone.0075952

Lin, S. C., Lin, K. J., Hsiao, I. T., Hsieh, C. J., Lin, W. Y., Lu, C. S., et al. (2014). In vivo detection of monoaminergic degeneration in early Parkinson disease by (18)F-9-fluoropropyl-(+)-dihydrotetrabenzazine PET. *J. Nucl. Med.* 55, 73–79. doi: 10.2967/jnumed.113.121897

Lotharius, J., and Brundin, P. (2002). Pathogenesis of Parkinson's disease: dopamine, vesicles and alpha-synuclein. *Nat. Rev. Neurosci.* 3, 932–942. doi: 10.1038/nrn983

Ma, K., Han, C., Zhang, G., Guo, X., Xia, Y., Wan, F., et al. (2019). Reduced VMAT2 expression exacerbates the hyposmia in the MPTP model of Parkinson's disease. *Biochem. Biophys. Res. Commun.* 513, 306–312. doi: 10.1016/j.bbrc.2019.03.159

Machtens, S., Boerner, A. R., Hofmann, M., Knapp, W. H., et al. (2004). [Positron emission tomography (PET) for diagnosis and monitoring of treatment for urological tumors]. *Urol. A* 43, 1397–1409.

Maino, B., Ciotti, M. T., Calissano, P., and Cavallaro, S. (2014). Transcriptional analysis of apoptotic cerebellar granule neurons following rescue by gastric inhibitory polypeptide. *Int. J. Mol. Sci.* 15, 5596–5622. doi: 10.3390/ijms15045596

Matos, M., Dublecz, K., Grafl, B., Liebhart, D., and Hess, M. (2018). Pancreatitis is an important feature of broilers suffering from inclusion body hepatitis leading to dysmetabolic conditions with consequences for zootechnical performance. *Avian. Dis.* 62, 57–64.

Moran, L. B., and Graeber, M. B. (2008). Towards a pathway definition of Parkinson's disease: a complex disorder with links to cancer, diabetes and inflammation. *Neurogenetics* 9, 1–13. doi: 10.1007/s10048-007-0116-y

Moroo, I., Yamada, T., Makino, H., Tooyama, I., McGeer, P. L., McGeer, E. G., et al. (1994). Loss of insulin receptor immunoreactivity from the substantia nigra pars compacta neurons in Parkinson's disease. *Acta Neuropathol.* 87, 343–348. doi: 10.1007/bf00313602

Naganawa, M., Lim, K., Nabulsi, N. B., Lin, S. F., Labaree, D., Ropchan, J., et al. (2018). Evaluation of pancreatic VMAT2 binding with active and inactive enantiomers of [(18)F]FP-DTBZ in healthy subjects and patients with type 1 diabetes. *Mol. Imaging Biol.* 20, 835–845. doi: 10.1007/s11307-018-1170-6

Naganawa, M., Lin, S. F., Lim, K., Labaree, D., Ropchan, J., Harris, P., et al. (2016). Evaluation of pancreatic VMAT2 binding with active and inactive enantiomers of (18)F-FP-DTBZ in baboons. *Nucl. Med. Biol.* 43, 743–751. doi: 10.1016/j.nucmedbio.2016.08.018

Normandin, M. D., Petersen, K. F., Ding, Y. S., Lin, S. F., Naik, S., Fowles, K., et al. (2012). In vivo imaging of endogenous pancreatic beta-cell mass in healthy and type 1 diabetic subjects using 18F-fluoropropyl-dihydrotetrabenazine and PET. *J. Nucl. Med.* 53, 908–916. doi: 10.2967/jnumed.111.100545

Ogama, N., Sakurai, T., Kawashima, S., Tanikawa, T., Tokuda, H., Satake, S., et al. (2018). Postprandial hyperglycemia is associated with white matter hyperintensity and brain atrophy in older patients with Type 2 diabetes mellitus. *Front. Aging Neurosci.* 10:273. doi: 10.3389/fnagi.2018.00273

Owens, W. A., Williams, J. M., Saunders, C., Avison, M. J., Galli, A., and Daws, L. C. (2012). Rescue of dopamine transporter function in hypoinsulinemic rats by a D2 receptor-ERK-dependent mechanism. *J. Neurosci.* 32, 2637–2647. doi: 10.1523/jneurosci.3759-11.2012

Pagano, G., Polychronis, S., Wilson, H., Giordano, B., Ferrara, N., Niccolini, F., et al. (2018). Diabetes mellitus and Parkinson disease. *Neurology* 90, e1654–e1662.

Palacios, N., Gao, X., McCullough, M. L., Jacobs, E. J., Patel, A. V., Mayo, T., et al. (2011). Obesity, diabetes, and risk of Parkinson's disease. *Mov. Disord.* 26, 2253–2259.

Park, C. R., Moon, M. J., Park, S., Kim, D. K., Cho, E. B., Millar, R. P., et al. (2013). A novel glucagon-related peptide (GCRP) and its receptor GCRPR account for coevolution of their family members in vertebrates. *PLoS One* 8:e65420. doi: 10.1371/journal.pone.0065420

Parker, W. D. Jr., Parks, J. K., et al. (2008). Complex I deficiency in Parkinson's disease frontal cortex. *Brain Res.* 1189, 215–218. doi: 10.1016/j.brainres.2007.10.061

Payer, D. E., Guttman, M., Kish, S. J., Tong, J., Adams, J. R., Rusjan, P., et al. (2016). D3 dopamine receptor-preferring [11C]PHNO PET imaging in Parkinson patients with dyskinesia. *Neurology* 86, 224–230. doi: 10.1212/wnl.0000000000002285

Pecic, S., Milosavic, N., Rayat, G., Maffei, A., and Harris, P. E. (2019). A novel optical tracer for VMAT2 applied to live cell measurements of vesicle maturation in cultured human beta-cells. *Sci. Rep.* 9:5403.

Petrisic, M. S., Augood, S. J., and Bicknell, R. J. (1997). Monoamine transporter gene expression in the central nervous system in diabetes mellitus. *J. Neurochem.* 68, 2435–2441. doi: 10.1046/j.1471-4159.1997.68062435.x

Purwana, I., Zheng, J., Li, X., Deurloo, M., Son, D. O., Zhang, Z., et al. (2014). GABA promotes human beta-cell proliferation and modulates glucose homeostasis. *Diabetes* 63, 4197–4205. doi: 10.2337/db14-0153

Raffo, A., Hancock, K., Polito, T., Xie, Y., Andan, G., Witkowski, P., et al. (2008). Role of vesicular monoamine transporter type 2 in rodent insulin secretion and glucose metabolism revealed by its specific antagonist tetrabenazine. *J. Endocrinol.* 198, 41–49. doi: 10.1677/joe-07-0632

Ray, N. J., Miyasaki, J. M., Zurowski, M., Ko, J. H., Cho, S. S., Pellecchia, G., et al. (2012). Extrastriatal dopaminergic abnormalities of DA homeostasis in Parkinson's patients with medication-induced pathological gambling: a [11C] FLB-457 and PET study. *Neurobiol. Dis.* 48, 519–525. doi: 10.1016/j.nbd.2012.06.021

Renaud, J., Bassareo, V., Beaulieu, J., Pinna, A., Schlich, M., Lavoie, C., et al. (2018). Dopaminergic neurodegeneration in a rat model of long-term hyperglycemia: preferential degeneration of the nigrostriatal motor pathway. *Neurobiol. Aging* 69, 117–128. doi: 10.1016/j.neurobiolaging.2018.05.010

Rodriguez-Diaz, R., Abdulreda, M. H., Formoso, A. L., Gans, I., Ricordi, C., Berggren, P. O., et al. (2011). Innervation patterns of autonomic axons in the human endocrine pancreas. *Cell. Metab.* 14, 45–54. doi: 10.1016/j.cmet.2011.05.008

Saeedi, P., Petersohn, I., Salpea, P., Malanda, B., Karuranga, S., Unwin, N., et al. (2019). Global and regional diabetes prevalence estimates for 2019 and projections for 2030 and 2045: results from the International Diabetes Federation Diabetes Atlas. *Diabetes Res. Clin. Pract.* 157:107843. doi: 10.1016/j.diabres.2019.107843

Samandari, R., Chizari, A., Hassanpour, R., Mousavi, Z., and Haghparast, A. (2013). Streptozotocin-induced diabetes affects the development and maintenance of morphine reward in rats. *Neurosci. Lett.* 543, 90–94. doi: 10.1016/j.neulet.2013.03.024

Santiago, J. A., Bottero, V., and Potashkin, J. A. (2017). Biological and clinical implications of comorbidities in Parkinson's disease. *Front. Aging Neurosci.* 9:394. doi: 10.3389/fnagi.2017.00394

Santiago, J. A., and Potashkin, J. A. (2014). System-based approaches to decode the molecular links in Parkinson's disease and diabetes. *Neurobiol. Dis.* 72(Pt A), 84–91. doi: 10.1016/j.nbd.2014.03.019

Sharma, A. N., Ligade, S. S., Sharma, J. N., Shukla, P., Elased, K. M., and Lucot, J. B. (2015). GLP-1 receptor agonist liraglutide reverses long-term atypical antipsychotic treatment associated behavioral depression and metabolic abnormalities in rats. *Metab. Brain Dis.* 30, 519–527. doi: 10.1007/s11011-014-9591-7

Shi, X., Zhang, Y., Xu, S., Kung, H. F., Qiao, H., Jiang, L., et al. (2019). Decreased striatal vesicular monoamine transporter type 2 correlates with the nonmotor symptoms in parkinson disease. *Clin. Nucl. Med.* 44, 707–713. doi: 10.1097/rlu.0000000000002664

Sinclair, A., Saeedi, P., Kaundal, A., Karuranga, S., Malanda, B., and Williams, R. (2020). Diabetes and global ageing among 65-99-year-old adults: findings from the International Diabetes Federation Diabetes Atlas. *Diabetes Res. Clin. Pract.* 162:108078. doi: 10.1016/j.diabres.2020.108078

Singhal, T., Ding, Y. S., Weinzimmer, D., Normandin, M. D., Labaree, D., Ropchan, J., et al. (2011). Pancreatic beta cell mass PET imaging and quantification with [11C]DTBZ and [18F]FP-(+)-DTBZ in rodent models of diabetes. *Mol. Imaging Biol.* 13, 973–984. doi: 10.1007/s11307-010-0406-x

Stahl, S. M. (2018). Mechanism of action of vesicular monoamine transporter 2 (VMAT2) inhibitors in tardive dyskinesia: reducing dopamine leads to less "go" and more "stop" from the motor striatum for robust therapeutic effects. *CNS Spectr.* 23, 1–6. doi: 10.1017/s1092852917000621

Stormezand, G. N., Chaves, L. T., Vallez Garcia, D., Doorduin, J., De Jong, B. M., Leenders, K. L., et al. (2020). Intrastriatal gradient analyses of 18F-FDOPA

PET scans for differentiation of Parkinsonian disorders. *Neuroimage Clin.* 25:102161. doi: 10.1016/j.nicl.2019.102161

Su, C. J., Shen, Z., Cui, R. X., Huang, Y., Xu, D. L., Zhao, F. L., et al. (2020). Thioredoxin-Interacting Protein (TXNIP) Regulates Parkin/PINK1-mediated Mitophagy in dopaminergic neurons under high-glucose conditions: implications for molecular links between Parkinson's disease and diabetes. *Neurosci. Bull.* 36, 346–358. doi: 10.1007/s12264-019-00459-5

Sun, X., Han, F., Yi, J., Han, L., and Wang, B. (2011). Effect of aspirin on the expression of hepatocyte NF-kappaB and serum TNF-alpha in streptozotocin-induced type 2 diabetic rats. *J. Korean Med. Sci.* 26, 765–770.

Sun, Y., Chang, Y. H., Chen, H. F., Su, Y. H., Su, H. F., and Li, C. Y. (2012). Risk of Parkinson disease onset in patients with diabetes: a 9-year population-based cohort study with age and sex stratifications. *Diabetes Care* 35, 1047–1049. doi: 10.2337/dc11-1511

Takahashi, N., Miner, L. L., Sora, I., Ujike, H., Revay, R. S., Kostic, V., et al. (1997). VMAT2 knockout mice: heterozygotes display reduced amphetamine-conditioned reward, enhanced amphetamine locomotion, and enhanced MPTP toxicity. *Proc. Natl. Acad. Sci. U.S.A.* 94, 9938–9943. doi: 10.1073/pnas.94.18.9938

Ter Horst, K. W., Lammers, N. M., Trinko, R., Opland, D. M., Figee, M., Ackermans, M. T., et al. (2018). Striatal dopamine regulates systemic glucose metabolism in humans and mice. *Sci. Transl. Med.* 10:eaar3752. doi: 10.1126/scitranslmed.aar3752

Tritsch, N. X., Ding, J. B., and Sabatini, B. L. (2012). Dopaminergic neurons inhibit striatal output through non-canonical release of GAB. *Nature A* 490, 262–266. doi: 10.1038/nature11466

Wahlqvist, M. L., Lee, M. S., Hsu, C. C., Chuang, S. Y., Lee, J. T., and Tsai, H. N. (2012). Metformin-inclusive sulfonylurea therapy reduces the risk of Parkinson's disease occurring with Type 2 diabetes in a Taiwanese population cohort. *Parkins. Relat. Disord.* 18, 753–758. doi: 10.1016/j.parkreldis.2012.03.010

Wang, C., Huang, X., Tian, S., Huang, R., Guo, D., Lin, H., et al. (2020). High plasma resistin levels portend the insulin resistance-associated susceptibility to early cognitive decline in patients with type 2 diabetes mellitus. *J. Alzheimers Dis.* 75, 807–815. doi: 10.3233/jad-200074

Wang, H., and Raleigh, D. P. (2014). The ability of insulin to inhibit the formation of amyloid by pro-islet amyloid polypeptide processing intermediates is significantly reduced in the presence of sulfated glycosaminoglycans. *Biochemistry* 53, 2605–2614. doi: 10.1021/bi4015488

Wang, Y. M., Gainetdinov, R. R., Fumagalli, F., Xu, F., Jones, S. R., Bock, C. B., et al. (1997). Knockout of the vesicular monoamine transporter 2 gene results in neonatal death and supersensitivity to cocaine and amphetamine. *Neuron* 19, 1285–1296. doi: 10.1016/s0896-6273(00)80419-5

Webb, J. L., Ravikumar, B., Atkins, J., Skepper, J. N., and Rubinsztein, D. C. (2003). Alpha-Synuclein is degraded by both autophagy and the proteasome. *J. Biol. Chem.* 278, 25009–25013. doi: 10.1074/jbc.m300227200

Wei, W., Ehlerding, E. B., Lan, X., Luo, Q. Y., and Cai, W. (2019). Molecular imaging of beta-cells: diabetes and beyond. *Adv. Drug Deliv. Rev.* 139, 16–31. doi: 10.1016/j.addr.2018.06.022

Wilcox, N. S., Rui, J., Hebrok, M., and Herold, K. C. (2016). Life and death of beta cells in Type 1 diabetes: a comprehensive review. *J. Autoimmun.* 71, 51–58. doi: 10.1016/j.jaut.2016.02.001

Wilson, J. M., and Kish, S. J. (1996). The vesicular monoamine transporter, in contrast to the dopamine transporter, is not altered by chronic cocaine self-administration in the rat. *J. Neurosci.* 16, 3507–3510. doi: 10.1523/jneurosci.16-10-03507.1996

Wood, H. (2014). Parkinson disease: 18F-DTBZ PET tracks dopaminergic degeneration in patients with Parkinson disease. *Nat. Rev. Neurol.* 10:305. doi: 10.1038/nrneurol.2014.81

Wu, Q., Xu, H., Wang, W., Chang, F., Jiang, Y., et al. (2016). Retrograde trafficking of VMAT2 and its role in protein stability in non-neuronal cells. *J. Biomed. Res.* 30, 502–509.

Wu, X., Zhou, X., Zhang, S., Zhang, Y., Deng, A., Han, J., et al. (2015). Brain uptake of a non-radioactive pseudo-carrier and its effect on the biodistribution of [(18)F]AV-133 in mouse brain. *Nucl. Med. Biol.* 42, 630–636. doi: 10.1016/j.nucmedbio.2015.03.009

Xu, Q., Park, Y., Huang, X., Hollenbeck, A., Blair, A., Schatzkin, A., et al. (2011). Diabetes and risk of Parkinson's disease. *Diabetes Care* 34, 910–915.

Yang, C. T., Ghosh, K. K., Padmanabhan, P., Langer, O., Liu, J., Halldin, C., et al. (2017). PET probes for imaging pancreatic islet cells. *Clin. Transl. Imaging* 5, 507–523. doi: 10.1007/s40336-017-0251-x

Yang, J., Zhang, L. J., Wang, F., Hong, T., and Liu, Z. (2019). Molecular imaging of diabetes and diabetic complications: beyond pancreatic beta-cell targeting. *Adv. Drug Deliv. Rev.* 139, 32–50. doi: 10.1016/j.addr.2018.11.007

Yu, M. G., Keenan, H. A., Shah, H. S., Frodsham, S. G., Pober, D., He, Z., et al. (2019). Residual beta cell function and monogenic variants in long-duration type 1 diabetes patients. *J. Clin. Invest.* 129, 3252–3263. doi: 10.1172/jci127397

Yue, X., Li, H., Yan, H., Zhang, P., Chang, L., et al. (2016). Risk of Parkinson disease in diabetes mellitus: an updated meta-analysis of population-based cohort studies. *Medicine* 95:e3549. doi: 10.1097/md.0000000000003549

Conflict of Interest: The authors declare that the research was conducted in the absence of any commercial or financial relationships that could be construed as a potential conflict of interest.

frontiers in Neurology

ORIGINAL RESEARCH
published: 17 July 2020
doi: 10.3389/fneur.2020.00684

Epilepsy-Related Brain Network Alterations in Patients With Temporal Lobe Glioma in the Left Hemisphere

Shengyu Fang[1,2], *Chunyao Zhou*[2], *Xing Fan*[1]*, *Tao Jiang*[1,2]* and *Yinyan Wang*[1,2]*

[1] Department of Neurosurgery, Beijing Neurosurgical Institute, Beijing, China, [2] Department of Neurosurgery, Beijing Tiantan Hospital, Capital Medical University, Beijing, China

Background: Seizures are a common symptom in patients with temporal lobe gliomas and may result in brain network alterations. However, brain network changes caused by glioma-related epilepsy (GRE) remain poorly understood.

Objective: In this study, we applied graph theory analysis to delineate topological networks with resting-state functional magnetic resonance images (rs-fMRI) and investigated characteristics of functional networks in patients with GRE.

Methods: Thirty patients with low-grade gliomas in the left temporal lobe were enrolled and classified into GRE (n = 15) and non-GRE groups. Twenty healthy participants matched for age, sex, and education level were enrolled. All participants had rs-fMRI data. Sensorimotor, visual, default mode, auditory, and right executive control networks were used to construct connection matrices. Topological properties of those sub-networks were investigated.

Results: Compared to that in the GRE group, four edges with higher functional connectivity were noted in the non-GRE group. Moreover, 21 edges with higher functional connectivity were identified in the non-GRE group compared to the healthy group. All significant alterations in functional edges belong to the visual network. Increased global efficiency and decreased shortest path lengths were noted in the non-GRE group compared to the GRE and healthy groups. Compared with that in the healthy group, nodal efficiency of three nodes was higher in the GRE and non-GRE groups and the degree centrality of six nodes was altered in the non-GRE group.

Conclusion: Temporal lobe gliomas in the left hemisphere and GRE altered visual networks in an opposing manner. These findings provide a novel insight into brain network alterations induced by GRE.

Keywords: functional network, glioma, graph theoretical analysis, resting-state fMRI, tumor-related epilepsy

OPEN ACCESS

Edited by:
Zsigmond Tamás Kincses, University of Szeged, Hungary

Reviewed by:
Gaelle Eve Doucet, Boys Town National Research Hospital, United States
Bo Gao, Affiliated Hospital of Guizhou Medical University, China
Benjamin Klugah-Brown, University of Electronic Science and Technology of China, China

***Correspondence:**
Xing Fan
xingkongyaoxiang@163.com
Tao Jiang
taojiang1964@163.com
Yinyan Wang
tiantanyinyan@126.com

Specialty section:
This article was submitted to Applied Neuroimaging, a section of the journal Frontiers in Neurology

Received: *17 March 2020*
Accepted: *08 June 2020*
Published: *17 July 2020*

Citation:
Fang S, Zhou C, Fan X, Jiang T and Wang Y (2020) Epilepsy-Related Brain Network Alterations in Patients With Temporal Lobe Glioma in the Left Hemisphere. Front. Neurol. 11:684. doi: 10.3389/fneur.2020.00684

INTRODUCTION

Seizures are a frequent symptom of brain tumors (1). Gliomas, particularly diffuse low-grade gliomas (DLGG, WHO grade 2), are highly epileptogenic (2). Most patients with DLGG experience glioma-related epilepsy (GRE) as a presenting symptom, especially for DLGGs growing in the temporal lobe (3). The prevailing view considers epilepsy to be a functional network disorder,

and previous studies have reported correlations between alterations in functional networks and epileptic characteristics (4, 5). However, the etiology of GRE remains unclear.

Resting-state functional magnetic resonance imaging (rs-fMRI) enables quantitative transformation of functional connections, permitting delineation of brain networks. Graph theory analysis is a useful approach to quantitatively reveal the topological properties of brain networks (6, 7). Numerous studies have focused on the association between primary seizures and alterations in functional networks. Temporal lobe seizures induce functional connectivity (FC) and decreased network efficiency as seizures decrease intercortical synchronous fluctuations (6, 8, 9). However, alterations in functional networks induced by GRE are affected by both the glioma and GRE. Hence, previous conclusions regarding alterations in functional networks in primary seizures are insufficient, occluding appropriate preoperative prevention and intraoperative treatment. Moreover, the alterations in functional networks induced by temporal gliomas are unknown. Consequently, investigating the characteristics of functional network alterations induced by temporal GRE is critical to optimize preoperative prevention and intraoperative treatment.

To address this gap in knowledge, this study retrospectively enrolled 30 patients with left temporal DLGG (including 15 patients with glioma-related generalized seizures) and 20 healthy controls to investigate how temporal GRE altered functional networks. Our results indicated that temporal DLGG and GRE caused distinct alterations in brain networks.

METHODS

The local institutional review board approved this study. All participants provided written informed consent before data acquisition.

Participants

Forty patients diagnosed with primary temporal lobe glioma and who had rs-fMRI data at Beijing Tiantan Hospital Glioma Treatment Center were recruited between January 2017 and July 2018. The patient inclusion criteria were as follows: (a) age $\geq$ 18 years, (b) histopathological diagnosis with primary DLGG according to the 2016 World Health Organization criteria; (c) more than 6 years of school education, and (d) no history of biopsy, radiotherapy, or chemotherapy. Exclusion criteria were as follows: (a) contraindications for MRI, or (b) head motion $>$ 3 mm in translation or 3° in rotation. The healthy participant inclusion criteria were as follows: (a) age $\geq$ 18 years, (b) no history of brain disease, and (c) more than 6 years of school education. The exclusion criteria were as follows: (a) contraindications for MRI, or (b) head motion $>$ 3 mm in translation or 3° in rotation.

Clinical Characteristics Collection

We retrospectively collected patient characteristics from inpatient records, including age, sex, education level, Karnofsky performance status, histopathology, isocitrate dehydrogenase mutation status, extent of tumor resection, information regarding preoperative seizures, type of seizure onset, and history of taking anti-epileptic drugs. Follow-up information about postoperative epileptic control was obtained by telephone interviews at 6 months postoperatively.

MRI Acquisition

A MAGNETOM Prisma 3-T MR scanner (Siemens, Erlangen, Germany) was used to acquire MR images. Anatomical images were collected by T1-magnetization prepared rapid acquisition gradient echo [repetition time [TR] = 2,300 ms; echo time [TE] = 2.3 ms; flip angle [FA] = 8°; field of view [FOV] = 220 × 220 mm; voxel size = 1.0 × 1.0 × 1.0 mm; slice number = 192]. A T2-FLAIR (fluid-attenuated inversion recovery) sequence was applied to acquire tumor images (TR = 3,200 ms; TE = 87 ms; FA = 150°; FOV = 220 × 220 mm; voxel size = 0.9 × 0.9 × 5 mm; slice number = 25). Additionally, the parameters for the rs-fMRI sequence were as follows: TR = 2,000 ms; TE = 30 ms; FA = 75°; FOV = 220 × 220 mm; voxel size = 3.0 × 3.0 × 5.0 mm; slice number = 30; acquisition duration: 8 min. All MRI data were acquired within 72 h before tumor resection.

Functional MRI Preprocessing

The Graph Theoretical Network Analysis (GRETNA) toolbox (https://www.nitrc.org/projects/gretna) (10) was used for rs-fMRI processing. For each participant, pre-processing was conducted as follows: (a) transformation to a NIFTI file, (b) removal of the first images (time point number to remove = 5), (c) slice timing correction, (d) realignment, (e) spatial normalization [normalized to EPI template (11)], (f) smoothing (full width half maximum = 4 mm), (g) temporal detrending (linear detrending), (h) regressing out covariance (white matter signal: with WMMask_3 mm; CSF signal: with CSFMask_3 mm; head motion: Friston−24 parameters), (i) temporal filtering (0.01–0.08 Hz), and (j) scrubbing (using default parameters and the interpolation strategy: linear interpolation, FD threshold: 0.5, previous time point number: 1, subsequent time point number: 2).

Regions of Tumor Invasion

Tumors were segmented into individual spaces based on hyper-intensive regions of FLAIR images. Regions of glioma invasion (shown in **Figure S1**) were manually drawn by two independent neuroradiologists. If the images drawn varied by more than 5%, a third neuroradiologist with over 20 years of clinical experience made the final decision regarding the region location. All tumor masks were then normalized into the Montreal Neurological Institute (MNI) standard space using the clinical toolbox package in SPM8 (http://www.fil.ion.ucl.ac.uk/spm/software/spm8).

Regions of Interest

To calculate FC within cerebral functional networks, regions of interest (ROIs) were extracted from an open-access brain atlas, "brainnetome atlas" (http://www.brainnetome.org/) (12), which comprises 246 brain regions. In the current study, sub-templates were extracted, including sensorimotor, visual, default mode, auditory, and right executive control networks. Areas of tumor overlays were not included in the network analysis.

Any potential effect of tumor invasion to registration would be highly decreased in this way. Details of each ROI are provided in **Tables S1–S5**.

Network Construction

To construct the FC matrix, Pearson correlation coefficients were used to compare regional mean time-series for all possible pairs of nodes. Consequently, five different FC matrices were extracted from the five sub-templates of the sensorimotor, visual, default mode, auditory, and right executive control networks.

Graph Theoretical Measures

Global and nodal topological properties, including the shortest path length, global efficiency, local efficiency, nodal efficiency, and degree centrality (DC), were calculated for all patients and healthy controls by using graph theory analysis. All matrices were transformed into absolute value and binary matrices before calculating topological properties.

Gamma, lambda, and sigma were indices of small worldness. Gamma (γ) = C_{real}/C_{random} >> 1 (C represented cluster coefficient), lambda (λ) = L_{real}/L_{random} ~ 1 (L represented shortest path length), sigma (σ) = $\gamma/\lambda > 1$ (13, 14). A high value of sigma indicates a high efficiency of information delivery.

Statistical Analyses

Clinical characteristics were compared between the patient and healthy groups by using two-sample *t*-tests, Mann-Whitney U tests, chi-squared tests, one-way ANOVA tests, and Fisher's exact tests according to data type using GraphPad 7.0 (GraphPad Software; San Diego, CA).

Group differences in FC were, respectively, calculated based on each sub-template in GRETNA. To explore group differences in topological properties, we applied a series of sparsity thresholds (from 0.17 to 0.33, interval 0.01) consistent with a previously published study (4). For each participant, topological properties were calculated according to the corresponding FC matrix of each sub-template, which was generated according to sparsity. The areas under the curves of global and nodal topological characteristics were evaluated by means of one-way ANOVA (corrected with false-positive adjustment). *Post-hoc* pairwise comparisons for global and nodal characteristics were performed with two-sample *t*-tests. False discovery rate (FDR) was used to correct the differences in FC of each sub-template and nodal property.

Data Availability Statement

Anonymized data will be made available on request.

RESULTS

Demographic Characteristics

Of the 40 patients enrolled, 10 were excluded; hence, only the data of 30 patients were analyzed in the study. These 30 patients were classified into GRE (n = 15, 8 men) and non-GRE (n = 15, 7 men) groups based on the presence of GRE (**Table 1**). All patients were defined as right-handed using the Edinburgh Handedness Inventory test. The type of seizure onset was secondary generalized epilepsy. All patients accompanying glioma-related epilepsy (GRE) had taken levetiracetam 0.5 g twice a day to control GRE from the glioma diagnosed to surgery. There were four patients with GRE who took anti-epileptic drugs and experienced recurring epilepsy. Our postoperative follow-up showed that no patient with preoperative GRE experienced epilepsy at 6 months after tumor resection. All patients achieved Engel class I. In addition, 20 healthy participants matched for age, sex, and education level were recruited (9 men; all right-handed).

No significant differences were observed in age, sex, or years of education among the three groups (GRE, Non-GRE, control).

TABLE 1 | Demographic and clinical characteristics of patient groups.

Demographic and clinical characteristics	GRE (n = 15)	Non-GRE (n = 15)	Healthy (n = 20)	p-value
Sex				
Male	8	7	9	0.88
Female	7	8	11	
Age (y)*	38.2 ± 3.4	41.4 ± 3.1	38.0 ± 1.9	0.63
Handness				
Right	15	15	20	–
Left	0	0	0	
KPS score (preoperative)				
100	15	14	20	
90~100	0	1	0	> 0.99
80~90	0	0	0	
Education level (y)*	12.8 ± 1.2	13.2 ± 1.1	12.7 ± 0.8	0.13
Histopathology				
Astrocytoma	7	8	–	0.71
Oligodendroglioma	8	7	–	
IDH status				
Mutation	9	10		
Wild-type	6	5		0.71
Tumor volume (mL)*	44.83 ± 8.37	38.57 ± 10.16	–	0.64
Onset age (y)*	38.15 ± 1.9			–
Frequency before diagnosis				
Low (only once)	12			
Medium (2~3 times)	2			–
High (>3 times)	1			
Preoperative anti-epileptic drugs				–
Levetiracetam (0.5 g, twice a day)	15			
Postoperative epileptic control				–
Engel Class I	15			

**Values are means ± standard deviations, unless indicated otherwise.*
Using Mann-Whitney U test to compare differences in the Karnofsky performance status between the GRE and non- GRE groups.
Using Student's t-test to compare differences in tumor volume between the GRE and non-GRE groups.
Using one-way ANOVA test to compare differences in age and education level between the GRE and non-GRE groups.
Using chi-squared test to compare differences in sex, tumor location, and IDH status between the GRE and non-GRE groups.
IDH, isocitrate dehydrogenase; KPS, Karnofsky performance status.

No differences in Karnofsky performance status ($p > 0.99$, Mann-Whitney U test) or isocitrate dehydrogenase mutation status ($p = 0.71$, chi-squared test) were observed between the GRE and non-GRE groups. No significant differences in tumor volume were noted between the GRE and non-GRE groups ($p = 0.64$).

Functional Connectivity Differences

FC was compared among GRE, non-GRE, and control groups in the matrices of sensorimotor, visual, default mode, auditory, and right executive control networks. Except for FC in the visual network, no significant differences in FC in the other five networks were noted after multiple correction.

In total, 231 functional edges belonged to the visual network. A significant difference in FC strength within the visual network among the three groups was observed after FDR correction (**Figure 1** and detailed in **Table S6**).

Compared with those in the GRE group, four functional edges were identified with significantly higher FC in the non-GRE group after FDR correction (threshold of p-value $= 6 \times 10^{-3}$). Three of these edges originated from the V5/MT+_L node, which mediates sensory aspects of the visual motion area in the left hemisphere, and were connected to the medial superior occipital (msOccG_L), middle occipital (mOccG_L), and caudal cuneus gyri (cCunG_L) in the left hemisphere. The other edge connected the caudal cuneus gyrus (cCunG_L) to the lateral superior occipital gyrus (lsOccG_L) in the left hemisphere.

Compared with those in the control group, 21 functional edges were identified with significantly higher FC in the non-GRE group after FDR correction (threshold of p-value $= 6 \times 10^{-3}$, **Table S7**). Seven edges originated from the inferior occipital gyrus (iOccG_L) node in the left hemisphere and were connected to the bilateral caudal cuneus (cCunG_L/R), bilateral rostral lingual (rLinG_L/R), bilateral medial superior occipital (msOccG_L/R), and rostral cuneus gyri in the right hemisphere (rCunG_R). Six edges originated from the inferior occipital gyrus (iOccG_R) in the right hemisphere and were connected to the bilateral rostral lingual (rLinG_L/R), bilateral medial superior occipital (msOccG_L/R), ipsilateral caudal cuneus (cCunG_R), and contralateral rostral cuneus gyri (rCunG_R). Two edges originated from the occipital polar cortex node in the left hemisphere (OPC_L) and were connected to the bilateral medial superior occipital gyrus (msOccG_L/R). Four edges originated from the occipital polar cortex node in the right hemisphere (OPC_R) and were connected to the bilateral medial rostral cuneus (rCunG_L/R), contralateral caudal cuneus (cCunG_L), and contralateral medial superior occipital gyri (msOccG_L). Two edges originated from the node of V5/MT + in the left hemisphere (V5/MT + _L), and were connected to the ipsilateral medial superior occipital gyrus (msOccG_L/R) and caudal lingual gyrus (cLinG_L).

Differences in Global Topological Properties

In the visual network, there were some differences in global efficiency ($p = 0.025$), shortest path length ($p = 0.048$), and vulnerability ($p = 0.003$) among patient and control groups by testing with one-way ANOVA.

The non-GRE group exhibited significantly greater global efficiency (0.614 ± 0.002) than the GRE (0.599 ± 0.004, $p = 0.013$, *post-hoc* analysis, multiple correction with Tamhane's test) and control groups (0.592 ± 0.004, $p < 0.001$, *post-hoc* analysis, multiple correction with Tamhane's test, **Figure 2A**). No significant difference in global efficiency was detected between the GRE and control groups ($p = 0.518$, *post-hoc* analysis, multiple correction with Tamhane's test).

The non-GRE group exhibited a significantly shorter length of the shortest path (1.987 ± 0.019) than the GRE (2.123 ± 0.043, $p = 0.039$, *post-hoc* analysis, multiple correction with Tamhane's test, **Figure 2B**) and healthy groups (2.209 ± 0.052, $p = 0.001$, *post-hoc* analysis, multiple correction with Tamhane's test). No significant difference was observed between GRE and control groups ($p = 0.385$, *post-hoc* analysis, multiple correction with Tamhane's test).

The GRE group exhibited significantly worse network vulnerability (0.104 ± 0.014) than the healthy group (0.153 ± 0.012, $p = 0.012$, *post-hoc* analysis, multiple correction with Least Significance Difference, **Figure 2C**). The non-GRE group demonstrated significantly worse vulnerability (0.092 ± 0.012, $p = 0.002$, *post-hoc* analysis, multiple correction with Least Significance Difference) than the healthy group. No significant difference was noted between GRE and non-GRE groups ($p = 0.606$, *post-hoc* analysis, multiple correction with Least Significance Difference).

No significant alterations of small-worldness properties, including gamma, lambda, and sigma, were found among the three groups.

Differences in Nodal Topological Properties

In the visual network, there were some differences in nodal efficiencies of the occipital polar cortex in the left hemisphere (OPC_L, $p = 0.001$), the occipital polar cortex in the right hemisphere (OPC_R, $p = 0.003$), and the inferior occipital gyrus in the left hemisphere (iOccG_L, $p < 0.001$) among patient and control groups by testing with one-way ANOVA. After *post-hoc* analysis, we found that compared with the healthy group, nodal efficiencies of the OPC_L, OPC_R, and iOccG_L of GRE and non-GRE groups significantly increased after multiple correction (**Table S8**). Hence, we respectively, compared differences in the nodal efficiency of these nodes between each of the patient and control groups.

Nodal efficiencies of the OPC_L, OPC_R, and iOccG_L were significantly lower in the non-GRE group (OPC_L: 0.577 ± 0.032, OPC_R: 0.527 ± 0.029, and iOccG_L: 0.588 ± 0.026) than those in the control group (OPC_L: 0.330 ± 0.048, OPC_R: 0.316 ± 0.039, and iOccG_L: 0.287 ± 0.049) after FDR correction, respectively (OPC_L: $p = 0.002$, OPC_R: $p = 0.002$, and iOccG_L: $p < 0.001$, threshold of p-value $= 0.002$). Moreover, the nodal efficiencies of the OPC_L, OPC_R, and iOccG_L were lower in the GRE group than those in the control group, respectively, but these differences were not significant after FDR correction. Additionally, no differences were identified in nodal efficiency of the bilateral occipital polar cortex or inferior occipital gyrus between GRE and non-GRE groups (**Figure 3** and **Table S8**).

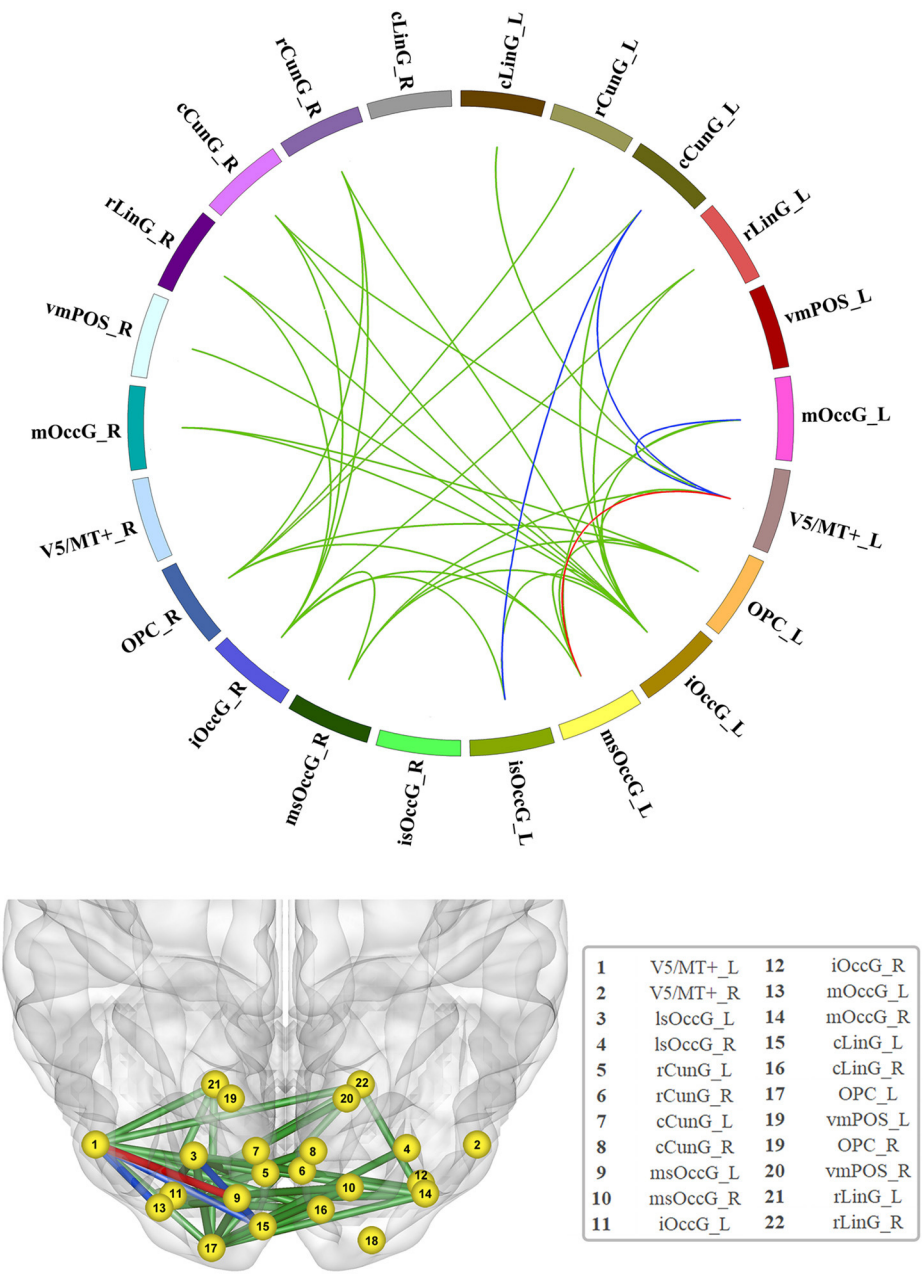

FIGURE 1 | Significant increase in functional connectivity (FC). The red line represents the edge of FC that was increased in the non-GRE group compared to the GRE and healthy groups. The blue lines represent the edges of FC that were increased in the non-GRE group compared to the GRE group. The green lines represent the edges of FC that were increased in the non-GRE group compared to the healthy group.

Compared to the control group (DC = 8.5), the DC of the ventromedial parieto-occipital sulcus node in the left hemisphere (vmPOS_L) was significantly lower in the GRE group (DC = 5, p = 0.002, Mann-Whitney U, FDR-corrected, p-value threshold = 0.011) and non-GRE group (DC = 5, p = 0.004, Mann-Whitney U, FDR-corrected, p-value threshold = 0.011). Compared with the control group (OPC_L: DC = 8.5, OPC_R: DC = 2.5), the DCs of occipital polar cortex nodes in the left (OPC_L), and right (OPC_R) hemispheres were significantly higher in the non-GRE group (OPC_L: DC = 6.5, p = 0.003, OPC_R: DC = 5, p = 0.009, Mann-Whitney U, FDR-corrected, p-value threshold = 0.011). Compared with the control group (DC = 2.5), the DC of the inferior occipital gyrus node in the left hemisphere (iOccG_L) was significantly higher in the non-GRE group (DC = 7, p = 0.002, Mann-Whitney U, FDR-corrected, p-value threshold = 0.011). Compared to the control group (vmPOS_R: DC =

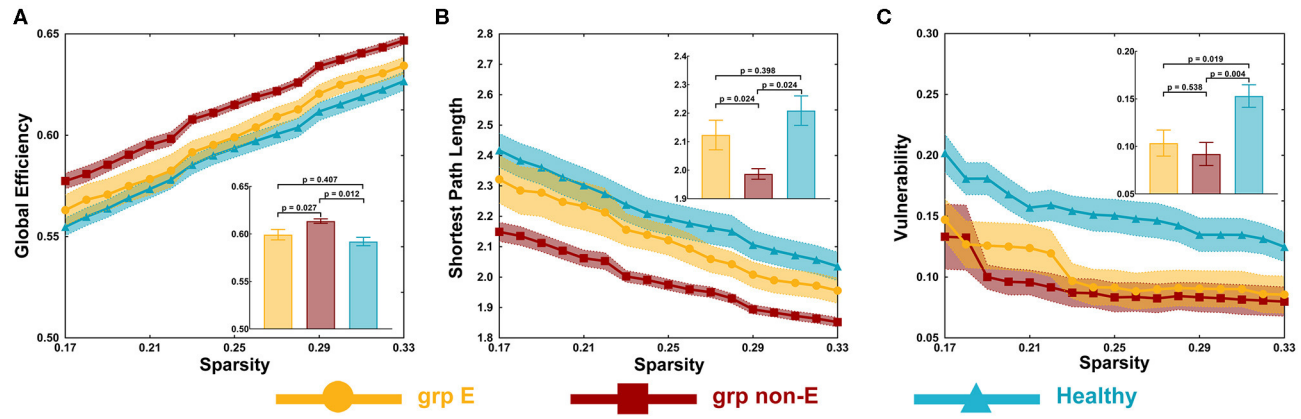

FIGURE 2 | Global topological properties. **(A)** Global efficiency. **(B)** Shortest path length. **(C)** Vulnerability. *P*-value threshold = 0.05. Grp E = GRE group. Grp non-E = non-GRE group.

8, rCunG_R: DC = 10), the DCs of the ventromedial parieto-occipital sulcus nodes in the right hemisphere (vmPOS_R) and the rostral cuneus gyrus in the left hemisphere (rCunG_L) were significantly lower in the non-GRE group (vmPOS_R: DC = 3, $p = 0.011$, and rCunG_L: DC = 7, $p = 0.002$, Mann-Whitney U, FDR-corrected, *p*-value threshold = 0.011, **Figure 4** and **Table S9**). Relative to those of the GRE group, no differences were identified in nodal efficiency in the ventromedial parieto-occipital sulcus, rostral cuneus gyrus, and inferior occipital gyrus nodes in the right hemisphere or the bilateral occipital polar cortex between non-GRE and control groups.

DISCUSSION

This study explored alterations in functional networks induced by temporal GRE. Our findings indicated that both temporal glioma and GRE altered both FC and topological properties of the healthy visual network. No significant alterations caused by glioma and GRE were detected in other networks. We identified that temporal GRE facilitated alterations in the visual network in an opposite manner to that of glioma-induced alterations.

An extensive increase in visual network FC was induced by temporal glioma. This extensive increase in FC was not significant in patients with GRE compared to that in healthy controls. DLGG is a slow-growing primary brain tumor and is associated with marked functional plasticity (15). DLGG facilitates reorganization of functional networks adjacent to the tumor (16–18), resulting in increased FC (19). In our study, gliomas were located in the left temporal lobe, which is close to the visual network. Hence, visual network FC was increased in patients with glioma and without GRE. Conversely, primary epilepsy disrupts healthy networks by decreasing neuronal activity and synchronous fluctuations (5, 20–22), resulting in decreased FC of networks in patients with epilepsy. For this reason, visual network FC in patients with both temporal glioma and GRE was not significantly different from that of healthy controls. Based on our findings of FC alterations in the visual network, a hypothesis was proposed that GRE further alters the visual network based on alterations caused by temporal glioma.

Global efficiency represents the ability to integrate and communicate information (23). Increased global efficiency and decreased shortest path lengths in the visual network were noted in patients with temporal glioma. These changes were not significant when comparing patients with GRE to healthy controls. Reduced global efficiency has been reported in idiopathic epilepsy patients (24–28); however, our findings differed from these results. This discrepancy may result from differences in pathogenesis and network reorganization (16–18). As discussed above, a glioma induces reorganization of functional networks. Hence, the shortest path length was significantly decreased in patients with glioma and without GRE. Simultaneously, decreased shortest path lengths indicate alterations in structural connectivity and communication pathways. Temporal glioma-induced topological properties of the visual network were altered. Epilepsy can induce cortical sclerosis (29), gray matter atrophy (30), and cortical hypometabolism (31), resulting in decreased global efficiency and increased shortest path lengths in patients with epilepsy. Compared to that in healthy controls, global efficiency and shortest path lengths were not significantly altered in patients with temporal glioma and GRE. However, the absence of significant alterations does not necessarily indicate that GRE facilitated recovery of the visual network. We believe that this apparent lack of change is due to a combination of glioma and GRE. For instance, glioma increases global efficiency and GRE induces decreased global efficiency.

Vulnerability is an index to evaluate network stability (32). We observed that the vulnerability of patients in GRE and non-GRE groups were lower than that in the control group. These findings indicate that the visual network was more stable in patients than in controls. Simultaneously, our findings verified that both glioma itself and GRE induced alterations in the visual network, rather than GRE facilitating glioma-induced alterations in the visual network.

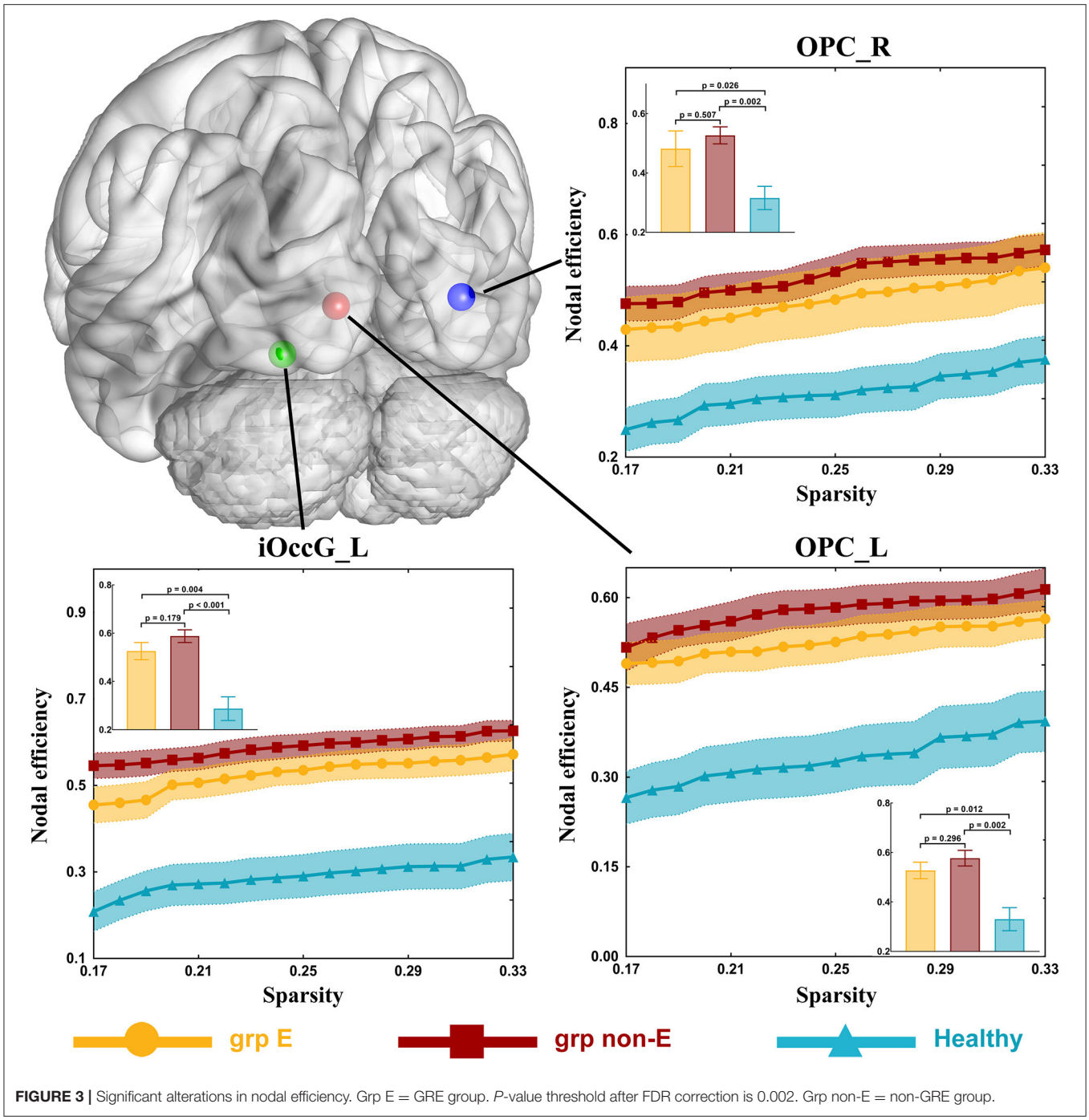

FIGURE 3 | Significant alterations in nodal efficiency. Grp E = GRE group. *P*-value threshold after FDR correction is 0.002. Grp non-E = non-GRE group.

Alterations in topological properties of nodes highlighted in detail the form of network alterations. Compared with the control group, the nodal efficiencies of OPC_L, OPC_R, and iOccG_L were increased in the non-GRE group. Similarly, the DCs of these nodes had increased. These findings indicated that the OPC_L, OPC_R, and iOccG_L nodes were activated by the glioma itself and were inhibited by GRE. Moreover, the DC of the vmPOS_L node was significantly decreased in both GRE and non-GRE groups compared to the control group, suggesting that the glioma itself disrupted connections originating from vmPOS_L. Further, the DCs of vmPOS_R and rCunG_L nodes were reduced in the non-GRE group compared to the GRE and control groups. These DC alterations suggested that GRE altered the visual network by disrupting connections originating from these nodes.

Consequently, our findings verified that both temporal glioma and GRE altered the visual network, and the alterations caused by GRE were opposite to those caused

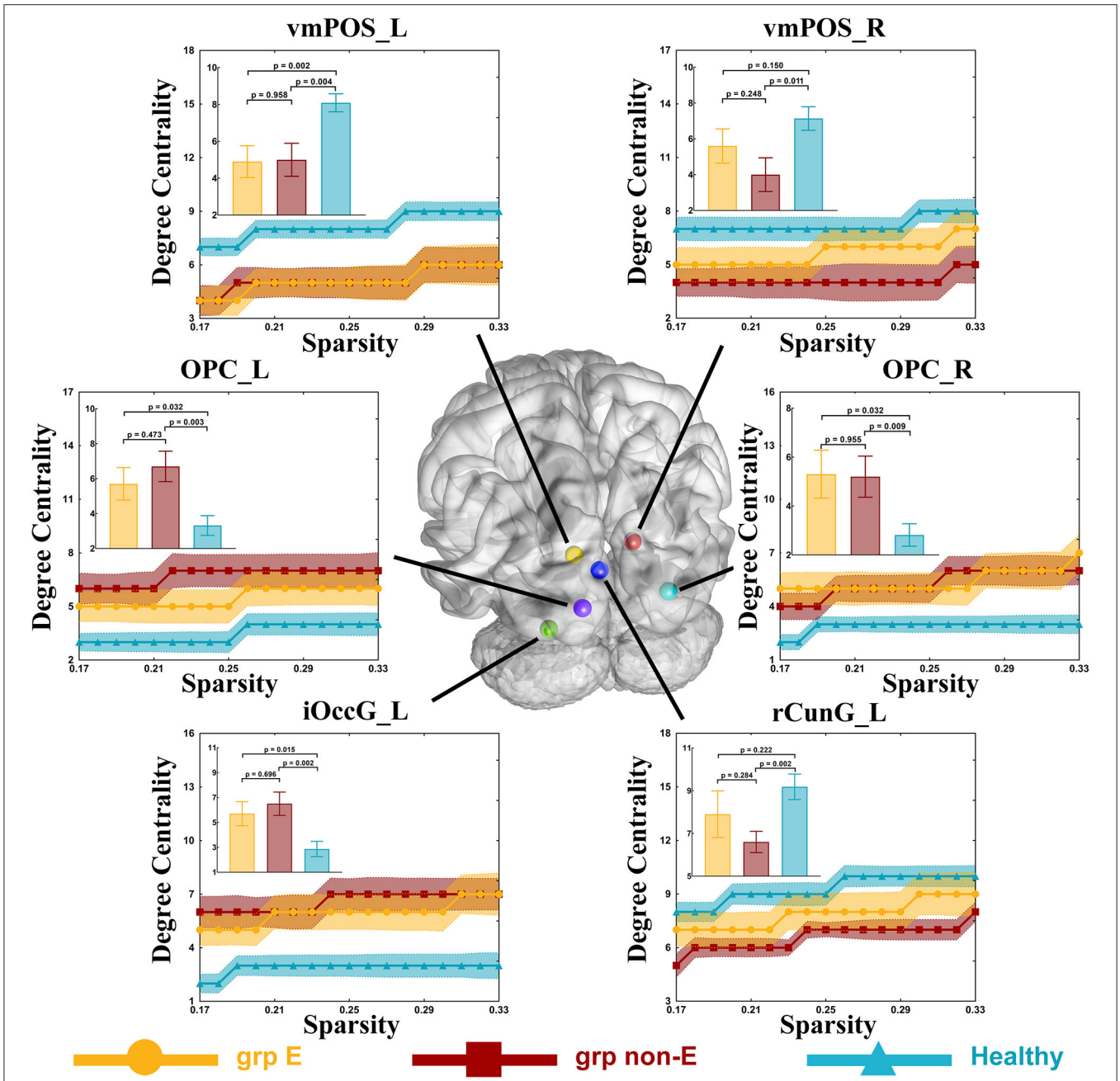

FIGURE 4 | Significant alterations in degree centrality. Grp E = GRE group. *P*-value threshold after FDR correction is 0.011. Grp non-E = non-GRE group.

by the glioma itself. Identifying the risk of preoperative seizures in patients with left temporal glioma requires analysis of nodal properties of nodes that were inhibited by GRE.

LIMITATIONS

Although the number of patients was limited, the positive result identified in this situation should be reliable with a strict correction. In this study, the topological properties were calculated by using functional matrices with absolute values as previous studies used (14, 33, 34). Our findings showed that there was no difference in FC between the GRE and healthy groups. The phenomenon that aberrant FC in specific cognitive networks tended to normalize with levetiracetam administration was firstly found in patients with primary temporal epilepsy who took levetiracetam over 3 months (35). In our study, all patients in the GRE group

took levetiracetam for a short period (< 14 days). To our knowledge, it is still not clear that whether alterations of FC can be induced by levetiracetam in a short time. Future studies should focus on the time effect of antiepileptic drugs on brain networks.

CONCLUSION

Temporal lobe glioma in the left hemisphere and GRE altered visual networks. Alterations in the visual network caused by GRE were opposite to those caused by the glioma itself. Our findings provide novel insight into GRE and contribute to improved understanding of functional network alterations in patients with glioma.

DATA AVAILABILITY STATEMENT

The datasets generated for this study are available on request to the corresponding author.

ETHICS STATEMENT

The studies involving human participants were reviewed and approved by IRB of Beijing Tiantan Hospital. The patients/participants provided their written informed consent to participate in this study. Written informed consent was obtained from the individual(s) for the publication of any potentially identifiable images or data included in this article.

AUTHOR CONTRIBUTIONS

SF and CZ: study concept and design and data acquisition and analysis. SF, CZ, XF, and YW: statistics/verified analytical method. SF, CZ, and XF: writing the first draft. XF, YW, and TJ: supervision study. All authors read and approved final version. SF is the first contributed author of this manuscript. XF, YW, and TJ were all correspondent for this manuscript but not equally contributed authors.

FUNDING

This study was supported by funds from the National High Technology Research and Development Program of China (863 program) (2015AA020504), the National Basic Research Program of China (No. 2015CB755500), and the National Natural Science Foundation of China (No. 81601452).

ACKNOWLEDGMENTS

Thanks to Dr. Meng Lanxi for imaging data acquisition and Dr. Qian Tianyi for guidance for this study.

SUPPLEMENTARY MATERIAL

The Supplementary Material for this article can be found online at: https://www.frontiersin.org/articles/10.3389/fneur.2020.00684/full#supplementary-material

REFERENCES

1. Liang S, Fan X, Zhao M, Shan X, Li W, Ding P, et al. Clinical practice guidelines for the diagnosis and treatment of adult diffuse glioma-related epilepsy. *Cancer Med.* (2019) 8:4527–35. doi: 10.1002/cam4.2362
2. Li Y, Shan X, Wu Z, Wang Y, Ling M, Fan X. IDH1 mutation is associated with a higher preoperative seizure incidence in low-grade glioma: a systematic review and meta-analysis. *Seizure.* (2018) 55:76–82. doi: 10.1016/j.seizure.2018.01.011
3. Shan X, Fan X, Liu X, Zhao Z, Wang Y, Jiang T. Clinical characteristics associated with postoperative seizure control in adult low-grade gliomas: a systematic review and meta-analysis. *Neuro Oncol.* (2018) 20:324–31. doi: 10.1093/neuonc/nox130
4. Ji GJ, Yu Y, Miao HH, Wang ZJ, Tang YL, Liao W. Decreased network efficiency in benign epilepsy with centrotemporal spikes. *Radiology.* (2017) 283:186–94. doi: 10.1148/radiol.2016160422
5. Li Q, Chen Y, Wei Y, Chen S, Ma L, He Z, et al. Functional network connectivity patterns between idiopathic generalized epilepsy with myoclonic and absence seizures. *Front Comput Neurosci.* (2017) 11:38. doi: 10.3389/fncom.2017.00038
6. Bernhardt BC, Chen Z, He Y, Evans AC, Bernasconi N. Graph-theoretical analysis reveals disrupted small-world organization of cortical thickness correlation networks in temporal lobe epilepsy. *Cereb Cortex.* (2011) 21:2147–57. doi: 10.1093/cercor/bhq291
7. He Y, Wang J, Wang L, Chen ZJ, Yan C, Yang H, et al. Uncovering intrinsic modular organization of spontaneous brain activity in humans. *PLoS ONE.* (2009) 4:e5226. doi: 10.1371/journal.pone.0005226
8. Englot DJ, Hinkley LB, Kort NS, Imber BS, Mizuiri D, Honma SM, et al. Global and regional functional connectivity maps of neural oscillations in focal epilepsy. *Brain.* (2015) 138(Pt 8):2249–62. doi: 10.1093/brain/awv130
9. Englot DJ, Gonzalez HFJ, Reynolds BB, Konrad PE, Jacobs ML, Gore JC, et al. Relating structural and functional brainstem connectivity to disease measures in epilepsy. *Neurology.* (2018) 91:e67–77. doi: 10.1212/WNL.0000000000005733
10. Wang J, Wang X, Xia M, Liao X, Evans A, He Y. GRETNA: a graph theoretical network analysis toolbox for imaging connectomics. *Front Hum Neurosci.* (2015) 9:386. doi: 10.3389/fnhum.2015.00386
11. Calhoun VD, Wager TD, Krishnan A, Rosch KS, Seymour KE, Nebel MB, et al. The impact of T1 versus EPI spatial normalization templates for fMRI data analyses. *Hum Brain Mapp.* (2017) 38:5331–42. doi: 10.1002/hbm.23737
12. Fan L, Li H, Zhuo J, Zhang Y, Wang J, Chen L, et al. The human brainnetome atlas: a new brain atlas based on connectional architecture. *Cereb Cortex.* (2016) 26:3508–26. doi: 10.1093/cercor/bhw157
13. Humphries MD, Gurney K, Prescott TJ. The brainstem reticular formation is a small-world, not scale-free, network. *Proc Biol Sci.* (2006) 273:503–11. doi: 10.1098/rspb.2005.3354
14. Gong Y, Wu H, Li J, Wang N, Liu H, Tang X. Multi-granularity whole-brain segmentation based functional network analysis using resting-state fMRI. *Front Neurosci.* (2018) 12:942. doi: 10.3389/fnins.2018.00942
15. Almairac F, Duffau H, Herbet G. Contralesional macrostructural plasticity of the insular cortex in glioma patients. *Neurology.* (2018) 91:e1902–8. doi: 10.1212/WNL.0000000000006517
16. Duffau H. Brain plasticity and tumors. *Adv Tech Stand Neurosurg.* (2008) 33:3–33. doi: 10.1007/978-3-211-72283-1_1
17. Duffau H. The "frontal syndrome" revisited: lessons from electrostimulation mapping studies. *Cortex.* (2012) 48:120–31. doi: 10.1016/j.cortex.2011.04.029
18. Herbet G, Maheu M, Costi E, Lafargue G, Duffau H. Mapping neuroplastic potential in brain-damaged patients. *Brain.* (2016) 139(Pt 3):829–44. doi: 10.1093/brain/awv394

19. van Dokkum LEH, Moritz Gasser S, Deverdun J, Herbet G, Mura T, D'Agata B, et al. Resting state network plasticity related to picture naming in low-grade glioma patients before and after resection. *Neuroimage Clin.* (2019) 24:102010. doi: 10.1016/j.nicl.2019.102010
20. Woodward KE, Gaxiola-Valdez I, Goodyear BG, Federico P. Frontal lobe epilepsy alters functional connections within the brain's motor network: a resting-state fMRI study. *Brain Connect.* (2014) 4:91–9. doi: 10.1089/brain.2013.0178
21. Cao X, Qian Z, Xu Q, Shen J, Zhang Z, Lu G. Altered intrinsic connectivity networks in frontal lobe epilepsy: a resting-state fMRI study. *Comput Math Methods Med.* (2014) 2014:864979. doi: 10.1155/2014/864979
22. Yang T, Luo C, Li Q, Guo Z, Liu L, Gong Q, et al. Altered resting-state connectivity during interictal generalized spike-wave discharges in drug-naive childhood absence epilepsy. *Hum Brain Mapp.* (2013) 34:1761–7. doi: 10.1002/hbm.22025
23. Zhao T, Cao M, Niu H, Zuo XN, Evans A, He Y, et al. Age-related changes in the topological organization of the white matter structural connectome across the human lifespan. *Hum Brain Mapp.* (2015) 36:3777–92. doi: 10.1002/hbm.22877
24. Sporns O, Zwi JD. The small world of the cerebral cortex. *Neuroinformatics.* (2004) 2:145–62. doi: 10.1385/NI:2:2:145
25. Besseling RM, Overvliet GM, Jansen JF, van der Kruijs SJ, Vles JS, Ebus SC, et al. Aberrant functional connectivity between motor and language networks in rolandic epilepsy. *Epilepsy Res.* (2013) 107:253–62. doi: 10.1016/j.eplepsyres.2013.10.008
26. Haneef Z, Lenartowicz A, Yeh HJ, Engel J, Stern JM Jr. Effect of lateralized temporal lobe epilepsy on the default mode network. *Epilepsy Behav.* (2012) 25:350–7. doi: 10.1016/j.yebeh.2012.07.019
27. Lee C, Im CH, Koo YS, Lim JA, Kim TJ, Byun JI, et al. Altered Network Characteristics of Spike-Wave Discharges in Juvenile Myoclonic Epilepsy. *Clin EEG Neurosci.* (2017) 48:111–17. doi: 10.1177/1550059415621831
28. Luo C, Qiu C, Guo Z, Fang J, Li Q, Lei X, et al. Disrupted functional brain connectivity in partial epilepsy: a resting-state fMRI study. *PLoS ONE.* (2011) 7:e28196. doi: 10.1371/journal.pone.0028196
29. Aparicio J, Carreno M, Bargallo N, Setoain X, Rubi S, Rumia J, et al. Combined (18)F-FDG-PET and diffusion tensor imaging in mesial temporal lobe epilepsy with hippocampal sclerosis. *Neuroimage Clin.* (2016) 12:976–89. doi: 10.1016/j.nicl.2016.05.002
30. Caciagli L, Bernasconi A, Wiebe S, Koepp MJ, Bernasconi N, Bernhardt BC. A meta-analysis on progressive atrophy in intractable temporal lobe epilepsy: time is brain? *Neurology.* (2017) 89:506–16. doi: 10.1212/WNL.0000000000004176
31. Celiker Uslu S, Yuksel B, Tekin B, Sariahmetoglu H, Atakli D. Cognitive impairment and drug responsiveness in mesial temporal lobe epilepsy. *Epilepsy Behav.* (2019) 90:162–7. doi: 10.1016/j.yebeh.2018.10.034
32. Latora V, Marchiori M. Vulnerability and protection of infrastructure networks. *Phys Rev E.* (2005) 71(1 Pt 2):015103. doi: 10.1103/PhysRevE.71.015103
33. Fornito A, Zalesky A, Bullmore ET. Network scaling effects in graph analytic studies of human resting-state FMRI data. *Front Syst Neurosci.* (2010) 4:22. doi: 10.3389/fnsys.2010.00022
34. Mazrooyisebdani M, Nair VA, Garcia-Ramos C, Mohanty R, Meyerand E, Hermann B, et al. Graph theory analysis of functional connectivity combined with machine learning approaches demonstrates widespread network differences and predicts clinical variables in temporal lobe epilepsy. *Brain Connect.* (2020) 10:39–50. doi: 10.1089/brain.2019.0702
35. Pang XM, Liang XL, Zhou X, Liu JP, Zhang Z, Zheng JO. Alterations in intra- and internetwork functional connectivity associated with levetiracetam treatment in temporal lobe epilepsy. *Neurol Sci.* (2020) doi: 10.1007/s10072-020-04322-8. [Epub ahead of print].

Conflict of Interest: The authors declare that the research was conducted in the absence of any commercial or financial relationships that could be construed as a potential conflict of interest.

frontiers in Psychiatry

BRIEF RESEARCH REPORT
published: 05 August 2020
doi: 10.3389/fpsyt.2020.00777

A Neglected Topic in Neuroscience: Replicability of fMRI Results With Specific Reference to ANOREXIA NERVOSA

Isabelle Horster[1], Kathrin Nickel[2], Lukas Holovics[1], Stefan Schmidt[1], Dominique Endres[2], Ludger Tebartz van Elst[2], Almut Zeeck[1], Simon Maier[1,2†] and Andreas Joos[1,3†]*

[1] Department of Psychosomatic Medicine and Psychotherapy, University Medical Center, University of Freiburg, Freiburg, Germany, [2] Department of Psychiatry and Psychotherapy, University Medical Center, University of Freiburg, Freiburg, Germany, [3] Department of Psychosomatic Medicine and Psychotherapy, Ortenau Klinikum, Offenburg, Germany

Functional magnetic resonance imaging (fMRI) studies report impaired functional correlates of cognition and emotion in mental disorders. The validity of preexisting studies needs to be confirmed through replication studies, which there is a lack of. So far, most replication studies have been conducted on non-patients (NP) and primarily investigated cognitive and motor tasks. To fill this gap, we conducted the first fMRI replication study to investigate brain function using disease-related food stimuli in patients with anorexia nervosa (AN). Using fMRI, we investigated 31 AN patients and 27 NP for increased amygdala and reduced midcingulate activation when viewing food and non-food stimuli, as reported by the original study (11AN, 11NP; Joos et al., 2011). Similar to the previous study, we observed in the within group comparisons (food>non-food) a frontoinsular activation for both groups. Although in AN the recorded activation clustered more prominently and extended into the cingulate cortex. In the between-group comparisons, the increased amygdala and reduced midcingulate activation could not be replicated. Instead, AN showed a higher activation of the cingulate cortices, the pre-/postcentral gyrus and the inferior parietal lobe. Unlike in the initial study, no significant differences between NP>AN could be observed. The inconsistency of results and the non-replication of the study could have several reasons, such as high inter-individual variance of functional correlates of emotion processing, as well as intra-individual variances and the smaller group size of the initial study. These results underline the importance of replication for assessing the reliability and validity of results from fMRI research.

Keywords: replicability, anorexia nervosa, food, functional magnetic resonance imaging (fMRI), neurobiology

OPEN ACCESS

Edited by:
Szilvia Anett Nagy,
University of Pécs, Hungary

Reviewed by:
Owen O'Daly,
King's College London, United Kingdom
Luke Norman,
University of Michigan, United States
Daniel John Halls,
King's College London, United Kingdom

***Correspondence:**
Simon Maier
simon.maier@uniklinik-freiburg.de

†These authors have contributed equally to this work and share senior authorship

Specialty section:
This article was submitted to Neuroimaging and Stimulation, a section of the journal Frontiers in Psychiatry

Received: *30 May 2020*
Accepted: *21 July 2020*
Published: *05 August 2020*

Citation:
Horster I, Nickel K, Holovics L, Schmidt S, Endres D, Tebartz van Elst L, Zeeck A, Maier S and Joos A (2020) A Neglected Topic in Neuroscience: Replicability of fMRI Results With Specific Reference to ANOREXIA NERVOSA. Front. Psychiatry 11:777. doi: 10.3389/fpsyt.2020.00777

BACKGROUND

Anorexia nervosa (AN) usually affects young women and shows high persistence rates of around 50% (1). Furthermore, it has the highest mortality of all mental disorders (2). The etiology is largely unknown, although an interplay of genetic and environmental factors is assumed (3). The AN pathophysiology consists largely of reduced weight, fear of weight gain and a distorted body perception, as well as a cognitive preoccupation with body and food related issues. For this reason, functional magnetic resonance imaging (fMRI) studies have focused on paradigms with disease-related food and body stimuli to investigate the neuronal correlation of the disorder.

The first fMRI study in AN with visual food cues (six patients, six non-patients (NP)) described greater activation of anterior cingulate cortices (ACC), left insular, and amygdala-hippocampal regions (4). Fourteen years later, a meta-analysis across nine studies applying food cues, reported increased activation of frontocingular cortices and lower activation of the parietal brain (5). However, the design and the results differed between the included studies. Three further reviews confirmed these inconsistencies (6–8) and therefore conclusions remain questionable. None of the studies were confirmed by replication, so the reported findings should not yet be regarded as established scientific knowledge.

The necessity of replications is not only increasingly recognized in the neurosciences, but in the entire scientific community (9–12). The awareness of a general lack of data replication in science, also referred to as a "reproducibility/replicability crisis" (13–16), has emerged in particular during the last decade (17). Although it is generally recognized that the replication and reproduction of scientific claims is essential in scientific research, the deficit of replications persists (9). Furthermore, there is no general agreement on the definition or directives of replication procedures (9, 16, 18, 19). The *Committee on Reproducibility and Replicability in Science* (9) suggested the following definition: "Reproducibility is obtaining consistent results using the same input data, computational steps, methods, and code, and conditions of analysis. (…) Replicability is obtaining consistent results across studies aimed at answering the same scientific question, each of which has obtained its own data. Two studies may be considered to have replicated if they obtain consistent results given the level of uncertainty inherent in the system under study." Other studies in the field also refer to this definition (15, 17, 20) and this publication adheres to it, too. In addition to exact definitions, the precise description of study protocols, data, and results is of importance (21). Replication serves the validation of exploratory results and therefore the transition from exploratory data into knowledge, to generate confirmable and generalizable principles (9).

There have been some replication efforts in the field of fMRI, but the studies are largely limited to NP and to motor and cognitive tasks (15, 17, 22, 23). However, Bennett and Miller (24) strongly assume that factors influencing the ability of replication (i.e., variance) are larger in emotional paradigms and in clinical populations, including eating disorders (25). Furthermore, low sample sizes, low power, and low effect-sizes, which reduce replicability, have been generally reported in the field of fMRI research (26–28). If replication attempts failed with sample sizes of 15–30, as a consequence of low power and low effect-sizes, this would have profound influences on planning further studies with respect to number of participants and study set-ups (29).

Against this background, the objective of the present study was to replicate for the first time an fMRI study in AN using visual food and non-food stimuli. Our aim was to replicate the original study (30) with the same research question in a larger but similar sample, using the identical study design and closely following the fMRI and analysis protocol.

In the original study (30), both AN (N=11) and NP (N=11) showed an involvement of frontoinsular and ACC areas when comparing food>non-food pictures (within-group effects) (**Figure 2A**). Comparing the two groups, AN had elevated blood oxygenation level dependent (BOLD) responses of the right amygdala and less activation in midcingulate cortices (MCC).

We assume that (1) there will be different neural correlates of the food-stimuli in AN compared to NP, uncovering disease-related responses, (2) that within-group data of food>non-food pictures will show an involvement of frontoinsular and cingulate cortices, and (3) between-group data will reveal elevated BOLD responses of the right amygdala and decreased activation in midcingulate cortices (MCC) in AN compared to NP similar to our earlier results.

In addition, we assessed emotional reactions to the stimuli by rating the images after scanning.

MATERIALS AND METHODS

This study was part of a multimodal MRI study, which assessed structural, metabolic and other functional data [see, e.g., (31–36)]. We replicated the aforementioned food paradigm with 31 AN and 27 NP.

In the following, we first describe Material and Methods of the current study and point towards differences with the earlier study in the second section.

Current Replication Study

Sample and State of Participants

For sample description see **Table 1**. All participants were studied in the second half of the menstrual cycle or the equivalent stage with estrogen and progesterone when taking oral contraception in the current investigation. All participants were offered a standardized breakfast before scanning. Caloric intake was (expectedly) lower in the AN group (**Table 1**). Of the 31 AN, 28 were diagnosed with a restrictive and 3 with a binge-eating/purging subtype.

Paradigm Presentation

The same visual food cues as in the previous study were presented in a block design showing 10 consecutive pictures of food followed by 10 consecutive non-food pictures per block – with a duration of 3 s per picture. As mentioned in Joos et al. (30)

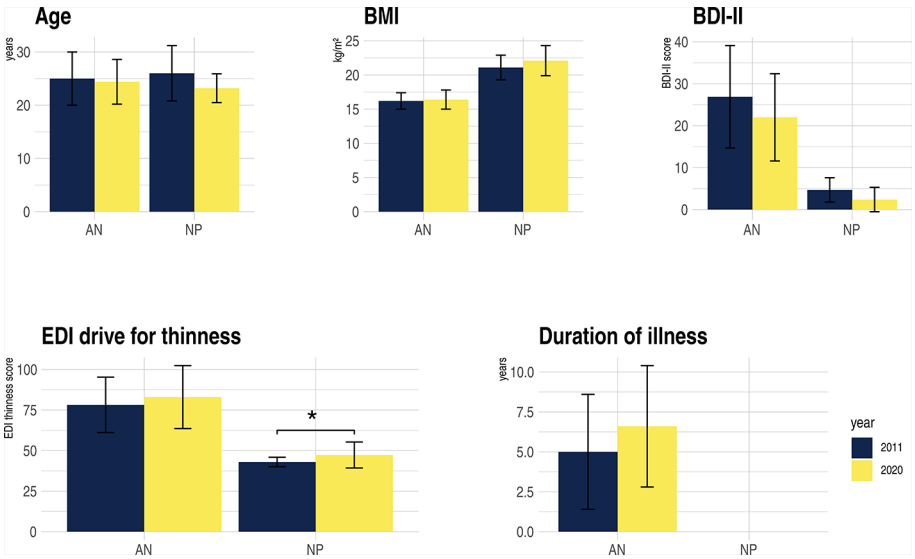

FIGURE 1 | Clinical characteristics of anorexia nervosa (AN) and non-patient (NP), study sample 2011 compared to 2020. BDI-II, Becks Depression-Inventary-2; BMI, Body-Mass-Index; EDI-drive for thinness, Eating Disorder Inventory; kg, kilograms; m^2, square meter; *p = 0.014. For further clinical characteristics of the replication study see **Table 1**.

TABLE 1 | Clinical characteristics of anorexia nervosa (AN) and non-patients (NP).

	Anorexia Nervosa(N=31)		*Non-Patients(N=27)*		*T-Test*	
					t-score	*p-value*
	Mean	SD	Mean	SD		
Age (years)	24.0	4.4	23.6	3.0	0.44	0.659
Duration of illness (years)	6.6	3.8	–	–		
Current BMI (kg/m²)	16.2	1.4	22.1	2.2	-11.97	<.001
Lowest-Lifetime BMI (kg/m²)	14.8	1.5	20.9	1.8	-11.08	<.001
EDI—total score	61.8	9.3	44.6	3.1	9.19	<.001
EDI—drive for thinness (t values)	83.5	19.6	44.6	6.4	9.85	<.001
EDI—body dissatisfaction (t values)	61.7	12.7	46.6	8.0	5.31	<.001
BDI-II	21.5	10.5	2.3	2.7	9.2	<.001
EDE total score	3.3	1.1	0.4	0.3	13.53	<.001
MWT-B	28.4	5.2	28.0	4.3	0.34	0.736
Caloric intake at breakfast	142.3	157.5	386.3	85.7	-7.12	<.001
STAI-state	38.7	6.6	32.8	4.8	3.83	<.001
STAI-trait	45.5	7.7	29.3	6.8	8.39	<.001

BDI-II, Becks Depression-Inventory-2; BMI, Body-Mass-Index; EDE, Eating Disorder Examination Interview; EDI-2, Eating Disorder Inventory-2; kg, kilogram; m2, square meter; MWT-B, Multiple-Choice-Vocabulary-Intelligence Test - German for Mehrfachwahl-Wortschatz-Test-Version (37); SD, standard deviation; STAI, State-Trait Anxiety Inventory.

some of the stimuli have been created by ourselves while others were kindly provided by R. Uher and colleagues (38).

Five blocks of each condition were presented. Examples of the stimuli used can be found in **Supplement 1**.

The instruction was identical to the previous study: participants should watch the pictures attentively (30).

MRI Data Acquisition and Preprocessing

A T1-weighted MPRAGE sequence was recorded as an anatomical reference (repetition time (TR): 2300ms, echo time (TE): 2.98ms, flip angle (FA): 90°, field-of-view (FOV): 240*256 mm, 176 slices, voxel size: 1x1x1 mm) using a Siemens 3T PRISMA Magnetom (Erlangen, Germany) equipped with a 20-channel head coil. The T1-weighted sequence was followed by the recording of 159 functional echo-planar T2*-weighted (EPI) images (TR: 2,500 ms, TE: 30 ms, FA: 90°, FOV: 192*192 mm, 38 slices, voxel size: 3x3x3 mm, interleaved). All EPI volumes were automatically rigid-body transformed to correct for head motion and a distortion correction algorithm was applied (39).

The statistical parametric mapping software SPM12 [Welcome Trust Centre of Imaging Neuroscience, London; for details, see (40)] was applied for the preprocessing and statistical analyses of the functional data. The first two volumes of each run were disregarded as so-called dummy scans, an artifact detection algorithm (ArtRepair toolbox, SPM) was applied to detect head motion and spiking artifacts. The realignment to the first volume of the raw functional images that were not motion corrected, was done to generate six head motion parameters (rotation and translation in x, y, z direction). To correct for influences of head motion those parameters were entered in the statistical first-level analysis as regressors of no interest. Using the anatomical MPRAGE image the remaining motion corrected images were spatially normalized with the Montreal National Institute (MNI) reference system followed by the smoothing of the functional images using a three-dimensional isotropic Gaussian kernel (8 mm full width at half maximum) to increase the signal-to-noise ratio and to compensate for inter-individual differences in location of corresponding functional areas. To remove low frequency artifacts across the time-series we applied a high-pass filter (128 s).

Statistical Analyses

Psychometric and behavioral data were assessed by two-sample t-test with a level of significance of $p<0.05$.

For functional data a linear regression model (general linear model [GLM]) with six regressors, modeling the head motion parameters of the realignment procedure, was fitted to the signal time courses of each voxel for each participant. The food and nonfood regressors were fitted with a canonical hemodynamic response function.

Whole Brain Second Level Analysis Replicating the Original Study

The resulting beta estimates for the two regressors were fed into a voxel-wise group-level random effects analyses using SPM's "full factorial" model with the factors condition (food and nonfood) and group (AN, NP) (30). Two different SPM t-contrasts of differential activation towards food versus nonfood condition were calculated for the comparisons AN(Food>non-food) >/< NP(Food>non-food). Bar graphs of activity were generated using the rfx plot as described by Gläscher (41). For the replication of Joos et al. (30) group activation maps (food versus nonfood) we used for the within-group comparisons a cluster-defining threshold of $p_{uncorr.}<0.001$ (> 10 voxels) and for the between-group comparison a cluster-defining threshold of $p_{uncorr.}<0.01$ (> 0 voxels). Results were considered significant at $p<0.05$, corrected for multiple comparisons (Family-wise error corrected (FWE)).

Region of Interest-Based Second Level Analysis Replicating the Original Study

In addition to the whole brain analysis, a region of interest (ROI) approach was conducted. As performed by Joos et al. (30), the following ROIs according to the Automated Anatomical Labeling Atlas [AAL; (42)] were used: medial and lateral orbitofrontal cortex (OFC), amygdala, ACC, insula and parietal lobe. Again, data were corrected for multiple comparison applying family wise error correction ($p<0.05$), as a small volume correction (SVC) for all voxels in the corresponding ROI.

Whole Brain Second Level Analysis According to Current Recommendations

Within-group food > nonfood differences were calculated using a one-sample t-test for both the AN and NP group. Further, the food > nonfood contrasts of the two groups were compared in a two-sample t-test. For both analyses the cluster-defining thresholding was set to $p_{uncorr.}<0.001$, $k \geq 10$ (43–46).

ROI-Based Second Level Analysis According to Current Recommendations

A SVC was conducted using the ROIs and the t-statistics described above.

Methodological Differences to the Original Study

Sample and State of Participants

The sample size was larger, however clinical characteristics were similar (**Figure 1**). In the earlier study we neither controlled for menstrual cycle nor hormonal contraception, nor was the breakfast standardized (30). Furthermore, the current study was undertaken in the morning, while the former took place in the afternoon hours.

Paradigm Presentation

Visual stimuli were now presented with a BOLD Screen system, which has a better contrast and resolution than the rear-projection system used in the Joos et al. (30) study. Additionally, other fMRI data were gathered before the food paradigm, which was not the case in the initial study. In the current study, we used the manikins of the International Affective Picture System (47) assessing the emotional response to the visual stimuli after scanning (outside the scanner) in three dimensions (arousal, valence, dominance), as we used this approach with another paradigm (32) as part of the multimodal study. In the previous study the Likert scale was applied.

MRI Data Acquisition and Preprocessing

A comparison of the scanner parameters of the two studies is presented in **Supplement 2**. Due to a scanner upgrade from a Siemens TRIO to a PRISMA system the original MRI parameters could not be adopted. The repetition time (TR) was lowered from 3 to 2.5 s to improve the sampling rate of the BOLD signal. All these changes aimed to increase the signal-to-noise ratio.

Post-processing of the two data sets was always conducted with the SPM standard settings. Yet, there are some differences in the two post-processing pipelines. Joos et al. (30) discarded 10 functional images, while in the current study two dummy scans were discarded in addition to five scans, which were discarded internally by the MR system. In the SPM5 analysis of the initial study the segmentation algorithm for the T1 images differs from the "new segment" procedure used in SPM12, which models the whole head, rather than just the brain. For further details we refer

to "SPM: A history" by J. Ashburner (2012, https://doi.org/10.1016/j.neuroimage.2011.10.025).

Statistical Analyses

Additionally to the identical second level and ROI analysis replicating Joos et al. (30) a statistical analysis according to current recommendations was conducted (see *Region of Interest-Based Second Level Analysis Replicating Joos et al. (30)*)

RESULTS

Clinical Characteristics

Clinical details are listed in **Table 1**. The AN and NP group of the current study were of the same age and no significant differences were found in the crystalline intelligence test [MWT-B, (30)]. NP had an expectedly higher BMI than AN. Psychopathology showed typically elevated scores of the questionnaires and interviews in AN (**Table 1**). With respect to the standardized breakfast before the measurement, the AN patients consumed fewer calories than the NP. **Figure 1** illustrates the similarities of the clinical characteristics of the original compared to the replication study.

Subject Rating of Stimuli

Affective ratings of the food stimuli were more aversive for AN (**Supplement 3**). The AN participants evaluated the food pictures more negatively than the NP in terms of valence, but simultaneously triggered a higher arousal in AN.

Within-Group Activation

In both groups, increased neuronal activity was found in the frontoinsular region and visual cortex observing the food stimuli compared to the neutral stimuli. In addition, AN showed increased activity of the precuneus, supramarginal, postcentral, and angular gyrus and NP of the superior parietal gyrus (**Figure 2A**, **Supplement 4**).

Group Comparison

Second Level Analysis Replicating the Original Study

Between-group effects yielded higher BOLD signals (AN>NP) in two clusters, one on each hemisphere, including the cingulate

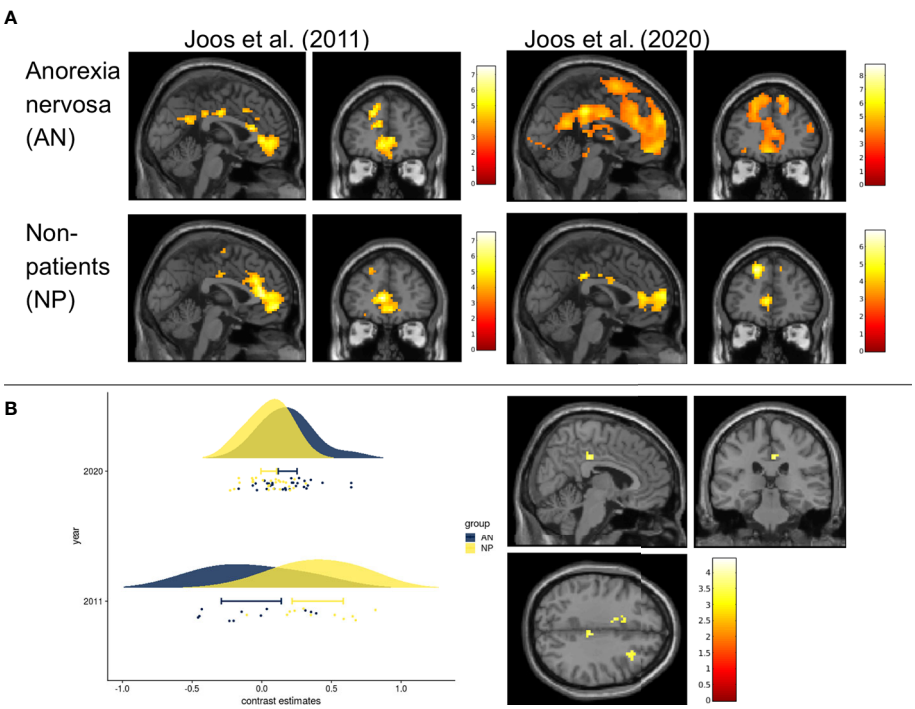

FIGURE 2 | Within group and between group contrasts of the replication study compared to results of Joos et al., 2011 **(A)** Cerebral activation of the within group contrast of anorexia nervosa and non-patients for food>non-food ($p_{uncorrected} <0.001$, k=10, for visualization purposes). Results of Joos et al., 2020 (one-sample t-test) compared to those of Joos et al., 2011 (full-factorial). All slices at MNI coordinates (0, 45, 0) where chosen as in Joos et al., 2011 for a good comparison. Color bars represent the t-scores (white/yellow = high, red = low). Maps from Joos et al., 2011 with kind permission of Elsevier. **(B)** Left Fig. Rain cloud plot of the contrast estimates (food>non-food) in the non-significant midcingulate cortices (MCC) of the replication study (MNI: x=6, y=-28, z=35, with 3mm radius), next to the MCC which derived from the NP>AN contrast reported by Joos et al., 2011 (MNI: x=9, y=-33, z=47). Right Fig: T-maps of the second level analysis (t-test AN(food>non-food) >NP (food>non-food)) according to the current recommendations (cluste-defining threshold p<0.001). Slices where chosen at non-significant peak cluster activity in the right MCC AN>NP (MNI coordinates x=6, y=-28, z=35); $p_{uncorrected}$ <0.001, k>0) Color bars represent the t-scores (white/yellow = high, red = low).

cortices, pre-/postcentral gyrus and inferior parietal lobe (IPL) (**Supplement 5**). The contrast NP>AN failed to reveal significant results. In the SVC analyses none of the ROIs showed any group differences.

Second Level Analysis According to Current Recommendations

The two-sample t-test with a threshold of $p_{uncorr.}<0.001$ did not yield any between-group effects (**Figure 2B**). Also in the SVC analyses no significant group differences emerged in the ROIs.

DISCUSSION

Our data indicates that within-group effects of food>non-food showed more extensive activation in similar cerebral regions (frontoinsular cortices) in AN and less extensively in NP compared to the previous work (30). Similar patterns of brain activation have been reported in earlier studies that used visual food cues (6). However, when contrasting these activations to NP in the between-group comparison, findings of increased amygdala and decreased MCC activation in AN could not be replicated. In both the current and the previous study (30), as well as in a similar study by Uher et al. (38) AN participants experienced the food stimuli more aversive compared to NP. Therefore, even though the aversive emotions were similar, the neural correlates in the between-group comparison of the studies differed.

The issue of replicability is gaining increased importance in the field of neuroscience, including eating disorders (14, 24, 25). There are several factors that can affect the replicability of results, ranging from the paradigmatic differences to hardware, to intra- and interindividual variances (17). Emotional paradigms seem to be much more critical, particularly in clinical populations (24), which we will discuss in detail below.

In addition to general reasons for poor replicability of studies, such as lack of statistical power, handling of outliers, reporting low p-values or trends (24, 25), and publication biases, the following factors are of particular importance:

1. Compared to within-group statistics, effect-sizes of between-groups in fMRI studies on mental disorders are usually lower (26, 28). From today's point of view, the original study in particular was conducted with a sample size that was too small, which, considering the relatively small effect sizes resulted in a low power of the study. It is therefore likely that the reported results of the original study were false positive or that at least the effect sizes were overestimated, which increases the likelihood of non-replicability. Since the replication study also failed to detect any group differences when applying conservative thresholds, only studies with a large sample size will have enough power to detect the probably rather weak effects. The only way to deal with relatively small effect-sizes is to increase sample size, and efforts such as those of the ENIGMA (Enhancing Neuro Imaging Genetics through Meta-Analysis) consortium pooling data from many sites (17, 25). Furthermore, larger sample sizes lead to an increase in power (17, 23, 48). As pointed out in several recent papers (43–45, 49), cluster-defining thresholds were often set too low, e.g., $p_{uncorr.} < 0.01$, which increases the risk of false-positive results. However, this procedure was common at the time of planning the initial study (Woo et al. (44) call it "endemic"). No significant group differences emerged when applying the currently recommended strict thresholds (for further details see, e.g., 42, 43, 44).
2. Heterogeneity across participants is an important confounder, not only in patients but also NP. In our two studies many factors are comparable (age, BMI, duration of disorder, psychopathology, in particular drive for thinness, and most being of the restrictive subtype, depression scores and perception of food pictures are more aversive in AN compared to NP – **Figure 1**), while other confounding genetic, environmental and stochastic factors are difficult or even impossible to account for. Some of these factors likely have larger effect-size than the investigated condition itself (50). Studies with small sample sizes might report results that are based on the effect of uncontrolled variables towards the dependent one (48). This also carries the risk of false-positive results due to sampling error. False-positive results may thus lead into a wrong direction, or even worse, may hinder detecting the real pathophysiological mechanisms (51).
3. Similarly, heterogeneity within participants can impact replicability. Depending on the paradigm, different intrinsic factors can influence the BOLD signal. The current study was controlled for effects of daytime (morning) and state of hunger (standardized meal beforehand), which was not the case in the original study. In the morning, hormonal levels like cortisol are higher; similarly, sex hormones exert cerebral effects (25), which was controlled for in the latter but not in the former study. This also increases the probability of false-positive results of the original study.
4. Heterogeneity across study sites arise from different sources. In addition to different fMRI protocols, scanner hardware and image post-processing pipelines, differences in experimental setup (instructions, interaction with the experimenter, order of tests) have an impact (25). In the current study, participants were subjected to other MRI paradigms before the food paradigm was assessed. In the former study participants started with the food paradigm. While an identical post-processing pipeline was used, fMRI protocols and the scanner hardware differed (see material and methods 2.2., **Supplement 2**). Still, person-related variance seems to be clearly greater than site-related variance (24, 25, 50).

Limitation

The cluster-defining threshold of $p<0.01$ and the full-factorial model in the between group comparisons are a limitation of the former study. This approach is not in line with the current recommendations. In order to ensure the replication of the former study, we applied a methodology as similar as possible, starting with the same statistical between-group analysis and

followed by a statistical analysis according to the current recommendations. Despite being considerably larger than in the previous study, the sample size was still too small. As recent studies point out, due to low effect sizes in the field of fMRI research sample sizes of 100 (52) or even more participants would be necessary (29) to achieve a sufficient power for many effects. Considering these issues, it will be difficult to recruit enough participants in diseases with low prevalence and often low motivation like AN within single center trials; also, costs and efforts will be very high.

Modern scanner hardware seem to influence variability only modestly (24, 25). Differences between SPM5 and SPM12 are mainly in the improved segmentation process and should explain only a minor part of the variance (53).

Another issue discussed in the literature is temporal and spatial stability of fMRI which is influenced by the sensitivity of detecting short-term metabolic changes and neuromodulatory effects (54). Therefore, Logothesis (54) points towards the fact that the fMRI signal of neuromodulatory effects may exceed the signals of purely task-related neuronal activity. This influences not only temporal but also spatial stability. Furthermore, temporal differences in attention, motivation, and excitement, as well as different cognitive strategies for task accomplishment, or changes in cognitive strategy when working on a task, can significantly influence neural activity in response (24). In the original as well as in the replication study, we performed a cross-sectional analysis with a onetime measurement of the participants. Therefore, we cannot assess the influences of short-term metabolic changes and neuromodulatory effects on the BOLD-signals measured. Especially task fMRI studies and within those particularly clinical populations with emotional paradigms seem to be influenced by temporal and spatial instability (24, 29).

CONCLUSION

In the replication study, we were not able to identify elevated BOLD responses of the right amygdala and decreased activation in midcingulate cortices (MCC) in AN compared to NP in the between-group analysis and therefore could not replicate the original study (30). As expected, we and other authors (24, 25) assume that human influences (inter- and intra-individual variances) are greater than most other factors and more difficult to control, especially in emotional tasks and in clinical populations.

Nevertheless, like most other fMRI studies that examine neural correlation of food compared to non-food stimuli (5–8), we found differences between AN and NP while processing food versus non-food stimuli applying the second level analysis replicating Joos et al. (30). The increased activation in AN>NP in the MCC together with the pre-/postcentral gyrus has also been reported by others: an increased cingulate activation was described by Ellison et al. (4) and Gizewski et al. (55), an pre-/postcentral gyrus activation by Boehm et al. (56). No increased IPL activation has been mentioned in AN, while a decreased IPL activation could be observed in three studies (38, 57, 58). Of those studies included in the meta-analysis and reviews only Kerr et al. (59) reported no differences between AN and NP for food versus non-food. Due to the heterogeneity of the previous results, no definitive conclusions can yet be drawn from these studies. Further, second level analysis according to current recommendations with a threshold of $p_{uncorr.}<0.001$ revealed neither between-group effects in the whole brain nor in the ROI analysis.

We aim to understand the cerebral pathophysiology of AN including the pathological eating behavior and maladaptive eating behavior. For valid and reliable conclusions of functionally altered brain regions, replications of fMRI studies examining neural processing of disease-specific food stimuli are paramount. As noted by others, study protocols as well as samples should be precisely described in order to be able to replicate and disentangle possible influences (17, 21, 24, 25). Likely, replication studies should be performed with larger sample sizes to increase the statistical power (26–28). Additionally, longitudinal studies or studies with repeated sessions of the same participants can be used to create replicability maps (17), which can improve the temporal and spatial stability. Besides the lack of replications, reproductions are necessary as well. Reproduction, i.e., the exact re-analysis of the same data (see *Background*), is a necessary step to establish stable data analysis pipelines and therefore also an important prerequisite for replication studies (60).

The issue of replication has been largely neglected in the past and is now increasingly coming into focus. It is of great importance to carefully control and/or describe modifying factors such as hardware, processing pipelines, statistics, experimental setups and clinical descriptions. Since almost all fMRI studies so far have not undergone replication, the validity of most findings in this field can be challenged.

DATA AVAILABILITY STATEMENT

The raw data supporting the conclusions of this article will be made available by the authors, without undue reservation. T-maps of the within and between group comparisons are available at: https://identifiers.org/neurovault.image:395600.

ETHICS STATEMENT

The studies involving human participants were reviewed and approved by Ethics commission of the Albert-Ludwig-University Freiburg (Nr. EK-Freiburg 520/13). The patients/participants provided their written informed consent to participate in this study.

AUTHOR CONTRIBUTIONS

Planning of the study: AJ, LT, and AZ. AJ is principal investigator of the DFG project JO 744-2/1. Recruitment and psychosomatic

assessment: AJ, SM, LH, and AZ. Measurement and data analysis: IH, AJ, SM, LH, KN. Writing: IH, AJ, SM, SS, KN, and DE. Proof reading: AJ, SM, IH, SS, LH, KN, DE, LT, and AZ. All authors contributed to the article and approved the submitted version. They agreed to be accountable for all aspects of the work.

FUNDING

The project was funded by the German Research Foundation (DFG Ref: JO 744-2/1). The article processing charge was funded by the University of Freiburg in the funding program Open Access Publishing.

ACKNOWLEDGMENTS

This study was carried out as part of the study DFG (German Research Foundation) of DFG-Grant JO 744-2/1. DE was funded by the Berta-Ottenstein-Programe for Advanced Clinician Scientists, Faculty of Medicine, University of Freiburg.

SUPPLEMENTARY MATERIAL

The Supplementary Material for this article can be found online at: https://www.frontiersin.org/articles/10.3389/fpsyt.2020.00777/full#supplementary-material

REFERENCES

1. Zipfel S, Giel KE, Bulik CM, Hay P, Schmidt U. Anorexia nervosa: aetiology, assessment, and treatment. *Lancet Psychiatry* (2015) 2:1099–111. doi: 10.1016/S2215-0366(15)00356-9
2. Fichter MM, Quadflieg N. Mortality in eating disorders - results of a large prospective clinical longitudinal study. *Int J Eat Disord* (2016) 49:391–401. doi: 10.1002/eat.22501
3. Treasure J, Zipfel S, Micali N, Wade T, Stice E, Claudino A, et al. Anorexia nervosa. *Nat Rev Dis Primer* (2015) 1:1–21. doi: 10.1038/nrdp.2015.74
4. Ellison Z, Foong J, Howard R, Bullmore E, Williams S, Treasure J. Functional anatomy of calorie fear in anorexia nervosa. *Lancet* (1998) 352:1192. doi: 10.1016/S0140-6736(05)60529-6
5. Zhu Y, Hu X, Wang J, Chen J, Guo Q, Li C, et al. Processing of Food, Body and Emotional Stimuli in Anorexia Nervosa: A Systematic Review and Meta-analysis of Functional Magnetic Resonance Imaging Studies. *Eur Eat Disord Rev* (2012) 20:439–50. doi: 10.1002/erv.2197
6. García-García I, Narberhaus A, Marqués-Iturria I, Garolera M, Rădoi A, Segura B, et al. Neural Responses to Visual Food Cues: Insights from Functional Magnetic Resonance Imaging. *Eur Eat Disord Rev* (2013) 21:89–98. doi: 10.1002/erv.2216
7. Lloyd EC, Steinglass JE. What can food-image tasks teach us about anorexia nervosa? A systematic review. *J Eat Disord* (2018) 6(1):31. doi: 10.1186/s40337-018-0217-z
8. Simon JJ, Stopyra MA, Friederich H-C. Neural Processing of Disorder-Related Stimuli in Patients with Anorexia Nervosa: A Narrative Review of Brain Imaging Studies. *J Clin Med* (2019) 8:17. doi: 10.3390/jcm8071047
9. Committee on Reproducibility and Replicability in Science, Board on Behavioral, Cognitive, and Sensory Sciences, Committee on National Statistics, Division of Behavioral and Social Sciences and Education, Nuclear and Radiation Studies Board and Division on Earth and Life Studies, et al. *Reproducibility and Replicability in Science*. Washington, D.C.: National Academies of Sciences, Engineering, and Medicine; Policy and Global Affairs (2019). doi: 10.17226/25303
10. Gilmore RO, Diaz MT, Wyble BA, Yarkoni. Progress Toward Openness T. Transparency, and Reproducibility in Cognitive Neuroscience. *Ann N. Y. Acad Sci* (2017) 1396:5–18. doi: 10.1111/nyas.13325
11. Makel MC, Plucker JA, Hegarty B. Replications in Psychology Research: How Often Do They Really Occur? *Perspect Psychol Sci* (2012) 7:537–42. doi: 10.1177/1745691612460688
12. Zwaan RA, Etz A, Lucas RE, Donnellan MB. Making replication mainstream. *Behav Brain Sci* (2018) 41:e120. doi: 10.1017/S0140525X17001972
13. Baker M. Is there a reproducibility crisis? A Nature survey lifts the lid on how researchers view the 'crisis' rocking science and what they think will help. *Nat News* (2016) 3:452–54. doi: 10.1038/533452a
14. Gorgolewski KJ, Poldrack. A Practical Guide for Improving Transparency RA. and Reproducibility in Neuroimaging Research. *PloS Biol* (2016) 14:e1002506. doi: 10.1371/journal.pbio.1002506
15. Kampa M, Sebastian A, Wessa M, Tüscher O, Kalisch R, Yuen K. Replication of fMRI group activations in the neuroimaging battery for the Mainz Resilience Project (MARP). *NeuroImage* (2020) 204:116223. doi: 10.1016/j.neuroimage.2019.116223
16. Schmidt S. Shall we Really do it Again? The Powerful Concept of Replication is Neglected in the Social Sciences. *Rev Gen Psychol* (2009) 13:90–100. doi: 10.1037/a0015108
17. Bossier H, Roels SP, Seurinck R, Banaschewski T, Barker GJ, Bokde ALW, et al. The empirical replicability of task-based fMRI as a function of sample size. *NeuroImage* (2020) 212:116601. doi: 10.1016/j.neuroimage.2020.116601
18. Barba LA. *Terminologies for Reproducible Research. Prepr ArXiv180203311* (2018). (Accessed December 2, 2019). Available at: http://arxiv.org/abs/1802.03311.
19. Patil P, Peng RD, Leek JT. What should we expect when we replicate? A statistical view of replicability in psychological science. *Perspect Psychol Sci J Assoc Psychol Sci* (2016) 11:539–44. doi: 10.1177/1745691616646366
20. Klapwijk E, van den Bos W, Tamnes CK, Mills K, Raschle N. Opportunities for increased reproducibility and replicability of developmental cognitive neuroscience. (2019) 1–58. doi: 10.31234/osf.io/fxjzt
21. Bollen K, Cacioppo JT, Kaplan RM, Krosnick JA, Olds JL. Social, behavioral, and economic sciences perspectives on robust and reliable science: Report of the Subcommittee on Replicability in Science, Advisory Committee to the National Science Foundation Directorate for Social, Behavioral, and Economic Sciences. *Advis. Comm. Natl Sci Found Dir. Soc Behav Econ. Sci* (2015).
22. Thirion B, Pinel P, Mériaux S, Roche A, Dehaene S, Poline J-B. Analysis of a large fMRI cohort: Statistical and methodological issues for group analyses. *NeuroImage* (2007) 35:105–20. doi: 10.1016/j.neuroimage.2006.11.054
23. Turner BO, Paul EJ, Miller MB, Barbey AK. Small sample sizes reduce the replicability of task-based fMRI studies. *Commun Biol* (2018) 1:1–10. doi: 10.1038/s42003-018-0073-z
24. Bennett CM, Miller MB. How reliable are the results from functional magnetic resonance imaging? *Ann N. Y. Acad Sci* (2010) 1191:133–55. doi: 10.1111/j.1749-6632.2010.05446.x
25. Frank GKW, Favaro A, Marsh R, Ehrlich S, Lawson. Toward valid EA. and reliable brain imaging results in eating disorders. *Int J Eat Disord* (2018) 51:250–61. doi: 10.1002/eat.22829
26. Chen G, Taylor PA, Cox RW. benn. *NeuroImage* (2017) 147:952–9. doi: 10.1016/j.neuroimage.2016.09.066
27. King JA, Frank GKW, Thompson PM, Ehrlich S. Structural Neuroimaging of Anorexia Nervosa: Future Directions in the Quest for Mechanisms Underlying Dynamic Alterations. *Biol Psychiatry* (2018) 83:224–34. doi: 10.1016/j.biopsych.2017.08.011
28. Poldrack RA, Baker CI, Durnez J, Gorgolewski KJ, Matthews PM, Munafò MR, et al. Scanning the horizon: towards transparent and reproducible neuroimaging research. *Nat Rev Neurosci* (2017) 18:115–26. doi: 10.1038/nrn.2016.167
29. Elliott ML, Knodt AR, Ireland D, Morris ML, Poulton R, Ramrakha S, et al. Poor test-retest reliability of task-fMRI: New empirical evidence and a meta-analysis. *bioRxiv* (2019) 681700. doi: 10.1101/681700
30. Joos AAB, Saum B, van Elst LT, Perlov E, Glauche V, Hartmann A, et al. Amygdala hyperreactivity in restrictive anorexia nervosa. *Psychiatry Res Neuroimaging* (2011) 191:189–95. doi: 10.1016/j.pscychresns.2010.11.008

31. Maier S, Nickel K, Perlov E, Kukies A, Zeeck A, van Elst LT, et al. Insular Cell Integrity Markers Linked to Weight Concern in Anorexia Nervosa—An MR-Spectroscopy Study. *J Clin Med* (2020) 9:1292. doi: 10.3390/jcm9051292
32. Maier S, Spiegelberg J, van Zutphen L, Zeeck A, van Elst LT, Hartmann A, et al. Neurobiological signature of intimacy in anorexia nervosa. *Eur Eat Disord Rev* (2019) 27:315–22. doi: 10.1002/erv.2663
33. Maier S, Schneider K, Stark C, Zeeck A, Tebartz van Elst L, Holovics L, et al. Fear Network Unresponsiveness in Women with Anorexia Nervosa. *Psychother Psychosom.* (2019) 88:238–40. doi: 10.1159/000495367
34. Nickel K, Joos A, van Elst LT, Holovics L, Endres D, Zeeck A, et al. Altered cortical folding and reduced sulcal depth in adults with anorexia nervosa. *Eur Eat Disord Rev* (2019) 27:655–70. doi: 10.1002/erv.2685
35. Nickel K, Tebartz van Elst L, Holovics L, Feige B, Glauche V, Fortenbacher T, et al. White Matter Abnormalities in the Corpus Callosum in Acute and Recovered Anorexia Nervosa Patients—A Diffusion Tensor Imaging Study. *Front Psychiatry* (2019) 10:490. doi: 10.3389/fpsyt.2019.00490
36. Nickel K, Joos A, van Elst LT, Matthis J, Holovics L, Endres D, et al. Recovery of cortical volume and thickness after remission from acute anorexia nervosa. *Int J Eat Disord* (2018) 51:1056–69. doi: 10.1002/eat.22918
37. Lehrl S, Triebig G, Fischer B. Multiple choice vocabulary test MWT as a valid and short test to estimate premorbid intelligence. *Acta Neurol Scand* (1995) 91:335–45. doi: 10.1111/j.1600-0404.1995.tb07018.x
38. Uher R, Murphy T, Brammer MJ, Dalgleish T, Phillips ML, Ng VW, et al. Medial Prefrontal Cortex Activity Associated With Symptom Provocation in Eating Disorders. *Am J Psychiatry* (2004) 161:1238–46. doi: 10.1176/appi.ajp.161.7.1238
39. Zaitsev M, Hennig J, Speck. Point spread function mapping with parallel imaging techniques O. and high acceleration factors: Fast, robust, and flexible method for echo-planar imaging distortion correction. *Magn. Reson. Med* (2004) 52:1156–66. doi: 10.1002/mrm.20261
40. Friston KJ, Jezzard P, Turner R. Analysis of functional MRI time-series. *Hum Brain Mapp.* (1994) 1:153–71. doi: 10.1002/hbm.460010207
41. Gläscher J. Visualization of Group Inference Data in Functional Neuroimaging. *Neuroinformatics* (2009) 7:73–82. doi: 10.1007/s12021-008-9042-x
42. Tzourio-Mazoyer N, Landeau B, Papathanassiou D, Crivello F, Etard O, Delcroix N, et al. Automated Anatomical Labeling of Activations in SPM Using a Macroscopic Anatomical Parcellation of the MNI MRI Single-Subject Brain. *NeuroImage* (2002) 15:273–89. doi: 10.1006/nimg.2001.0978
43. Eklund A, Nichols TE, Knutsson H. Cluster failure: Why fMRI inferences for spatial extent have inflated false-positive rates. *Proc Natl Acad Sci* (2016) 113:7900–5. doi: 10.1073/pnas.1602413113
44. Woo C-W, Krishnan A, Wager TD. Cluster-extent based thresholding in fMRI analyses: Pitfalls and recommendations. *NeuroImage* (2014) 91:412–9. doi: 10.1016/j.neuroimage.2013.12.058
45. Eklund A, Knutsson H, Nichols TE. Cluster failure revisited: Impact of first level design and physiological noise on cluster false positive rates. *Hum Brain Mapp.* (2019) 40:2017–32. doi: 10.1002/hbm.24350
46. Roiser JP, Linden DE, Gorno-Tempinin ML, Moran RJ, Dickerson BC, Grafton ST. Minimum statistical standards for submissions to Neuroimage: Clinical. *NeuroImage Clin* (2016) 12:1045–7. doi: 10.1016/j.nicl.2016.08.002
47. Bradley MM, Lang PJ. International Affective Picture System. In: Zeigler-Hill V, Shackelford TK, editors. *Encyclopedia of Personality and Individual Differences*. Cham: Springer International Publishing. (2017) p. 1–4. doi: 10.1007/978-3-319-28099-8_42-1
48. Button KS, Ioannidis JPA, Mokrysz C, Nosek BA, Flint J, Robinson ESJ, et al. Power failure: why small sample size undermines the reliability of neuroscience. *Nat Rev Neurosci* (2013) 14:365–76. doi: 10.1038/nrn3475
49. Cox RW, Chen G, Glen DR, Reynolds RC, Taylor. fMRI clustering PA. and false-positive rates. *Proc Natl Acad Sci* (2017) 114:E3370–1. doi: 10.1073/pnas.1614961114
50. Gee DG, McEwen SC, Forsyth JK, Haut KM, Bearden CE, Addington J, et al. Reliability of an fMRI paradigm for emotional processing in a multisite longitudinal study. *Hum Brain Mapp.* (2015) 36:2558–79. doi: 10.1002/hbm.22791
51. Geissberger N, Tik M, Sladky R, Woletz M, Schuler A-L, Willinger D, et al. Reproducibility of amygdala activation in facial emotion processing at 7T. *NeuroImage* (2020) 211:116585. doi: 10.1016/j.neuroimage.2020.116585
52. Geuter S, Qi G, Welsh RC, Wager TD, Lindquist MA. Effect Size and Power in fMRI Group Analysis. *bioRxiv* (2018) 295048. doi: 10.1101/295048
53. Ashburner J, Barnes G, Chen C, Daunizeau J, Flandin G, Friston K, et al. *SPM12 manual*. London, UK: Functional Imaging Laboratory Wellcome Trust Centre for Neuroimaging Institute of Neurology (2014). p. 2464.
54. Logothetis. What we can do NK. and what we cannot do with fMRI. *Nature* (2008) 453:869–78. doi: 10.1038/nature06976
55. Gizewski ER, Rosenberger C, de Greiff A, Moll A, Senf W, Wanke I, et al. Influence of Satiety and Subjective Valence Rating on Cerebral Activation Patterns in Response to Visual Stimulation with High-Calorie Stimuli among Restrictive Anorectic and Control Women. *Neuropsychobiology* (2010) 62:182–92. doi: 10.1159/000319360
56. Boehm I, King JA, Bernardoni F, Geisler D, Seidel M, Ritschel F, et al. Subliminal and supraliminal processing of reward-related stimuli in anorexia nervosa. *Psychol Med* (2018) 48:790–800. doi: 10.1017/S0033291717002161
57. Santel S, Baving L, Krauel K, Münte TF, Rotte. Hunger M. and satiety in anorexia nervosa: fMRI during cognitive processing of food pictures. *Brain Res* (2006) 1114:138–48. doi: 10.1016/j.brainres.2006.07.045
58. Scaife JC, Godier LR, Reinecke A, Harmer CJ, Park RJ. Differential activation of the frontal pole to high vs low calorie foods: The neural basis of food preference in Anorexia Nervosa? *Psychiatry Res* (2016) 258:44–53. doi: 10.1016/j.pscychresns.2016.10.004
59. Kerr KL, Moseman SE, Avery JA, Bodurka J, Simmons WK. Influence of visceral interoceptive experience on the brain's response to food images in anorexia nervosa. *Psychosom. Med* (2017) 79:777–84. doi: 10.1097/PSY.0000000000000486
60. Asendorpf JB, Conner M, Fruyt FD, Houwer JD, Denissen JJA, Fiedler K, et al. Recommendations for Increasing Replicability in Psychology. *Eur J Pers* (2013) 27:108–19. doi: 10.1002/per.1919

Conflict of Interest: The authors declare that the research was conducted in the absence of any commercial or financial relationships that could be construed as a potential conflict of interest.

frontiers in Psychiatry

ERRATUM
published: 04 September 2020
doi: 10.3389/fpsyt.2020.599179

Erratum: A Neglected Topic in Neuroscience: Replicability of fMRI Results With Specific Reference to ANOREXIA NERVOSA

Frontiers Production Office *

Frontiers Media SA, Lausanne, Switzerland

OPEN ACCESS

Approved by:
Frontiers Editorial Office, Frontiers Media SA, Switzerland

***Correspondence:**
Frontiers Production Office
production.office@frontiersin.org

Specialty section:
This article was submitted to Neuroimaging and Stimulation, a section of the journal Frontiers in Psychiatry

Received: *26 August 2020*
Accepted: *27 August 2020*
Published: *04 September 2020*

Citation:
Frontiers Production Office (2020) Erratum: A Neglected Topic in Neuroscience: Replicability of fMRI Results With Specific Reference to ANOREXIA NERVOSA. Front. Psychiatry 11:599179. doi: 10.3389/fpsyt.2020.599179

Keywords: replicability, anorexia nervosa, food, functional magnetic resonance imaging (fMRI), neurobiology

An Erratum on

A Neglected Topic in Neuroscience: Replicability of fMRI Results With Specific Reference to ANOREXIA NERVOSA
by Horster I, Nickel K, Holovics L, Schmidt S, Endres D, Tebartz van Elst L, Zeeck A, Maier S and Joos A. (2020). Front. Psychiatry 11:777. doi: 10.3389/fpsyt.2020.00777

Due to a production error, there was a mistake in **Table 1** as published. The footnote text was incorrectly placed and there was an error in the column names. The corrected **Table 1** appears below. The publisher apologizes for this mistake.

The original version of this article has been updated.

TABLE 1 | Clinical characteristics of anorexia nervosa (AN) and non-patients (NP).

	Anorexia Nervosa(N=31)		***Non-Patients(N=27)***		***T-Test***	
					t-score	***p-value***
	Mean	SD	Mean	SD		
Age (years)	24.0	4.4	23.6	3.0	0.44	0.659
Duration of illness (years)	6.6	3.8	-	-		
Current BMI (kg/m^2)	16.2	1.4	22.1	2.2	-11.97	<.001
Lowest-Lifetime BMI (kg/m^2)	14.8	1.5	20.9	1.8	-11.08	<.001
EDI—total score	61.8	9.3	44.6	3.1	9.19	<.001
EDI—drive for thinness (t values)	83.5	19.6	44.6	6.4	9.85	<.001
EDI—body dissatisfaction (t values)	61.7	12.7	46.6	8.0	5.31	<.001
BDI-II	21.5	10.5	2.3	2.7	9.2	<.001
EDE total score	3.3	1.1	0.4	0.3	13.53	<.001
MWT-B	28.4	5.2	28.0	4.3	0.34	0.736
Caloric intake at breakfast	142.3	157.5	386.3	85.7	-7.12	<.001
STAI-state	38.7	6.6	32.8	4.8	3.83	<.001
STAI-trait	45.5	7.7	29.3	6.8	8.39	<.001

BDI-II, Becks Depression-Inventory-2; BMI, Body-Mass-Index; EDE, Eating Disorder Examination Interview; EDI-2, Eating Disorder Inventory-2; kg, kilogram; m2, square meter; MWT-B, Multiple-Choice-Vocabulary-Intelligence Test - German for Mehrfachwahl-Wortschatz-Test-Version (37); SD, standard deviation; STAI, State-Trait Anxiety Inventory.

frontiers in Neuroscience

ORIGINAL RESEARCH
published: 21 August 2020
doi: 10.3389/fnins.2020.00867

Comparison of Activation Patterns in Mirror Neurons and the Swallowing Network During Action Observation and Execution: A Task-Based fMRI Study

Ying-hua Jing[1†], Tuo Lin[1†], Wan-qi Li[2], Cheng Wu[1], Xue Li[2], Qian Ding[1], Man-feng Wu[1], Guang-qing Xu[3,4] and Yue Lan[1,2*]*

[1] Department of Rehabilitation Medicine, Guangzhou First People's Hospital, School of Medicine, South China University of Technology, Guangzhou, China, [2] Department of Rehabilitation Medicine, Guangzhou First People's Hospital, Guangzhou Medical University, Guangzhou, China, [3] Department of Rehabilitation Medicine, Beijing Tian Tan Hospital, Capital Medical University, Beijing, China, [4] China National Clinical Research Center for Neurological Diseases, Beijing, China

OPEN ACCESS

Edited by:
Szilvia Anett Nagy,
University of Pécs, Hungary

Reviewed by:
Jiu Chen,
Nanjing Medical University, China
Lihua Qiu,
The Second People's Hospital of Yibin, China

***Correspondence:**
Guang-qing Xu
guangchingx@163.com
Yue Lan
bluemooning@163.com

[†] These authors have contributed equally to this work

Specialty section:
This article was submitted to Brain Imaging Methods, a section of the journal Frontiers in Neuroscience

Received: 04 June 2020
Accepted: 27 July 2020
Published: 21 August 2020

Citation:
Jing Y, Lin T, Li W, Wu C, Li X, Ding Q, Wu M, Xu G and Lan Y (2020) Comparison of Activation Patterns in Mirror Neurons and the Swallowing Network During Action Observation and Execution: A Task-Based fMRI Study. Front. Neurosci. 14:867. doi: 10.3389/fnins.2020.00867

Background: Observation of a goal-directed motor action can excite the respective mirror neurons, and this is the theoretical basis for action observation (AO) as a novel tool for functional recovery during stroke rehabilitation. To explore the therapeutic potential of AO for dysphagia, we conducted a task-based functional magnetic resonance imaging (fMRI) study to identify the brain areas activated during observation and execution of swallowing in healthy participants.

Methods: Twenty-nine healthy volunteers viewed the following stimuli during fMRI scanning: an action-video of swallowing (condition 1, defined as AO), a neutral image with a Chinese word for "watching" (condition 2), and a neutral image with a Chinese word for "swallowing" (condition 3). Action execution (AE) was defined as condition 3 minus condition 2. One-sample *t*-tests were performed to define the brain regions activated during AO and AE.

Results: Many brain regions were activated during AO, including the middle temporal gyrus, inferior frontal gyrus, pre- and postcentral gyrus, supplementary motor area, hippocampus, brainstem, and pons. AE resulted in activation of motor areas as well as other brain areas, including the inferior parietal lobule, vermis, middle frontal gyrus, and middle temporal gyrus. Two brain areas, BA6 and BA21, were activated with both AO and AE.

Conclusion: The left supplementary motor area (BA6) and left middle temporal gyrus (BA21), which contains mirror neurons, were activated in both AO and AE of swallowing. In this study, AO activated mirror neurons and the swallowing network in healthy participants, supporting its potential value in the treatment of dysphagia.

Keywords: mirror neurons, swallowing network, action observation, action execution, functional magnetic resonance imaging

INTRODUCTION

Mirror neurons are a specific neuronal population that discharge not only during the performance of a particular action, but also during observation of others performing a similar action (Cook et al., 2014; Marshall, 2014). These neurons are found throughout the brain, including in the Broca's area, ventral premotor region, premotor cortex (PMC), posterior regions of the inferior frontal gyrus (IFG), inferior parietal lobule (IPL), insula, amygdala, and prefrontal cortex (PFC) (Casile et al., 2011; Kilner and Lemon, 2013; Cook et al., 2014; Zhang et al., 2018). Current theories in cognitive neuroscience suggest that mirror neurons are central to the basic neural mechanisms underlying action recognition, motion intention coding, and motor learning (Maranesi et al., 2014; Amoruso et al., 2018; Catmur et al., 2018; Mazurek et al., 2018). Previous studies revealed a neuronal mechanism of mirror neurons that matches perception and action as well as cognition and motility, and permits action recognition and understanding (Rizzolatti and Sinigaglia, 2016; Tramacere et al., 2017). In other words, observation of others' actions can activate brain regions similar to those involved in the execution of that action and then can induce the same action. For example, Fawcett et al. illustrated that infants learn to replicate others' joint activity through observation (Fawcett and Liszkowski, 2012). Given the properties of the action observation–execution matching mechanism, mirror neurons may influence plasticity-related functional reorganization after stroke or brain injury, re-activating the top-down neural pathway, leading to recovery of motor function (Sale and Franceschini, 2012; Small et al., 2013). In recent years, action observation (AO), in which patients observe a specific video describing an action to recruit the relevant action-related mirror neurons and enable a direct matching between others' gestures and their own motor system, has emerged as a novel and effective option as an add-on intervention to rehabilitation therapy (Hetu et al., 2010; Sale and Mattingley, 2013; Bassolino et al., 2014; Vesia et al., 2019). To date, this approach has been successfully applied in the rehabilitation of upper limb motor functions in chronic stroke patients (Borges et al., 2018), in the language rehabilitation of post-stroke aphasia patients (Gili et al., 2017), in motor recovery of Parkinson's disease patients (Pelosin et al., 2013), including those presenting with freezing of gait (Pelosin et al., 2018), and in children with cerebral palsy (Kirkpatrick et al., 2016).

Swallowing is a coordinated physiological process, involving complex neuromuscular interactions (Ertekin and Aydogdu, 2003). Extensive research has shown that the swallowing network includes the brain regions of the primary sensorimotor system, supplementary motor area (SMA), insula, cingulate cortex, IFG, IPL, temporal lobe, precuneus, cerebellum, and brain stem (Hamdy et al., 1999a; Lang, 2009; Soros et al., 2009; Lima et al., 2015; Toogood et al., 2017). When any area of the swallowing network is damaged, dysphagia occurs (Domenech and Kelly, 1999; Gonzalez-Fernandez and Daniels, 2008). Dysphagia can result in serious complications, including pneumonia, malnutrition, dehydration, and even death, and is strongly linked to a deteriorated quality of life (Clavé and Shaker, 2015; Rommel and Hamdy, 2016). Regrettably, because traditional dysphagia therapies (e.g., compensatory strategies, external stimulation of oral, and pharyngeal structures) are aimed at recovering the function of swallowing biomechanics rather than directly repairing the central nervous system (Martino and McCulloch, 2016; Easterling, 2017; Lazarus, 2017), the cycle of rehabilitation is long and the outcome of clinical treatment is typically poor. Therefore, repairing the damaged networks directly to improve swallowing function has become a challenge demanding a prompt answer. We found that some brain areas of swallowing regulation overlap those with mirror neurons, such as the motor regions, IFG, IPL and others. Additionally, animal studies have shown that observation of eating behavior can stimulate observers to execute swallowing-related action (Rizzolatti and Craighero, 2004). Based on the aforementioned exploration of the literature, we speculated that AO might be useful in treating dysphagia. In contrast to other body movements, swallowing is regulated by motor and sensory feedback and is particularly difficult to observe directly (Dodds, 1989). As yet, there is paucity of evidence demonstrating that an action-video of swallowing can activate mirror neurons and the swallowing network, prompting us to conduct the current experiment.

Functional magnetic resonance imaging (fMRI), which detects changes in the blood oxygen level-dependent (BOLD) signal as an indirect measure of neuronal activity, is a powerful tool for exploring brain functions non-invasively (Ogawa et al., 1992). Compared to other neuroimaging methods [e.g., electroencephalography (EEG), magnetoencephalography (MEG), near-infrared spectroscopy (NIRS)], fMRI offers good contrast resolution and excellent spatial resolution for accurately determining the location and activation patterns of a neural source. The rapid development of neuroimaging technology has facilitated task-based fMRI, which can accurately reveal the brain regions that are activated when one executes a certain task. This approach provides a good foundation for our research on the activation of mirror neurons and the swallowing network induced by AO (Ugurbil, 2016). In 12 healthy adults, Kawai et al. (2009) used fMRI to verify that visual and audiovisual stimuli related to swallowing motion contribute to activation of the brain regions related to swallowing. However, in comparison to a still image or auditory stimuli associated with swallowing, action-video stimuli of swallowing promote better integral transmission of coherent information regarding the swallowing motion. Additionally, the single-trial paradigm used in Kawai et al.'s study can track only the chronological changes activated by a single stimulus, decreases the BOLD-signals caused by the stimulus, and offers weak contrast-to-noise ratios. Moreover, previous studies were limited by small sample sizes. To address these problems and improve the detection efficiency for mirror neurons, we devised a block-design fMRI study in 29 health volunteers. This type of design was previously shown to be applicable for the swallowing task by Soltysik and Hyde (2006).

In the current study, based on our assumption that AO of swallowing in daily life can activate brain regions similar to those required for the action execution (AE) of swallowing, we employed task-based fMRI in a reasonably large subject population to identify the regions of the brain that are activated

during observation of the action-video of swallowing and the neuronal responses that occur during swallowing, as well as to investigate interactions among the brain areas activated by the task. Furthermore, we examined whether the specific swallowing video can modulate voluntarily participants' mirror neurons to induce brain activity related to swallowing and estimated whether AO represents a feasible intervention for dysphasia that warrants further research in patients.

MATERIALS AND METHODS

Participants

Twenty-nine healthy volunteers (15 female, 14 male, mean age: 22.76 ± 2.63 years; education level: 15.48 ± 1.06 years) participated in the study after providing written informed consent. All participants had normal or corrected-to-normal vision, and volunteers were excluded if they had a personal history of dysphagia, current sore throat due to respiratory infection or chronic pharyngitis, neurological or psychiatric illness, or drug or alcohol abuse. The experiment was approved by the Medical Ethics Committee of medical college of South China University of Technology and was performed in accordance with the ethical standards of the Declaration of Helsinki.

Experimental Design

Before the fMRI experiment, all participants underwent an operant training to ensure they fully understand the entire procedure, including the task-related functional and structural scans.

During the functional image acquisition, participants were asked to lie down quietly in a comfortable supine position on the magnetic resonance scanner. They then viewed the session through a tilted mirror mounted above their eyes on the head coil, and completed a total session lasting 14.4 min and comprised of three different task blocks of 36 s (with 18 s trial duration and 18 s rest period). In the task blocks, three stimuli were presented: a video of the left profile of a man biting into an apple, chewing, and then swallowing; a neutral picture of a desk with a Chinese word for "watching"; and the same neutral picture with a Chinese word for "swallowing." A dark image was shown during the rest periods. When the video of swallowing appeared on the screen, participants were instructed to attentively watch and understand the swallowing movements of the man. When the image of the desk with the "swallowing" message was shown, they were instructed to execute the swallowing motion in a regular, comfortable, self-paced rhythm. When viewing the image with the word "watching," they needed to remain quiet (with the absence of swallowing movements or thought) and focus on the screen. Each block was repeated eight times in pseudo-random order with sequence randomized according to a computer-generated list of random numbers. A 10 s blank block was allowed for elimination of the influence of blood signal saturation and adaption to the MRI environment initially. In the same way, a 10 s blank block was used to avoid end-effects and data corruption at the end of the session. Then, a T1 scan for the structural image was performed after the task session, in which participants were instructed to remain awake but relaxed with their eyes closed, remaining motionless as much as possible. The detailed experimental design is illustrated in **Figure 1**.

MRI Data Acquisition

All brain imaging data were acquired on a 3.0 T MRI scanner (Siemens, Erlangen, Germany) with an 8-channel head coil at Guangzhou First People's Hospital, China. The MRI scanning sessions consisted of an approximately 14.4 min task-based session and a 9 min anatomical scan. All participants underwent T2-sensitive gradient reflection echo (GRE) sequence scanning (parameters: TR = 2000 ms, TE = 21 ms, flip angle = 78°, matrix = 64 × 64, slice thickness = 4.0 mm, voxel dimensions = 3.5 × 3.5 × 4.0 mm), which provided whole-brain coverage in 33 slices during task completion. T1-weighted structural images were recorded using a 3D magnetization-prepared rapid gradient echo (MPRAGE) sequence (parameters: TR = 2530 ms, TE = 2.93 ms, TI = 900 ms, flip angle = 9°, matrix = 256 × 256, slice thickness = 1.0 mm, voxel dimensions = 1.0 × 1.0 × 1.0 mm). The MRI sequence and image-acquisition parameters were kept constant during the scanning period. Participants wore earplugs to reduce scanner noise, and pads were used to reduce head motion. During the MRI scanning sessions, participants lay supine on the scanner bed and viewed the experimental tasks on a screen through a mirror mounted onto the head coil.

fMRI Data Preprocessing

Image preprocessing was performed using RESTplus (Jia et al., 2019), which runs with the statistical parametric mapping software SPM12[1]. Briefly, all images were preprocessed with the following steps:

I. Conversion of the DICOM data format into NIFTI format and visual inspection for quality for the convenience of data processing.
II. Slice timing to correct for differences in the time of slice acquisition.
III. Head motion correction using six parameters, with the first volume as a reference slice.
IV. Normalization of all functional images to the Montreal Neurological Institute (MNI) space via the Rigid Body deformation fields derived from tissue segmentation of structural images (resampling voxel size = 3 mm × 3 mm × 3 mm) for accurate spatial localization within the brain.
V. Spatial smoothing after normalization to improve the quality of group-level statistics with an isotropic Gaussian kernel with a full width at half maximum (FWHM) of 6 mm.

No participants were excluded from further analysis due to image registration error or large head motion (more than 3.0 mm of maximal translation in any direction of x, y or z or 3.0° of maximal rotation throughout the course of scanning).

[1]http://www.fil.ion.ucl.ac.uk/spm

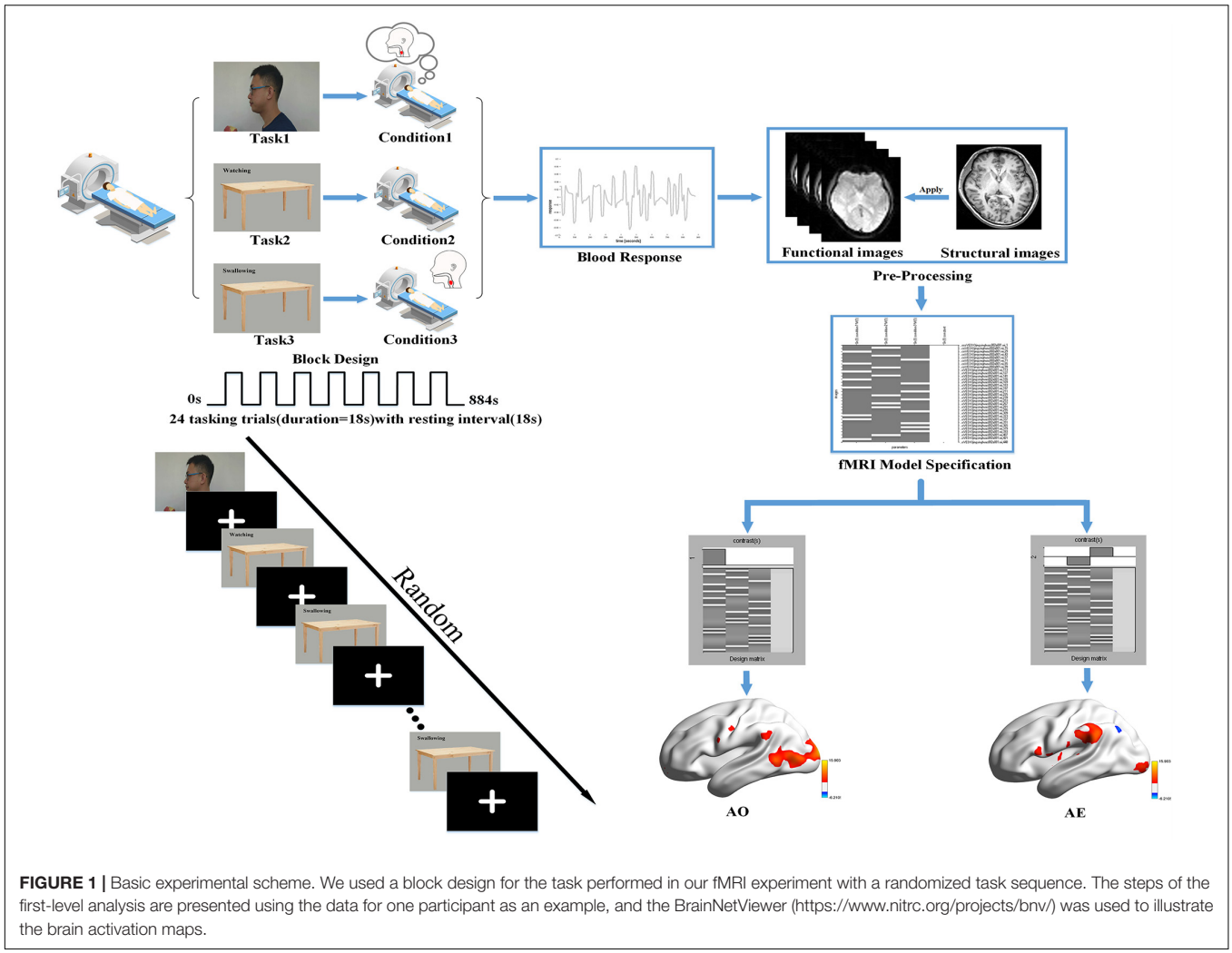

FIGURE 1 | Basic experimental scheme. We used a block design for the task performed in our fMRI experiment with a randomized task sequence. The steps of the first-level analysis are presented using the data for one participant as an example, and the BrainNetViewer (https://www.nitrc.org/projects/bnv/) was used to illustrate the brain activation maps.

fMRI Data Analysis

SPM12 was used in a block design to analyze functional whole-brain data with the purpose of determining group effects. The General Linear Model (GLM) was used in the first-level analysis. First, to observe the activation in each condition, we used the following design matrix: video task (condition 1) versus rest period; neutral picture of a desk with a Chinese word for "watching" (condition 2) versus rest period; neutral picture with a Chinese word for "swallowing" (condition 3) versus rest period. Second, whole-brain analysis of the following contrasts of task conditions was performed: we defined condition 1 as the AO and condition 3 minus condition 2 as the action execution (AE). Hence, the analysis revealed the activation patterns of mirror neurons during AO and the activation patterns of the swallowing network during AE. In order to detail and check the activation pattern in each participant, the resultant T-maps were considered with a threshold of $P < 0.001$ uncorrected for multiple comparisons. The first-level analysis is outlined in **Figure 1**.

In the second-level analysis, the statistical analysis, the beta weights of two contrasts were statistically compared separately using one sample *t*-test, with the age and sex of participants as covariates. The results were corrected for multiple comparisons using the false discovery rate (FDR) correction at the voxel-level, and the significance threshold was set at FDR-corrected $P < 0.01$ with a minimum cluster size (the number of voxels) of 10 voxels.

RESULTS

AO-Condition 1

As shown in **Figure 2** and **Table 1**, observation of the action-video of swallowing motion led to activation patterns in the bilateral middle temporal gyrus (BA37\21), left pre- and postcentral gyrus (BA6\4), left hippocampus, right inferior frontal gyrus (BA45), right SMA (BA6), left brainstem, and pons ($P < 0.01$, FDR corrected, cluster size > 10 voxels).

AE-Condition 3 Minus Condition 2

As shown in **Figure 3** and **Table 2**, compared with the task image without action, execution of swallowing movements activated the brain network in the motor areas (left SMA [BA6]), bilateral inferior parietal lobule (BA40), left anterior

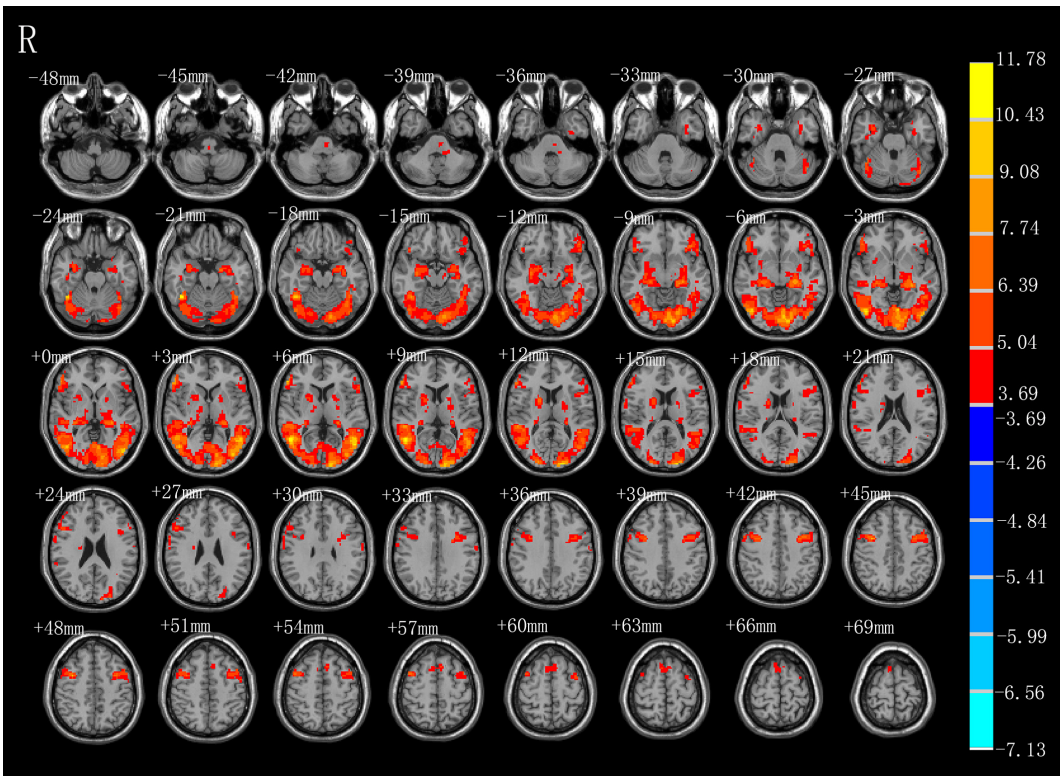

FIGURE 2 | T-score map showing activation for AO (hot colors) in transverse slices ($P < 0.01$, FDR corrected, cluster size > 10 voxels).

cingulate (BA32), vermis of the cerebellum, left middle frontal gyrus (BA45), left superior frontal gyrus (BA11), left thalamus, left precuneus (BA7), left cuneus, left middle temporal gyrus (BA37\21), left inferior temporal gyrus (BA20), left middle occipital gyrus (BA39), left calcarine (BA18), and bilateral caudate ($P < 0.01$, FDR corrected, cluster size > 10 voxels).

TABLE 1 | Brain regions activated by AO.

Regions (AAL)	BA	Cluster size	Peak *T*-value	MNI coordinate (mm)		
				X	*Y*	*Z*
AO						
Temporal_Mid_R	37	5270	11.7835	51	−57	6
Frontal_Inf_Tri_R	45	325	10.1845	57	36	6
Precentral_R	6	272	9.6466	36	3	45
Supp_Motor_Area_R	6	109	5.5840	9	12	72
Precentral_L	6	688	7.3714	−36	6	45
Hippocampus_L	N.A	589	8.8161	−24	−24	−6
Postcentral_L	4	16	4.6161	−63	−9	30
Temporal_Mid_L	21	10	4.2366	−57	−24	−6
Left Brainstem	N.A	17	4.7916	−9	−21	−42
Pons	N.A	10	4.6971	−18	−33	−39

BA, Brodman's area; Cluster size, the number of voxels; MNI, Montreal Neurological Institute; R right, L left; P < 0.01, FDR corrected, cluster size > 10 voxels.

AO Versus AE

As shown in **Figure 4**, BA6 and BA21 were activated during both AO and AE states.

DISCUSSION

In the present study, we examined and compared the patterns of brain activation in healthy participants as they observed an action-video and as they actually executed the swallowing motion using task-based fMRI. We identified the brain regions of BA6 and BA21 as commonly activated during the two sessions and speculated on the role of AO in swallowing.

AO-Condition 1

During condition 1, observation of the video of the task, the most critical task of our experiment, we observed activated of not only similar mirror neurons reported in a prior study (Cook et al., 2014), but also increased activity of classical swallowing network. Consistent with the findings in the previous review (Ferrari et al., 2017), activation of brain regions in the left pre- and postcentral gyrus (BA6\4), right inferior frontal gyrus (BA45), and right supplementary motor area (BA6) did correspond to mouth mirroring in the present study. In our

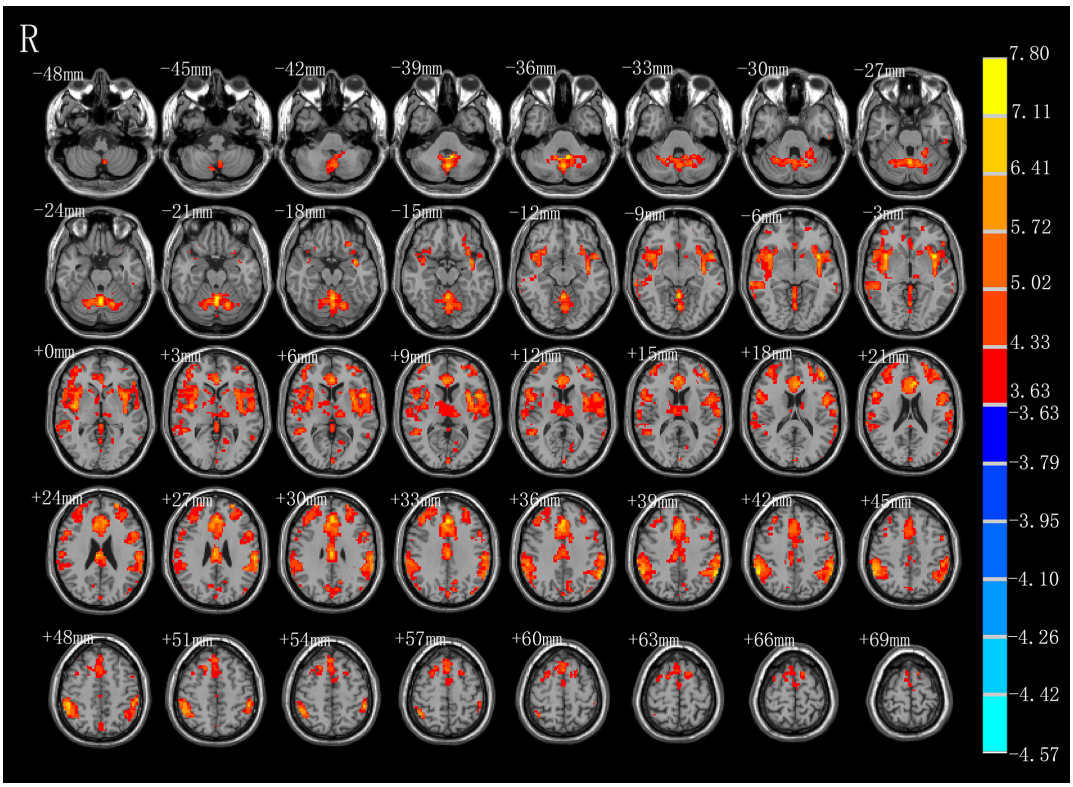

FIGURE 3 | T-score map showing stronger activation of brain areas with AE (hot colors) in transverse slices ($P < 0.01$, FDR corrected, cluster size > 10 voxels).

results, the bilateral precentral (BA6) and right SMA (BA6) were strongly activated when the healthy participants watched the video of swallowing action, which is consistent with the findings of a previous MEG study (Ushioda et al., 2012). In general, the SMA (BA6), located in the superior and middle frontal gyri, often processes sequential motions, especially those associated with the beginning of the motions, and the precentral gyrus (BA6), including the premotor areas and primary motor cortex, is involved in complex experienced motions. However, different from the prior MEG study, observation of our action-video of swallowing led to the activation of many other brain regions (e.g., BA37, BA45, BA4, and BA21) rather than BA40. In addition to the intrinsic advantage of fMRI for extracting deep or multiple BOLD signals, we considered that observation of the action-video for a daily performance activity may be better than animation or auditory stimuli for activating the brain regions of mirror neurons related to swallowing. Specifically, considering our results in comparison with those of prior studies, due to the complementary role of the inferior frontal gyrus (BA45) in swallowing regulation, it is possible that activation of BA45 during our video task is associated with taste and imagery of the apple in the action-video. In addition, the left brainstem and pons are associated with voluntary swallowing more than spontaneous swallowing in humans, which might explain why observation of the action-video of swallowing proactively stimulated swallowing among healthy participants (Ertekin, 2011). The hippocampus is the site in the brain responsible for memory and learning and may therefore be conducive to evoked memory of swallowing and play a role in the swallowing process (Downar et al., 2000). We also hypothesized that the hippocampus receives information from the action-video, coordinates with the precentral gyrus, and then relays the neural signals to SMA, and further research is needed to confirm this hypothesis. More importantly, the most meaningful finding from this experiment is that activation of the specific brain regions, including the bilateral middle temporal gyrus (BA37\21), inferior frontal gyrus (BA45), primary motor cortex, and SMA (BA6), is consistent with the hypothesis of Small et al. that the mirror neurons activated by the action-video of swallowing may promote reorganization of the cortical motor loop and thereby improve swallowing function (Small et al., 2012).

AE-Condition 3 Minus Condition 2

In line with the previous studies, our comparison of condition 2 with condition 3, which excluded the visual effects and emotional reactions, showed that the AE of swallowing activated many different brain areas related to swallowing. Martin et al. reported that the SMA (BA6) and anterior cingulate (BA32) are vital for the control of voluntary swallowing (Martin et al., 2001). As mentioned above, the SMA (BA6) plays a dynamic role in the execution of different swallowing tasks and is mainly involved in comprehensive oral movements. One explanation for the activation of the anterior cingulate (BA32) is that voluntary saliva swallowing may rely on attention and concentration.

TABLE 2 | Brain regions activated more strongly with AE.

Regions (AAL)	BA	Cluster size	Peak *T*-value	MNI coordinate (mm)		
				X	*Y*	*Z*
AE						
Parietal_Inf_R	40	2728	7.4847	57	−48	42
Caudate_R	N.A	17	4.9357	15	21	3
Parietal_Inf_L	40	1995	7.5035	−60	−48	39
Cingulum_Ant_L	32	1829	7.2223	0	36	30
Frontal_Mid_L	45	415	6.6479	−42	45	15
Thalamus_L	N.A	293	4.6826	−15	−18	6
Cuneus_L	N.A	150	5.2192	−9	−75	36
Supp_Motor_Area_L	6	56	4.8467	−12	12	66
Calcarine_L	18	39	4.2421	−12	−75	9
Caudate_L	N.A	32	5.2077	−15	18	0
Occipital_Mid_L	39	27	5.2851	−42	−78	36
Precuneus_L	7	24	4.1871	0	−72	48
Temporal_Mid_L	37	16	4.3757	−60	−57	3
Frontal_Sup_Orb_L	11	13	4.5128	−21	57	−3
Temporal_Mid_L	37	11	4.4436	−60	−57	15
Temporal_Mid_L	21	11	4.1524	−66	−39	−6
Temporal_Inf_L	20	10	5.0509	−54	−18	−30
Vermis_6	N.A	1230	7.8017	0	−60	−24

BA, Brodman's area; Cluster size, the number of voxels; MNI, Montreal Neurological Institute; R right, L left; P < 0.01, FDR corrected, cluster size > 10 voxels.

Additionally, Kawai et al. reported that the pre-SMA receives input signals from the cingulate gyrus and pre-frontal area to facilitate the performance of a series of swallowing motions (Kawai et al., 2009). During the execution of swallowing, we propose that activation of the left superior frontal gyrus (BA11) and left middle frontal gyrus (BA45), which are associated with emotion, motivation, and learning-set formation, reflects the processing of swallowing information and its delivery to the SMA. The temporal gyrus that was activated in prior experiments and corresponds to the left middle temporal gyrus (BA37\21) and left inferior temporal gyrus (BA20) in our experiment, has been implicated in taste and imagery of food and may play a supplementary role in the regulation of swallowing and feeding (Hamdy et al., 1999b; Ertekin and Aydogdu, 2003). However, it is also possible that the noise produced by the MRI scanner and the sounds of swallowing by themselves activated the auditory cortex. Because all participants wore ear plugs, we instead suggest that the activation of the temporal gyrus may reflect the acoustic correlates of swallowing. In this study, activation of bilateral inferior parietal lobules (BA40) located near the insula and bilateral caudate, which are related to oral movements and sensation, may be a characteristic of bilateral movements such as swallowing, as reported by a previous MEG study (Ushioda et al., 2012). However, while the meta-analysis by Soros et al. observed activation in the basal ganglia, they also reported involvement of the putamen but not of the caudate during swallowing, in contrast with the present findings (Soros et al., 2009). Moreover, the cluster of precuneus (BA7), cuneus, and calcarine (BA18) also are likely to play a sensory role in the control of swallowing (Kober et al., 2019). Activation of the vermis of the cerebellum and thalamus was shown to contribute to swallowing and to effective connectivity within the swallowing network in recent neuroimaging studies (Ushioda et al., 2012; Babaei et al., 2013). The brain region of the middle occipital gyrus (BA39) is a well-established component of the visual cortex that processes visual information. We speculate that, due to the difference in the Chinese words presented in condition 2 versus condition 3, the activity in the left middle occipital gyrus (BA39) mainly aims to distinguish different task instructions. Yet, Hamdy et al. proposed that the left brain is the dominant side for the swallowing network (Hamdy et al., 1999a), a conclusion that is not supported by our findings. Indeed, in our study (**Figure 1**), large clusters of activation were observed in the right brain whereas the activated areas in the left brain were dispersed among a number of spatially discrete cortical regions. Further research is required to determine the dominant hemisphere for swallowing.

AO Versus AE

In the present study, both the BA6 and BA21 areas were activated during both AO and AE. The Ba6 brain area, which includes the premotor cortex and SMA, is a dominant area for motor function bilaterally. Undoubtedly, BA6 responds consistently during AE of swallowing, and this findings is in agreement with the results of a meta-analysis on swallowing (Soros et al., 2009). Compared to AE of swallowing, AO of swallowing also activated BA6, and this might be related to the activation of mirror neurons in this area. We hypothesize that activation of BA6 appears is not only motor marker, but also a marker of the ability of mirror neurons to relay visual information to the executive control network to achieve goal-directed behaviors (Zhang et al., 2018). Although the BA21 brain area was also activated during both AO and AE, the specific anatomical location of this activation remains unclear (**Figure 4**). We hypothesize that BA21 actively focuses on visual processing during AO (Small et al., 2012), whereas it may participate in swallowing regulation with taste and imagery of food during AE (Ertekin and Aydogdu, 2003). The detailed activation pattern requires further exploration.

Study Limitations and Future Directions

The present study provided a simple comparison of neuronal correlates between mirror neurons and the swallowing network, and showed that the left supplementary motor area (BA6) and left middle temporal gyrus (BA21) may be foundational to the role of AO in treatment for dysphagia. However, our results did not reveal the precise neural mechanisms of the two neuronal networks, and thus, we are planning future neuroimaging analyses to elucidate these mechanisms. Furthermore, a limitation of the present study is that we could not control for head movement during swallowing. Because swallowing and head movement are highly correlated, we did not use head motion as a covariate in our statistical analysis to rule out the effects of the head motion on the current results.

Dysphagia seriously affects the general condition as well as the quality of life of the patient. Novel treatments to

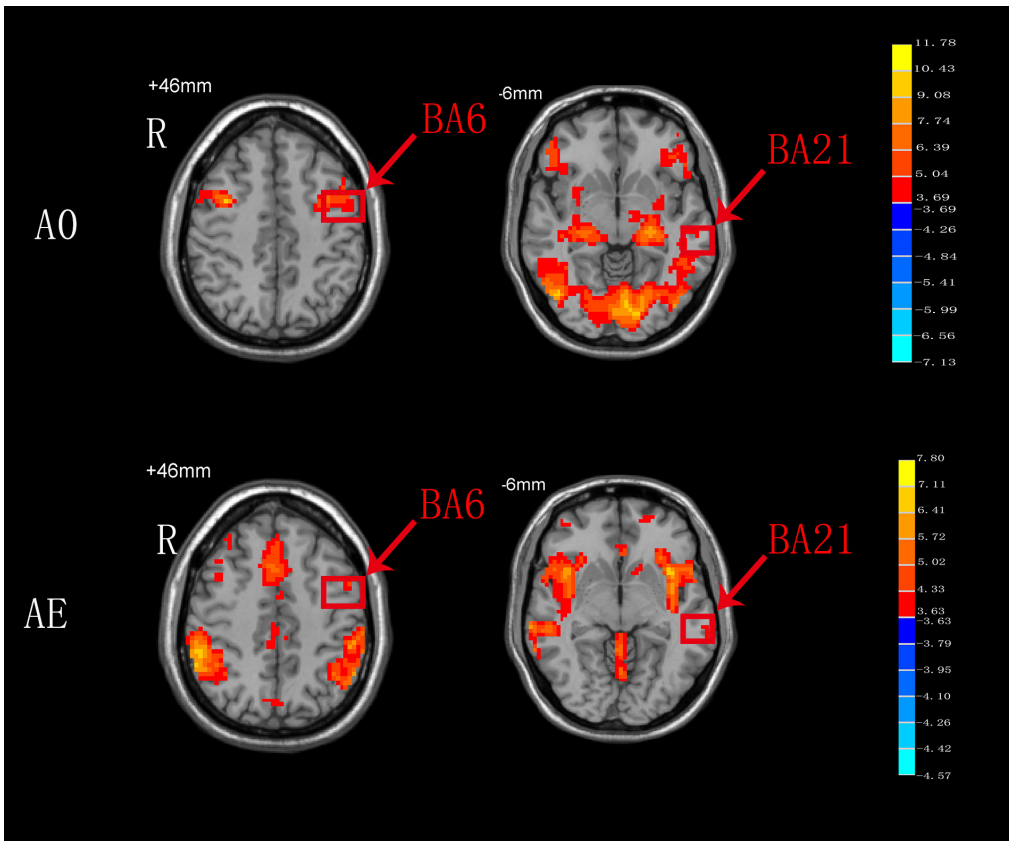

FIGURE 4 | T-score map showing the brain areas activated during both AO and AE (hot colors) in transverse slices ($P < 0.01$, FDR corrected, cluster size > 10 voxels).

repair the injured nerves are urgently needed to improve the clinical efficacy. Our findings suggest that AO can be applied to dysphagia directly via impacting the connection of mirror neurons and swallowing network. Additionally, we can stimulate BA6 and BA21 to enhance and regulate the swallowing network and mirror neurons dynamically via non-invasive stimulation, and then repair the swallowing network by AO. Further studies in dysphagia patients are warranted to evaluate whether the action-video of swallowing could be used as a stimulus for AO in the treatment of dysphagia and to elucidate the neural mechanisms of AO.

CONCLUSION

Our results preliminarily indicate that AO using an action-video of swallowing practically activates the mirror neurons related to swallowing in healthy individuals. We believe that AO can be used as an effective therapy to repair the damaged swallowing network for dysphagia. Particular attention should be paid to two brain regions, BA6 and BA21, which were commonly activated during the observation and execution of swallowing, in future patient studies.

DATA AVAILABILITY STATEMENT

The raw data supporting the conclusions of this article will be made available by the authors, without undue reservation.

ETHICS STATEMENT

The studies involving human participants were reviewed and approved by the Medical Ethics Committee of medical college of South China University of Technology. The patients/participants provided their written informed consent to participate in this study. Written informed consent was obtained from the individual(s) for the publication of any potentially identifiable images or data included in this article.

AUTHOR CONTRIBUTIONS

YL and GX guided the experiment design. YJ and TL conceived, designed, and completed the experiment. YJ analyzed the data and drafted the manuscript. TL reviewed and edited the manuscript. CW, XL, QD, and MW collected the data. All authors contributed to the article and approved the submitted version.

FUNDING

This study was supported by grants from the Natural Science Foundation of China (Nos. 81772438, 81802227, and 81974357), the Fundamental Research Funds for the Central University (2018PY03), the Guangzhou Municipal Science and Technology Program (No. 201803010083), and the Guangdong Provincial Science and Technology Program (No. 2016A020213003).

REFERENCES

Amoruso, L., Finisguerra, A., and Urgesi, C. (2018). Contextualizing action observation in the predictive brain: causal contributions of prefrontal and middle temporal areas. *Neuroimage* 177, 68–78. doi: 10.1016/j.neuroimage.2018.05.020

Babaei, A., Ward, B. D., Siwiec, R. M., Ahmad, S., Kern, M., Nencka, A., et al. (2013). Functional connectivity of the cortical swallowing network in humans. *NeuroImage* 76, 33–44. doi: 10.1016/j.neuroimage.2013.01.037

Bassolino, M., Campanella, M., Bove, M., Pozzo, T., and Fadiga, L. (2014). Training the motor cortex by observing the actions of others during immobilization. *Cereb. Cortex* 24, 3268–3276. doi: 10.1093/cercor/bht190

Borges, L. R., Fernandes, A. B., Melo, L. P., Guerra, R. O., and Campos, T. F. (2018). Action observation for upper limb rehabilitation after stroke. *Cochrane Database Syst. Rev.* 10:CD011887. doi: 10.1002/14651858.CD011887.pub2

Casile, A., Caggiano, V., and Ferrari, P. F. (2011). The mirror neuron system: a fresh view. *Neuroscientist* 17, 524–538. doi: 10.1177/1073858410392239

Catmur, C., Thompson, E. L., Bairaktari, O., Lind, F., and Bird, G. (2018). Sensorimotor training alters action understanding. *Cognition* 171, 10–14. doi: 10.1016/j.cognition.2017.10.024

Clavé, P., and Shaker, R. (2015). Dysphagia: current reality and scope of the problem. *Nat. Rev. Gastroenterol. Hepatol.* 12, 259–270. doi: 10.1038/nrgastro.2015.49

Cook, R., Bird, G., Catmur, C., Press, C., and Heyes, C. (2014). Mirror neurons: from origin to function. *Behav. Brain Sci.* 37, 177–192. doi: 10.1017/S0140525X13000903

Dodds, W. J. (1989). Physiology of swallowing. *Dysphagia* 3, 171–178. doi: 10.1007/bf02407219

Domenech, E., and Kelly, J. (1999). Swallowing disorders. *Med. Clin. North Am.* 83, 97–113. doi: 10.1016/s0025-7125(05)70090-0

Downar, J., Crawley, A. P., Mikulis, D. J., and Davis, K. D. (2000). A multimodal cortical network for the detection of changes in the sensory environment. *Nat. Neurosci.* 3, 277–283. doi: 10.1038/72991

Easterling, C. (2017). 25 years of dysphagia rehabilitation: what have we done, what are we doing, and where are we going? *Dysphagia* 32, 50–54. doi: 10.1007/s00455-016-9769-8

Ertekin, C. (2011). Voluntary versus spontaneous swallowing in man. *Dysphagia* 26, 183–192. doi: 10.1007/s00455-010-9319-8

Ertekin, C., and Aydogdu, I. (2003). Neurophysiology of swallowing. *Clin. Neurophysiol.* 114, 2226–2244. doi: 10.1016/s1388-2457(03)00237-2

Fawcett, C., and Liszkowski, U. (2012). Observation and initiation of joint action in infants. *Child Dev.* 83, 434–441. doi: 10.1111/j.1467-8624.2011.01717.x

Ferrari, P. F., Gerbella, M., Coude, G., and Rozzi, S. (2017). Two different mirror neuron networks: the sensorimotor (hand) and limbic (face) pathways. *Neuroscience* 358, 300–315. doi: 10.1016/j.neuroscience.2017.06.052

Gili, T., Fiori, V., De Pasquale, G., Sabatini, U., Caltagirone, C., and Marangolo, P. (2017). Right sensory-motor functional networks subserve action observation therapy in aphasia. *Brain Imaging Behav.* 11, 1397–1411. doi: 10.1007/s11682-016-9635-1

Gonzalez-Fernandez, M., and Daniels, S. K. (2008). Dysphagia in stroke and neurologic disease. *Phys. Med. Rehabil. Clin. N. Am.* 19, 867–888. doi: 10.1016/j.pmr.2008.07.001

Hamdy, S., Mikulis, D. J., Crawley, A., Xue, S., Lau, H., Henry, S., et al. (1999a). Cortical activation during human volitional swallowing: an event-related fMRI study. *Am. J. Physiol.* 277, G219–G225. doi: 10.1152/ajpgi.1999.277.1.G219

Hamdy, S., Rothwell, J. C., Brooks, D. J., Bailey, D., Aziz, Q., and Thompson, D. G. (1999b). Identification of the cerebral loci processing human swallowing with H2(15)O PET activation. *J. Neurophysiol.* 81, 1917–1926. doi: 10.1152/jn.1999.81.4.1917

Hetu, S., Gagne, M., Jackson, P. L., and Mercier, C. (2010). Variability in the effector-specific pattern of motor facilitation during the observation of everyday actions: implications for the clinical use of action observation. *Neuroscience* 170, 589–598. doi: 10.1016/j.neuroscience.2010.07.015

Jia, X.-Z., Wang, J., Sun, H.-Y., Zhang, H., Liao, W., Wang, Z., et al. (2019). RESTplus: an improved toolkit for resting-state functional magnetic resonance imaging data processing. *Sci. Bull.* 64, 953–954. doi: 10.1016/j.scib.2019.05.008

Kawai, T., Watanabe, Y., Tonogi, M., Yamane, G. Y., Abe, S., Yamada, Y., et al. (2009). Visual and auditory stimuli associated with swallowing: an FMRI study. *Bull. Tokyo Dent. Coll.* 50, 169–181. doi: 10.2209/tdcpublication.50.169

Kilner, J. M., and Lemon, R. N. (2013). What we know currently about mirror neurons. *Curr. Biol.* 23, R1057–R1062. doi: 10.1016/j.cub.2013.10.051

Kirkpatrick, E., Pearse, J., James, P., and Basu, A. (2016). Effect of parent-delivered action observation therapy on upper limb function in unilateral cerebral palsy: a randomized controlled trial. *Dev. Med. Child Neurol.* 58, 1049–1056. doi: 10.1111/dmcn.13109

Kober, S. E., Grössinger, D., and Wood, G. (2019). Effects of motor imagery and visual neurofeedback on activation in the swallowing network: a real-time fMRI study. *Dysphagia* 34, 879–895. doi: 10.1007/s00455-019-09985-w

Lang, I. M. (2009). Brain stem control of the phases of swallowing. *Dysphagia* 24, 333–348. doi: 10.1007/s00455-009-9211-6

Lazarus, C. L. (2017). History of the use and impact of compensatory strategies in management of swallowing disorders. *Dysphagia* 32, 3–10. doi: 10.1007/s00455-016-9779-6

Lima, M. S., Mangilli, L. D., Sassi, F. C., and Andrade, C. R. (2015). Functional magnetic resonance and swallowing: critical literature review. *Braz. J. Otorhinolaryngol.* 81, 671–680. doi: 10.1016/j.bjorl.2015.08.006

Maranesi, M., Livi, A., Fogassi, L., Rizzolatti, G., and Bonini, L. (2014). Mirror neuron activation prior to action observation in a predictable context. *J. Neurosci.* 34, 14827–14832. doi: 10.1523/jneurosci.2705-14.2014

Marshall, J. (2014). Mirror neurons. *Proc. Natl. Acad. Sci. U.S.A.* 111:6531. doi: 10.1073/pnas.1404652111

Martin, R. E., Goodyear, B. G., Gati, J. S., and Menon, R. S. (2001). Cerebral cortical representation of automatic and volitional swallowing in humans. *J. Neurophysiol.* 85, 938–950. doi: 10.1152/jn.2001.85.2.938

Martino, R., and McCulloch, T. (2016). Therapeutic intervention in oropharyngeal dysphagia. *Nat. Rev. Gastroenterol. Hepatol.* 13, 665–679. doi: 10.1038/nrgastro.2016.127

Mazurek, K. A., Rouse, A. G., and Schieber, M. H. (2018). Mirror neuron populations represent sequences of behavioral epochs during both execution and observation. *J. Neurosci.* 38, 4441–4455. doi: 10.1523/jneurosci.3481-17.2018

Ogawa, S., Tank, D. W., Menon, R., Ellermann, J. M., Kim, S. G., Merkle, H., et al. (1992). Intrinsic signal changes accompanying sensory stimulation: functional brain mapping with magnetic resonance imaging. *Proc. Natl. Acad. Sci. U.S.A.* 89, 5951–5955. doi: 10.1073/pnas.89.13.5951

Pelosin, E., Barella, R., Bet, C., Magioncalda, E., Putzolu, M., Di Biasio, F., et al. (2018). Effect of group-based rehabilitation combining action observation with physiotherapy on freezing of gait in Parkinson's disease. *Neural Plast.* 2018:4897276. doi: 10.1155/2018/4897276

Pelosin, E., Bove, M., Ruggeri, P., Avanzino, L., and Abbruzzese, G. (2013). Reduction of bradykinesia of finger movements by a single session of action observation in parkinson disease. *Neurorehabil. Neural Repair* 27, 552–560. doi: 10.1177/1545968312471905

Rizzolatti, G., and Craighero, L. (2004). The mirror-neuron system. *Annu. Rev. Neurosci.* 27, 169–192. doi: 10.1146/annurev.neuro.27.070203.144230

Rizzolatti, G., and Sinigaglia, C. (2016). The mirror mechanism: a basic principle of brain function. *Nat. Rev. Neurosci.* 17, 757–765. doi: 10.1038/nrn.2016.135

Rommel, N., and Hamdy, S. (2016). Oropharyngeal dysphagia: manifestations and diagnosis. *Nat. Rev. Gastroenterol. Hepatol.* 13, 49–59. doi: 10.1038/nrgastro.2015.199

Sale, M. V., and Mattingley, J. B. (2013). Selective enhancement of motor cortical plasticity by observed mirror-matched actions. *Neuroimage* 74, 30–36. doi: 10.1016/j.neuroimage.2013.02.009

Sale, P., and Franceschini, M. (2012). Action observation and mirror neuron network: a tool for motor stroke rehabilitation. *Eur. J. Phys. Rehabil. Med.* 48, 313–318.

Small, S. L., Buccino, G., and Solodkin, A. (2012). The mirror neuron system and treatment of stroke. *Dev. Psychobiol.* 54, 293–310. doi: 10.1002/dev.20504

Small, S. L., Buccino, G., and Solodkin, A. (2013). Brain repair after stroke—a novel neurological model. *Nat. Rev. Neurol.* 9, 698–707. doi: 10.1038/nrneurol.2013.222

Soltysik, D. A., and Hyde, J. S. (2006). Strategies for block-design fMRI experiments during task-related motion of structures of the oral cavity. *Neuroimage* 29, 1260–1271. doi: 10.1016/j.neuroimage.2005.08.063

Soros, P., Inamoto, Y., and Martin, R. E. (2009). Functional brain imaging of swallowing: an activation likelihood estimation meta-analysis. *Hum. Brain Mapp.* 30, 2426–2439. doi: 10.1002/hbm.20680

Toogood, J. A., Smith, R. C., Stevens, T. K., Gati, J. S., Menon, R. S., Theurer, J., et al. (2017). Swallowing preparation and execution: insights from a delayed-response functional magnetic resonance imaging (fMRI) study. *Dysphagia* 32, 526–541. doi: 10.1007/s00455-017-9794-2

Tramacere, A., Pievani, T., and Ferrari, P. F. (2017). Mirror neurons in the tree of life: mosaic evolution, plasticity and exaptation of sensorimotor matching responses. *Biol. Rev.* 92, 1819–1841. doi: 10.1111/brv.12310

Ugurbil, K. (2016). What is feasible with imaging human brain function and connectivity using functional magnetic resonance imaging. *Philos. Trans. R. Soc. Lond. B Biol. Sci.* 371:20150361. doi: 10.1098/rstb.2015.0361

Ushioda, T., Watanabe, Y., Sanjo, Y., Yamane, G.-Y., Abe, S., Tsuji, Y., et al. (2012). Visual and auditory stimuli associated with swallowing activate mirror neurons: a magnetoencephalography study. *Dysphagia* 27, 504–513. doi: 10.1007/s00455-012-9399-8

Vesia, M., Pellicciari, R., Cash, R. F. H., Isayama, R., Kunaratnam, N., Jegatheeswaran, G., et al. (2019). Learning from goal and action based observations differentially modulates functional motor cortical plasticity. *Neuroscience* 404, 387–395. doi: 10.1016/j.neuroscience.2019.02.019

Zhang, J. J. Q., Fong, K. N. K., Welage, N., and Liu, K. P. Y. (2018). The activation of the mirror neuron system during action observation and action execution with mirror visual feedback in stroke: a systematic review. *Neural Plast.* 2018:2321045. doi: 10.1155/2018/2321045

Conflict of Interest: The authors declare that the research was conducted in the absence of any commercial or financial relationships that could be construed as a potential conflict of interest.

frontiers in Psychiatry

ORIGINAL RESEARCH
published: 28 August 2020
doi: 10.3389/fpsyt.2020.00788

Volumetric Abnormalities in Violent Schizophrenia Patients on the General Psychiatric Ward

FengJu Liu[1†], *Yang Shao*[1†], *Xin Li*[2], *Li Liu*[1], *Rong Zhao*[1], *Bin Xie*[1*] *and Yi Qiao*[1*]

[1] Shanghai Mental Health Center, Shanghai Jiao Tong University School of Medicine, Shanghai, China, [2] Shanghai Pudong New Area Mental Health Center, School of Medicine, Tongji University, Shanghai, China

Background: In recent years, neuroimaging has been used increasingly to explore the biological underpinnings of violence carried out by schizophrenia patients (SPs). Studies have focused mostly on patients with a history of carrying out severe physical assaults, or comorbid with substance abuse/personality disorder (SA/PD). As a result, participants were unrepresentative and the interpretation of brain-structure changes was confusing. Here, we concentrated on SPs on a general psychiatric ward with a history of relatively lower violence, and individuals comorbid with SA or PD were excluded. We expected to identify the characteristics of brain morphometry in this population, and to explore whether the morphometric changes were universal.

Methods: Forty-eight violent schizophrenia patients (VSPs), twenty-seven non-VSPs (nVSPs) and 28 nonviolent healthy controls (HCs) were investigated. Voxel-based morphometry was used to evaluate the gray matter volume (GMV) of all study participants. Whole-brain analyses were used to reveal group effects and differences between any two groups. Correlation analyses were undertaken between significant brain regions and behavioral measurements in the VSP group.

Results: Patients showed a significantly smaller GMV in widespread frontal, temporal, and limbic regions compared with HCs. No region was found in which the two patient groups had significantly larger volumes compared with that in HCs. A significant decrease in the GMV of the right fusiform gyrus was found in the VSP group compared with that in the nVSP group ($p = 0.004$), where the GMV of this region had a negative correlation with the Physical Aggression [subscale of the Modified Overt Aggression Scale (MOAS)] or Hostility score. The VSP group showed a trend of GMV decrease in the left middle temporal cortex compared with that in the nVSP group ($p = 0.077$). Negative correlation was also found between the GMV of left inferior temporal gyrus/left Superior frontal gyrus, medial and the Hostility score.

Conclusions: Our results provide initial evidence demonstrating the generalizability of GMV abnormalities in SPs engaged in varying levels of violence, even when SA or PD have not been implicated. GMV reduction was correlated with only the Physical Aggression

OPEN ACCESS

Edited by:
Zsigmond Tamás Kincses, University of Szeged, Hungary

Reviewed by:
Nikoletta Szabó, University of Szeged, Hungary
Luke Norman, University of Michigan, United States

***Correspondence:**
Bin Xie
xiebin@smhc.org.cn
Yi Qiao
qiaoyi2004@msn.com

[†]*These authors have contributed equally to this work*

Specialty section:
This article was submitted to Neuroimaging and Stimulation, a section of the journal Frontiers in Psychiatry

Received: *25 March 2020*
Accepted: *23 July 2020*
Published: *28 August 2020*

Citation:
Liu F, Shao Y, Li X, Liu L, Zhao R, Xie B and Qiao Y (2020) Volumetric Abnormalities in Violent Schizophrenia Patients on the General Psychiatric Ward. Front. Psychiatry 11:788. doi: 10.3389/fpsyt.2020.00788

subscale score of the MOAS, suggesting that this change in brain morphology may be dependent upon different types of violent actions.

Keywords: structural brain alterations, violence, schizophrenia, MRI voxel-based morphometry, neuroimaging

INTRODUCTION

There is robust evidence that people with schizophrenia are more likely to carry out violence than members of the general population (1, 2). Such violence can result in physical harm, stigmatization, and enormous economic cost to society (3, 4). Therefore, it is important to develop a better understanding of the aggression and violence involved in schizophrenia. In addition, neurological soft signs have been shown to be present in violent schizophrenia patients (VSPs) compared with non-VSPs (nVSPs) and normal populations (5, 6), which suggests that neuropathologic predispositions contribute to aggression in schizophrenia.

Certain brain regions have important roles in the violent behavior associated with schizophrenia (7). These are regions involved in affective regulation, such as the orbital frontal cortex (OFC) and anterior cingulate cortex (ACC) (6, 8, 9) as well as egions involved in psychiatric symptoms, such as the hippocampus and prefrontal cortex (PFC) (10–12).

Several structural magnetic resonance imaging (MRI) studies have been conducted in VSPs. Hoptman and colleagues reported a correlation between the Urgency Score and reduced cortical thickness in the OFC and ACC (13). Similarly, the Impulsiveness Score was found to be correlated significantly and negatively with the gray matter volume (GMV) of the OFC and hippocampus in SPs with a history of severe violence (14). Few studies have focused on the relationship between brain structure and violence. Only a few studies have reported significant GMV differences among VSPs when compared with nVSPs. Yang and colleagues revealed that people convicted of murder and suffering from schizophrenia showed a reduced GMV in their hippocampus compared with that of patients without a history of violence (10). Kuroli and coworkers found reduced temporal, fusiform, and insular volumes in SPs who had carried out severe violence compared with nVSPS (15). In contrast, in a study undertaken in SPs who had carried out physical assaults, widespread morphometric abnormalities were found in VSPs compared with healthy controls (HCs), but shared volumetric abnormalities were not found between VSPs and nVSPs (16). Similarly, a reduced volume of the ACC was revealed in SPs who had carried out severe violence only when they were compared with HCs (17). In another study undertaken on SPs who had carried out severe violence, the volume differences in putamen and amygdala between VSPs and nVSPs disappeared when the influence of the Positive and Negative Syndrome Scale (PANSS) score was minimized (18).

Results between studies have been inconsistent, with some particular areas of concern: different definitions of violence; small sample size; comorbidity with substance dependence, personality disorder (PD) and other factors. Substance abuse and PD, as confounding factors, can affect violent behavior (19, 20), and might play an important part in morphologic changes (15, 18, 21), which can complicate interpretation of volumetric changes. Structural-MRI studies have been carried out mostly on SPs who have carried out severe physical violence (14, 15), near-fatal violent behavior against another person (18) or murder (10). These are extreme cases of SPs, so these participants are unrepresentative.

With the limitations mentioned above in mind, we concentrated on SPs on a general psychiatric ward with a history of relatively low-level violence, and individuals comorbid with substance abuse or PD were excluded. We used voxel-based morphometry to detect neural differences in VSPs, nVSPs and non-violent HCs to explore the neurobiological basis underlying these categories of the population.

METHODS

Ethical Approval of the Study Protocol

All participants and/or their authorized legal representatives provided written informed consent. The study protocol was approved by the Ethics Committee of Shanghai Mental Health Center (Shanghai, China).

Participants

The study cohort comprised 75 SPs and 28 HCs. SPs were recruited on the general psychiatry ward of Shanghai Mental Health Center (Shanghai, China). All patients met ICD-10 diagnostic criteria, including 48 SPs who had a history of violence and ultimately 27 age-matched nVSPs. One participant dropped out of the nVSP group for not being able to tolerate MRI. All patients were medicated. In the VSP group, 30 patients were on atypical agents, one was on typical agents, and 17 were on both types of agents. In the nVSP group, 17 patients were on atypical agents, one was on typical agents, and nine were on both types of agents. None of the patients had a history of substance dependence. Urine tests were undertaken when patients were admitted to the ward. HCs were recruited from the local community. Diagnostic interviews were conducted by two independent psychiatrists to screen for a history of mental disorders. HCs were screened for PD using the Structured Clinical Interview for DSM-IV Axis II Disorders (SCID-II). Self-reporting indicated that no patients had a history of substance abuse. All participants were required to be aged 18–45 years and right-handed to minimize the influence of hemispheric lateralization between three groups. Participants with severe physical diseases, head injuries, or diagnosed with other psychiatric disorders were excluded.

Clinical Measurements

Psychiatric symptoms in patients were rated using the PANSS. We used the Modified Overt Aggression Scale (MOAS) to

evaluate acts of violence, as noted previously (22, 23). The MOAS is composed of four subscales: Verbal Aggression; Aggression Against Objects; Physical Aggression Against Oneself; Physical Aggression Against Other People. This scale has good reliability and validity, and is also applicable to Chinese populations (24, 25).

All individuals in the VSP group were required to have a MOAS score >4 in the past 6 months. Otherwise the participants were classified into the nVSP group. In the PANSS, the Excitement item (P4), Hostility item (P7) and Poor Impulse Control item (G14) were also used to describe aggressive behavior (26).

Acquisition and Preprocessing of Images

All participants were images on the same Magnetom Verio 3.0-T MRI scanner (Siemens, Munich, Germany) at Shanghai Mental Health Center. The T1-weighted sequence was scanned with the parameters of repetition time = 2530 ms, echo time = 2.34 ms, inversion time = 1100 ms, flip angle = 7°, field of view = 256 mm, with 192 1-mm slices (no gap).

Data were processed using Statistical Parametric Mapping (SPM8) (www.fil.ion.ucl.ac.uk/spm) and voxel-based morphometry (VBM8) toolbox with default parameters (http://dbm.neuro.uni-jena.de/vbm/) in Matlab 2012a. Structural T1-weighted MR images were bias-corrected and segmented into gray matter (GM), white matter, and cerebrospinal fluid. Images of GM and white matter were normalized spatially to the standard Montreal Neurological Institute template and modulated to account for the volume changes caused by normalization. The modulated GM images were smoothed further with a Gaussian kernel of 8-mm full-width-at-half maximum.

Statistical Analyses

Demographic and Behavioral Data

Analyses were undertaken with SPSS 18.0 (IBM, Armonk, NY, USA). Continuous variables were analyzed using one-way analysis of variance (ANOVA) with *post hoc* comparisons of the mean (least square difference method) or independent *t*-test, as appropriate. The chi-square test was used to examine categorical variables.

Data on Whole-Brain Structure

Differences in the GMV were analyzed by a one-way ANOVA in the three groups controlling for the whole-brain GMV and education level. A whole-brain F-test was undertaken to determine differences among the three groups. Then, significant clusters were saved and extracted as region of interest (ROI) "masks." The mean value of a cluster for each participant was calculated for *post hoc* analysis to reveal GMV differences between any two groups.

For the whole-brain F-test, the familywise error (FWE) was corrected using a voxel-level correction implemented in SPM8 and the significance level was set at corrected $p < 0.05$ with a minimum of 10 voxels. For *post hoc* analyses, the significance level was set at $p < 0.05$.

Correlation Analyses

In the VSP group, correlation analyses were carried out between significant brain regions according to whole-brain analyses and behavioral measurements. Spearman's correlation (using SPSS v18.0) was used for these steps.

RESULTS

Comparisons of Demographic Statistics

As reported in **Table 1**, no significant group differences existed for age ($F = 1.565$, $p = 0.214$) or sex ($c^2 = 0.463$, $p = 0.793$), with the sample being comprised mainly of men. Groups differed in terms of years of education ($F = 10.648$, $p < 0.000$), with HCs having spent more years at school than the nVSP group and VSP group. When comparing VSPs and nVSPs, no significant group differences existed for illness duration ($t = 0.762$, $p = 0.449$). The medication dose (as measured using chlorpromazine equivalency values) did not differ ($t = 0.589$, $p = 0.746$) (27). All patients were taking antipsychotic medications during the study. As expected, VSPs showed significantly higher scores on the MOAS than

TABLE 1 | Demographic and clinical characteristics of the study groups.

	Mean (SD)			F/χ^2/T	P
	VSP(n = 48)	nVSP(n = 27)	HC(n = 28)		
Age, years	28.98 (7.85)	27.70 (6.41)	26.07 (5.57)	1.565	0.214
Education, years	12.90 (2.81)	13.11 (2.82)	15.57 (1.64)	10.648	**0.000**
MOAS score	14.10 (5.12)	0.37 (0.79)	0.36 (0.83)	191.242	**0.000**
Age at illness onset, years	21.42 (5.81)	21.52 (5.02)		–0.076	0.939
Illness duration, years	7.17 (4.71)	6.23 (5.80)		0.762	0.449
Medication dose (chlorpromazine equivalent)	539.42 (275.56)	500.30 (277.06)		0.589	0.746
PANSS total score	84.65 (13.59)	83.78 (9.51)		0.294	0.770
PANSS positive score	25.00 (4.98)	21.30 (4.29)		3.245	**0.002**
PANSS negative score	17.13 (6.14)	19.89 (5.26)		–1.976	0.053
Sex (M/F)	32/16	20/7	19/9	0.463	0.793

VSP, violent schizophrenia patient; nVSP, nonviolent schizophrenia patient; HC, healthy control; PANSS, Positive and Negative Symptom Scale; MOAS, Modified Overt Aggression Scale. The results for P < .05 were marked in bold.

nVSPs and HCs (F = 191.242, p < 0.000). No significant differences in the negative score or total score of the PANSS were found in VSP and nVSP group. However, VSP group had higher scores on the PANSS positive scale, this mainly because VSP group had higher rating on items measuring violent traits.

Whole-Brain Analyses and Post Hoc Comparisons

As presented in **Figure 1**, voxel-wise whole-brain analyses showed significant GMV differences in widespread brain regions between three groups (FWE-corrected p < 0.05). These regions were: (i) frontal regions of bilateral orbital part of middle frontal gyri, left medial of the superior frontal cortex, and right middle frontal cortex; (ii) temporal regions of bilateral middle temporal gyri, left superior temporal cortex, left inferior temporal cortex, and right fusiform gyrus; (iii) limbic system of the left parahippocampus, and hippocampus, and left middle cingulate gyrus. Descriptive statistics for these brain regions of the three groups and *post hoc* results are presented in **Tables 2** and **3**. Details were shown in **Data Sheet 1** and **Data Sheet 2** in the supplementary data.

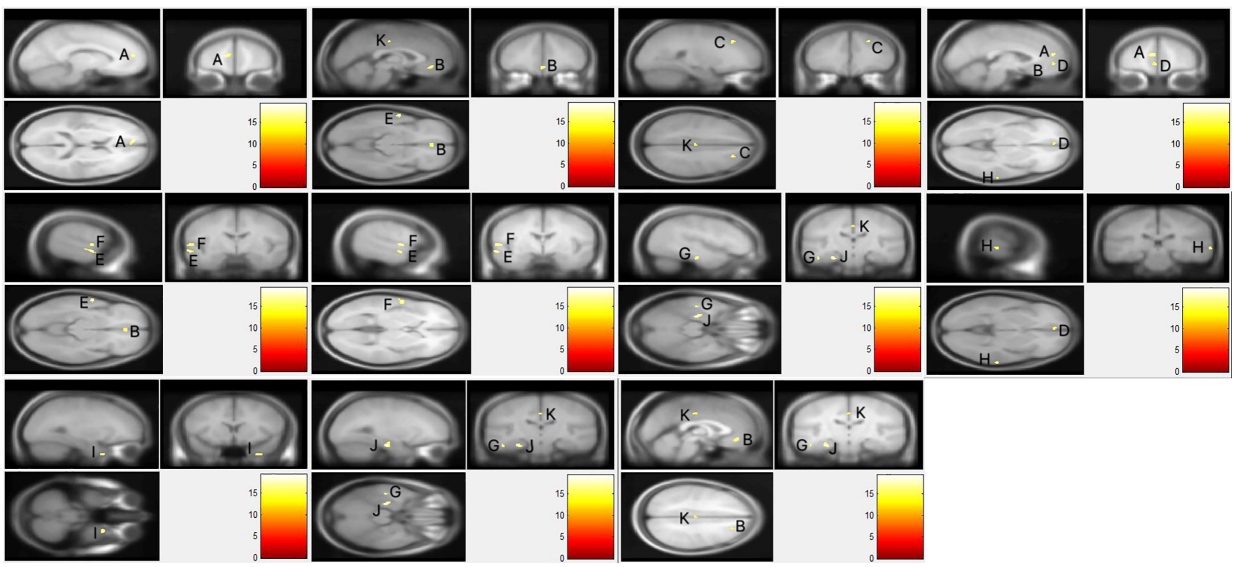

FIGURE 1 | The whole brain gray matter volume differences of three groups. Using F-test, the familywise error (FWE) was corrected using a voxel-level correction and the significance level was set at corrected p < 0.05 with a minimum of 10 voxels. **(A)** Left Superior frontal gyrus, medial; **(B)** left/right middle frontal gyrus, orbital part; **(C)** right middle frontal gyrus; **(D)** left superior frontal gyrus, medial orbital; **(E)** left middle temporal gyrus; **(F)** left superior temporal gyrus; **(G)** left inferior temporal gyrus; **(H)** right middle temporal gyrus; **(I)** right fusiform gyrus; **(J)** left parahippocampal gyrus/left hippocampus; **(K)** left median cingulate gyrus.

TABLE 2 | *Post hoc* analyses (differences between any two groups).

Anatomic Location	MNI peak coordinate			Voxels	F	P	VSP vs. nVSP		VSP vs. HC		nVSP vs. HC	
	x	y	z			FWE- corrected	T	P	T	P	T	P
Frontal lobe												
Left Superior frontal gyrus, medial	−11	54	13	134	19.432	0.002	−0.797	0.432	−6.137	**0.000**	−4.699	**0.000**
Left /right middle frontal gyrus, orbital part	0	38	−12	86	17.305	0.009	0.813	0.409	−5.363	**0.000**	−5.453	**0.000**
Right middle frontal gyrus	24	33	40	29	16.905	0.011	0.554	0.579	−5.358	**0.000**	−5.218	**0.000**
Left superior frontal gyrus, medial orbital	−3	51	−5	28	15.883	0.022	0.438	0.657	−5.301	**0.000**	−5.065	**0.000**
Temporal lobe												
Left middle temporal gyrus	−60	−6	−11	90	19.250	0.002	−1.750	0.077	−6.894	**0.000**	−4.517	**0.000**
Left superior temporal gyrus	−59	−4	3	80	18.500	0.004	−1.088	0.282	−6.285	**0.000**	−4.571	**0.000**
Left inferior temporal gyrus	−47	−21	−24	39	17.499	0.008	−1.350	0.183	−5.946	**0.000**	−4.099	**0.000**
Right middle temporal gyrus	68	−28	−3	26	17.305	0.009	−1.474	0.144	−6.110	**0.000**	−4.073	**0.000**
Right fusiform gyrus	30	12	−45	47	17.250	0.009	−2.923	**0.004**	−6.000	**0.000**	−2.683	**0.000**
Limbic system												
Left parahippocampal gyrus /left hippocampus	−27	−21	−24	106	19.346	0.002	−0.887	0.346	−5.504	**0.000**	−4.062	**0.000**
Left median cingulate gyrus	0	−19	40	13	15.628	0.027	0.731	0.467	−5.028	**0.000**	−5.085	**0.000**

VSP, violent schizophrenia patient; nVSP, nonviolent schizophrenia patient; HC, healthy controls; peak voxel significant at P < 0.05; corrected for multiple comparisons after Family Wise Error (FWE). The results for P < .05 were marked in bold.

TABLE 3 | Mean volumes of the ROI-defined gray-matter regions and their correlations with aggression.

Anatomic Location	MNI peak coordinate			VSP	nVSP	HC	Hostility		Physical Aggression Against Other People	
	x	y	z		Mean (SD)		rho	P	rho	P
Frontal lobe										
Left Superior frontal gyrus, medial	−11	54	13	0.52(0.06)	0.53(0.06)	0.61(0.06)	−0.285	**0.050***	−0.097	0.512
Left/right middle frontal gyrus, orbital part	0	38	−12	0.72(0.07)	0.70(0.09)	0.82(0.07)	−0.087	0.557	−0.193	0.190
Right middle frontal gyrus	24	33	40	0.58(0.08)	0.57(0.07)	0.69(0.10)	−0.036	0.811	0.215	0.142
Left superior frontal gyrus, medial orbital	−3	51	−5	0.53(0.06)	0.52(0.07)	0.61(0.06)	−0.113	0.446	0.076	0.607
Temporal lobe										
Left middle temporal gyrus	−60	−6	−11	0.55(0.05)	0.57(0.07)	.65(0.06)	−0.144	0.329	−0.126	0.394
Left superior temporal gyrus	−59	−4	3	0.48(0.06)	0.50(0.06)	0.57(0.07)	−0.202	0.169	−0.086	0.562
Left inferior temporal gyrus	−47	−21	−24	0.49(0.07)	0.51(0.07)	0.59(0.08)	−0.347	**0.016***	−0.232	0.112
Right middle temporal gyrus	68	−28	−3	0.50(0.06)	0.52(0.05)	0.58(0.05)	−0.186	0.205	−0.123	0.405
Right fusiform gyrus	30	12	−45	0.58(0.14)	0.67(0.13)	0.76(0.11)	−0.365	**0.011***	−0.382	**0.007***
Limbic system										
Left parahippocampal gyrus/left hippocampus	−27	−21	−24	0.77(0.05)	0.78(0.06)	0.83(0.05)	−0.006	0.968	0.042	0.778
Left median cingulate gyrus	0	−19	40	0.70(0.07)	0.70(0.07)	0.78(0.06)	−0.033	0.823	−0.010	0.944

*Hostility, PANSS hostility item (P7); physical aggression against other people, fourth subscale of MOAS; ROI, regions of interest. *P < .05. The results for P < .05 were marked in bold.*

Comparison of the nVSP vs. HCs (**Table 2**) revealed that nVSPs exhibited a volume decrease, relative to HCs, in all of the regions mentioned in the group comparisons. No region was found in which the nVSP group had a significantly larger volume compared with that of HCs.

When compared VSPs vs. HCs, the VSP group showed a smaller GMV compared with that of HCs in regions with significant group effects. Overall, the VSP group showed a more pronounced decrease in the GMV in most brain regions. We did not find a brain region in which the VSP group showed a larger GMV than that in HCs.

In addition, we compared VSPs vs. nVSPs. A significant decrease in the GMV of the right fusiform gyrus was observed in the VSP group compared with that in the nVSP group ($p = 0.004$). A decreased GMV in the left middle temporal gyrus in the VSP group was noted compared with that in the nVSP group ($p = 0.077$). We did not find a brain region in which the VSP group showed a larger GMV than that in nVSPs.

Correlation Analyses

In the VSP group, Spearman correlation analyses showed a significant negative association between scores of Physical Aggression Against Other People (the fourth subscale of the MOAS) and volume of the right fusiform. Negative correlations were also seen between the Hostility item scores of the PANSS and the volumes of left inferior temporal, right fusiform, and the left medial of superior frontal GM (**Table 3** and **Figure 2**).

DISCUSSION

In our study, a decreased GMV in a widespread network of frontotemporal and limbic systems was detected in SPs compared with HCs. When considering violent or violent traits, the volume of the right fusiform was significantly smaller in the VSP group compared with that in the nVSP group and HCs. The volume decrease in this brain region appeared to be associated with physical aggression (subscale of the MOAS) and hostility. The VSP group also showed a trend in GMV decrease in the left middle temporal gyrus compared with that in the nVSP group. Negative correlation was also found between the GMV of several brain regions and behavioral measurements. These findings revealed different and shared abnormalities compared with studies on severely violent SPs (10, 14, 15, 18).

Frontal Lobe

The VSP group and nVSP group showed a significantly decreased GMV in the bilateral medial of orbital frontal gyri, left medial of superior frontal gyrus, and right middle of frontal gyrus, compared with that in HCs. Similar abnormalities have been reported in SPs who have carried out severe physical violence. Compared with HCs, VSPs showed a reduced GMV and cortex thickness in the OFC and inferior frontal cortex (14, 28). The PFC plays an important part in the inhibitory control of aggression (29). GM abnormalities in the OFC and ventrolateral prefrontal cortex are considered to be associated with information-processing (30), decision-making (31), and emotion-regulation (9) mechanisms in violent behavior. We did not observe a significant difference in the GMV in frontal regions between VSPs and nVSPs, but noted a negative correlation between the volume of the superior frontal gyrus, medial and Hostility score in the VSP group. In accordance with our study, most studies have failed to find significant differences at the group level in the GMV of prefrontal regions when comparing VSPs with nVSPs (15, 18, 32). These observations might be because structural abnormalities in prefrontal regions seem to be more characteristic of schizophrenia or other violent traits than the violent act itself: violent behavior is perhaps more likely to result from a combination of several risk factors, including psychosis.

Temporal Gyrus

We revealed brain-structure abnormalities in the temporal lobe (including the bilateral middle temporal gyri, left superior temporal cortex and inferior temporal cortex) in the two patient groups when compared with that in HCs. Consistent

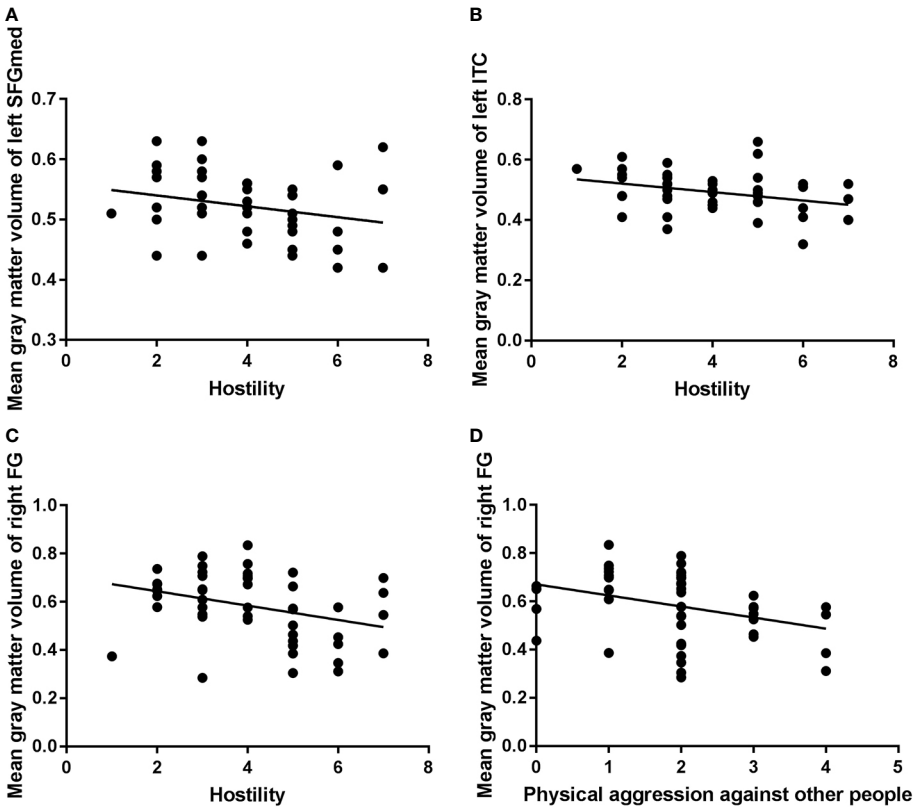

FIGURE 2 | Correlation analysis of mean gray-matter volume of significant brain regions and aggressive behavior in the violent schizophrenia patient (VSP) group (n = 48). ITC, inferior temporal cortex; FG, fusiform gyrus; SFGmed, superior frontal gyrus, medial; P7, PANSS Hostility item. Negative correlations were seen between left SFGmed and P7 [**(A)**: rho = –0.285, P = 0.050)], left ITC and P7 [**(B)**: rho = –0.347, P = 0.016)], right FG and P7 [**(C)**: rho = –0.365, P = 0.011)], right FG and Physical Aggression Against Other People (subscale of the MOAS) [**(D)**: rho = –0.382, P = 0.007)] in the VSP group.

with our study, structural abnormalities in the temporal lobe have been reported in SPs (33) as well as in populations with psychopathy or antisocial behavioral problems (18, 34, 35). We did not find a volume difference in temporal regions between VSPs and nVSPs, but a negative correlation was found between the left inferior temporal cortex and the Hostility score. Contrary to our study, Kuroki and colleagues reported a reduced GMV in the right inferior gyrus in male SPs with a history of severe violence compared with that in nVSPs (15). Those differences were explained (at least in part) by varying levels of violence and other violent traits. In our study, violent behavior was mild, and correlations were found between the GMV and behavioral measurements instead of brain-structure differences. The temporal lobe is an important component of frontotemporal circuitry. It is involved in emotional processing and executive cognitive function, including the ability to use feedback to modulate behavior (36).

Limbic Systems

A decreased GMV was observed in limbic systems, such as the left parahippocampal gyrus, hippocampal gyrus, and left middle cingulate gyrus, in the two patient groups compared with that in HCs. Similar to our findings, a reduced hippocampus volume was found in two studies of SPs with a history of severe physical assault (14, 18) compared with that in HCs. A reduced ACC volume and cortical thickness have been observed in SPs with a history of severe violence when compared with that in HCs (17, 28). A GMV difference in the hippocampal gyrus has been found between VSPs and nVSPs in several studies: those data are inconsistent with our study results. When compared with nVSPs, people convicted of murder and diagnosed with schizophrenia have exhibited a significant reduction in the GMV in the bilateral hippocampus (10). Such data indicate that volume changes in the hippocampus are dependent on the degree of violence. Abnormalities in the hippocampus may contribute toward neuropsychological disturbances and violence in schizophrenia. The hippocampus and ACC are critical components of the limbic system, and are involved in the regulation of violent behavior (30). The hippocampus is also involved in cognition, emotion, and regulation of the stress response (37). Structural abnormalities in the hippocampus may contribute to affective dysregulation and promote impulsive behavior which, in turn, might lead to higher chance of aggression (30).

Fusiform Gyrus

VSPs showed a decreased GMV in the right fusiform compared with that in nVSPs. Similar findings were seen in two recent studies on SPs with a history of severe violence. Del Bene and colleagues revealed a reduced GMV in the right fusiform in SPs with a history of severely violent behaviors against others (15) compared with that in nVSPs. Storvestre and collaborators demonstrated that VSPs had a reduced thickness in the fusiform gyrus compared with that in nVSPs (38). Those findings demonstrated that the fusiform gyrus plays an important part in varying degrees of violence. The fusiform gyrus is part of the visual system, and has been proved to be involved in brain activity during anger-induced imagery tasks (39). Together with amygdala and other brain regions, the fusiform gyrus participates in processing affective visual stimuli in humans, contributing to the evaluation of which stimuli should be approached and which should be avoided (15, 40). This region is also part of the ventral stream, which is involved in facial recognition (41) and recognition of emotional stimuli (42).

Here we reported, for the first time, that the right fusiform gyrus has a close correlation with carrying out violent acts. One possibility why this has not been reported before is that previously scholars have chosen the OFC, PFC, amygdala, and hippocampus as ROI; the fusiform gyrus has often been excluded in such analyses. Future research should focus on the fusiform gyrus to ascertain the role of this brain region in violent behavior. Interestingly, in our study, the GMV of the right fusiform gyrus was correlated negatively only with physical aggression against other people, not with the total score or other subscale scores of the MOAS, which indicated the violence-specificity of this association. One reason for this finding could be that the neuropsychological traits of violence in SPs may be heterogeneous. Brain structure varies depending on the type of violent behavior carried out by SPs. For instance, physical aggression is associated with impulsivity, callousness, and lack of empathy, whereas suicide is caused by impairments of cognitive control of mood, pessimism, reactive aggressive traits, and excessive emotional pain (43–45).

Strengths of Our Study

Unlike most studies on individuals with a history of severe violence, we focused on patients on a general psychiatry ward with a history of relatively lower severity of violence. In addition, patients in our study were free of substance abuse and PD, which simplified the interpretation of results. Therefore, the characteristics of participants in our investigation contributed to the study on violent behaviors in SPs. We were able to identify alterations in structure brain in VSPs on a general psychiatry ward so as to provide neuroimaging information for early recognition of violent behaviors in SPs.

Limitations of Our Study

Our study had four main limitations. First, participants in the VSP group and nVSP group were taking antipsychotic medications. Though no significant differences in the chlorpromazine-equivalent dose were found in the two patient groups, we could not totally eliminate the influence of a long duration of medication use. Second, the education duration in participants with and without a history of violence was significantly less than that in HCs. Although we used education as a covariate, the influence of a confounding factor may not have been eliminated fully. Third, we did not correct for multiple comparisons in the correlation analysis, which would increase the probability of a type-I error. Finally, the absence of a group of non-psychotic violent patients prevented us from assessing whether the results were explained by an effect of violence or by an interaction between psychosis and violence.

CONCLUSION

Findings provide initial evidence demonstrating the generalizability of GMV abnormalities in schizophrenia patients engaged in varying levels of violence. In our study, abnormality in the right fusiform was seen in violent schizophrenia group compared with non-violent patients. Gray matter volume decrease of this brain region was also associated with physical aggression (subscale of the MOAS) and hostility scores, which revealed an important role of right fusiform in violent behavior. Further study on the neurobiological mechanisms underlying this population may contribute to early detection and intervention on aggressive behavior in schizophrenia patients on general psychiatry ward.

DATA AVAILABILITY STATEMENT

All datasets presented in this study are included in the article/supplementary material.

ETHICS STATEMENT

The studies involving human participants were reviewed and approved by Ethics Committee of Shanghai Mental Health Center. The patients/participants provided their written informed consent to participate in this study.

AUTHOR CONTRIBUTIONS

FL, YS, BX, and YQ designed the study and wrote the protocol. FL undertook the statistical analysis and wrote the first draft of the manuscript. XL, LL, and RZ collected clinical data. All authors contributed to the article and approved the submitted version.

FUNDING

This investigation was supported by grants from the Three-Year Action Plan for the Construction of Public Health System in

Shanghai (GWIV-5; principal investigator, BX), Key Projects in the National Science & Technology Pillar Program during the Twelfth Five-Year Plan Period (2012BAK16B04; principal investigator, BX), and the top priority of National Natural Science Foundation of China (81302624; principal investigator, YQ).

SUPPLEMENTARY MATERIAL

The Supplementary Material for this article can be found online at: https://www.frontiersin.org/articles/10.3389/fpsyt.2020.00788/full#supplementary-material

REFERENCES

1. Iozzino L, Ferrari C, Large M, Nielssen O, de Girolamo G. Prevalence and risk factors of violence by psychiatric acute inpatients: a systematic review and meta-analysis. *PloS One* (2015) 10(6):e0128536. doi: 10.1371/journal.pone.0128536
2. Nederlof AF, Muris P, Hovens JE. The epidemiology of violent behavior in patients with a psychotic disorder: a systematic review of studies since 1980. *Aggression Violent Behav* (2013) 18(1):183–9. doi: 10.1016/j.avb.2012.11.018
3. McEvoy JP. The costs of schizophrenia. *J Clin Psychiatry* (2007) 68(14):4–7. doi: 10.1055/s-2007-995290
4. Van Dorn RA, Swanson JW, Elbogen EB. Swartz MS. A comparison of stigmatizing attitudes toward persons with schizophrenia in four stakeholder groups: perceived likelihood of violence and desire for social distance. *Psychiatry* (2005) 68(2):152–63. doi: 10.1521/psyc.2005.68.2.152
5. Hoptman MJ, Antonius D. Neuroimaging correlates of aggression in schizophrenia: an update. *Curr Opin Psychiatry* (2011) 24(2):100–6. doi: 10.1097/YCO.0b013e328342c8e0
6. Schug RA, Raine A. Comparative meta-analyses of neuropsychological functioning in antisocial schizophrenic persons. *Clin Psychol Rev* (2009) 29 (3):230–42. doi: 10.1016/j.cpr.2009.01.004
7. Fjellvang M, Groning L, Haukvik UK. Imaging violence in schizophrenia: a systematic review and critical discussion of the MRI literature. *Front Psychiatry* (2018) 9:333. doi: 10.3389/fpsyt.2018.00333
8. Coccaro EF, Sripada CS, Yanowitch RN, Phan KL. Corticolimbic function in impulsive aggressive behavior. *Biol Psychiat* (2011) 69(12):1153–9. doi: 10.1016/j.biopsych.2011.02.032
9. Davidson RJ, Putnam KM, Larson CL. Dysfunction in the neural circuitry of emotion regulation–a possible prelude to violence. *Science* (2000) 289 (5479):591–4. doi: 10.1126/science.289.5479.591
10. Yang Y, Raine A, Han CB, Schug RA, Toga AW, Narr KL. Reduced hippocampal and parahippocampal volumes in murderers with schizophrenia. *Psychiatry Res* (2010) 182(1):9–13. doi: 10.1016/j.pscychresns.2009.10.013
11. Tamminga CA, Stan AD. Wagner ADJAJoP. The hippocampal formation in schizophrenia. *Am J Psychiatry* (2010) 167(10):1178–93. doi: 10.1176/appi.ajp.2010.09081187
12. Kumari V, Das M, Taylor PJ, Barkataki I, Andrew C, Sumich A, et al. Neural and behavioural responses to threat in men with a history of serious violence and schizophrenia or antisocial personality disorder. *Schizophr Res* (2009) 110 (1-3):47–58. doi: 10.1016/j.schres.2009.01.009
13. Hoptman MJ, Antonius D, Mauro CJ, Parker EM, Javitt DC. Cortical thinning, functional connectivity, and mood-related impulsivity in schizophrenia: relationship to aggressive attitudes and behavior. *Am J Psychiatry* (2014) 171(9):939–48. doi: 10.1176/appi.ajp.2014.13111553
14. Veena K, Ian B, Sangeeta G, Satinder F, Mrigendra D, Pamela T. Dysfunctional, but not functional, impulsivity is associated with a history of seriously violent behaviour and reduced orbitofrontal and hippocampal volumes in schizophrenia. *Psychiatry Res* (2009) 1(173):39–44. doi: 10.1016/j.pscychresns.2008.09.003
15. Kuroki N, Kashiwagi H, Ota M, Ishikawa M, Kunugi H, Sato N, et al. Brain structure differences among male schizophrenic patients with history of serious violent acts: an MRI voxel-based morphometric study. *BMC Psychiatry* (2017) 17(1):136. doi: 10.1186/s12888-017-1302-6
16. Del Bene VA, Foxe JJ, Ross LA, Krakowski MI, Czobor P, De Sanctis P. Neuroanatomical abnormalities in violent individuals with and without a diagnosis of schizophrenia. *PloS One* (2016) 11(12):e0168100. doi: 10.1371/journal.pone.0168100
17. Kumari V, Uddin S, Premkumar P, Young S, Gudjonsson GH, Raghuvanshi S, et al. Lower anterior cingulate volume in seriously violent men with antisocial personality disorder or schizophrenia and a history of childhood abuse. *Aust N Z J Psychiatry* (2014) 48(2):153–61. doi: 10.1177/0004867413512690
18. Barkataki I, Kumari V, Das M, Taylor P, Sharma T. Volumetric structural brain abnormalities in men with schizophrenia or antisocial personality disorder. *Behav Brain Res* (2006) 169(2):239–47. doi: 10.1016/j.bbr.2006.01.009
19. Fazel S, Långström N, Hjern A, Grann M, Lichtenstein P. Schizophrenia, substance abuse, and violent crime. *JAMA* (2009) 301(19):2016–23. doi: 10.1001/jama.2009.675
20. Swanson JW, Van Dorn RA, Swartz MS, Smith A, Elbogen EB, Monahan J. Alternative pathways to violence in persons with schizophrenia: the role of childhood antisocial behavior problems. *Law Hum Behav* (2008) 32(3):228–40. doi: 10.1007/s10979-007-9095-7
21. Schiffer B, Leygraf N, Muller BW, Scherbaum N, Forsting M, Wiltfang J, et al. Structural brain alterations associated with schizophrenia preceded by conduct disorder: a common and distinct subtype of schizophrenia? *Schizophr Bull* (2013) 39(5):1115–28. doi: 10.1093/schbul/sbs115
22. Qiao Y, Mei Y, Han H, Liu F, Yang XM, Shao Y, et al. Effects of Omega-3 in the treatment of violent schizophrenia patients. *Schizophr Res* (2018) 195:283–5. doi: 10.1016/j.schres.2017.08.026
23. Qiao Y, Xie B, Du X. Abnormal response to emotional stimulus in male adolescents with violent behavior in China. *Eur Child Adolesc Psychiatry* (2012) 21(4):193–8. doi: 10.1007/s00787-012-0252-2
24. Huang HC, Wang YT, Chen KC, Yeh TL, Lee IH, Chen PS, et al. The reliability and validity of the Chinese version of the Modified Overt Aggression Scale. *Int J Psychiatry Clin Pract* (2009) 13(4):303–6. doi: 10.3109/13651500903056533
25. Silver JM, Yudofsky SC. The Overt Aggression Scale: overview and guiding principles. *J Neuropsychiatry Clin Neurosci* (1991) 3(2):S22–29.
26. Hoptman MJ, Volavka J, Czobor P, Gerig G, Chakos M, Blocher J, et al. Aggression and quantitative MRI measures of caudate in patients with chronic schizophrenia or schizoaffective disorder. *J Neuropsychiatry Clin Neurosci* (2006) 18(4):509–15. doi: 10.1176/jnp.2006.18.4.509
27. Kane JM, Leucht S, Carpenter D, Docherty JP. Expert consensus panel for optimizing pharmacologic treatment of psychotic D. The expert consensus guideline series. Optimizing pharmacologic treatment of psychotic disorders. Introduction: methods, commentary, and summary. *J Clin Psychiatry* (2003) 64(Suppl 12):5–19. doi: 10.1530/EJE-10-0859
28. Narayan VM, Narr KL, Kumari V, Woods RP, Thompson PM, Toga AW, et al. Regional cortical thinning in subjects with violent antisocial personality disorder or schizophrenia. *Am J Psychiatry* (2007) 164(9):1418–27. doi: 10.1176/appi.ajp.2007.06101631
29. Nelson RJ, Trainor BC. Neural mechanisms of aggression. *Nat Rev Neurosci* (2007) 8(7):536–46. doi: 10.1038/nrn2174
30. Leclerc MP, Regenbogen C, Hamilton RH, Habel U. Some neuroanatomical insights to impulsive aggression in schizophrenia. *Schizophr Res* (2018) 201:27–34. doi: 10.1016/j.schres.2018.06.016
31. Salmond CH, Menon DK, Chatfield DA, Pickard JD, Sahakian BJ. Deficits in decision-making in head injury survivors. *J Neurotraum* (2005) 22(6):613–22. doi: 10.1089/neu.2005.22.613
32. Treasaden IH, Bustos MG, Nadeem S, Counsell SJ, Puri BK, Bydder GMJBP. Regional grey matter volumetric changes in forensic schizophrenia patients: an MRI study comparing the brain structure of patients who have seriously and violently offended with that of patients who have not. *BMC Psychiatry* (2008) 8(Suppl 1):1–6. doi: 10.1186/1471-244X-8-S1-S6
33. Shah C, Zhang W, Xiao Y, Yao L, Zhao Y, Gao X, et al. Common pattern of gray-matter abnormalities in drug-naive and medicated first-episode schizophrenia: a multimodal meta-analysis. *Psychol Med* (2016) 47(3):1–13. doi: 10.1017/S0033291716002683

34. Muller JL, Ganssbauer S, Sommer M, Dohnel K, Weber T, Schmidt-Wilcke T, et al. Gray matter changes in right superior temporal gyrus in criminal psychopaths. Evidence from voxel-based morphometry. *Psychiatry Res* (2008) 163(3):213–22. doi: 10.1016/j.pscychresns.2007.08.010
35. Dolan MC, Deakin JF, Roberts N, Anderson IM. Quantitative frontal and temporal structural MRI studies in personality-disordered offenders and control subjects. *Psychiatry Res* (2002) 116(3):133–49. doi: 10.1016/S0925-4927(02)00085-9
36. Weiss EM. Neuroimaging and neurocognitive correlates of aggression and violence in schizophrenia. *Scientifica (Cairo)* (2012) 2012:158646. doi: 10.6064/2012/158646
37. Fanselow MS, Dong HW. Are the dorsal and ventral hippocampus functionally distinct structures? *Neuron* (2010) 65(1):7–19. doi: 10.1016/j.neuron.2009.11.031
38. Storvestre GB, Valnes LM, Jensen A, Nerland S, Tesli N, Hymer KE, et al. A preliminary study of cortical morphology in schizophrenia patients with a history of violence. *Psychiatry Res Neuroimaging* (2019) 288:29–36. doi: 10.1016/j.pscychresns.2019.04.013
39. Ueltzhoffer K, Herpertz SC, Krauch M, Schmahl C, Bertsch K. Whole-brain functional connectivity during script-driven aggression in borderline personality disorder. *Prog Neuropsychopharmacol Biol Psychiatry* (2019) 93:46–54. doi: 10.1016/j.pnpbp.2019.03.004
40. Pessoa L, Adolphs R. Emotion processing and the amygdala: from a 'low road' to 'many roads' of evaluating biological significance. *Nat Rev Neurosci* (2010) 11(11):773–83. doi: 10.1038/nrn2920
41. Bilalić MJJCN. Revisiting the role of the fusiform face area in expertise. *J Cogn Neurosci* (2016) 28(9):1345–57. doi: 10.1162/jocn_a_00974
42. Kark SM, Kensinger EA. Effect of emotional valence on retrieval-related recapitulation of encoding activity in the ventral visual stream. *Neuropsychologia* (2015) 78:221–30. doi: 10.1016/j.neuropsychologia.2015.10.014
43. van Heeringen K, Mann JJ. The neurobiology of suicide. *Lancet Psychiatry* (2014) 1(1):63–72. doi: 10.1016/s2215-0366(14)70220-2
44. Szeszko PR. Aggression in schizophrenia and its relationship to neural circuitry of urgency. *Am J Psychiatry* (2014) 171(9):897–900. doi: 10.1176/appi.ajp.2014.14050629
45. Hodgins S, Piatosa MJ, Schiffer B. Violence among people with schizophrenia: phenotypes and neurobiology. *Curr Top Behav Neurosci* (2014) 17:329–68. doi: 10.1007/7854_2013_259

Conflict of Interest: The authors declare that the research was conducted in the absence of any commercial or financial relationships that could be construed as a potential conflict of interest.

frontiers in Psychiatry

ORIGINAL RESEARCH
published: 11 September 2020
doi: 10.3389/fpsyt.2020.555836

Enhanced Connectivity of Thalamo-Cortical Networks in First-Episode, Treatment-Naive Somatization Disorder

Jin Zhao[1,2], *Qinji Su*[3], *Feng Liu*[4], *Zhikun Zhang*[3], *Ru Yang*[5], *Wenbin Guo*[1,6*] *and Jingping Zhao*[1*]

[1] National Clinical Research Center for Mental Disorders, and Department of Psychiatry, The Second Xiangya Hospital of Central South University, Changsha, China, [2] Department of Psychiatry, Henan Mental Hospital, Second Affiliated Hospital of Xinxiang Medical University, Xinxiang, China, [3] Mental Health Center, the Second Affiliated Hospital of Guangxi Medical University, Nanning, China, [4] Department of Radiology, Tianjin Medical University General Hospital, Tianjin, China, [5] Department of Radiology, The Second Xiangya Hospital of Central South University, Changsha, China, [6] Department of Psychiatry, The Third People's Hospital of Foshan, Foshan, China

OPEN ACCESS

Edited by:
Szilvia Anett Nagy,
University of Pécs, Hungary

Reviewed by:
Gergely Darnai,
University of Pécs, Hungary
Cheng Luo,
University of Electronic Science and Technology of China, China

***Correspondence:**
Jingping Zhao
zhaojingping@csu.edu.cn
Wenbin Guo
guowenbin76@csu.edu.cn

Specialty section:
This article was submitted to Neuroimaging and Stimulation, a section of the journal Frontiers in Psychiatry

Received: 26 April 2020
Accepted: 18 August 2020
Published: 11 September 2020

Citation:
Zhao J, Su Q, Liu F, Zhang Z, Yang R, Guo W and Zhao J (2020) Enhanced Connectivity of Thalamo-Cortical Networks in First-Episode, Treatment-Naive Somatization Disorder. Front. Psychiatry 11:555836. doi: 10.3389/fpsyt.2020.555836

Background: Dysfunctions of the thalamus and its projections to cortical cortices have been implicated in patient with somatization disorder (SD). However, changes in the anatomical specificity of thalamo-cortical functional connectivity (FC) in SD remain unclear.

Methods: Resting-state fMRI scans were collected in 25 first-episode, drug-naive patients with SD, as well as 28 sex-, age-, and education-matched healthy controls. We parcellated the thalamus with seven predefined regions of interest (ROIs) and used them as seeds to map whole-brain FC. Correlation analysis was conducted in the patients.

Results: We found an increased pattern of thalamic ROI-cortex connectivity in patients with SD. Patients with SD demonstrated enhanced thalamic connectivity to the bilateral anterior/middle cingulum, motor/sensory cortex, visual cortex, and auditory cortex. A significantly negative correlation was found between the right occipital thalamic ROI to the anterior cingulum and EPQ extraversion scores (r=0.404, p=0.045) after the Benjamini-Hochberg correction.

Conclusions: This study demonstrates that anatomical specificity of enhanced thalamo-cortical FCs exists in first-episode, drug-naive patients with SD. These findings further highlight the importance of the thalamic subregions in the pathophysiology of SD.

Keywords: thalamus, functional connectivity, somatization disorder, anterior/middle cingulum, motor/sensory cortex

INTRODUCTION

Somatization disorder (SD) is a common mental disease with a prevalence of 4% to 7% in general individuals (1). Patients with SD are always stressed because of their unexplained physical symptoms (e.g. pain, gastrointestinal distress, and pseudoneurological symptoms) and repeated hospital visits. SD places a huge burden on patients and families, and continues to lead patients experiencing a low life quality and high emotional stress. Although many studies have been conducted on SD, the pathophysiology of SD remains unclear.

With the progress of neuroimaging techniques, MRI has become a promising tool for observation of brain structure, activity, and connectivity of SD. Structural MRI studies show that patients with SD have increased gray matter volume in the caudate nuclei (2), but reduced gray volumes in the amygdala and pituitary (3, 4). Zhao et al. found increased white matter volume in the right inferior frontal gyrus and decreased white matter volume in the left inferior longitudinal fasciculus in patients with SD (5). Functional MRI studies also report altered activity and connectivity in patients with SD. Fayed et al. used spectroscopy to evaluate resting-state glutamate and glutamine levels in patients with fibromyalgia, patients with SD and healthy controls, and found that patients with SD showed enhanced glutamate and glutamine levels in the posterior cingulate cortex (6). Moreover, increased activity in the bilateral superior medial prefrontal cortex and left precuneus have been observed in patients with SD by Su et al.(7), who also found enhanced FC strength in the inferior temporal gyrus (ITG) in SD (8). Li et al. found increased/decreased bidirectional corticolimbic connectivity and bidirectional cortico-cerebellar and limbic-cerebellar connectivity in patients with SD (9). Despite these findings supporting abnormal FCs in patients with SD, the effects of important FCs (such as thalamo-cortical FC) on the pathophysiology of SD remain unclear.

The thalamus, a relay station that organizes information routes within the cortex, may play an important role in the FC network of the brain. Previous studies have shown disrupted thalamo-cortical FC in mental diseases. For example, deformed thalamic shape (10), reduced regional thalamic volumes (11), altered correlational patterns between thalamic and cortical volumes (12, 13), and abnormal functional connectivity (14) were reported in schizophrenia. Wang et al. found increased and reduced thalamic FCs in patients with schizophrenia (15). Skåtun et al. conducted thalamo-cortical FC in schizophrenia and found that one increased thalamic-sensory connectivity and eight reductions with frontal and posterior areas in schizophrenia (16). Greicius et al. observed increased FC between the thalamus and the default mode network in major depressive disorder (MDD) (17). However, changes in the thalamo-cortical networks in patients with SD remain unknown.

The thalamus comprises many distinct nuclei and reciprocal topographically organized fibers that connect with the sensory, motor, limbic, and cognitive regions of the cortex (18, 19). For example, the ventral lateral and ventral posteriolateral portions of the thalamus connect to the motor and somatosensory areas, whereas the anterior and dorsomedial areas of the thalamus are linked to the prefrontal cortex (20). De Greck et al. conducted a reward task-fMRI, and patients with acute somatoform disorder patients showed hemodynamic changes in the right ventroposterior thalamus (21). Kang et al. reported enhanced FC between the thalamus and the primary somatosensory cortex in MDD (22). In addition, the thalamus exhibited discrimination-related activation during spatial or non-spatial discrimination of pain stimuli (23), and dynamic analysis identified the thalamus as a critical region in the prediction of pain intensity (24).Thus, topographical division of the FC between the thalamus and the cortex may improve the possibility that mental diseases (such as SD) can be characterized by specific dysfunction connectivity in the thalamic subdivision (or cortical regions).

Based on a previous study, the thalamus can be segmented as bilateral seven subregions, including primary motor, sensory, occipital, pre-frontal, pre-moto, posterior parietal, and temporal of thalamus (25). Higher-order associative nucleuses are in the thalamic subregions, including the ventral anterior (VA) nuclei, ventral lateral posterior (VLp) nuclei, and most partial mediodorsal (MD) nuclei in the pre-frontal thalamus; the ventral lateral anterior (VLa) nuclei in the pre-motor thalamus; the ventral posterior lateral (VPL) nuclei in the sensory thalamus; the lateral posterior (LP) nuclei and partial pulvinar (Pu) nuclei in the parietal thalamus; the partial MD nuclei and partial Pu nuclei in the temporal thalamus, and the partial Pu nuclei in the occipital thalamus (25, 26). Abnormal thalamo-cortical FC was observed in previous studies. For example, Brown et al. found increased FC between medial thalamus and temporal areas, and between medial thalamus and somatosensory areas in MDD (27). Han et al. found increased and decreased FC between thalamic-subregions and cortex in long-term primary dysmenorrhea (28). Since thalamic subregions have different nucleuses and functions, examining the thalamo-cortical FC may promote our understanding of the pathophysiology of SD.

A number of studies have reported cognitive function deficits in patients with SD. Hall et al. found that physical complaints were correlated to poor performance in attention and psychomotor speed (29). Although the findings vary considerably across studies, there is an agreement that some domains of cognitive functions, such as memory (29–31), attention (29), executive function (29, 30), emotional awareness (32) and perceptual awareness (33) are impaired in patients with SD.

In addition, personality traits may be involved in the pathophysiological process of SD. A high prevalence of personality disorders in patients with SD has been reported about 20 years ago (34). Song et al. found a significantly positive correlation between the neuroticism scores of Eysenck Personality Questionnaire (EPQ) and increased regional homogeneity (ReHo) in the left angular gyrus (AG) in patients with SD (35). However, the relationship between cognitive function, personality, and thalamo-cortical FC remain unclear.

In the present study, we aimed to examine the thalamo-cortical FC in first-episode, treatment-naive patients with SD and conducted correlation analysis to explore the potential

relationship between clinical symptoms, cognitive function, personality, and thalamo-cortical connectivity in SD. According to the Harvard Oxford subcortical structural atlases (25, 36), the thalamus can be subdivided into 7 bilateral subregions based on previous study (25). Based on previous studies (37, 38), we hypothesized that enhanced thalamo-cortical FC would exist in SD, and we also examined whether FC changes was positively correlated with cognitive function and personality traits in patients with SD.

METHODS

Subjects

Twenty-six first-episode, drug-naive patients with SD from the Mental Health Center of the Second Affiliated Hospital, Guangxi Medical University in China from 2012.01 to 2013.12 were recruited, and 30 age-, sex-, and education-matched healthy controls from the local community were included. Each patient was diagnosed based on the Structured Clinical Interview of DSM-IV. The inclusion criteria for participants were as follows: Han Chinese ethnicity, 18 to 60 years old, drug-naive and right handedness. The exclusion criteria for patients with SD were as follows: any previous or current use of psychotropic medications, a history of neuropsychiatric disorders (comorbidity with depression is allowed because of the high comorbidity), and any contraindications for MRI scanning. The exclusion for healthy controls was as follows: no lifetime neuropsychiatric disorder, no family history of neuropsychiatric disorders, and no history of using of psychotropic drugs.

All participants were required to complete several questionnaires. Symptom severity was examined with Symptom checklist-90 (Scl-90) (39), Hamilton depression scale (HAMD; 17 items) (40) and Hamilton anxiety scale (HAMA) (41). Cognitive function was assessed by Wisconsin Card Sorting Test (WCST, including number of categories achieved, number of errors, and number of persistent error response of the test) (42) and digit symbol coding of Wechsler Adult Intelligence Scale (DSC-WAIS, including number of correctly decoded symbols in 90 seconds) (43). Personality traits were evaluated by EPQ (44), including four subscales (extraversion, neuroticism, psychoticism, and lie). These four subscales can represent positive affect/outgoing, negative affect/emotional unstableness, psychotic episode/aggression, and unsophisticated feature of an individual.

The present study was approved by the Ethics Committee of the Second Affiliated Hospital, Guangxi Medical University. All participants were given a complete description of the study and they provided a written informed consent.

Image Acquisition

A 3.0 T Siemens scanner was used to collect data. All participants were required to lie motionless, eye-closed, and keeping quiet and awake for 500s during the image capturing. The MRI sequence type was an echo-planar imaging (EPI) sequence. The imaging-sequence parameters used were as follows: repetition time/echo time = 2000/30 ms, slices = 30, thickness= 4 mm, gap = 0.4 mm, field of view = 24 cm, flip angle= 90°, and data matrix = 64×64.

Data Preprocessing

Data processing and analysis for (resting-state) brain imaging (45) was used to preprocess the entire MRI data.

The detailed procedure of FC analysis was as follows. First, slice timing and head motion were corrected. Subjects who had more than 2.0 mm maximum displacement in any direction (x, y, or z) and 2° of angular motion were excluded from the study. Second, the images were normalized to the standard Montreal Neurological Institute space in SPM8 with each voxel resampled to 3×3×3 mm^3. Afterwards, the images were smoothed with a 4 mm full-width at half-maximum (FWHM) Gaussian kernel. The images were then temporally band-pass filtered (0.01–0.08 Hz) and linearly detrended. Moreover, sources of spurious covariates of head-motion parameters, cerebrospinal fluid signal, and white matter signal were removed. To address the residual effects of head motion, we computed the framewise displacement (FD) as described in the study of Power et al. (46) and used it as a covariate in group comparisons.

FC Processing

Seven bilateral subregions of the thalamus from the Harvard Oxford subcortical structural atlases were selected as seeds for whole-brain FC processing with the REST software. The detail placement of each seed in direction (x, y, z) was shown in **Supplementary Material Figure S1**. The FC analysis was conducted as follows. First, to obtain a whole-brain FC matrix for each participant, Pearson correlation coefficients between the seeds and other voxels of the whole brain were calculated. Afterwards, the coefficients were standardized to *z*-scores to generate seed-based FC maps. Two sample *t*-tests were used to compare group differences, with HAMA scores, HAMD scores, age, sex, and the mean FD as covariates. The significance level was set at $p<0.05$ corrected by Gaussian random field (GRF) theory with a voxel threshold of $p<0.001$ and a cluster threshold of $p<0.05$(minimum cluster size=22 voxels).

Statistical Analysis

Chi-square and *t*-tests were used to analyze the demographic characteristics. Correlation analyses between mean values of thalamo-cortical FC and clinical variables (including total questionnaire score and its factors, which reflect the severity of anxiety, depression and somatization symptoms, cognitive function, and personality dimensions) were performed by Pearson's correlation analyses in patients with SD. Benjamini-Hochberg correction was used to limit type I error. Significance level was set at $p<0.05$.

RESULTS

Demographics and Clinical Characteristics

We excluded data with excessive head movement, and then the data of 25 patients with SD and 28 healthy controls were analyzed. No significant difference was observed in terms of age, sex ratio, and education level. However, compared with healthy controls, patients with SD expressed higher scores in

terms of HAMD scores, HAMA scores, somatization subscale of Scl-90, and EPQ psychoticism/neuroticism scores. Demographic information and clinical characteristics are shown in **Table 1**.

Seed-Based FC Analyses: Group Comparisons

Table 2 and **Figures 1**, **2** show hyperconnectivity between thalamic seeds and whole brain in patients with SD. Enhanced connectivity was found between the right primary motor thalamic ROI and the right middle occipital gyrus (MOG) and right precentral gyrus. We also found that right sensory thalamic ROI was positively connected with right precentral gyrus/right postcentral gyrus, the right ITG, and the right precentral gyrus. We observed significantly enhanced connectivity between the left occipital thalamic ROI and the right precentral gyrus/right postcentral gyrus, and between the right occipital thalamic ROI and the anterior cingulum and middle cingulum. Increased connectivity was found between the right pre-motor thalamic ROI and the right MOG and right precentral gyrus/right postcentral gyrus. The left posterior parietal thalamic ROI was positively connected with the right precentral gyrus, and the right posterior parietal thalamic ROI was positively connected with the right ITG, right precentral gyrus/right postcentral gyrus, and right paracentral lobule, respectively. Positive connectivity was also found between the left temporal thalamic ROI and the right precentral gyrus/right postcentral gyrus. The right temporal thalamic ROI was positively connected with the left superior temporal gyrus (STG), right precentral gyrus/right postcentral gyrus, and right SMA.

Correlations Between Increased FC and Clinical Variables in the Patients

The right primary motor thalamic ROI to the precentral gyrus was negatively correlated to scores of DSC-WAIS scores (r = −0.425, p = 0.034); the right sensory thalamic ROI to the right ITG was positively correlated to scl-90 somatic scores (r=0.407, p=0.043); the left occipital thalamic ROI to the right precentral gyrus/postcentral gyrus was negatively correlated to DSC-WAIS scores (r = −0.447, p=0.025); the right occipital thalamic ROI to the anterior cingulum was positively correlated to EPQ extraversion scores (r=0.404, p=0.045); the right occipital thalamic ROI to the anterior cingulum was positively correlated to HAMA total scores (r=0.397, p=0.050); the right occipital thalamic ROI to the middle cingulum was positively correlated to HAMA total scores (r=0.406, p=0.044); the right pre-motor thalamic ROI to the right precentral gyrus/postcentral gyrus was negatively correlated to DSC-WAIS scores (r = −0.470, p=0.018); the right posterior parietal thalamic ROI to the right ITG was positively correlated to scl-90 somatic scores (r=0.494, p=0.012); the left temporal thalamic ROI to the right precentral gyrus/postcentral gyrus was negatively correlated to DSC-WAIS scores (r = −0.540, p=0.005); and the right temporal thalamic ROI to the right precentral gyrus/postcentral gyrus was negatively correlated to DSC-WAIS scores (r = −0.427, p=0.033).

After the Benjamini-Hochberg correction, significant negative correlation was found between the right occipital thalamic ROI to the anterior cingulum and EPQ extraversion scores (r=0.404, p=0.045). See **Figure 3**.

DISCUSSION

We used thalamic subregions as seeds to conduct thalamo-cortical seed-based connectivity analysis and examine the specific thalamo-cortical FC in SD. To our knowledge, this report is the first on anatomically inferences of abnormal connectivity between thalamic subregions and cortex in patients with SD. The main findings were enhanced thalamic nuclei connectivity to the bilateral anterior/middle cingulum,

TABLE 1 | Characteristics of participants.

Variables	Patients (n = 25)	Controls (= 28)	*p* value
Age (years)	41.00 ± 10.76	38.71 ± 9.59	0.42[b]
Sex (male/female)	4/21	6/22	0.73[a]
Years of education (years)	7.72 ± 4.39	7.82 ± 2.59	0.92[b]
Illness duration (months)	59.12 ± 62.22		
Somatization subscale of SCL-90	28.48 ± 10.37	14.32 ± 3.44	<0.001[b]
HAMD	18.84 ± 7.31	2.60 ± 1.83	<0.001[b]
HAMA	22.96 ± 10.95	0.53 ± 0.99	<0.001[b]
Digit symbol-coding of WAIS	8.28 ± 2.87	9.64 ± 2.15	0.06[b]
EPQ			
Extraversion	46.84 ± 11.02	49.75 ± 9.65	0.31[b]
Psychoticism	50.52 ± 9.01	45.00 ± 8.54	0.03[b]
Neuroticism	57.36 ± 9.18	46.78 ± 10.24	<0.001[b]
Lie	49.44 ± 12.31	47.96 ± 11.01	0.65[b]
WCST			
Number of categories achieved	3.52 ± 1.76	3.89 ± 1.66	0.43[b]
Number of errors	22.84 ± 9.12	24.71 ± 8.91	0.45[b]
WCST-Pre	20.04 ± 9.48	\22.82 ± 8.72	0.27[b]

[a]*The p value for sex distribution was obtained by a chi-square test.*

[b]*The p values were obtained by two samples t-tests.*

HAMD, Hamilton depression scale; HAMA, Hamilton anxiety scale; SCL-90, Symptom Checklist-90; EPQ, Eysenck Personality Questionnaire; WAIS, Wechsler Adult Intelligence Scale; WCST-Pre, persistent error response of Wisconsin Card Sorting Test.

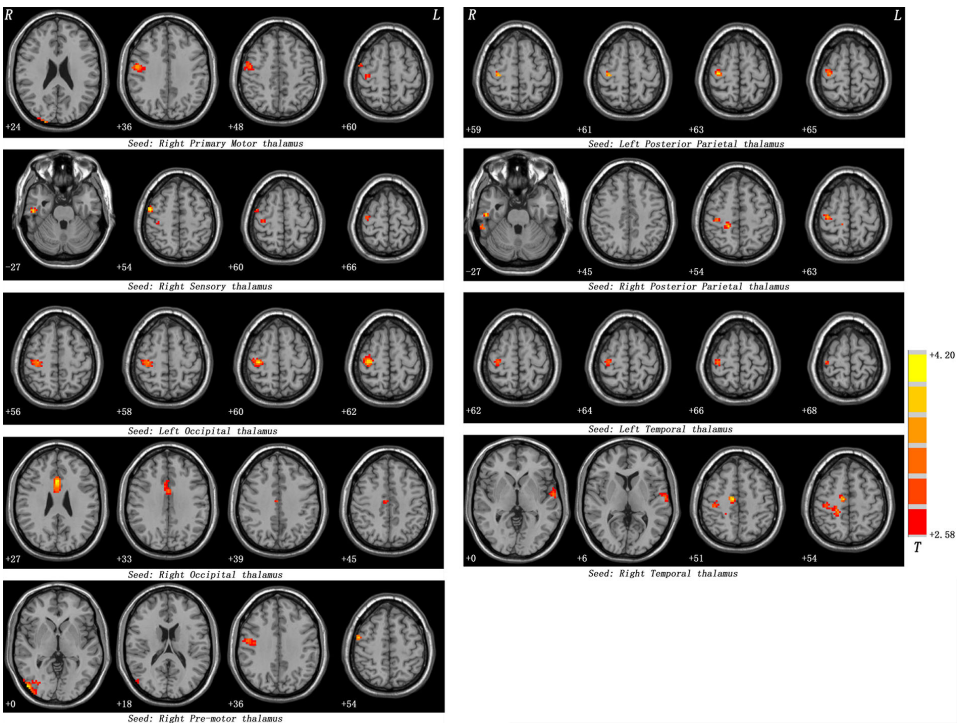

FIGURE 1 | Maps of thalamo-cortical FC changes in patients with SD compared with healthy controls. Red denotes high FC values in patients and the color bar represents the *t* value from two-sample *t*-tests. Correction for multiple comparisons was conducted based on the Gaussian random field theory at $p < 0.05$ (voxel significance: $p < 0.001$, cluster significance: $p < 0.05$).

motor/sensory cortex, visual cortex, and auditory cortex in patients with SD. These results suggested that patients with SD had increased thalamo-cortical FC with some specific regions which might be involved in the pathogenesis of SD. These findings may provide new insights into thalamo-cortical connectivity in patients with SD and help reveal the neurobiological mechanisms of SD.

One of the most important findings is the widespread increase in the thalamo-cortical network, including hyperconnectivity of the thalamic seeds to the bilateral anterior/middle cingulum, motor/sensory cortex, auditory cortex, and visual cortex. The findings of increased connectivity in the thalamo-cortical network may suggest a compensatory effort for either neuronal deficits or insufficient performance or nonselective recruitment occurring when appropriate regions have decreased accessibility (47). For example, Hua et al. found hyperconnectivity in the thalamus-prefrontal circuit, which implied a compensatory mechanism that additional cortical regions were recruited to subserve "normal" functions (48, 49). Moreover, given that the thalamo-cortical system modulates the transmission of sensory and motivation information, increased FCs reflect thalamic subregions hyper-responsiveness to negative emotions and cognitive function biased in patients with SD. We can infer that hyperconnectivity of the thalamus to the anterior/middle cingulum, motor/sensory cortex, auditory cortex, and visual cortex in the present study may be interpreted as a compensatory effort, a nonselective recruitment, or some combination of these two possibilities to reduce connectivity between thalamic nuclei and cortex in patients with SD.

Positive connectivity was found between the right occipital thalamic ROI and the anterior cingulum and middle cingulum. The occipital thalamus (Otha) includes Pu, which is involved in visual processing, attention, social cognition, and speech processing. Rafal et al. proposed a model for the posterior attention system, and found that patients with Pu lesions showed a deficit in the ability to hold attention on the target stimulus when competing information was also present in the visual field (50). The Pu was reported to act as an critical role in attentional modulation (51, 52). Zhou et al. provided causal information that Pu played an important role in attentive visual stimulus processing and maintaining and modulating neuronal oscillatory dynamics in visual cortex (53). Lemche et al. considered that the Pu was involved in separate brain system of depression (54). Furthermore, research considered that the Otha was related to the reward function (55). Li et al. found increased FC between the right occipital thalamus and right middle occipital gyrus, right amygdala, and right fusiform area, and decreased FC between the right Otha and left inferior parietal gyrus and left triangular inferior frontal gyrus in patients with obsessive-compulsive disorder (56). They suggested that the altered Otha-related FC was associated with reward processing, attention and emotion regulation (56). The

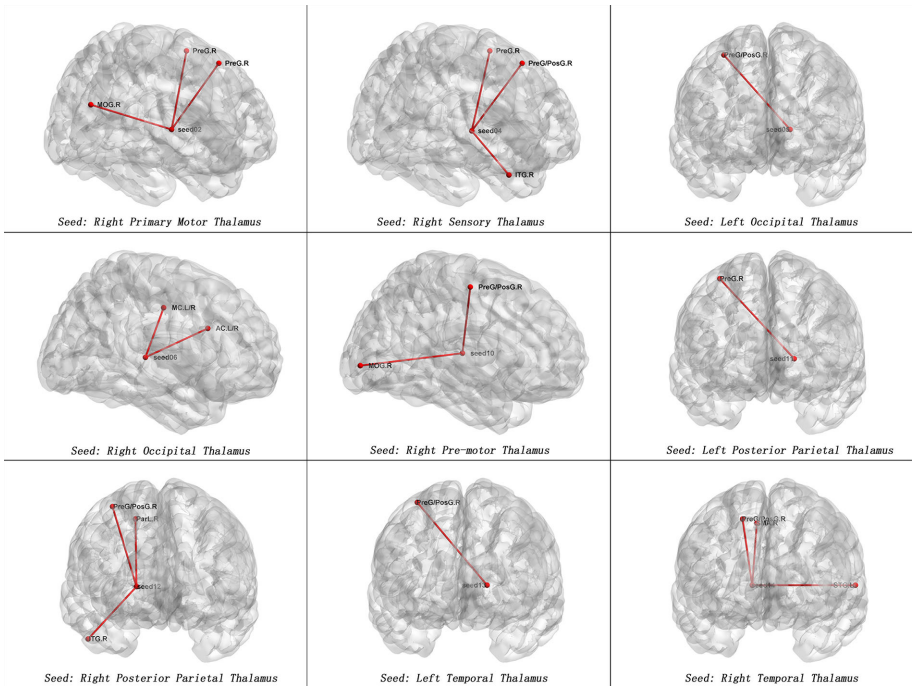

FIGURE 2 | Maps of increased seed-based thalamo-cortical FC in patients with SD compared with healthy controls. The red line represents the significant increased FCs between subregions of thalamus and cortex. Correction for multiple comparisons was conducted based on the Gaussian random field theory at $p < 0.05$(voxel significance: $p < 0.001$, cluster significance: $p < 0.05$). MOG.R, right middle occipital gyrus, PreG.R, right precentral gyrus; ITG.R, right inferior temporal gyrus; PreG/PosG.R, right precentral gyrus/right postcentral gyrus; AC.L/R. anterior cingulum; MC.L/R, middle cingulum; ParL.R, right paracentral lobule; STG.L, left superior temporal gyrus, SMA.R = right supplementary motor area.

anterior cingulum and middle cingulum play an important role in cognitive control by putting sensory input together to guide attention to salient stimuli and response selection through the recruitment of appropriate brain FC networks to modulate behavior. Dysfunction of anterior cingulum and middle cingulum may affect self-regulation of cognition, behavior, and emotion (57–59). In line with the results that the anterior cingulum and middle cingulum play a key role in cognitive control (60), researchers have reported that impaired cognition is widespread in patients with somatization symptoms (61, 62). Thus, we speculate that abnormal connectivity in Otha to the anterior/middle cingulum may play a potential role in imbalance of cognitive function in patients with SD. We also found a positive correlation between the connectivity of the right occipital thalamic ROI to the anterior cingulum and EPQ extraversion scores in the patients. The positive correlation suggests that a talkative patient has a strengthened connectivity of thalamic nuclei to the anterior cingulum cortex.

We found significantly increased connectivity between the right primary motor/sensory and left posterior parietal thalamic ROI and the right precentral gyrus; between the right sensory/pre-motor/posterior parietal/temporal and left occipital/temporal thalamic ROI and the right precentral gyrus/right postcentral gyrus; and between the right temporal thalamic ROI and the right SMA. The primary motor, sensory, pre-motor, posterior parietal, occipital, and temporal thalamus includes LP nucleus, VA nuclei, VLa nuclei, VPL nuclei, partial MD nuclei and partial Pu nuclei that project to the somatosensory cortices, temporal lobe, pre-motor areas, primary motor cortex and posterior parietal lobe (25). These nucleuses were involved in sensory and motivation information transmutation. Patients with SD pay overfull concentration on physical sensations, that leads to a decrease in awareness of events in the external world (63, 64), resulting in an imbalance between internal and external stimuli (21). Therefore, impaired top-down and bottom-up modulations of sensory and motivation exist in SD (65, 66). The motor/sensory cortex, including somatosensory (postcentral gyrus), motor (precentral gyrus), and SMA (67), is specialized in processing of sensory stimuli and motor responses. Studies have reported that the motor/sensory cortex plays an important role in bipolar disorder (68, 69), suggesting the potential compensatory effort of the motor/sensory cortex in emotional regulation. Patients with SD have unexplained physical complaints leading to frequently visit hospitals for physical examinations (70). Thus, increased thalamic FC with motor/sensory cortex shown in the present study partially explains specific behaviors in patients with SD.

Furthermore, we observed that hyperconnectivity existed between the right temporal thalamic ROI and the left STG; between the right sensory/right posterior parietal thalamic ROI

and the right ITG; and between the right premotor thalamic ROI and the right MOG in the patients. These findings suggested hyperconnectivity in thalamus nuclei to the auditory and visual cortex. The STG and ITG are responsible for processing sounds. As essential structures involved in auditory processing, including language, the STG and ITG are also associated with social cognition processes (71, 72). The MOG, which is located in the occipital lobe, participates in visual processing (73). These increased FCs in thalamus nuclei to the auditory and visual cortex further support the disturbance of somatosensory processing and the motor/sensory cortex.

In the present study, patients with SD scored higher in HAMA and HAMD than healthy controls. To reduce possible effects of HAMA and HAMD scores on thalamo-cortical FC, we used age, sex, the mean FD, HAMA scores and HAMD scores as covariates in the analyses. In addition, we used age, sex and the mean FD (without HAMA and HAMD scores) as covariates to reanalyze the data, and obtained similar results (**Table 2** and **Supplementary Material Table S1**). This issue indicates that HAMA and HAMD scores have little effects on the present results, which suggests that abnormal thalamo-cortical FC may be an inherent characteristic for SD that can be used as a potential endophenotype for SD.

Limitations exist in the study. First, the relatively small sample cannot be ignored. Second, this study is based on resting-state fMRI, so we cannot eliminate physiologic noise. Third, we found high levels of anxiety and depression symptom severity in the patients. A high ratio of comorbidities is known to exist among depression, anxiety, and somatization (74). Since anxiety and depression may be inherent characteristics of SD, the influence cannot be completely removed in the analysis. Given the imbalanced sex ratio (female-to-male ratio= 5:1) in the

TABLE 2 | Regions with increased connectivity with seeds in the patients.

Cluster location	Peak (MNI)			Number of voxels	*T* value
	x	y	z		
Seed: left primary motor thalamus					
None					
Seed: right primary motor thalamus					
Right middle occipital gyrus	21	−99	24	99	3.2895
Right precentral gyrus	51	−3	54	165	3.9532
Right precentral gyrus	36	−21	63	35	3.0798
Seed: left sensory thalamus					
None					
Seed: right sensory thalamus					
Right inferior temporal gyrus	54	−18	−27	29	3.464
Right precentral gyrus/right postcentral gyrus	51	−3	54	129	3.747
Right precentral gyrus	36	−21	63	27	3.0372
Seed: Left occipital thalamus					
Right precentral gyrus/right postcentral gyrus	33	−24	60	179	3.5828
Seed: right occipital thalamus					
Bilateral anterior cingulum	3	18	27	123	4.1951
Bilateral middle cingulum	6	−15	42	30	3.1134
Seed: left pre-frontal thalamus					
None					
Seed: right pre-frontal thalamus					
None					
Seed: left pre-motor thalamus					
None					
Seed: right pre-motor thalamus					
Right middle occipital gyrus	51	−84	0	200	4.1579
Right precentral gyrus/right postcentral gyrus	51	−3	57	122	3.7314
Seed: left posterior parietal thalamus					
Right Precentral Gyrus	36	−21	63	48	3.2562
Seed: right posterior parietal thalamus					
Right inferior temporal gyrus	54	−18	−33	62	3.4951
Right precentral gyrus/right postcentral gyrus	36	−21	63	57	3.1615
Right paracentral lobule	18	−36	54	28	3.2906
Seed: left temporal thalamus					
Right precentral gyrus/right postcentral gyrus	36	−24	66	57	3.0031
Seed: Right Temporal thalamus					
Left superior temporal gyrus	−63	−12	6	59	2.9629
Right precentral gyrus/right postcentral gyrus	21	−33	54	138	3.1737
Right supplementary motor area	9	−15	51	36	3.4222

The significance level was set at $p < 0.05$ corrected by Gaussian random field (GRF) theory (voxel significance: $p < 0.001$, cluster significance: $p < 0.05$, minimum cluster size = 22 voxels). HAMA scores, HAMD scores, sex, age, and the mean FD as covariates.
MNI, Montreal Neurological Institute; FD, framewise displacement.

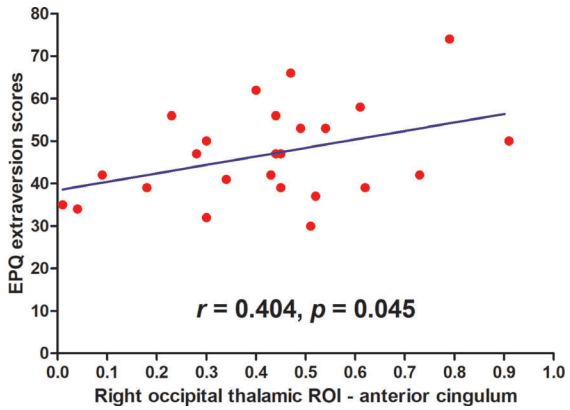

FIGURE 3 | Maps of correlations between abnormal thalamo-cortical connectivity and personality traits. A significantly negative correlation was found between the right occipital thalamic ROI to the anterior cingulum and EPQ extraversion scores (r = 0.404, p = 0.045) after the Benjamini-Hochberg correction.

general population, we recruited high proportion of females in the study.

In conclusion, our findings demonstrated increased FC between the thalamic subregions and cortex in patients with SD. Increased connectivity in thalamus nuclei to the anterior/middle cingulum and motor/sensory cortex were observed, indicating the important role of disturbed functional networks in the pathophysiology of SD. Overall, our study highlights the importance of the thalamic subregions in the pathophysiology of SD.

DATA AVAILABILITY STATEMENT

All datasets presented in this study are included in the article/**Supplementary Material**.

ETHICS STATEMENT

The studies involving human participants were reviewed and approved by The Ethics Committee of the First Affiliated Hospital, Guangxi Medical University. The patients/participants provided their written informed consent to participate in this study. Written informed consent was obtained from the individual(s) for the publication of any potentially identifiable images or data included in this article.

AUTHOR CONTRIBUTIONS

WG and JPZ designed the study. JZ and QS collected the original imaging data. FL, RY, and WG managed and analyzed the imaging data. JZ and ZZ wrote the first draft of the manuscript.

FUNDING

This study was supported by grants from the National Key R&D Program of China (grant nos. 2016YFC1307100 and 2016YFC1306900), the National Natural Science Foundation of China (grant nos. 81771447 and 81630033), and the Natural Science Foundation of Tianjin (grant no. 18JCQNJC10900).

ACKNOWLEDGMENTS

We are grateful to the patients, their families, and the subjects who offered their time to participate in this study.

SUPPLEMENTARY MATERIAL

The Supplementary Material for this article can be found online at: https://www.frontiersin.org/articles/10.3389/fpsyt.2020.555836/full#supplementary-material

REFERENCES

1. Rief W, Hessel A, Braehler E. Somatization symptoms and hypochondriacal features in the general population. *Psychosom Med* (2001) 63:595–602. doi: 10.1097/00006842-200107000-00012
2. Hakala M, Karlsson H, Kurki T, Aalto S, Koponen S, Vahlberg T, et al. Volumes of the caudate nuclei in women with somatization disorder and healthy women. *Psychiatry Res* (2004) 131:71–8. doi: 10.1016/j.pscychresns.2004.03.001
3. Atmaca M, Sirlier B, Yildirim H, Kayali A. Hippocampus and amygdalar volumes in patients with somatization disorder. *Prog Neuropsychopharmacol Biol Psychiatry* (2011) 35:1699–703. doi: 10.1016/j.pnpbp.2011.05.016
4. Yildirim H, Atmaca M, Sirlier B, Kayali A. Pituitary volumes are reduced in patients with somatization disorder. *Psychiatry Investig* (2012) 9:278–82. doi: 10.4306/pi.2012.9.3.278
5. Zhao J, Su Q, Liu F, Zhang Z, Li R, Zhu F, et al. Regional white matter volume abnormalities in first-episode somatization disorder. *Int J Psychophysiol* (2018) 133:12–6. doi: 10.1016/j.ijpsycho.2018.09.003
6. Fayed N, Andres E, Rojas G, Moreno S, Serrano-Blanco A, Roca M, et al. Brain dysfunction in fibromyalgia and somatization disorder using proton magnetic resonance spectroscopy: a controlled study. *Acta Psychiatr Scand* (2012) 126:115–25. doi: 10.1111/j.1600-0447.2011.01820.x
7. Su Q, Yao D, Jiang M, Liu F, Jiang J, Xu C, et al. Dissociation of regional activity in default mode network in medication-naive, first-episode somatization disorder. *PLoS One* (2014) 9:e99273. doi: 10.1371/journal.pone.0099273
8. Su Q, Yao D, Jiang M, Liu F, Jiang J, Xu C, et al. Increased functional connectivity strength of right inferior temporal gyrus in first-episode, drug-naive somatization disorder. *Aust N Z J Psychiatry* (2015) 49:74–81. doi: 10.1177/0004867414553949
9. Li R, Liu F, Su Q, Zhang Z, Zhao J, Wang Y, et al. Bidirectional causal connectivity in the cortico-limbic-cerebellar circuit related to structural alterations in first-episode, drug-naive somatization disorder. *Front Psychiatry* (2018) 9:162. doi: 10.3389/fpsyt.2018.00162
10. Smith MJ, Wang L, Cronenwett W, Mamah D, Barch DM, Csernansky JG. Thalamic morphology in schizophrenia and schizoaffective disorder. *J Psychiatr Res* (2011) 45:378–85. doi: 10.1016/j.jpsychires.2010.08.003

11. Konick LC, Friedman L. Meta-analysis of thalamic size in schizophrenia. *Biol Psychiatry* (2001) 49:28–38. doi: 10.1016/s0006-3223(00)00974-4
12. Corradi-Dell'Acqua C, Tomelleri L, Bellani M, Rambaldelli G, Cerini R, Pozzi-Mucelli R, et al. Thalamic-insular dysconnectivity in schizophrenia: evidence from structural equation modeling. *Hum Brain Mapp* (2012) 33:740–52. doi: 10.1002/hbm.21246
13. Zhang D, Guo L, Hu X, Li K, Zhao Q, Liu T. Increased cortico-subcortical functional connectivity in schizophrenia. *Brain Imaging Behav* (2012) 6:27–35. doi: 10.1007/s11682-011-9138-z
14. Gong J, Luo C, Li X, Jiang S, Khundrakpam BS, Duan M, et al. Evaluation of functional connectivity in subdivisions of the thalamus in schizophrenia. *Br J Psychiatry* (2019) 214:288–96. doi: 10.1192/bjp.2018.299
15. Wang HL, Rau CL, Li YM, Chen YP, Yu R. Disrupted thalamic resting-state functional networks in schizophrenia. *Front Behav Neurosci* (2015) 9:45. doi: 10.3389/fnbeh.2015.00045
16. Skatun KC, Kaufmann T, Brandt CL, Nhat Trung D, Alnaes D, Tonnesen S, et al. Thalamo-cortical functional connectivity in schizophrenia and bipolar disorder. *Brain Imaging Behav* (2018) 12:640–52. doi: 10.1007/s11682-017-9714-y
17. Greicius MD, Flores BH, Menon V, Glover GH, Solvason HB, Kenna H, et al. Resting-state functional connectivity in major depression: abnormally increased contributions from subgenual cingulate cortex and thalamus. *Biol Psychiatry* (2007) 62:429–37. doi: 10.1016/j.biopsych.2006.09.020
18. Carlesimo GA, Lombardi MG, Caltagirone C. Vascular thalamic amnesia: a reappraisal. *Neuropsychologia* (2011) 49:777–89. doi: 10.1016/j.neuropsychologia.2011.01.026
19. Herrero MT, Barcia C, Navarro JM. Functional anatomy of thalamus and basal ganglia. *Childs Nerv Syst* (2002) 18:386–404. doi: 10.1007/s00381-002-0604-1
20. Zhang D, Snyder AZ, Shimony JS, Fox MD, Raichle ME. Noninvasive functional and structural connectivity mapping of the human thalamocortical system. *Cereb Cortex* (2010) 20:1187–94. doi: 10.1093/cercor/bhp182
21. de Greck M, Scheidt L, Boelter AF, Frommer J, Ulrich C, Stockum E, et al. Multimodal psychodynamic psychotherapy induces normalization of reward related activity in somatoform disorder. *World J Biol Psychiatry* (2011) 12:296–308. doi: 10.3109/15622975.2010.539269
22. Kang LJ, Zhang AX, Sun N, Liu PH, Yang CX, Li GZ, et al. Functional connectivity between the thalamus and the primary somatosensory cortex in major depressive disorder: a resting-state fMRI study. *BMC Psychiatry* (2018) 18:339. doi: 10.1186/s12888-018-1913-6
23. Oshiro Y, Quevedo AS, McHaffie JG, Kraft RA, Coghill RC. Brain mechanisms supporting discrimination of sensory features of pain: a new model. *J Neurosci* (2009) 29:14924–31. doi: 10.1523/jneurosci.5538-08.2009
24. Wager TD, Atlas LY, Lindquist MA, Roy M, Woo C-W, Kross E. An fMRI-Based neurologic signature of physical pain. *New Engl J Med* (2013) 368:1388–97. doi: 10.1056/NEJMoa1204471
25. Behrens TEJ, Johansen-Berg H, Woolrich MW, Smith SM, Wheeler-Kingshott CAM, Boulby PA, et al. Non-invasive mapping of connections between human thalamus and cortex using diffusion imaging. *Nat Neurosci* (2003) 6:750–57. doi: 10.1038/nn1075
26. Anticevic A, Cole MW, Repovs G, Murray JD, Brumbaugh MS, Winkler AM, et al. Characterizing thalamo-cortical disturbances in Schizophrenia and bipolar illness. *Cereb Cortex* (2014) 24:3116–30. doi: 10.1093/cercor/bht165
27. Brown EC, Clark DL, Hassel S, MacQueen G, Ramasubbu R. Thalamocortical connectivity in major depressive disorder. *J Affect Disord* (2017) 217:125–31. doi: 10.1016/j.jad.2017.04.004
28. Han F, Liu HJ, Wang K, Yang J, Yang L, Liu J, et al. Correlation between Thalamus-related functional connectivity and serum BDNF levels during the periovulatory phase of primary dysmenorrhea. *Front Hum Neurosci* (2019) 13:333. doi: 10.3389/fnhum.2019.00333
29. Hall NM, Kuzminskyte R, Pedersen AD, Ornbol E, Fink P. The relationship between cognitive functions, somatization and behavioural coping in patients with multiple functional somatic symptoms. *Nord J Psychiatry* (2011) 65:216–24. doi: 10.3109/08039488.2010.528024
30. Al-Adawi S, Al-Zakwani I, Obeid YA, Zaidan Z. Neurocognitive functioning in women presenting with undifferentiated somatoform disorders in Oman. *Psychiatry Clin Neurosci* (2010) 64:555–64. doi: 10.1111/j.1440-1819.2010.02117.x
31. Martin A, Buech A, Schwenk C, Rief W. Memory bias for health-related information in somatoform disorders. *J Psychosom Res* (2007) 63:663–71. doi: 10.1016/j.jpsychores.2007.05.005
32. Subic-Wrana C, Beutel ME, Knebel A, Lane RD. Theory of mind and emotional awareness deficits in patients with somatoform disorders. *Psychosom Med* (2010) 72:404–11. doi: 10.1097/PSY.0b013e3181d35e83
33. Katzer A, Oberfeld D, Hiller W, Witthoft M. Tactile perceptual processes and their relationship to medically unexplained symptoms and health anxiety. *J Psychosom Res* (2011) 71:335–41. doi: 10.1016/j.jpsychores.2011.03.009
34. Stern J, Murphy M, Bass C. Personality disorders in patients with somatisation disorder. A controlled study. *Br J Psychiatry* (1993) 163:785–9. doi: 10.1192/bjp.163.6.785
35. Song Y, Su Q, Jiang M, Liu F, Yao D, Dai Y, et al. Abnormal regional homogeneity and its correlations with personality in first-episode, treatment-naive somatization disorder. *Int J Psychophysiol* (2015) 97:108–12. doi: 10.1016/j.ijpsycho.2015.05.012
36. Behrens TEJ, Woolrich MW, Jenkinson M, Johansen-Berg H, Nunes RG, Clare S, et al. Characterization and propagation of uncertainty in diffusion-weighted MR imaging. *Magn Reson Med* (2003) 50:1077–88. doi: 10.1002/mrm.10609
37. Kong QM, Qiao H, Liu CZ, Zhang P, Li K, Wang L, et al. Aberrant intrinsic functional connectivity in thalamo-cortical networks in major depressive disorder. *CNS Neurosci Ther* (2018) 24:1063–72. doi: 10.1111/cns.12831
38. Sun X, Pan X, Ni K, Ji C, Wu J, Yan C, et al. Aberrant thalamic-centered functional connectivity in patients with persistent somatoform pain disorder. *Neuropsychiatr Dis Treat* (2020) 16:273–81. doi: 10.2147/ndt.S231555
39. Derogatis LR, Rickels K, Rock AF. The SCL-90 and the MMPI: a step in the validation of a new self-report scale. *Br J Psychiatry* (1976) 128:280–9. doi: 10.1192/bjp.128.3.280
40. Hamilton M. A rating scale for depression. *J Neurol Neurosurg Psychiatry* (1960) 23:56–62. doi: 10.1136/jnnp.23.1.56
41. Hamilton M. The assessment of anxiety states by rating. *Br J Med Psychol* (1959) 32:50–5. doi: 10.1111/j.2044-8341.1959.tb00467.x
42. Greve KW, Stickle TR, Love JM, Bianchini KJ, Stanford MS. Latent structure of the Wisconsin Card Sorting Test: a confirmatory factor analytic study. *Arch Clin Neuropsychol* (2005) 20:355–64. doi: 10.1016/j.acn.2004.09.004
43. Christensen BK, Girard TA, Bagby RM. Wechsler adult intelligence scale-third edition short form for index and IQ scores in a psychiatric population. *Psychol Assess* (2007) 19:236–40. doi: 10.1037/1040-3590.19.2.236
44. Eysenck SB, Eysenck HJ. The questionnaire measurement of psychoticism. *Psychol Med* (1972) 2:50–5. doi: 10.1017/s0033291700045608
45. Yan CG, Wang XD, Zuo XN, Zang YF. DPABI: data processing & analysis for (resting-state) brain imaging. *Neuroinformatics* (2016) 14:339–51. doi: 10.1007/s12021-016-9299-4
46. Power JD, Barnes KA, Snyder AZ, Schlaggar BL, Petersen SE. Spurious but systematic correlations in functional connectivity MRI networks arise from subject motion. *Neuroimage* (2012) 59:2142–54. doi: 10.1016/j.neuroimage.2011.10.018
47. Logan JM, Sanders AL, Snyder AZ, Morris JC, Buckner RL. Under-recruitment and nonselective recruitment: dissociable neural mechanisms associated with aging. *Neuron* (2002) 33:827–40. doi: 10.1016/s0896-6273(02)00612-8
48. Hua J, Blair NIS, Paez A, Choe A, Barber AD, Brandt A, et al. Altered functional connectivity between sub-regions in the thalamus and cortex in schizophrenia patients measured by resting state BOLD fMRI at 7T. *Schizophr Res* (2019) 206:370–77. doi: 10.1016/j.schres.2018.10.016
49. Anticevic A, Haut K, Murray JD, Repovs G, Yang GJ, Diehl C, et al. Association of thalamic dysconnectivity and conversion to psychosis in youth and young adults at elevated clinical risk. *JAMA Psychiatry* (2015) 72:882–91. doi: 10.1001/jamapsychiatry.2015.0566
50. Rafal RD, Posner MI. Deficits in human visual spatial attention following thalamic lesions. *Proc Natl Acad Sci U S A* (1987) 84:7349–53. doi: 10.1073/pnas.84.20.7349
51. Lakatos P, O'Connell MN, Barczak A. Pondering the pulvinar. *Neuron* (2016) 89:5–7. doi: 10.1016/j.neuron.2015.12.022

52. Buschman TJ, Miller EK. Top-down versus bottom-up control of attention in the prefrontal and posterior parietal cortices. *Science* (2007) 315:1860–62. doi: 10.1126/science.1138071
53. Zhou H, Schafer RJ, Desimone R. Pulvinar-Cortex Interactions in Vision and Attention. *Neuron* (2016) 89:209–20. doi: 10.1016/j.neuron.2015.11.034
54. Lemche E, Surguladze SA, Brammer MJ, Phillips ML, Sierra M, David AS, et al. Dissociable brain correlates for depression, anxiety, dissociation, and somatization in depersonalization-derealization disorder. *CNS Spectr* (2016) 21:35–42. doi: 10.1017/s1092852913000588
55. Fan L, Li H, Zhuo J, Zhang Y, Wang J, Chen L, et al. The Human Brainnetome Atlas: A New Brain Atlas Based on Connectional Architecture. *Cereb Cortex* (2016) 26:3508–26. doi: 10.1093/cercor/bhw157
56. Li K, Zhang H, Yang Y, Zhu J, Wang B, Shi Y, et al. Abnormal functional network of the thalamic subregions in adult patients with obsessive-compulsive disorder. *Behav Brain Res* (2019) 371. doi: 10.1016/j.bbr.2019.111982
57. Shepherd GM. Corticostriatal connectivity and its role in disease. *Nat Rev Neurosci* (2013) 14:278–91. doi: 10.1038/nrn3469
58. Webb CA, Dillon DG, Pechtel P, Goer FK, Murray L, Huys QJ, et al. Neural correlates of three promising endophenotypes of depression: evidence from the EMBARC study. *Neuropsychopharmacology* (2016) 41:454–63. doi: 10.1038/npp.2015.165
59. Dong D, Luo C, Guell X, Wang Y, He H, Duan M, et al. Compression of cerebellar functional gradients in Schizophrenia. *Schizophr Bull* (2020). doi: 10.1093/schbul/sbaa016
60. Ham T, Leff A, de Boissezon X, Joffe A, Sharp DJ. Cognitive control and the salience network: an investigation of error processing and effective connectivity. *J Neurosci* (2013) 33:7091–8. doi: 10.1523/JNEUROSCI.4692-12.2013
61. Bailey PE, Henry JD. Alexithymia, somatization and negative affect in a community sample. *Psychiatry Res* (2007) 150:13–20. doi: 10.1016/j.psychres.2006.05.024
62. Roth RS, Geisser ME, Theisen-Goodvich M, Dixon PJ. Cognitive complaints are associated with depression, fatigue, female sex, and pain catastrophizing in patients with chronic pain. *Arch Phys Med Rehabil* (2005) 86:1147–54. doi: 10.1016/j.apmr.2004.10.041
63. van Wijk CM, Kolk AM. Sex differences in physical symptoms: the contribution of symptom perception theory. *Soc Sci Med (1982)* (1997) 45:231–46. doi: 10.1016/s0277-9536(96)00340-1
64. van der Werf SP, de Vree B, van der Meer JWM, Bleijenberg G. The relations among body consciousness, somatic symptom report, and information processing speed in chronic fatigue syndrome. *Neuropsychiatry Neuropsychol Behav Neurol* (2002) 15:2–9.
65. Vertes RP, Linley SB, Hoover WB. Limbic circuitry of the midline thalamus. *Neurosci Biobehav Rev* (2015) 54:89–107. doi: 10.1016/j.neubiorev.2015.01.014
66. Wolff M, Alcaraz F, Marchand AR, Coutureau E. Functional heterogeneity of the limbic thalamus: From hippocampal to cortical functions. *Neurosci Biobehav Rev* (2015) 54:120–30. doi: 10.1016/j.neubiorev.2014.11.011
67. Chenji S, Jha S, Lee D, Brown M, Seres P, Mah D, et al. Investigating default mode and sensorimotor network connectivity in amyotrophic lateral sclerosis. *PLoS One* (2016) 11:e0157443. doi: 10.1371/journal.pone.0157443
68. Doucet GE, Bassett DS, Yao N, Glahn DC, Frangou S. The role of intrinsic brain functional connectivity in vulnerability and resilience to bipolar disorder. *Am J Psychiatry* (2017) 174:1214–22. doi: 10.1176/appi.ajp.2017.17010095
69. Martino M, Magioncalda P, Huang Z, Conio B, Piaggio N, Duncan NW, et al. Contrasting variability patterns in the default mode and sensorimotor networks balance in bipolar depression and mania. *Proc Natl Acad Sci U S A* (2016) 113:4824–9. doi: 10.1073/pnas.1517558113
70. Katon W, Lin E, Von Korff M, Russo J, Lipscomb P, Bush T. Somatization: a spectrum of severity. *Am J Psychiatry* (1991) 148:34–40. doi: 10.1176/ajp.148.7.A34
71. Bigler ED, Mortensen S, Neeley ES, Ozonoff S, Krasny L, Johnson M, et al. Superior temporal gyrus, language function, and autism. *Dev Neuropsychol* (2007) 31:217–38. doi: 10.1080/87565640701190841
72. Jou RJ, Minshew NJ, Keshavan MS, Vitale MP, Hardan AY. Enlarged right superior temporal gyrus in children and adolescents with autism. *Brain Res* (2010) 1360:205–12. doi: 10.1016/j.brainres.2010.09.005
73. Flores LP. Occipital lobe morphological anatomy: anatomical and surgical aspects. *Arq Neuropsiquiatr* (2002) 60:566–71. doi: 10.1590/s0004-282x2002000400010
74. Bjelland I, Dahl AA, Haug TT, Neckelmann D. The validity of the Hospital Anxiety and Depression Scale. An updated literature review. *J Psychosom Res* (2002) 52:69–77. doi: 10.1016/s0022-3999(01)00296-3

Conflict of Interest: The authors declare that the research was conducted in the absence of any commercial or financial relationships that could be construed as a potential conflict of interest.

frontiers in Neurology

ORIGINAL RESEARCH
published: 11 September 2020
doi: 10.3389/fneur.2020.01016

Altered Functional Hubs and Connectivity in Type 2 Diabetes Mellitus Without Mild Cognitive Impairment

Yifan Li[1,2†], *Yi Liang*[1,2†‡], *Xin Tan*[2], *Yuna Chen*[1,2], *Jinquan Yang*[1,2], *Hui Zeng*[3], *Chunhong Qin*[2], *Yue Feng*[1,2], *Xiaomeng Ma*[1,2] *and Shijun Qiu*[1,2*]

[1] First Clinical Medical College, Guangzhou University of Chinese Medicine, Guangzhou, China, [2] Department of Radiology, The First Affiliated Hospital of Guangzhou University of Chinese Medicine, Guangzhou, China, [3] Department of Radiology, The First Affiliated Hospital of Guangdong Pharmaceutical University, Guangzhou, China

OPEN ACCESS

Edited by:
Nicola Toschi,
University of Rome Tor Vergata, Italy

Reviewed by:
Alessia Sarica,
University of Magna Graecia, Italy
Nicola Amoroso,
University of Bari Aldo Moro, Italy

***Correspondence:**
Shijun Qiu
qiu-sj@163.com

†These authors have contributed equally to this work

‡These authors share first authorship

Specialty section:
This article was submitted to Applied Neuroimaging, a section of the journal Frontiers in Neurology

Received: 13 May 2020
Accepted: 03 August 2020
Published: 11 September 2020

Citation:
Li Y, Liang Y, Tan X, Chen Y, Yang J, Zeng H, Qin C, Feng Y, Ma X and Qiu S (2020) Altered Functional Hubs and Connectivity in Type 2 Diabetes Mellitus Without Mild Cognitive Impairment. Front. Neurol. 11:1016. doi: 10.3389/fneur.2020.01016

Background: Type 2 diabetes mellitus (T2DM)-related cognitive decline is associated with neuroimaging changes. However, only a few studies have focused on early functional alteration in T2DM prior to mild cognitive impairment (MCI). This study aimed to investigate the early changes of global connectivity patterns in T2DM by using a resting-state functional magnetic resonance imaging (rs-fMRI) technique.

Methods: Thirty-four T2DM subjects and 38 age-, sex-, and education-matched healthy controls (HCs) underwent rs-fMRI in a 3T MRI scanner. Degree centrality (DC) was used to identify the functional hubs of the whole brain in T2DM without MCI. Then the functional connectivity (FC) between hubs and the rest of the brain was assessed by using the hub-based approach.

Results: Compared with HCs, T2DM subjects showed increased DC in the right cerebellum lobules III–V. Hub-based FC analysis found that the right cerebellum lobules III–V of T2DM subjects had increased FC with the right cerebellum crus II and lobule VI, the right temporal inferior/middle gyrus, and the right hippocampus.

Conclusions: Increased DC in the right cerebellum regions III–V, as well as increased FC within cerebellar regions and ipsilateral cerebrocerebellar regions, may indicate an important pathophysiological mechanism for compensation in T2DM without MCI.

Keywords: type 2 diabetes mellitus, resting state, functional connectivity, degree centrality, cognitive function

INTRODUCTION

Type 2 diabetes mellitus (T2DM) is a systemic metabolic disease, resulting in severe complications of multiple systems. Recently, T2DM-related cognitive dysfunction has been paid more attention (1–3). Mild cognitive impairment (MCI), an important complication of T2DM, is intermediate transition state between age-appropriate cognition and dementia (4). Although the integral cognitive function kept "normal" up for a long time before MCI, there has been a gradually imperceptible decline in some aspects of cognitive function (5, 6). Early detection of the brain

functional changes of this stage could be clinically significant, because it might provide theoretical evidence for explaining cognitive changes related to T2DM and might greatly postpone the onset of MCI.

Currently, neuroimaging methods have been generally applied to probe the mechanism of T2DM-related cognitive impairment (7–10). However, only a few studies kept a watchful eye on the early neuroimaging changes in T2DM subjects without MCI, and the underlying mechanisms have not been entirely elaborated. In a previous study, neurovascular decoupling pattern in T2DM without MCI was assessed using a variety of imaging methods (5). In another study, alterations in connectivity within the Papez circuit in T2DM patients without MCI were identified, and the relationships between these alterations and insulin resistance have been determined (11). However, there were no comprehensive and sensitive assessments on cognitive function, or subjects in these studies were older. Sun et al. found that functional connectivity (FC) between the hippocampus and certain brain structures had decreased significantly in T2DM subjects without MCI (12). However, results of the region of interest (ROI)-based FC analysis should be interpreted in caution, as the selected ROIs are mainly based on the prior knowledge, leading to different and unpredictable findings (13). Our previous studies showed microstructure of the white matter changes in T2DM without MCI in several brain regions including the bilateral cingulum lobe and thalami (14), pons, and left temporal pole (15). It is believed that alterations in brain structure may lead to changes in brain function (16–19). Abnormalities in FC are largely related to cognitive abnormalities (20). Therefore, comprehensive whole-brain FC analyses were needed.

Another neuroimaging method, the degree centrality (DC), is used to explore the distribution of the local FC by using resting-state functional magnetic resonance imaging (rs-fMRI) technique (21–23). It does not need to pick out seed points, nor does it need to consider the relationships between brain regions. It can investigate the overall performances and patterns of functional connectome with higher speed than traditional methods, and it can perform whole-brain analysis at the voxel level to eliminate biases caused by selection of brain regions based on prior assumptions (22, 23).

DC has been widely used to quantify node features of networks, and increased DC regions are defined as functional hubs (22). Previous researches using DC analysis showed altered brain functional hubs and connectivity in T2DM subjects (5, 23, 24). However, subjects enrolled in these studies had clinical cognitive impairment or lacked cognitive assessment. In the present work, we aimed to explore the early neurological changes of T2DM without MCI based on DC. Specifically, DC was firstly performed to evaluate the altered brain functional hubs of T2DM patients compared with the control group; then a hub-based analysis of the interactions among these functional hubs or FC between hubs and the rest of brain was conducted to further explore internal changes of connections. A large number of cognitive scales were used to assess the cognitive function of T2DM subjects as a whole.

MATERIALS AND METHODS

Subjects

All the T2DM subjects were enrolled from inpatients and outpatients of the First Affiliated Hospital of Guangzhou University of Chinese Medicine from November 1, 2017, to December 20, 2019 (**Table 1**). The diagnostic criteria for T2DM were defined by the American Diabetes Association (ADA). The healthy control (HC) group consisted of healthy people who underwent routine physical examination. All subjects were right-handed and had more than 6 years of education. They were all Han Chinese and native Chinese speakers. None of the subjects had obvious cognitive impairment or dementia, and their Montreal Cognitive Assessment (MoCA, Beijing edition) scores were $\geq$26. The study was authorized by the Medical Research Ethics Committee of Guangzhou University of Chinese Medicine, and written informed consent was obtained from each participant before the experiment. HC subjects were matched with T2DM subjects in reference to age, sex, and education. Participants associated with neurological and psychiatric diseases (e.g., brain injury and cerebrovascular accident, brain tumors, epilepsy, depression, schizophrenia, and Parkinson's disease), or systematic disease(s), complications associated with diabetes (such as diabetic retinopathy, diabetic nephropathy, and peripheral neuropathy), alcohol dependence or history of drug abuse, other types of diabetes, and contraindications to MRI were excluded. Finally, a total of 38 HC subjects and 34 T2DM subjects were enrolled. All the T2DM subjects enrolled in the current study received initiating oral metformin following insulin via a pump or subcutaneous injection during hospitalization. Their blood sugar levels were well-controlled. None of the T2DM subjects received intranasal insulin.

Demographic and Clinical Characteristics

General demographic information and clinical measurement of all the subjects were collected, including age, gender, education level, body mass index (BMI), and blood pressure. The laboratory tests were available for T2DM, including fasting blood glucose (FBG), fasting insulin (FINS), triglyceride (TG), total cholesterol (TC), low-density lipoprotein (LDL), and glycosylated hemoglobin (HbA1c).

Cognitive Assessment

All subjects received a range of neuropsychological tests, which were sensitive and commonly used in T2DM-related studies, including the MoCA (25), auditory verbal learning test (AVLT) (26), trail making test (TMT; including parts A and B) (27), grooved pegboard test (GPT) (28), symbol digit test (SDT) (29), the clock drawing test (CDT) (30), and the digital span test (DST, including forward and backward) (31). The AVLT involved four parts: immediate recall, short-term delayed recall, long-term delayed recall, and recognition. The whole process took at least 35 min to complete assessment.

Image Acquisition

MRI data were acquired on a 3-T GE SIGNA clinical MRI scanner with an eight-channel phased-array head coil. Scanning consisted of two parts: conventional sequences were used

for screening lesions, and functional sequences were used for experiment processing. First, all participants underwent conventional brain axial T1-weighted, T2-weighted, and fluid-attenuated inversion recovery (FLAIR) images to rule out brain organic diseases and white matter hyperintensity (WMH) lesions (15). Images of conventional sequences (T1, T2, and FLAIR) were inspected, respectively, by two radiologists who had a wealth of work experience, and none of the subjects were excluded after the conventional scans. Functional images were obtained using a gradient-echo planar sequence. The scanning parameters were consistent with our previous research (7).

The scan was performed within 2–3 h after dinner (7–8p.m.), and the time interval between the scanning and the neuropsychological tests should be at least 0.5 h. Needle injection (for blood tests or therapies) or sleeplessness before scanning also was avoided. The blood glucose levels were all well-controlled before scanning. During the scanning, the subjects were asked to avoid systemic thinking or falling asleep.

TABLE 1 | Demographics, clinical data, cognitive assessment of T2DM and HCs.

	Diabetic subjects ($n = 34$)	Healthy controls ($n = 38$)	Statistics	*P*-value
DEMOGRAPHICS				
Age (years)	49.41 ± 5.58	47.42 ± 6.81	$t = 1.347$	0.182
Gender (M/F)	22/12	19/19	$\chi^2 = 1.58$	0.208
Education (years)	9 (6, 16)	10 (6, 16)	$z = -0.187$	0.852
CLINICAL DATA				
BMI (kg/m^2)	25.04 ± 2.40	22.72 ± 2.55	$t = 3.945$	0.000*
SBP (mmHg)	133.06 ± 15.64	117.82 ± 11.10	$t = 4.808$	0.000*
DBP (mmHg)	85 (66, 120)	76 (71, 110)	$z = -3.117$	0.002*
HbA1c (%)	8.73 ± 2.15	N/A	N/A	N/A
FBG (mmol/L)	7.59 (3.66, 17.50)	N/A	N/A	N/A
FINS (μIU/ml)	5.94 (0.79, 18.90)	N/A	N/A	N/A
TG (mmol/L)	1.64 (0.64, 7.61)	N/A	N/A	N/A
TC (mmol/L)	4.51 ± 0.98	N/A	N/A	N/A
LDL (mmol/L)	3.28 ± 1.11	N/A	N/A	N/A
COGNITIVE ASSESSMENT				
MoCA score	26 (26, 29)	28 (26, 30)	$z = -3.174$	0.002*
AVLT (immediate)	20.00 ± 4.83	21.18 ± 5.48	$t = -0.968$	0.337
AVLT (5 min)	7 (4, 12)	8 (4, 14)	$z = -1.494$	0.135
AVLT (20 min)	7.74. ± 2.47	8.34 ± 2.47	$t = -1.041$	0.302
AVLT (recall)	11.5 (6, 12)	12 (5, 13)	$z = -1.245$	0.213
Grooved pegboard (R)	77.05 (59.3, 181)	73.5 (55, 130.8)	$z = -1.574$	0.115
Grooved pegboard (L)	83 (70, 182)	80.35 (53, 193)	$z = -1.055$	0.291
TMT-A	53.5 (21, 156)	54 (23, 124)	$z = -0.914$	0.361
TMT-B	45.5 (19, 118)	42.8 (23, 89)	$z = -0.790$	0.430
DST (forward)	8 (5, 12)	8 (6, 11)	$z = -0.536$	0.592
DST (inverse)	4 (2, 10)	4 (2, 10)	$z = -0.442$	0.659
CDT	3 (1, 3)	3 (2, 3)	$z = -1.967$	0.049*
SDT	42.29 ± 10.28	50.29 ± 14.32	$t = -2.694$	0.009*

Values distributed normally or non-normally are presented as mean ± SD or median (minimum, maximum).

BMI, body mass index; SBP, systolic blood pressure; DBP, diastolic blood pressure; FBG, fasting blood glucose; FINS, fasting insulin; TG, triglyceride; TC, total cholesterol; LDL, low-density lipoprotein; MoCA, Montreal Cognitive Assessment; AVLT, auditory verbal learning test; TMT, trail making test; GPT, grooved pegboard test; SDT, symbol digit test; CDT, the clock drawing test; DST, the digital span test.

**P < 0.05.*

Data Preprocessing

The entire calculation process was carried out on the MATLAB R2014a platform. Data analysis tool RESTplus was used to preprocess the original rs-fMRI data (32). The first 10 images were discarded and the remaining 175 time-point images were preprocessed. The main procedure was conducted as follows: (1) DICOM-NIFTI format conversion. (2) Slice timing: the acquisition time of all voxels was kept consistent through rectification, and each time point was aligned to the time point of the most middle layer. (3) Head movement correction: subjects were excluded if the maximum cumulative head motion exceeded 2 mm in translation or 2° in rotation along any direction. (4) Spatial normalization: the brain images of all subjects were aligned to the same standard space to solve the problems of individual differences in brain size and scanning positions. After alignment, statistical comparison based on voxel could be conducted in the Montreal Neurological Institute (MNI) space, and the resampled voxel size was 3 × 3 × 3 mm. (5) Remove linear drift: the trend signal generated during scanning period should be decomposed from the original time series data. (6) Regression covariates: the interference signal should be removed by a linear regression model, which includes (6) head motion parameters, white matter signal, and cerebrospinal fluid signal. (7) Filtering: data were filtered from 0.01 to 0.08 Hz.

The brain intrinsic connectivity network was constructed at the voxel level. The temporal Pearson's correlation of time series and the similarity of rs-fMRI signals between pairs of voxels were measured to calculate a correlation matrix. For a weighted graph, which is more robust against confounding factors, DC is defined as the sum of weights from edges connecting to a node (also sometimes referred to as the node strength) (22).

The DC in RESTplus software was used to calculate the DC value based on correlation thresholds (absolute value of

TABLE 2 | Brain regions with increased DC in T2DM compared with HCs.

Cluster	Brain regions	Peak MNI			Number of voxels	*t*-value
		X	Y	Z		
	Right cerebellum III Right cerebellum IV–V	12	−33	−24	183	4.9013

DC, degree centrality; MNI, Montreal Neurological Institute; X, Y, Z, coordinates of primary peak locations in the MNI space.

Pearson's $r > 0.2$) to exclude weak correlations, which may be caused by signal noise based on previous studies (22, 33, 34). Then smooth was performed with a $6 \times 6 \times 6$ mm^3 Gaussian kernel.

The hub-based FC analysis was also conducted by RESTplus. Peak MNI coordinates of the brain functional hubs were acquired by group comparison of DC maps, and the hubs were considered to be the center of ROI with a 6-mm radius. The average time series of ROI was extracted by using the anatomical automatic labeling (AAL) template in the RESTplus software package and correlated with the time series of voxel in other brain regions of the whole brain. And then a Fisher z-transform was used to improve the normality of the correlation coefficients.

Statistical Analysis

Demographic and Clinical Characteristics Analysis

Kolmogorov–Smirnov test (33) was applied to detect the normality of the continuous variables, including the demographic data and biochemical characteristics of the T2DM subjects and HCs. Independent two-sample *t*-tests were used if the data meet normal distribution and variance homogeneity; otherwise, Mann–Whitney non-parametric tests were used. The chi-square test was used to evaluate intergroup difference in gender. All statistical analyses were using the IBM Statistical Package for the Social Sciences 22.0 software (IBM SPSS Inc., Chicago, IL, USA). The significance level was set at $P < 0.05$.

Intergroup Comparison of Resting-State Degree Centrality and Hub-Based Functional Connectivity

The two-sample *t*-test in the RESTplus data analysis kit V1.21 software was used to compare the DC statistical parameter charts of the two groups of subjects. The built-in brain mask of RESTplus ($61 \times 73 \times 61$ mm) was used as the registration template, and the initial threshold was $P < 0.01$, and the Gaussian random field (GRF) correction was performed. Voxel $P < 0.01$ and cluster $P < 0.05$ were set. The inspection is double tail inspection. The corrected cluster size threshold is 179 voxels. Then, an independent sample *t*-test and a GRF were also used to explore the differences between T2DM subjects and HCs in terms of FC.

These brain regions were positioned, and the location, size, peak MNI coordinates, and *t*-values of statistically significant brain regions were recorded according to the AAL partition template.

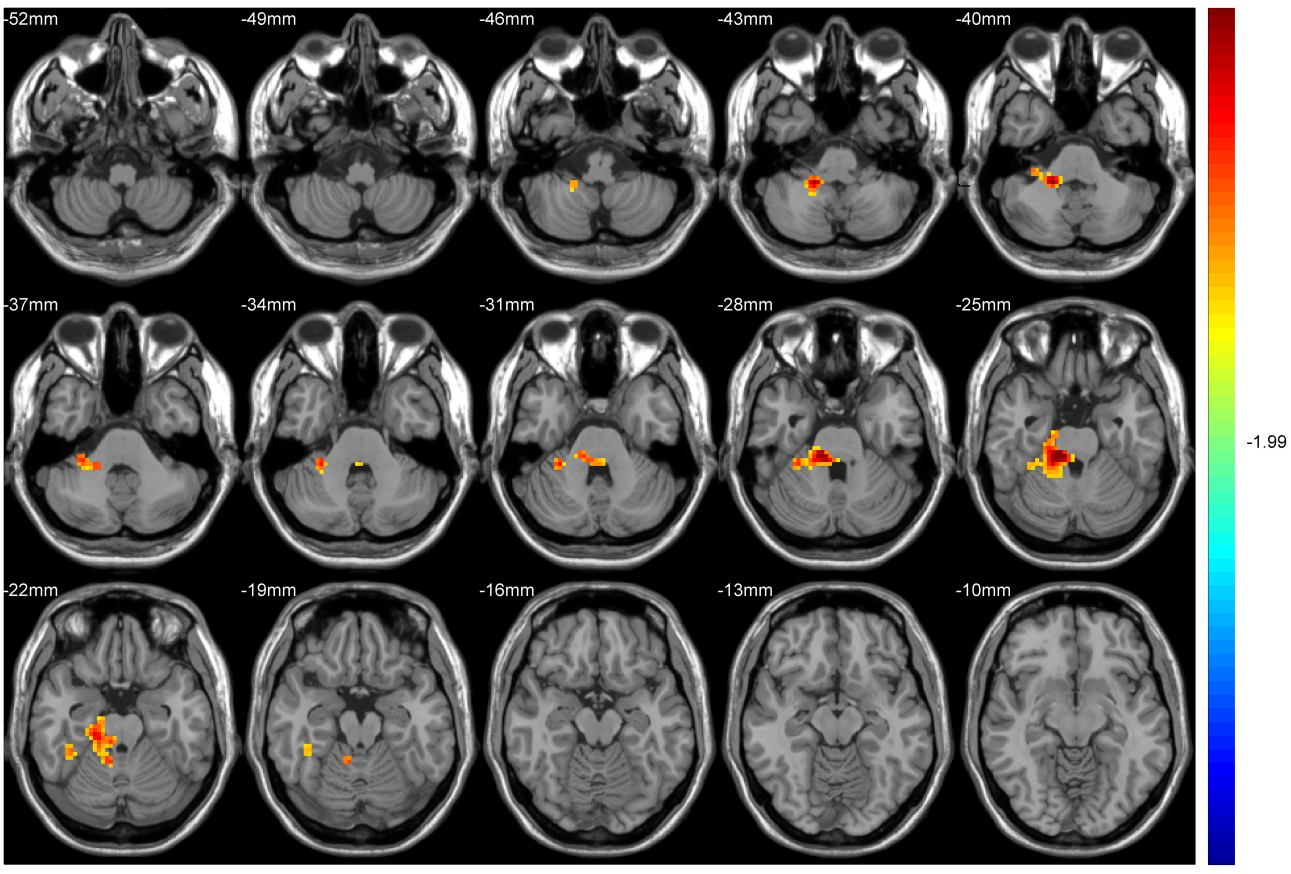

FIGURE 1 | The colored brain regions represent significantly increased degree centrality (DC) in type 2 diabetes mellitus (T2DM) subjects compared with healthy controls (HCs). The color bar indicates the *t*-value from two-sample *t*-tests.

The Relationship Between Clinical Biochemical Index and Neurocognitive Function

Partial correlation analysis was applied to analyze the correlation between various clinical biochemical indicators (HbA1c, TC, TG, FINS, FBG, and LDL) and scores of different neurocognitive function scales (MoCA, AVLT, TMT-a, TMT-b, GPT, DST, CDT, and SDT) in the T2DM group after controlling for gender, age, and education level. $P < 0.05$ was considered statistically significant.

RESULTS

Demographic, Clinical, and Cognitive Characteristics

Demographic, clinical, and cognitive information of all the subjects is listed in **Table 1**. There was no statistical difference in age, gender, and education levels between the two groups. Compared with HCs, the T2DM group had significantly higher levels of BMI and blood pressure and exhibited worse performance on the tests of MoCA, CDT, and SDT ($P < 0.05$).

Intergroup Differences in Degree Centrality

After GRF multiple comparison correction (voxel $P < 0.01$, cluster $P < 0.05$), only one cluster survived in the T2DM group compared with the HC group in the brain areas with increased DC (**Table 2**, **Figure 1**), involving the right cerebellum areas III–V. To further verify the validity and reliable of the results by using 0.2 as threshold in the DC analysis, the thresholds of 0.1 and 0.3 had also been processed (**Supplementary Figures 1, 2**). The location of the peak MNI point and the cluster were consistent, but the size of the cluster was slightly altered.

Intergroup Differences in Functional Connectivity

Hub-based FC analysis showed the brain regions with increased FC in the T2DM group mainly involving the right cerebellum crus II, right cerebellum lobule VI, right temporal inferior gyrus, right temporal middle gyrus, and right hippocampus (**Table 3**, **Figure 2**).

Correlation Analysis Results

Partial correlation analysis found that HbA1c was negatively correlated with AVLT immediate memory scores in the T2DM group and FBG was negatively correlated with TMT-B (**Figure 3**). However, there were no correlations between increased DC or FC and scores of the neuropsychological tests.

DISCUSSION

This study focused on changes of brain functional hubs and their connectivity in T2DM without MCI by using DC and FC. Compared with the HCs, the T2DM subjects exhibited significantly increased DC in the right cerebellum regions III–V. And according to the hub-based analysis, we found that FC increased between the right cerebellum regions III–V and the right cerebellum crus II/VI, right inferior/middle temporal gyrus, and right hippocampus in the T2DM group. The increased DC and FC may provide evidence of early compensatory mechanism in T2DM without MCI.

TABLE 3 | Brain regions with increased FC in T2DM compared with HCs.

Cluster	Brain regions	Peak MNI			Number of voxels	*t*-value
		X	Y	Z		
Cluster 1	Right cerebellum crus II Right Cerebellum lobule VI	−12	−69	−39	404	3.6218
Cluster 2	Right temporal inferior gyrus Right temporal middle gyrus Right Hippocampus	51	−27	−12	477	4.0098

FC, functional connectivity; GRF correction (P < 0.01, voxel P < 0.01, cluster P < 0.05).

Cognition Assessment of Type 2 Diabetes Mellitus and Healthy Controls

There was no significant difference of neuropsychological assessment between T2DM and HCs, except for a few scales, i.e., MoCA-B, CDT, and SDT. Most of the T2DM subjects were younger than 50 years and had no obvious vascular complications, such as retinopathy and cerebrovascular diseases. This may explain why cognitive functions of the T2DM group are not significantly impaired (5). MoCA-B mainly assesses attention and concentration and has different sensitivity in different mental disorder diseases (35). Longer test durations of CDT and SDT were commonly reported in T2DM patients compared with HCs, indicating that mild impairment of executive function and inflexibility of movement firstly exist at the early stage of the disease (36, 37). Negative correlation between cognitive function and clinical measurement (i.e., HbA1c and FBG) suggested that higher blood sugar level may have some impact on cognitive decline in preclinical stage (38).

Degree Centrality Alteration in Cerebellum Regions in Type 2 Diabetes Mellitus

DC quantifies local degree, which measures the centrality of every voxel in the human brain connectome (22, 24). The increased DC may imply the transition from an economic connection to the costly connection; that is, brain regions with high energy-consumption such as brain hubs can be reconfigured to meet different and variable cognitive needs through negotiations between connection costs and the topological characteristics of the networks (39, 40). In the current study, increased DC of the right cerebellum regions III–V in T2DM compared with HCs could be attributed to a compensatory mechanism invoked following dysfunction of the neuro architectural network that typically would support a cognitive task (41, 42). The compensation mechanisms of the cerebellum in neural functions in T2DM individuals with the early stage had been reported via not only rs-fMRI but also task fMRI or structure MRI studies (42–45). Our previous study also indicated that T2DM subjects exhibited increased nodal efficiency in the right cerebellum

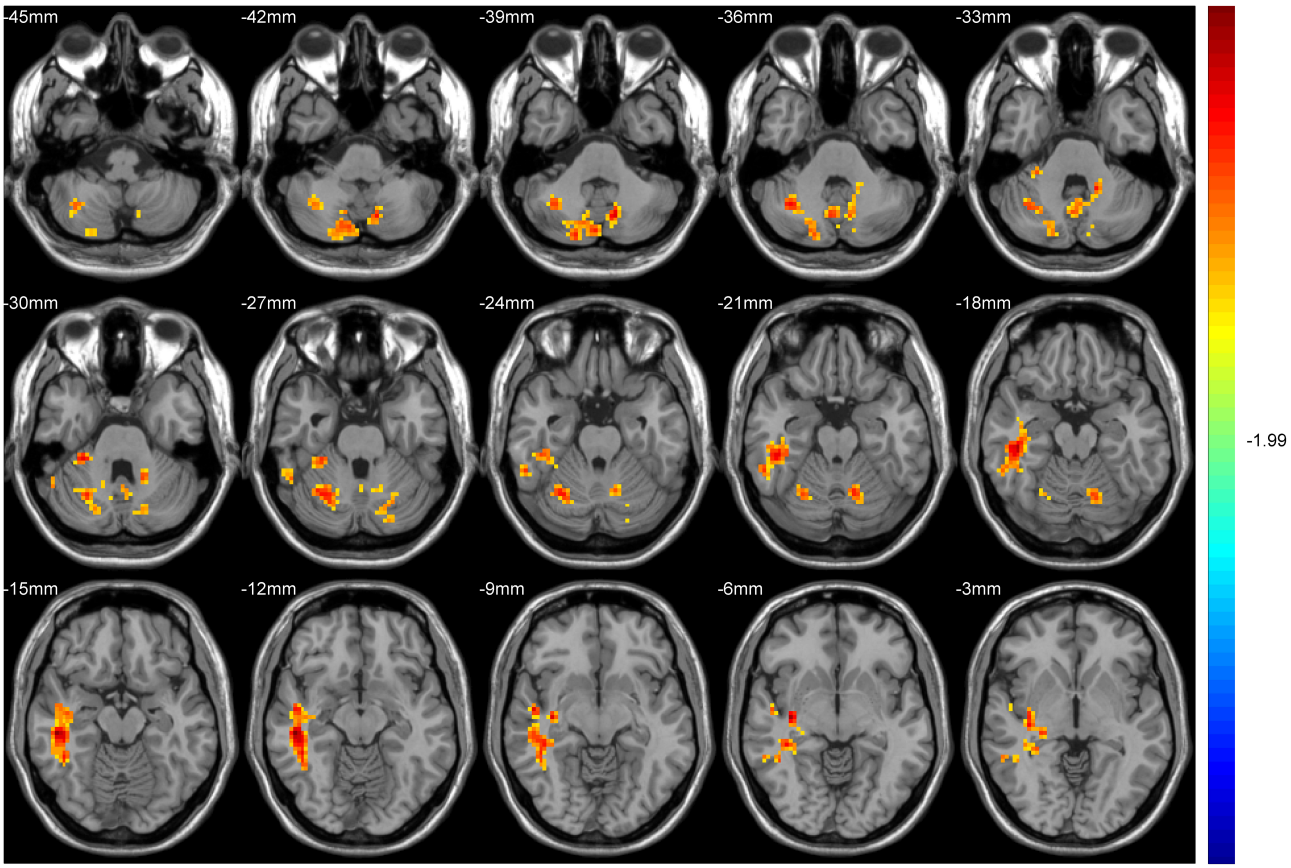

FIGURE 2 | The colored brain regions represent significantly increased functional connectivity (FC) in type 2 diabetes mellitus (T2DM) patients compared with healthy controls (HCs). The color bar indicates the *t*-value from two-sample *t*-tests.

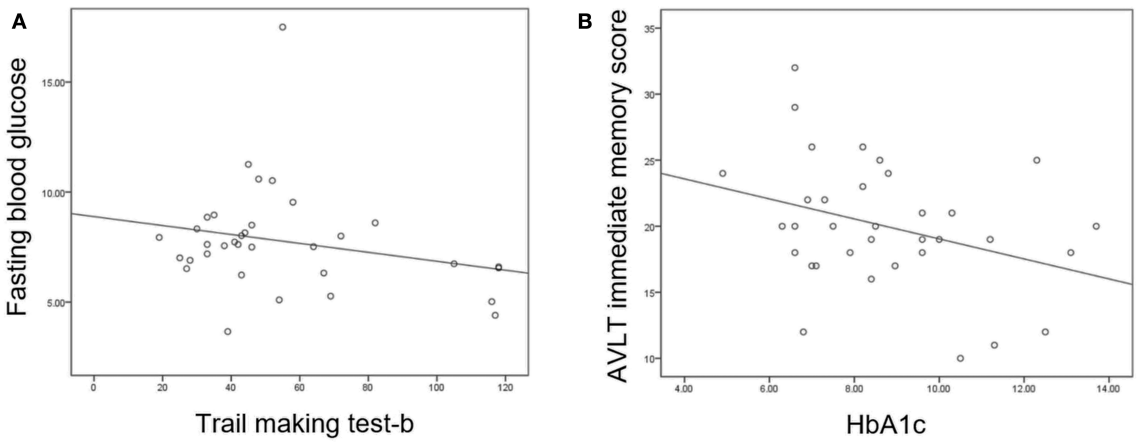

FIGURE 3 | (A) Fasting blood glucose was negatively correlated with trail making test-B score ($P = 0.047$, $r = -0.360$). **(B)** Glycosylated hemoglobin (HbA1c) was negatively correlated with auditory verbal learning test (AVLT) immediate recall score ($P = 0.021$, $r = -0.413$).

III, which were associated with cognitive performance (41). However, some previous studies reported that T2DM subjects showed significant decreased anatomical connections, mean regional homogeneity (mReHo), cerebral blood flow (CBF), and DC in cerebellar regions (46–48), providing evidence to the significant role of the cerebellum in terms of cognitive function. Although inconsistent results were obtained, it is believed that the cerebellum might play an important role in maintaining normal

cognitive functions in T2DM before the onset of symptoms or even at the prediabetic stage (15, 43).

Functional Connectivity Alteration in Type 2 Diabetes Mellitus

The FCs are accumulation of the paired regional connections in the brain and are rich in information associated with the intrinsic interactions among the brain regions, which are caused by the spontaneous neural activities. Higher FCs indicate the enhancement of temporal consistency of the different brain regions. In the present study, increased FC based on the hub DC analysis was found not only within different cerebellar regions but also between ipsilateral cerebrocerebellar regions, suggesting sophisticated recruitment capacity of the cerebellum in T2DM (15, 42, 43). Though the cognitive functions of the cerebellum are not yet well-understood, a study based on exceptionally large and high-quality dataset analysis indicated that functional gradients of the cerebellum correspond to intrinsic connectivity of cerebellar voxels with the rest of the cerebellum (49). On the other hand, correlation studies have shown interactions between the cerebellum and non-motor areas of the cerebral cortex (50). The inferior and middle temporal lobes contain fiber tracks (e.g., middle cerebellar peduncle and unciform fasciculus) crossing several brain regions and associating with language processing, verbal working memory, visual spatial perception (51), and so forth. The hippocampus is involved in different aspects of memory formation and learning process (10) and plays an important role during the cognitive process of normal cognition to Alzheimer's disease. It was reported that T2DM subjects usually has existing atrophy of the hippocampus and reduced cortical thickness in the right middle and inferior temporal gyri and at the early stage of the disease (12, 52). The increased FC between the cerebellum and temporal gyrus (including the hippocampus) might present the potential impairment of cognition, which could be compensated by means of adjustment of functions of other regions to "recover" the potential impairments before the clinical onset of cognitive impairment.

We did not find any correlation between the aberrant FC and the multiple neurocognitive assessment scale scores. This is probably because the subjects' cognitive function was still in the normal range, and it was not linear enough with the increased DC or FC brain regions. In addition, in most of the cases, correlations could exist in any area, even that without group difference. Even further searching correlations in an area with group difference itself do not guarantee that only patients show a correlation but controls do not. Therefore, we feel that it is more reasonable to do exactly the same exhausted search, for group difference detection, as well as for correlation identification, based on the exploratory nature of this work (53).

Limitations

There were some limitations in this study. Firstly, it was a cross-sectional investigation and had relatively small sample size. Further longitudinal studies are needed to elaborate the changes in the whole brain DC associated with cognitive impairment, particularly as it develops to MCI or AD. Secondly, uncontrolled thoughts and/or other activities during the resting-state scan could confound the result (43, 54). In addition, different doses of hypoglycemic agents may affect the results, though the blood sugar level of all the T2DM individuals was well-controlled, and we have tried to control for confounding factors. Future studies should take these into consideration, and multimodal MRI that provide comprehensive channels of information should be conducted (55).

CONCLUSION

The present study found increased DC in the right cerebellum regions III–V, as well as increased FCs within cerebellar regions and ipsilateral cerebrocerebellar regions, indicating complicated compensatory mechanisms of the cerebellum in the early stage of T2DM without MCI. These results provide valuable insights into the neurological pathophysiology of T2DM-related of cognitive decline and hold great potential in detecting early imaging markers of T2DM.

DATA AVAILABILITY STATEMENT

The raw data supporting the conclusions of this article will be made available by the authors, without undue reservation.

ETHICS STATEMENT

The studies involving human participants were reviewed and approved by Medical Research Ethics Committee of Guangzhou University of Chinese Medicine. The patients/participants provided their written informed consent to participate in this study.

AUTHOR CONTRIBUTIONS

YLi and YLia designed the entire experiment and completed the data analysis and manuscript writing. XT analyzed the data and revised the manuscript. YC has made contributions to statistical analysis. JY administered the neuropsychological tests. HZ and CQ contributed to the review of conventional sequence images. YF and XM contributed to data collection. SQ is the guarantor of this study and had complete access to all data in the study. All the authors accept responsibility for the integrity of the data and the accuracy of the data analysis.

FUNDING

The study work was in part funded by the National Natural Science Foundation of China (81771344 and 91649117) and the Key International Cooperation Project of National Natural Science Foundation of China (81920108019).

SUPPLEMENTARY MATERIAL

The Supplementary Material for this article can be found online at: https://www.frontiersin.org/articles/10.3389/fneur.2020.01016/full#supplementary-material

REFERENCES

1. Groeneveld O, Reijmer Y, Heinen R, Kuijf H, Koekkoek P, Janssen J, et al. Brain imaging correlates of mild cognitive impairment and early dementia in patients with type 2 diabetes mellitus. *Nutr Metab Cardiovasc Dis.* (2018) 28:1253–60. doi: 10.1016/j.numecd.2018.07.008
2. Manschot SM, Brands AM, van der Grond J, Kessels RP, Algra A, Kappelle LJ, et al. Brain magnetic resonance imaging correlates of impaired cognition in patients with type 2 diabetes. *Diabetes.* (2006) 55:1106–13. doi: 10.2337/diabetes.55.04.06.db05-1323
3. Liu Z, Liu J, Yuan H, Liu T, Cui X, Tang Z, et al. Identification of cognitive dysfunction in patients with T2DM using whole brain functional connectivity. *Genomics Proteomics Bioinformatics.* (2019) 17:441–52. doi: 10.1016/j.gpb.2019.09.002
4. Pal K, Mukadam N, Petersen I, Cooper C. Mild cognitive impairment and progression to dementia in people with diabetes, prediabetes and metabolic syndrome: a systematic review and meta-analysis. *Soc psychiatry Psychiatr Epidemiol.* (2018) 53:1149–60. doi: 10.1007/s00127-018-1581-3
5. Yu Y, Yan LF, Sun Q, Hu B, Zhang J, Yang Y, et al. Neurovascular decoupling in type 2 diabetes mellitus without mild cognitive impairment: potential biomarker for early cognitive impairment. *NeuroImage.* (2019) 200:644–58. doi: 10.1016/j.neuroimage.2019.06.058
6. Ma F, Wu T, Miao R, Xiao YY, Zhang W, Huang G. Conversion of mild cognitive impairment to dementia among subjects with diabetes: a population-based study of incidence and risk factors with five years of follow-up. *J Alzheimer's Dis.* (2015) 43:1441–9. doi: 10.3233/JAD-141566
7. Tan X, Liang Y, Zeng H, Qin C, Li Y, Yang J, et al. Altered functional connectivity of the posterior cingulate cortex in type 2 diabetes with cognitive impairment. *Brain Imaging Behav.* (2019) 13:1699–707. doi: 10.1007/s11682-018-0017-8
8. van Bussel FC, Backes WH, Hofman PA, van Boxtel MP, Schram MT, Stehouwer CD, et al. Altered hippocampal white matter connectivity in type 2 diabetes mellitus and memory decrements. *J Neuroendocrinol.* (2016) 28:12366. doi: 10.1111/jne.12366
9. Yang SQ, Xu ZP, Xiong Y, Zhan YF, Guo LY, Zhang S, et al. Altered intranetwork and internetwork functional connectivity in type 2 diabetes mellitus with and without cognitive impairment. *Sci Rep*. (2016) 6:32980. doi: 10.1038/srep32980
10. Zhang H, Hao Y, Manor B, Novak P, Milberg W, Zhang J, et al. Intranasal insulin enhanced resting-state functional connectivity of hippocampal regions in type 2 diabetes. *Diabetes.* (2015) 64:1025–34. doi: 10.2337/db14-1000
11. Xia W, Chen YC, Luo Y, Zhang D, Chen H, Ma J, et al. Alterations in effective connectivity within the Papez circuit are correlated with insulin resistance in T2DM patients without mild cognitive impairment. *Brain Imaging Behav.* (2019) 14:1238–46. doi: 10.1007/s11682-019-00049-z
12. Sun Q, Chen GQ, Wang XB, Yu Y, Hu YC, Yan LF, et al. Alterations of white matter integrity and hippocampal functional connectivity in type 2 diabetes without mild cognitive impairment. *Front Neuroanat.* (2018) 12:21. doi: 10.3389/fnana.2018.00021
13. Qin W, Xuan Y, Liu Y, Jiang T, Yu C. Functional connectivity density in congenitally and late blind subjects. *Cereb Cortex.* (2015) 25:2507–16. doi: 10.1093/cercor/bhu051
14. Tan X, Fang P, An J, Lin H, Liang Y, Shen W, et al. Micro-structural white matter abnormalities in type 2 diabetic patients: a DTI study using TBSS analysis. *Neuroradiology.* (2016) 58:1209–16. doi: 10.1007/s00234-016-1752-4
15. Liang Y, Zhang H, Tan X, Liu J, Qin C, Zeng H, et al. Local diffusion homogeneity provides supplementary information in T2DM-related WM microstructural abnormality detection. *Front Neurosci.* (2019) 13:63. doi: 10.3389/fnins.2019.00063
16. Huang H, Ding M. Linking functional connectivity and structural connectivity quantitatively: a comparison of methods. *Brain Connect.* (2016) 6:99–108. doi: 10.1089/brain.2015.0382
17. Farooq H, Chen Y, Georgiou TT, Tannenbaum A, Lenglet C. Network curvature as a hallmark of brain structural connectivity. *Nat Commun.* (2019) 10:4937. doi: 10.1038/s41467-019-12915-x
18. Fernandes HM, Cabral J, van Hartevelt TJ, Lord LD, Gleesborg C, Moller A, et al. Disrupted brain structural connectivity in pediatric bipolar disorder with psychosis. *Sci Rep.* (2019) 9:13638. doi: 10.1038/s41598-019-50093-4
19. Amoroso N, La Rocca M, Bruno S, Maggipinto T, Monaco A, Bellotti R, et al. Multiplex networks for early diagnosis of alzheimer's disease. *Front Aging Neurosci.* (2018) 10:365. doi: 10.3389/fnagi.2018.00365
20. Liu H, Liu J, Liu H, Peng L, Feng Z, Rong P, et al. Pathological between-network positive connectivity in early type 2 diabetes patients without cerebral small vessel diseases. *Front Neurosci.* (2019) 13:731. doi: 10.3389/fnins.2019.00731
21. Buckner RL, Sepulcre J, Talukdar T, Krienen FM, Liu H, Hedden T, et al. Cortical hubs revealed by intrinsic functional connectivity: mapping, assessment of stability, and relation to Alzheimer's disease. *J Neurosci.* (2009) 29:1860–73. doi: 10.1523/JNEUROSCI.5062-08.2009
22. Zuo XN, Ehmke R, Mennes M, Imperati D, Castellanos FX, Sporns O, et al. Network centrality in the human functional connectome. *Cereb Cortex.* (2012) 22:1862–75. doi: 10.1093/cercor/bhr269
23. Cui Y, Li SF, Gu H, Hu YZ, Liang X, Lu CQ, et al. Disrupted brain connectivity patterns in patients with type 2 diabetes. *AJNR Am J Neuroradiol.* (2016) 37:2115–22. doi: 10.3174/ajnr.A4858
24. Liu D, Duan S, Zhou C, Wei P, Chen L, Yin X, et al. Altered brain functional hubs and connectivity in type 2 diabetes mellitus patients: a resting-state fMRI study. *Front Aging Neurosci.* (2018) 10:55. doi: 10.3389/fnagi.2018.00055
25. Li X, Jia S, Zhou Z, Jin Y, Zhang X, Hou C, et al. The role of the montreal cognitive assessment (MoCA) and its memory tasks for detecting mild cognitive impairment. *Neurol Sci.* (2018) 39:1029–34. doi: 10.1007/s10072-018-3319-0
26. Zhao Q, Guo Q, Liang X, Chen M, Zhou Y, Ding D, et al. Auditory verbal learning test is superior to rey-osterrieth complex figure memory for predicting mild cognitive impairment to Alzheimer's disease. *Curr Alzheimer Res.* (2015) 12:520–6. doi: 10.2174/1567205012666150530202729
27. Muir RT, Lam B, Honjo K, Harry RD, McNeely AA, Gao FQ, et al. Trail making test elucidates neural substrates of specific poststroke executive dysfunctions. *Stroke.* (2015) 46:2755–61. doi: 10.1161/STROKEAHA.115.009936
28. Tolle KA, Rahman-Filipiak AM, Hale AC, Kitchen Andren KA, Spencer RJ. Grooved pegboard test as a measure of executive functioning. *Appl Neuropsychol Adult.* (2019) 27:414–20. doi: 10.1080/23279095.2018.1559165
29. Silva PHR, Spedo CT, Baldassarini CR, Benini CD, Ferreira DA, Barreira AA, et al. Brain functional and effective connectivity underlying the information processing speed assessed by the symbol digit modalities test. *NeuroImage.* (2019) 184:761–70. doi: 10.1016/j.neuroimage.2018.09.080
30. Zhou H, Lu W, Shi Y, Bai F, Chang J, Yuan Y, et al. Impairments in cognition and resting-state connectivity of the hippocampus in elderly subjects with type 2 diabetes. *Neurosci Lett.* (2010) 473:5–10. doi: 10.1016/j.neulet.2009.12.057
31. Diamond A. Executive functions. *Ann Rev Psychol.* (2013) 64:135–68. doi: 10.1146/annurev-psych-113011-143750
32. Jia XZ, Wang J, Sun HY, Zhang H, Liao W, Wang Z, et al. RESTplus: an improved toolkit for resting-state functional magnetic resonance imaging data processing. *Sci Bull.* (2019) 64:953–4. doi: 10.1016/j.scib.2019.05.008
33. Liu L, Li W, Zhang Y, Qin W, Lu S, Zhang Q. Weaker functional connectivity strength in patients with type 2 diabetes mellitus. *Front Neurosci.* (2017) 11:390. doi: 10.3389/fnins.2017.00390
34. Wang L, Dai Z, Peng H, Tan L, Ding Y, He Z, et al. Overlapping and segregated resting-state functional connectivity in patients with major depressive disorder with and without childhood neglect. *Hum Brain Mapp.* (2014) 35:1154–66. doi: 10.1002/hbm.22241
35. Liu D, Chen L, Duan S, Yin X, Yang W, Shi Y, et al. Disrupted balance of long- and short-range functional connectivity density in type 2 diabetes mellitus: a resting-state fMRI study. *Front Neurosci.* (2018) 12:875. doi: 10.3389/fnins.2018.00875
36. Liu D, Duan S, Zhang J, Zhou C, Liang M, Yin X, et al. Aberrant brain regional homogeneity and functional connectivity in middle-aged T2DM patients: a resting-state functional MRI study. *Front Hum Neurosci.* (2016) 10:490. doi: 10.3389/fnhum.2016.00490
37. Zhang Y, Lu S, Liu C, Zhang H, Zhou X, Ni C, et al. Altered brain activation and functional connectivity in working memory related networks in patients with type 2 diabetes: an ICA-based analysis. *Sci Rep.* (2016) 6:23767. doi: 10.1038/srep23767
38. Biessels GJ, Staekenborg S, Brunner E, Brayne C, Scheltens P. Risk of dementia in diabetes mellitus: a systematic review.

Lancet Neurol. (2006) 5:64–74. doi: 10.1016/S1474-4422(05)70284-2
39. Kitzbichler MG, Henson RN, Smith ML, Nathan PJ, Bullmore ET. Cognitive effort drives workspace configuration of human brain functional networks. *J Neurosci.* (2011) 31:8259–70. doi: 10.1523/JNEUROSCI.0440-11.2011
40. Bullmore E, Sporns O. The economy of brain network organization. *Nat Rev Neurosci.* (2012) 13:336–49. doi: 10.1038/nrn3214
41. Qin C, Liang Y, Tan X, Leng X, Lin H, Zeng H, et al. Altered whole-brain functional topological organization and cognitive function in type 2 diabetes mellitus patients. *Front Neurol.* (2019) 10:599. doi: 10.3389/fneur.2019.00599
42. Baker LD, Cross DJ, Minoshima S, Belongia D, Watson GS, Craft S. Insulin resistance and Alzheimer-like reductions in regional cerebral glucose metabolism for cognitively normal adults with prediabetes or early type 2 diabetes. *Arch Neurol.* (2011) 68:51–7. doi: 10.1001/archneurol.2010.225
43. Xia W, Wang S, Sun Z, Bai F, Zhou Y, Yang Y, et al. Altered baseline brain activity in type 2 diabetes: a resting-state fMRI study. *Psychoneuroendocrinology.* (2013) 38:2493–501. doi: 10.1016/j.psyneuen.2013.05.012
44. Hsu JL, Chen YL, Leu JG, Jaw FS, Lee CH, Tsai YF, et al. Microstructural white matter abnormalities in type 2 diabetes mellitus: a diffusion tensor imaging study. *Neuroimage.* (2012) 59:1098–105. doi: 10.1016/j.neuroimage.2011.09.041
45. Xia W, Chen YC, Ma J. Resting-state brain anomalies in type 2 diabetes: a meta-analysis. *Front Aging Neurosci.* (2017) 9:14. doi: 10.3389/fnagi.2017.00014
46. Dai W, Duan W, Alfaro FJ, Gavrieli A, Kourtelidis F, Novak V. The resting perfusion pattern associates with functional decline in type 2 diabetes. *Neurobiol Aging.* (2017) 60:192–202. doi: 10.1016/j.neurobiolaging.2017.09.004
47. Peng J, Qu H, Peng J, Luo TY, Lv FJ, Chen L, et al. Abnormal spontaneous brain activity in type 2 diabetes with and without microangiopathy revealed by regional homogeneity. *Eur J Radiol.* (2016) 85:607–15. doi: 10.1016/j.ejrad.2015.12.024
48. Fang P, An J, Tan X, Zeng LL, Shen H, Qiu S, et al. Changes in the cerebellar and cerebro-cerebellar circuit in type 2 diabetes. *Brain Res Bull.* (2017) 130:95–100. doi: 10.1016/j.brainresbull.2017.01.009
49. Guell X, Schmahmann JD, Gabrieli J, Ghosh SS. Functional gradients of the cerebellum. *eLife.* (2018) 7:e36652. doi: 10.7554/eLife.36652
50. Carulli D, Broersen R, de Winter F, Muir EM, Meskovic M, de Waal M, et al. Cerebellar plasticity and associative memories are controlled by perineuronal nets. *Procee Natl Acad Sci USA.* (2020) 117:6855–65. doi: 10.1073/pnas.1916163117
51. Sanjari Moghaddam H, Ghazi Sherbaf F, Aarabi MH. Brain microstructural abnormalities in type 2 diabetes mellitus: a systematic review of diffusion tensor imaging studies. *Front Neuroendocrinol.* (2019) 55:100782. doi: 10.1016/j.yfrne.2019.100782
52. Fang F, Lai MY, Huang JJ, Kang M, Ma MM, Li KA, et al. Compensatory hippocampal connectivity in young adults with early-stage type 2 diabetes. *J Clin Endocrinol Metab.* (2019) 104:3025–38. doi: 10.1210/jc.2018-02319
53. Liu Z, Zhang J, Zhang K, Zhang J, Li X, Cheng W, et al. Distinguishable brain networks relate disease susceptibility to symptom expression in schizophrenia. *Hum Brain Mapp.* (2018) 39:3503–15. doi: 10.1002/hbm.24190
54. Brundel M, Kappelle LJ, Biessels GJ. Brain imaging in type 2 diabetes. *Eur Neuropsychopharmacol.* (2014) 24:1967–81. doi: 10.1016/j.euroneuro.2014.01.023
55. Hoogenboom WS, Marder TJ, Flores VL, Huisman S, Eaton HP, Schneiderman JS, et al. Cerebral white matter integrity and resting-state functional connectivity in middle-aged patients with type 2 diabetes. *Diabetes.* (2014) 63:728–38. doi: 10.2337/db13-1219

Conflict of Interest: The authors declare that the research was conducted in the absence of any commercial or financial relationships that could be construed as a potential conflict of interest.

frontiers in Neurology

REVIEW
published: 12 November 2020
doi: 10.3389/fneur.2020.548568

Applications of Functional Magnetic Resonance Imaging in Determining the Pathophysiological Mechanisms and Rehabilitation of Spatial Neglect

Yuqian Zhang[1], *Yan Hua*[2] *and Yulong Bai*[1]*

[1] Department of Rehabilitation Medicine, Huashan Hospital, Fudan University, Shanghai, China, [2] Department of Rehabilitation Medicine, Huashan Hospital North, Fudan University, Shanghai, China

Functional magnetic resonance imaging (fMRI) is a neuroimaging tool which has been applied extensively to explore the pathophysiological mechanisms of neurological disorders. Spatial neglect is considered to be the failure to attend or respond to stimuli on the side of the space or body opposite a cerebral lesion. In this review, we summarize and analyze fMRI studies focused specifically on spatial neglect. Evidence from fMRI studies have highlighted the role of dorsal and ventral attention networks in the pathophysiological mechanisms of spatial neglect, and also support the concept of interhemispheric rivalry as an explanatory model. fMRI studies have shown that several rehabilitation methods can induce activity changes in brain regions implicated in the control of spatial attention. Future investigations with large study cohorts and appropriate subgroup analyses should be conducted to confirm the possibility that fMRI might offer an objective standard for predicting spatial neglect and tracking the response of brain activity to clinical treatment, as well as provide biomarkers to guide rehabilitation for patients with SN.

Keywords: functional magnetic resonance imaging, dorsal attention network, ventral attention network, interhemispheric rivalry, pathophysiological mechanisms, spatial neglect, rehabilitation

OPEN ACCESS

Edited by:
Rick M. Dijkhuizen, University Medical Center Utrecht, Netherlands

Reviewed by:
Flavia Di Pietro, The University of Sydney, Australia
Szilvia Anett Nagy, University of Pécs, Hungary
Lenny E. Ramsey, Carroll University, United States

***Correspondence:**
Yulong Bai
dr_baiyl@fudan.edu.cn

Specialty section:
This article was submitted to Applied Neuroimaging, a section of the journal Frontiers in Neurology

Received: *07 April 2020*
Accepted: *25 September 2020*
Published: *12 November 2020*

Citation:
Zhang Y, Hua Y and Bai Y (2020) Applications of Functional Magnetic Resonance Imaging in Determining the Pathophysiological Mechanisms and Rehabilitation of Spatial Neglect. Front. Neurol. 11:548568. doi: 10.3389/fneur.2020.548568

INTRODUCTION

"Spatial neglect" (SN) is a contralesional spatial bias (i.e., the failure to attend or respond to stimuli on the side of the space or body opposite the lesion) (1). It is correlated with impaired vigilance/arousal that results in delayed responses and non-spatial deficits in attentional capacity (2).

SN can occur subsequent to neurodegenerative disease (3, 4), cancer (5), trauma (6), but it occurs most commonly subsequent to stroke (7, 8). Research on patients with stroke has shown that SN occurs in 43% of right brain-lesioned patients and 20% of left brain-lesioned patients at baseline (8). At 3 months, SN continues to be present in 17% of right brain-lesioned patients and 5% of left brain-lesioned patients (8). SN negatively affects motor and cognitive function, activities of daily living (ADL), and duration of hospital stay (9–12).

SN is a heterogeneous syndrome and has several subtypes, such as perceptual vs. intentional (13), personal space vs. extra-personal space (14), or egocentric vs. allocentric representation (15). A battery of neuropsychological tests is administered to assess SN symptoms in the clinic, including conventional pencil-and-paper tests [e.g., line bisection, cancellation, copying or drawing figures, reading/writing; (16)], and ecological evaluations [e.g., Catherine Bergego Scale, Behavioral

Inattention Test, Subjective Neglect Questionnaire, Baking Tray Task, wheelchair obstacle course, ADL-based SN battery; (17, 18)]. These tests can assess various classes of SN symptoms, and different patients may show deficits in different subsets of tests.

FUNCTIONAL MAGNETIC RESONANCE IMAGING (fMRI)

fMRI is a neuroimaging tool that employs MRI to image regional, time-varying changes in neural activity (19). The blood-oxygen-level-dependent (BOLD) signal is detected in fMRI. The BOLD signal represents an indirect measure of neuronal activity through neurovascular coupling. The latter is a cascade of physiological processes linking local neuronal activity to orchestrated changes in local blood flow and blood oxygenation (20). Researchers can document specific signal changes from the entire brain in a relatively short time during a specific task or at rest, which contributes to the popularity of fMRI in neuroscience research. The increasing popularity of fMRI also derives from its non-invasive nature and excellent spatial resolution.

Task-based fMRI and resting-state fMRI are the two main types of fMRI. Task-based fMRI is acquired while the individual is instructed to perform a particular task, such as a motor task, social cognition, working memory, incentive processing, emotion processing, language processing, attention, or object location (21). Task-based fMRI is highly dependent upon the applied task, which is a minor drawback. Resting-state fMRI measures spontaneous, low-frequency fluctuations (<0.1 Hz) in the BOLD signal without a task or stimulus (22). The individual should stay still and avoid cognitive, language or motor tasks with eyes either closed or open or staring at a fixed point while data are acquired (23, 24). Widely separated (though functionally related) brain regions showing temporally correlated fluctuations constitute a brain functional network. Functional networks identified through resting-state fMRI can be identified similarly through task-based fMRI (25, 26). Also, measurements of the temporal correlation of BOLD signals between different brain regions in the resting state, called "resting-state functional connectivity," can be used to map topography between different brain networks (27, 28).

Two main limitations of fMRI impede its wide application in the clinic. First, the BOLD signal can be affected by several factors: movements or tasks during scans; temperature and technical noise of the MR system; hormonal rhythms, blood pressure and heart rate of individual; diet; time of day (23, 29). This variability in the BOLD signal affects the reliability of task-based fMRI and resting-state fMRI. Second, a lack of standardized acquisition and analytical methods also hinder its use for diagnostic purposes (30).

Abbreviations: ADL, activities of daily living; AI, anterior insula; AG, angular gyrus; BOLD, blood-oxygen-level-dependent; DAN, dorsal attention network; DMN, default mode network; FEFs, frontal eye fields; fMRI, functional magnetic resonance imaging; IFG, inferior frontal gyrus; IPL, inferior parietal lobule; IPS, intraparietal sulcus; MFG, middle frontal gyrus; MI, motor imagery; NIBS, non-invasive brain stimulation; OKS, optokinetic stimulation; PA, prismatic adaptation; PPC, posterior parietal cortex; SMG, supramarginal gyrus; SMA, supplementary motor area; SN, spatial neglect; SPL, superior parietal lobe; STS, superior temporal sulcus; STG, superior temporal gyrus; TMS, transcranial magnetic stimulation; TPJ, temporal–parietal junction; VAN, ventral attention network; VFC, ventral frontal cortex; VR, virtual reality.

PATHOPHYSIOLOGICAL MECHANISMS UNDERLYING SN

SN is dependent not only upon localized damage to specific brain structures but also the function of brain regions that are far from the local lesion (31). Brain networks are referred to sets of brain regions that contribute to the performance of a particular set of functions, or set of related tasks (32). Increasingly, fMRI studies have explored the effects of stroke on brain networks, and linked abnormalities in those networks on the behavioral deficits in SN [(31, 33, 34); **Figure 1**]. Evidence from fMRI has also demonstrated the validity of "interhemispheric rivalry mechanisms" as an explanatory model of SN [(31, 35); **Figure 1**]. The concept of interhemispheric rivalry proposed originally by Kinsbourne suggests that each hemisphere contains a processor of spatial attention for the contralateral visual field, and reciprocal transcallosal inhibition has been postulated to underlie the balance of attention toward the left vs. right visual fields (36).

Dysfunction of Attention Networks

Attention networks comprise the dorsal attention network (DAN) and ventral attention network (VAN). Dysfunction of attention networks has a critical role in SN (37–40). The DAN is composed mainly of the superior parietal lobe (SPL), intraparietal sulcus (IPS), and frontal eye fields (FEFs). The DAN is a goal-driven, "top–down" network and supports top–down endogenous attention based on prior knowledge, expectations, and current goals (38, 41, 42). The VAN mainly comprises the temporal–parietal junction (TPJ) and ventral frontal cortex (VFC). The VAN is a stimulus-driven or "bottom–up" network and is implicated in detecting task-relevant sensory events, particularly if they are unexpected (43–45). The TPJ includes the posterior sector of the superior temporal sulcus (STS) and superior temporal gyrus (STG), as well as the ventral part of the supramarginal gyrus (SMG). The VFC includes the inferior frontal gyrus (IFG) and the middle frontal gyrus (MFG) in the anterior insula (AI), and frontal operculum. If attention is reoriented to a new target, a reorienting signal from the VAN interrupts the ongoing task in the DAN, which shifts attention toward the novel source of information (46). Furthermore, the DAN contributes to the suppression of exogenous task-irrelevant information (41). Thus, except perhaps when individuals are not carrying out an ongoing task, the VAN cannot be activated by exogenous task-irrelevant stimuli, but environmental task-relevant stimuli. The posterior parietal cortex (PPC) (including the IPS and TPJ) interacts with the visual cortex for the selection of relevant targets (46).

SN is observed commonly in stroke patients with lesions restricted to the right VAN (31, 47). However, it can also occur if lesions are restricted to the component of the DAN,

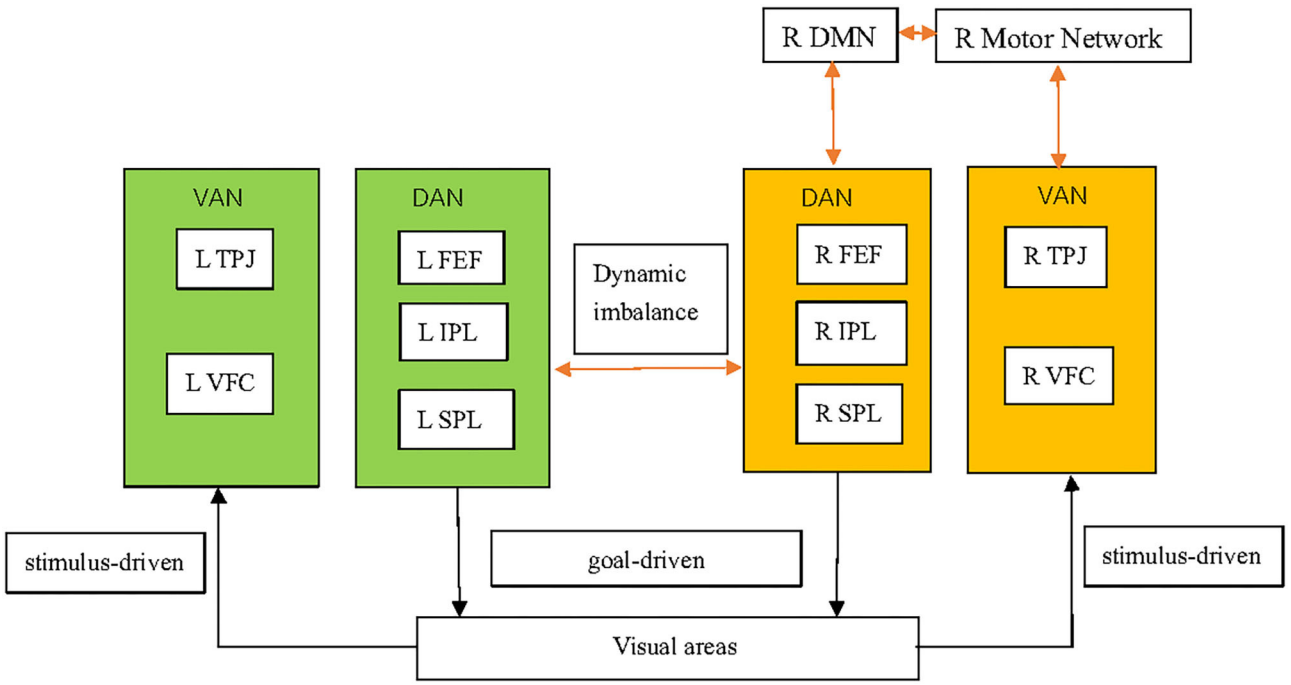

FIGURE 1 | Pathophysiological mechanisms underlying spatial neglect. The DAN, which mainly comprises the SPL, IPS, and FEFs, is a goal-driven, "top–down" network and supports top–down endogenous attention. The VAN, which mainly comprises the TPJ and VFC, is a stimulus-driven or "bottom–up" network and is implicated in detecting exogenous task-relevant stimuli. Structural damage in VAN regions can induce DAN dysfunction. A virtual lesion on the DAN induced by transcranial magnetic stimulation can exert DAN dysfunction. SN might involve not only dysfunction of the DAN and VAN, but also other brain functional networks, including the DMN and motor networks. SN patients have decreased inter-network connectivity between the VAN and motor network. SN patients also have decreased inter-network connectivity between the DAN/motor network and the DMN in the right hemisphere. Functional imbalance of brain activity in left (hyperactive) and right (hypoactive) brain regions involved in the control of spatial attention is observed in SN patients, which supports the concept of the interhemispheric-rivalry mechanism as an explanatory model. The shading in orange and green indicate, respectively, relative decreases and increases in functional activity. The orange arrows indicate decreased connectivity between networks. DAN, dorsal attention network; VAN, ventral attention network; SPL, superior parietal lobe; IPS, intraparietal sulcus; FEFs, frontal eye fields; TPJ, temporal–parietal junction; VFC, ventral frontal cortex; DMN, default mode network.

such as the IPS (48). There is a complex interaction between these two attention networks during target detection under sustained spatial attention. Lesions in parts of the VAN have been shown to evoke profound activation changes in parts of the structurally intact DAN measured by resting-state functional connectivity MRI which, in turn, correlates with SN severity in stroke patients (39, 49). The fractional amplitude of low-frequency fluctuations of the BOLD signal in resting-state fMRI in the structurally intact right SPL (as part of the DAN) is strongly correlated with the SN-related functional impairment and pathological attention bias in SN patients with structural damage to the VAN (39). Studies using task-based fMRI have found that an anatomically intact DAN (especially the IPS and SPL) of damaged hemispheres shows weak or no task-related activity during the Posner Cuing Task in SN patients with VAN lesions (31). In short, physiological dysfunction of the DAN induced by structural damage to the VAN is observed not only at rest, but also during task performance by fMRI. SN-like symptoms can be evoked temporally by transcranial magnetic stimulation (TMS) to model the virtual lesion on the dorsal right parietal cortex in healthy individuals (50). One task-based fMRI study demonstrated that TMS, as a causal perturbation approach on the IPS (a critical component of the DAN), could exert profound directional causal influences on the TPJ (a critical component of the VAN) during target detection under sustained spatial attention (51).

Increasing numbers of fMRI studies have reported that SN might involve not only attention networks but also other brain functional networks (34, 40, 52). One study on resting-state functional connectivity found that SN patients had decreased interhemispheric connectivity in the VAN and decreased inter-network connectivity between the VAN and the motor network (primary motor cortices) (52). Moreover, Baldassarre et al. found that SN in first-ever stroke patients was associated with correlated multi-network patterns of abnormal functional connectivity by resting-state fMRI (34). Specifically, the DAN and sensory–motor networks showed a loss of intra-hemispheric anti-correlation with the default mode network (DMN) in the right hemisphere (34). Also, improvement of attention deficits was correlated with a restoration of the normal anti-correlation between dorsal attention/motor regions and the DMN, as assessed by resting-state functional connectivity, particularly in the damaged hemisphere (40). The DMN encompasses a group of discrete, bilateral, symmetrical

and functionally connected brain regions, in the medial and lateral parietal, medial prefrontal, as well as medial and lateral temporal cortices (53). It exhibits higher levels of activity during relaxed states than during performance of externally oriented cognitive tasks (54). Another study based on resting-state fMRI focused specifically on attention deficits and motor deficits. The authors demonstrated that behavioral attention deficits were associated significantly more with decreased interhemispheric functional connectivity of the DAN than with motor networks, whereas motor deficits were associated significantly more with decreased interhemispheric functional connectivity of motor networks than with the DAN (33).

Model of Interhemispheric Rivalry

Supporting evidence for the model of interhemispheric rivalry stems from clinical observation of a patient who suffered from sequential strokes in both hemispheres with severe SN after a first right-sided parietal infarct and abrupt disappearance of SN after a second left-sided frontal infarct (55). Emerging evidence from fMRI supports the validity of interhemispheric-rivalry mechanisms as an explanatory model of SN (31, 34, 35, 40, 49).

Functional imbalance of task-evoked brain activity in the left (hyperactive) and right (hypoactive) dorsal parietal cortex has been observed in patients with SN after right frontal damage, even though these areas were structurally intact (31). The hyperactivity of the unaffected hemisphere might result from a loss of inter-hemispheric inhibition, which may be reflected by interhemispheric functional connectivity using resting-state functional connectivity MRI. Furthermore, an imbalance in the interhemispheric coherence of regions involved in the control of spatial attention (as measured by resting-state functional connectivity MRI) correlates with deficits in spatial attention (35). One study based on functional connectivity fMRI acquired fMRI data while study participants undertook an event-related attention task, but with the deterministic task-evoked effects removed, to conduct functional connectivity analyses. The authors found that interhemispheric connectivity in the posterior IPS was disrupted acutely but recovered at the chronic stage. This finding was in accordance with the observation that the right posterior IPS was less recruited than the left posterior IPS at the acute stage, and that they returned to balanced activation at the chronic stage in patients with SN (49). Also, improvement of attention deficits was closely related to increases in inter-hemispheric functional connectivity between regions of the dorsal attention, motor, visual, and auditory networks as assessed by resting-state functional connectivity MRI (40). In conclusion, SN involves the relative hyperactivity of the unaffected hemisphere due to release from reciprocal inhibition by the affected hemisphere. Also, improvement of attention deficits is correlated with rebalance in brain regions implicated in the control of spatial attention between the unaffected and affected hemispheres, which suggests the validity of the interhemispheric-rivalry model.

TMS can deactivate the brain cortex temporally to model the virtual lesion and to induce SN-like behaviors in healthy people. The validity of interhemispheric-rivalry mechanisms has also been supported by studies on task-based fMRI and resting-state fMRI using TMS to induce SN-like behaviors in healthy individuals (56, 57). Petitet et al. used TMS to transiently inhibit activity in the right caudal part of the angular gyrus at the junction with the IPS, and assessed the changes of functional brain activity by task-based fMRI during a bilateral target-detection task (56). They demonstrated that the direction of TMS-induced attentional bias and changes in brain activity (i.e., the leftward shift in parietal activity and rightward shift in attentional bias) was consistent, which suggested that the balance of functional brain activity between the left and right parietal cortex determined the spatial allocation of attention (56). Wang and colleagues, using repetitive TMS and resting-state functional connectivity fMRI, indicated that a TMS-induced unbalanced interaction between the interhemispheric top–down network of posterior SPL and V1 correlated with lateralization of visuospatial attention in healthy individuals (57). The interhemispheric-rivalry model has also been supported by evidence showing that behavioral deficits of SN patients were improved when TMS over the left PPC or left frontal cortex was employed to normalize the over-excitability of the contralesional hemisphere for interhemispheric rebalance (58, 59).

REHABILITATION METHODS

SN affects the rehabilitation of other stroke-related symptoms negatively, and is associated with reduced functional independence in ADL (60). Development of efficacious treatment strategies for SN provides an important opportunity to improve the functional outcome of stroke (60–62). Consensus on the most efficacious therapy for SN is lacking. However, several promising interventions have been proposed to improve SN symptoms: prismatic adaptation (PA), non-invasive brain stimulation (NIBS), motor imagery (MI), optokinetic stimulation (OKS) and virtual reality (VR) (61–76). Besides, there is a low level of evidence in favor of mirror therapy, neck-muscle vibration, family involvement, motor activation and spatial cueing for SN (77). These methods can be classified into three main types: top–down, bottom–up, and modulation of intracerebral inhibition processes [i.e., NIBS; (77)]. Top–down methods are based on a voluntary effort of the patient following a therapist's instructions, such as MI (77). Bottom–up methods are based on the patient's sensory environment or visuomotor adaptation, such as PA and OKS (61, 71). NIBS–TMS and transcranial direct current stimulation (tDCS), which were developed on a model of interhemispheric competition, can also ameliorate the behavioral deficits of SN by reducing the activity of the unaffected hemisphere or by increasing the activity of the affected hemisphere (78, 79). fMRI has been used as an additional assessment of existing therapy strategies to evaluate changes in the neural activity of the brain cortex. In this review, we focus on changes in fMRI

signals induced by the promising rehabilitation methods mentioned above.

PA

PA can be used to alleviate SN (64, 71, 80–87). PA is dependent upon the mismatch between the perceived position of a target seen through prismatic goggles and its real position relative to the body (68). PA includes two adaptive processes: recalibration (which contributes to early error correction) and spatial realignment (which contributes to after-effect development). In a typical protocol for PA, individuals wear prismatic goggles with a rightward deviation of the visual image and perform tasks to reach visual targets. At first, participants will miss the real target, pointing erroneously in the direction of prismatic displacement. With repeated pointing movements, participants can adapt gradually to the prismatic displacement and correct their errors to reach the real target. After removal of the prisms, participants exhibit pointing errors in the direction opposite to the prismatic shift, which denotes the adaptation "after-effect" (88).

fMRI studies have investigated the effect of PA on brain activation in healthy people to determine visuomotor plasticity, which can indirectly explain neural substrates underlying the therapeutic benefits of PA. One study using resting-state fMRI explored transient changes of resting-state functional connectivity in the right DAN induced by a session of pointing tasks with a prism in healthy people. The authors found that a rightward prism modulated resting-state functional connectivity between the right IPS and FEFs belonging to the right DAN and functional connectivity between the right anterior cingulate cortex and FEFs (89). Furthermore, Wilf et al. discovered that PA-induced functional modulation was not limited within attention networks, but was characterized instead by enhancement of the decoupling between the DMN and DAN/VAN. Their findings were based on comparison of patterns of resting-state functional connectivity before and after a 3-min pointing task with a rightward-shifting prism in healthy individuals (90). The cerebellum is also involved in visuomotor adaptation (91–94).

Some fMRI studies investigated changes in brain activity induced by PA to directly explain neural substrates underlying the therapeutic effect of PA on patients with SN. One task-based fMRI study examined the effect of PA by comparing brain activity during three tasks (bisection, search, and memory) before and after a single PA session (95). The authors found increased activation in the bilateral PPC, mid-frontal cortex, and occipital cortex during bisection and visual-searching tasks accompanied by significant behavioral improvement (95). Another study on task-based fMRI using a detection task reported that the PA-induced alleviation of SN predominately involved the left superior temporal region (64). The fMRI studies mentioned above suggest that the beneficial effect of PA on SN is derived from modulation of cortical regions implicated in spatial cognition in damaged and undamaged hemispheres. Furthermore, the effect of PA on SN is dependent upon the site of brain damage. Compared with SN patients with parietal lesions, PA can induce a higher level of improvement in SN patients with frontal lesions, accompanied by enhanced activity of posterior parietal and mid-frontal areas bilaterally, as measured by task-based fMRI during bisection and search tasks (96). Differences in brain plasticity induced by PA were documented among the fMRI studies mentioned above. More fMRI studies in SN patients with different lesion sites and subtypes of SN are needed to explain the underlying neural mechanisms of PA.

OKS

OKS is a promising therapeutic method that can induce enduring and functionally relevant positive effects in patients with right-hemisphere stroke and SN (97). OKS requires patients to perform smooth-pursuit eye movements following visual stimuli that move coherently from the ipsilesional to the contralesional side on a screen. OKS can lead to an exogenously triggered directing of spatial attention to the neglected side.

Several fMRI studies in healthy individuals have provided evidence that OKS can induce almost symmetrical activations in multiple brain regions, including frontoparietal regions (FEFs, IPS) as well as the primary and associated visual cortices, insula, basal ganglia, cerebellum, and brainstem in both hemispheres independent of the stimulus direction (98–100).

Some fMRI studies investigating the neural mechanisms of OKS in SN patients have shown inconsistent results. One study based on task-based fMRI found that OKS led to increased neural activity bilaterally in the middle frontal gyrus and precuneus. In addition, OKS activated the cingulate gyrus, middle temporal gyrus, angular gyrus and occipital cortex in the left hemisphere as measured by task-based fMRI during a spatial-attention task, accompanied by amelioration of SN symptoms in SN patients suffering from chronic right-hemisphere lesions (97). A compensatory recruitment of left-hemisphere areas induced by OKS contributes to SN amelioration in stroke patients with chronic right-hemisphere lesions. In patients with an acute right-hemisphere stroke, leftward OKS led to mostly bilateral activations in the visual cortex (V1–V4), IPS, FEFs, supplementary eye fields and thalamus, as measured by task-based fMRI during OKS, which was negatively correlated with behavioral impairment (101). The differences in neural activity induced by OKS among the two fMRI studies mentioned above might be because the study participants were in different stages of stroke.

MI

MI involves the mental execution of an action in the absence of movement. MI can be used as a complement to physical training for stroke patients (102, 103).

MI can recruit brain networks consisting of premotor regions [e.g., IFG and supplementary motor area (SMA)], parietal regions (e.g., SMG, IPL, SPL), and subcortical regions (e.g., putamen and cerebellum) in healthy people (104, 105). However, few scholars have investigated the changes in brain activity induced by MI in SN patients. One pilot study examined neuronal activation by task-based fMRI in patients with chronic SN with right-hemispheric stroke during MI whereby patients had to imagine touching each of their four fingers with the tip of the thumb (106).

The authors found that the left primary somatosensory, premotor cortices and SMA were activated during MI of the unaffected hand. However, MI of the affected hand was related to activations in the left premotor cortex, left AI, left dorsolateral prefrontal cortex, medial SMA, right rolandic operculum and right SPL (106). The authors also revealed that SN severity was positively related to brain activation in the SMA during MI of the affected hand (106). Although the results should be treated with caution due to absence of a matched control group and small sample size, they suggested that MI can activate functionally relevant brain areas in SN patients.

TMS

Repetitive transcranial magnetic stimulation (rTMS) is a method of NIBS. rTMS may be useful for exploring the SN pathophysiology and ameliorating its symptoms (107). Low-frequency rTMS ($\leq$1 Hz) lowers cortical excitability, whereas high-frequency rTMS ($\geq$10 Hz) increases cortical excitability, likely by modulating neurotransmitters such as gamma-aminobutyric acid and dopamine. Theta burst stimulation (TBS), a variant of rTMS, involves application of short trains of stimuli at high frequency repeated at intervals of 200 ms (108). TBS can be subclassified as intermittent theta-burst stimulation (iTBS) and continuous TBS (cTBS) based on the pattern of stimulation (109). iTBS influences motor-evoked potentials to produce long-term potentiation, whereas cTBS induces prolonged depression of brain activity.

The mechanism underlying SN might involve the relative hyperactivity of the unaffected hemisphere due to release from reciprocal inhibition by the affected hemisphere (35, 49). Thus, inhibitory low-frequency rTMS or cTBS over the unaffected PPC could improve SN (78, 79). One case report revealed that cTBS applied over the left PPC improved SN symptoms in one patient with traumatic brain injury (110). That observation was associated with decreased excitability of the PPC–M1 connections in the left hemisphere and bilateral increased functional connectivity in the frontoparietal network shown by resting-state fMRI (110). Thus, the authors considered that cTBS could have partially reduced the interhemispheric imbalance due to a decrease in the hyper-excitability of the left PPC-M1 connections and increased connectivity in frontal-parietal networks.

Several studies have explored the effect of high-frequency rTMS or iTBS on SN. A double-blind, sham-controlled study compared the therapeutic effect of low- and high-frequency rTMS applied over the PPC. The authors found that high-frequency rTMS over the lesioned PPC improved SN significantly more than low-frequency rTMS over the non-lesioned PPC in patients with acute stroke (111). Cao and colleagues applied iTBS to the left dorsal lateral prefrontal cortex in patients with right-hemisphere stroke and SN (112). They found that increasing the activity of the left dorsal lateral prefrontal cortex through iTBS could ameliorate SN symptoms (112). They also found that iTBS at a resting motor threshold of 80% induced a large-scale reduction in the extent of resting-state functional connectivity, mostly in right attention networks, and more significant amelioration of behavioral performance compared with iTBS at a resting motor threshold of 40% (112).

VR

VR is a computer-based, multisensory, stimulating, and interactive environment that occurs in real-time whereby the individual is engaged in activities that appear similar to real-world objects and events (113, 114). VR combines top–down and bottom–up treatments for SN. RehAtt^{TM}, a novel multisensory VR device, can combine scanning training in a three-dimensional game with intense multisensory stimulation (70). Fordell et al. found that 5-week RehAtt training improved spatial attention and ADL in older patients with chronic SN (70).

A pilot study used task-based fMRI to evaluate the change in brain activity during the Posner Cuing Task before and after RehAtt intervention in patients with chronic SN (115). They demonstrated that 5-week RehAtt training improved performance in patients with chronic SN and increased their brain activity during cue-induced focus of attention in the prefrontal cortex (e.g., dorsolateral prefrontal cortex and anterior cingulate cortex), middle and superior temporal gyrus, but showed no training effects during target presentations (115). Another pilot study revealed that 5-week iRehAtt intervention improved SN symptoms, and increased inter-hemispheric resting-state functional connectivity in the DAN between the right FEF and left IPS in patients with chronic SN as measured by resting-state fMRI (116). The studies mentioned above suggest that VR is a promising approach to post-stroke management of SN due to changes in relative brain activities. However, a more extensive prospective controlled study is needed to explain the different results among studies, and to obtain a potential marker that would allow a priori identification of patients as responders or non-responders for VR training.

CONCLUSIONS

fMRI opens the way for greater understanding of the pathophysiological mechanisms underlying SN and potentially improves our ability to evaluate the effect of rehabilitation methods. fMRI studies have demonstrated that SN might result from abnormal changes in attention networks and other brain functional networks, including the DMN and motor network. Several promising interventions (PA, NIBS, MI, OKS, and VR) could modulate the cortical regions implicated in spatial cognition measured by fMRI, which might contribute to a beneficial effect to the clinical presentation of SN.

However, differences between fMRI studies have been documented, and caution needs to be taken in utilizing their conclusions due to three main reasons. First, SN is a heterogeneous syndrome and can be fractionated into several subtypes. However, fMRI studies have employed mostly small study cohorts and included patients were barely divided into different subgroups of SN. Second, task-based fMRI is highly dependent upon the applied task during scans, but task-based fMRI studies have used different tasks while fMRI is acquired. Third, acquisition and analytical methods of fMRI influence its results. Thus, fMRI cannot yet offer an objective standard for

diagnosing or predicting SN in the clinic. fMRI can be used to track the response of SN to various treatments in clinical trials, but it cannot provide a biomarker to determine which treatment is most appropriate for a specific subtype of SN in the clinic.

Prospective controlled studies or randomized controlled trials of large sample size, appropriate subgroup analyses, as well as standard acquisition and analytical methods of fMRI should be conducted. In this way, fMRI might prognosticate the risk of SN, track its response of brain activity to treatment, and provide biomarkers to guide rehabilitation for patients with SN.

AUTHOR CONTRIBUTIONS

YZ wrote the first draft. YB and YH provided critical revisions. All authors contributed to the article and approved the submitted version.

FUNDING

This study was supported financially by the Natural Science Foundation of China (No. 81871841) and the hospital-level start-up foundation of Huashan Hospital, Fudan University (No. 2020QD016).

REFERENCES

1. Halligan PW, Marshall JC, Wade DT. Visuospatial neglect: underlying factors and test sensitivity. *Lancet.* (1989) 2:908. doi: 10.1016/S0140-6736(89)91561-4
2. Husain M, Rorden C. Non-spatially lateralized mechanisms in hemispatial neglect. *Nat Rev Neurosci.* (2003) 4:26–36. doi: 10.1038/nrn1005
3. Zilli EM, Heilman KM. Allocentric spatial neglect with posterior cortical atrophy. *Neurocase.* (2014) 21:190–7. doi: 10.1080/13554794.2013.878731
4. Andrade K, Samri D, Sarazin M, de Souza LC, Cohen L, Thiebaut DSM, et al. Visual neglect in posterior cortical atrophy. *Bmc Neurol.* (2010) 10:68. doi: 10.1186/1471-2377-10-68
5. Emanuele B, Santini B, Talacchi A, Gerosa M, Savazzi S. Pre- and post-operative assessment of visuo-spatial functions in right hemisphere tumour patients: a pilot study. *J Neuro-Oncol.* (2012) 108:261–7. doi: 10.1007/s11060-012-0820-9
6. Chen P, Ward I, Khan U, Liu Y, Hreha K. Spatial neglect hinders success of inpatient rehabilitation in individuals with traumatic brain injury. *Neurorehab Neural Re.* (2015) 30:451–60. doi: 10.1177/1545968315604397
7. Kamtchum Tatuene J, Allali G, Saj A, Bernati T, Sztajzel R, Pollak P, et al. Incidence, risk factors and anatomy of peripersonal visuospatial neglect in acute stroke. *Eur Neurol.* (2016) 75:157–63. doi: 10.1159/000444709
8. Ringman JM, Saver JL, Woolson RF, Clarke WR, Adams HP. Frequency, risk factors, anatomy, and course of unilateral neglect in an acute stroke cohort. *Neurology.* (2004) 63:468–74. doi: 10.1212/01.WNL.0000133011.10689.CE
9. Chen P, Hreha K, Kong Y, Barrett AM. Impact of spatial neglect on stroke rehabilitation: evidence from the setting of an inpatient rehabilitation facility. *Arch Phys Med Rehab.* (2015) 96:1458–66. doi: 10.1016/j.apmr.2015.03.019
10. Spaccavento S, Cellamare F, Falcone R, Loverre A, Nardulli R. Effect of subtypes of neglect on functional outcome in stroke patients. *Ann Phys Rehabilit Med.* (2017) 60:376–81. doi: 10.1016/j.rehab.2017.07.245
11. Bosma MS, Nijboer TCW, Caljouw MAA, Achterberg WP. Impact of visuospatial neglect post-stroke on daily activities, participation and informal caregiver burden: a systematic review. *Ann Phys Rehabilit Med.* (2019) 63:344–58. doi: 10.1016/j.rehab.2019.05.006
12. Vanbellingen T, Ottiger B, Maaijwee N, Pflugshaupt T, Bohlhalter S, Müri RM, et al. Spatial neglect predicts upper limb use in the activities of daily living. *Cerebrovasc Dis.* (2017) 44:122–7. doi: 10.1159/000477500
13. Bisiach E, Geminiani G, Berti A, Rusconi Ml. Perceptual and premotor factors of unilateral neglect. *Neurology.* (1990) 40:1278–81. doi: 10.1212/WNL.40.8.1278
14. Committeri G, Pitzalis S, Galati G, Patria F, Pelle G, Sabatini U, et al. Neural bases of personal and extrapersonal neglect in humans. *Brain.* (2007) 130:431–41. doi: 10.1093/brain/awl265
15. Chechlacz M, Rotshtein P, Roberts KL, Bickerton W, Lau JKL, Humphreys GW. The prognosis of allocentric and egocentric neglect: evidence from clinical scans. *PLoS ONE.* (2012) 7:e47821. doi: 10.1371/journal.pone.0047821
16. Saj A, Verdon V, Vocat R, Vuilleumier P. "The anatomy underlying acute versus chronic spatial neglect" also depends on clinical tests. *Brain.* (2012) 135(Pt 2):e207. doi: 10.1093/brain/awr227
17. Pitteri M, Chen P, Passarini L, Albanese S, Meneghello F, Barrett AM. Conventional and functional assessment of spatial neglect: clinical practice suggestions. *Neuropsychology.* (2018) 32:835–42. doi: 10.1037/neu0000469
18. Azouvi P. The ecological assessment of unilateral neglect. *Ann Phys Rehabilit Med.* (2017) 60:186–90. doi: 10.1016/j.rehab.2015.12.005
19. Glover GH. Overview of functional magnetic resonance imaging. *Neurosurg Clin N Am.* (2011) 22:133–9. doi: 10.1016/j.nec.2010.11.001
20. Hillman EMC. Coupling mechanism and significance of the BOLD signal: a status report. *Annu Rev Neurosci.* (2014) 37:161–81. doi: 10.1146/annurev-neuro-071013-014111
21. Turner BO, Paul EJ, Miller MB, Barbey AK. Small sample sizes reduce the replicability of task-based fMRI studies. *Commun Biol.* (2018) 1:62. doi: 10.1038/s42003-018-0073-z
22. Lee MH, Smyser CD, Shimony JS. Resting-state fMRI: a review of methods and clinical applications. *Am J Neuroradiol.* (2013) 34:1866–72. doi: 10.3174/ajnr.A3263
23. Specht K. Current challenges in translational and clinical fMRI and future directions. *Front Psychiatry.* (2020) 10:924. doi: 10.3389/fpsyt.2019.00924
24. Lv H, Wang Z, Tong E, Williams LM, Zaharchuk G, Zeineh M, et al. Resting-state functional MRI: everything that nonexperts have always wanted to know. *Am J Neuroradiol.* (2018) 39:1390–9. doi: 10.3174/ajnr.A5527
25. Kristo G, Rutten G, Raemaekers M, de Gelder B, Rombouts SARB, Ramsey NF. Task and task-free FMRI reproducibility comparison for motor network identification. *Hum Brain Mapp.* (2014) 35:340–52. doi: 10.1002/hbm.22180
26. Fornito A, Bullmore ET. What can spontaneous fluctuations of the blood oxygenation-level-dependent signal tell us about psychiatric disorders? *Curr Opin Psychiatr.* (2010) 23:239–49. doi: 10.1097/YCO.0b013e328337d78d
27. Gordon EM, Laumann TO, Adeyemo B, Huckins JF, Kelley WM, Petersen SE. Generation and evaluation of a cortical area parcellation from resting-state correlations. *Cereb Cortex.* (2016) 26:288–303. doi: 10.1093/cercor/bhu239
28. Siegel JS, Shulman GL, Corbetta M. Measuring functional connectivity in stroke: approaches and considerations. *J Cereb Blood Flow Metab.* (2017) 37:2665–78. doi: 10.1177/0271678X17709198
29. Herting MM, Gautam P, Chen Z, Mezher A, Vetter NC. Test-retest reliability of longitudinal task-based fMRI: implications for developmental studies. *Dev Cogn Neuros-Neth.* (2018) 33:17–26. doi: 10.1016/j.dcn.2017.07.001
30. O'Connor EE, Zeffiro TA. Why is clinical fMRI in a resting state? *Front Neurol.* (2019) 10:420. doi: 10.3389/fneur.2019.00420
31. Corbetta M, Kincade MJ, Lewis C, Snyder AZ, Sapir A. Neural basis and recovery of spatial attention deficits in spatial neglect. *Nat Neurosci.* (2005) 8:1603–10. doi: 10.1038/nn1574
32. Petersen SE, Sporns O. Brain networks and cognitive architectures. *Neuron.* (2015) 88:207–19. doi: 10.1016/j.neuron.2015.09.027
33. Baldassarre A, Ramsey L, Rengachary J, Zinn K, Siegel JS, Metcalf NV, et al. Dissociated functional connectivity profiles for motor and attention deficits in acute right-hemisphere stroke. *Brain.* (2016) 139:2024–38. doi: 10.1093/brain/aww107
34. Baldassarre A, Ramsey L, Hacker CL, Callejas A, Astafiev SV, Metcalf NV, et al. Large-scale changes in network interactions as a physiological signature of spatial neglect. *Brain.* (2014) 137(Pt 12):3267–83. doi: 10.1093/brain/awu297

35. Carter AR, Astafiev SV, Lang CE, Connor LT, Rengachary J, Strube MJ, et al. Resting inter-hemispheric fMRI connectivity predicts performance after stroke. *Ann Neurol.* (2010) 3:365–75. doi: 10.1002/ana.21905
36. Kinsbourne M. Hemi-neglect and hemisphere rivalry. *Adv Neurol.* (1977) 18:41–9.
37. Corbetta M, Shulman GL. Spatial neglect and attention networks. *Annu Rev Neurosci.* (2011) 34:569–99. doi: 10.1146/annurev-neuro-061010-113731
38. Ptak R, Schnider A. The attention network of the human brain: relating structural damage associated with spatial neglect to functional imaging correlates of spatial attention. *Neuropsychologia.* (2011) 49:3063–70. doi: 10.1016/j.neuropsychologia.2011.07.008
39. Machner B, von der Gablentz J, Gottlich M, Heide W, Helmchen C, Sprenger A, et al. Behavioral deficits in left hemispatial neglect are related to a reduction of spontaneous neuronal activity in the right superior parietal lobule. *Neuropsychologia.* (2020) 138:107356. doi: 10.1016/j.neuropsychologia.2020.107356
40. Ramsey LE, Siegel JS, Baldassarre A, Metcalf NV, Zinn K, Shulman GL, et al. Normalization of network connectivity in hemispatial neglect recovery. *Ann Neurol.* (2016) 80:127–41. doi: 10.1002/ana.24690
41. Lanssens A, Pizzamiglio G, Mantini D, Gillebert CR. Role of the dorsal attention network in distracter suppression based on features. *Cogn Neurosci.* (2020) 11:37–46. doi: 10.1080/17588928.2019.1683525
42. Lunven M, Bartolomeo P. Attention and spatial cognition: neural and anatomical substrates of visual neglect. *Ann Phys Rehabil Med.* (2017) 60:124–9. doi: 10.1016/j.rehab.2016.01.004
43. Fox MD, Corbetta M, Snyder AZ, Vincent JL, Raichle ME. Spontaneous neuronal activity distinguishes human dorsal and ventral attention systems. *Proc Natl Acad Sci USA.* (2006) 103:10046–51. doi: 10.1073/pnas.0604187103
44. DiQuattro NE, Sawaki R, Geng JJ. Effective connectivity during feature-based attentional capture: evidence against the attentional reorienting hypothesis of TPJ. *Cereb Cortex.* (2014) 24:3131–41. doi: 10.1093/cercor/bht172
45. Shulman GL, Astafiev SV, Franke D, Pope DLW, Snyder AZ, McAvoy MP, et al. Interaction of stimulus-driven reorienting and expectation in ventral and dorsal frontoparietal and basal ganglia-cortical networks. *J Neurosci.* (2009) 29:4392–407. doi: 10.1523/JNEUROSCI.5609-08.2009
46. Corbetta M, Patel G, Shulman GL. The reorienting system of the human brain: from environment to theory of mind. *Neuron.* (2008) 58:306–24. doi: 10.1016/j.neuron.2008.04.017
47. Verdon V, Schwartz S, Lovblad KO, Hauert CA, Vuilleumier P. Neuroanatomy of hemispatial neglect and its functional components: a study using voxel-based lesion-symptom mapping. *Brain.* (2010) 133(Pt 3):880–94. doi: 10.1093/brain/awp305
48. Gillebert CR, Mantini D, Thijs V, Sunaert S, Dupont P, Vandenberghe R. Lesion evidence for the critical role of the intraparietal sulcus in spatial attention. *Brain.* (2011) 134:1694–709. doi: 10.1093/brain/awr085
49. He BJ, Snyder AZ, Vincent JL, Epstein A, Shulman GL, Corbetta M. Breakdown of functional connectivity in frontoparietal networks underlies behavioral deficits in spatial neglect. *Neuron.* (2007) 53:905–18. doi: 10.1016/j.neuron.2007.02.013
50. Hilgetag CC, Pascual-Leone A, Théoret H. Enhanced visual spatial attention ipsilateral to rTMS-induced 'virtual lesions' of human parietal cortex. *Nat Neurosci.* (2001) 4:953–7. doi: 10.1038/nn0901-953
51. Leitao J, Thielscher A, Tunnerhoff J, Noppeney U. Concurrent TMS-fMRI reveals interactions between dorsal and ventral attentional systems. *J Neurosci.* (2015) 35:11445–57. doi: 10.1523/JNEUROSCI.0939-15.2015
52. Barrett AM, Boukrina O, Saleh S. Ventral attention and motor network connectivity is relevant to functional impairment in spatial neglect after right brain stroke. *Brain Cogn.* (2019) 129:16–24. doi: 10.1016/j.bandc.2018.11.013
53. Raichle ME. The brain's default mode network. *Annu Rev Neurosci.* (2015) 38:433–47. doi: 10.1146/annurev-neuro-071013-014030
54. Buckner RL, Andrews-Hanna JR, Schacter DL. The brain's default network. *Ann Ny Acad Sci.* (2008) 1124:1–38. doi: 10.1196/annals.1440.011
55. Vuilleumier P, Hester D, Assal G, Regli F. Unilateral spatial neglect recovery after sequential strokes. *Neurology.* (1996) 46:184–9. doi: 10.1212/WNL.46.1.184
56. Petitet P, Noonan MP, Bridge H, O Reilly JX, O Shea J. Testing the inter-hemispheric competition account of visual extinction with combined TMS/fMRI. *Neuropsychologia.* (2015) 74:63–73. doi: 10.1016/j.neuropsychologia.2015.04.021
57. Wang J, Tian Y, Wang M, Cao L, Wu H, Zhang Y, et al. A lateralized top-down network for visuospatial attention and neglect. *Brain Imaging Behav.* (2016) 10:1029–37. doi: 10.1007/s11682-015-9460-y
58. Koch G, Oliveri M, Cheeran B, Ruge D, Gerfo EL, Salerno S, et al. Hyperexcitability of parietal-motor functional connections in the intact left-hemisphere of patients with neglect. *Brain.* (2008) 131:3147–55. doi: 10.1093/brain/awn273
59. Oliveri M, Rossini PM, Traversa R, Cicinelli P, Filippi MM, Pasqualetti P, et al. Left frontal transcranial magnetic stimulation reduces contralesional extinction in patients with unilateral right brain damage. *Brain.* (1999) 122 (Pt 9):1731–9. doi: 10.1093/brain/122.9.1731
60. Barrett AM, Houston KE. Update on the clinical approach to spatial neglect. *Curr Neurol Neurosci.* (2019) 19:25. doi: 10.1007/s11910-019-0940-0
61. Gammeri R, Iacono C, Ricci R, Salatino A. Unilateral spatial neglect after stroke: current insights. *Neuropsych Dis Treat.* (2020) 16:131–52. doi: 10.2147/NDT.S171461
62. Evald L, Wilms IL, Nordfang M. Treatment of spatial neglect in clinical practice: a nationwide survey. *Acta Neurol Scand.* (2019) 141:81–9. doi: 10.1111/ane.13179
63. Salazar A, Vaz PG, Marchese RR, Stein C, Pinto C, Pagnussat AS. Noninvasive brain stimulation improves hemispatial neglect after stroke: a systematic review and meta-analysis. *Arch Phys Med Rehabil.* (2018) 99:355–66. doi: 10.1016/j.apmr.2017.07.009
64. Crottaz-Herbette S, Fornari E, Notter MP, Bindschaedler C, Manzoni L, Clarke S. Reshaping the brain after stroke: the effect of prismatic adaptation in patients with right brain damage. *Neuropsychologia.* (2017) 104:54–63. doi: 10.1016/j.neuropsychologia.2017.08.005
65. Cotoi A, Mirkowski M, Iruthayarajah J, Anderson R, Teasell R. The effect of theta-burst stimulation on unilateral spatial neglect following stroke: a systematic review. *Clin Rehabil.* (2019) 33:183–94. doi: 10.1177/0269215518804018
66. Kashiwagi FT, El DR, Gomaa H, Gawish N, Suzumura EA, Da ST, et al. Noninvasive brain stimulations for unilateral spatial neglect after stroke: a systematic review and meta-analysis of randomized and nonrandomized controlled trials. *Neural Plast.* (2018) 2018:1638763. doi: 10.1155/2018/1638763
67. Dionísio A, Duarte IC, Patrício M, Castelo-Branco M. Transcranial magnetic stimulation as an intervention tool to recover from language, swallowing and attentional deficits after stroke: a systematic review. *Cerebrovasc Dis.* (2018) 46:178–85. doi: 10.1159/000494213
68. Gammeri R, Turri F, Ricci R, Ptak R. Adaptation to virtual prisms and its relevance for neglect rehabilitation: a single-blind dose-response study with healthy participants. *Neuropsychol Rehabil.* (2018) 30:753–66. doi: 10.1080/09602011.2018.1502672
69. Ogourtsova T, Souza Silva W, Archambault PS, Lamontagne A. Virtual reality treatment and assessments for post-stroke unilateral spatial neglect: a systematic literature review. *Neuropsychol Rehabil.* (2017) 27:409–54. doi: 10.1080/09602011.2015.1113187
70. Fordell H, Bodin K, Eklund A, Malm J. RehAtt - scanning training for neglect enhanced by multi-sensory stimulation in Virtual Reality. *Top Stroke Rehabil.* (2016) 23:191–9. doi: 10.1080/10749357.2016.1138670
71. Spaccavento S, Cellamare F, Caffario E, Loverre A, Craca A. Efficacy of visual-scanning training and prism adaptation for neglect rehabilitation. *Appl Neuropsychol Adult.* (2016) 23:313–21. doi: 10.1080/23279095.2015.1038386
72. Wang W, Ji X, Ni J, Ye Q, Zhang S, Chen W, et al. Visual spatial attention training improve spatial attention and motor control for unilateral neglect patients. *CNS Neurol Disord Drug Targets.* (2015) 14:1277–82. doi: 10.2174/1871527315666151111122926
73. Liu K, Hanly J, Fahey P, Fong S, Bye R. A systematic review and meta-analysis of rehabilitative interventions for unilateral spatial neglect and hemianopia poststroke from 2006 through 2016. *Arch Phys Med Rehabil.* (2019) 100:956–79. doi: 10.1016/j.apmr.2018.05.037

74. De Luca R, Lo BV, Leo A, Russo M, Aragona B, Leonardi S, et al. Use of virtual reality in improving poststroke neglect: promising neuropsychological and neurophysiological findings from a case study. *Appl Neuropsychol Adult.* (2019) 26:96–100. doi: 10.1080/23279095.2017.1363040
75. Pedroli E, Serino S, Cipresso P, Pallavicini F, Riva G. Assessment and rehabilitation of neglect using virtual reality: a systematic review. *Front Behav Neurosci.* (2015) 9:226. doi: 10.3389/fnbeh.2015.00226
76. Klinke ME, Hafsteinsdottir TB, Hjaltason H, Jonsdottir H. Ward-based interventions for patients with hemispatial neglect in stroke rehabilitation: a systematic literature review. *Int J Nurs Stud.* (2015) 52:1375–403. doi: 10.1016/j.ijnurstu.2015.04.004
77. Azouvi P, Jacquin-Courtois S, Luauté J. Rehabilitation of unilateral neglect: Evidence-based medicine. *Ann Phys Rehabilit Med.* (2017) 60:191–7. doi: 10.1016/j.rehab.2016.10.006
78. Nyffeler T, Vanbellingen T, Kaufmann BC, Pflugshaupt T, Bauer D, Frey J, et al. Theta burst stimulation in neglect after stroke: functional outcome and response variability origins. *Brain.* (2019) 142:992–1008. doi: 10.1093/brain/awz029
79. Yang W, Liu T, Song X, Zhang Y, Li Z, Cui Z, et al. Comparison of different stimulation parameters of repetitive transcranial magnetic stimulation for unilateral spatial neglect in stroke patients. *J Neurol Sci.* (2015) 359:219–25. doi: 10.1016/j.jns.2015.08.1541
80. Clarke S, Crottaz-Herbette S. Modulation of visual attention by prismatic adaptation. *Neuropsychologia.* (2016) 92:31–41. doi: 10.1016/j.neuropsychologia.2016.06.022
81. Panico F, Rossetti Y, Trojano L. On the mechanisms underlying prism adaptation: a review of neuro-imaging and neuro-stimulation studies. *Cortex.* (2020) 123:57–71. doi: 10.1016/j.cortex.2019.10.003
82. Goedert KM, Zhang JY, Barrett AM. Prism adaptation and spatial neglect: the need for dose-finding studies. *Front Hum Neurosci.* (2015) 9:243. doi: 10.3389/fnhum.2015.00243
83. De Wit L, Ten Brink AF, Visser-Meily JMA, Nijboer TCW. Does prism adaptation affect visual search in spatial neglect patients: a systematic review. *J Neuropsychol.* (2018) 12:53–77. doi: 10.1111/jnp.12100
84. Hreha K, Gillen G, Noce N, Nilsen D. The feasibility and effectiveness of using prism adaptation to treat motor and spatial dysfunction in stroke survivors with multiple incidents of stroke. *Top Stroke Rehabil.* (2018) 25:305–11. doi: 10.1080/10749357.2018.1437937
85. Anelli F, Avanzi S, Damora A, Mancuso M, Frassinetti F. Mental time travel and functional daily life activities in neglect patients: recovery effects of rehabilitation by prism adaptation. *Cortex.* (2019) 113:141–55. doi: 10.1016/j.cortex.2018.12.003
86. Fortis P, Ronchi R, Velardo V, Calzolari E, Banco E, Algeri L, et al. A home-based prism adaptation training for neglect patients. *Cortex.* (2020) 122:61–80. doi: 10.1016/j.cortex.2018.09.001
87. Vaes N, Nys G, Lafosse C, Dereymaeker L, Oostra K, Hemelsoet D, et al. Rehabilitation of visuospatial neglect by prism adaptation: effects of a mild treatment regime. A randomised controlled trial. *Neuropsychol Rehabil.* (2018) 28:899–918. doi: 10.1080/09602011.2016.1208617
88. Redding GM, Rossetti Y, Wallace B. Applications of prism adaptation: a tutorial in theory and method. *Neurosci Biobehav Rev.* (2005) 29:431–44. doi: 10.1016/j.neubiorev.2004.12.004
89. Tsujimoto K, Mizuno K, Nishida D, Tahara M, Yamada E, Shindo S, et al. Prism adaptation changes resting-state functional connectivity in the dorsal stream of visual attention networks in healthy adults: a fMRI study. *Cortex.* (2019) 119:594–605. doi: 10.1016/j.cortex.2018.10.018
90. Wilf M, Serino A, Clarke S, Crottaz-Herbette S. Prism adaptation enhances decoupling between the default mode network and the attentional networks. *Neuroimage.* (2019) 200:210–20. doi: 10.1016/j.neuroimage.2019.06.050
91. Panico F, Sagliano L, Grossi D, Trojano L. Bi-cephalic parietal and cerebellar direct current stimulation interferes with early error correction in prism adaptation: toward a complex view of the neural mechanisms underlying visuomotor control. *Cortex.* (2018) 109:226–33. doi: 10.1016/j.cortex.2018.09.020
92. Panico F, Sagliano L, Grossi D, Trojano L. Cerebellar cathodal tDCS interferes with recalibration and spatial realignment during prism adaptation procedure in healthy subjects. *Brain Cogn.* (2016) 105:1–8. doi: 10.1016/j.bandc.2016.03.002
93. Panico F, Sagliano L, Nozzolillo C, Trojano L, Rossetti Y. Cerebellar contribution to spatial realignment: A tDCS study during multiple-step prism adaptation. *Neuropsychologia.* (2018) 112:58–65. doi: 10.1016/j.neuropsychologia.2018.03.008
94. Chapman HL, Eramudugolla R, Gavrilescu M, Strudwick MW, Loftus A, Cunnington R, et al. Neural mechanisms underlying spatial realignment during adaptation to optical wedge prisms. *Neuropsychologia.* (2010) 48:2595–601. doi: 10.1016/j.neuropsychologia.2010.05.006
95. Saj A, Cojan Y, Vocat R, Luauté J, Vuilleumier P. Prism adaptation enhances activity of intact fronto-parietal areas in both hemispheres in neglect patients. *Cortex.* (2013) 49:107–19. doi: 10.1016/j.cortex.2011.10.009
96. Saj A, Cojan Y, Assal F, Vuilleumier P. Prism adaptation effect on neural activity and spatial neglect depend on brain lesion site. *Cortex.* (2019) 119:301–11. doi: 10.1016/j.cortex.2019.04.022
97. Thimm M, Fink GR, Küst J, Karbe H, Willmes K, Sturm W. Recovery from hemineglect: Differential neurobiological effects of optokinetic stimulation and alertness training. *Cortex.* (2009) 45:850–62. doi: 10.1016/j.cortex.2008.10.007
98. Bense S, Janusch B, Schlindwein P, Bauermann T, Vucurevic G, Brandt T, et al. Direction-dependent visual cortex activation during horizontal optokinetic stimulation (fMRI study). *Hum Brain Mapp.* (2006) 27:296–305. doi: 10.1002/hbm.20185
99. Dieterich M, Bucher SF, Seelos KC, Brandt T. Cerebellar activation during optokinetic stimulation and saccades. *Neurology.* (2000) 54:148. doi: 10.1212/WNL.54.1.148
100. Konen CS, Kleiser R, Seitz RJ, Bremmer F. An fMRI study of optokinetic nystagmus and smooth-pursuit eye movements in humans. *Exp Brain Res.* (2005) 165:203–16. doi: 10.1007/s00221-005-2289-7
101. von der Gablentz J, Könemund I, Sprenger A, Heide W, Heldmann M, Helmchen C, et al. Brain activations during optokinetic stimulation in acute right-hemisphere stroke patients and hemispatial neglect: an fMRI study. *Neurorehab Neural Re.* (2019) 33:581–92. doi: 10.1177/1545968319855038
102. Tong Y, Pendy JT, Li WA, Du H, Zhang T, Geng X, et al. Motor imagery-based rehabilitation: potential neural correlates and clinical application for functional recovery of motor deficits after stroke. *Aging Dis.* (2017) 8:364. doi: 10.14336/AD.2016.1012
103. Guerra ZF, Lucchetti ALG, Lucchetti G. Motor imagery training after stroke: a systematic review and meta-analysis of randomized controlled trials. *J Neurol Phys Ther.* (2017) 41:205–14. doi: 10.1097/NPT.0000000000000200
104. Hétu S, Grégoire M, Saimpont A, Coll M, Eugène F, Michon P, et al. The neural network of motor imagery: an ALE meta-analysis. *Neuroscience & Biobehavioral Reviews.* (2013) 37:930–49. doi: 10.1016/j.neubiorev.2013.03.017
105. Hardwick RM, Caspers S, Eickhoff SB, Swinnen SP. Neural correlates of action: comparing meta-analyses of imagery, observation, and execution. *Neurosci Biobehav Rev.* (2018) 94:31–44. doi: 10.1016/j.neubiorev.2018.08.003
106. Simon JJ, Welfringer A, Leifert-Fiebach G, Brandt T. Motor imagery in chronic neglect: an fMRI pilot study. *J Clin Exp Neuropsychol.* (2019) 41:58–68. doi: 10.1080/13803395.2018.1500527
107. Klomjai W, Lackmy-Vallée A, Roche N, Pradat-Diehl P, Marchand-Pauvert V, Katz R. Repetitive transcranial magnetic stimulation and transcranial direct current stimulation in motor rehabilitation after stroke: an update. *Ann Phys Rehabilit Med.* (2015) 58:220–4. doi: 10.1016/j.rehab.2015.05.006
108. Oberman L, Edwards D, Eldaief M, Pascual-Leone A. Safety of theta burst transcranial magnetic stimulation: a systematic review of the literature. *J Clin Neurophysiol.* (2011) 28:67–74. doi: 10.1097/WNP.0b013e318205135f
109. Suppa A, Huang YZ, Funke K, Ridding MC, Cheeran B, Di Lazzaro V, et al. Ten years of theta burst stimulation in humans: established knowledge, unknowns and prospects. *Brain Stimul.* (2016) 9:323–35. doi: 10.1016/j.brs.2016.01.006

110. Bonnì S, Mastropasqua C, Bozzali M, Caltagirone C, Koch G. Theta burst stimulation improves visuo-spatial attention in a patient with traumatic brain injury. *Neurol Sci.* (2013) 34:2053–6. doi: 10.1007/s10072-013-1412-y
111. Kim BR, Chun MH, Kim D, Lee SJ. Effect of high- and low-frequency repetitive transcranial magnetic stimulation on visuospatial neglect in patients with acute stroke: a double-blind, sham-controlled trial. *Arch Phys Med Rehab.* (2013) 94:803–7. doi: 10.1016/j.apmr.2012.12.016
112. Cao L, Fu W, Zhang Y, Huo S, Du J, Zhu L, et al. Intermittent θ burst stimulation modulates resting-state functional connectivity in the attention network and promotes behavioral recovery in patients with visual spatial neglect. *Neuroreport.* (2016) 27:1261–5. doi: 10.1097/WNR.0000000000000689
113. Freeman D, Reeve S, Robinson A, Ehlers A, Clark D, Spanlang B, et al. Virtual reality in the assessment, understanding, and treatment of mental health disorders. *Psychol Med.* (2017) 47:2393–400. doi: 10.1017/S003329171700040X
114. Hung Y, Gordon AM. Virtual reality training for children with unilateral cerebral palsy. *Dev Med Child Neurol.* (2018) 60:334–5. doi: 10.1111/dmcn.13699
115. Ekman U, Fordell H, Eriksson J, Lenfeldt N, Wåhlin A, Eklund A, et al. Increase of frontal neuronal activity in chronic neglect after training in virtual reality. *Acta Neurol Scand.* (2018) 138:284–92. doi: 10.1111/ane.12955
116. Wåhlin A, Fordell H, Ekman U, Lenfeldt N, Malm J. Rehabilitation in chronic spatial neglect strengthens resting-state connectivity. *Acta Neurol Scand.* (2019) 139:254–9. doi: 10.1111/ane.13048

Conflict of Interest: The authors declare that the research was conducted in the absence of any commercial or financial relationships that could be construed as a potential conflict of interest.

frontiers in Psychiatry

ORIGINAL RESEARCH
published: 17 November 2020
doi: 10.3389/fpsyt.2020.587803

Altered Patterns of the Fractional Amplitude of Low-Frequency Fluctuation in Drug-Naive First-Episode Unipolar and Bipolar Depression

Xue Chai[1†], Rongrong Zhang[2†], Chen Xue[1], Zonghong Li[1], Wang Xiao[1], Qingling Huang[1], Chaoyong Xiao[1] and Shiping Xie[2*]*

[1] Department of Radiology, The Affiliated Brain Hospital of Nanjing Medical University, Nanjing, China, [2] Department of Psychiatry, The Affiliated Brain Hospital of Nanjing Medical University, Nanjing, China

OPEN ACCESS

Edited by:
Zsigmond Tamás Kincses, University of Szeged, Hungary

Reviewed by:
Gianluca Serafini, San Martino Hospital (IRCCS), Italy
Yu-Feng Zang, Hangzhou Normal University, China

***Correspondence:**
Chaoyong Xiao
xchaoyong@163.com
Shiping Xie
xieshiping@njmu.edu.cn

[†]These authors have contributed equally to this work and share first authorship

Specialty section:
This article was submitted to Neuroimaging and Stimulation, a section of the journal Frontiers in Psychiatry

Received: *27 July 2020*
Accepted: *12 October 2020*
Published: *17 November 2020*

Citation:
Chai X, Zhang R, Xue C, Li Z, Xiao W, Huang Q, Xiao C and Xie S (2020) Altered Patterns of the Fractional Amplitude of Low-Frequency Fluctuation in Drug-Naive First-Episode Unipolar and Bipolar Depression. Front. Psychiatry 11:587803. doi: 10.3389/fpsyt.2020.587803

Background: An early and correct diagnosis is crucial for treatment of unipolar depression (UD) and bipolar disorder (BD). The fractional amplitude of low-frequency fluctuations (fALFFs) has been widely used in the study of neuropsychiatric diseases, as it can detect spontaneous brain activities. This study was conducted to survey changes of fALFF within various frequency bands of the UD and BD patients, as well as to explore the effects on changes in fALFF on cognitive function.

Methods: In total, 58 drug-naive first-episode patients, including 32 UD and 26 BD, were enrolled in the study. The fALFF values were calculated under slow-5 band (0.01–0.027 Hz) and slow-4 band (0.027–0.073 Hz) among UD patients, BD patients, and healthy control (HC). Additionally, we conducted correlation analyses to examine the association between altered fALFF values and cognitive function.

Results: Under the slow-5 band, compared to the HC group, the UD group showed increased fALFF values in the right cerebellum posterior lobe, whereas the BD group showed increased fALFF values in the left middle temporal gyrus (MTG). Under the slow-4 band, in comparison to HC, the UD group showed increased fALFF values in the left superior temporal gyrus, whereas the right inferior parietal lobule (IPL) and BD group showed increased fALFF values in the bilateral postcentral gyrus. Notably, compared to BD, the UD group showed increased fALFF values in the right IPL under the slow-4 band. Furthermore, altered fALFF values in the left MTG and the right IPL were significantly positively correlated with Verbal Fluency Test scores.

Conclusions: This current study indicated that there were changes in brain activities in the early UD and BD groups, and changes were related to executive function. The fALFF values can serve as potential biomarker to diagnose and differentiate UD and BD patients.

Keywords: bipolar disorder, unipolar depression, amplitude of low-frequency fluctuations, fractional amplitude low-frequency fluctuations, resting-state functional magnetic resonance imaging

INTRODUCTION

Unipolar depression (UD) and bipolar disorder (BD) are highly disabling diseases that seriously impact the patients' quality of life and are associated with high suicide rates (1, 2). In particular, studies have suggested that anxiety/depression, alexithymia, and extreme sensory processing patterns in psychiatric disorders are risk factors for suicide (3, 4) The distinction between UD and BD depends on whether the patient presents with a manic or hypomanic episode (2, 5, 6). It is almost impossible to correctly diagnose BD patients without a history of mania/hypomania episode (6, 7). Studies have shown that about 60% of BD patients are initially misdiagnosed as UD, and they are treated differently, which can cause serious consequences, including inducing manic episodes and emotional instability. These disabling consequences are often associated with abnormal use of antidepressants (8, 9). Therefore, promoting an understanding of the pathological mechanism of UD and BD will be of great help to diagnosis and treat this disease. According to previous studies, brain activities in the resting state, which reflect the baseline status of the brain, contributes to a better understanding of the pathophysiological features of mental illness, including UD and BD.

The resting-state functional magnetic resonance imaging (fMRI), a non-invasive fMRI technique, has been suggested as a useful way to measure spontaneous brain activities and detect internal changes in brain function that are inherent in pathological condition, including mental disorders such as UD and BD (10). The amplitude of low-frequency fluctuations (ALFFs) and the fractional ALFF (fALFF) are two credible indicators that are used to examine the regional features of low-frequency oscillations (LFOs) (11, 12). The ALFF measures voxel-wise amplitude of LFOs at very low frequencies (typically 0.01–0.08 Hz) and reflects local characteristics of brain oscillatory activities, whereas fALFF is the ALFF of a given frequency band and is part of the sum of amplitudes over an entire frequency range (13). Notably, the fALFF is a modified index of ALFF, which is less likely to produce any noise and is more sensitive and specific to the detection of spontaneous brain activities in comparison to ALFF (13). Convergent evidence suggests that the whole frequency range can be divided into four bands, including slow-5: 0.01–0.027 Hz, slow-4: 0.027–0.073 Hz, slow-3: 0.073–0.198 Hz, and slow-2: 0.198–0.25 Hz, in which the slow-4 and slow-5 bands can sensitively reveal pathology behind neuropsychiatric disorders (13, 14). Previous studies have indicated that ALFF/fALFF values under slow-4 and slow-5 bands are of great significance in the diagnosis of depression, but few studies have assessed its application in the UD and BD patients (14).

Most neuroimaging studies of UD and BD patients have found abnormal neuronal activities, which manifest as abnormal ALFF/fALFF values (15, 16). Chun et al. found that the BD group indicated abnormal ALF values that mainly exist in the prefrontal-limbic networks and associated striatal systems (17). The pediatric BD patients have also shown abnormal ALFF values in the basal ganglia, parietal cortex, and occipital cortex (10). Moreover, ALFF values in the bilateral superior frontal gyrus and left superior temporal gyrus can contribute to differentiate early-onset depression from late-onset depression (18). Notably, studies have shown that suicidal ideation is relevant to the changing resting-state brain activities in major depressive disorder (19). Electroconvulsive therapy, as a quick and effective treatment for severe depression, can relieve symptoms of depression, as well as alter resting-state brain activities (20). Therefore, application of ALFF in depression can play a role in diagnosing depression, judging the period of depression, and even providing a new perspective for selection of therapeutic targets.

In this current study, we calculated fALFF values in the slow-4 and slow-5 bands in drug and treatment-naive, first-episode, and short-illness-duration patients with UD and BD. In addition, correlation analyses were applied to study the relationship between altered fALFF values of UD and BD and cognitive function. We hypothesized the fALFF values were conducive to identification of UD and BD patients, and changed fALFF values affected cognitive function of patients.

MATERIALS AND METHODS

Subjects

In total, 58 drug-naive first-episode patients, including 32 UD and 26 BD patients, were recruited from the inpatient and outpatient clinic at the Affiliated Brain Hospital of Nanjing Medical University, Jiangsu Province, China. The inclusion criteria for UD patients included the following: (1) met the criteria outlined in the fourth edition of the *Diagnostic and Statistical Manual of Mental Disorders, Fourth Edition* (*DSM-IV*) for major depressive episode; (2) had a 17-item Hamilton Depression Rating Scale ($HAMD_{17}$) score $\geq$17; (3) between the ages of 14 and 45 years; (4) right-handed Han Chinese; and (5) never received psychotropic medication, electroconvulsive therapy, or psychotherapy. The inclusion criteria for BD patients included the following: (1) met the *DSM-IV* criteria for BD; (2) currently in the midst of a depressive episode; (3) Young Mania Rating Scale (YMRS) score <7 and 17-item HAMD score $\geq$17; (4) between the ages of 14 and 45 years; (5) right-handed Han Chinese; and (6) never received psychotropic medication, electroconvulsive therapy, or psychotherapy. The exclusion criteria for the patients included the following: (1) diagnosis of other mental disorders; (2) a history of severe brain injury, organic brain diseases, or systemic illnesses; (3) alcohol or drug abuse; (4) pregnancy and lactation; and (5) contraindications to MRI scanning. Overall, 30 healthy control (HC) individuals were recruited from the community. The inclusion criteria for HC comprise (1) no history of mental disorders, according to *DSM-IV*; (2) $HAMD_{17}$ score <7; and (3) no family history of mental disorders. All participants and their families provided written informed consent, and the study was granted approval by the Institutional Ethical Committee for Clinical Research of Nanjing Brain Hospital.

Neurocognitive Assessments

The study adopted the Chinese version of the MATRICS Consensus Cognitive Battery (MCCB) in order to assess cognitive function. The MCCB is a comprehensive and systematic

assessment that can be divided into seven domains: (1) speed of processing: Trail Making Test A, Brief Assessment of Cognition in Schizophrenia, and Semantic Verbal Fluency Test (VFT); (2) verbal learning: Hopkins Vocabulary Learning Test; (3) working memory: Wechsler Memory Scale; (4) reasoning and problem-solving: Neuropsychological Assessment Battery (NAB); (5) visual learning: the Brief Visuospatial Memory Test; (6) social cognitive: Mayer–Salovey–Caruso Emotional Intelligence Test; and (7) attention/vigilance: Continuous Performance Test, Identical Pairs version (CPT-IP) (21).

MRI Data Acquisition

Neuroimaging was conducted through the use of a 3.0-T Verio Siemens scanner with an eight-channel head-coil at the Nanjing Brain Hospital. Participants were instructed to rest with their eyes open, to not fall asleep, and to not think about anything in particular.

The gradient-echo echoplanar imaging sequence contained 149 volumes. The parameters included repetition time (TR) = 2,500 ms, echo time (TE) = 30 ms, flip angle = 90°, slice thickness = 3.5 mm, number of slices = 37, field of view (FOV) = 224 × 224 mm^2, matrix size = 64 × 64, and voxel size = 3.5 × 3.5 × 3.5 mm^3.

High-resolution T1-weighted images were obtained using magnetization-prepared rapid gradient-echo sequence. The parameters included TR = 2,300 ms, TE = 2.98 ms, flip angle = 9°, inversion time = 900 ms, thickness = 1 mm, number of slices = 192, FOV = 256 × 240 mm^2, and voxel size = 1 × 1 × 1 mm^3.

Image Preprocessing

The fMRI data were preprocessed using Data Processing and Analysis for Brain Imaging (DPABI, http://rfmri.org/DPABI) software in MATLAB 2013b (http://www.mathworks.com/products/matlab/). The first five volumes of functional images were discarded, and the remaining 142 volumes were used for subsequent processing, including slice timing, head-motion correction, and nuisance covariate regression. There were no subjects with excessive head motion (>2.5 mm of displacement or >2.5° of rotation in any direction). Next, 24 motion parameters, global signal, white matter signal, and cerebrospinal fluid signal were chosen as nuisance covariate. Then, the functional images were spatially normalized to the standard space of the Montreal Neurological Institute and resampled to an isotropic voxel size of 3 mm. Finally, the resulting functional images were smoothed with a 6-mm full-width half-maximum Gaussian kernel, and the linear trends were removed.

fALFF Measurement

The fALFF computed using the DPABI software. The time series of each voxel was transformed into a frequency domain, and the power spectrum was obtained using the fast Fourier transform. The square root was measured at each frequency of the power spectrum, and the averaged square root, i.e., ALFF value, was acquired over the range of 0.01–0.08 Hz. The fALFF value was obtained by dividing total ALFF values from 0.01 to 0.025 Hz. Finally, the resulting fALFF maps were normalized with each voxel divided by mean of the fALFF values of the whole-brain signal, providing mfALFF spatial maps. In addition, this study calculated and analyzed fALFF at slow-4 band (0.027–0.073) and slow-5 band (0.01–0.027), according to previous studies.

Statistical Analysis

The Statistical Package for the Social Sciences software version 22.0 (IBM, Armonk, New York) was used for statistical analysis. The analysis of variance (ANOVA), the two-sample *t*-test, and χ^2-test were performed compared with the demographics and neurocognition among the groups, including UD, BD, and HC. The threshold for statistical significance difference was set at $p < 0.05$.

One-way ANOVA was conducted in order to compare differences in mfALFF value between the three groups, including UD, BD, and HC using age, gender, and education as covariates, Non-parametric permutation test was conducted in the study in order to reduce the false-positive rate, and the permutation times were set at 1,000. $p < 0.05$ was set for statistical significance, and cluster size >200 voxels (5,400 mm^3) was used for multiple comparisons. The *post-hoc* comparisons were calculated using a mask obtained from ANOVA using age, gender, and education as covariates. The non-parametric threshold-free cluster enhancement (TFCE) and the family-wise error (FWE) corrected at $p < 0.05$ with cluster size >20 voxels (540 mm^3) were set for statistical significance. The mfALFF values of significantly changed regions were extracted using the Resting-State fMRI Data Analysis Toolkit (Rest) (http://

TABLE 1 | Demographics and MCCB assessments of patients with UD, BD, and HC subjects.

	UD (32)	BD (26)	HC (30)	F/χ^2	*p*
Age (years)	26.2 (7.0)	22.7 (5.7)	22.5 (4.0)	4.023	0.021
Gender (male/female)	17/15	10/16	12/18	1.594	0.451
Education level (years)	14.6 (2.6)	13.8 (2.4)	14.4 (3.1)	0.939	0.395
Course of disease (month)	18.5 (22.9)	25.0 (20.7)	—	−1.060	0.294
TMT	31.5 (8.4)	33.04 (10.2)	27.3 (6.6)	2.754	0.070
BACS	62.7 (11.1)	61.1 (10.2)	66.8 (4.4)	2.436	0.094
HVLT-R	27.8 (4.7)	27.8 (4.7)	28.2 (3.2)	0.083	0.920
WMS	16.9 (3.6)	16.3 (2.8)	17.7 (1.7)	1.256	0.291
NAB	17.5 (7.2)*	17.7 (5.7)*	22.0 (3.2)	4.331	0.016
BVMT-R	27.4 (4.9)	27.9 (5.0)	29.1 (3.6)	0.387	0.680
VFT	22.2 (5.9)*	22.3 (3.8)*	25.9 (4.1)	4.666	0.012
MSCEIT	86.6 (8.5)	87.5 (9.7)	89.1 (6.3)	0.408	0.666
CPT-IP	2.8 (0.6)	2.5(0.6)*	3.0 (0.4)	5.097	0.008

*Numbers are given as means (standard deviation) unless stated otherwise. Significant group differences were found at p < 0.05 (ANOVA test and post-hoc analysis). *Compared to HC. UD, unipolar depression; BD, bipolar disorder; HC, healthy control; TMT, Trail Making Test; BACS, Brief Assessment of Cognition in Schizophrenia; HVLT-R, Hopkins Vocabulary Learning Test; WMS, Wechsler Memory Scale; NAB, Neuropsychological Assessment Battery; BVMT-R, the Brief Visuospatial Memory Test; VFT, Verbal Fluency Test; MSCEIT, Mayer–Salovey–Caruso Emotional Intelligence Test; CPT-IP, Continuous Performance Test, Identical Pairs version.*

www.restfmri.net/forum/REST_V1.8) and used for correlation analysis. The correlation analysis was conducted to reveal the relationships between altered mfALFF values and MCCB assessments with age, gender, and years of education as covariates ($p < 0.05$, Bonferroni-corrected).

RESULTS

Demographic and Neurocognitive Characteristics

The demographic and MCCB information of all subjects, including 32 UD, 26 BD, and 30 HC patients, is shown in **Table 1**. The results indicated significant differences in NAB, VFT, and CPT-IP across the three groups. In comparison to HC, both UD and BD showed significantly reduced NAB and VFT scores, whereas only BD showed significantly reduced CPT-IP ($p < 0.05$). All results were obtained using age, gender, and education as covariates.

Altered mfALFF Values in the Three Groups

For mfALFF values in slow-5, the ANOVA indicated significant differences across the three groups, including UD, BD, and HC, and included the right cerebellum posterior lobe (CPL), the left middle temporal gyrus (MTG), the bilateral thalamus, the left inferior parietal lobule (IPL), and the left precentral gyrus. Compared to HC, the BD group showed significantly increased mfALFF value in the left MTG, whereas the UD group demonstrated increased mfALFF value in right CPL (TFCE-FWE corrected, cluster size ≥20, $p < 0.05$). All results were obtained using age, gender, and education as covariates (**Table 2**, **Figure 1**).

For mfALFF values in slow-4, ANOVA showed significant differences across three groups, including UD, BD, and HC, as well as the bilateral lingual, the left superior temporal gyrus (STG), the left postcentral gyrus (PoCG), the right IPL, the right PoCG, and the bilateral middle cingulum gyrus. Compared to the HC group, the BD group showed significantly increased mfALFF values in the bilateral PoCG, whereas the UD group showed significantly increased mfALFF values in the left STG and right IPL. Notably, in comparison to the BD group, the UD group showed increased mfALFF values in the right IPL (TFCE-FWE corrected, cluster size ≥20, $p < 0.05$). All results were obtained using age, gender, and education as covariates (**Table 3**, **Figure 2**).

TABLE 2 | The difference of fALFF values under slow-5 band across three groups.

Brain region	Peak MNI coordinate			*F/t*	Cluster number
	x	*y*	*z*		
ANOVA					
R cerebellum posterior lobe	6	−42	−63	10.4337	225
L middle temporal gyrus/superior temporal gyrus	−42	9	−36	11.2087	223
B thalamus	18	−6	9	9.8102	572
L inferior parietal lobule/postcentral gyrus	−60	−18	21	7.1453	244
L precentral gyrus	6	−9	78	7.8028	202
BD vs. HC					
L middle temporal gyrus	−45	9	−36	3.976	23
UD vs. HC					
R cerebellum posterior lobe	9	−42	−63	4.6847	211

The x, y, and z coordinates is the primary peak locations in the MNI space. Cluster size >200 voxels in ANOVA, p < 0.05; cluster size >19 voxels in post-hoc analysis, TFCE-FEW corrected, p < 0.05. L, left; R, right.

Correlations Between the Abnormal mfALFF Values and MCCB in the Three Groups

Pearson correlation analysis was performed between altered mfALFF-values regions and MCCB assessments using age, gender, and years of education as covariates ($p < 0.05$, Bonferroni corrected). Under the slow-5 band, mfALFF values of the left MTG were significantly positively correlated with VFT scores in the BD and HC groups ($r = 0.574$, $p = 0.010$). Under the slow-4 band, the mfALFF values of the right IPL were significantly positively correlated with VFT scores in the groups of BD and MD ($r = 0.374$, $p = 0.007$) and the mfALFF values of the right IPL were positively associated with VFT scores in the MD and HC groups ($r = 0.490$, $p = 0.007$) (**Figure 3**).

DISCUSSION

This current study analyzed fALFF values under the slow-4 (0.027–0.073) and slow-5 (0.01–0.027 Hz) bands in BD and UD patients and further explored the relationship between altered fALFF values and MCCB assessments. Our study had several findings that were highly congruent with our hypothesis. First, local brain regions, including the left MTG, the right CPL, the bilateral PoCG, the left STG, and the right IPL, showed significantly increased fALFF under the two separate frequency bands of the patient group. Second, under the slow-4 band, the fALFF values of the right IPL served as a potential biological marker in order to identify the BD and UD groups. Finally, Pearson correlation analysis proved that regions with altered fALFF were positively correlated with impaired VFT scores. In conclusion, the present study revealed that the fALFF values under slow-4 and slow-5 bands play an important and different role in the identification and diagnosis of the very early BD and UD.

Increased fALFF Values in the BD and UD Groups Under Slow-4 and Slow-5 Bands

Our study indicated that several regions of the BD and UD groups had significantly increased fALFF values in the slow-4 and slow-5 bands. In general, abnormal fALFF values in early BD and UD patients were mainly located in the temporal and parietal lobes, similar to previous studies (22–24).

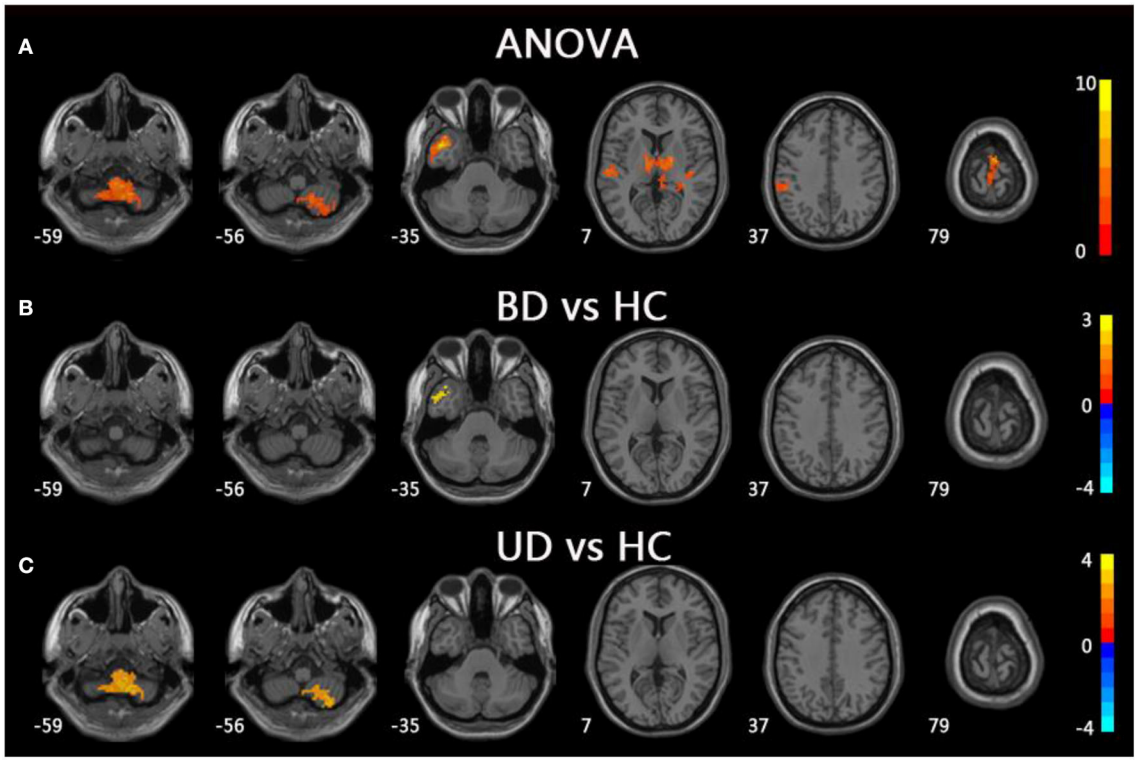

FIGURE 1 | Brain regions exhibiting significant differences from ANOVA and *post-hoc* analysis in fALFF values under slow-5 band. **(A)** Brain regions showing significant differences in fALFF values between UD, BD, and HC (cluster size >200, $p < 0.05$). **(B)** Brain regions showing significant differences in fALFF values between BD and HC (cluster size >19, TFCE-FWE corrected, $p < 0.05$). **(C)** Brain regions showing significant differences in fALFF values between UD and HC (cluster size >19, TFCE-FWE corrected, $p < 0.05$). UD, unipolar depression; BD, bipolar disorder; HC, healthy control.

TABLE 3 | The difference of fALFF values under slow-4 band across three groups.

Brain region	Peak MNI coordinate			*F/t*	Cluster number
	x	*y*	*z*		
ANOVA					
B lingual	−3	−81	−6	8.0345	238
L superior temporal gyrus/postcentral gyrus/inferior parietal lobule	−63	−27	27	9.5035	549
R inferior parietal lobule/angular/postcentral gyrus	45	−69	45	12.5965	419
B cingulum_mid/medial frontal gyrus	12	−27	36	9.9791	357
BD vs. HC					
R postcentral gyrus	51	−21	24	4.1787	26
L postcentral gyrus	−42	−27	63	4.3138	89
UD vs. HC					
L superior temporal gyrus	−57	−27	12	3.9197	22
R Inferior Parietal Lobule	51	−63	42	3.6236	20
UD vs. BD					
R inferior parietal lobule	45	−72	45	5.2864	78

The x, y, and z coordinates is the primary peak locations in the MNI space. Cluster size >200 voxels in ANOVA, p < 0.05; cluster size >19 voxels in post-hoc analysis, TFCE-FEW corrected, p < 0.05. L, left; R, right.

Under the slow-5 band, compared to the HC group, BD patients showed increased fALFF values in the left MTG, whereas UD patients showed increased fALFF values in the right CPL. Evidence also suggested that BD patients had structural and functional abnormalities in the temporal lobe and that increased fALFF values in the left MTG were consistent with the results of previous studies (15, 25). The cerebellum was thought to be involved in motor processing. However, a growing body of research suggests that the cerebellum is involved in pathogenesis of depression and CPL, which belongs to the default mode network (DMN) and regulates emotional processing and cognition (26). Sun et al. found that both major depressive disorder and cognitive vulnerability to depression showed increased regional homogeneity (ReHo) compared to the HC group, and the abnormal ReHo values were associated with the Center for Epidemiologic Studies Depression Scale (27). Additionally, the decreased functional connection in the bilateral CPL, as well as decreased cerebellar volume, was reported in UD patients in prior studies (28). In combination with increased fALFF values in UD patients of the study, our data suggest that the CPL abnormal resting-state brain activities of CPL may be potential biomarkers of UD patients (29, 30).

Under the slow-4 bands, compared to the HC group, the BD group showed increased fALFF values in the bilateral PoCG,

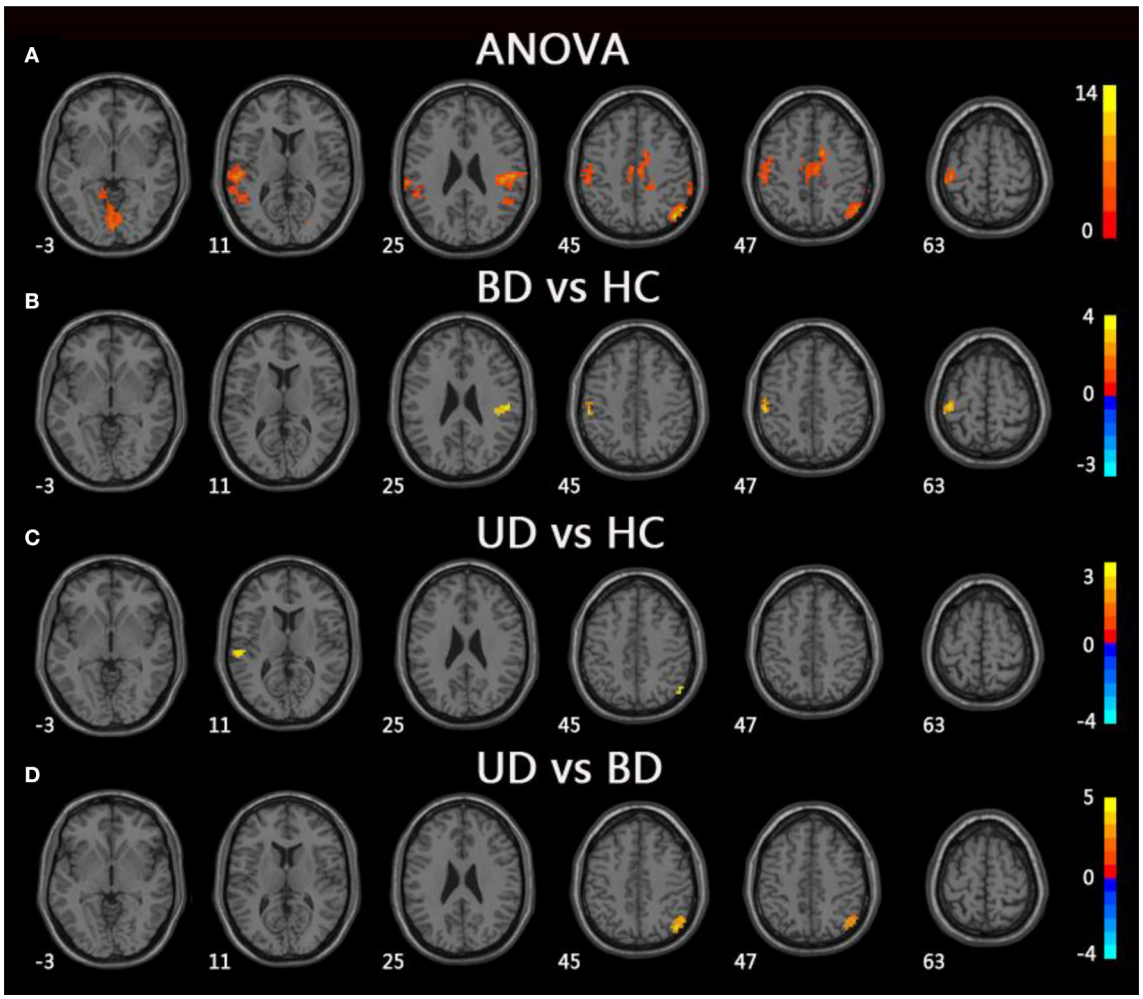

FIGURE 2 | Brain regions exhibiting significant differences from ANOVA and *post-hoc* analysis in fALFF values under slow-4 band. **(A)** Brain regions showing significant differences in fALFF values between UD, BD, and HC (cluster size >200, $p < 0.05$). **(B)** Brain regions showing significant differences in fALFF values between BD and HC (cluster size >19, TFCE-FWE corrected, $p < 0.05$). **(C)** Brain regions showing significant differences in fALFF values between UD and HC (cluster size >19, TFCE-FWE corrected, $p < 0.05$). **(D)** Brain regions showing significant differences in fALFF values between UD and BD (cluster size >19, TFCE-FWE corrected, $p < 0.05$). UD, unipolar depression; BD, bipolar disorder; HC, healthy control.

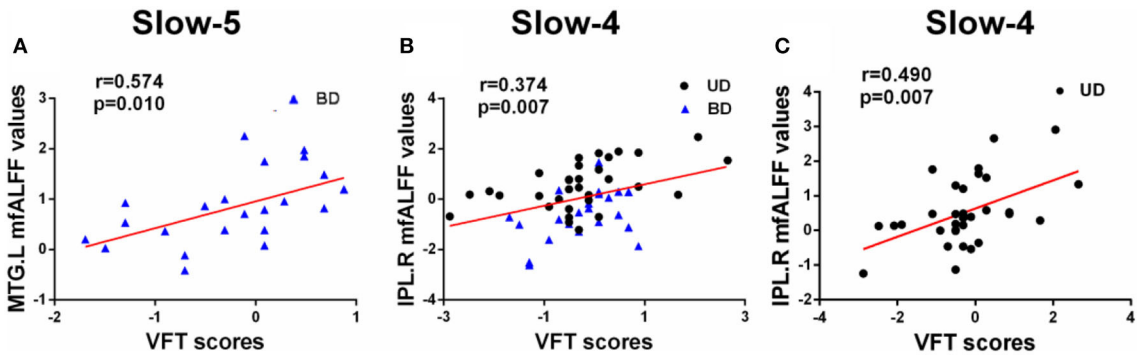

FIGURE 3 | (A–C) Significant correlations between altered fALFF values under slow-5 and slow-4 bands and MCCB assessments (Bonferroni corrected, $p < 0.05$). UD, unipolar depression; BD, bipolar disorder; VFT, Verbal Fluency Test; MTG, middle temporal gyrus; IPL, inferior parietal lobule; R, right; L, left.

whereas the UD group showed increased fALFF values in the left STG and right IPL. The PoCG, part of the parietal lobe, is widely known to be an important region that is responsible for proprioception (31). A growing body of study suggests that the PoCG is important in emotional processing, including the production of an emotional state and regulation of emotion (31). Abnormalities in the emotional processing circuit in BD patients are related to abnormal brain activities in the PoCG. Moreover, numerous studies have discovered that STG is the key brain region for pathological development of BD patients (32–34). An abnormal fatty acid pattern in STG was even believed to be the specific change in BD patients (35). Interestingly, results from this study showed that fALFF values were increased in the UD group, which is consistent with a meta-analysis, suggesting that both BD and UD patients had functional changes in STG (36). Notably, compared to the BD group, the UD group showed increased fALFF values in the right IPL. The IPL, which is widely considered to be the posterior region of the DMN, is a heterogeneous area that integrates information from different sensory patterns (37, 38). Moreover, the IPL was thought to be involved in cognitive functions, including executive control and episodic memory (39). Previous studies have reported that the UD group showed significantly increased ReHo in the right IPL compared to the HC group. Additionally, Sawamura et al. found that the average kurtosis of gray matter in the right IPL can help distinguish BD from major depressive disorder with a high accuracy (40, 41). It is worth noting that there were no significant differences with regard to the fALFF values of right IPL between BD patients and the HC group, and there was significantly increased fALFF of right IPL in the UD group compared to the HC group. This might suggest the fALFF of right IPL is a specific indicator that can be used to diagnose and identify UD patients.

It is worth noting that there is no reduction in fALFF values of the BD and UD groups in either the slow-4 or slow-5 band, which is clearly inconsistent with prior studies. The reason may be that the patients enrolled in this study were first-episode, drug-naive patients and had a short illness duration and thus belonged to a very early stage of depression and had not yet progressed to a decline in fALFF values. The increased fALFF values might be a compensatory mechanism for early BD and UD. In conclusion, the fALFF values under slow-4 and slow-5 bands can reveal the difference in brain activities between the depression patients and HC. Compared to the slow-5 band, the slow-4 band was more sensitive to differences in brain activities between the BD and UD groups. The combination of the slow-4 and slow-5 bands is beneficial to a clinical diagnosis and differentiation of UD and BD patients.

Behavioral Significance of Altered fALFF in Three Groups

The current study showed a significantly positive relationship between altered fALFF values and VFT scores in UD and BD patients. Under the slow-5 band, increased fALFF values of the MTG in BD patients were obviously positively correlated with VFT scores. Under the slow-4 band, increased fALFF values of the right IPL in BD and UD patient groups were positively correlated with VFT scores, and increased fALFF values of the right IPL in UD patients were positively correlated to VFT scores. The VFT scale is an important scale that can effectively reflect executive function. The IPL is considered to support control processes, and IPL activity is related to performance accuracy (42, 43). Notably, MTG and IPL are part of the DMN, which is deemed to be involved in self-referential processing, including internal monitoring, memory retrieval, theory of mind, and future planning (44, 45). Therefore, the left MTG and right IPL are regarded to play vital roles in executive function in early BD and UD patients.

LIMITATIONS

There are two limitations in the current study that should be mentioned. First, the small sample size in the study may influence the authenticity of results. Therefore, we will continue to recruit volunteers and continue the analysis. Second, there were significant differences in age among the three groups, which may have influenced the results. To solve this problem, we performed all statistical analyses using age, gender, and years of education as covariates.

CONCLUSION

Distinctively abnormal fALFF values were found among three groups, including UD, BD, and HC under the slow-4 and slow-5 bands, which revealed varying degrees of altered brain activities in UD and BD patients. In comparison to slow-5 bands, the slow-4 bands were more sensitive to differences in brain activities between the BD and UD groups. Moreover, the positive correlation between altered fALFF values and VFT scores further suggested that abnormal fALFF may contribute to a cognitive decline in UD and BD patients. In summary, the fALFF values can be used as a biological marker in the BD and UD patients.

DATA AVAILABILITY STATEMENT

The raw data supporting the conclusions of this article will be made available by the authors, without undue reservation.

ETHICS STATEMENT

The studies involving human participants were reviewed and approved by the Institutional Ethical Committee for clinical research of Nanjing Brain Hospital. Written informed consent to participate in this study was provided by the participants' legal guardian/next of kin.

AUTHOR CONTRIBUTIONS

XC, RZ, CXi, and SX: designed the study. XC, RZ, CXu, ZL, WX, QH, CXi, and SX: collected the data. XC and RZ: analyzed the data and prepared the manuscript. All authors contributed to the article and approved the submitted version.

FUNDING

This study was supported by Nanjing Municipal Commission of Science and Technology (No. 21803032); the Nanjing Medical Science and Technique Development Foundation (No. QRX17181 and YKK17134).

REFERENCES

1. Murray CJ, Vos T, Lozano R, Naghavi M, Flaxman AD, Michaud C, et al. Disability-adjusted life years (DALYs) for 291 diseases and injuries in 21 regions, 1990-2010: a systematic analysis for the global burden of disease study 2010. *Lancet.* (2012) 380:2197–223. doi: 10.1016/S0140-6736(12)61690-0
2. Cardoso de Almeida JR, Phillips ML. Distinguishing between unipolar depression and bipolar depression: current and future clinical and neuroimaging perspectives. *Biol Psychiatry.* (2013) 73:111–8. doi: 10.1016/j.biopsych.2012.06.010
3. Engel-Yeger B, Muzio C, Rinosi G, Solano P, Geoffroy PA, Pompili M, et al. Extreme sensory processing patterns and their relation with clinical conditions among individuals with major affective disorders. *Psychiatry Res.* (2016) 236:112–8. doi: 10.1016/j.psychres.2015.12.022
4. De Berardis D, Fornaro M, Orsolini L, Valchera A, Carano A, Vellante F, et al. Alexithymia and suicide risk in psychiatric disorders: a mini-review. *Front Psychiatry.* (2017) 8:148. doi: 10.3389/fpsyt.2017.00148
5. Perlis RH, Brown E, Baker RW, Nierenberg AA. Clinical features of bipolar depression versus major depressive disorder in large multicenter trials. *Am J Psychiatry.* (2006) 163:225–31. doi: 10.1176/appi.ajp.163.2.225
6. Grotegerd D, Suslow T, Bauer J, Ohrmann P, Arolt V, Stuhrmann A, et al. Discriminating unipolar and bipolar depression by means of fMRI and pattern classification: a pilot study. *Eur Arch Psychiatry Clin Neurosci.* (2013) 263:119–31. doi: 10.1007/s00406-012-0329-4
7. Woo YS, Shim IH, Wang HR, Song HR, Jun TY, Bahk WM. A diagnosis of bipolar spectrum disorder predicts diagnostic conversion from unipolar depression to bipolar disorder: a 5-year retrospective study. *J Affect Disord.* (2015) 174:83–8. doi: 10.1016/j.jad.2014.11.034
8. Han KM, De Berardis D, *Fornaro* M, Kim YK. Differentiating between bipolar and unipolar depression in functional and structural MRI studies. *Prog Neuropsychopharmacol Biol Psychiatry.* (2019) 91:20–7. doi: 10.1016/j.pnpbp.2018.03.022
9. Burger C, Redlich R, Grotegerd D, Meinert S, Dohm K, Schneider I, et al. Differential abnormal pattern of anterior cingulate gyrus activation in unipolar and bipolar depression: an fMRI and pattern classification approach. *Neuropsychopharmacology.* (2017) 42:1399–408. doi: 10.1038/npp.2017.36
10. Lu D, Jiao Q, Zhong Y, Gao W, Xiao Q, Liu X, et al. Altered baseline brain activity in children with bipolar disorder during mania state: a resting-state study. *Neuropsychiatr Dis Treat.* (2014) 10:317–23. doi: 10.2147/NDT.S54663
11. Zang YF, He Y, Zhu CZ, Cao QJ, Sui MQ, Liang M, et al. Altered baseline brain activity in children with ADHD revealed by resting-state functional MRI. *Brain Dev.* (2007) 29:83–91. doi: 10.1016/j.braindev.2006.07.002
12. Zou QH, Zhu CZ, Yang Y, Zuo XN, Long XY, Cao QJ, et al. An improved approach to detection of amplitude of low-frequency fluctuation (ALFF) for resting-state fMRI: fractional ALFF. *J Neurosci Methods.* (2008) 172:137–41. doi: 10.1016/j.jneumeth.2008.04.012
13. Zuo XN, Di Martino A, Kelly C, Shehzad ZE, Gee DG, Klein DF, et al. The oscillating brain: complex and reliable. *Neuroimage.* (2010) 49:1432–45. doi: 10.1016/j.neuroimage.2009.09.037
14. Wang L, Kong Q, Li K, Su Y, Zeng Y, Zhang Q, et al. Frequency-dependent changes in amplitude of low-frequency oscillations in depression: a resting-state fMRI study. *Neurosci Lett.* (2016) 614:105–11. doi: 10.1016/j.neulet.2016.01.012
15. Liu CH, Li F, Li SF, Wang YJ, Tie CL, Wu HY, et al. Abnormal baseline brain activity in bipolar depression: a resting state functional magnetic resonance imaging study. *Psychiatry Res.* (2012) 203:175–9. doi: 10.1016/j.pscychresns.2012.02.007
16. Xu K, Liu H, Li H, Tang Y, Womer F, Jiang X, et al. Amplitude of low-frequency fluctuations in bipolar disorder: a resting state fMRI study. *J Affect Disord.* (2014) 152–154:237–42. doi: 10.1016/j.jad.2013.09.017
17. Liu CH, Ma X, Wu X, Li F, Zhang Y, Zhou FC, et al. Resting-state abnormal baseline brain activity in unipolar and bipolar depression. *Neurosci Lett.* (2012) 516:202–6. doi: 10.1016/j.neulet.2012.03.083
18. Guo WB, Liu F, Xun GL, Hu MR, Guo XF, Xiao CQ, et al. Reversal alterations of amplitude of low-frequency fluctuations in early and late onset, first-episode, drug-naive depression. *Prog Neuropsychopharmacol Biol Psychiatry.* (2013) 40:153–9. doi: 10.1016/j.pnpbp.2012.08.014
19. Lan MJ, Rizk MM, Pantazatos SP, Rubin-Falcone H, Miller JM, Sublette ME, et al. Resting-state amplitude of low-frequency fluctuation is associated with suicidal ideation. *Depress Anxiety.* (2019) 36:433–41. doi: 10.1002/da.22888
20. Kong XM, Xu SX, Sun Y, Wang KY, Wang C, Zhang J, et al. Electroconvulsive therapy changes the regional resting state function measured by regional homogeneity (ReHo) and amplitude of low frequency fluctuations (ALFF) in elderly major depressive disorder patients: an exploratory study. *Psychiatry Res Neuroimaging.* (2017) 264:13–21. doi: 10.1016/j.pscychresns.2017.04.001
21. Smelror RE, Jorgensen KN, Lonning V, Kelleher I, Cannon M, DeRosse P, et al. Healthy adolescent performance with standardized scoring tables for the MATRICS consensus cognitive battery: a multisite study. *Schizophr Bull.* (2019) 45:773–83. doi: 10.1093/schbul/sby131
22. Yang C, Zhang A, Jia A, Ma JX, Sun N, Wang Y, et al. Identify abnormalities in resting-state brain function between first-episode, drug-naive major depressive disorder and remitted individuals: a 3-year retrospective study. *Neuroreport.* (2018) 29:907–16. doi: 10.1097/WNR.0000000000001054
23. Guo W, Liu F, Yu M, Zhang J, Zhang Z, Liu J, et al. Functional and anatomical brain deficits in drug-naive major depressive disorder. *Prog Neuropsychopharmacol Biol Psychiatry.* (2014) 54:1–6. doi: 10.1016/j.pnpbp.2014.05.008
24. Xu Z, Zhang S, Huang L, Zhu X, Zhao Q, Zeng Y, et al. altered resting-state brain activities in drug-naive major depressive disorder assessed by fmri: associations with somatic symptoms defined by Yin-Yang theory of the traditional Chinese medicine. *Front Psychiatry.* (2018) 9:195. doi: 10.3389/fpsyt.2018.00195
25. Jones LD, Payne ME, Messer DF, Beyer JL, MacFall JR, Krishnan KR, et al. Temporal lobe volume in bipolar disorder: relationship with diagnosis and antipsychotic medication use. *J Affect Disord.* (2009) 114:50–7. doi: 10.1016/j.jad.2008.07.003
26. Liu X, Hou Z, Yin Y, Xie C, Zhang H, Zhang H, et al. CACNA1C Gene rs11832738 polymorphism influences depression severity by modulating spontaneous activity in the right middle frontal gyrus in patients with major depressive disorder. *Front Psychiatry.* (2020) 11:73. doi: 10.3389/fpsyt.2020.00073
27. Sun H, Luo L, Yuan X, Zhang L, He Y, Yao S, et al. Regional homogeneity and functional connectivity patterns in major depressive disorder, cognitive vulnerability to depression and healthy subjects. *J Affect Disord.* (2018) 235:229–35. doi: 10.1016/j.jad.2018.04.061
28. Wang Y, Zhong S, Jia Y, Zhou Z, Wang B, Pan J, et al. Interhemispheric resting state functional connectivity abnormalities in unipolar depression and bipolar depression. *Bipolar Disord.* (2015) 17:486–95. doi: 10.1111/bdi.12315
29. Wang L, Dai W, Su Y, Wang G, Tan Y, Jin Z, et al. Amplitude of low-frequency oscillations in first-episode, treatment-naive patients with major depressive disorder: a resting-state functional MRI study. *PLoS ONE.* (2012) 7:e48658. doi: 10.1371/journal.pone.0048658
30. Liu F, Guo W, Liu L, Long Z, Ma C, Xue Z, et al. Abnormal amplitude low-frequency oscillations in medication-naive, first-episode patients with

major depressive disorder: a resting-state fMRI study. *J Affect Disord.* (2013) 146:401–6. doi: 10.1016/j.jad.2012.10.001
31. Kropf E, Syan SK, Minuzzi L, Frey BN. From anatomy to function: the role of the somatosensory cortex in emotional regulation. *Braz J Psychiatry.* (2019) 41:261–9. doi: 10.1590/1516-4446-2018-0183
32. Takahashi T, Malhi GS, Wood SJ, Yucel M, Walterfang M, Kawasaki Y, et al. Gray matter reduction of the superior temporal gyrus in patients with established bipolar I disorder. *J Affect Disord.* (2010) 123:276–82. doi: 10.1016/j.jad.2009.08.022
33. Ratnanather JT, Poynton CB, Pisano DV, Crocker B, Postell E, Cebron S, et al. Morphometry of superior temporal gyrus and planum temporale in schizophrenia and psychotic bipolar disorder. *Schizophr Res.* (2013) 150:476–83. doi: 10.1016/j.schres.2013.08.014
34. Kandilarova S, Stoyanov D, Sirakov N, Maes M, Specht K. Reduced grey matter volume in frontal and temporal areas in depression: contributions from voxel-based morphometry study. *Acta Neuropsychiatr.* (2019) 31:252–7. doi: 10.1017/neu.2019.20
35. McNamara RK, Rider T, Jandacek R, Tso P. Abnormal fatty acid pattern in the superior temporal gyrus distinguishes bipolar disorder from major depression and schizophrenia and resembles multiple sclerosis. *Psychiatry Res.* (2014) 215:560–7. doi: 10.1016/j.psychres.2013.12.022
36. Zhou M, Hu X, Lu L, Zhang L, Chen L, Gong Q, et al. Intrinsic cerebral activity at resting state in adults with major depressive disorder: a meta-analysis. *Prog Neuropsychopharmacol Biol Psychiatry.* (2017) 75:157–64. doi: 10.1016/j.pnpbp.2017.02.001
37. Wang J, Fan L, Zhang Y, Liu Y, Jiang D, Zhang Y, et al. Tractography-based parcellation of the human left inferior parietal lobule. *Neuroimage.* (2012) 63:641–52. doi: 10.1016/j.neuroimage.2012.07.045
38. Xue C, Yuan B, Yue Y, Xu J, Wang S, Wu M, et al. Distinct disruptive patterns of default mode subnetwork connectivity across the spectrum of preclinical alzheimer's disease. *Front Aging Neurosci.* (2019) 11:307. doi: 10.3389/fnagi.2019.00307
39. Vilberg, KL. Rugg MD. Memory retrieval and the parietal cortex: a review of evidence from a dual-process perspective. *Neuropsychologia.* (2008) 46:1787–99. doi: 10.1016/j.neuropsychologia.2008.01.004
40. Sawamura D, Narita H, Hashimoto N, Nakagawa S, Hamaguchi H, Fujima N, et al. Microstructural alterations in bipolar and major depressive disorders: a diffusion kurtosis imaging study. *J Magn Reson Imaging.* (2020) 52:1187–96. doi: 10.1002/jmri.27174
41. Liang MJ, Zhou Q, Yang KR, Yang XL, Fang J, Chen WL, et al. Identify changes of brain regional homogeneity in bipolar disorder unipolar depression using resting-state FMRI. *PLoS ONE.* (2013) 8:e79999. doi: 10.1371/journal.pone.0079999
42. Chan, YC, Lavallee JP. Temporo-parietal and fronto-parietal lobe contributions to theory of mind and executive control: an fMRI study of verbal jokes. *Front Psychol.* (2015) 6:1285. doi: 10.3389/fpsyg.2015.01285
43. Stegmayer K, Bohlhalter S, Vanbellingen T, Federspiel A, Wiest R, Muri RM, et al. Limbic interference during social action planning in schizophrenia. *Schizophr Bull.* (2018) 44:359–68. doi: 10.1093/schbul/sbx059
44. Buckner RL, Andrews-Hanna JR, *Schacter* DL. The brain's default network: anatomy, function, and relevance to disease. *Ann N Y Acad Sci.* (2008) 1124:1–38. doi: 10.1196/annals.1440.011
45. Spreng RN, Mar RA, *Kim* AS. The common neural basis of autobiographical memory, prospection, navigation, theory of mind, and the default mode: a quantitative meta-analysis. *J Cogn Neurosci.* (2009) 21:489–510. doi: 10.1162/jocn.2008.21029

Conflict of Interest: The authors declare that the research was conducted in the absence of any commercial or financial relationships that could be construed as a potential conflict of interest.

frontiers in Psychiatry

ORIGINAL RESEARCH
published: 15 January 2021
doi: 10.3389/fpsyt.2020.566518

PET Hypometabolism of the Prefrontal-Cingulate Cortices in Internet Gaming Disorder

Sun Ki Kim[1], *Hyeonseok Jeong*[1,2], *Jooyeon Jamie Im*[2], *Sang Hoon Lee*[3] *and Yong-An Chung*[1,2]*

[1] *Department of Radiology, College of Medicine, Incheon St. Mary's Hospital, The Catholic University of Korea, Seoul, South Korea,* [2] *Department of Nuclear Medicine, College of Medicine, Incheon St. Mary's Hospital, The Catholic University of Korea, Seoul, South Korea,* [3] *Department of Radiology, College of Medicine, Yeouido St. Mary's Hospital, The Catholic University of Korea, Seoul, South Korea*

Recently, excessive and uncontrolled use of online games has been recognized as a public concern. Although previous neuroimaging studies have reported structural and functional brain deficits in Internet gaming disorder (IGD), very few studies have investigated the regional cerebral metabolic rate of glucose (rCMRglu). This study investigated the differences in rCMRglu between individuals with IGD and healthy controls using 18F-fluoro-2-deoxyglucose positron emission tomography (18F-FDG PET). A total of 23 adults with IGD and 23 controls underwent brain 18F-FDG PET scans and completed self-report questionnaires. A whole-brain voxel-wise analysis of rCMRglu was conducted and associations between rCMRglu and severity of IGD were assessed. The IGD group showed higher impulsivity ($p = 0.04$) and lower self-control ($p = 0.002$) than the control group. In addition, the IGD group had lower FDG uptake in the left medial orbitofrontal gyrus, left middle cingulate cortex, left superior frontal gyrus, and right anterior cingulate cortex ($p < 0.001$). A significant negative association was found between the rCMRglu in the right anterior cingulate cortex and the number of fulfilled diagnostic criteria for IGD ($\beta = -0.50$, $p = 0.02$). Our results suggest that IGD may be associated with deficits of glucose metabolism in the prefrontal-cingulate cortices.

Keywords: Internet gaming disorder, regional cerebral metabolic rate of glucose, positron emission tomography, prefrontal cortex, anterior cingulate cortex

OPEN ACCESS

Edited by:
Szilvia Anett Nagy,
University of Pécs, Hungary

Reviewed by:
Eric Guedj,
Aix-Marseille Université, France
Baoci Shan,
Chinese Academy of Sciences, China

***Correspondence:**
Yong-An Chung
yongan@catholic.ac.kr

Specialty section:
This article was submitted to Neuroimaging and Stimulation, a section of the journal Frontiers in Psychiatry

Received: *28 May 2020*
Accepted: *14 December 2020*
Published: *15 January 2021*

Citation:
Kim SK, Jeong H, Im JJ, Lee SH and Chung YA (2021) PET Hypometabolism of the Prefrontal-Cingulate Cortices in Internet Gaming Disorder. Front. Psychiatry 11:566518. doi: 10.3389/fpsyt.2020.566518

INTRODUCTION

As online gaming has become one of the most popular leisure activities, excessive and uncontrolled use of online games has been recognized as a public concern since it can interfere with various aspects of daily life including academic performance and mental health (1). Therefore, Internet gaming disorder (IGD) has been suggested as a tentative psychiatric disorder that needs further research in the fifth edition of Diagnostic and Statistical Manual of Mental Disorders (DSM-5) (2). In addition, IGD is associated with impairment in response-inhibition, working memory, decision-making, and psychopathology such as depression, anxiety, and attention deficit hyperactivity disorder (3).

Several neuroimaging studies have reported structural and functional brain alterations in IGD. A meta-analysis indicated that abnormalities in the fronto-cingulate-striatal regions are consistently found in IGD (4). These findings suggest IGD may share neurobiological characteristics with other behavioral and substance addiction (4).

Compared to other imaging modalities, very few studies have investigated the regional cerebral metabolic rate of glucose (rCMRglu) in IGD. rCMRglu reflects the energy demand of neural activity and can be measured using 18F-fluoro-2-deoxyglucose positron emission tomography (18F-FDG PET). A previous study reported increased rCMRglu of the orbitofrontal cortex (OFC), caudate nucleus, and insula and decreased rCMRglu of the postcentral gyrus, precentral gyrus, and occipital cortex in Internet game overusers (5). Another 18F-FDG PET study found lower rCMRglu of the prefrontal, temporal, and limbic systems in IGD individuals (6). In addition, hypometabolism of the anterior cingulate cortex (ACC), frontal, temporal, parietal, and striatum regions was observed in a recent study (7). However, further research is required due to small sample size, lack of female subjects, and relatively lenient statistical thresholds in these previous studies (5–7).

The current study investigated the differences in rCMRglu between IGD individuals and controls using a whole-brain voxel-wise comparison of 18F-FDG PET images. Moreover, we examined the correlations between rCMRglu and addiction severity within the IGD group.

MATERIALS AND METHODS

Participants

Participants with IGD and healthy controls of age $\geq$ 20 years were recruited. IGD was diagnosed based on the Diagnostic and Statistical Manual of Mental Disorders-5 (DSM-5) criteria (2). Exclusion criteria included significant neurological or psychiatric disorders including major depressive disorder, anxiety disorder, psychotic disorder, and alcohol or other substance dependence, history of traumatic brain injury, taking psychotropic medication, and pregnancy.

The severity of the addiction symptoms was evaluated with the Internet Addiction Test, which was modified to assess online gaming instead of general online activities. Levels of self-control were examined using the Brief Self-Control Scale (BSCS). The Barratt Impulsiveness Scale-11 (BIS-11) was used to assess impulsivity.

The study protocol was approved by the Institutional Review Board of Incheon St. Mary's Hospital (Incheon, South Korea). All participants provided written informed consent.

Image Acquisition and Analysis

A Discovery STE PET-CT scanner (GE Healthcare, Milwaukee, WI, USA) was used for brain 18F-FDG PET scans. The participants received an intravenous injection of 185–222 MBq of FDG and remained lying comfortably with eyes closed in a quiet and dark room for 45 min. Forty-seven transaxial emission images were acquired (matrix = 128 × 128, voxel size = 1.95 × 1.95 × 3.27 mm). In addition, brain CT images were obtained for attenuation correction. To reconstruct the PET images, standard filtering techniques and ordered subset expectation maximization algorithm were used.

Image processing and analysis were performed using the Statistical Parametric Mapping 12 (SPM; Wellcome Department of Cognitive Neurology, Institute of Neurology, London, UK). The PET images were normalized to the Montreal Neurological Institute (MNI) space, resliced to 2 mm isotropic resolution, and smoothed with an 8 mm full-width at half-maximum isotropic Gaussian kernel. Global mean normalization was applied to estimate relative FDG uptake at each voxel as a ratio using proportional scaling.

A whole-brain voxel-wise two-sample *t*-test was conducted to compare rCMRglu between the two groups. Age and sex were included as covariates. The statistical threshold was $p < 0.001$ and 50 or more contiguous voxels. For each significant cluster, rCMRglu was extracted using MarsBar toolbox (http://marsbar.sourceforge.net/).

Statistical Analysis

Demographic and clinical characteristics were compared using independent *t*-test, Chi-square test, or Fisher's exact test. For each significant cluster, correlations between the rCMRglu and the number of fulfilled diagnostic criteria for IGD were tested within the IGD group using linear regression.

The significance level was $p < 0.05$ (two-tailed). Statistical tests were carried out using STATA version 16 (StataCorp., College Station, TX, USA).

RESULTS

A total of 23 IGD individuals and 23 controls were included in this study. Demographic and clinical characteristics of the participants are demonstrated in **Table 1**. There were no significant differences in age ($t = -0.29$, $p = 0.77$), sex ($\chi^2 = 0.11$, $p = 0.74$), education ($p = 0.19$), and years of gaming ($t = -0.61$, $p = 0.54$). However, the IGD group showed higher scores of IAT ($t = 6.70$, $p < 0.001$) and BIS-11 ($t = 2.09$, $p = 0.04$), and lower scores of BSCS ($t = -3.27$, $p = 0.002$).

The differences in rCMRglu are presented in **Table 2** and **Figures 1**, **2**. The IGD group had lower FDG uptake in the left

TABLE 1 | Characteristics of study participants.

Characteristics	IGD ($n = 23$)	Control ($n = 23$)	Test
Age (years)	22.8 ± 2.2	23.0 ± 2.8	$t = -0.29$, $p = 0.77$
Sex (male/female)	17/6	16/7	$\chi^2 = 0.11$, $p = 0.74$
Higher education[a]	18	22	$p = 0.19$
Years of gaming	6.4 ± 3.8	7.1 ± 4.4	$t = -0.61$, $p = 0.54$
IAT	48.4 ± 9.8	28.0 ± 10.9	$t = 6.70$, $p < 0.001$
BSCS	34.0 ± 6.1	40.7 ± 7.6	$t = -3.27$, $p = 0.002$
BIS-11	67.3 ± 9.3	61.7 ± 8.8	$t = 2.09$, $p = 0.04$

[a] *College or higher.*

BIS-11, Barratt Impulsiveness Scale-11; BSCS, Brief Self-Control Scale; IAT, Internet Addiction Test; IGD, Internet gaming disorder.

medial orbitofrontal gyrus (t = 4.64, 126 voxels), left middle cingulate cortex (t = 4.29, 387 voxels), left superior frontal gyrus (t = 4.28, 86 voxels), and right ACC (t = 4.19, 51 voxels). Brain areas with higher rCMRglu in the IGD group were not found.

The correlation analysis revealed that a significant negative association was found between the glucose metabolism in the right ACC cluster and the number of fulfilled diagnostic criteria for IGD ($\beta = -0.50$, $p = 0.02$) (**Figure 3**).

DISCUSSION

This study investigated the brain glucose metabolism and its association with addiction severity in participants with IGD. The 18F-FDG PET analysis revealed that the IGD group had hypometabolism in the prefrontal and cingulate cortices compared to the control group. In addition, lower rCMRglu in the ACC was associated with having more addiction symptoms. These results may suggest the important roles of the prefrontal-cingulate cortices in the pathophysiology of IGD.

Although previous 18F-FDG PET studies in IGD included only male participants (5–7), our IGD group demonstrated a similar male-to-female ratio (2.8:1) to that of the global prevalence (2.5:1) of gaming disorder (8). The IGD group in this study showed higher impulsivity and lower self-control than the control group. Like other behavioral and substance addictions, core symptoms of IGD include failure to control the addictive patterns of gaming behavior and continued use in spite of negative consequences (9). Elevated impulsivity and reduced self-control were suggested as important characteristics of IGD (10). Consistent with our results, a previous study has reported increased impulsivity in IGD individuals compared with healthy controls (11). In addition, reduced self-control was found in both IGD and smartphone addiction (12, 13).

In alignment with our results, previous 18F-FDG PET studies reported lower rCMRglu of the prefrontal and ACC regions in IGD individuals (6, 7). Although some studies showed hypermetabolism of some cortical and subcortical areas in individuals with IGD or Internet game overusers (5, 6), another study did not find higher rCMRglu (7). These inconsistencies may result from differences in inclusion criteria, sample characteristics, and statistical thresholds. Compared to the relatively liberal thresholds ($p < 0.005$ or $p < 0.01$) used in previous studies (6, 7), our study used the more stringent threshold of $p < 0.001$.

TABLE 2 | Differences in regional cerebral metabolic rate of glucose between participants with Internet gaming disorder and controls.

No.	Region	t	p	MNI coordinates (x, y, z)	Cluster size (voxels)
IGD > Control					
	None				
IGD < Control					
1	L medial orbitofrontal gyrus	4.64	<0.001	−8, 40, −6	126
2	L middle cingulate cortex	4.29	<0.001	−4, −8, 34	387
3	L superior frontal gyrus	4.28	<0.001	−26, 60, 24	86
4	R anterior cingulate cortex	4.19	<0.001	14, 40, 8	51

IGD, Internet gaming disorder; L, left; MNI, Montreal Neurological Institute; R, right.

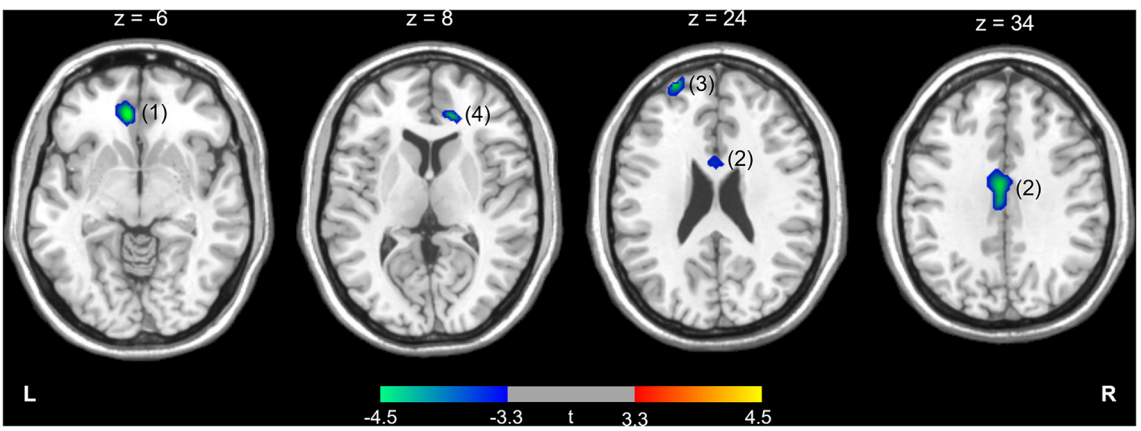

FIGURE 1 | Higher (red-yellow) or lower (blue-green) regional cerebral metabolic rate of glucose in participants with Internet gaming disorder compared with controls. The numbers above the brain slices indicate z coordinates in the Montreal Neurological Institute space. The color bar represents t value at each voxel. The numbers in parentheses show the cluster numbers listed in **Table 2**. L, left; R, right.

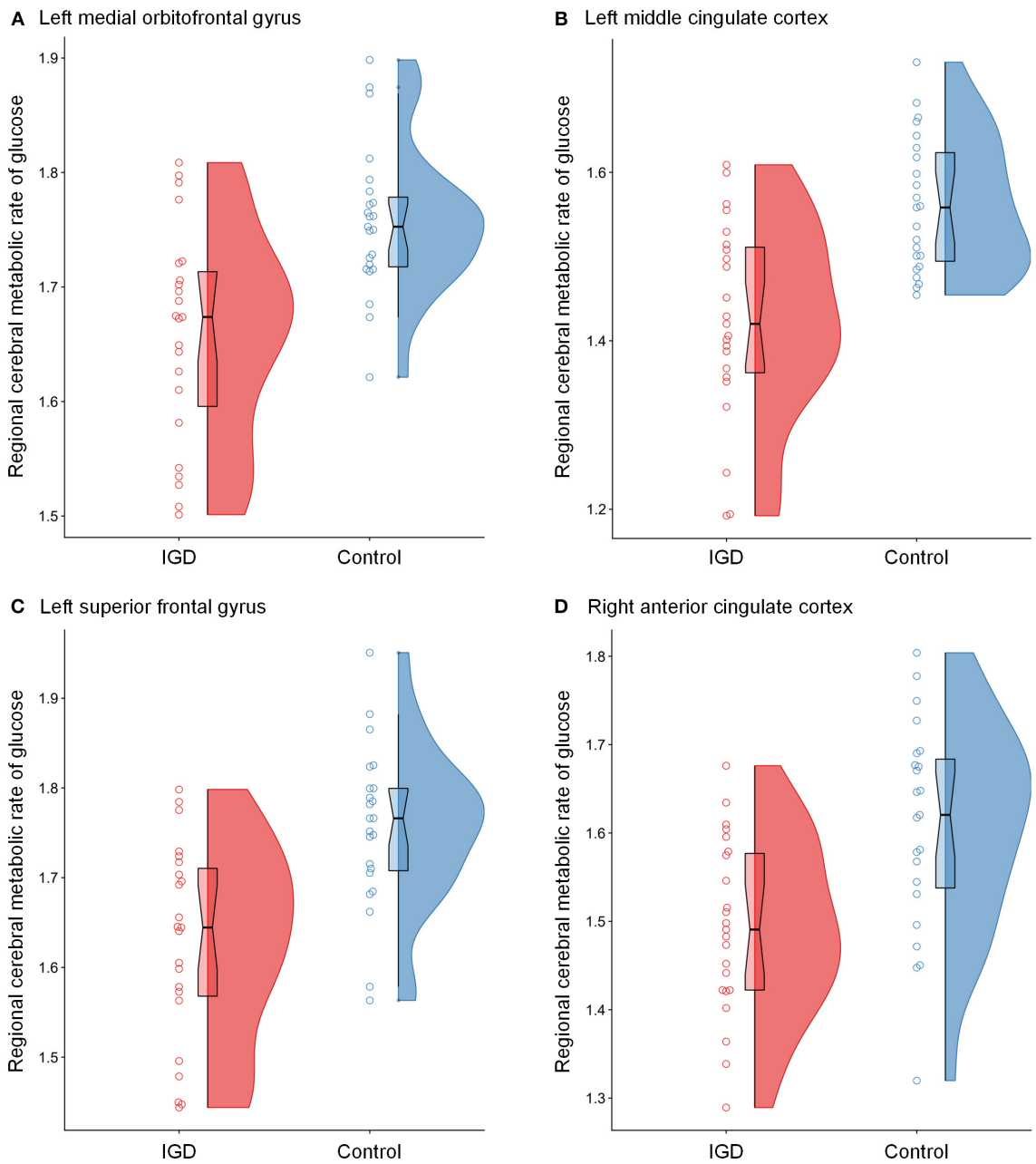

FIGURE 2 | Raincloud plots for regional cerebral metabolic rate of glucose (rCMRglu) in the **(A)** left medial orbitofrontal gyrus, **(B)** left middle cingulate cortex, **(C)** left superior frontal gyrus, and **(D)** right anterior cingulate cortex clusters with significant group differences between Internet gaming disorder (IGD) and controls. The dots represent each individual's rCMRglu. The boxplots are overlaid on the split-half violin plots of the distribution. The detailed cluster information is listed in **Table 2**.

The IGD group demonstrated hypometabolism in the orbitofrontal, superior frontal, and anterior/middle cingulate cortices. A previous neuroimaging meta-analysis in IGD suggested that structural and functional alterations are prominent in the prefrontal, cingulate, and striatal regions (4). The prefrontal-cingulate circuit may play key roles in the pathophysiology of addiction through the regulation of limbic reward circuits and higher-order executive functions such as self-control, salience attribution, and self-awareness (14). Specifically, a meta-analysis suggested that the dorsolateral prefrontal cortex (DLPFC), OFC, and ACC were most consistently implicated in reward/risk-related decision making (15). The OFC and DLPFC are implicated in the control of impulsive decision-making. For instance, previous studies reported that both humans and

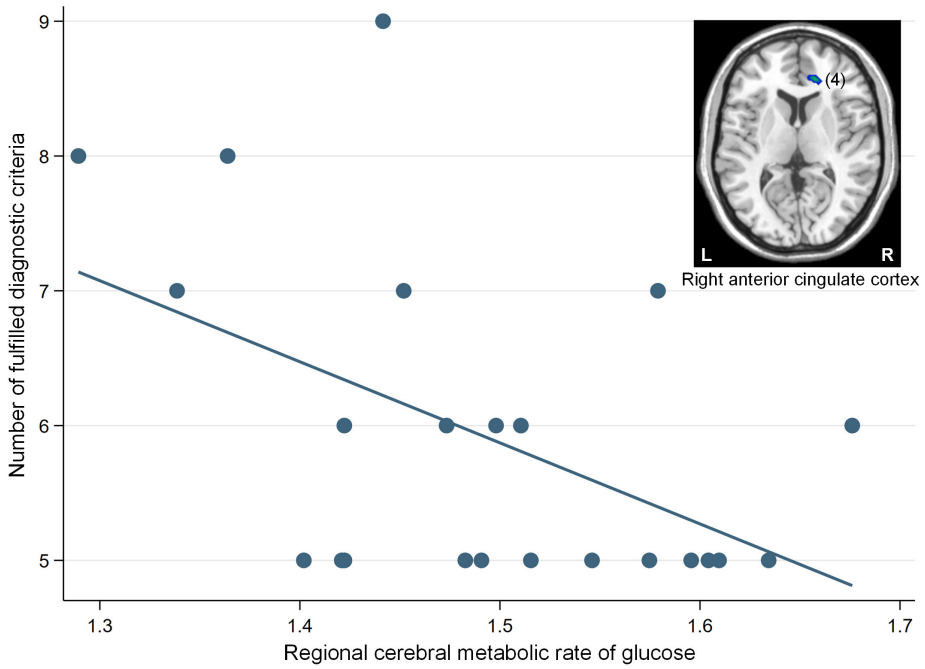

FIGURE 3 | A significant negative correlation between the regional cerebral metabolic rate of glucose in the right anterior cingulate cortex (cluster number 4) and the number of fulfilled diagnostic criteria for Internet gaming disorder (IGD) in participants with IGD ($\beta = -0.50$, $p = 0.02$). The number in parentheses show the cluster number listed in **Table 2**. L, left; R, right.

rodents with lesions in the OFC demonstrated more impulsive behaviors than normal controls (16, 17). In addition, functional interactions between the OFC and DLPFC were associated with self-control of cigarette craving (18). Previous studies in drug addiction suggested that the OFC and ACC, which are anatomically connected to the limbic system, are closely involved in higher-order motivational and cognitive functions including monitoring and modulating the salience of a reinforcer based on context and expectation and controlling and inhibiting prepotent responses (19).

Previous neuroimaging studies have suggested that IGD may be associated with both functional and structural deficits of the OFC, DLPFC, and ACC. During the Probabilistic Guessing task, online game addicts demonstrated higher activation levels of the orbitofrontal gyrus in gain conditions and lower activation levels of the ACC in loss conditions (20). Other functional magnetic resonance imaging studies in excessive online gamers reported altered activation of the ACC and OFC during the Stroop task (21, 22). With regard to the prefrontal-ACC networks, IGD individuals had lower resting-state functional connectivity of the OFC with both the DLPFC and ACC (23). Another study found altered static and dynamic resting-state functional connectivity of the DLPFC with several cortical and subcortical structures in IGD (24). In addition, excessive engagement in online gaming may be associated with gray matter deficits of the OFC and ACC (25). Reduced cortical thickness of the OFC in online gaming addiction was correlated with higher impulsivity and lower performance in the Stroop task, indicating impaired cognitive control ability (25, 26).

Some limitations of the current study should be considered. First, the cross-sectional design cannot determine the causal relationships between brain glucose metabolism and IGD. Prefrontal deficits were suggested as both predisposing factors and consequences for substance addiction (27). Recently, a longitudinal study revealed progressive volume loss of the OFC during the progression of IGD (28). To further establish the causality, more prospective longitudinal studies are required. Second, our study sample was consisted of young adults. Although there is a paucity of study in adolescents with IGD, they may have different neural correlates compared to adults (4). Thus, comparisons of IGD-related brain alterations in different age groups would be needed. Third, since multiple comparison correction was not applied in the analysis due to the relatively small sample size, future studies with larger samples should consider more stringent statistical thresholds.

The present study highlights the deficits in glucose metabolism of the prefrontal-cingulate regions among IGD individuals. Previous clinical trials suggested that treatment with antidepressant or transcranial direct current stimulation improves functional alterations of the DLPFC in IGD (29, 30). Further studies are warranted to investigate whether the prefrontal-cingulate circuit can be

used as neuroimaging biomarkers and potential treatment targets for IGD.

DATA AVAILABILITY STATEMENT

The datasets presented in this article are not readily available because the IRB has restrictions on sharing datasets. Requests to access the datasets should be directed to YAC (yongan@catholic.ac.kr).

ETHICS STATEMENT

The studies involving human participants were reviewed and approved by Institutional Review Board of Incheon St. Mary's Hospital. The patients/participants provided their written informed consent to participate in this study.

AUTHOR CONTRIBUTIONS

HJ, SL, and YAC were responsible for the study concept, design, and performed the data analysis and interpretation of findings. SK, HJ, and JI contributed to the acquisition of human data and drafted the manuscript. All authors provided critical revision of the manuscript and approved the final version of the manuscript. All authors contributed to the article and approved the submitted version.

FUNDING

This study was supported by the National Research Foundation of Korea funded by the Korean government (2020R1C1C1007254) and Institute of Information & Communications Technology Planning & Evaluation (2020-0-00238).

REFERENCES

1. Kuss DJ. Internet gaming addiction: current perspectives. *Psychol Res Behav Manag.* (2013) 6:125–37. doi: 10.2147/PRBM.S39476
2. American Psychiatric Association. *Diagnostic and Statistical Manual of Mental Disorders (DSM-5)*. Arlington, VA: American Psychiatric Association (2013).
3. González-Bueso V, Santamaría JJ, Fernández D, Merino L, Montero E, Ribas J. Association between internet gaming disorder or pathological video-game use and comorbid psychopathology: a comprehensive review. *Int J Environ Res Public Health.* (2018) 15:668. doi: 10.3390/ijerph15040668
4. Yao YW, Liu L, Ma SS, Shi XH, Zhou N, Zhang JT, et al. Functional and structural neural alterations in Internet gaming disorder: a systematic review and meta-analysis. *Neurosci Biobehav Rev.* (2017) 83:313–24. doi: 10.1016/j.neubiorev.2017.10.029
5. Park HS, Kim SH, Bang SA, Yoon EJ, Cho SS, Kim SE. Altered regional cerebral glucose metabolism in internet game overusers: a 18F-fluorodeoxyglucose positron emission tomography study. *CNS Spectr.* (2010) 15:159–66. doi: 10.1017/s1092852900027437
6. Tian M, Chen Q, Zhang Y, Du F, Hou H, Chao F, et al. PET imaging reveals brain functional changes in internet gaming disorder. *Eur J Nucl Med Mol Imaging.* (2014) 41:1388–97. doi: 10.1007/s00259-014-2708-8
7. Kim H, Kim YK, Lee JY, Choi AR, Kim DJ, Choi JS. Hypometabolism and altered metabolic connectivity in patients with internet gaming disorder and alcohol use disorder. *Prog Neuropsychopharmacol Biol Psychiatry.* (2019) 95:109680. doi: 10.1016/j.pnpbp.2019.109680
8. Stevens MW, Dorstyn D, Delfabbro PH, King DL. Global prevalence of gaming disorder: a systematic review and meta-analysis. *Aust N Z J Psychiatry.* (2020). doi: 10.1177/0004867420962851. [Epub ahead of print].
9. Brand M, Young KS, Laier C, Wolfling K, Potenza MN. Integrating psychological and neurobiological considerations regarding the development and maintenance of specific Internet-use disorders: an interaction of Person-Affect-Cognition-Execution (I-PACE) model. *Neurosci Biobehav Rev.* (2016) 71:252–66. doi: 10.1016/j.neubiorev.2016.08.033
10. Rho MJ, Lee H, Lee TH, Cho H, Jung DJ, Kim DJ, et al. Risk factors for internet gaming disorder: psychological factors and internet gaming characteristics. *Int J Environ Res Public Health.* (2017) 15:40. doi: 10.3390/ijerph15010040
11. Choi SW, Kim HS, Kim GY, Jeon Y, Park SM, Lee JY, et al. Similarities and differences among Internet gaming disorder, gambling disorder and alcohol use disorder: a focus on impulsivity and compulsivity. *J Behav Addict.* (2014) 3:246–53. doi: 10.1556/JBA.3.2014.4.6
12. Kim Y, Jeong JE, Cho H, Jung DJ, Kwak M, Rho MJ, et al. Personality factors predicting smartphone addiction predisposition: behavioral inhibition and activation systems, impulsivity, and self-control. *PLoS ONE.* (2016) 11:e0159788. doi: 10.1371/journal.pone.0159788
13. Na E, Lee H, Choi I, Kim DJ. Comorbidity of Internet gaming disorder and alcohol use disorder: a focus on clinical characteristics and gaming patterns. *Am J Addict.* (2017) 26:326–34. doi: 10.1111/ajad.12528
14. Goldstein RZ, Volkow ND. Dysfunction of the prefrontal cortex in addiction: neuroimaging findings and clinical implications. *Nat Rev Neurosci.* (2011) 12:652–69. doi: 10.1038/nrn3119
15. Krain AL, Wilson AM, Arbuckle R, Castellanos FX, Milham MP. Distinct neural mechanisms of risk and ambiguity: a meta-analysis of decision-making. *Neuroimage.* (2006) 32:477–84. doi: 10.1016/j.neuroimage.2006.02.047
16. Berlin HA, Rolls ET, Kischka U. Impulsivity, time perception, emotion and reinforcement sensitivity in patients with orbitofrontal cortex lesions. *Brain.* (2004) 127(Pt 5):1108–26. doi: 10.1093/brain/awh135
17. Winstanley CA, Theobald DE, Cardinal RN, Robbins TW. Contrasting roles of basolateral amygdala and orbitofrontal cortex in impulsive choice. *J Neurosci.* (2004) 24:4718–22. doi: 10.1523/JNEUROSCI.5606-03.2004
18. Hayashi T, Ko JH, Strafella AP, Dagher A. Dorsolateral prefrontal and orbitofrontal cortex interactions during self-control of cigarette craving. *Proc Natl Acad Sci USA.* (2013) 110:4422–7. doi: 10.1073/pnas.1212185110
19. Goldstein RZ, Volkow ND. Drug addiction and its underlying neurobiological basis: neuroimaging evidence for the involvement of the frontal cortex. *Am J Psychiatry.* (2002) 159:1642–52. doi: 10.1176/appi.ajp.159.10.1642
20. Dong G, Huang J, Du X. Enhanced reward sensitivity and decreased loss sensitivity in Internet addicts: an fMRI study during a guessing task. *J Psychiatr Res.* (2011) 45:1525–9. doi: 10.1016/j.jpsychires.2011.06.017
21. Dong G, Devito EE, Du X, Cui Z. Impaired inhibitory control in 'internet addiction disorder': a functional magnetic resonance imaging study. *Psychiatry Res.* (2012) 203:153–8. doi: 10.1016/j.pscychresns.2012.02.001
22. Dong G, Shen Y, Huang J, Du X. Impaired error-monitoring function in people with Internet addiction disorder: an event-related fMRI study. *Eur Addict Res.* (2013) 19:269–75. doi: 10.1159/000346783
23. Kim JY, Chun JW, Park CH, Cho H, Choi J, Yang S, et al. The Correlation between the Frontostriatal Network and Impulsivity in Internet Gaming Disorder. *Sci Rep.* (2019) 9:1191. doi: 10.1038/s41598-018-37702-4
24. Han X, Wu X, Wang Y, Sun Y, Ding W, Cao M, et al. Alterations of resting-state static and dynamic functional connectivity of the dorsolateral prefrontal cortex in subjects with internet gaming disorder. *Front Hum Neurosci.* (2018) 12:41. doi: 10.3389/fnhum.2018.00041
25. Lee D, Park J, Namkoong K, Kim IY, Jung YC. Gray matter differences in the anterior cingulate and orbitofrontal cortex of young adults with Internet gaming disorder: Surface-based morphometry. *J Behav Addict.* (2018) 7:21–30. doi: 10.1556/2006.7.2018.20
26. Yuan K, Cheng P, Dong T, Bi Y, Xing L, Yu D, et al. Cortical thickness abnormalities in late adolescence with online gaming addiction. *PLoS ONE.* (2013) 8:e53055. doi: 10.1371/journal.pone.0053055

27. Ersche KD, Williams GB, Robbins TW, Bullmore ET. Meta-analysis of structural brain abnormalities associated with stimulant drug dependence and neuroimaging of addiction vulnerability and resilience. *Curr Opin Neurobiol.* (2013) 23:615–24. doi: 10.1016/j.conb.2013.02.017
28. Zhou F, Montag C, Sariyska R, Lachmann B, Reuter M, Weber B, et al. Orbitofrontal gray matter deficits as marker of Internet gaming disorder: converging evidence from a cross-sectional and prospective longitudinal design. *Addict Biol.* (2019) 24:100–9. doi: 10.1111/adb.12570
29. Han DH, Hwang JW, Renshaw PF. Bupropion sustained release treatment decreases craving for video games and cue-induced brain activity in patients with Internet video game addiction. *Exp Clin Psychopharmacol.* (2010) 18:297–304. doi: 10.1037/a0020023
30. Lee SH, Im JJ, Oh JK, Choi EK, Yoon S, Bikson M, et al. Transcranial direct current stimulation for online gamers: A prospective single-arm feasibility study. *J Behav Addict.* (2018) 7:1166–70. doi: 10.1556/2006.7.2018.107

Conflict of Interest: The authors declare that the research was conducted in the absence of any commercial or financial relationships that could be construed as a potential conflict of interest.

frontiers in Psychiatry

ORIGINAL RESEARCH
published: 22 January 2021
doi: 10.3389/fpsyt.2020.596337

Amplitude of Low-Frequency Oscillations in Major Depressive Disorder With Childhood Trauma

Zhuoying Wu[1†], Qianyi Luo[1†], Huawang Wu[2], Zhiyao Wu[1], Yingjun Zheng[2], Yuling Yang[1], Jianfei He[1], Yi Ding[2], Rongjun Yu[3] and Hongjun Peng[1*]*

[1] Department of Clinical Psychology, The Affiliated Brain Hospital of Guangzhou Medical University, Guangzhou, China, [2] Department of Psychiatry, The Affiliated Brain Hospital of Guangzhou Medical University, Guangzhou, China, [3] Department of Management, Hong Kong Baptist University, Hong Kong, China

Major Depressive Disorder (MDD) with childhood trauma is one of the functional subtypes of depression. Frequency-dependent changes in the amplitude of low-frequency fluctuations (ALFF) have been reported in MDD patients. However, there are few studies on ALFF about MDD with childhood trauma. Resting-state functional magnetic resonance imaging was used to measure the ALFF in 69 MDD patients with childhood trauma (28.7 ± 9.6 years) and 30 healthy subjects (28.12 ± 4.41 years). Two frequency bands (slow-5: 0.010–0.027 Hz; slow-4: 0.027–0.073 Hz) were analyzed. Compared with controls, the MDD with childhood trauma had decreased ALFF in left S1 (Primary somatosensory cortex), and increased ALFF in left insula. More importantly, significant group × frequency interactions were found in right dorsal anterior cingulate cortex (dACC). Our finding may provide insights into the pathophysiology of MDD with childhood trauma.

Keywords: major depressive disorder, childhood trauma, low-frequency fluctuation, resting state, MRI, insula, primary somatosensory cortex, dorsal anterior cingulate cortex

OPEN ACCESS

Edited by:
Boldizsar Czeh,
University of Pécs, Hungary

Reviewed by:
Jiajia Zhu,
First Affiliated Hospital of Anhui Medical University, China
Hong Yang,
Zhejiang University, China

***Correspondence:**
Hongjun Peng
penghjgz@163.com
Rongjun Yu
yu.rongjun@gmail.com

† These authors have contributed equally to this work

Specialty section:
This article was submitted to Neuroimaging and Stimulation, a section of the journal Frontiers in Psychiatry

Received: *19 August 2020*
Accepted: *29 December 2020*
Published: *22 January 2021*

Citation:
Wu Z, Luo Q, Wu H, Wu Z, Zheng Y, Yang Y, He J, Ding Y, Yu R and Peng H (2021) Amplitude of Low-Frequency Oscillations in Major Depressive Disorder With Childhood Trauma. Front. Psychiatry 11:596337. doi: 10.3389/fpsyt.2020.596337

INTRODUCTION

Major depressive disorder (MDD) is described as long sadness and interest loss in generally pleasant activities, following with inability to perform daily activities, over a period of at least 2 weeks (1). At present, depending on its characteristics, MDD can be divided into different subtypes (2).

Childhood trauma is considered as a key factor affecting the occurrence of depression (3, 4). Some scholars believe that MDD with childhood trauma may be one of the functional subtypes of depression (5). To gain an insight of MDD and its heterogeneity, latest studies have been focusing on its clinically relevant depression hypotypes (6). Previous studies have found that nearly half of depression patients have experienced childhood trauma (7, 8), and their clinical characteristics are different from those of ordinary depression patients (9). For instance, symptoms of MDD are often more serious. The symptoms of MDD include higher suicide risk, serious cognitive impairment, and decreased response to antidepressants (10). In addition, there are some specific changes in brain imaging of depression patients with childhood trauma. Brain network studies reported that there are constant disruptions of resting-state networks (RSNs) in patients with MDD, including increased connection between the DMN and FPN, hyperconnectivity in the default mode network (DMN), and hyporconnectivity in the frontoparietal network (FPN) (11). Saleh et al. reported that in depressive subjects, greater early life stress exposure was linked to slower processing speeds and smaller orbitofrontal cortex volumes; however, in non-depressive subjects, it was associated

with faster speeds and larger volumes (12). Some studies have found that, compared with the healthy control subjects, amplitude of low-frequency fluctuations (ALFF) in bilateral amygdala and left orbit/cerebellum is increased, while fALFF in the left inferior temporal gyrus and right middle frontal gyrus is decreased in children with MDD after trauma. On MDD, early life stress was positively correlated with regional activity in the left cerebellum and the right posterior central/infratemporal/superior frontal cingulate gyrus and inferior frontal gyrus (13).

Since typical task-based functional magnetic resonance imaging (fMRI) scans can filter out low-frequency physiological noise and keep the high-frequency component of the signal it may lead to confusion about performance differences or activity patterns of specific tasks between healthy subjects and patients. Resting-state fMRI (rs-FMRI), which is applied to evaluate interactions between brain regions when a subject is not performing a specific task (14), has been widely applied to identify the neural correlation to psychiatric disorders. Low frequency fluctuation amplitude analysis (ALFF) measures voxel-by-voxel fluctuations in the amplitude of a blood oxygen level related (BOLD) signal at very low frequencies (typically 0.010–0.080 Hz) (15), which are pointed out to reflect autonomous brain activity (16). Signals in different frequency bands may lead to distinguish brain oscillations with physiological functions and specific characteristics (17). Entire low-frequency spectrum is usually subdivided into four bands (slow-2, 0.198–0.250 Hz; slow-3, 0.073–0.198 Hz; slow-4, 0.027–0.073 Hz; slow-5, 0.010–0.027 Hz) (18). The slow-4 and slow-5 bands are the most associated to gray matter (GM) signals, which are helpful for identifying associations between the functional processing and disease (19). More recent studies have examined ALFF at slow-4 (0.027–0.073 Hz) and slow-5 (0.010–0.027 Hz).

Although ALFF analyses are widely used to study depression, few ALFF studies on MDD have specifically examined MDD with childhood trauma. Therefore, more research is needed to examine the pathophysiology and etiology of MDD with childhood trauma, to help with the early diagnosis and treatment of this subtype of depression, and further to enhance patients' quality of life. The search for biological markers of disease mechanism, treatment choices, diagnosis, or prognosis has become one of the principal goals of depression' neuroimaging (11). Our research aims to identify potential biomarkers to differentiate individuals with MDD with childhood trauma from individuals with ordinary depression.

Abbreviations: ALFF, amplitude of low-frequency fluctuations; BOLD, blood oxygenation level dependent; DMN, Default-mode network; CTQ-SF, Childhood Truama Questinnaire; dACC, dorsal anterior cingulate cortex; FC, functional connectivity; FWE, family-wise error; FFT, fast Fourier transforms; fMRI, functional magnetic resonance imaging; fALFF, fractional amplitude of low frequency fluctuations; GM, gray matter; HC, healthy controls; HAMD, Hamilton Depressive Rating Scale; LFO, low-frequency oscillations; MDD, Major Depressive Disorder; MRI, magnetic resonance imaging; MPFC, medial prefrontal cortex; MNI, Montreal Neurological Institute; MTG, middle temporal gyrus; S1, primary somatosensory cortex; SCID, structured clinical interview; STD, subthreshold depression; SDS, Zung's Self-Rating Depression Scale; TRD, treatment-resistant depression.

MATERIALS AND METHODS

Subjects

Ninety-nine subjects were recruited for this study. Among them, 69 were unmedicated MDD patients with childhood trauma and 30 were non-depressed comparison subjects (HC). Sixty-nine unmedicated subjects with MDD ranging from 18 to 45 were recruited from the outpatient and inpatient units The Affiliated Brain Hospital of Guangzhou Medical University. The absence or presence of MDD was evaluated by the structured clinical interview (SCID) for DSM-V diagnostic criteria. Patients with other neurological disorders, psychiatric axis-I or axis-II disorders, electroconvulsive therapy, medication used in the past 6 months, clinically relevant abnormalities in laboratory examinations or their medical history, and contraindication for magnetic resonance imaging (MRI) were excluded. Depression severity were evaluated by Zung's Self-Rating Depression Scale (SDS) and The 17-item Hamilton Depressive Rating Scale (HAMD) (20). The Childhood Truama Questinnaire (CTQ-SF) was used to measure childhood adversity. The CTQ-SF consist of five subscales: sexual abuse (SA), emotional abuse (EA), physical abuse (PA), emotional neglect (EN) and physical neglect (PN) (21). The cut off points for subscales are: SA grade $\geq$ 8, EA grade $\geq$ 13, PA grade $\geq$ 10, PN grade $\geq$ 10, and EN grade $\geq$ 15 (8, 22). In addition, 30 gender- age-, and education-matched healthy subjects were recruited from the community near the hospital. Before enrollment, all participants were fully gave notice of the information of the research, and written informed consent was formal obtained. Researches were executed under the Declaration of Helsinki and ratified by The Affiliated Brain Hospital of Guangzhou Medical University Ethics Committee.

MRI Data Acquisition

Philips 3T MR systems (Philips, Best, The Netherlands) were used to acquire imaging data. Subjects were asked to wear earplugs and positioned in the coil for support. Participants were requested to lie still with their eyes closed but to remain awake, and all participants reported that they did not fall asleep during the whole experiment. A total of 180 volumes of echo planar images were obtained axially (repetition time, 3,000 ms; echo time, 30 ms; slices, 36; thickness, 4 mm, no slice gap; field of view, 240 $\times$ 240 mm^2; resolution, 64$\times$ 64; flip angle, 90°).

Image Pre-processing

The first 10 volumes of each functional time series for the instability of the initial MRI signal and the adaptation of participants to the circumstance were discarded. The fMRI images were sliced acquisition corrected, head-motion corrected, normalized to the standard SPM5 Montreal Neurological Institute (MNI) template, and then re-sampled to 3-mm cubic voxels. Data were filtered using typical temporal bandpass (0.010–0.080 Hz), slow-4 bandpass (0.027–0.073 Hz), and slow-5 bandpass (0.010–0.027 Hz) separately after linear detrending. REST software was used to calculate ALFF (by Dr. Yong He, http://resting-fmri.sourceforge.net). The filtered time series was transformed into a frequency domain with a fast Fourier transform (FFT) (parameters: taper percent = 0, FFT length

TABLE 1 | Demographics and clinical characteristics.

	HC ($n = 30$)		MDD with childhood trauma ($n = 69$)		T/*P*-value
	Mean	SD	Mean	SD	
Age(y)	28.12	4.41	28.70	9.6	0.23
Gender (male/female) (n)	19/11		39/30		0.42
Education (years)	14.12	3.24	13.27	3.32	0.32
Illness duration (m)	n.a.	n.a.	21.32	12.08	n.a.
HAMD	n.a.	n.a.	28.39	9.42	n.a.
SDS	n.a.	n.a.	52.81	9.26	n.a.

HC, healthy controls; SD, standard deviation; MDD, major depression disorder; HAMD, Hamilton Depressive Rating Scale; SDS, Self-Rating Depression scale.

= shortest), and the power spectrum was then obtained. Since the power of a given frequency is proportional to the square of the amplitude of this frequency component of the original time series in the time domain, the square root was calculated at each frequency of the power spectrum and the averaged square root was obtained across 0.010–0.080 Hz at each voxel. This averaged square root was taken as the ALFF. For standardization purposes, the ALFF of each voxel was divided by the global mean ALFF value.

A corrected threshold of family-wise error (FWE) of $p < 0.05$ at cluster level was set. Coordinates were reported in MNI coordinates, as used by SPM.

Statistical Analysis

SPSS 17.0 software was used to analysis the general data. Mean ± SD was used to describe the continuous data that conformed the normal distribution. Between the data analysis of MDD with childhood trauma group and health control group, independent sample *t*-test was performed. When calculating the group differences within the ALFF measurement and the correlation between the clinical measurements and ALFF, age, gender, and education level were included as covariates. In depressed subjects, relationship between depression severity and ALFF values were analyzed by Pearson's correlations. Respectively, *post-hoc* test and simple effect analyses were conducted with the mALFF values averaged in order to further investigate the differences in frequency bands and groups. The above results are statistically significant with $P < 0.05$.

RESULTS

Demographics

Clinical data and demographic of healthy and depressed subjects are showed in **Table 1**. The mean age of the 69 patients is 28.7 ± 9.6 years, and the average year of education is 13.27 ± 3.32 years. The illness duration is 21.32 ± 12.08 months. Thirty controls are recruited, of which the average age is 28.12 ± 4.41 years, and the mean years of education is 14.12 ± 3.24. There is no significant difference in gender, education state, age between two groups.

TABLE 2 | Brain regions showing statistically significant correlation between ALFF and depression severity in terms of HAMD scores in subjects with MDD with CT.

Brain regions	Brodmann areas	Cluster size	MNI coordinates			*R*-values
			x	y	z	
Anterior Insula	13	87	−39	9	0	+0.54
S1	3a, 3b, 1, and 2	44	9	−42	75	−0.66
dACC	32	155	12	−6	39	−0.73

BA, Brodmann area; MNI, Montreal Neurologic Institute; MDD, major depressive disorder; S1, primary somatosensory cortex; dACC, dorsal Anterior Cingulate Cortex.

Correlations Between Clinical Data and the ALFF

In insula, a highly positive correlation between HAMD total score and the ALFF ($p < 0.01$) was found. On the contrary, a strong negative correlation between depressive symptom severity and ALFF was detected in the S1 and dACC ($p < 0.01$) (**Table 2**).

ALFF Frequency Main Effect

Main effects from the two-way repeated measure ANOVA are shown in **Figure 1**. In midbrain, basal ganglia, cingulate cortex and fusiform gyrus, ALFF of slow 4 is obviously larger than that of slow 5, while ALFF of slow 5 is larger in lingual gyrus, middle temporal gyrus, inferior frontal gyrus and medial frontal ventral gyrus (see **Figure 1**).

ALFF Group Main Effect

Differences between groups are demonstrated in **Table 3** and **Figure 2**. Compared to controls, patients exhibited decreased ALFF in a cluster in the postcentral gyrus (sensorimotor cortex), [$x = 9, -42, 75$], $Z = 5.72$, voxels = 154, PFWE < 0.05, see **Figure 2A**. Patients had higher ALFF in the left anterior insula, [−39, 9, 0], $Z = 3.29$, voxels = 22, PFWE < 0.05 (**Figure 2B**).

Group X Frequency Interaction

We found the significant group by frequency interaction in dACC, [12, −6, 39], $Z = 5.20$, voxels = 56, PFWE < 0.05, corrected at cluster-level see **Figure 3A**. The interaction is plotted in **Figure 3**.

DISCUSSION

Functional MRI has been **broadly** used to explore the brain systems's dysfunction in patients with psychiatric disorders. Our study found that the frequency-dependent changes in the ALFF occur in MDD patients with childhood trauma. ALFF analysis is applied to examine the amplitude of low-frequency oscillations (LFOs) in MDD with childhood trauma in different frequency bands, namely slow-5 and slow-4.

Our study is the first systematic investigation to explore frequency-dependent changes in LFO amplitudes (as indexed by the ALFF) from resting-state fMRI signals in MDD patients with childhood trauma. In different brain regions, the main frequency-dependent effects varies according to the different frequency bands: slow-4 oscillations were greater than slow-5

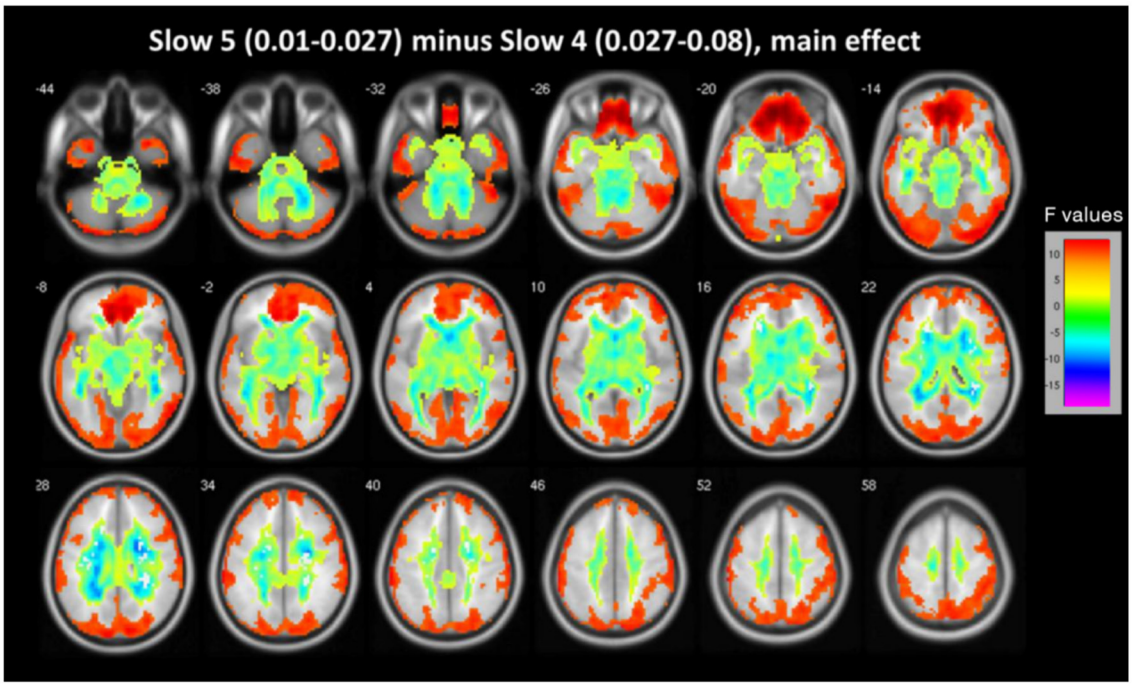

FIGURE 1 | The main effect for frequency band on ALFF. Most of the brain showed marked differences in ALFF between the two frequency bands (slow-4 vs. slow-5). Warm color represents greater ALFF in the slow-5 band than in the slow-4 band, while cool color represents lower ALFF. A two-way repeated measures ANOVA obtained the results.

TABLE 3 | The brain region showing marked group main effect and interaction effect of group and frequency (slow−4 and slow−5) on ALFF.

	Anatomical region	Left/ right	Size (voxels)	Peak level P (FWE-corrected)	MNI(mm)			Voxel *Z*-value
					x	y	z	
Depression-control	Anterior insula	L	22	0.042	−39	9	0	3.29
Control-depression	S1	L	154	0.021	9	−42	75	5.72
Group × Frequency interaction	dACC	R	56	0.017	12	−6	39	5.20

dACC, dorsal Anterior Cingulate Cortex; S1, primary somatosensory cortex.

oscillations primarily in subcortical regions, such as midbrain, basal ganglia, cingulate cortex, and fusiform gyrus; and slow-5 oscillations were greater than slow-4 oscillations in several cortical areas, such as the inferior frontal gyrus, ventromedial frontal gyrus and middle temporal gyrus. Compared with controls, major depressive patients with childhood trauma indicated decreased ALFF values in S1 and increased ALFF values in insula. Moreover, a remarkable interaction was identified between frequency bands and groups in dACC, which suggests that the observed dynamic changes in low-frequency fluctuations may be related to frequency-dependent. Due to this reason, we decided to analyze group differences in the ALFF across the slow-5 and slow-4 ranges.

Group Differences in ALFF Between Frequency Bands

Previous studies of the ALFF have also detected the differences between brain areas in the slow-4 and slow-5 bands (18, 23, 24). Although, from different frequency bands, the significance and source of signals are not clear, it has been suggested that the different low-frequency bands relate to different neural processes and physiological functions (17, 25). Lower frequency oscillations have been linked with long-range connections and the integration of large neuronal systems, while signals from higher frequency bands have been linked to more local neuronal assemblies and short-range connections (25). Therefore, regions of the cerebral cortex such as the inferior frontal gyrus, ventromedial frontal gyrusand, and middle temporal gyrus, may facilitate long-distance connectivity in many large networks. Conversely, subcortical regions such as fusiform gyrus, cingulate cortex, and basal ganglia may mainly contribute to fast local events, which are regulated by extensive slow oscillations (25, 26). Additionally, compared with the slow-4 band, we found higher ALFF values in the slow-5 band in most of the main subregions of the default mode network (DMN) (27), including inferior frontal gyrus, middle temporal gyrus and ventromedial frontal gyrus.

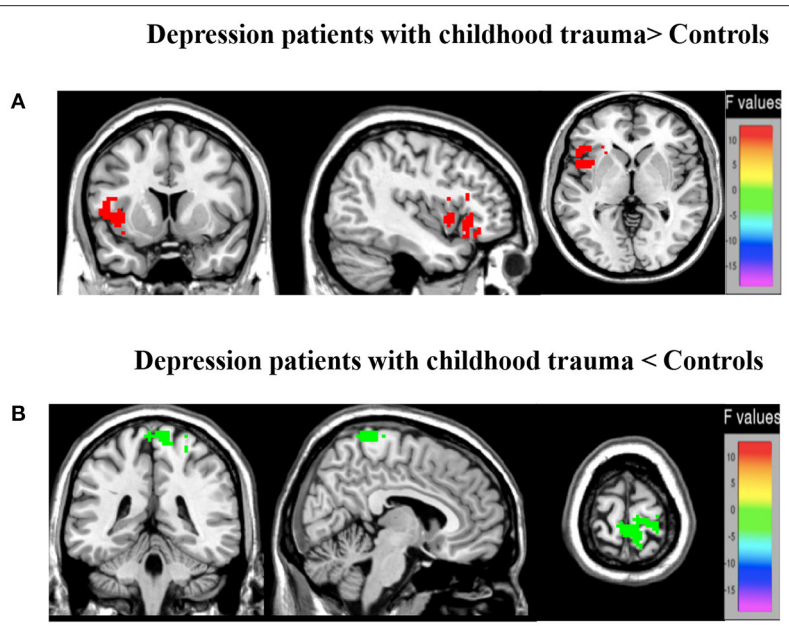

FIGURE 2 | Brain regions showing marked group main effect **(A,B)** on ALFF. **(A)** Warm colors represent reduced ALFF in the MDD with CT when compared with HC; **(B)** cool colors represent the decreased ALFF in the young depression group when compared with HC.

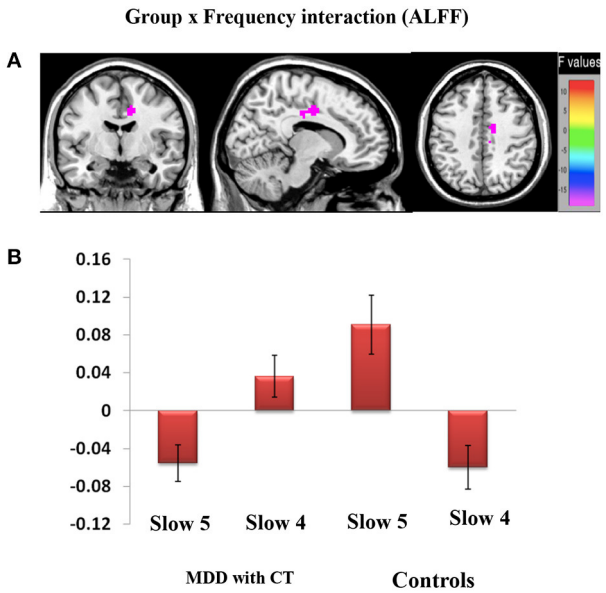

FIGURE 3 | Brain regions showing significant group and frequency (slow-4 and slow-5) interaction **(A,B)** effects on ALFF. **(A)** The interaction between frequency band and group on ALFF. A two-way repeated-measure ANOVA and *post-hoc* test obtained the results. The beta values for dACC were plotted **(B)** to show the directions of the interaction.

Our results are in accord with the previous studies on MDD patients which suggested that the slow-5 band shows stronger LFOs and higher functional activity in the majority of DMN subregions (18, 28, 29). It seems that differences in ALFF between frequency bands in MDD with childhood trauma are similar to MDD patients. Interestingly, in the cingulate cortex, lower ALFF were found in the slow-5 band, which differ from the results of ALFF studies into other diseases (28, 29). The cingulate cortex, a key DMN region shows a strong connectivity in primates with the parahippocampal gyrus and entorhinal cortex, and thus with the hippocampal memory system (30). It has also been reported that the functional connectivity of the cingulate cortex is related to rumination in depression (31). We assume that MDD patients with childhood trauma suffer mainly from a dysfunction of the cingulate cortex.

Increased ALFF Activity in Insular in MDD With CT Patients

The insula is regarded as a hub for external and internal information exchange (32). Accumulating evidence are based on studying changes in insula function in MDD patients, abnormalities in the insula caused by MDD, and dysregulation of the interaction between the insula and other important functional brain networks (such as DMN and central executive network) show can be explored (33–35). The insula plays an important role in generating and processing emotional information, including feelings of anxiety and disgust (36, 37). In short, previous findings demonstrate that the insula plays an important role in the pathogenesis of MDD patients with childhood trauma. Previous neuroimaging studies have found that the abnormal function of the insula is tightly related to the symptoms of depression, including reports that resting-state brain functional connectivity in insula can more accurately distinguish healthy controls from patients with depression (38). Numerous studies have shown a close relationship between

changes in insula function and depression, but the results of these studies are inconsistent. Su et al. found that the ALFF decreases in the insula of depressive patients (39, 40), but some scholars found that the ALFF was increased in the insula of depressive patients (41). Whether MDD patients experience childhood trauma may be one of the reasons leading to the inconsistent. In our study, we found that the ALFF in the insula of the depressive group is observably higher than that in the HC group, indicating the dysfunction of insular in MDD patients with childhood trauma. This dysfunction may be the key factor that severely impairs the ability of MDD patients with childhood trauma to regulate their emotions. Our results show that compared to HC, MDD patients have an increased ALFF in the insula, which indicates abnormal insula activities, and it may further lead to a declined in the ability of regulating the negative emotions.

Decreased ALFF Activity in S1 in MDD With CT Patients

S1, parallel to the central sulcus, is located in the postcentral gyrus (42). S1 is responsible for integrating pain-related information. In animal models, researchers have made a solid conclusion that S1 is involved in sensory-discriminative pain processing; that is, it encodes the location and intensity of pain stimulation (43–45). A number of studies have found that empathizing with others' pain can also activate S1 (46). Moreover, research has shown that the cognitive processing of pain usually begins with activation in prefrontal brain regions, which then further regulates activity in pain-related regions of S1 (47–49). It indicates that the painful somatic symptoms of MDD may relate to functional changes in S1. Several studies have found that when subjects experience different emotions, the activity in S1 also changes and it is highly activated when the subjects focus on their own emotions (50). The result has indicated that S1 takes part in the processing of emotional experience, primarily in the generation of somatosensory emotions. More and more research is supporting the conclusion that S1 is involved in modulating and controlling associatively learned behaviors (51, 52). Schaefer et al. even suggested that S1 functions as an "embodied mind," which supports the existence of the unconscious self in concert with the embodied aspect of the self (53). In short, these findings suggest that S1 is likely to be an important structure closely related to cognitive function. MDD patients with childhood trauma typically have many symptoms related to cognitive impairment, which may be associated with S1 dysfunction. Previous studies have found an increased GM volume in right S1 in patients with comorbid anxiety and MDD (54), while the total area of the somatosensory cortex is reduced in adolescent patients with MDD and in patients with bipolar disorder (55, 56). Kang et al. reported MDD patient's abnormalities in S1–thalamic functional connectivity related to the typical clinical symptoms of MDD, which indicates that such changes are neurobiological characteristics and potential biomarkers of MDD with childhood trauma (57). However, there has still been no research to report the relationship between changes in functional signals in S1 and the development of MDD. In our study, we found that compared to the healthy controls, MDD with CT patients had a lower ALFF in S1, indicating a lower level of spontaneous neural activity. This implies that the dysfunction in left S1 seems to be related to the development of MDD and lead to a possible decline or loss of sensation. We assume that a lower ALFF in S1 may be a specific signal of MDD with the subtype of childhood trauma.

Group × Frequency Interaction in dACC

In this study, a significant group × frequency interaction effect on the ALFF value in dACC is observed. This result indicates that the difference in resting brain function may result from an interaction between frequency bands and disease states. Moreover, it suggests that pathological conditions may increase the influence of some particular frequency bands in the brain, especially in dACC, and that each frequency band may have a specific pathological significance. The dACC is connected with areas of the central executive network and the salience network, which are involved in target maintenance and the integration of sensorimotor and visuomotor inputs, and therefore, guides the output of corresponding behaviors (58). Many studies have shown that functional changes in dACC are involved in the pathophysiological process of MDD (59, 60). In addition, some studies have shown that the components of emotional experience related to pain are processed by the anterior insula and dACC (61), and dACC mainly encodes the psychological aspect of pain sensation (62). These conclusions demonstrate that dACC plays a key role in dealing with social pain and functions as a negative information processing system. A number of animal studies have showed that the dACC was activated when infant mammals were separated from their mothers; however, after the damage to dACC, animal infants reduced their whining during separation. This result has indicated that the brain activities that take part in processing pain-related emotional components are closely related to the degree of painful feelings caused by negative social events.

Researchers also investigated whether different forms of negative social events will have the same effect on activating the brain areas that involved in processing painful components of emotion. In conclusion, in the tasks of social evaluation and social loss, brain areas involved in processing painful emotional components were activated (63). The tasks of negative emotional experiences (such as fear, anxiety, anger, disgust, and sadness) and physiological pain both can lead to the increased activity in insula and dACC. Based on that, a conclusion made is that the damage to the function of dACC may lead to an imbalance in negative information processing in MDD with childhood trauma, activating brain areas related to painful emotional components and producing various negative emotions.

We assume that the disease state and spontaneous brain activity may inhibit individuals' functions to each other, thus causing dysfunction in dACC. The remarkable correlation observed between ALFF in the right dACC within slow-5 suggests that the LFO amplitude in the region may be applied to monitor the disease progress of MDD with childhood trauma.

Limitations

Our study used a cross-sectional design with a relatively small sample. Other confounding differences between the two groups, such as social economic status and mood, may also explain

our findings. Future studies may further investigate how ALFF changes as the depression progresses. Importantly, it would be interesting to directly compare MDD with childhood trauma with MDD without such trauma to isolate the effect of childhood trauma on brain networks in MDD. The exact origins and mechanisms underlying ALFF remain elusive. More studies are needed to comprehend the functional significance of ALFF changes in MDD.

CONCLUSIONS

In conclusion, our results show that changes in the ALFF occur in various brain regions in patients suffering MDD with CT, which indicates that the subtypes of MDD involve the dysfunction of multiple areas of the brain. The CT results of MDD patients demonstrate abnormal LFO amplitudes in many brain regions, consist of subcortical regions, cortical areas, insula, and S1, which highlight abnormalities in LFO amplitudes in MDD with CT and provide insights into understanding the pathophysiology of major depressive disorder.

DATA AVAILABILITY STATEMENT

The raw data supporting the conclusions of this article will be made available by the authors, without undue reservation.

ETHICS STATEMENT

The studies involving human participants were reviewed and approved by Ethics Committee of Affiliated Brain Hospital of Guangzhou Medical University. Written informed consent to participate in this study was provided by the participants' legal guardian/next of kin.

AUTHOR CONTRIBUTIONS

ZW and QL designed the study and drafted the primary manuscript. HW, ZW, and YZ supervised the recruitment and made statistical analyses. YY, JH, and YD took part in recruitment and data management. RY and HP made further revisions of the manuscript. All the authors had read and approved the final manuscript.

FUNDING

The Guangdong Natural Science Foundation, China (2015A030313800 to HP) supported the design of the study. The Guangzhou municipal key discipline in medicine for Guangzhou Brain Hospital (GBH2014-ZD04 to HP) supported the data collection of the study. The Science and Technology Plan Project of Guangdong Province, China (2019B030316001 to Yuping Ning) and the Guangzhou Municipal Psychiatric Disease Clinical Transformation Laboratory (201805010009 to Yuping Ning) supported the interpretation of data of this study.

ACKNOWLEDGMENTS

We would like to thank our subjects for their readiness to engage in this study.

REFERENCES

1. Park LT, Zarate CA. Depression in the primary care setting. *N Engl J Med.* (2019) 380:559–68. doi: 10.1056/NEJMcp1712493
2. Alexopoulos GS. Depression in the elderly. *Lancet.* (2005) 365:1961–70. doi: 10.1016/S0140-6736(05)66665-2
3. Heim C, Newport DJ, Mletzko T, Miller AH, Nemeroff CB. The link between childhood trauma and depression: insights from HPA axis studies in humans. *Psychoneuroendocrinology.* (2008) 33:693–710. doi: 10.1016/j.psyneuen.2008.03.008
4. Scheuer S, Wiggert N, Brückl TM, Awaloff Y, Uhr M, Lucae S, et al. Childhood abuse and depression in adulthood: the mediating role of allostatic load. *Psychoneuroendocrinology.* (2018) 94:134–42. doi: 10.1016/j.psyneuen.2018.04.020
5. Heim C, Mletzko T, Purselle D, Musselman DL, Nemeroff CB. The dexamethasone/corticotropin-releasing factor test in men with major depression: role of childhood trauma. *Biol Psychiatr.* (2008) 63:398–405. doi: 10.1016/j.biopsych.2007.07.002
6. Ulbricht CM, Chrysanthopoulou SA, Levin L, Lapane KL. The use of latent class analysis for identifying subtypes of depression: a systematic review. *Psychiatr Res.* (2018) 266:228–46. doi: 10.1016/j.psychres.2018.03.003
7. Nelson J, Klumparendt A, Doebler P, Ehring T. Childhood maltreatment and characteristics of adult depression: meta-analysis. *Br J Psychiatr.* (2017) 210:96–104. doi: 10.1192/bjp.bp.115.180752
8. Xie P, Wu K, Zheng Y, Guo Y, Yang Y, He J, et al. Prevalence of childhood trauma and correlations between childhood trauma, suicidal ideation, and social support in patients with depression, bipolar disorder, and schizophrenia in southern China. *J Affect Disord.* (2018) 228:241–8. doi: 10.1016/j.jad.2017.11.011
9. Wiersma JE, Hovens JG, van Oppen P, Giltay EJ, van Schaik DJ, Beekman AT, et al. The importance of childhood trauma and childhood life events for chronicity of depression in adults. *J Clin Psychiatr.* (2009) 70:983–9. doi: 10.4088/jcp.08m04521
10. Gamble SA, Talbot NL, Duberstein PR, Conner KR, Franus N, Beckman AM, et al. Childhood sexual abuse and depressive symptom severity: the role of neuroticism. *J Nerv Ment Dis.* (2006) 194:382–5. doi: 10.1097/01.nmd.0000218058.96252.ac
11. Yu M, Shinohara RT, Oathes DJ, Cook PA, Duprat R, Moore TM, et al. Childhood trauma history is linked to abnormal brain connectivity in major depression. *Proc Natl Acad Sci USA.* (2019) 116:8582–90. doi: 10.1073/pnas.1900801116
12. Saleh A, Potter GG, McQuoid DR, Boyd B, Turner R, MacFall JR, et al. Effects of early life stress on depression, cognitive performance and brain morphology. *Psychol Med.* (2017) 47:171–81. doi: 10.1017/S0033291716002403
13. Du L, Wang J, Meng B, Yong N, Yang X, Huang Q, et al. Early life stress affects limited regional brain activity in depression. *Sci Rep.* (2016) 6:25338. doi: 10.1038/srep25338
14. Arnone D, McIntosh AM, Ebmeier KP, Munafò MR, Anderson IM. Magnetic resonance imaging studies in unipolar depression: systematic review and meta-regression analyses. *Eur Neuropsychopharmacol.* (2012) 22:1–16. doi: 10.1016/j.euroneuro.2011.05.003
15. Zhou Y, Wang K, Liu Y, Song M, Song SW, Jiang T. Spontaneous brain activity observed with functional magnetic resonance imaging as a potential

biomarker in neuropsychiatric disorders. *Cognitive Neurodyn.* (2010) 4:275–94. doi: 10.1007/s11571-010-9126-9
16. Fox MD, Raichle ME. Spontaneous fluctuations in brain activity observed with functional magnetic resonance imaging. *Nat Rev Neurosci.* (2007) 8:700–11. doi: 10.1038/nrn2201
17. Knyazev GG. Motivation, emotion, and their inhibitory control mirrored in brain oscillations. *Neurosci Biobehav Rev.* (2007) 31:377–95. doi: 10.1016/j.neubiorev.2006.10.004
18. Wang L, Kong Q, Li K, Su Y, Zeng Y, Zhang Q, et al. Frequency-dependent changes in amplitude of low-frequency oscillations in depression: a resting-state fMRI study. *Neurosci. Lett.* (2016) 614:105–11. doi: 10.1016/j.neulet.2016.01.012
19. Zuo XN, Di Martino A, Kelly C, Shehzad ZE, Gee DG, Klein DF, et al. The oscillating brain: complex and reliable. *Neuroimage.* (2010) 49:1432–45. doi: 10.1016/j.neuroimage.2009.09.037
20. Helmreich I, Wagner S, Mergl R, Allgaier A-K, Hautzinger M, Henkel V, et al. Sensitivity to changes during antidepressant treatment: a comparison of unidimensional subscales of the Inventory of Depressive Symptomatology (IDS-C) and the Hamilton Depression Rating Scale (HAMD) in patients with mild major, minor or subsyndromal depression. *Eur Arch Psychiatr Clin Neurosci.* (2011) 262:291–304. doi: 10.1007/s00406-011-0263-x
21. Bernstein DP, Stein JA, Newcomb MD, Walker E, Pogge D, Ahluvalia T, et al. Development and validation of a brief screening version of the childhood trauma questionnaire. *Child Abuse Negl.* (2003) 27:169–90. doi: 10.1016/s0145-2134(02)00541-0
22. Jansen K, Cardoso TA, Fries GR, Branco JC, Silva RA, Kauer-Sant'Anna M, et al. Childhood trauma, family history, and their association with mood disorders in early adulthood. *Acta Psychiatr Scand.* (2016) 134:281–136. doi: 10.1111/acps.12551
23. Yu R, Chien Y-L, Wang H-LS, Liu C-M, Liu C-C, Hwang T-J, et al. Frequency-specific alternations in the amplitude of low-frequency fluctuations in schizophrenia. *Human Brain Mapp.* (2014) 35:627–37. doi: 10.1002/hbm.22203
24. Yang L, Yan Y, Li Y, Hu X, Lu J, Chan P, et al. Frequency-dependent changes in fractional amplitude of low-frequency oscillations in Alzheimer's disease: a resting-state fMRI study. *Brain Imag Behav.* (2019) 14:2187–201. doi: 10.1007/s11682-019-00169-6
25. Buzs aki G, Draguhn A. Neuronal oscillations in cortical networks. *Science.* (2004) 304:1926–9. doi: 10.1126/science.1099745
26. Salvador R, Suckling J, Schwarzbauer C, Bullmore E. Undirected graphs of frequency-dependent functional connectivity in whole brain networks. *Philos Trans R Soc B: Biol Sci.* (2005) 360:937–46. doi: 10.1098/rstb.2005.1645
27. Raichle ME, MacLeod AM, Snyder AZ, Powers WJ. A default mode of brain function. *PNAS.* (2001) 98:676–82. doi: 10.1073/pnas.98.2.676
28. Liu X, Wang S, Zhang X, Wang Z, Tian X, He Y. Abnormal amplitude of low-frequency fluctuations of intrinsic brain activity in Alzheimer's disease. *J Alzheimers Dis.* (2014) 40:387–97. doi: 10.3233/JAD-131322
29. Wei L, Duan X, Zheng C, Wang S, Gao Q, Zhang Z, et al. Specific frequency bands of amplitude low-frequency oscillation encodes personality. *Hum Brain Mapp.* (2014) 35:331–9. doi: 10.1002/hbm.22176
30. Bubb EJ, Kinnavane L, Aggleton JP. Hippocampal–diencephalic–cingulate networks for memory and emotion: An anatomical guide. *Brain Neurosci Adv.* (2017) 1:2398212817723443. doi: 10.1177/2398212817723443
31. Berman MG, Peltier S, Nee DE, Kross E, Deldin PJ, Jonides J. Depression, rumination and the default network. *Soc Cogn Affect Neurosci.* (2011) 6:548–55. doi: 10.1093/scan/nsq080
32. Mufson EJ, Mesulam MM. Insula of the old world monkey. II: Afferent cortical input and comments on the claustrum. *J Comp Neurol.* (1982) 212:223–37. doi: 10.1002/cne.902120103
33. Menon V. Large-scale brain networks and psychopathology: a unifying triple network model. *Trends Cogn Sci.* (2011) 15:483–506. doi: 10.1016/j.tics.2011.08.003
34. Manoliu A, Meng C, Brandl F, Doll A, Tahmasian M, Scherr M, et al. Insular dysfunction within the salience network is associated with severity of symptoms and aberrant inter-network connectivity in major depressive disorder. *Front Human Neurosci.* (2014) 7:930. doi: 10.3389/fnhum.2013.00930
35. Kaiser RH, Andrews-Hanna JR, Wager TD, Pizzagalli DA. Large-scale network dysfunction in major depressive disorder: a meta-analysis of resting-state functional connectivity. *JAMA Psychiatr.* (2015) 72:603–11. doi: 10.1001/jamapsychiatry.2015.0071
36. Singer T, Critchley HD, Preuschoff K. A common role of insula in feelings, empathy and uncertainty. *Trends Cogn Sci.* (2009) 13:334–40. doi: 10.1016/j.tics.2009.05.001
37. Lamm C, Singer T. The role of anterior insular cortex in social emotions. *Brain Struct Funct.* (2010) 214:579–91. doi: 10.1007/s00429-010-0251-3
38. Ambrosi E, Arciniegas DB, Madan A, Curtis KN, Patriquin MA, Jorge RE, et al. Insula and amygdala resting-state functional connectivity differentiate bipolar from unipolar depression. *Acta Psychiatr Scand.* (2017) 136:129–39. doi: 10.1111/acps.12724
39. Fitzgerald PB, Laird AR, Maller J, Daskalakis ZJ. A meta-analytic study of changes in brain activation in depression. *Human Brain Mapp.* (2008) 29:683–95. doi: 10.1002/hbm.20426
40. Su L, Cai Y, Xu Y, Dutt A, Shi S, Bramon E. Cerebral metabolism in major depressive disorder: a voxel-based meta-analysis of positron emission tomography studies. *BMC Psychiatr.* (2014) 14:321. doi: 10.1186/s12888-014-0321-9
41. Liu CH, Ma X, Song LP, Fan J, Wang WD, Lv XY, et al. Abnormal spontaneous neural activity in the anterior insular and anterior cingulate cortices in anxious depression. *Behav Brain Res.* (2015) 281:339–47. doi: 10.1016/j.bbr.2014.11.047
42. Kaas JH, Nelson RJ, Sur M, Lin CS, Merzenich MM. Multiple representations of the body within the primary somatosensory cortex of primates. *Science.* (1979) 204:521–3. doi: 10.1126/science.107591
43. Guilbaud G, Benoist JM, Levante A, Gautron M, Willer JC. Primary somatosensory cortex in rats with pain-related behaviours due to a peripheral mononeuropathy after moderate ligation of one sciatic nerve: neuronal responsivity to somatic stimulation. *Exp Brain Res.* (1992) 92:227–45. doi: 10.1007/BF00227967
44. Follett KA, Dirks B. Characterization of responses of primary somatosensory cerebral cortex neurons to noxious visceral stimulation in the rat. *Brain Res.* (1994) 656:627–32. doi: 10.1016/0006-8993(94)91362-5
45. Canavero S, Bonicalzi V. Role of primary somatosensory cortex in the coding of pain. *Pain.* (2013) 154:1156–8. doi: 10.1016/j.pain.2013.02.032
46. Apkarian AV, Bushnell MC, Treede RD, Zubieta JK. Human brain mechanisms of pain perception and regulation in health and disease. *Eur J Pain.* (2005) 9:463–84. doi: 10.1016/j.ejpain.2004.11.001
47. Rainville P, Duncan GH, Price DD, Carrier B, Bushnell MC. Pain affect encoded in human anterior cingulate but not somatosensory cortex. *Science.* (1997) 277:5968–71. doi: 10.1126/science.277.5328.968
48. Peyron R, Laurent B, García-Larrea L. Functional imaging of brain responses to pain. A review and meta-analysis. *Neurophysiol Clin.* (2000) 30:263–88. doi: 10.1016/s0987-7053(00)00227-6
49. Rainville P. Brain mechanisms of pain affect and pain modulation. *Curr Opin Neurobiol.* (2002) 12:195–204. doi: 10.1016/s0959-4388(02)00313-6
50. Damasio AR, Grabowski TJ, Bechara A, Damasio H, Ponto LL, Parvizi J, et al. Subcortical and cortical brain activity during the feeling of self-generated emotions. *Nat Neurosci.* (2000) 3:1049–56. doi: 10.1038/79871
51. Galvez R, Weiss C, Weible AP, Disterhoft JF. Vibrissa-signaled eyeblink conditioning induces somatosensory cortical plasticity. *J Neurosci.* (2006) 26:6062–8. doi: 10.1523/JNEUROSCI.5582-05.20
52. Chau LS, Davis AS, Galvez R. Neocortical synaptic proliferation following forebrain-dependent trace associative learning. *Behav Neurosci.* (2013) 127:285–92. doi: 10.1037/a0031890
53. Schaefer M, Northoff G. Who am i: the conscious and the unconscious self. *Front Hum Neurosci.* (2017) 11:126. doi: 10.3389/fnhum.2017.00126
54. Qi H, Ning Y, Li J, Guo S, Chi M, Gao M, et al. Gray matter volume abnormalities in depressive patients with and without anxiety disorders. *Medicine.* (2014) 93:e345. doi: 10.1097/MD.0000000000000345
55. Koutsouleris N, Meisenzahl EM, Borgwardt S, Riecher-Rössler A, Frodl T, Kambeitz J, et al. Individualized differential diagnosis of schizophrenia and mood disorders using neuroanatomical biomarkers. *Brain.* (2015) 138:2059–73. doi: 10.1093/brain/awv111
56. Schmaal L, Hibar DP, Sämann PG, Hall GB, Baune BT, Jahanshad N, et al. Cortical abnormalities in adults and adolescents with major depression

based on brain scans from 20 cohorts worldwide in the ENIGMA Major depressive disorder working group. *Mol Psychiatr.* (2017) 22:900–9. doi: 10.1038/mp.2016.60

57. Kang L, Zhang A, Sun N, Liu P, Yang C, Li G, et al. Functional connectivity between the thalamus and the primary somatosensory cortex in major depressive disorder: a resting-state fMRI study. *BMC Psychiatr.* (2018) 18:339. doi: 10.1186/s12888-018-1913-6
58. Seeley WW, Menon V, Schatzberg AF, Keller J, Glover GH, Kenna H, et al. Dissociable intrinsic connectivity networks for salience processing and executive control. *J Neurosci.* (2007) 27:2349–56. doi: 10.1523/JNEUROSCI.5587-06.2007
59. Wagner G, Köhler S, Bär KJ. Treatment associated changes of functional connectivity of midbrain/brainstem nuclei in major depressive disorder. *Sci Rep.* (2017) 7:8675. doi: 10.1038/s41598-017-09077-5
60. Schwartz J, Ordaz SJ, Kircanski K, Ho TC, Davis EG, Camacho MC, et al. Resting-state functional connectivity and inflexibility of daily emotions in major depression. *J Affect Disord.* (2019) 249:226–34. doi: 10.1016/j.jad.2019.01.040
61. Price DD. Psychological and neural mechanisms of the affective dimension of pain. *Science.* (2000) 288:1769–72. doi: 10.1126/science.288.5472.1769
62. Treedea R-D, Kenshalo DR, Gracelyb RH, Jones AK. The cortical representation of pain. *Pain.* (1999) 79:105–11. doi: 10.1016/s0304-3959(98)00184-5
63. Eisenberger NI, Inagaki TK, Muscatell KA, Byrne Haltom KE, Leary MR. The neural sociometer: brain mechanisms underlying state self-esteem. *J Cogn Neurosci.* (2011) 23:3448–55. doi: 10.1162/jocn_a_00027

Conflict of Interest: The authors declare that the research was conducted in the absence of any commercial or financial relationships that could be construed as a potential conflict of interest.

frontiers in Neuroscience

ORIGINAL RESEARCH
published: 05 February 2021
doi: 10.3389/fnins.2021.605115

Diagnosis of Alzheimer's Disease Using Brain Network

*Ramesh Kumar Lama and Goo-Rak Kwon**

The Alzheimer's Disease Neuroimaging Initiative, Department of Information and Communication Engineering, Chosun University, Gwangju, South Korea

Recent studies suggest the brain functional connectivity impairment is the early event occurred in case of Alzheimer's disease (AD) as well as mild cognitive impairment (MCI). We model the brain as a graph based network to study these impairment. In this paper, we present a new diagnosis approach using graph theory based features from functional magnetic resonance (fMR) images to discriminate AD, MCI, and healthy control (HC) subjects using different classification techniques. These techniques include linear support vector machine (LSVM), and regularized extreme learning machine (RELM). We used pairwise Pearson's correlation-based functional connectivity to construct the brain network. We compare the classification performance of brain network using Alzheimer's disease neuroimaging initiative (ADNI) datasets. Node2vec graph embedding approach is employed to convert graph features to feature vectors. Experimental results show that the SVM with LASSO feature selection method generates better classification accuracy compared to other classification technique.

Keywords: Alzhieimer's disease, brain network, node2vec, extreme learning machine, support vector machine

OPEN ACCESS

Edited by:
Szilvia Anett Nagy,
University of Pécs, Hungary

Reviewed by:
Kewei Chen,
Banner Alzheimer's Institute, United States
Alexandra L. Young,
University College London, United Kingdom

***Correspondence:**
Goo-Rak Kwon
grkwon@chosun.ac.kr

Specialty section:
This article was submitted to Brain Imaging Methods, a section of the journal Frontiers in Neuroscience

Received: *11 September 2020*
Accepted: *06 January 2021*
Published: *05 February 2021*

Citation:
Lama RK and Kwon G-R (2021) Diagnosis of Alzheimer's Disease Using Brain Network. Front. Neurosci. 15:605115. doi: 10.3389/fnins.2021.605115

INTRODUCTION

Alzheimer's disease (AD), which causes majority of dementia is a progressive neurodegenerative disease (American Psychiatric Association, 1994; Liu F. et al., 2014; Schmitter et al., 2015; Alzheimer's association, 2016). The subtle AD neuropathological process begins years before the visible progressive cognitive impairment, which is trouble to remember and learn new information. Currently there is no cure and treatment to slow or stop its progression. Currently, more research works are focused toward earlier intervention of AD. Thus accurate diagnosis of disease at its early stage makes great significance in such scenario.

With the availability of recent neuroimaging technology, promising result is obtained in the early and accurate detection of AD (Hanyu et al., 2010; Górriz et al., 2011; Gray et al., 2012). The study of progression of disease and early detection is carried out by using different imaging models, such as electroencephalography (EEG) (Pfefferbaum et al., 2000), functional magnetic resonance imaging (fMRI) (Masliah et al., 1993), single-photon emission computed tomography (SPECT) (Chen et al., 2013) and positron emission tomography (PET) (Ly et al., 2014).

Similarly, structural magnetic resonance imaging (MRI) (Hanyu et al., 1999; Canu et al., 2010; Bendlin et al., 2012) is the most commonly used imaging system for study of AD. The feature extracted from MRI is typically gray matter volumes and measured as important biomarker for the study of neurodegeneration, alterations of hippocampal white matter pathways is often observed in AD (Delbeuck et al., 2003; Liu Y. et al., 2014). Several studies reveal the alterations in widely distributed functional and structural connectivity pairs are prevalent in AD and mild cognitive impairment (MCI) (Delbeuck et al., 2007; Acosta-Cabronero et al., 2012). Additionally, in recent studies, the resting-state functional magnetic resonance imaging (rs-fMRI) has been widely used

for the investigations of progression of AD (Stam et al., 2006; Sorg et al., 2007; Supekar et al., 2008; Doan et al., 2017). This imaging system evaluates the impulsive variabilities seen in the blood oxygenation level-dependent (BOLD) indications in various regions of the brain. Several studies are carried out based on aberrant regional spontaneous fluctuation of BOLD, functional connectivity and alteration in functional brain network. These studies are carried out in different networks, such as default mode network, somatomotor network, dorsal attention network, limbic network, and frontoparietal control network (Bullmore and Sporns, 2009). Thus, the graph theory based network analyses of human brain functional connectomes, provides better insights of the network structure to reveal abnormal patterns of organization of functional connectivity in AD infected brain (Rubinov and Sporns, 2010; Sporns, 2011).

Graph theory is a mathematical approach to study complex networks. Network is constructed of vertices which are interconnected by edges. Vertices in our case are brain regions. Graph theory is widely used as tool for identifying anatomically localized subnetworks associated with neuronal alterations in different neurodegenerative diseases (Bajo et al., 2010). In fMRI images, graph represents causal relations or correlations of different nodes in constructed networks. However, the brain network built by graph has non-Euclidian characteristics. Thus, applying machine learning techniques to analyze the brain networks is challenging. We use graph embedding to transform graphs to a vector or set of vectors to overcome this problem. Embedding captures the graph topology, vertex-vertex relationship, and other relevant graph information. In the current study, we used node2vec graph embedding technique to transform vertex and edge of brain network graph to feature vector. With the help of this model we have analyzed and classified the networks of brain from fMRI data into AD, MCI, and HC.

MATERIALS FOR THE STUDY

fMRI Dataset

In our study, we have used the dataset from Alzheimer's disease neuroimaging initiative database (ADNI)[1]. The ADNI database was launched in 2004. The database consists of subjects of age ranging from 55–90 years. The goal of ADNI is to study the progression of the disease using different biomarkers. This includes clinical measures and assesses of the structures and functions of brain for the course of different disease states.

All participants were scanned using 3.0-Telsa Philips Achieva scanners at different centers. Same scanning protocol were followed for all participants and the set parameters were ratio of Repetition Time (TR) to Echo Time (TE) i.e., TR/TE = 3000/30 *ms*, 140 volumes, also voxel thickness as 3.3 mm, acquisition matrix size = 64 × 64, 48 slices, flip angle = 80° Similarly, 3D T1-weighted images were collected using MPRAGE sense2 sequences with acquisition type 3D, field strength = 3 Tesla, flip angle 9.0 degree, pixel spacing X = 1.0547000169754028 mm; Pixel Spacing Y = 1.0547000169754028 mm, slice thickness = 1.2000000476837158 mm; echo time (TE) 2.859 ms, inversion time (TI) 0.0 ms, repetition time (TR) 6.6764 ms and weighting T1. We selected subjects as specified in Table.

[1]http://adni.loni.usc.edu/

Subjects

We selected 93 subjects from ADNI2 cohort. The purpose of ADNI2 is to examine how brain imaging and other biomarkers can be used to measure the progression of MCI and early AD. The ADNI selects and categorizes participants in specific group based on certain inclusion criteria. The criteria are well defined in[2]. We selected the subjects according to availability of both MRI and fMRI data. Thus, the subjects with following demographic status as shown in **Table 1** with following average age, clinical dementia rating (CDR) and mini-mental state estimation (MMSE) out of all available data in ADNI2 cohort were selected in our study.

1. 31 HC subjects: 14 males, 17 females; age ± SD = 73.9 ± 5.4 years with the mini-mental state estimation (MMSE) score of 28.9 ± 1.65 and the range was 24–30.
2. 31 MCI subjects: 17 males, 14 females; age ± SD = 74.5 ± 5.0 with the MMSE score of 27.5 ± 2.02, and range was 22–30.
3. 31 AD subjects: 13 males, 18 females; age ± SD = 72.7 ± 7.0 with MMSE = 20.87 ± 3.6, and the range was 14–26.

Data Preprocessing

We used data processing subordinate for the resting state fMRI via DPARSF[3] (Chao-Gan and Yu-Feng, 2010) and the statistical parametric mapping platform via SPM8[4] aimed at the preprocessing of rs-fMRI data. All the images initially obtained from scanner were in the format of digital imaging and communications in medicine (DICOM). We converted these images to neuroimaging informatics technology initiative (NIfTI) file format. Signal standardization and participant's adaptation to the noise while scanning each participant are carried out by discarding the first 10 time points for each participant. Next, we preformed preprocessing operation through following steps:

For slice-timing correction last slice was referred reference slice. Friston 24-parameter model with 6 parameters of head motion, 6 parameters of head motion from the previous time point, and 12 corresponding squared items were employed for

[2]https://www.nia.nih.gov/alzheimers/clinical-trials/alzheimers-disease-neuroimaging-initiative-2-adni2

[3]http://www.restfmri.net

[4]http://www.fil.ion.ucl.ac.uk/spm

TABLE 1 | Summary of subject's demographic status.

Number of	HC (*n* = 31)	MCI (*n* = 31)	AD (*n* = 31)
subjects	Mean (SD)	Mean (SD)	Mean (SD)
Age (years)	73.9 ± 5.4	74.5 ± 5.0	SD = 72.7 ± 7.0
Global CDR	0.04 ± 0.13	0.5 ± 0.18	0.95 ± 0.30
MMSE	28.9 ± 1.65	27.5 ± 2.02	20.87 ± 3.6

realignment for head movement compensation. Similarly, after the realignment, individual structural images (T1-weighted MPRAGE) were registered to the mean functional image. For the standardization of the rs-fMRI toward the original place was accomplished with the help of diffeomorphic anatomical registration through exponentiated lie algebra (DARTEL) as in Ashburner (2007) (resampling voxel size = 3 mm × 3 mm × 3 mm). A 6 mm full width at half-maximum (FWHM) Gaussian kernel spatial smoothing was employed for the smoothing. Next, we performed linear trend exclusion and also the temporal band pass filtering which ranges at (0.01 Hz < f < 0.08 Hz) on the time series of each voxel. Finally, cerebrospinal as well as white matter signals along with six head-motion parameters were regressed out to reduce the effects of nuisance signals.

Proposed Framework

This proposed method consists of the following four major functional steps as shown in **Figure 1**:

1. Construct a brain network using graph theory.
2. Convert graph to feature vector using node2vec graph embedding.
3. Reduce the features.
4. Perform the classification using regularized extreme learning machine (RELM) and linear support vector machine (LSVM).

Construction of Brain Networks

For the construction of network from fMR images, we first preprocessed the raw fMR data as described in data preprocessing section. Next, we used the automated anatomical labeling (AAL) atlas to identify the brain regions of interest (ROI). The whole image was divided in 116 regions with each hemisphere. Next, we calculate the average time series of each ROI for each subject by averaging their time series across the voxels within each ROI. For each subject, a matrix of 130 rows and 116 columns was obtained. In the matrix, every row denotes the time series conforming to a give ROI, while information of total regions at a definite time point are stored at each column. The mean time series of each brain region were obtained for each individual by averaging the time series within the region. For $L_i = (l_i(1), l_i(2), \ldots, l_i(n))$ and $L_j = (l_j(1), l_j(2), \ldots, l_j(n))$ are two n length time series of brain region i and j, the Pearson's correlation (PC) between them can be calculated as

$$PC_{ij} = \frac{cov(L_i, L_j)}{\sigma_{L_i}\sigma_{L_j}} \quad (1)$$

Where $cov(L_i, L_j)$ is covariance of variables L_i and L_j. Similarly, σ_{L_i} and σ_{L_j} are standard deviation of variables L_i and L_j. This operation results into 116 × 116 correlation matrix which defines the relation amongst different regions of brain and matches to the functional connectivity network.

Graph-Embedding

Graphs are complex data structures, consisting a finite set of vertices and set of edges which connect a pair of nodes. One of the possible solutions to manipulate prevalent pattern recognition algorithms on graphs is embedding the graph into vector space. Indeed, graph embedding is a bridge between statistical pattern recognition and graph mining. We employ the node2vec (Grover and Leskovec, 2016) algorithm as graph embedding tool in this study. The node2vec algorithm aims to learn a vectorial representation of nodes in a graph by optimizing a neighborhood preserving objective. It extends the previous node embedding algorithm Deepwalk (Canu et al., 2010) and it is inspired from the state of art word embedding algorithm word2vec (Delbeuck et al., 2003).

In word2vec, given a set of sentences also known as corpus, the model learns word embedding by analyzing the context of each word in the body. The word2vec uses the neural network with one hidden layer to transform words into embedding vectors. This neural network is known as Skip-gram. This network is trained to

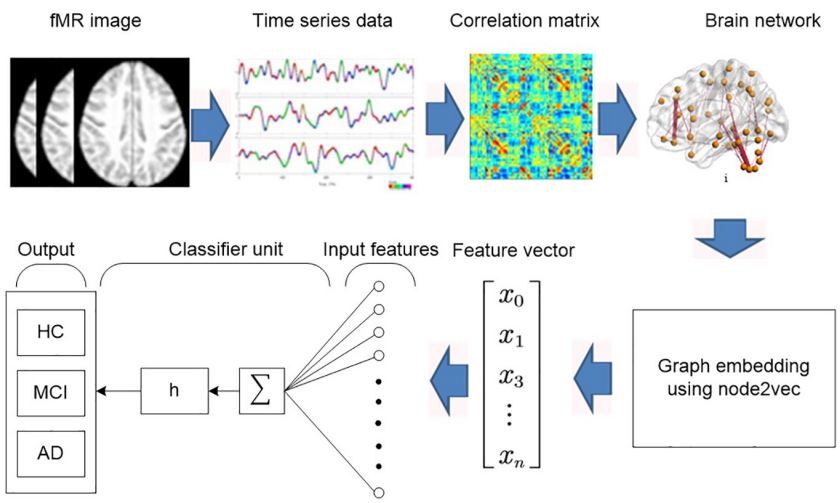

FIGURE 1 | Block diagram of the proposed diagnosis system.

predict the neighboring word in the sentence. It accepts the word at the input and is optimized such that it predicts the neighboring words in a sentence with high probability.

node2vec applies the same embedding approach to train and predict the neighborhood of a node in graph. However, word is replaced by the node and the bag of nodes is used instead of corpus. The sampling is used to generate this bag of nodes from a graph. Generally, the graph embedding consists of three steps:

Sampling

A graph is sampled with random walks. This random walk results in bag of nodes of neighborhood from sampling. The bag of nodes acts as a collection of contexts for each node in the network. The innovation of node2vec with respect to Deepwalk is the use of flexible biased random walks on the network. In Deepwalk, random walk is obtained by a uniform random sampling over the linked nodes, while node2vec combine two different strategies for the network exploration: depth-first search (DFS) and breadth-first-search (BFS). For current random walk position at node v and traversed position at previous step at node t and neighboring nodes x_1, x_2 and x_3, the sampling of next node x is determined by evaluating the unnormalized transition probabilities π_{vx} on edge (t, v) with the static edge weight w_{vx} as shown in **Figure 2**. This unnormalized transition probability is estimated based on search bias α defined by two parameters p and q such that $\pi_{vx} = \alpha_{pq}(t, x) \cdot w_{vx}$ where.

$$\alpha_{pq}(t,x) = \begin{cases} \frac{1}{p}, & \text{if } d_{tx} = 0 \\ 1, & \text{if } d_{tx} = 1 \\ \frac{1}{q}, & \text{if } d_{tx} = 2 \end{cases} \quad (2)$$

Here d_{tx} denotes the shortest path distance between nodes t and x.

The parameter p determines the likelihood of sampling the node t again during random walk. When the value of p is high revisit of the node possibility is low. Similarly the parameter q allows to different between local and global nodes. If $q > 1$, the random walk has the likelihood of sampling the nodes around the node v is high.

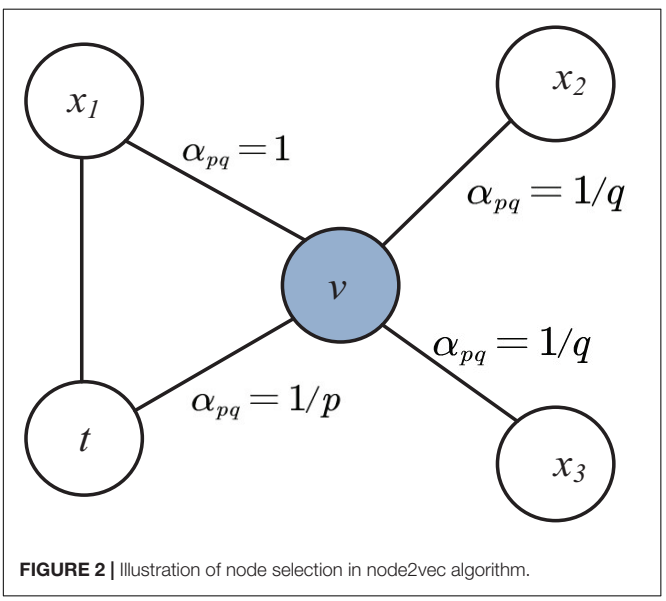

FIGURE 2 | Illustration of node selection in node2vec algorithm.

Training Skip-Gram

The bag of nodes generated from the random walk is fed into the skip-gram network. Each node is represented by a one-hot vector and maximizes the probability for predicting neighbor nodes. The one-hot vector has size same as the size of the set of unique words used in the text corpus. For each node only one dimension is equal to one and remaining are zeros. The position of dimension having one in vector defines the individual node.

Computing Embedding

The output of the hidden layer of the network is taken as the embedding of the graph.

Feature Reduction Techniques

Support Vector Machine-Recursive Feature Elimination (SVM-RFE)

Support vector machine-recursive feature elimination is a multivariate feature reduction algorithm is based on wrapper model. This method is recursive and in each of iteration of the RFE, LSVM model is trained. This method starts by constructing a model on the complete set of features and computing the importance score for each feature. The least important features are removed and the model is rebuilt and the importance scores are again computed. This recursive procedure is continued until all the features are eliminated. Then, the features are ranked according to the order of elimination. A detailed description of SVM-RFE procedure presented in a previous paper (Guyon et al., 2002). In this work, after applying SVM-RFE, the most significant training features that make the most of cross-validated accurateness are kept to train the classifiers.

Least Absolute Shrinkage and Selection Operator (LASSO)

Least absolute shrinkage and selection operator (Tibshirani, 1996) is a powerful method which is used to remove insignificant features. Two major tasks of this method are regularization and feature selection. This method minimizes residual sum of squares of the model using ordinary least square regression (OLS) by placing a constraint on the sum of the absolute values of the model parameters. LASSO computes model coefficients β by minimizing the following function:

$$RSS_{LASSO}(\beta_i, \beta_0) = \underset{\beta}{\arg\min} \left[\sum_{i=1}^{n} \left(y_i - (\beta_i x_i + \beta_0)\right)^2 + \alpha \sum_{j=1}^{k} |\beta_j| \right] \quad (3)$$

Where, x_i is the graph embedded feature input data, a vector of k values at observation j, and n is the number of observations. y_i is the response at observation i. α is a non-negative user defined regularization parameter. This parameter controls the strength of penalty. When α is sufficiently large then coefficients are forced

to be zero which leads to produce few relevant features. If α approaches 0 the model becomes OLS with more relevant features (Hanyu et al., 2010).

Features Selection With Adaptive Structure Learning (FSASL)

Features selection with adaptive structure learning is an unsupervised method which performs data manifold learning and feature selection. This method first utilizes the adaptive structure of the data to construct the global learning and the local learning. Next, the significant features are selected by integrating both of them with $L_{2,1}$-norm regularizer. This method utilizes the sparse reconstruction coefficients to extract the global structure of data for global learning. In sparse representation, each data sample x_i can be approximated as a linear combination of all the other samples, and the optimal sparse combination weight matrix.

For local learning, this method directly learns a Euclidean distance induced probabilistic neighborhood matrix (Du and Shen, 2015).

$$\min_{W,S,P} (\|W^T X - W^T XS\|^2 + \alpha\|S\|_1) + \beta \sum_{i,j}^{n} (\|W^T x_i - W^T x_j\|^2 P_{ij} + \mu P_{ij}^2) + \gamma\|W\|_{21}$$
$$\text{s.t. } S_{ii} = 0, P1_n = 1_n, P \geq 0, W^T XX^T X = I \quad (4)$$

Where, α is used to balancing the sparsity and the reconstruction error, β and γ are regularization parameters for global and local structure learning in first and second group and the sparsity of feature selection matrix in the third group. Similarly, S is used to guide the search of relevant global feature and P defines the local neighborhood of data sample x_i.

Local Learning and Clustering Based Feature Selection (LLCFS)

LLCFS is clustering based feature selection method. This method learns the adaptive data structure with selected features by constructing the k-nearest neighbor graph in the weighted feature space (Zeng and Cheung, 2011). The joint clustering and feature weight learning is performed by solving the following problem.

$$\min_{Y,\{W^i,b^i\}_{i=1}^n,z} \sum_{i=1}^{n} \sum_{c'=1}^{c} \left[\sum_{x_j \in N_{x_i}} \beta(Y_{ic'} - x_j^T W_{c'}^i - b_c^i)^2 + (W_{c'}^i)^T \text{diag}(z^{-1}) W_{c'}^i \right]$$
$$\text{s.t. } 1_d^T z = 1, z \geq 0 \quad (5)$$

Where z the feature weight vector and N_{x_i} is the k-nearest neighbor of x_i based on z weighted features.

Pairwise Correlation Based Feature Selection (CFS)

CFS selects features based on the ranks attributes according to an empirical evaluation function based on correlations (Hall, 2000). Subsets made of attribute vectors are evaluated by evaluation function, which are associated with the labels of class, however autonomous among each another. CFS accepts that unrelated structures express a low correspondence with the class and hence they are ought to be overlooked by the procedure. Alternatively, additional features must be studied, as they are typically hugely correlated with one or additional amount of other features.

Classification

Two of the prevalent machine-learning classification algorithms namely, LSVM, and RELM are studied in this article. The results acquired through the experiments of these classifiers show that RELM classifier performs better than others respective of the computation time required and accuracy value. Each of the methods is described in brief in the subsections below.

Support Vector Machine Classifier

Linear support vector machine (Cortes and Vapnik, 1995) is principally a supervised binary classifier that classifies separable and non-separable data. This type of classification is usually used in the field of neuroimaging and is deliberated as one of the finest machine-learning method in the domain of the neuroscience for past decades. It discovers the best hyperplane to split both classes which has optimum boundary from support vectors for the duration of the training. The classifier decides on the basis of the estimated hyperplane to test the new data points. For the patterns that are linearly separable, LSVM can be used. Alternatively, LSVM is not capable of guaranteeing improved performance in the complex circumstances with the patterns that are not separable. In such circumstances, Kernel trick is used to extend the LSVM. The input arrays of linear SVM are plotted to the space dimensions using the kernels. Both the linear as well as non-linear radial basis function (RBF) kernels are extensively trained using SVM kernels.

Extreme Learning Machine

ELM (Extreme Learning Machine) is single layer feedforward neural networks (Huang et al., 2006; Zhang et al., 2015). This neural network is implemented using Moore-Penrose generalized inverse to set its weights (Peng et al., 2013; Cao et al., 2016). Thus, this learning algorithm doesn't require iterative gradient-based backpropagation to tune the artificial hidden nodes. Thus this method is considered as effective solution with extremely reduced complexity (Cambria and Huang, 2013; Qureshi et al., 2016). ELM with L number of hidden nodes and g(x) as activation function is expressed as

$$Y_L(x) = \sum_{i=1}^{L} \beta_i h_i(x) = h(x)\beta_i \quad (6)$$

Where x is an input vector. $h_i(x)$ is the input to output node from hidden node output. $\beta = [\beta_1, \ldots\ldots, \beta_2]^T$ is the weight matrix of i^{th} node. The input weight w_i and the hidden layer biases b_i are generated randomly before the training samples are acquired. Thus iterative back-propagation to tune these parameters is not

needed. Given N training samples $\{(x_j, t_j)\}_{j=1}^{N}$. The objective function of ELM is expressed as,

$$\|H\left(w_1, ...w_{\tilde{N}}, b_1, ..., b_{\tilde{N}}\right)\hat{\beta} - T\| = \min_{\beta} \|H\hat{\beta} - T\| \quad (7)$$

with

$$H\left(w_1, ...w_{\tilde{N}}, b_1, ..., b_{\tilde{N}}\right) = \begin{bmatrix} g\left(w_1.x_1 + b_1\right) & \cdots & g\left(w_L.x_1 + b_L\right) \\ \vdots & \cdots & \vdots \\ g\left(w_1.x_N + b_1\right) & \cdots & g\left(w_L.x_N + b_L\right) \end{bmatrix} \quad (8)$$

$$, \beta = \begin{bmatrix} \beta_1^T \\ \vdots \\ \beta_L^T \end{bmatrix} T = \begin{bmatrix} t_1^T \\ \vdots \\ t_L^T \end{bmatrix}$$

Here H represents the hidden layer output matrix and T represents output label of training data matrix. The output weight matrix β is calculated as

$$\beta = H^{+}T \quad (9)$$

Here, H^{+} represents the Moore-Penrose generalized inverse of the matrix H. Since ELM learning approach requires no backpropagation, this method is best suited for the binary and multiclass classification of big data and neuroimaging features. However the decrease in computation time comes with the expense of increase in the error in the output, which ultimately decreases the accuracy. Thus, a regularization term is added to improve generalization performance and make the solution more robust. The output weight of the regularized ELM can be expressed as

$$\beta = \left(\frac{I}{C} + H^T H\right)^{-1} H^T T \quad (10)$$

Performance Evaluation

We evaluated the performance using the SVM and RELM classifiers for each specific test including the binary and multiclass test. Confusion matrix is constructed to visualize the performance of the binary classifier in a form of a as shown in **Table 2**. Correct numbers of prediction of classifier are placed on the diagonal of the matrix. These components are further divided into true positive (TP), true negative (TN), which represent correctly identified controls. Similarly, the false positive (FP) and false negative (FN) represent the number of wrongly classified subjects.

TABLE 2 | Confusion matrix.

Accurate Class	Predicted Class	
	C1	C2
C1	TP	FN
C2	FP	TN

The proportion of subjects which are correctly classified by the classifier is expressed as the accuracy.

$$ACC = \frac{TP + TN}{TP + TN + FP + FN} \quad (11)$$

However, for dataset with unbalanced class distribution accuracy may be a good performance metric. Thus two more performance are used. These metrics are known as sensitivity and specificity are used.

$$SEN = \frac{TP}{TP + FN} \quad (12)$$

$$SPE = \frac{TN}{TN + FP} \quad (13)$$

The sensitivity (SEN) measures the rate of true positives (TP) while the specificity (SPE) measures rate of true negatives (TN).

RESULTS

Demographic and Clinical Findings

We did not find a significant group difference in age in AD versus HC, AD versus MCI and MCI versus HC. However significant group difference was found in MMSE ($P < 0.01$) and CDR ($P<0.01$) in all group combinations. The gender proportion on both AD and HC is male dominant. AD has 54.83% and HC has 45.16% male dominance. **Table 1** shows the detailed descriptions and analysis of these variables.

Classification Results

We have observed the performance of our proposed algorithm and compared it with that of the RELM classifier and LSVM classifier for respective test comprising the binary classification. The performance shown by the binary classifier is envisaged as a confusion matrix as presented in **Table 1**. Elements on the diagonal elements of the matrix specify the accurate estimations by the classifier. These elements are further divided as true positive (TP) and true negative (TN), which signifies appropriately recognized controls. Correspondingly, all the erroneously classified matters can be symbolized by false positive (FP) and false negative (FN). We evaluated the feature selection and classification algorithms on data set using a 10-flold cross validation (CV). First, we divided the subjects into 10 equally sized subsets: each of these subsets (folds), containing 10% of the subjects as test set and remaining 90% for training set. Then feature ranking was performed on the training sets. We used different algorithms to rank the features. Linear SVM and RELM classifiers were trained using these top-ranked features. For each training and test we performed separate feature selection to avoid the feature selection bias during 10-fold cross validation. We calculated cross validated average classification accuracy and standard deviation for specific feature using k-top most ranked features, where k ranges from 1 to 50. We repeatedly tested for 5 iterations and plotted the mean accuracy and standard deviation as shown in **Figure 3** for LASSO feature selection and RELM classifier.

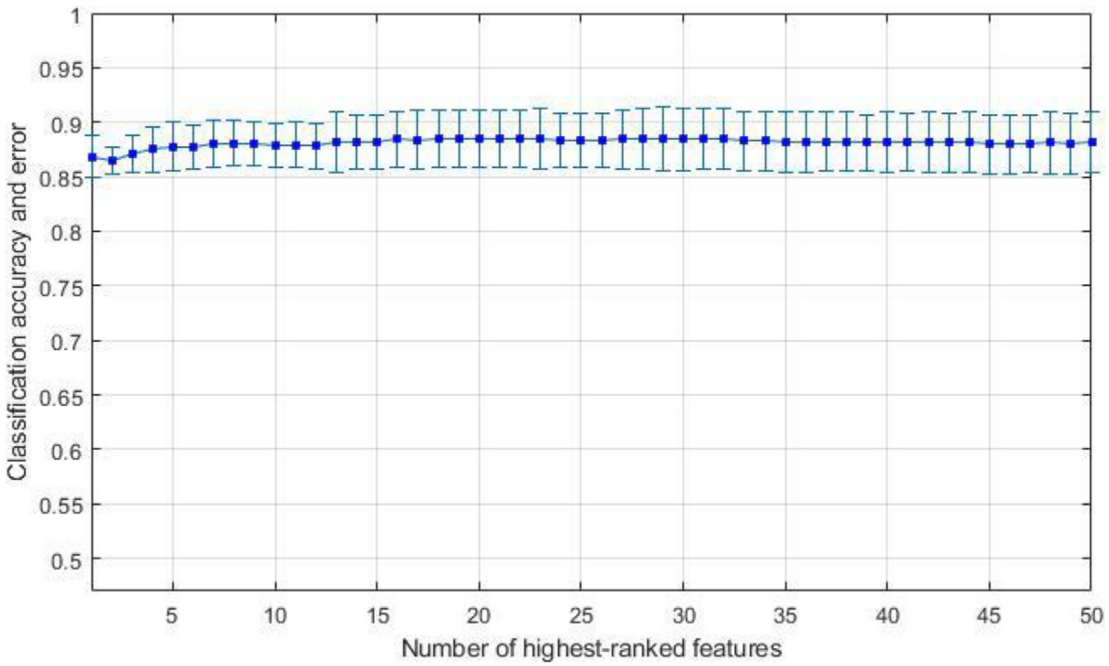

FIGURE 3 | Average accuracy and standard deviation for AD against HC using RELM classification method on reduced datasets using LASSO feature selection.

TABLE 3 | 10-fold cross-validation binary mean classification performance for AD against HC using RELM classifier using different feature selection methods.

Feature selection method	Performance metrics	Mean (%)	Standard deviation	Max (%)	Min (%)
LASSO	Accuracy	**87.723**	0.468	88.663	85.82
	Sensitivity	**90.93**	0.341	91.525	89.50
	Specificity	**84.52**	0.792	85.891	82.14
	F-measure		0.883		
FSASL	Accuracy	76.181	1.069	78.551	73.45
	Sensitivity	76.233	1.255	78.839	72.58
	Specificity	75.664	1.264	77.868	72.20
	F-measure		0.785		
LLCFS	Accuracy	75.737	1.004	78.690	71.64
	Sensitivity	74.205	1.069	77.031	70.11
	Specificity	77.881	1.378	81.036	73.64
	F-measure		0.817		
CFS	Accuracy	80.517	1.737	82.86	74.005
	Sensitivity	80.035	1.813	82.22	73.25
	Specificity	79.16	1.977	81.79	73.084
	F-measure		0.867		
SVM-RFE	Accuracy	68.57	1.186	70.474	65.60
	Sensitivity	75.99	1.676	78.832	71.715
	Specificity	60.92	1.301	63.426	57.34
	F-measure		0.6743		

TABLE 4 | 10-fold cross-validation binary mean classification performance for HC against MCI using RELM classifier using different feature selection methods.

Feature selection method	Performance metrics	Mean (%)	Standard deviation	Max (%)	Min (%)
LASSO	Accuracy	**96.11**	0.859	96.88	91.33
	Sensitivity	**95.03**	1.080	95.93	89.84
	Specificity	**97.18**	0.798	97.84	92.93
	F-measure		0.973		
FSASL	Accuracy	85.85	0.9129	87.503	80.88
	Sensitivity	79.27	0.986	81.484	76.01
	Specificity	92.03	1.4433	93.308	85.40
	F-measure		0.937		
LLCFS	Accuracy	82.29	0.624	83.39	80.77
	Sensitivity	77.54	0.73	78.566	75.408
	Specificity	86.81	1.081	88.41	83.74
	F-measure		0.85		
CFS	Accuracy	80.67	1.68	90.427	74.48
	Sensitivity	88.43	2.328	74.968	80.49
	Specificity	72.38	1.3677	74.486	68.58
	F-measure		0.795		
SVM-RFE	Accuracy	80.20	0.920	82.001	77.89
	Sensitivity	84.00	1.207	85.99	79.86
	Specificity	75.91	1.251	77.806	73.29
	F-measure		0.815		

Finally, we calculated the mean accuracy and standard deviation of highest ranked features for different feature selection and classification methods as depicted in **Tables 3–8** and the bold values in each table indicate the maximum value of accuracy, sensitivity and specificity. Maximum and minimum value of accuracy, sensitivity

TABLE 5 | 10-fold cross-validation binary mean classification performance for MCI against AD using RELM classifier using different feature selection methods.

Feature selection method	Performance metrics	Mean (%)	Standard deviation	Max (%)	Min (%)
LASSO	Accuracy	**93.86**	0.766	94.90	89.128
	Sensitivity	**91.93**	0.757	93.67	89.836
	Specificity	**95.92**	1.204	96.61	88.580
	F-measure		0.968		
FSASL	Accuracy	85.358	1.030	86.76	80.29
	Sensitivity	85.088	0.951	86.61	80.47
	Specificity	85.201	1.4227	86.829	79.27
	F-measure		0.879		
LLCFS	Accuracy	90.32	1.06316	91.88	86.50
	Sensitivity	93.33	2.0782	95.63	87.43
	Specificity	87.49	0.9471	89.56	85.75
	F-measure		0.895		
CFS	Accuracy	79.13	1.2768	81.595	75.10
	Sensitivity	83.59	1.2281	85.60	78.94
	Specificity	74.83	1.7084	78.927	70.54
	F-measure		0.795		
SVMRFE	Accuracy	77.5974	0.8177	78.93	74.98
	Sensitivity	76.802	1.1299	79.225	73.26
	Specificity	78.182	0.8359	79.289	75.44
	F-measure		0.8169		

TABLE 6 | 10-fold cross-validation binary mean classification performance for AD against HC using LSVM classifier using different feature selection methods.

Feature selection method	Performance metrics	Mean (%)	Standard deviation	Max (%)	Min (%)
LASSO	Accuracy	**90.63**	0.515	91.51	88.52
	Sensitivity	87.044	0.585	88.03	85.44
	Specificity	**94.315**	0.671	95.35	90.95
	F-measure		0.958		
FSASL	Accuracy	82.895	1.4020	85.60	80.19
	Sensitivity	78.206	1.5118	81.99	75.21
	Specificity	87.712	1.7666	90.02	82.85
	F-measure		0.8360		
LLCFS	Accuracy	81.19	1.438	83.37	77.68
	Sensitivity	85.15	2.087	88.068	80.49
	Specificity	76.39	1.25	78.983	73.65
	F-measure		0.8095		
CFS	Accuracy	88.37	1.78	91.18	83.25
	Sensitivity	**87.95**	1.72	91.98	84.52
	Specificity	88.79	2.17	90.71	81.28
	F-measure		0.903		
SVMRFE	Accuracy	65.99	1.48	68.51	62.05
	Sensitivity	65.03	1.41	67.73	61.46
	Specificity	67.40	2.327	70.53	61.27
	F-measure		0.671		

TABLE 7 | 10-fold cross-validation binary mean classification performance for HC against MCI using LSVM classifier using different feature selection methods.

Feature selection method	Performance metrics	Mean (%)	Standard deviation	Max (%)	Min (%)
LASSO	Accuracy	**98.91**	0.456	99.25	95.82
	Sensitivity	**99.68**	0.56	100.0	95.48
	Specificity	**98.11**	0.46	98.51	96.00
	F-measure		0.9856		
FSASL	Accuracy	81.28	1.010	83.01	77.64
	Sensitivity	84.61	1.389	86.62	79.81
	Specificity	77.92	1.121	79.81	73.038
	F-measure		0.833		
LLCFS	Accuracy	76.27	0.631	78.31	74.70
	Sensitivity	71.08	1.388	75.37	68.23
	Specificity	81.40	1.005	82.69	76.80
	F-measure		0.800		
CFS	Accuracy	86.16	2.25	88.96	80.47
	Sensitivity	92.28	2.33	95.11	86.14
	Specificity	79.72	2.375	82.75	73.88
	F-measure		0.8517		
SVMRFE	Accuracy	71.92	0.832	74.43	69.93
	Sensitivity	66.90	1.493	71.14	63.53
	Specificity	76.68	1.187	79.61	72.88
	F-measure		0.7762		

TABLE 8 | 10-fold cross-validation binary mean classification performance for MCI against AD using LSVM classifier using different feature selection methods.

Feature selection method	Performance metrics	Mean (%)	Standard deviation	Max (%)	Min (%)
LASSO	Accuracy	**97.80**	0.9862	98.32	91.99
	Sensitivity	**97.62**	1.0065	97.92	91.73
	Specificity	**97.74**	1.0720	98.5	92.07
	F-measure		0.98		
FSASL	Accuracy	83.71	0.90	85.00	78.15
	Sensitivity	90.63	1.57	92.23	84.12
	Specificity	77.10	1.098	79.74	72.55
	F-measure		0.838		
LLCFS	Accuracy	90.04	1.43	92.02	86.07
	Sensitivity	90.23	1.43	91.94	86.74
	Specificity	90.09	1.77	92.52	84.62
	F-measure		0.903		
CFS	Accuracy	84.41	1.95	86.81	79.18
	Sensitivity	90.37	2.14	93.26	83.73
	Specificity	78.10	1.90	80.79	72.84
	F-measure		0.83		
SVMRFE	Accuracy	82.87	0.903	83.96	78.832
	Sensitivity	81.68	1.22	84.34	77.10
	Specificity	84.11	0.94	85.21	80.72
	F-measure		0.854		

and specificity are calculated amongst corresponding values estimated for highest ranked features as shown in **Figure 3**.

Tables 3–5 show the binary classification results using RELM classifier with five different feature selections. Results obtained through the feature selection methods are compared in

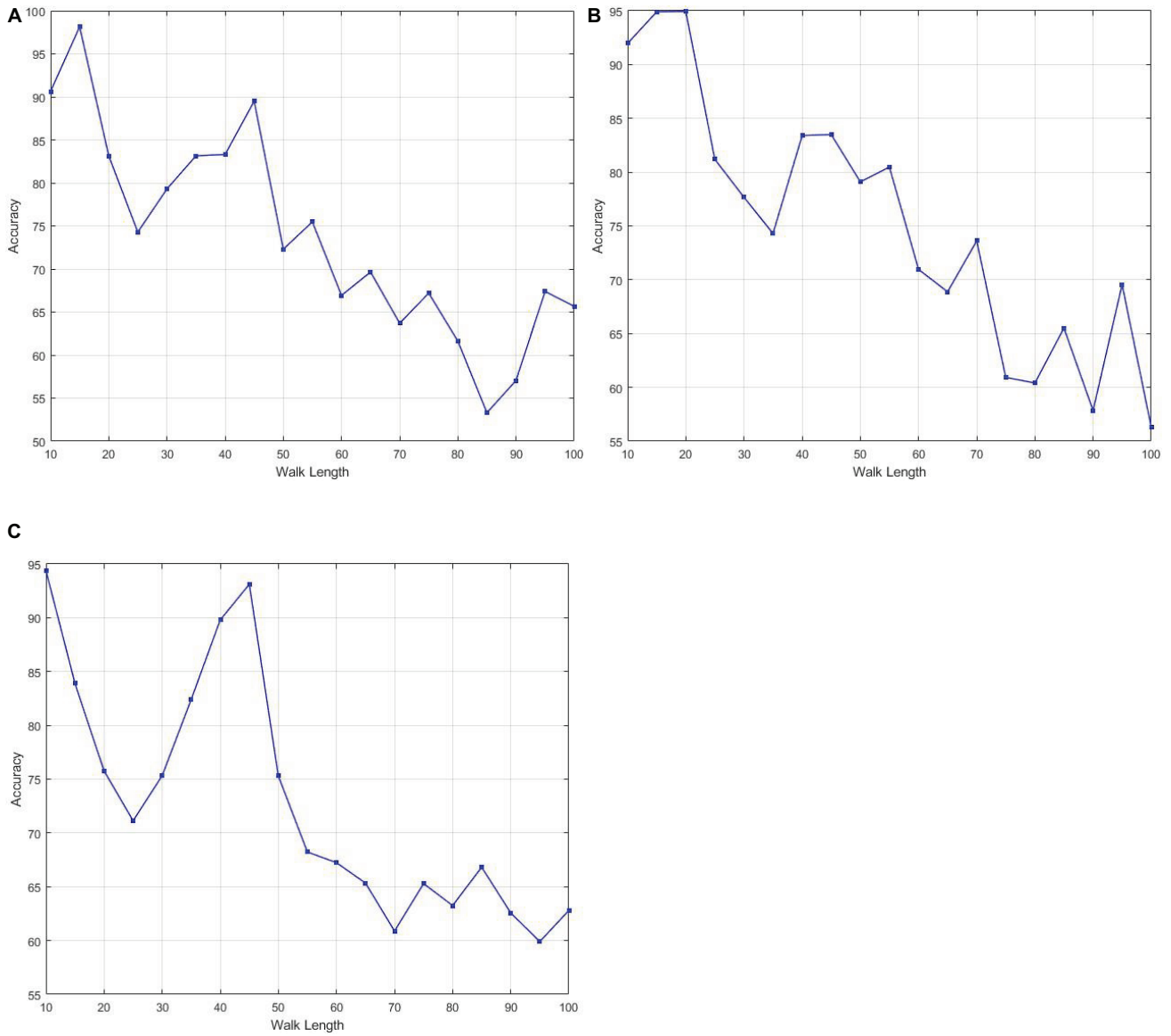

FIGURE 4 | The effect of different parameter values of Walk Length of Node2vec on performance **(A)** AD against HC, **(B)** HC against MCI, **(C)** AD against MCI.

regards to the performance metrics such as accuracy, sensitivity specificity and f-measure. **Table 3** summarizes the AD versus HC classification. The LASSO feature selection method outperforms all other methods consider with the highest mean accuracy of 87.72%, mean specificity of 90.93% and mean sensitivity of 84.52%. Additionally, the standard deviation of LASSO is 0.4 which is less than less than 1. Similarly, the classification results of AD versus MCI and NC versus MCI using RELM are shown in **Tables 4**, **5**. As shown in **Table 4**, the highest mean accuracy is 96.11 (±0.859) for HC against MCI classification and 93.86 (±0.766) for MCI against AD classification. The standard deviation is less than 1 in both mean classifications. Additionally the F-score is high in all three classifications (0.883 for HC against AD, 0.973 for HC against MCI, 0.968 for AD against MCI) using LASSO feature section method compared to other feature selection methods. The value of standard deviation less than one indicates that the data points of accuracy estimated tend to be close to the mean. Hence from the result it is very evident that the less inflated accuracy can be obtained using LASSO. Similarly, the high F-score indicates precision of classification is high compared to other feature selection methods.

Similarly, the comparison of classification of HC, MCI and AD using LSVM classifier with different feature selection methods are shown in **Tables 6**–**8**. Similar to RELM, the highest performance result in terms of mean accuracy, specificity, sensitivity and F-score was obtained by using LASSO for all three classification tests. As shown in **Table 6**, we obtained the accuracy of 90.63% specificity of 94.315% and sensitivity

of 87.95% and F-score of 0.958 for AD against HC. In **Table 7** the highest mean accuracy, specificity, sensitivity and F-score are obtained as 98.9, 99.68, 98.11, and 0.9856% for HC against MCI classification. Similarly, **Table 8** shows the classification performance of AD against MCI. The highest mean accuracy, specificity, sensitivity and F-score are 97.81, 97.62, 97.74, and 0.98%.

From all these results, it is clearly evident that the use of LASSO as feature selection method is ideal choice for the classification using RELM and LSVM classifiers for the graph embedded data.

From **Tables 3**–**5** the highest classification accuracies of RELM classifier using LASSO feature selection for AD against HC, HC against MCI and MCI against AD are 87.723% (±0.468), 96.11% (±0.859), and 93.86 %(±0.766). Similarly, from **Tables 6**–**8** the highest classification accuracies of RELM classifier using LASSO feature selection for AD against HC, HC against MCI and MCI against AD are 90.63% (±0.515), 98.91% (±0.456), and 97.80% (±0.9862).

Now, the comparison of performance between two classifiers shows that the SVM can classify the given dataset more accurately with the highest mean accuracy for all three binary classifications. However, the small standard deviation of the classification HC against MCI and MCI against AD suggest that the classification accuracy values are less inflated in RELM as compared to LSVM.

The number of hidden layer nodes influences the performance of the RELM classifier. In our experiment, we found 1000 number of hidden layer generated the best performance in terms of accuracy. Similarly, for SVM we set the default parameter defined for the MATLAB library. We performed the classification by varying different parameters on node2vec graph embedding. **Figure 4** shows the effect of different parameters of node2vec on the performance of RELM classifier. We varied the walk length of node2vec from 10 to 100. In all experiments, increased value of walk length decreases the performance of classifier. For this experiment, we fixed two other parameters, dimension and number of walks to 32 and 200. Similarly, we set the parameters p and q to correspond localized random walks. With the smaller value of p and larger value of q, the random walk is easy to sample to the high-order -order proximity. Thus, we selected p and q randomly and performed graph embedding with $p = 0.1$ and $q = 1.6$.

DISCUSSION

Several studies based on rs-fMRI have been carried out for the classification of AD and MCI from HC subjects. Binary classification in combination of different classifier with different feature measure reported the accuracy ranging from 85 to 95% for AD against HC and 62.90 to 72.58% to and MCI against HC as shown in **Tables 9**, **10**. These studies used the same MCI and HC subjects from the ADNI2 cohort. One can clearly notice that the number of subjects directly influences the accuracy. As the number of subjects increase the accuracy is decreased. As reported in previous section the highest accuracy for the classification of AD from is obtained in proposed work is 90.63% using the combination of LASSO and LSVM. If we compare the results for MCI against HC, the results obtained in current study outperform all the state of art methods. However, it is not fair to compare performance with other studies directly because each work employ different datasets, preprocessing pipelines, feature measures, and classifiers. Majority of works including (Eavani et al., 2013; Leonardi et al., 2013; Wu et al., 2013; Wee et al., 2014; Suk et al., 2016) have used subjects less than or nearly equal to 30 in each subject class. The main reason behind small number of dataset is the availability of fMRI data in ADNI2 cohort. All of these studies performed classification and made conclusion. Likewise, we also conducted our study using ADNI2 cohort with nearly equal number of subjects with

TABLE 9 | Comparison of performance of binary classification AD against HC with state of the art methods using rs-fMRI.

Dataset	Feature measures	Classifier	Accuracy (%)	Reference
AD:77, HC: 173	Combination of FC matrices, FC dynamics, ALFF	AUC	85	de Vos et al., 2018
AD: 12, HC: 12	Difference between DMN and SN map	LDA	92	Zhou et al., 2010
AD: 34, HC: 45	Graph measures	Naïve Bayes	93.3	Khazaee et al., 2017
AD: 15, HC: 16	Averaged voxel intensities of core regions in resting state networks: DMN, DAN, VAN	Multivariate ROC	95	Wu et al., 2013

TABLE 10 | Comparison of performance of binary classification MCI against HC with state of the art methods using rs-fMRI.

Dataset	Feature measures	Classifier	Accuracy (%)	References
MCI: 31, HC: 31	Functional activity co-variations of ROIs	SVM	62.90	Eavani et al., 2013
MCI: 31, HC: 31	Group sparse representation	SVM	66.13	Wee et al., 2014
MCI: 31, HC: 31	SDFN	SVM	70.97	Leonardi et al., 2013
MCI: 31, HC: 31	Deep auto encoder and HMM	SVM	72.58	Suk et al., 2016

FC, functional connectivity; ALFF, amplitude of low-frequency fluctuation; AUC, area under the curve; DMN, default mode network; SN, salience network; LDA, linear discriminant analysis; ROC, receiver operating characteristic; ROI, region of interest; AAL, automated anatomical labeling; DMN, default mode network; SDFN, sliding window-based dynamic functional network; HMM, hidden markov model.

previous studies and the cross validation was also done using these dataset.

Mild cognitive impairment is a transitional stage between the healthy non dementia and dementia stage[2]. This stage is further divided into early MCI (EMCI) and late MCI (LMCI), according to extent of episodic memory impairment. The risk conversion from MCI to AD is higher in LMCI than in EMCI. In this study, we included only EMCI subjects in MCI group. The MCI converted and non-converted to is classified according to CDR and MMSE score. MCI subjects whose CDR undergoes change from 0.5 to 1 and MMSE score goes below 26 in subsequent visits are considered to have fulfilled the criteria to be MCI converted. In our study majority of subjects fulfill to be non-converted MCI. Only few subjects either have changed CDR score or MMSE score during the visits in the interval of 3, 6, 12, and 18 months. Additionally, none of the MCI subjects are recorded in the list of AD subjects.

Limitations

While this study is focused on the stage diagnosis of AD progression using fMRI alone using ADNI2 cohort, the major limitation of this study is the limited sample size of ADNI2 (31 AD, 31 MCI, and 31 HC). In this context, the entire population is not represented adequately with the dataset we used. Thus, we cannot guarantee the generalization of our results to other groups.

CONCLUSION

It is widely accepted that the early diagnosis of AD and MCI plays an import role to take preventive action and to delay the future progression of AD. Thus the accurate classification task of different stages of AD progression is essential. In this study, we demonstrated graph based features from functional magnetic resonance (fMR) images can be used for the classification of AD and MCI from HC. Additionally, we used multiple feature selection techniques to cope with the smaller number of subjects with larger number of feature representations. The appropriate amount of features is extracted from standard Alzheimer's disease Neuroimaging Initiative cohort that lead to maximal classification accuracies as compared to all other recent researches. Among different feature section methods LASSO together with LSVM on graph based features significantly improved the classification accuracy.

DATA AVAILABILITY STATEMENT

The raw data supporting the conclusions of this article will be made available by the authors, without undue reservation.

ETHICS STATEMENT

The studies involving human participants were reviewed and approved by Alzheimer's Disease Neuroimaging Initiative (ADNI). The patients/participants provided their written informed consent to participate in this study.

AUTHOR CONTRIBUTIONS

RL has generated the idea and conducted the experiments. G-RK has reviewed idea and final verification of results. All authors contributed to the article and approved the submitted version.

FUNDING

This work was supported by the National Research Foundation of Korea (NRF) grant funded by the Korea Government (MSIT) (No. NRF-2019R1A4A1029769).

ACKNOWLEDGMENTS

Data collection and sharing for this project was funded by the Alzheimer's Disease Neuroimaging Initiative (ADNI) (National Institutes of Health Grant U01 AG024904) and DOD ADNI (Department of Defense award number W81XWH-12-2-0012). As such, the investigators within the ADNI contributed to the design and implementation of ADNI and/or provided data but did not participate in analysis or writing of this report. A complete listing of ADNI investigators can be found at: http://adni.loni.usc.edu/wp-content/uploads/how_to_apply/ADNI_Acknowledgement_List.pdf. ADNI is funded by the National Institute on Aging, the National Institute of Biomedical Imaging and Bioengineering, and through generous contributions from the following: AbbVie, Alzheimer's Association; Alzheimer's Drug Discovery Foundation; Araclon Biotech; BioClinica, Inc.; Biogen; Bristol-Myers Squibb Company; CereSpir, Inc.; Cogstate; Eisai Inc.; Elan Pharmaceuticals, Inc.; Eli Lilly and Company; EuroImmun; F. Hoffmann-La Roche Ltd and its affiliated company Genentech, Inc.; Fujirebio; GE Healthcare; IXICO Ltd.; Janssen Alzheimer Immunotherapy Research & Development, LLC.; Johnson & Johnson Pharmaceutical Research and Development LLC.; Lumosity; Lundbeck; Merck & Co., Inc.; Meso Scale Diagnostics, LLC.; NeuroRx Research; Neurotrack Technologies; Novartis Pharmaceuticals Corporation; Pfizer Inc.; Piramal Imaging; Servier; Takeda Pharmaceutical Company; and Transition Therapeutics. The Canadian Institutes of Health Research is providing funds to support ADNI clinical sites in Canada. Private sector contributions are facilitated by the Foundation for the National Institutes of Health (www.fnih.org). The grantee organization is the Northern California Institute for Research and Education, and the study is coordinated by the Alzheimer's Therapeutic Research Institute at the University of Southern California. ADNI data are disseminated by the Laboratory for Neuro Imaging at the University of Southern California. Correspondence should be addressed to GR-K, grkwon@chosun.ac.kr.

REFERENCES

Acosta-Cabronero, J., Alley, S., Williams, G. B., Pengas, G., and Nestor, P. J. (2012). Diffusion tensor metrics as biomarkers in Alzheimer's disease. *PLoS One* 7:e49072. doi: 10.1371/journal.pone.0049072

Alzheimer's association (2016). 2016 Alzheimer's disease facts and figures. *Alzheimers Dement.* 12, 459–509. doi: 10.1016/j.jalz.2016.03.001

American Psychiatric Association (1994). "Task force on DSM-IV," in *Diagnostic and Statistical Manual of Mental Disorders," DSM-IV*, 4th Edn, Vol. xxv, (Washington, DC: American Psychiatric Association).

Ashburner, J. (2007). A fast diffeomorphic image registration algorithm. *Neuroimage* 38, 95–113. doi: 10.1016/j.neuroimage.2007.07.007

Bajo, R., Maestú, F., Nevado, A., Sancho, M., Gutiérrez, R., Campo, P., et al. (2010). Functional connectivity in mild cognitive impairment during a memory task: implications for the disconnection hypothesis. *J. Alzheimers Dis.* 22, 183–193. doi: 10.3233/jad-2010-100177

Bendlin, B. B., Carlsson, C. M., Johnson, S. C., Zetterberg, H., Blennow, K., and Willette, A. (2012). CSF T-Tau/Aβ42 predicts white matter microstructure in healthy adults at risk for Alzheimer's disease. *PLoS One* 7:e37720. doi: 10.1371/journal.pone.0037720

Bullmore, E., and Sporns, O. (2009). Complex brain networks: graph theoretical analysis of structural and functional systems. *Nat. Rev. Neurosci.* 10, 186–198. doi: 10.1038/nrn2575

Cambria, E., and Huang, G.-B. (2013). Extreme learning machines. *IEEE Intell. Syst.* 28, 2–31.

Canu, E., McLaren, D. G., Fitzgerald, M. E., Bendlin, B. B., Zoccatelli, G., and Alessandrini, F. (2010). Microstructural diffusion changes are independent of macrostructural volume loss in moderate to severe Alzheimer's disease. *J. Alzheimers Dis.* 19, 963–976. doi: 10.3233/jad-2010-1295

Cao, J., Zhang, K., Luo, M., Yin, C., and Lai, X. (2016). Extreme learning machine and adaptive sparse representation for image classification. *Neural Netw.* 81, 91–102. doi: 10.1016/j.neunet.2016.06.001

Chao-Gan, Y., and Yu-Feng, Z. (2010). DPARSF: a MATLAB toolbox for "Pipeline" data analysis of resting-State fMRI. *Front. Syst. Neurosci.* 4:13. doi: 10.3389/fnsys.2010.00013

Chen, Y. J., Deutsch, G., Satya, R., Liu, H. G., and Mountz, J. M. (2013). A semi-quantitative method for correlating brain disease groups with normal controls using SPECT: Alzheimer's disease versus vascular dementia. *Comput. Med. Imaging Graph.* 37, 40–47. doi: 10.1016/j.compmedimag.2012.11.001

Cortes, C., and Vapnik, V. (1995). Support-vector networks. *Mach. Learn.* 20, 273–297.

de Vos, F., Koini, M., Schouten, T. M., Seiler, S., van der Grond, J., Lechner, A., et al. (2018). A comprehensive analysis of resting state fMRI measures to classify individual patients with Alzheimer's disease. *Neuroimage* 167, 62–72. doi: 10.1016/j.neuroimage.2017.11.025

Delbeuck, X., Collette, F., and Van der Linden, M. (2007). Is Alzheimer's disease a disconnection syndrome? Evidence from a crossmodal audio-visual illusory experiment. *Neuropsychologia* 45, 3315–3323.

Delbeuck, X., Van der Linden, M., and Collette, F. (2003). Alzheimer's disease as a disconnection syndrome? *Neuropsychol. Rev.* 13, 79–92.

Doan, N. T., Engvig, A., Persson, K., Alnæs, D., Kaufmann, T., Rokicki, J., et al. (2017). Dissociable diffusion MRI patterns of white matter microstructure and connectivity in Alzheimer's disease spectrum. *Sci. Rep.* 7:45131.

Du, L., and Shen, Y. D. (2015). "Unsupervised feature selection with adaptive structure learning," in *Proceedings of the 21th ACM SIGKDD International Conference on Knowledge Discovery and Data Mining*, 209–218.

Eavani, H., Satterthwaite, T. D., Gur, T. E., Gur, R. C., and Davatzikos, C. (2013). Unsupervised learning of functional network dynamics in resting state fMRI. *Inf. Process Med. Imaging* 23, 426–437. doi: 10.1007/978-3-642-38868-2_36

Górriz, J. M., Segovia, F., Ramírez, J., Lassl, A., and Gonzalez, D. S. (2011). GMM based SPECT image classification for the diagnosis of Alzheimer's disease. *Appl. Soft. Comput.* 11, 2313–2325. doi: 10.1016/j.asoc.2010.08.012

Gray, K. R., Wolz, R., Heckemann, R. A., Aljabar, P., Hammers, A., and Rueckert, D. (2012). Multi-region analysis of longitudinal FDG-PET for the classification of Alzheimer's disease. *Neuroimage* 60, 221–229. doi: 10.1016/j.neuroimage.2011.12.071

Grover, A., and Leskovec, J. (2016). "Node2Vec: scalable feature learning for networks," in *Proceedings of the 22nd ACM SIGKDD International Conference on Knowledge Discovery and Data Mining*, (New York, NY: ACM).

Guyon, I., Weston, J., Barnhill, S., and Vapnik, V. (2002). Gene selection for cancer classification using support vector machines. *Mach. Learn.* 46, 389–422.

Hall, M. A. (2000). Correlation-based feature selection for discrete and numeric class machine learning. *Proc. 17th Int'l Conf. Machine Learning* 359–366.

Hanyu, H., Asano, T., Sakurai, H., Imon, Y., Iwamoto, T., Takasaki, M., et al. (1999). Diffusion-weighted and magnetization transfer imaging of the corpus callosum in Alzheimer's disease. *J. Neurol. Sci.* 167, 37–44. doi: 10.1016/s0022-510x(99)00135-5

Hanyu, H., Sato, T., Hirao, K., Kanetaka, H., Iwamoto, T., and Koizumi, K. (2010). The progression of cognitive deterioration and regional cerebral blood flow patterns in Alzheimer's disease: a longitudinal SPECT study. *J. Neurol. Sci.* 290, 96–101. doi: 10.1016/j.jns.2009.10.022

Huang, G. B., Zhu, Q. Y., and Siew, C. K. (2006). Extreme learning machine: theory and applications. *Neurocomputing* 70, 489–501. doi: 10.1016/j.neucom.2005.12.126

Khazaee, A., Ebrahimzadeh, A., and Babajani-Feremi, A. (2017). Classification of patients with MCI and AD from healthy controls using directed graph measures of resting-state fMRI. *Behav. Brain Res.* 322, 339–350. doi: 10.1016/j.bbr.2016.06.043

Leonardi, N., Richiardi, J., Gschwind, M., Simioni, S., Annoni, J.-M., Schluep, M., et al. (2013). Principal components of functional connectivity: a new approach to study dynamic brain connectivity during rest. *Neuroimage* 83, 937–950. doi: 10.1016/j.neuroimage.2013.07.019

Liu, F., Zhou, L., Shen, C., and Yin, J. (2014). Multiple kernel learning in the primal for multi-modal Alzheimer's disease classification. *IEEE J. Biomed. Health Inform.* 18, 984–990. doi: 10.1109/jbhi.2013.2285378

Liu, Y., Yu, C., Zhang, X., Liu, J., Duan, Y., Alexander-Bloch, A. F., et al. (2014). Impaired long distance functional connectivity and weighted network architecture in Alzheimer's disease. *Cereb. Cortex* 24, 1422–1435. doi: 10.1093/cercor/bhs410

Ly, M., Canu, E., Xu, G., Oh, J., McLaren, D. G., Dowling, N. M., et al. (2014). Midlife measurements of white matter microstructure predict subsequent regional white matter atrophy in healthy adults. *Hum. Brain Mapp.* 35, 2044–2054. doi: 10.1002/hbm.22311

Masliah, E., Mallory, M., Hansen, L., DeTeresa, D., and Terry, R. (1993). Quantitative synaptic alterations in the human neocortex during normal aging. *Neurology* 43, 192–197. doi: 10.1212/wnl.43.1_part_1.192

Supekar, K., Menon, V., Rubin, D., Musen, M., and Greicius, M. D. (2008). Network analysis of intrinsic functional brain connectivity in Alzheimer's disease. *PLoS Comput. Biol.* 4:e1000100. doi: 10.1371/journal.pcbi.1000100

Peng, X., Lin, P., Zhang, T., and Wang, J. (2013). Extreme learning machine-based classification of ADHD using brain structural MRI data. *PLoS One* 8:e79476. doi: 10.1371/journal.pone.0079476

Pfefferbaum, A., Sullivan, E., Hedehus, M., Lim, K., Adalsteinsson, E., and Moseley, M. (2000). Age-related decline in brain white matter anisotropy measured with spatially corrected echo-planar diffusion tensor imaging. *Magn. Reson. Med.* 44, 259–268. doi: 10.1002/1522-2594(200008)44:2<259::aid-mrm13>3.0.co;2-6

Qureshi, M. N. I., Min, B., Jo, H. J., and Lee, B. (2016). Multiclass classification for the differential diagnosis on the ADHD subtypes using recursive feature elimination and hierarchical extreme learning machine:structural MRI Study. *PLoS One* 11:e0160697. doi: 10.1371/journal.pone.0160697

Rubinov, M., and Sporns, O. (2010). Complex network measures of brain connectivity: uses and interpretations. *Neuroimage* 52, 1059–1069. doi: 10.1016/j.neuroimage.2009.10.003

Schmitter, D., Roche, A., Maréchal, B., Ribes, D., Abdulkadir, A., Bach-Cuadra, M., et al. (2015). An evaluation of volume-based morphometry for prediction of mild cognitive impairment and Alzheimer's disease. *NeuroImage* 7, 7–17.

Sorg, C., Riedl, V., Mühlau, M., Calhoun, V. D., Eichele, T., Läer, L., et al. (2007). Selective changes of resting-state networks in individuals at risk for Alzheimer's disease. *Proc. Nat. Acad. Sci. U.S.A.* 104, 18760–18765. doi: 10.1073/pnas.0708803104

Sporns, O. (2011). The human connectome: a complex network. *Ann. N. Y. Acad. Sci.* 1224, 109–125. doi: 10.1111/j.1749-6632.2010.05888.x

Stam, C. J., Jones, B. F., Manshandena, I., van Cappellen van Walsum, A. M., Montez, T., Verbunt, J. P. A., et al. (2006). Magnetoencephalographic evaluation of resting-state functional connectivity in Alzheimer's disease. *Neuroimage* 32, 1335–1344. doi: 10.1016/j.neuroimage.2006.05.033

Suk, H. I., Wee, C. Y., Lee, S. W., and Shen, D. (2016). State-space model with deep learning for functional dynamics estimation in resting-state fMRI. *Neuroimage* 129, 292–307. doi: 10.1016/j.neuroimage.2016.01.005

Tibshirani, R. (1996). Regression shrinkage and selection via the lasso. *J. R. Stat. Soc. Ser. B Stat. Methodol.* 58, 267–288. doi: 10.1111/j.2517-6161.1996.tb02080.x

Wee, C. Y., Yap, P. T., Zhang, D., Wang, L., and Shen, D. (2014). Group-constrained sparse fMRI connectivity modeling for mild cognitive impairment identification. *Brain Struct. Funct.* 219, 641–656. doi: 10.1007/s00429-013-0524-8

Wu, X., Li, J., Ayutyanont, N., Protas, H., Jagust, W., Fleisher, A., et al. (2013). The receiver operational characteristic for binary classification with multiple indices and its application to the neuroimaging study of Alzheimer's disease. *IEEE/ACM Trans. Comput. Biol. Bioinform.* 10, 173–180. doi: 10.1109/tcbb.2012.141

Zeng, H., and Cheung, Y. (2011). Feature selection and kernel learning for local learning-based clustering. *IEEE Transactions on PAMI* 33, 1532–1547. doi: 10.1109/TPAMI.2010.215

Zhang, W., Shen, H., Ji, Z., Meng, G., and Wang, B. (2015). "Identification of mild cognitive impairment using extreme learning machines model," intelligent computing theories and methodologies," in *Proceedings of the 11th International Conference, ICIC 2015*, Fuzhou.

Zhou, J., Greicius, M. D., Gennatas, E. D., Growdon, M. E., Jang, J. Y., Rabinovici, G. D., et al. (2010). Divergent network connectivity changes in behavioural variant frontotemporal dementia and Alzheimer's disease. *Brain* 133, 1352–1367. doi: 10.1093/brain/awq075

Conflict of Interest: The authors declare that the research was conducted in the absence of any commercial or financial relationships that could be construed as a potential conflict of interest.

frontiers in Neuroscience

ORIGINAL RESEARCH
published: 01 March 2021
doi: 10.3389/fnins.2021.614220

Exosomal MicroRNAs Contribute to Cognitive Impairment in Hypertensive Patients by Decreasing Frontal Cerebrovascular Reactivity

Junyi Ma[1†], Xiang Cao[1,2,3,4†], Fangyu Chen[1†], Qing Ye[1], Ruomeng Qin[1,2,3], Yue Cheng[1,2,3,4], Xiaolei Zhu[1,2,3,4] and Yun Xu[1,2,3,4*]*

[1] The State Key Laboratory of Pharmaceutical Biotechnology, Department of Neurology, Medical School, Drum Tower Hospital, Institute of Brain Science, Nanjing University, Nanjing, China, [2] Jiangsu Key Laboratory for Molecular Medicine, Medical School of Nanjing University, Nanjing, China, [3] Jiangsu Province Stroke Center for Diagnosis and Therapy, Nanjing, China, [4] Nanjing Neurology Clinic Medical Center, Nanjing, China

OPEN ACCESS

Edited by:
Boldizsar Czeh, University of Pécs, Hungary

Reviewed by:
Gergely Feher, University of Pécs, Hungary
Zhenghua Hou, Southeast University, China

***Correspondence:**
Yun Xu
xuyun20042001@aliyun.com
Xiaolei Zhu
zhuquelee@126.com

† These authors have contributed equally to this work

Specialty section:
This article was submitted to Brain Imaging Methods, a section of the journal Frontiers in Neuroscience

Received: *05 October 2020*
Accepted: *14 January 2021*
Published: *01 March 2021*

Citation:
Ma J, Cao X, Chen F, Ye Q, Qin R, Cheng Y, Zhu X and Xu Y (2021) Exosomal MicroRNAs Contribute to Cognitive Impairment in Hypertensive Patients by Decreasing Frontal Cerebrovascular Reactivity. Front. Neurosci. 15:614220. doi: 10.3389/fnins.2021.614220

Mechanisms underlying cognitive impairment (CI) in hypertensive patients remain relatively unclear. The present study aimed to explore the relationship among serum exosomal microRNAs (miRNAs), cerebrovascular reactivity (CVR), and cognitive function in hypertensive patients. Seventy-three hypertensive patients with CI (HT-CI), 67 hypertensive patients with normal cognition (HT-NC), and 37 healthy controls underwent identification of exosomal miRNA, multimodal magnetic resonance imaging (MRI) scans, and neuropsychological tests. CVR mapping was investigated based on resting-state functional MRI data. Compared with healthy subjects and HT-NC subjects, HT-CI subjects displayed decreased serum exosomal miRNA-330-3p. The group difference of CVR was mainly found in the left frontal lobe and demonstrated that HT-CI group had a lower CVR than both HT-NC group and control group. Furthermore, both the CVR in the left medial superior frontal gyrus and the miRNA-330-3p level were significantly correlated with executive function ($r = -0.275$, $P = 0.021$, and $r = -0.246$, $P = 0.04$, respectively) in HT-CI subjects, and the CVR was significantly correlated with the miRNA-330-3p level ($r = 0.246$, $P = 0.040$). Notably, path analysis showed that the CVR mediated the association between miRNA-330-3p and executive function. In conclusion, decreased miRNA-330-3p might contribute to CI in hypertensive patients by decreasing frontal CVR and could be a biomarker of early diagnosis.

Keywords: hypertension, exosomal microRNA, cerebrovascular reactivity, mediation, cognitive impairment

INTRODUCTION

As a worldwide public health problem, hypertension is detected in 31.1% of adults worldwide (Mills et al., 2016). It has been reported that hypertension is one of the major risk factors for dementia. There is a strong correlation between hypertension and the progression of dementia (Li et al., 2016). High blood pressure has been correlated with multiple cognitive dysfunctions such as executive

dysfunction, reduced mental processing speed, as well as memory deficit (Gąsecki et al., 2013). A 40-year follow-up study of a population-based cohort investigated the association of vascular risk factors with all types of dementia and found that high systolic blood pressure was consistently associated with all types of dementia (Ronnemaa et al., 2011). In a 17-year observational study of 668 non-demented elderly Japanese, subjects with hypertension had at least three-fold greater risk of vascular dementia compared to subjects with normal blood pressure (Ninomiya et al., 2011).

Hypertension is thought to affect the structure and function of cerebral blood vessels. There are multiple adaptive changes in the extravascular environment, local signaling molecules, or hemodynamic demands in the healthy arteries to keep blood pressure homeostasis, but these adaptive changes do not return to baseline and induce pathological vascular alterations in disease states. Multiple cellular components such as vascular smooth muscle cells (VSMCs) in the vessel wall of both large and small arteries, endothelial cells, and elastin and collagen content were changed in hypertension (Wong et al., 2010; Savoia et al., 2011; Wagenseil and Mecham, 2012; Duca et al., 2016). With the development of chronic hypertension, the structure of arterial wall has remodeled, such as thickening, stiffening, and narrowing, which are reactions to the stress of arterial walls (Wilstein et al., 2018). However, how these hypertension-related cerebrovascular alterations result in cognitive impairment (CI) remains relatively unknown. Cerebrovascular reactivity (CVR) is a vasodilatory index that is related to the important function of dilation and constriction of cerebral vessels in response to changes of resource requirement in vessel system. Compared with other cerebral vascular indexes such as cerebral blood flow (CBF), CVR is regarded as a more specific vascular signal (Liu et al., 2017). Two major techniques in testing cerebrovascular reactivity are functional magnetic resonance imaging (fMRI) and transcranial Doppler sonography (Grant et al., 2015). fMRI represents a unique and noninvasive technique in measuring cerebral vascular state. Blood oxygen level-dependent (BOLD) signal, detected with fMRI technique, is equipped with the advantage of high signal-to-noise ratio, which is capable of measuring CVR (Kannurpatti et al., 2014). Previous studies have suggested that BOLD-based fMRI signal is basically adjusted by physiology of vessels (Kannurpatti et al., 2010; Liu et al., 2013). Reduced CVR has been observed in specific regions of the brain in hypertensive patients. However, the molecular mechanism underlying the altered CVR and the relationship between CVR and cognitive function in hypertensive patients are relatively unclear.

Exosomes are small extracellular membrane vesicles with a diameter of 30–150 nm. They are secreted by all living cells and contain microRNAs (miRNAs), DNA, lipid, protein, and mRNAs (Chopp and Zhang, 2015; Mathieu et al., 2019). Exosomes exist in different types of body fluid, including saliva, blood, and urine, and serve as important carriers that transfer both proteomic and genomic materials between cells. As a kind of endogenous and small non-coding RNAs, miRNAs play a critical role in restraining target RNAs' translation or facilitating decomposition of target RNAs (Bartel, 2004). MiRNAs are more stable in serum exosomes compared with those free in serum due to the features of exosomes to protect the structure and biological activity of miRNA from RNase digestion. Therefore, specific serum exosomal miRNAs are regarded as novel regulators of neural behavior not only in protein translation but also in inflammatory processing (Wood et al., 2011).

Plentiful studies have shown that miRNA levels related to neurological insult are significantly changed in essential hypertension and secondary hypertension (Shi et al., 2015). MiRNAs are involved in the pathogenesis of hypertension through a variety of mechanisms, including the regulations of endothelial function, nitric oxide-dependent vasodilatation, and sympathetic activity (Klimczak et al., 2017). Specifically, altered circulating miRNAs including miRNA-1, 21, 133, 145, 505, and 510 have been strongly associated with the pathogenesis and progression of essential hypertension (Kontaraki et al., 2014; Yang et al., 2014; Krishnan et al., 2017). MiRNAs regulate a series of vascular processes, such as angiogenesis, apoptosis, proliferation, and migration by targeting specific mRNA (Ballantyne et al., 2016), and most of the processes are related to endothelial cell function. Moreover, endothelial dysfunction is considered as an important contributor to the imbalance between vasoconstrictors and vasodilators in the pathogenesis of hypertension (Widlansky et al., 2003; Nemecz et al., 2016; Zhang et al., 2018). Since CVR serves as a specific measurement for the dilation and constriction of cerebral vessels, abnormal miRNA might lead to altered CVR in hypertensive patients.

The present study recruited hypertensive patients with cognitive impairment (CI), hypertensive patients with normal cognition, and healthy subjects. All subjects underwent identification of exosomal miRNA, multimodal MRI scans, and neuropsychological tests. We explored the patterns of exosomal miRNA, CVR maps, and cognitive function in hypertensive patients and the relationship among them. We also explored whether there were mediating effects of CVR on the relationship between miRNA and CI in hypertensive patients with CI. We hypothesized that CI of hypertensive patients would be related to abnormal exosomal miRNA and altered CVR patterns, and CVR might mediate the link between exosomal miRNA and CI.

MATERIALS AND METHODS

Participants

Individuals were recruited from the outpatients and inpatients of the Department of Neurology of Nanjing Drum Tower Hospital between January 2017 and June 2019. The present study was approved by the Nanjing Drum Tower Hospital Research Ethics Committee. All participants provided written informed consent ahead of participation. Inclusion criteria for the hypertension group were as follows: (1) $\geq$50 years of age and (2) classified as hypertension by experienced physician based on standard guidelines (systolic blood pressure (SBP) >140 mmHg or/and diastolic blood pressure (DBP) >90 mmHg) (Mancia et al., 2013), with/without CI. The control group was selected from participants with normal blood pressure and cognition. The CI of

participants was evaluated based on the standard of our previous study, and the cut-off was based on the Mini Mental State Examination (MMSE)/Montreal Cognitive Assessment (MoCA) scores and educational experience of the subjects (Gu et al., 2019). The participants with scores less than the cut-off (for MMSE score, the cut-off was ≤26 for >6 educational years, ≤22 for 1–6 educational years, and ≤19 for 0 educational years, and for MoCA score, the cut-off was ≤25 for >12 educational years, ≤24 for 7–12 educational years, ≤19 for 1–6 educational years, and ≤13 for 0 educational years) were defined as cognitive impairment (**Table 1**). Exclusion criteria were as follows: (1) severe chronic diseases (e.g., cardiac insufficiency, renal insufficiency, cancer, severe anemia, shock, systemic lupus erythematosus, or thyroid dysfunction); (2) anxiety, depression, or other mental diseases; (3) contraindications of MRI scanning or obvious motion artifacts on any image series; (4) a history of Alzheimer's disease, Parkinson's disease, multiple sclerosis, neuromyelitis optica, or epilepsy; (5) severe carotid artery or vertebral stenosis; and (6) severe impaired vision or audition.

A total of 177 subjects were recruited, namely, 73 hypertensive patients with CI (HT-CI), 67 hypertensive patients with normal cognition (HT-NC), and 37 healthy controls. All subjects underwent MRI examination, serum collection, neuropsychological tests, and B-mode ultrasonography of the carotid and vertebral arteries or coronal computed tomography angiography (CTA).

Neuropsychological Examination

Neuropsychological tests were performed by a professional neuropsychologist on the day of MRI scanning. Six domains of cognitive function were evaluated, including global cognition, processing speed, memory, executive function, visuospatial function, and language. All the raw scores were transformed into Z scores according to means and standard deviation (SD) of the row scores: ($Z = \frac{X-\overline{X}}{\mathrm{SD}}$), and $\overline{X}$ indicates mean of raw score. MMSE and MoCA were used to evaluate general cognition. The mean of Z scores of Visual Reproduction-delayed recall test (VR-DR) and the Auditory Verbal Learning Test-long time delayed recall test (AVLT-DR) were used to assess memory. Processing speed was examined via the average Z scores of Trail Making Test A (TMT-A) and Stroop Color and Word Test (SCWT) A. Executive function was evaluated from the mean Z scores from Category Verbal Fluency (CVF), Trail Making Test A and B, and the Stroop-C test. Language was assessed using the average Z scores from Boston Naming Test (BNT) and the Category Verbal Fluency. In addition, visuospatial ability was evaluated using the average Z scores of Visual Reproduction (VR)-copy and the clock-drawing test (CDT).

Serum Collection

Venous blood samples were collected in vacutainer tubes in the morning and then were centrifuged at 3,000 rpm for 10 min. The serum was transferred to a fresh Eppendorf tube and centrifuged at 10,000 rpm for another 10 min to eliminate cellular debris and red blood cells.

Isolation and Characterization of Exosomes

To separate exosomes from serum, ExoQuick serum prep and exosome precipitation kit (System Biosciences Inc., Mountain View, CA, United States) was used according to the manufacturer's protocol. Briefly, a one-fourth volume of exosome precipitation solution was added to the serum and mixed gently by inverting the tube and then the sample was refrigerated for 30 min at 4°C. After centrifuging (1,500 *g*) for 30 min, the supernatant was removed carefully and the pellets were resuspended in sterile PBS. Exosomes were visualized by transmission electron microscopy (TEM) and detected on a nanoparticle-tracking analyzer (NTA; Malvern Panalytical, Malvern, United Kingdom) as described previously (Ji et al., 2016).

Western Blotting Analysis

Exosomes were lysed with lysis buffer (Thermo Fisher Scientific, Rockford, IL, United States) for 30 min at 4°C. The concentration was measured via BCA methods after centrifuging at 12,500 rpm for 30 min. Equal quantities of proteins were separated with 10% SDS-PAGE and then transferred onto PVDF membranes (Millipore, Billerica, MA, United States). After blocking with 5% slim milk for 1 h, the membranes were incubated with primary antibodies against Alix, CD54, Flotillin-1, CD9, and CD63, which are specific proteins of exosomes (Cell Signaling Biotechnology, Hertfordshire, England). The proteins were scanned with a Gel-Pro system (Tanon Technologies, Shanghai, China).

RNA Extraction and Quantitative Reverse Transcription Polymerase Chain Reaction

An exosome RNA Purification Kit (System Biosciences Inc) was used to extract total RNA from serum exosomes following the manufacturer's conditions. RNA was quantified using an Agilent Bioanalyzer 2100 (Santa Clara, CA, United States). Then, the isolated RNA was reverse transcribed using a miRNA Reverse Transcription Kit (Thermo Fisher Scientific, Rockford, IL, United States) according to the following protocols: 16°C for 30 min, 42°C for 30 min, and 85°C for 5 min. Quantitative reverse transcription polymerase chain reaction (qRT-PCR) was carried out on a StepOne Plus Real-Time PCR System (Applied Biosystems, Foster City, United States) with TaqMan Universal Master Mix (Thermo Fisher Scientific). The expression levels of selected miRNAs detected by qRT-PCR were normalized to spiked-in *Caenorhabditis elegans* cel-miR-39 (RiboBio, Guangzhou, China) and the data were analyzed using the $2^{-\Delta Ct}$ (ΔCt = CtmiRNA − CtmiR39) method.

Exosomal miRNA Profile

MiRNA deep sequencing was performed from the serum of the most typical subjects, including six HT-NC patients, six HT-CI patients, and three control individuals in Nanjing Geneseeq Inc., Nanjing, China. Briefly, serum exosomal total RNA quality was assessed using Agilent Bioanalyzer 2100. Then, the sequencing libraries were generated using NEBNext Multiplex Small RNA

TABLE 1 | The evaluation standard of cognitive impairment.

	MMSE			MoCA			
Education (years)	0	1–6	>6	0	1–6	7–12	>12
Threshold value of cognitive impairment (score)	≤19	≤22	≤26	≤13	≤19	≤24	≤25

The subjects with scores equal to or lower than the threshold in MMSE or MoCA tests in different educational experience layers were defined as cognitive impairment. MMSE, Mini-Mental State Examination; MoCA, Montreal Cognitive Assessment.

Library Prep Set (New England Biolabs, United States) following manufacturer's recommendations, and index codes were added to attribute sequences to each sample. Libraries were pooled and sequenced on an Illumina X-ten PE150 platform. A minimum of 300 M reads was generated per sample.

MRI Acquisition

All experiments were performed on a Philips Ingenia 3.0T scanner (Philips, Eindhoven, Netherlands), equipped with a 32-channel head coil. All the images were collected through a same MRI machine to keep homogeneity of images. Head motion was minimized using foam padding, and scanner noise were reduced using a pair of earplugs. Resting-state functional imaging was obtained using a gradient-echo echo-planar imaging (GRE-EPI) sequence, and the imaging parameters were as follows: repetition time (TR) = 2000 ms, flip angle (FA) = 90°, echo time (TE) = 30 ms, matrix = 64 × 64, thickness = 4.0 mm, voxel size = 3 × 3 × 3 mm, field of view = 192 × 192 mm, number of slices = 35, and gap = 0 mm. The scan process totally continued for 8 min and 7 s, and subjects received an instruction to keep still during the whole procedure. The three-dimensional T1-weighted sagittal imaging were acquired by turbo fast echo sequence: TR = 9.8 ms, FA = 8°, TE = 4.6 ms, matrix = 256 × 256, thickness = 1.0 mm, voxel size = 1 × 1 × 1 mm, field of view = 256 × 256 mm, number of slices = 192, and gap = 0 mm. The three-dimensional FLAIR sagittal imaging was acquired by the following sequence: TR = 4,500 ms, FA = 90°, TE = 344 ms, matrix = 272 × 272, thickness = 1.0 mm, number of slices = 200, and gap = 0 mm.

MRI Processing

Data were analyzed using the toolbox for Statistical Parametric Mapping (SPM) and Data Processing and Analysis for Brain Image (DPABI 4.0)[1] software, which are performed in MATLAB (MathWorks, Natick, MA, United States). Preprocessing of the BOLD image series was performed including transformation from DICOM to NIFIT format, head motion correction, smoothing with a Gaussian filter of an 8-mm full-width half-maximum (FWHM), and linear detrending. The end-tidal CO_2 ($EtCO_2$) time course was shifted using a step-wise searching procedure mentioned previously to figure up the time for the blood travel from the lung to the brain. Afterward, the shifted $EtCO_2$ time course was in sync with BOLD imaging and was used for the following analysis. Previous study has shown that the correlation between $EtCO_2$ and BOLD signal time courses was highest when the time course was at the 0.02–0.04 Hz frequency range (Liu et al., 2017); thus, the BOLD signal was filtered at the frequency range of 0.02–0.04 Hz. The average whole-brain BOLD time course was obtained using the whole-brain mask and was used as a reference signal. Then, the CVR index was calculated by employing a general linear model with an independent variable of the reference BOLD signal and dependent variable of the voxel's signal time course and was normalized to the reference region values, yielding a relative CVR map. Relative CVR map was obtained in individual space and then normalized to Montreal Neurological Institute (MNI) standard space with the resample size set at 3 mm × 3 mm × 3 mm. Voxel-wise group comparison and ROI relative CVR value extraction based on the group comparison were performed on DPABI. Automated white matter hyperintensity (WMH) was performed using a brain quantification tool AccuBrain (Wang et al., 2019). The preprocessing steps included noise reduction, bias field correction, and intensity normalization, which was used to normalize intensity level of MRIs acquired from multiple MRI scanners. The segmentation and quantification of WMH are based on a deep learning framework on T1 and FLAIR images, which was trained on hundreds of MRI acquired from different individuals using different scanners and with highly variable degrees of hyperintensity.

Statistical Analysis

Statistical evaluation was conducted using the software SPSS 22.0. For the first analysis, we investigated demographic data in one-way analysis of variance (ANOVA) or chi-square test. As the data of miRNA concentrations were not normally distributed, log transformation was made in miRNA data. The neuropsychological data and miRNA data were performed by covariance analysis, controlling for age, years of education, and history of lacunar stroke. The second analysis focuses on the CVR, and all the BOLD data were analyzed by DPABI 4.0. The analysis of covariance (ANCOVA) was conducted on individual normalized maps in a voxel-wise manner within a whole-brain mask to analyze the differences of CVR among the three groups, controlling for the age, years of education, and history of lacunar stroke. The threshold was determined using Gaussian random field (GRF) for multiple comparisons in the whole brain (voxel-wise p-value < 0.005, cluster p-value < 0.001, and cluster size > 20 voxels). The average CVR significant regions of interest were extracted in every subgroup. Then, the mean CVR in each significant cluster was extracted in each subject. A *post hoc t*-test was performed to detect the detailed group CVR difference in each region using the SPSS 22.0 software. Finally, mediation analysis was performed on the question whether miRNA mediates the relationship between CVR and cognitive

[1] http://rfmri.org/DPABI

performance, which was conducted in PROCESS, controlling for age, years of education, and history of lacunar stroke. The significance was set at $p < 0.05$.

RESULTS

Demographic, Neuropsychological Characteristic, and WMH Volumes

The HT-NC group, the HT-CI group, and the control group did not significantly differ in gender, the ratio of diabetes, hyperlipidemia, smoking, or drinking. However, the control group was significantly younger than the two hypertensive groups. The educational year of the HT-CI group was less than that of the HT-NC group and the control group. Moreover, the ratio of the history of lacunar stroke in the HT-CI group was higher than that in the HT-NC group and the control group (**Table 2**). The results of covariance analysis of cognitive performance and WMH volumes are shown in **Table 2**, controlling for age, years of education, and history of lacunar stroke. The HT-CI group was significantly worse than the HT-NC group and control group in all six domains of cognition. The difference of WMH volume between groups has no significance.

Morphological and Biochemical Characterization of the Exosomes From Patients

The isolated exosomes were characterized by TEM, nanoparticle tracking analysis, and western blotting. TEM analysis indicated that the serum micro-vesicles from patients exhibited a typical round or "cup-shape" appearance (**Figure 1A**). As shown in **Figure 1B**, the exosome markers including Alix, CD54, Flotillin-1, CD9, and CD63 were detected in the serum exosomes by western blotting. The main peak size was within the exosome particle size range (30–150 nm, **Figures 1C,D**). Taken together, these results confirmed that the observed exosomes showed the majority characteristics of exosomes through our isolation operation.

Discovery of Candidate Exosomal MiRNA in the Screen Stage

Three stages, including screening, training, and validation, were performed to define potential serum exosome miRNA biomarkers for hypertensive patients with CI (**Figure 2A**). Deep sequencing was used on the isolated exosomal miRNA from HT-NC and HT-CI patients and corresponding controls. The results showed that there were 2,489 common and novel miRNAs in all samples. There were a total of 25 elevated exosomal miRNAs and 14 downregulated exosomal miRNAs in the HT-CI groups as compared to controls (**Figure 2B**). Compared to the HT-NC group, 42 miRNAs were changed (25 miRNAs were elevated and 17 miRNAs were downregulated) (**Figure 2C**). Among them, nine miRNAs were elevated (miRNA-107, miRNA-191-3p, miRNA-223-3p, miRNA-330-3p, miRNA-339-3p, miRNA-432-5p, miRNA-625-3p, miRNA-671-3p, and miRNA-7641) and one miRNA was downregulated (miRNA-6852-3p) in the HT-CI group as compared to the control group and the HT-NC group.

TABLE 2 | Demographic, neuropsychological, and volume data.

Items	Control (*N* = 37)	HT-NC (*N* = 67)	HT-CI (*N* = 73)	*F* or χ^2	*P*
Sex, male/female	19/18	38/29	37/36	0.568	0.753
Age, years	58.51 ± 7.194	63.85 ± 8.214[a]	66.03 ± 8.197[a]	10.853	< 0.001***
Education, years	12.95 ± 4.453	11.97 ± 3.622	11.07 ± 3.634[ab]	3.080	0.048*
Lacunar stroke, *n* (%)	6 (16)	13 (19)	26 (36)[ab]	6.935	0.031*
Diabetes, *n* (%)	5 (14)	16 (24)	16 (22)	1.627	0.443
Coronary disease, *n* (%)	1 (3)	2 (3)	6 (8)	2.533	0.282
Hyperlipidemia, *n* (%)	7 (19)	16 (24)	15 (21)	2.127	0.712
Smoking, *n* (%)	8 (22)	17 (25)	13 (18)	1.186	0.553
Alcohol, *n* (%)	10 (27)	16 (24)	12 (16)	2.005	0.367
Global cognition	0.52 ± 0.56	0.39 ± 0.55	−0.62 ± 0.87[ab]	39.409	< 0.001***
Processing speed	0.35 ± 0.70	0.18 ± 0.83	−0.35 ± 0.78[ab]	5.138	0.008**
Executive function	0.15 ± 0.59	0.13 ± 0.53	−0.20 ± 0.50[ab]	4.708	0.010*
Memory	0.32 ± 0.68	0.14 ± 0.63	−0.30 ± 0.96[ab]	3.746	0.026*
Language	0.43 ± 0.71	0.18 ± 0.74	−0.41 ± 0.82[ab]	13.407	< 0.001***
Visuospatial function	0.14 ± 0.64	0.26 ± 0.31	−0.32 ± 1.12[ab]	7.893	0.001**
WMH volume (ml)	1.49 ± 1.58	4.37 ± 6.38	5.61 ± 10.17	0.934	0.395

Data are represented as mean ± SD or n (%). One-way ANOVA was performed on normal distributed data. χ^2 analysis was performed on sex data. Covariance analysis was performed on the comparison of Z scores in global cognition, processing speed, executive function, memory, language, visuospatial function, and WMH volume data, controlling for age, years of education, and history of lacunar stroke.

[a] $P < 0.05$, compared with control group.

[b] $P < 0.05$, compared with HT-NC group.

**$P < 0.05$, **$P < 0.01$, ***$P < 0.001$.*

HT-NC, hypertensive patients with normal cognition; HT-CI, hypertensive patients with cognitive impairment.

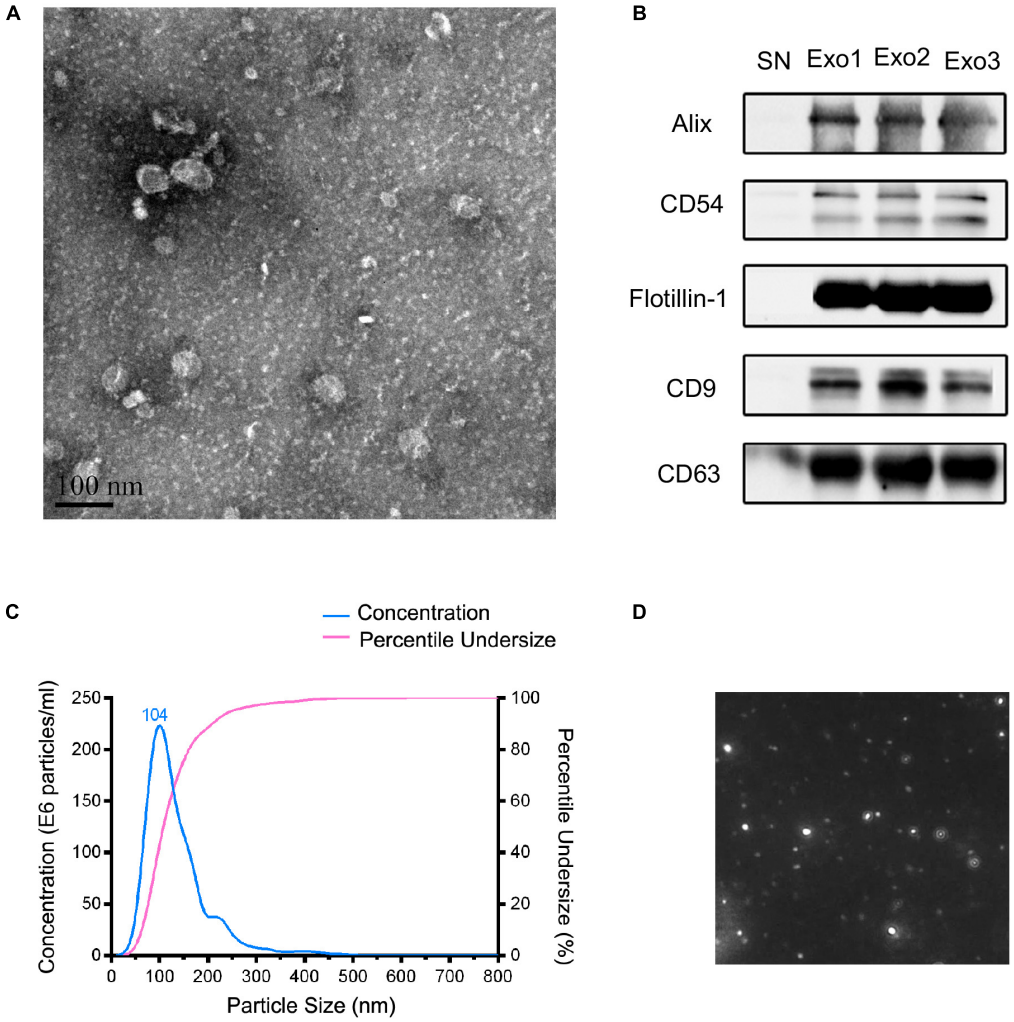

FIGURE 1 | Characteristics of the obtained exosomes from human serum in this study. **(A)** The transmission electron microscopy of the exosomes from the serum. Scale bar = 100 nm. **(B)** Identification of exosomal markers with indicated antibodies by western blot. Measurement of size distribution **(C)** and morphology **(D)** of exosomes purified from serum by nanoparticle-tracking analyzer.

Validation of Candidate Exosomal MiRNA by qRT-PCR

To determine the accuracy of the miRNA sequencing results, we validated the expression of exosomal miRNAs by qRT-PCR. The 10 candidate miRNAs were firstly analyzed from 37 HT-NC patients, 39 HT-CI patients, and 18 controls in the training stage. Only five miRNAs (miRNA-330-3p, miRNA-339-3p, miRNA-432-5p, miRNA-625-3p, and miRNA-6852-3p) showed consistent up- or downregulation tendency (**Supplementary Figures 1A–E**). In contrast, no significant differences of miRNA-107, miRNA-191-3p, miRNA-223-3p, miRNA-671-3p, and miRNA-7641 were observed among HT-NC, HT-CI, and control groups (**Supplementary Figures 1F–J**). The difference of miRNAs among three groups was further measured in a larger cohort of 30 HT-NC patients, 34 HT-CI patients, and 19 control serum samples using covariant analysis in validation stage. The result is shown in **Figure 3**, controlling for age, years of education, and history of lacunar stroke. There were four miRNAs screened out to be related to hypertension and CI, including miRNA-330-3p, miRNA-432-5p, miRNA-625-3p, and miRNA-6852-3p (**Figure 3**). *Post hoc* analysis showed that the HT-CI group had lower miRNA-330-3p and miRNA-625-3p than the control group and had lower miRNA-330-3p and miRNA-432-5p than the HT-NC group. Furthermore, both the HT-NC group and HT-CI group had higher miRNA-6852-3p than the control group.

Bioinformatics Analysis of Identified Exosomal MiRNAs

To investigate the potential role of four identified exosomal miRNAs, we identified the target genes of the differentially expressed miRNAs with miRDB, miRanda, and TargetScan software. It was found that there were 202 target genes recruited. Then, Gene Ontology (GO) category analysis and Kyoto Encyclopedia of Genes and Genomes (KEGG) analysis

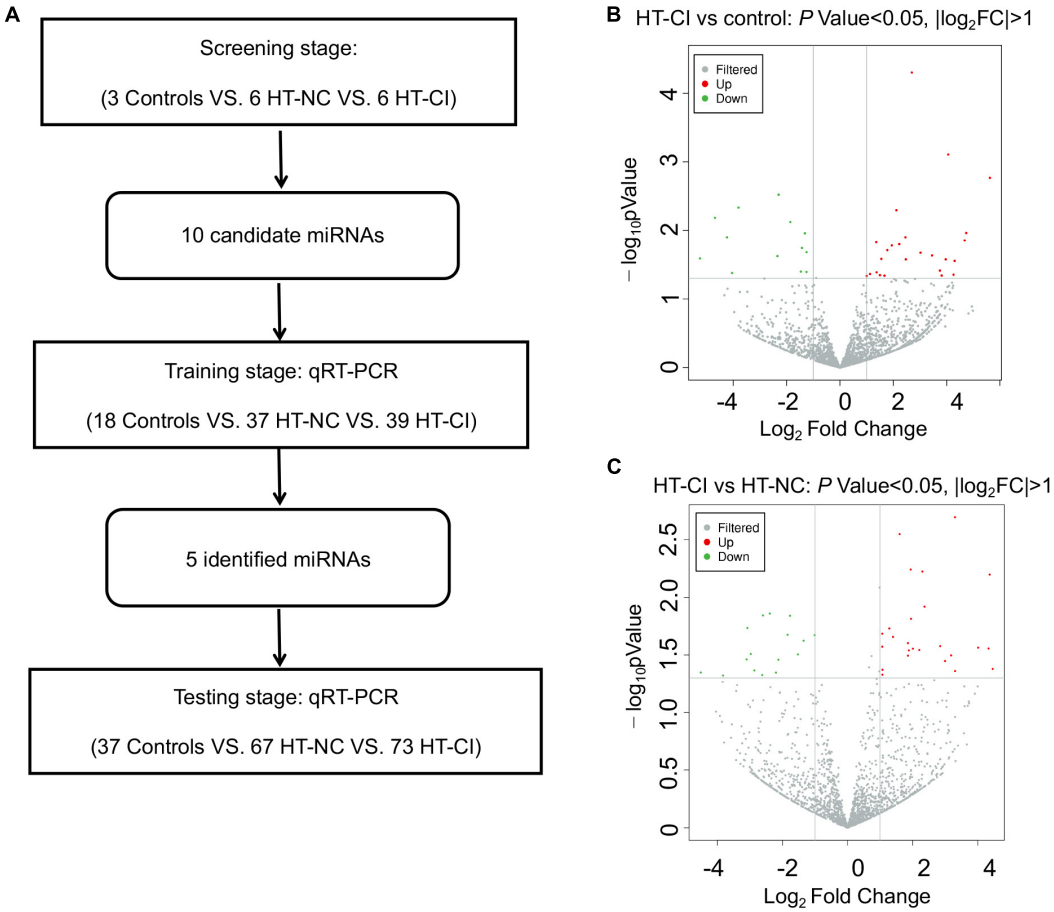

FIGURE 2 | Screening on differentially expressed miRNA. **(A)** Flow chart of study design. **(B)** Volcano plot of differentially expressed miRNAs between HT-CI and control groups. **(C)** Volcano plot of differentially expressed miRNAs between HT-CI and HT-NC groups. HT-NC, hypertensive patients with normal cognition; HT-CI, hypertensive patients with cognitive impairment.

were used to elucidate the biological function of these target genes. GO category analysis identified 676 biological process (BP) entries, 174 cellular component (CC) entries, and 251 molecular function (MF) entries, respectively (**Figure 4A**). Positive regulation of cholesterol biosynthetic process, negative regulation of synapse maturation, and blood vessel maturation are the top three enriched BP terms. The top enriched CC and MF were synapse and amyloid-beta binding, respectively. According to the KEGG pathway enrichment analysis, our identified four exosomal miRNAs were involved in several inflammation and proliferation-related pathways, such as glucagon signaling pathway, TNF signaling pathway, ErbB signaling pathway, PI3K-Akt signaling pathway, and FoxO signaling pathway (**Figure 4B**).

CVR Data

The comparison of CVR variability among the three groups is shown in **Figure 5**. After adjustment for age, years of education, and history of lacunar stroke, significant differences of CVR were mainly found in the left prefrontal white matter, left triangular inferior frontal gyrus, left medial superior frontal gyrus, and left precentral gyrus (**Table 3**). *Post hoc* analysis showed the following: Firstly, significant differences of CVR were shown between HT subjects and control subjects. Compared with the control group, both the HT-NC group and the HT-CI group displayed decreased CVR in the left precentral gyrus. Secondly, the HT-CI group displayed lower CVR than the HT-NC group in the left prefrontal white matter, left triangular inferior frontal gyrus, and left medial superior frontal gyrus. Finally, compared with the control group, the HT-NC group displayed increased CVR in the left prefrontal white matter and left medial superior frontal gyrus.

The Relationship Between CVR, Exosomal MiRNA, and Cognition in Hypertensive Patients With Cognitive Impairment

No significant correlation between CVR in the left prefrontal white matter or left precentral gyrus and cognition were observed in the HT-CI group. The CVR value in the left triangular inferior frontal gyrus was negatively correlated with visuospatial function

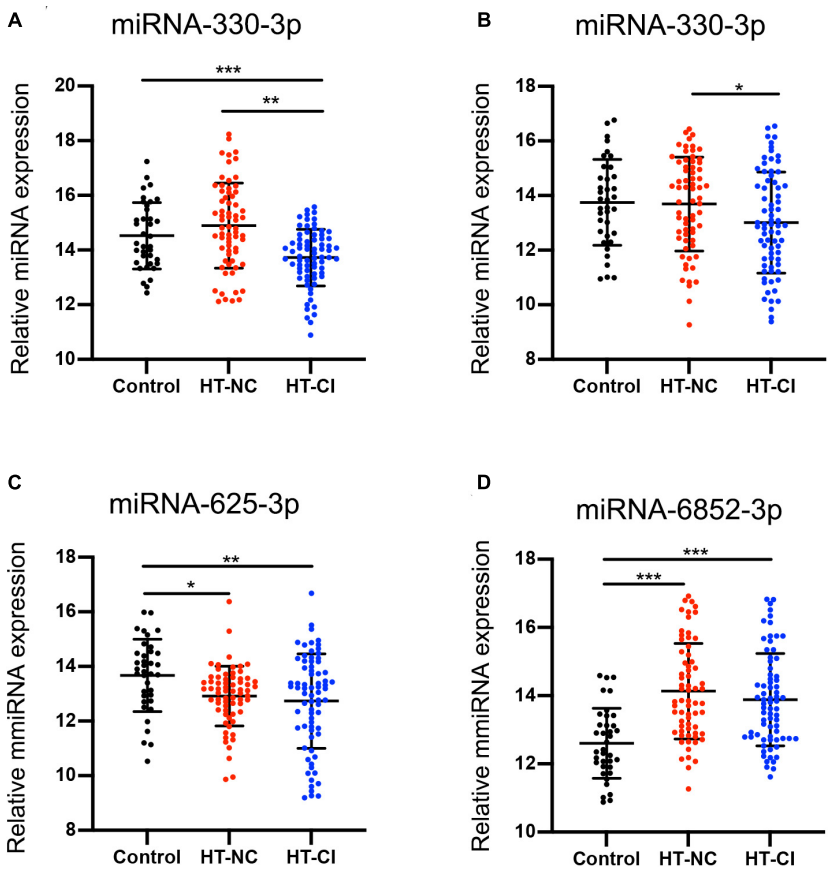

FIGURE 3 | MicroRNA difference among the three groups. **(A)** Subjects in the HT-CI group demonstrated significantly lower concentration of miRNA-330-3p than the other two groups. **(B)** Subjects in the HT-CI group displayed significantly lower concentration of miRNA-432-5p than the HT-NC group. **(C)** Subjects in the HT-CI group and HT-NC group showed significantly lower miRNA-625-3p than the control group. **(D)** Subjects in the HT-CI group and HT-NC group showed significantly higher miRNA-6852-3p than the control group. Error bar indicates standard deviation. $^{*}P < 0.05$, $^{**}P < 0.01$, $^{***}P < 0.001$. HT-NC, hypertensive patients with normal cognition; HT-CI, hypertensive patients with cognitive impairment.

($r = -0.254$, $P = 0.034$) (**Figure 6A**). The correlation was also observed between CVR in the left medial superior frontal gyrus and executive function ($r = -0.275$, $P = 0.021$) (**Figure 6B**) or language ($r = -0.26$, $P = 0.029$) (**Figure 6C**), after adjustment for age, years of education, and history of lacunar stroke.

A significant correlation between serum miRNA-330-3p and executive function was found in the HT-CI group ($r = -0.32$, $P = 0.007$) (**Figure 6D**). There was no correlation between cognitive performance and other serum miRNA (miRNA-432-5p, miRNA-6852-3p, and miRNA-625-3p).

The CVR in the region of interest of the left medial superior frontal lobe was associated with the levels of exosomal miRNAs including miRNA-330-3p ($r = 0.246$, $P = 0.040$) (**Figure 6E**) and miRNA-432-5p ($r = 0.297$, $P = 0.012$) (**Figure 6F**) after controlling for age, years of education, and history of lacunar stroke.

Path Analysis

When the effect of CVR on the association between the exosomal miRNAs and CI was investigated, we used the factors that showed significant correlation to build path models. We previously demonstrated that both miRNA-330-3p and CVR in the left medial superior frontal lobe were significantly correlated with executive function, and miRNA-330-3p was associated with CVR. Thus, we analyzed whether the CVR in the left medial superior frontal lobe mediated the association between miRNA-330-3p and executive function, controlling for age, years of education, and history of lacunar stroke. The association between miRNA-330-3p and executive function was mediated by CVR in the left medial superior frontal lobe (indirect effect: −0.023; 95% CI of bootstrap: −0.0583, −0.001; total effect: −0.1427, 95% CI of bootstrap: −0.2450, −0.0404) (**Figure 7**).

DISCUSSION

The major findings of the present study were as follows. HT-CI subjects displayed several decreased miRNAs (miRNA-330-3p, miRNA-432-5p, and miRNA-625-3p) and increased miRNA-6852-3p in serum exosomes, most of which were related to inflammation and proliferation pathways. HT-CI subjects also displayed significantly lower CVR in the left frontal regions

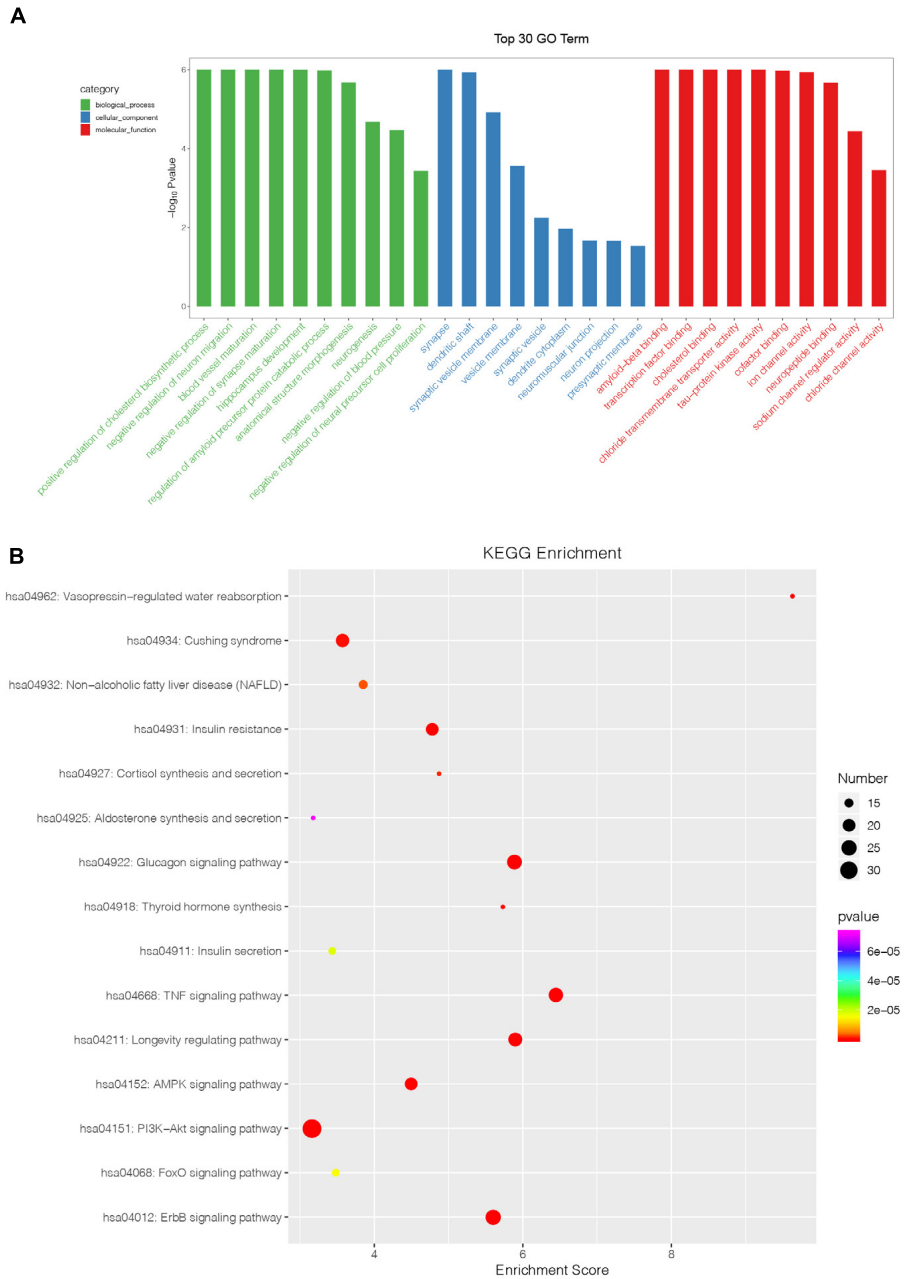

FIGURE 4 | Bioinformatics analysis of identified miRNAs. **(A)** The results of Gene Ontology function analysis on differentially expressed miRNA target genes. **(B)** The entries of Kyoto Encyclopedia of Genes and Genomes pathway enrichment analysis on differentially expressed miRNA target genes.

than HT-NC subjects and healthy subjects. Correlation analysis showed that both exosomal miRNA-330-3p level and the CVR in the left medial frontal gyrus were negatively correlated with executive function in HT-CI subjects. Notably, the CVR in the left medial frontal gyrus mediated the association between miRNA-330-3p level and executive function. These findings furthered the understanding of mechanisms underlying the development of CI in hypertensive patients.

Previous studies have detected a variety of abnormal miRNA expression in hypertensive patients. Li et al. (2011) found that 18 miRNAs were decreased and nine miRNAs were increased in the plasma of hypertensive patients, and one of the miRNAs, human cytomegalovirus (HCMV)-encoded miRNA, hcmv-miR-UL112, was independently associated with the risk of hypertension. Hijmans et al. found that circulating expression of miRNA-34a was increased and the expression of miRNA-21, miRNA-126, and miRNA-146a were decreased in hypertensive patients. Furthermore, the levels of miRNA-34a, miRNA-21, miRNA-126, and miRNA-146a were associated with blood pressure (Hijmans et al., 2018). The heterogeneity

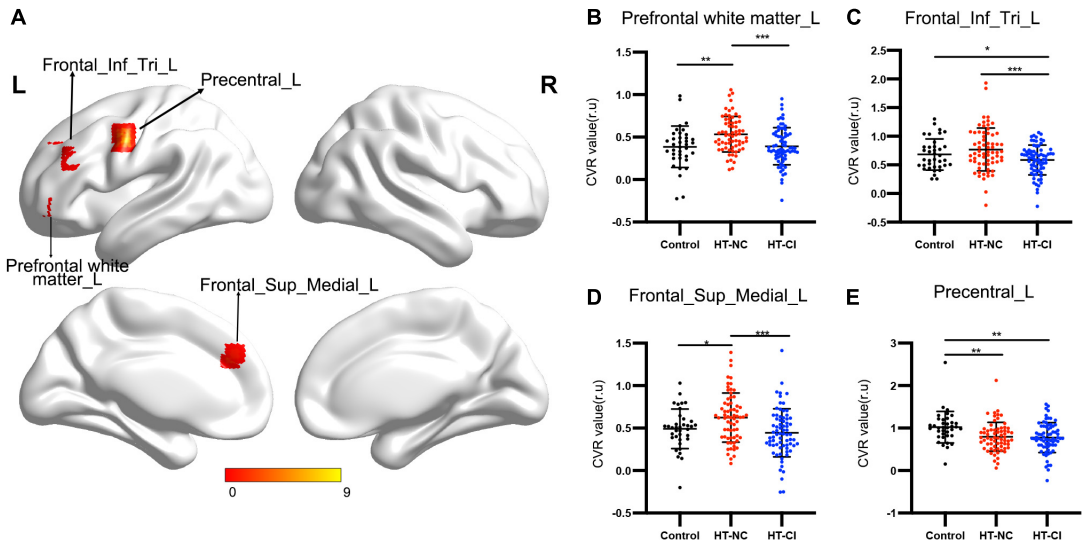

FIGURE 5 | The CVR difference among the three groups. **(A)** Significant CVR regions on the brain. The four regions with significant difference were all located in the left frontal lobe. **(B)** Subjects in the HT-NC group demonstrated significantly higher CVR in the left prefrontal white matter than the other two groups. **(C)** Subjects in the HT-CI group demonstrated significantly lower CVR in the left triangular inferior frontal gyrus. **(D)** Subjects in the HT-NC group demonstrated significantly higher CVR in the left medial superior frontal gyrus than the other two groups. **(E)** Subjects in the HT-CI group and HT-NC group showed significantly lower CVR in the left precentral gyrus than the control group. The threshold was set at corrected *P*-value < 0.005, determined by Gaussian random field for multiple comparisons. Error bar indicates standard deviation. $^{*}P < 0.05$, $^{**}P < 0.01$, $^{***}P < 0.001$. Prefrontal white matter_L, left prefrontal white matter; Frontal_Inf_Tri_L, left triangular inferior frontal gyrus; Frontal_Sup_Medial_L, left medial superior frontal gyrus; Precentral_L, left precentral gyrus; r.u., relative unit.

of abnormal miRNAs has been shown by previous studies. These abnormal miRNAs are mainly involved in inflammation, angiogenesis, renin-angiotensin-aldosterone system, nitric oxide release, and ROS production, and most of the pathways are related to endothelial function (Nemecz et al., 2016). Thus, these abnormal miRNAs may eventually lead to endothelial dysfunction in hypertensive patients. The present study explored exosomal miRNA levels in hypertensive patients and found abnormal exosomal miRNAs related to hypertension and CI. These abnormal miRNAs, including decreased miRNA-330-3p, miRNA-432-5p, and miRNA-625-3p and increased miRNA-6852-3p, in HT-CI subjects, were mainly related to inflammation and proliferation pathways. Notably, the results were displayed by hypertensive patients with MCI, suggesting that these abnormal miRNAs played a major role in the onset of both hypertension and hypertension-related CI. The findings also suggested that although miRNAs contributed to hypertension through many pathways, the inflammation and proliferation pathways may be more related to hypertension-related CI.

TABLE 3 | Clusters with significant difference in the cerebrovascular reactivity among groups.

	BA	Volume (mm^3)	Peak MNI coordinate (mm)	*F*-value
			X*, *Y*, *Z	
Prefrontal white matter_L	11.47	117	−24, 39, 0	8.866
Frontal_Inf_Tri_L	48	21	−36, 30, 24	6.7435
Frontal_Sup_Medial_L	32	39	−15, 39, 30	7.9402
Precentral_L	6	28	−48, −6, 42	6.7351

(X, Y, Z) coordinates of primary peak locations in the MNI space. BA, Brodmann area; MNI, Montreal Neurological Institute; Prefrontal white matter_L, left prefrontal white matter; Frontal_Inf_Tri_L, left triangle inferior frontal gyrus; Frontal_Sup_Medial_L, left medial superior frontal gyrus; Precentral_L, left precentral gyrus.

The CVR pattern in hypertensive patients has been investigated by studies using transcranial Doppler or fMRI technique. Traditionally, transcranial Doppler is useful for measuring global CVR. Decreased global CVR was shown in both children and adolescents with hypertension and was associated with increased diastolic blood pressure (Wong et al., 2011). Elderly people with hypertension also displayed decreased global CVR, which was associated with lower executive function scores (Hajjar et al., 2014). These findings suggested that global CVR reflected the diastolic blood pressure and might predict the onset of CI in hypertensive patients. On the other hand, fMRI technique has been used to detect the regional CVR. Decreased CVR has been shown across different cortical regions, including the frontal cortex, parietal cortex, and cingulum cortex, in hypertensive patients (Savoia et al., 2011; Haight et al., 2015). In the present study, CVR differences were detected not only between hypertensive patients and healthy subjects but also between hypertensive patients with MCI and those with normal cognition. Both HT-NC subjects and HT-CI subjects displayed lower CVR in the left precentral gyrus than healthy subjects. Compared with HT-NC subjects, HT-CI subjects also displayed lower CVR in the frontal regions, including the left prefrontal white matter, the left inferior frontal gyrus, and the left medial

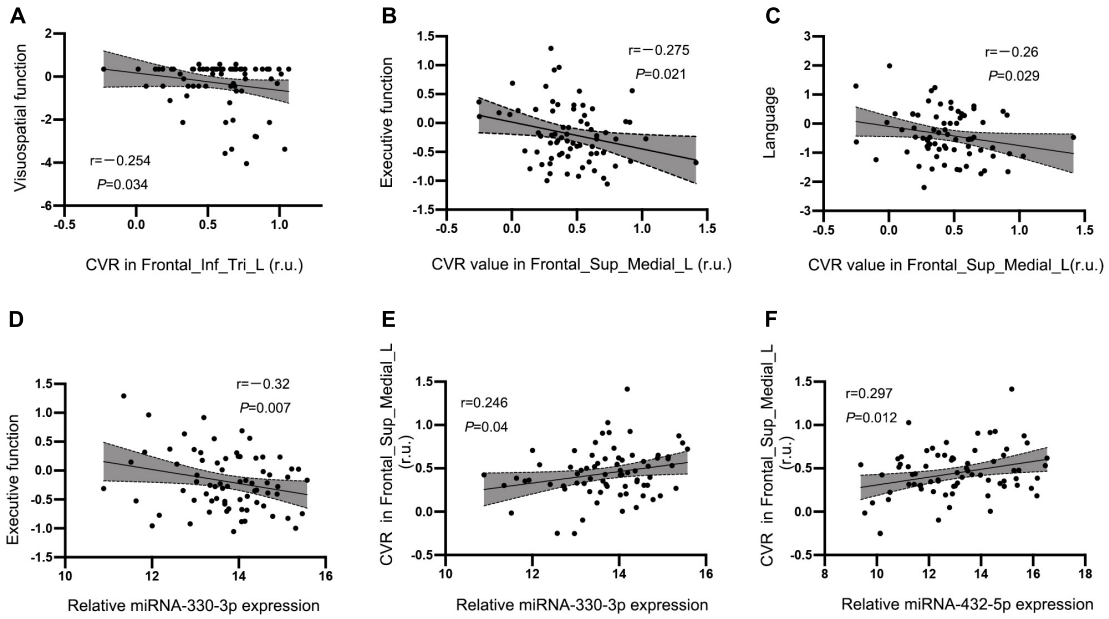

FIGURE 6 | Correlations between CVR, miRNA, and cognitive performance in the HT-CI group. **(A)** The CVR value in the left triangular inferior frontal gyrus was negatively correlated with visuospatial function. **(B,C)** The CVR of the left medial superior frontal lobe had a negative correlation with executive function and language. **(D)** A significant inverse correlation between serum miRNA-330-3p and executive function was discovered in the HT-CI group. **(E,F)** The CVR of the left medial superior frontal lobe had a positive correlation with serum miRNA-330-3p and miRNA-452-5p. Frontal_Inf_Tri_L, left triangular inferior frontal gyrus; Frontal_Sup_Medial_L, left medial superior frontal gyrus; r.u., relative unit.

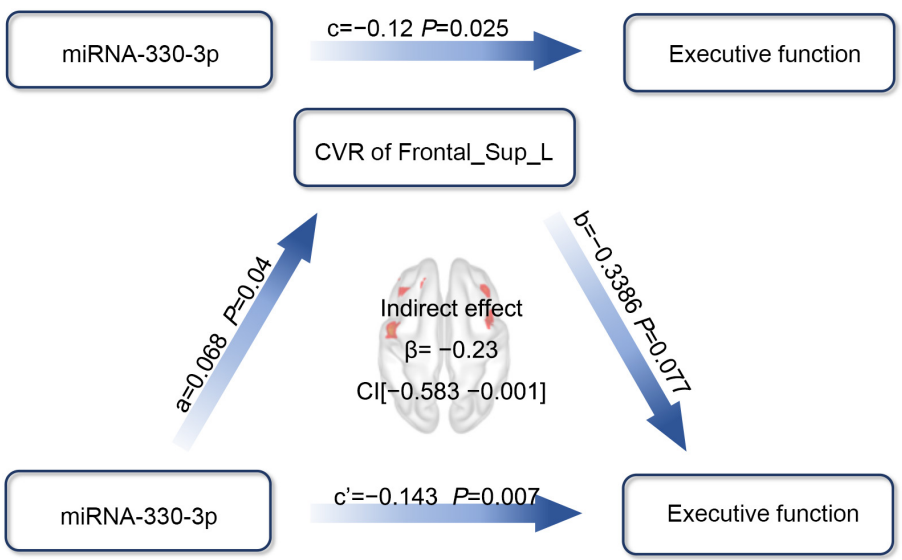

FIGURE 7 | The mediation effect analysis of CVR in the left medial superior frontal lobe on the association between miRNA-330-3p and executive function in HT-CI patients. The standard coefficient and *P*-value were displayed on the pathway controlling for age, years of education, and history of lacunar stroke. The indirect mediation effect of β = –0.23 and a 95% CI as (–0.583, –0.001) was present in the center of the diagram. Red block indicated the significant CVR region. Frontal_Sup_Medial_L, left medial superior frontal gyrus.

frontal gyrus. The results suggested that the impaired cerebral vasodilatory activity of hypertensive patients was prominently shown in the frontal lobe, and the impaired vasodilatory activity played an important role in the development of CI related to hypertension. Furthermore, compared with healthy subjects, HT-NC subjects displayed increased CVR in the frontal regions, suggesting that compensatory vasodilatory activity in the frontal lobe might happen before the onset of CI in hypertensive patients.

Generally, vascular CI is characterized by impaired executive function, information processing, attention, and visuospatial function (O'Brien et al., 2003). Deficits in these domains are related to vascular lesions within the frontal lobe and basal ganglia regions, reflecting impairments of the frontal–subcortical loop (Román et al., 2002; Hsu et al., 2016). A great deal of evidence supports the hypothesis that the frontal cortex coordinates the transfer of various perceptual information from contextual cues and executes corresponding behavioral responses to achieve specific goals, which is known as the perception–action cycle (Fuster, 2001; Miller and Cohen, 2001). While many studies found that fMRI activity in the frontal cortex was associated with multiple cognitive performances (Wierenga et al., 2008; Obler et al., 2010; Gu et al., 2019; Liu R. et al., 2019), the present study extended these associations to regional vasodilatory activity and cognitive performance, i.e., the CVR in the frontal regions was significantly associated with executive function, visuospatial function, and language. Thus, not only the brain activity but also the vasodilatory activity in the frontal regions could reflect the development of CI in hypertensive patients. Notably, both exosomal miRNA-330-3p level and the CVR in the left medial frontal gyrus were negatively correlated with executive function in HT-CI subjects, and the CVR mediated the association between miRNA-330-3p level and executive function. To the best of our knowledge, the present study was the first to show the mediation effect of CVR on the association between miRNA and cognition in hypertensive patients. The mediation of CVR may be explained with the pathology of vascular CI.

Previous studies indicated that the expression of miRNA-330 was significantly decreased in human prostate cancer, melanoma skin cancer, and colorectal cancer, which inversely correlated with its direct target specificity protein 1 (Sp1), E2F1 transcription factors, and thymidylate synthase (TYMS) expression. After overexpression of miRNA-330 in these cancer cells, cell growth, migration, and invasion capability were suppressed (Lee et al., 2009; Mao et al., 2013; Xu et al., 2017; Sehati et al., 2020). However, miRNA-330 overexpression promoted cellular proliferation of glioblastoma through directly targeting the 3′UTR of SH3GL2 gene (Qu et al., 2012). A recent study reported that miRNA-330 overexpression in Alzheimer's disease contributed to the reduction of amyloid β, oxidative stress, and mitochondrial dysfunction by targeting VAV1 through the MAPK pathway (Zhou et al., 2018). In addition, downregulated miRNA-330 could reduce myocardial infarction size through suppressing left ventricular remodeling (Liu Z. Y. et al., 2019). The discrepancy in miRNA-330 biological effects may result from the different diseases, tissues, and experimental conditions used. In the current study, we found that the HT-CI group had lower miRNA-330-3p than the control group and HT-NC group. Besides, the results of KEGG pathway analysis showed that many inflammation and proliferation-related pathways were significantly enriched in HT-CI subjects. The abnormal inflammation and proliferation could be accompanied by massive release of prostanoids and vascular endothelial growth factor, which accelerated vascular leakage, protein extravasation, and cytokine production. These processes disrupted endothelial function and reduced cerebral blood flow through various cerebral arteries, reflected by the decreased CVR in hypertensive patients. Specifically, the deep penetrating arteries supplying cortical projection fibers, association fibers, and subcortical nuclei were more susceptible to be damaged than other arteries. Then, the brain activity and connectivity were disrupted and the CI happened in hypertensive patients. The potential mechanism of miRNA-330 in the pathogenesis of hypertension-related CI needs further investigation.

Several limitations of the present study should be addressed. Firstly, the present study was a single-center, retrospective cohort study design. In consideration of the heterogeneity of the miRNA and the CVR in hypertensive patients, our findings should be validated with a larger sample from multiple centers. Secondly, the approach of resting-state BOLD applied in measuring cerebrovascular disease based on the finding that global BOLD signal within the frequency of 0.02–0.04 Hz has a significant correlation with end-tidal (Et) CO_2 (Liu et al., 2017). However, it is possible the signal contains interference from some non-CO_2 material. Finally, as the miRNA levels varied in different stages of hypertension, further experiments were needed to detect the expression levels of miRNAs at different time points.

CONCLUSION

In conclusion, hypertensive patients with MCI displayed abnormal exosomal miRNA expression and decreased frontal CVR, both of which were related to the CI in these patients. The mediation of the decreased CVR on the association between exosomal miRNA and CI revealed the link between exosomal miRNA, cerebral vasodilatory activity, and CI in hypertensive patients. The decreased frontal CVR and the decreased exosomal miRNA-330-3p might become early biomarkers for the CI related to hypertension.

DATA AVAILABILITY STATEMENT

The datasets presented in this study can be found in online repositories. The names of the repository/repositories and accession number(s) can be found below: https://www.ncbi.nlm.nih.gov/sra/PRJNA685950.

ETHICS STATEMENT

The studies involving human participants were reviewed and approved by the Drum Tower Hospital Research Ethics Committee. The patients/participants provided their written informed consent to participate in this study.

AUTHOR CONTRIBUTIONS

JM, XC, and QY contributed to conduct and analysis of the study, and writing of the manuscript. FC, RQ, and YC contributed to conduct the study. XZ contributed to concept and design of the study and conduct the study. YX contributed to

concept and design of the study, and review and editing of the manuscript. All authors contributed to the article and approved the submitted version.

FUNDING

This study was supported by the National Key Research and Development Program of China (2016YFC1300504), National Natural Science Foundation of China (81630028, 81971112, and 81701170), and Key Research and Development Program of Jiangsu Province of China, Jiangsu Province Key Medical Discipline (ZDXKA2016020).

SUPPLEMENTARY MATERIAL

The Supplementary Material for this article can be found online at: https://www.frontiersin.org/articles/10.3389/fnins.2021.614220/full#supplementary-material

REFERENCES

Ballantyne, M. D., McDonald, R. A., and Baker, A. H. (2016). Lncrna/microrna interactions in the vasculature. *Clin. Pharmacol. Ther.* 99, 494–501. doi: 10.1002/cpt.355

Bartel, D. P. (2004). Micrornas: genomics, biogenesis, mechanism, and function. *Cell* 116, 281–297. doi: 10.1016/s0092-8674(04)00045-5

Chopp, M., and Zhang, Z. G. (2015). Emerging potential of exosomes and noncoding micrornas for the treatment of neurological injury/diseases. *Expert Opin. Emerg. Drugs* 20, 523–526. doi: 10.1517/14728214.2015.1061993

Duca, L., Blaise, S., Romier, B., Laffargue, M., Gayral, S., El Btaouri, H., et al. (2016). Matrix ageing and vascular impacts: focus on elastin fragmentation. *Cardiovasc. Res.* 110, 298–308. doi: 10.1093/cvr/cvw061

Fuster, J. M. (2001). The prefrontal cortex–an update: time is of the essence. *Neuron* 30, 319–333.

Gąsecki, D., Kwarciany, M., Nyka, W., and Narkiewicz, K. (2013). Hypertension, brain damage and cognitive decline. *Curr. Hypertens. Rep.* 15, 547–558. doi: 10.1007/s11906-013-0398-4

Grant, H., Bhambhani, Y., Singhal, A., Haennel, R., and Warren, S. (2015). Reliability and reactivity of the prefrontal hemodynamic responses in essential hypertension: a functional near infrared spectroscopy study. *J. Am. Soc. Hypertens.* 9, 811–820. doi: 10.1016/j.jash.2015.07.010

Gu, Y., Liu, R., Qin, R., Chen, X., Zou, J., Jiang, Y., et al. (2019). Characteristic changes in the default mode network in hypertensive patients with cognitive impairment. *Hypertens. Res.* 42, 530–540. doi: 10.1038/s41440-018-0176-4

Haight, T. J., Bryan, R. N., Erus, G., Davatzikos, C., Jacobs, D. R., D'Esposito, M., et al. (2015). Vascular risk factors, cerebrovascular reactivity, and the default-mode brain network. *Neuroimage* 115, 7–16. doi: 10.1016/j.neuroimage.2015.04.039

Hajjar, I., Marmerelis, V., Shin, D. C., and Chui, H. (2014). Assessment of cerebrovascular reactivity during resting state breathing and its correlation with cognitive function in hypertension. *Cerebrovasc. Dis.* 38, 10–16. doi: 10.1159/000365349

Hijmans, J. G., Diehl, K. J., Bammert, T. D., Kavlich, P. J., Lincenberg, G. M., Greiner, J. J., et al. (2018). Association between hypertension and circulating vascular-related micrornas. *J. Hum. Hypertens.* 32, 440–447. doi: 10.1038/s41371-018-0061-2

Hsu, Y. H., Huang, C. F., Lo, C. P., Wang, T. L., Yang, C. C., and Tu, M. C. (2016). Frontal assessment battery as a useful tool to differentiate mild cognitive impairment due to subcortical ischemic vascular disease from alzheimer disease. *Dement. Geriatr. Cogn. Disord.* 42, 331–341. doi: 10.1159/000452762

Ji, Q., Ji, Y., Peng, J., Zhou, X., Chen, X., Zhao, H., et al. (2016). Increased brain-specific mir-9 and mir-124 in the serum exosomes of acute ischemic stroke patients. *PLoS One* 11:e0163645. doi: 10.1371/journal.pone.0163645

Kannurpatti, S. S., Motes, M. A., Biswal, B. B., and Rypma, B. (2014). Assessment of unconstrained cerebrovascular reactivity marker for large age-range fmri studies. *PLoS One* 9:e88751. doi: 10.1371/journal.pone.0088751

Kannurpatti, S. S., Motes, M. A., Rypma, B., and Biswal, B. B. (2010). Neural and vascular variability and the fmri-bold response in normal aging. *Magn. Reson. Imaging* 28, 466–476. doi: 10.1016/j.mri.2009.12.007

Klimczak, D., Jazdzewski, K., and Kuch, M. (2017). Regulatory mechanisms in arterial hypertension: role of microrna in pathophysiology and therapy. *Blood Press.* 26, 2–8. doi: 10.3109/08037051.2016.1167355

Kontaraki, J. E., Marketou, M. E., Zacharis, E. A., Parthenakis, F. I., and Vardas, P. E. (2014). Differential expression of vascular smooth muscle-modulating micrornas in human peripheral blood mononuclear cells: novel targets in essential hypertension. *J. Hum. Hypertens.* 28, 510–516. doi: 10.1038/jhh.2013.117

Krishnan, R., Mani, P., Sivakumar, P., Gopinath, V., and Sekar, D. (2017). Expression and methylation of circulating microrna-510 in essential hypertension. *Hypertens. Res.* 40, 361–363. doi: 10.1038/hr.2016.147

Lee, K. H., Chen, Y. L., Yeh, S. D., Hsiao, M., Lin, J. T., Goan, Y. G., et al. (2009). Microrna-330 acts as tumor suppressor and induces apoptosis of prostate cancer cells through e2f1-mediated suppression of akt phosphorylation. *Oncogene* 28, 3360–3370. doi: 10.1038/onc.2009.192

Li, J. Q., Tan, L., Wang, H. F., Tan, M. S., Tan, L., Xu, W., et al. (2016). Risk factors for predicting progression from mild cognitive impairment to alzheimer's disease: a systematic review and meta-analysis of cohort studies. *J. Neurol. Neurosurg. Psychiatry* 87, 476–484. doi: 10.1136/jnnp-2014-310095

Li, S., Zhu, J., Zhang, W., Chen, Y., Zhang, K., Popescu, L. M., et al. (2011). Signature microrna expression profile of essential hypertension and its novel link to human cytomegalovirus infection. *Circulation* 124, 175–184. doi: 10.1161/CIRCULATIONAHA.110.012237

Liu, P., Hebrank, A. C., Rodrigue, K. M., Kennedy, K. M., Park, D. C., and Lu, H. (2013). A comparison of physiologic modulators of fmri signals. *Hum. Brain Mapp.* 34, 2078–2088. doi: 10.1002/hbm.22053

Liu, P., Li, Y., Pinho, M., Park, D. C., Welch, B. G., and Lu, H. (2017). Cerebrovascular reactivity mapping without gas challenges. *Neuroimage* 146, 320–326. doi: 10.1016/j.neuroimage.2016.11.054

Liu, R., Wu, W., Ye, Q., Gu, Y., Zou, J., Chen, X., et al. (2019). Distinctive and pervasive alterations of functional brain networks in cerebral small vessel disease with and without cognitive impairment. *Dement. Geriatr. Cogn. Disord.* 47, 55–67. doi: 10.1159/000496455

Liu, Z. Y., Pan, H. W., Cao, Y., Zheng, J., Zhang, Y., Tang, Y., et al. (2019). Downregulated microrna-330 suppresses left ventricular remodeling via the tgf-beta1/smad3 signaling pathway by targeting sry in mice with myocardial ischemia-reperfusion injury. *J. Cell Physiol.* 234, 11440–11450. doi: 10.1002/jcp.27800

Mancia, G., Fagard, R., Narkiewicz, K., Redon, J., Zanchetti, A., Bohm, M., et al. (2013). 2013 esh/esc guidelines for the management of arterial hypertension: the task force for the management of arterial hypertension of the european society of hypertension (esh) and of the european society of cardiology (esc). *Eur. Heart J.* 34, 2159–2219. doi: 10.1093/eurheartj/eht151

Mao, Y., Chen, H., Lin, Y., Xu, X., Hu, Z., Zhu, Y., et al. (2013). Microrna-330 inhibits cell motility by downregulating sp1 in prostate cancer cells. *Oncol. Rep.* 30, 327–333. doi: 10.3892/or.2013.2452

Mathieu, M., Martin-Jaular, L., Lavieu, G., and Thery, C. (2019). Specificities of secretion and uptake of exosomes and other extracellular vesicles for cell-to-cell communication. *Nat. Cell Biol.* 21, 9–17. doi: 10.1038/s41556-018-0250-9

Miller, E. K., and Cohen, J. D. (2001). An integrative theory of prefrontal cortex function. *Annu. Rev. Neurosci.* 24, 167–202. doi: 10.1146/annurev.neuro.24.1.167

Mills, K. T., Bundy, J. D., Kelly, T. N., Reed, J. E., Kearney, P. M., Reynolds, K., et al. (2016). Global disparities of hypertension prevalence and control: a systematic analysis of population-based studies from 90 countries. *Circulation* 134, 441–450. doi: 10.1161/CIRCULATIONAHA.115.018912

Nemecz, M., Alexandru, N., Tanko, G., and Georgescu, A. (2016). Role of microrna in endothelial dysfunction and hypertension. *Curr. Hypertens. Rep.* 18:87. doi: 10.1007/s11906-016-0696-8

Ninomiya, T., Ohara, T., Hirakawa, Y., Yoshida, D., Doi, Y., Hata, J., et al. (2011). Midlife and late-life blood pressure and dementia in japanese elderly: the hisayama study. *Hypertension* 58, 22–28. doi: 10.1161/HYPERTENSIONAHA.110.163055

Obler, L. K., Rykhlevskaia, E., Schnyer, D., Clark-Cotton, M. R., Spiro, A. III, Hyun, J., et al. (2010). Bilateral brain regions associated with naming in older adults. *Brain Lang.* 113, 113–123. doi: 10.1016/j.bandl.2010.03.001

O'Brien, J. T., Erkinjuntti, T., Reisberg, B., Roman, G., Sawada, T., Pantoni, L., et al. (2003). Vascular cognitive impairment. *Lancet Neurol.* 2, 89–98. doi: 10.1016/s1474-4422(03)00305-3

Qu, S., Yao, Y., Shang, C., Xue, Y., Ma, J., Li, Z., et al. (2012). Microrna-330 is an oncogenic factor in glioblastoma cells by regulating sh3gl2 gene. *PLoS One* 7:e46010. doi: 10.1371/journal.pone.0046010

Román, G. C., Erkinjuntti, T., Wallin, A., Pantoni, L., and Chui, H. C. (2002). Subcortical ischaemic vascular dementia. *Lancet Neurol.* 1, 426–436. doi: 10.1016/s1474-4422(02)00190-4

Ronnemaa, E., Zethelius, B., Lannfelt, L., and Kilander, L. (2011). Vascular risk factors and dementia: 40-year follow-up of a population-based cohort. *Dement. Geriatr. Cogn. Disord.* 31, 460–466. doi: 10.1159/000330020

Savoia, C., Sada, L., Zezza, L., Pucci, L., Lauri, F. M., Befani, A., et al. (2011). Vascular inflammation and endothelial dysfunction in experimental hypertension. *Int. J. Hypertens.* 2011:281240. doi: 10.4061/2011/281240

Sehati, N., Sadeghie, N., Mansoori, B., Mohammadi, A., Shanehbandi, D., and Baradaran, B. (2020). Microrna-330 inhibits growth and migration of melanoma a375 cells: in vitro study. *J. Cell Biochem.* 121, 458–467. doi: 10.1002/jcb.29211

Shi, L., Liao, J., Liu, B., Zeng, F., and Zhang, L. (2015). Mechanisms and therapeutic potential of micrornas in hypertension. *Drug Discov. Today* 20, 1188–1204. doi: 10.1016/j.drudis.2015.05.007

Wagenseil, J. E., and Mecham, R. P. (2012). Elastin in large artery stiffness and hypertension. *J. Cardiovasc. Transl. Res.* 5, 264–273. doi: 10.1007/s12265-012-9349-8

Wang, C., Zhao, L., Luo, Y., Liu, J., Miao, P., Wei, S., et al. (2019). Structural covariance in subcortical stroke patients measured by automated mri-based volumetry. *Neuroimage Clin.* 22:101682. doi: 10.1016/j.nicl.2019.101682

Widlansky, M. E., Gokce, N., Keaney, J. F., and Vita, J. A. (2003). The clinical implications of endothelial dysfunction. *J. Am. Coll. Cardiol.* 42, 1149–1160. doi: 10.1016/s0735-1097(03)00994-x

Wierenga, C. E., Benjamin, M., Gopinath, K., Perlstein, W. M., Leonard, C. M., Rothi, L. J., et al. (2008). Age-related changes in word retrieval: role of bilateral frontal and subcortical networks. *Neurobiol. Aging* 29, 436–451. doi: 10.1016/j.neurobiolaging.2006.10.024

Wilstein, Z., Alligood, D. M., McLure, V. L., and Miller, A. C. (2018). Mathematical model of hypertension-induced arterial remodeling: a chemo-mechanical approach. *Math. Biosci.* 303, 10–25. doi: 10.1016/j.mbs.2018.05.002

Wong, L. J., Kupferman, J. C., Prohovnik, I., Kirkham, F. J., Goodman, S., Paterno, K., et al. (2011). Hypertension impairs vascular reactivity in the pediatric brain. *Stroke* 42, 1834–1838. doi: 10.1161/STROKEAHA.110.607606

Wong, W. T., Wong, S. L., Tian, X. Y., and Huang, Y. (2010). Endothelial dysfunction: the common consequence in diabetes and hypertension. *J. Cardiovasc. Pharmacol.* 55, 300–307. doi: 10.1097/fjc.0b013e3181d7671c

Wood, M. J., O'Loughlin, A. J., and Samira, L. (2011). Exosomes and the blood-brain barrier: implications for neurological diseases. *Ther. Deliv.* 2, 1095–1099. doi: 10.4155/tde.11.83

Xu, W., Jiang, H., Zhang, F., Gao, J., and Hou, J. (2017). Microrna-330 inhibited cell proliferation and enhanced chemosensitivity to 5-fluorouracil in colorectal cancer by directly targeting thymidylate synthase. *Oncol. Lett.* 13, 3387–3394. doi: 10.3892/ol.2017.5895

Yang, Q., Jia, C., Wang, P., Xiong, M., Cui, J., Li, L., et al. (2014). Microrna-505 identified from patients with essential hypertension impairs endothelial cell migration and tube formation. *Int. J. Cardiol.* 177, 925–934. doi: 10.1016/j.ijcard.2014.09.204

Zhang, H. N., Xu, Q. Q., Thakur, A., Alfred, M. O., Chakraborty, M., Ghosh, A., et al. (2018). Endothelial dysfunction in diabetes and hypertension: role of micrornas and long non-coding rnas. *Life Sci.* 213, 258–268. doi: 10.1016/j.lfs.2018.10.028

Zhou, Y., Wang, Z. F., Li, W., Hong, H., Chen, J., Tian, Y., et al. (2018). Protective effects of microrna-330 on amyloid beta-protein production, oxidative stress, and mitochondrial dysfunction in alzheimer's disease by targeting vav1 via the mapk signaling pathway. *J. Cell Biochem.* 119, 5437–5448. doi: 10.1002/jcb.26700

Conflict of Interest: The authors declare that the research was conducted in the absence of any commercial or financial relationships that could be construed as a potential conflict of interest.

frontiers in Neuroscience

ORIGINAL RESEARCH
published: 08 March 2021
doi: 10.3389/fnins.2021.622423

[^{18}F]F13640, a 5-HT$_{1A}$ Receptor Radiopharmaceutical Sensitive to Brain Serotonin Fluctuations

*Matthieu Colom[1,2], Benjamin Vidal[1], Sylvain Fieux[1], Jérôme Redoute[3], Nicolas Costes[3], Franck Lavenne[3], Inés Mérida[3], Zacharie Irace[3], Thibaud Iecker[3], Caroline Bouillot[3], Thierry Billard[3], Adrian Newman-Tancredi[4] and Luc Zimmer[1,2,3,5]**

[1] Lyon Neuroscience Research Center, INSERM, CNRS, Université de Lyon, Université Claude Bernard Lyon 1, Lyon, France, [2] Hospices Civils de Lyon, Lyon, France, [3] CERMEP-Imagerie du Vivant, Bron, France, [4] Neurolixis, Castres, France, [5] Institut National des Sciences et Techniques Nucléaires, Gif-sur-Yvette, France

Introduction: Serotonin is involved in a variety of physiological functions and brain disorders. In this context, efforts have been made to investigate the *in vivo* fluctuations of this neurotransmitter using positron emission tomography (PET) imaging paradigms. Since serotonin is a full agonist, it binds preferentially to G-protein coupled receptors. In contrast, antagonist PET ligands additionally interact with uncoupled receptors. This could explain the lack of sensitivity to serotonin fluctuations of current 5-HT$_{1A}$ radiopharmaceuticals which are mainly antagonists and suggests that agonist radiotracers would be more appropriate to measure changes in neurotransmitter release. The present study evaluated the sensitivity to endogenous serotonin release of a recently developed, selective 5-HT$_{1A}$ receptor PET radiopharmaceutical, the agonist [^{18}F]F13640 (a.k.a. befiradol or NLX-112).

Materials and Methods: Four cats each underwent three PET scans with [^{18}F]F13640, i.e., a control PET scan of 90 min, a PET scan preceded 30 min before by an intravenous injection 1 mg/kg of d-fenfluramine, a serotonin releaser (blocking challenge), and a PET scan comprising the intravenous injection of 1 mg/kg of d-fenfluramine 30 min after the radiotracer injection (displacement challenge). Data were analyzed with regions of interest and voxel-based approaches. A lp-ntPET model approach was implemented to determine the dynamic of serotonin release during the challenge study.

Results: D-fenfluramine pretreatment elicited a massive inhibition of [^{18}F]F13640 labeling in regions known to express 5-HT$_{1A}$ receptors, e.g., raphe nuclei, hippocampus, thalamus, anterior cingulate cortex, caudate putamen, occipital, frontal and parietal cortices, and gray matter of cerebellum. Administration of d-fenfluramine during PET acquisition indicates changes in occupancy from 10% (thalamus) to 31% (gray matter of cerebellum) even though the dissociation rate of [^{18}F]F13640 over the 90 min acquisition time was modest. The lp-ntPET simulation succeeded in differentiating the control and challenge conditions.

Conclusion: The present findings demonstrate that labeling of 5-HT$_{1A}$ receptors with [^{18}F]F13640 is sensitive to serotonin concentration fluctuations *in vivo*. Although the

OPEN ACCESS

Edited by:
Nicola Toschi,
University of Rome Tor Vergata, Italy

Reviewed by:
Laetitia Lemoine,
Karolinska Institutet (KI), Sweden
Hanne Demant Hansen,
Copenhagen University Hospital, Denmark

***Correspondence:**
Luc Zimmer
luc.zimmer@univ-lyon1.fr

Specialty section:
This article was submitted to Brain Imaging Methods, a section of the journal Frontiers in Neuroscience

Received: *28 October 2020*
Accepted: *17 February 2021*
Published: *08 March 2021*

Citation:
Colom M, Vidal B, Fieux S, Redoute J, Costes N, Lavenne F, Mérida I, Irace Z, Iecker T, Bouillot C, Billard T, Newman-Tancredi A and Zimmer L (2021) [^{18}F]F13640, a 5-HT$_{1A}$ Receptor Radiopharmaceutical Sensitive to Brain Serotonin Fluctuations. Front. Neurosci. 15:622423. doi: 10.3389/fnins.2021.622423

data underline the need to perform longer PET scan to ensure accurate measure of displacement, they support clinical development of [^{18}F]F13640 as a tool to explore experimental paradigms involving physiological or pathological (neurological or neuropsychiatric pathologies) fluctuations of extracellular serotonin.

Keywords: [^{18}F]F13640, 5-HT$_{1A}$ receptors, PET imaging, serotonin release, agonist, fenfluramine

INTRODUCTION

The 5-HT$_{1A}$ receptor is a subtype of serotonin (5-HT) receptors that belongs to the G-protein coupled receptor family. 5-HT$_{1A}$ receptors couple to $G_{i/o}$ protein and their activation induces an inhibition of cyclase adenylate and a decrease of cAMP synthesis, leading to hyperpolarization of neuron membrane and inhibition of neuron activity (Nichols and Nichols, 2008). 5-HT$_{1A}$ receptors are widely distributed in the central nervous system, being localized in raphe nuclei as somatodendritic receptors (Riad et al., 2000), or in cortical and limbic areas as post-synaptic receptors (Verge et al., 1985; Radja et al., 1991; Miquel et al., 1992). The wide regional expression of 5-HT$_{1A}$ receptors is in accordance with their involvement in many physiological functions, including cognition (Buhot, 1997), cognitive behaviors (Buhot, 1997), pain (Kristian Eide et al., 1990) and in numerous brain disorders such as anxiety (Akimova et al., 2009), depression (Richardson-Jones et al., 2010), schizophrenia (Maćkowiak et al., 2000), Alzheimer's disease (Truchot et al., 2007), and Parkinson's disease (Shimizu and Ohno, 2013). In view of the complexity of the functions controlled by 5-HT$_{1A}$ receptors, efforts have been made to investigate them using various positron emission tomography (PET) imaging tools, notably as concerns the fluctuations of endogenous neurotransmitter levels in physiological or pathological conditions. This objective can be pursued by using radiotracers that bind to the target receptors with comparable affinity as the neurotransmitter of interest. Such an approach has been largely applied to the study of the dopaminergic system, using radiotracers of D_2/D_3 receptors such as [^{11}C]raclopride (Laruelle, 2000). Unfortunately, measuring endogenous 5-HT release using PET has proved more challenging (Paterson et al., 2010; Tyacke and Nutt, 2015). Currently, very few radiotracers display sensitivity to changes in 5-HT levels, including [^{11}C]Cimbi-36, a 5-HT$_{2A}$ receptor agonist radioligand (da Cunha-Bang et al., 2019) and [^{11}C]AZ10419369, a 5-HT$_{1B}$ receptor agonist radioligand (Yang et al., 2018). As concerns 5-HT$_{1A}$ receptors, some studies were carried out in rodent models with the antagonist [^{18}F]MPPF (Zimmer et al., 2002, 2003) but did not show sufficient sensitivity to robustly evaluate physiological changes of endogenous serotonin levels,

The main reason cited for the lack of sensitivity of 5-HT$_{1A}$ radiopharmaceuticals is the fact that they are antagonists or, at best, partial agonists (Colom et al., 2019). *In vitro* studies indicate that antagonist ligands bind similarly to receptors in both coupled and uncoupled states (Laruelle, 2000). Since serotonin is a full agonist which binds preferentially to G-protein-coupled receptors, competition with a PET antagonist is therefore "diluted" by the latter's additional interaction with uncoupled receptors. In this context, using agonist radiotracers seems a more promising strategy, as they directly compete with endogenous serotonin on the same G-protein-coupled sites. Accordingly, [^{11}C]Cimbi-36 shows a higher sensitivity to serotonin fluctuations compared to the antagonist radiotracer, [^{18}F]altanserin (Jørgensen et al., 2017).

We previously evaluated a series of full-agonist ligands of 5-HT$_{1A}$ receptors, F13714, F15599 (a.k.a. NLX-101) and F13640 (a.k.a. befiradol or NLX-112), as potential radiotracers. Although the labeling of F13714 and F15599 with fluorine-18 was successful, their first use *in vivo* as radiotracers showed that the signal to noise ratio was too low for [^{18}F]F15599, and that [^{18}F]F13714 binding appeared to be irreversible (Lemoine et al., 2010, 2012). In contrast, [^{18}F]F13640 showed satisfying properties for neuroimaging. PET studies in rats, cats and non-human primates revealed that it specifically targets 5-HT$_{1A}$ receptors, and showed a good signal to noise ratio (Vidal et al., 2018a). Moreover, *ex vivo* autoradiography studies in rat showed that [^{18}F]F13640 was almost ten times more sensitive to competition binding with serotonin than the antagonist [^{18}F]MPPF (Vidal et al., 2018a), thus justifying the current study.

The aim of the present PET study was therefore to further investigate the PET sensitivity of [^{18}F]F13640 to changes in endogenous serotonin levels induced by 1 mg/kg of d-fenfluramine, a serotonin releaser. Studies were conducted in cat due to its higher imaging resolution than mice and rats (Aznavour et al., 2006), as shown in our previous experiments (Vidal et al., 2018a,b). We performed two type of pharmacological PET protocols with [^{18}F]F13640: (i) a d-fenfluramine pretreatment 30 min before PET acquisition (5-HT blocking paradigm); and (ii) a challenge of d-fenfluramine 30 min after start of PET acquisition (5-HT displacement paradigm). Additional *in vitro* autoradiography experiments were also carried out and the data were analyzed using a ROI-based and a voxel-based approaches, with simple estimations of 5-HT$_{1A}$ receptors occupancy by serotonin or kinetic modeling of serotonin release using the lp-ntPET protocol (Normandin et al., 2012).

MATERIALS AND METHODS

[^{18}F]F13640 Radiosynthesis

Synthesis of [^{18}F]F13640 and quality controls pathways were previously described (Vidal et al., 2018a). Briefly, after production of fluoride preparation $^{18}O(p,n)^{18}F$ cyclotron reaction, 5 mg of F13640 nitro precursor are introduced. After nucleophile substitution, [^{18}F]F13640 is obtained by separation on a preparative HPLC column (SymmetryPrepC18, 7 μm,

7.80 mm × 300 mm, Waters). The radiotracer is formulated *via* solid phase extraction techniques using a Sep-Pak Light C18 cartridge (Waters). The final product is eluted with 1 mL of ethanol, diluted with saline and finally sterilized by filtration (sterile filter Millex-GS, 0.22 μm; Millipore).

Autoradiography Studies

The brain of one cat was extracted after euthanasia obtained by short inhalation of isoflurane and in accordance with European guidelines for care of laboratory animals (2010:63:EU). The brain was immediately frozen in 2-methylbutane cooled with dry ice (−29°C). Coronal sections (30 μm thick) were cut using a −20°C cryostat, thaw-mounted on glass slides, and allowed to air dry before storage at −80°C until used. At the day of the experiment, all slides were incubated for 20 min in Tris phosphate-buffered saline buffer, pH 7.5, containing 37 kBq/ml of [^{18}F]F13640 (F13640 1 μmol/L). For competition studies, slices were placed in the same buffer plus four different concentrations of serotonin (1 nM, 2 nM, 5 nM, and 10 nM). For coupling studies, 10 μM of Gpp(NH)p, a non-hydrolysable analog of guanosine 5′-triphosphate, was added. After incubation, slides were dipped in distilled cold water (4°C) and then dried and juxtaposed to a phosphor imaging plate and scanned for 60 min (BAS-1800 II; Fujifilm). Regions of interest (ROIs) were manually drawn using Multigauge software (Fujifilm). The results were expressed in optical densities (PSL/mm^2).

PET Studies

Animals and Procedures

Four male cats (Isoquimen S.L., Barcelona, Spain) weighting 3.5–5.5 kg underwent PET scans in 12 separate sessions. All experiments were performed in accordance with European guidelines for care of laboratory animals (2010:63:EU). Before each exam, cats underwent a premedication with medetomidine (30–60 μg/kg subcutaneous) followed by anesthesia induction using intramuscular injection of 30 μg/kg medetomidine plus 2 mg/kg ketamine. Radiotracer injection was ensured by a catheter insertion into the cephalic vein of the forearm continuously perfused by NaCl 9%. Endotracheal intubation was performed to ensure a respiration rate of 15 breaths/min and anesthesia was maintained by constant insufflation of 2% isoflurane. Heart rate and SpO2 were continuously monitored. Cats were placed in ventral decubitus in an acrylic stereotactic apparatus with ear bars. Body temperature was maintained using a heated water blanket.

Study Design

Each cat underwent three PET acquisitions, i.e., one control acquisition, one d-fenfluramine intravenous pretreatment acquisition, and one challenge acquisition consisting in d-fenfluramine injected intravenously during acquisition. The agonist radiotracer of 5-HT$_{1A}$ receptors [^{18}F]F13640 was injected in a bolus at the start of the PET acquisition over 30 s (108 ± 19 MBq), diluted in 1 mL of NaCl 0.9%. D-fenfluramine was administered at 1 mg/kg diluted in 1 mL of NaCl 0.9%, 30 min before PET acquisition, for the pre-treatment study, and 30 min after radiotracer injection, for the pharmacological challenge. The corresponding control experiments consisted in a 1 mL saline administration 30 min after the radiotracer injection.

Data Acquisition and Reconstruction

Images were acquired on a PET/CT Biograph mCT (Siemens) at the CERMEP-imaging platform. Before PET emission scan, a rapid CT acquisition was performed to compute a brain attenuation map. The PET emission scan was performed for 90 min in list mode immediately after intravenously injection of [^{18}F]F13640. A dynamic PET image was reconstructed in a series of 28 sequential frames (4 × 30 s; 4 × 60 s; 8 × 180 s and 12 × 300 s). PET images were reconstructed with a fully three-dimensional (3D) ordinary Poisson OSEM reconstruction (OP-OSEM). PET data were preprocessed using MINC Toolkit (McConnell Brain Imaging Centre, Montreal, QC, Canada) and modeled with programs of the Turku PET Center library. For each cat, a PET sum image was computed and used as target for the warping of a multi-subject MRI template (Lancelot et al., 2010), which allows the parcellation of the brain into 20 anatomical brain regions of interest. In addition, a bisymmetrical anterior part of centrum semiovale was manually drawn on display software and was considered as a reference region. Time-activity curves in kBq/cc were extracted for each ROI, bilaterally averaged. Each time point of the TAC was converted into binding ratios compared to the centrum semiovale, which was chosen as region of reference.

PET Data Analysis

Occupancy Analysis in Pretreatment and Challenge Studies

In pretreatment experiments, averaged binding ratios between 40 and 88 min were compared with the control experiments by Student *t*-tests ($p < 0.01$; non-corrected; GraphPad Prism 6). In the pretreatment study, blocking rates in the frame [40;88] min were calculated as below:

$$Blocking\ rate\ \ (\%) = \frac{Ratio\left(Control\right) - Ratio\left(Pretreatment\right)}{Ratio\left(Control\right) - 1} \times 100$$

In the pharmacological challenge experiments, post-injection binding ratios between 40 and 88 min were compared with pre-injection binding ratios between 15 and 30 min to estimate occupancy rates (Zhang and Fox, 2012):

$$Occupancy\ \ (\%) = \frac{Ratio\ \ \left(Pre-injection\right) - Ratio\left(Post-injection\right)}{Ratio\left(Pre-injection\right) - 1} \times 100$$

The occupancy values obtained for each scan were averaged and compared to the control condition by Student *t*-tests ($p < 0.01$; non-corrected; GraphPad Prism 6). The occupancy rates in challenge condition were subtracted with the occupancy rates

calculated in the control condition to finally obtain a corrected occupancy rates, taking into account non-specific changes that could occur without any challenge.

Voxel-Based Analysis of the Pharmacological Challenge Study

Ratio images were generated by dividing the PET signal in each voxel by the mean signal in the centrum semiovale using the Turku PET Center software (*Imgratio* function) to generate one baseline image from 15 to 30 min and one global post injection image from 30 to 90 min. These ratio images were smoothed using a 1 mm × 1 mm × 1 mm isotropic Gaussian filter, spatially normalized in the template space, and statistically analyzed with SPM 12. Pooling the four subjects, a statistical map of the significant decreases of [^{18}F]F13640 binding after the pharmacological challenge was computed with two successive paired *t*-test, the first performed for each scan using the relative contrast (Baseline image – Post injection), the second to compare the saline and challenge conditions, corresponding to the final contrast [(Baseline image – Post injection)$_{challenge}$ – (Baseline image – Post injection)$_{saline}$] for each post-injection time interval. Statistical significance was set at $p < 0.01$ uncorrected.

Kinetic Modeling of [^{18}F]F13640 Displacement in the Pharmacological Challenge Study

We applied the lp-ntPET model (Normandin et al., 2012) optimized with the 2-step method (Merida et al., 2018) on control and challenge conditions in order to characterize the transient tracer displacement induced by an endogenous serotonin release. This model computes the perfusion ratio of the ROI relative to the reference region (R1), the efflux rate in the reference region (k_2), and in the ROI (k_{2a}), as well as four parameters describing the analytical curve of the endogenous serotonin discharge (modeled as a gamma variate function) underlying the TAC curve decrease after pharmacological challenge. The discharge equation parameters are, start time of the discharge (t_D), time of the peak of the discharge (t_P), a parameter controlling the shape of the discharge (α), and the amplitude of the discharge (γ). The following constraints were applied on parameters: t_D was searched between 30 and 50 min with a step of 1 min, t_P was searched between 31 and 90 min with a step of 1 min, and α ranged from 0.5 to 10 with a step of 0.5.

Curves of k_{2a} variation across time (expressed as the % of baseline) were calculated to highlight dynamic changes in regional 5-HT receptors (Kyme et al., 2019). Receptor occupancies were obtained, in each region, from the dynamic BP_{ND} (DBP_{ND}) (Sander et al., 2013) estimated with the 2-step lp-ntPET model.

$$Occupancy\ lp-ntPET\ (\%) = \frac{DBP_{ND}\left(Baseline\right) - DBP_{ND}\left(Post\ injection\right)}{DBP_{ND}\left(Baseline\right)} \times 100$$

Where DBP_{ND} (baseline) is the averaged DBP_{ND} on the interval 20–30 min and DBP_{ND} (post injection) is the averaged DBP_{ND} on the interval 40–90 min.

RESULTS

Radiosynthesis

Radiolabeling of the nitro-precursor with fluorine achieved a radiochemical yield of 6% corrected for decay and 90 min-radiosynthesis time. The synthesis led to no other radioactive derivatives and the chosen HPLC conditions ensured good separation of [^{18}F]F13640 from its precursor (Vidal et al., 2018a). Radiochemical purity was higher than 98%, and specific activity at EOS ranged between 25 and 124 GBq/μmol. Radioactivity injected ranged from 76 to 137 MBq.

In vitro Studies

In vitro sensitivity of [^{18}F]F13640 was evaluated by incubation of cat brain slices with increasing concentrations of serotonin in buffer. Binding was decreased in a concentration-dependent manner especially for the cingulate cortex (52% inhibition at 10 nM), the frontal cortex (32% at 10 nM), and the lateral septum (48% at 10 nM) (**Figure 1A**). No changes were observed in the cerebellum. Incubation of cat brain slices with 10 μM of Gpp(NH)p, a receptor/G-protein uncoupling agent, induced significant reduction of [^{18}F]F13640 binding in comparison with control experiment: 52% in the cingulate cortex, 48% in the frontal cortex, 50% in lateral septum and no changes in the cerebellum (**Figure 1B**).

In vivo Distribution of [^{18}F]F13640

[^{18}F]F13640 kinetics showed rapid uptake in the whole cat brain, and a slow wash-out during the 90 min of acquisition (**Figures 2**, **3**). The dorsal raphe nucleus (DRN), the anterior cingulate cortex, the hippocampus, and the thalamus showed the higher uptake values. The cortical parts of the cerebellum showed an intermediate uptake unlike the cerebellar nuclei. We also identified the anterior part of centrum semiovale as a region displaying a very low uptake (**Figure 2**). Given that this region was unlikely to be impacted by partial volume effects compared to the cerebellar nuclei (due to their proximity with the cortical parts displaying high uptake) and that the signal was low and constant in the three conditions (**Figure 3**), this region was chosen as a reliable reference region.

Pretreatment Study With D-Fenfluramine

The intravenous administration of d-fenfluramine (1 mg/kg) 30 min before radiotracer injection induced a drastic decrease of [^{18}F]F13640 uptake (**Figure 2**). Significant decreases of binding ratios control occurred in caudate, thalamus, hippocampus, anterior cingulate cortex, frontal cortex, parietal cortex, and DRN. The average blocking rate varied between 96% (gray matter of the cerebellum) and 33% (pontine nuclei) (**Table 1**).

Challenge Study With D-Fenfluramine

The intravenous injection of d-fenfluramine (1 mg/kg), 30 min after radiotracer injection, slightly decreased the time activity curves/increased the wash-out rate of [^{18}F]F13640. The impact of d-fenfluramine on TAC slope started at 40 min (**Figure 3**). Significant changes in occupancy rate were observed in

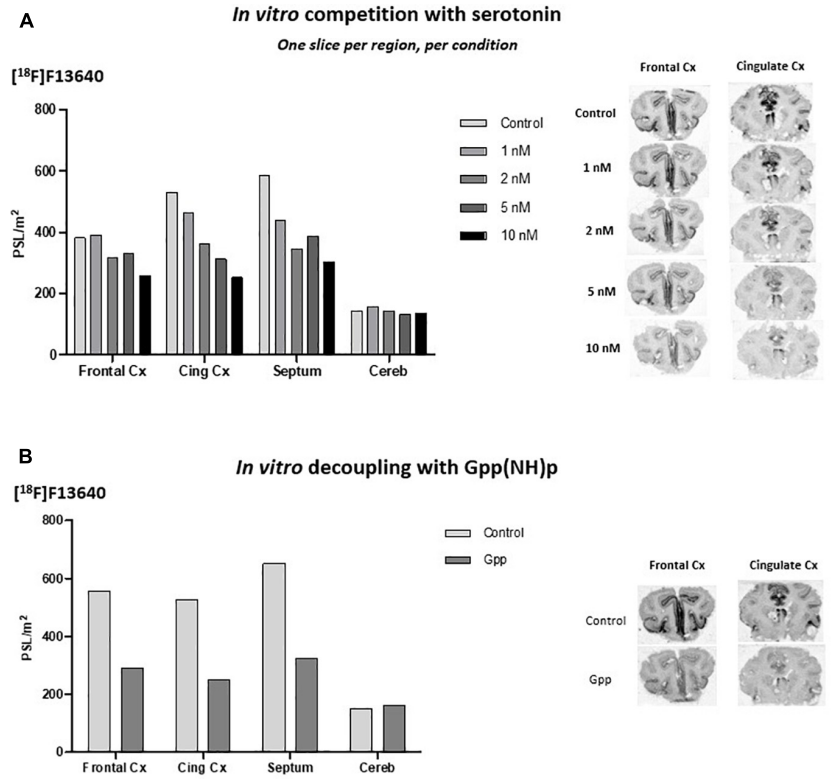

FIGURE 1 | (A) [^{18}F]F13640 *in vitro* binding in cat brain with increasing concentrations of serotonin (Front Cx, frontal cortex; Cing, cingulate cortex; Septum, lateral septum; Cereb, cerebellum). **(B)** [^{18}F]F13640 *in vitro* binding in cat brain with addition of 10 μM of Gpp(NH)p (Front Cx, frontal cortex; Cing Cx, cingulate cortex; Septum, lateral septum; Cereb, cerebellum).

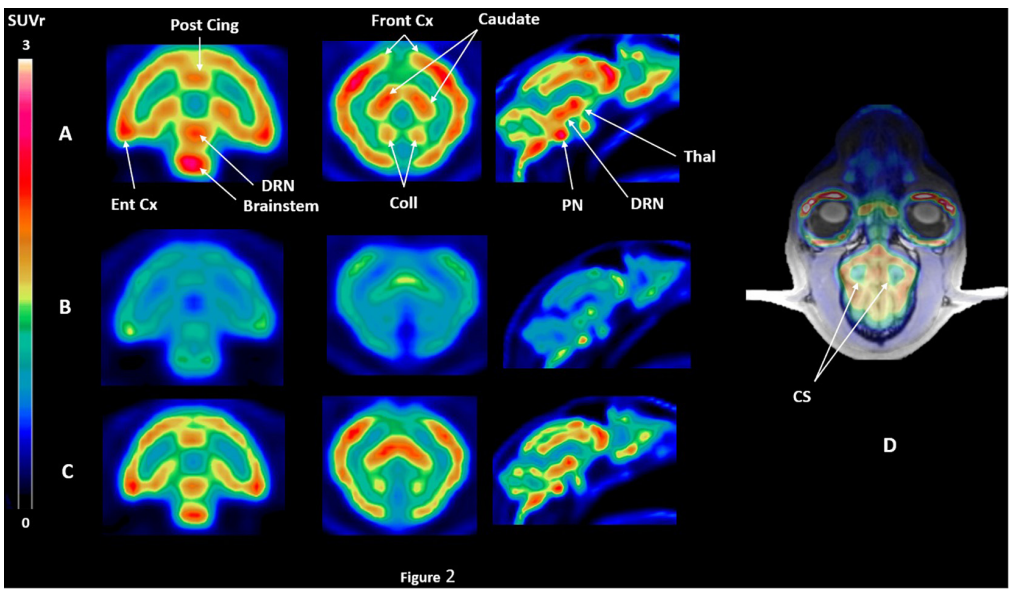

FIGURE 2 | SUVr PET images of [^{18}F]F13640 binding in the three experimental conditions for one cat, i.e., **(A)** control conditions, **(B)** pre-injection of d-fenfluramine 30 min before PET acquisition, using the centrum semiovale as a reference region **(D)**. SUVr images are averaged from 32 to 90 min time of acquisition; **(C)** injection of d-fenfluramine 30 min after PET acquisition beginning (Post cing, posterior cingulate cortex; Front Cx, frontal cortex; Caudate, caudate putamen; Ent Cx, entorhinal cortex; DRN, dorsal raphe nucleus; PN, pontine nucleus; Thal, thalamus; Coll, colliculi; CS, centrum semiovale).

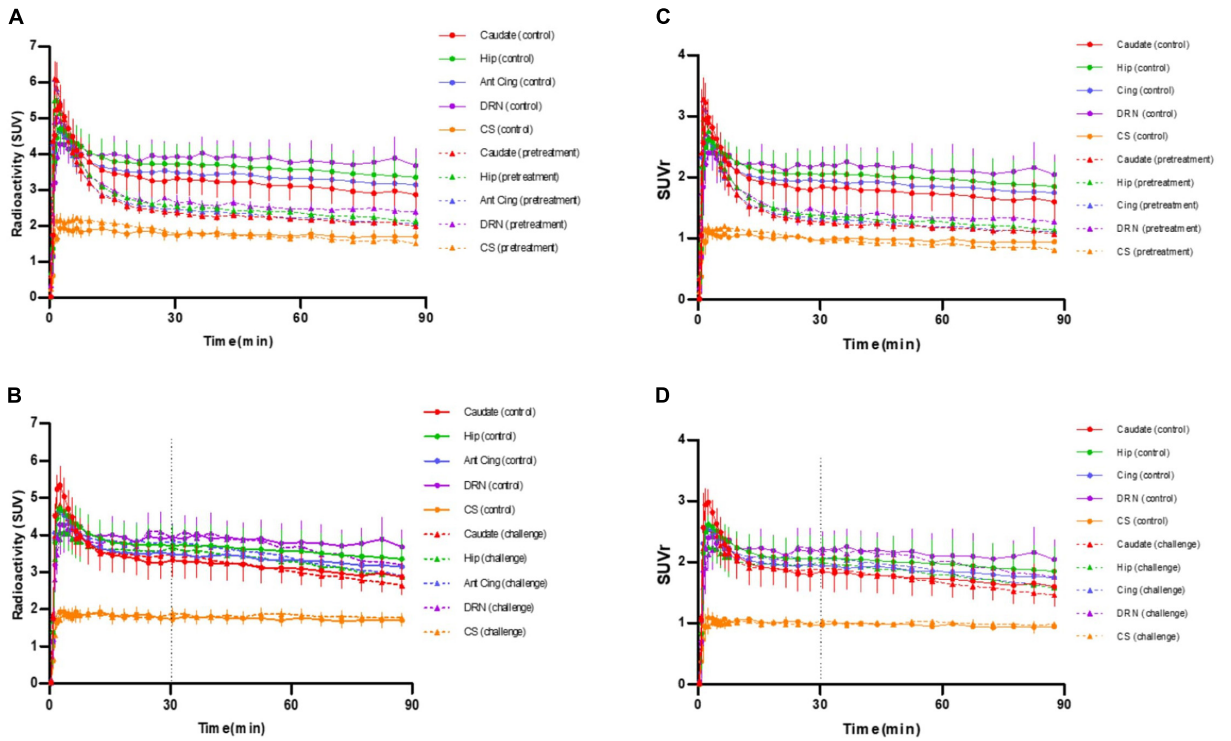

FIGURE 3 | (A) Averaged time-activity curves of [^{18}F]F13640 ± SEM (circles, control conditions; triangles, pretreatment study with a pre-injection of 1 mg/kg of d-fenfluramine, 30 min before PET acquisition). **(B)** Averaged time-activity curves of [^{18}F]F13640 ± SEM (circles, control conditions; triangles, challenge study with a post-injection of 1 mg/kg of d-fenfluramine, 30 min after beginning of PET acquisition). **(C)** Averaged SUVr of [^{18}F]F13640 ± SEM (circles, control conditions; triangles, pretreatment study with a pre-injection of 1 mg/kg of d-fenfluramine, 30 min before PET acquisition). **(D)** Averaged SUVr of [^{18}F]F13640 ± SEM (circles, control conditions; triangles, challenge study with a post-injection of 1 mg/kg of d-fenfluramine, 30 min after beginning of PET acquisition) Caudate, caudate putamen; Hip, hippocampus; Cereb, cerebellum; Ant Cing, anterior cingulate cortex; DRN, dorsal raphe nucleus; CS, centrum semiovale.

TABLE 1 | 5-HT$_{1A}$ receptor occupancy rate calculated for pretreatment study, challenge study (standard analysis and lp-ntPET modeling) and *p*-value of Wilcoxon paired test comparing occupancy computed with BP or with lp-ntPET.

	Caudate	Thal	Hip	Cereb	Ant Cing	Front Cx	Occ Cx
Pretreatment study							
Cat 1	67.7	59.2	64.9	94.7	68.7	73.7	93.4
Cat 2	47.4	33.9	45.7	77.2	50.1	44.3	71.4
Cat 3	41.1	30.3	40.3	93.2	47.1	50.2	57.3
Cat 4	67.6	66.5	76.2	95.5	73.8	83.7	86.1
Blocking rate (% ± sd)	56.0 ± 13.8	47.5 ± 18.1	56.8 ± 16.7	90.2 ± 8.7	59.9 ± 13.3	63.0 ± 18.8	77.1 ± 16.0
Challenge study							
Cat 1	17.5	10.8	18.5	31.7	20.5	15.9	26.4
Cat 2	16.2	12.1	15.1	30.0	19.8	16.2	23.5
Cat 3	19.1	5.5	11.8	32.7	12.9	6.6	23.8
Cat 4	15.6	13.1	18.0	31.1	21.0	16.6	24.8
Occupancy* (% ± sd)	17.1 ± 1.5	10.4 ± 3.4	15.8 ± 3.1	31.4 ± 1.2	18.5 ± 3.8	13.8 ± 4.8	24.6 ± 1.3
Lp-ntPET							
Cat 1	11.2	11.0	15.6	15.7	9.1	11.0	16.0
Cat 2	11.9	14.0	11.7	16.3	15.8	13.6	14.8
Cat 3	12.2	12.0	16.2	16.9	11.0	9.0	14.9
Cat 4	10.8	14.0	12.5	15.5	15.3	14.8	10.9
Occupancy lp-ntPET*(% ± sd)	11.5 ± 0.6	12.8 ± 1.5	14.0 ± 2.2	16.1 ± 0.6	12.8 ± 3.3	12.1 ± 2.6	14.2 ± 2.2
p-value	0.125	0.125	0.625	0.125	0.125	0.375	0.125

**Occupancy rate were adjusted on control condition for challenge study (Caudate, caudate putamen; Thal, thalamus; Hip, hippocampus; Cereb, cerebellum; Ant Cing, anterior cingulate cortex; Front Cx, frontal cortex; Temp Cx, temporal cortex; Occ Cx, occipital cortex).*

cerebellum, hippocampus, caudate, occipital cortex, parietal cortex, and thalamus. The average corrected rate of occupancy ranged from 10% for the thalamus to 31% for the cerebellum (**Figure 4**). The voxel analysis underlined a progressive effect of the competition between the radiotracer and 5-HT induced by d-fenfluramine. Regions statistically concerned by this effect ($p < 0.01$) were rostral colliculus, cerebellar gray matter, raphe nuclei, marginal gyrus, precuneus, cingulate gyrus, and lateral septum (**Figure 5**).

Kinetic Modeling With 2-Step lp-ntPET

Occupancy rates estimated using the 2-step lp-ntPET model displayed high displacement of the tracer in cerebellum, hippocampus, and the cingulate, frontal, temporal and occipital cortices, ranging from 12% in caudate to 16% in cerebellum (**Figure 4**). Interestingly, the curves of estimated parameter k2a displayed slight differences among animals and regions of interest. For cat 1, the shape of the curve was similar for all regions, with the detected start time of discharge at 15 min and a peak at 45–50 min after d-fenfluramine administration. Cat 2 displayed similar curves with a lower peak amplitude. For cat 3 the curves were slightly different, with a start time occurring later, at around 20 min, and a peak at 50 min after d-fenfluramine administration in the anterior cingulate cortex, cerebellum and caudate. In the hippocampus, the curve was even sharper with a start time at 25 min and a peak at 45 min after the challenge. For cat 4, two different kinetics were observed. In the cerebellum and the anterior cingulate cortex, the start time occurred very early, just after d-fenfluramine administration, followed by a slow increase to a peak reached between 45 and 50 min. In the caudate and the hippocampus, the start time was about 10 min after the challenge and k2a values increased rapidly, reaching a plateau 30 min after the challenge. We also noticed variations in terms of peak amplitude among regions (anterior cingulate cortex: cat4 > cat1 > cat2 > cat3; caudate: cat1 > cat4 > cat3 > cat2; cerebellum: cat1 > cat4 > cat2 > cat3; hippocampus: cat3 > cat1 > cat4 > cat2) and among cats (cat1: cerebellum > caudate > anterior cingulate cortex > hippocampus; cat2 and cat4: cerebellum > anterior cingulate cortex > caudate > hippocampus; cat3: hippocampus > cerebellum > caudate > anterior cingulate cortex). The amplitude of peak ranged from 110 to 140% of k2a basal values (**Figure 6**). Finally, a Wilcoxon Rank paired test showed that there is no statistical difference comparing occupancy computed with BP or with lp-ntPET for any of the regions (**Table 1**).

DISCUSSION

In certain controlled paradigms, PET imaging enables the *in vivo* measure of neurotransmitter fluctuations in the living brain. For example, the determination of changes in extracellular dopamine levels elicited by dopamine-releasers has been well described, but equivalent exploration of serotonin neurotransmission has proven to be difficult (Laruelle, 2000; Zimmer et al., 2002, 2003; Paterson et al., 2010; Tyacke and Nutt, 2015; Yang et al., 2018; Colom et al., 2019; da Cunha-Bang et al., 2019). Several teams have attempted to identify and characterize serotoninergic radiotracers that are sufficiently sensitive to detect changes in endogenous serotonin concentrations following an acute pharmacological challenge, but with limited success. Recently, a European consortium demonstrated that [^{11}C]CIMBI-36 binding is sensitive to increased levels of brain serotonin release following a d-amphetamine challenge (Erritzoe et al., 2020). In the present preclinical study, we propose an alternative radiopharmaceutical with a number of advantages. On the one hand, [^{18}F]F13640 binds widely to 5-HT$_{1A}$ receptors in the brain

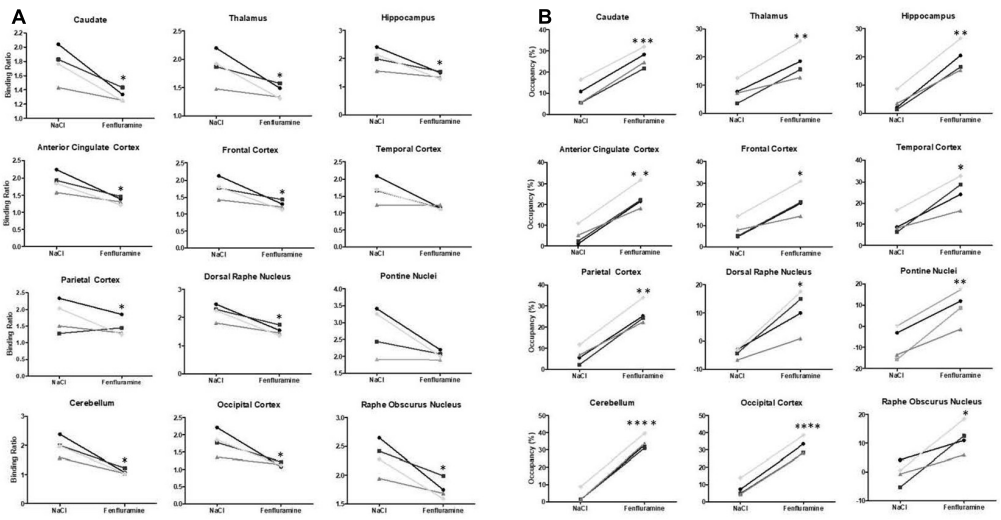

FIGURE 4 | (A) Averaged binding ratios of [^{18}F]F13640 calculated in control (NaCl) and pretreatment (d-fenfluramine) conditions in the four cats (*$p < 0.05$; **$p < 0.01$; ****$p < 0.0001$ paired *t*-test, non-corrected). **(B)** Occupancy (%) of serotonin calculated in control (NaCl) and challenge (d-fenfluramine) conditions in the four cats (*$p < 0.05$; **$p < 0.01$; ****$p < 0.0001$). For values see **Table 1**.

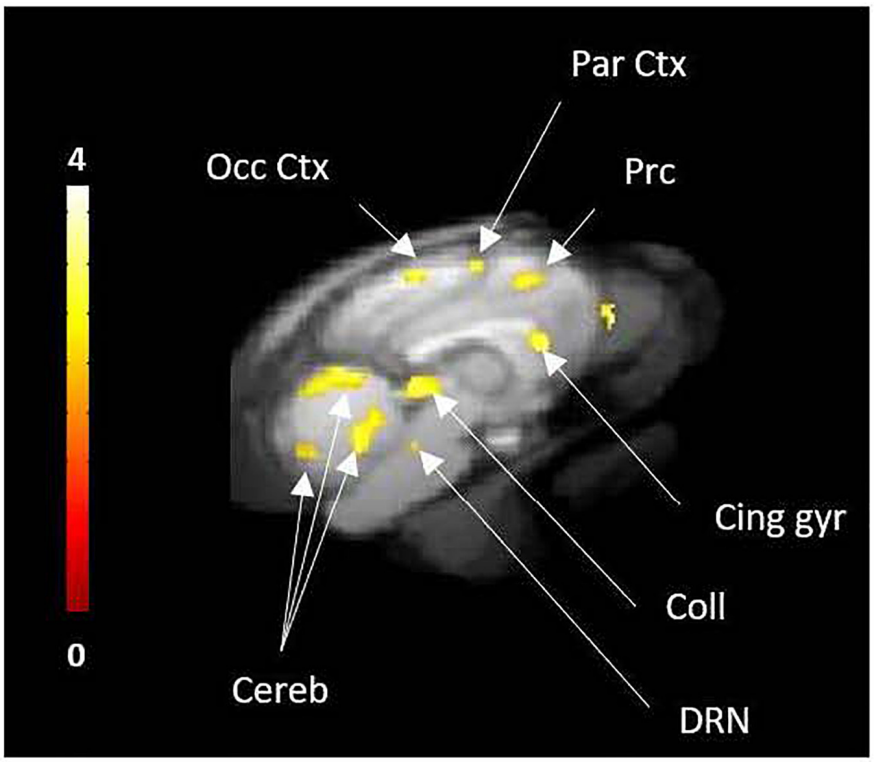

FIGURE 5 | Voxel-to-voxel analysis from 30 to 90 min PET acquisition, showing the significant decreases of [^{18}F]F13640 binding after d-fenfluramine challenge compared to control scans ($p < 0.01$, non-corrected). Occ Ctx, Occipital Cortex; Par Ctx, Parietal Cortex; Cing gyr, Cingulate gyrus; Coll, Colliculi; DRN, Dorsal raphe Nuclei; Cereb, Cerebellum; Prc, precuneus.

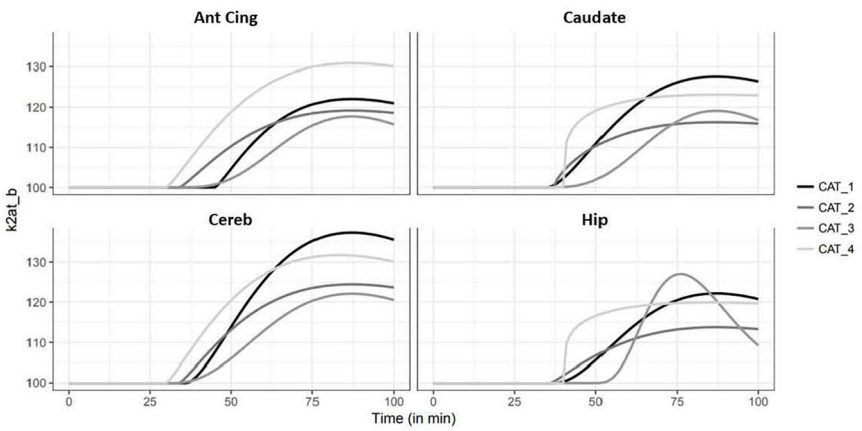

FIGURE 6 | Simulation of the kinetics of serotonin release illustrated by variation (%) of the efflux rate k2at_b of four regions of interest (Ant Cing, anterior cingulate cortex; Caudate, caudate putamen; Cereb, cerebellum; Hip, hippocampus).

and covers many brain regions in both animals (Vidal et al., 2018a) and, as recently shown, in humans (Colom et al., 2020). On the other hand, this radiopharmaceutical is radiolabeled with fluorine 18, allowing prolonged experimental protocols as well as broader dissemination to other research sites.

As previously mentioned, the pharmacological characteristics of F13640 (a highly specific 5-HT$_{1A}$ receptor agonist, a.k.a. NLX-112 or befiradol) and promising *in vitro* results prompted us to initiate this preclinical proof-of-concept study.

Effect of D-Fenfluramine on Brain Serotonin Levels

The choice of d-fenfluramine, a well-described 5-HT releaser, was justified by its very low affinity for 5-HT$_{1A}$ receptors

(K_i = 831 nM), ruling out the possibility of a direct competition with [^{18}F]F13640 at administered doses (33). Although the binding profile of d-fenfluramine is well-known, there is a lack of data concerning effects of d-fenfluramine in different brain regions in terms of 5-HT release in cat. One study reported that basal serotonin concentrations in dorsal raphe of cats ranged from 0.32 nM during REM sleep to 0.8 nM during waking (Portas and McCarley, 1994). In the anesthetized rat, previous data indicated basal levels of serotonin of 0.24–0.25 nM in the ventral hippocampus (Assié and Koek, 1996). The intraperitoneal injection of 10 mg/kg of d-fenfluramine increased 5-HT levels to a maximum of about 7 nM (that is, nearly 3000% of baseline levels) after 40 min. In rat striatum, basal levels of serotonin were reported at 0.11 nM, with 1 mg/kg of d-fenfluramine ip increasing the concentration to 282% of basal levels after 2 h in conscious animals (Balcioglu and Wurtman, 1998). Basal levels in frontal cortex were estimated at 1.2 nM and administration of 10 mg/kg d-fenfluramine induced an increase to 420% of the baseline 30 min after ip injection (Gardier et al., 1994). Hume et al. (2001) reported that, after 40 min, d-fenfluramine 10 mg/kg ip increased 5-HT levels 4.5 fold in frontal cortex and 15 fold in hippocampus. In pig, a d-fenfluramine dose of 0.5 mg/kg induced an increase of 1123% of serotonin in medial prefrontal cortex, 15 min after intravenous injection (Jørgensen et al., 2017). These results and others show heterogenous basal levels of serotonin among brain regions and a widespread effect of d-fenfluramine, with some variability depending on the regions and species considered. A major limitation of many of these microdialysis studies is that high doses of d-fenfluramine can lead to large increases in extracellular serotonin concentrations that may not reflect normal-physiological conditions. In view of these multiple experimental results, the present study therefore used a modest dose of fenfluramine in order to mimic physiological levels of serotonin fluctuation.

Effect of D-Fenfluramine on PET Radiotracers Binding

Measuring endogenous levels of serotonin by competition with a PET radiotracer is a real challenge and no 5-HT$_{1A}$ receptor radiotracer has previously been successfully used for this purpose. The development of such a radiotracer faces many challenges related to both its own kinetic properties and to the characteristics of the serotonin system (Paterson et al., 2010). For instance, the *in vivo* density of 5-HT$_{1A}$ receptors in the high affinity (i.e., G-protein-coupled) state is considered to be low, as suggested by *in vitro* findings, which may explain the lack of sensitivity of antagonist radiotracers to changes in 5-HT levels: serotonin would compete with a very small portion of the total binding pool of such tracers (Nénonéné et al., 1994; Udo de Haes et al., 2005). This was also suggested by *in vivo* PET studies where agonists only show occupancies of 10–20% of the [^{18}F]antagonist-labeled sites (Bantick et al., 2004). Numerous attempts with other 5-HT$_{1A}$ radiotracers to demonstrate changes of binding induced by pretreatment or challenge with d-fenfluramine showed contrasted results. While pretreatment with d-fenfluramine at 10 mg/kg ip (Hume et al., 2001) and challenge studies with d-fenfluramine at 10 mg/kg iv in rats induced a significant decrease of [^{11}C]WAY100635 uptake in hippocampus (19), iv infusion of 5 mg/kg and 10 mg/kg of d-fenfluramine in conscious non-human primates did not induce significant changes in [^{18}F]MPPF binding (Udo de Haes et al., 2006). By contrast, [^{18F}]MPPF was sensitive to d-fenfluramine challenge in a dose dependent manner in anesthetized rats (Zimmer et al., 2002). For [^{11}C]CUMI-101, a pre-injection with 2.5 mg/kg of d-fenfluramine and 2–4 mg/kg of citalopram iv in baboon was responsible for a binding decrease of 15–30% across brain regions (Milak et al., 2010). In humans, one study showed no changes in binding potential of this radiotracer after infusion of 0.15 mg/kg of citalopram (Pinborg et al., 2012) whereas another study showed few increases of binding potential at post-synaptic areas after infusion of 10 mg of citalopram (Selvaraj et al., 2012). No significant evidence of sensitivity to 5-HT release was shown for [^{18}F]FCWAY and [^{18}F]FPWAY (Jagoda et al., 2006).

Pretreatment Study With D-Fenfluramine

All these previous studies contrasted with our preliminary findings with the full agonist [^{18}F]F13640. *Ex vivo* autoradiography studies in rat brain revealed a significant binding reduction following d-fenfluramine iv pre-administration at doses of 0.5 mg/kg, 1 mg/kg, and 5 mg/kg in hippocampus, anterior cingulate cortex and dorsal raphe whereas only a tendency was observed for [^{18}F]MPPF at in the same conditions (Vidal et al., 2018a). These results suggested that [^{18}F]F13640 is very sensitive to changes in 5-HT levels, especially in view of the fact that the doses of d-fenfluramine needed for a significant effect were ten times lower than those used for [^{18}F]MPPF. For the present study, we therefore chose to use a dose of 1 mg/kg of d-fenfluramine, which is lower than the doses used in previous studies investigating the sensitivity of 5-HT$_{1A}$ radiotracers but that were anticipated to be high enough to induce strong decreases of [^{18}F]F13640 binding. As expected, 1 mg/kg of d-fenfluramine administered in pretreatment or a challenge induced marked changes in [^{18}F]F13640 labeling kinetics (**Figures 2**, **3**). The pre-administration of d-fenfluramine induced a highly significant decrease of agonist radiotracer signal, and the blocking rate calculated was higher for hippocampus, anterior cingulate cortex and dorsal raphe in comparison with the previous *ex vivo* autoradiography study (58%, 60%, and 55%, respectively) (Vidal et al., 2018a). The gray matter of the cerebellum was the most impacted region (90%), see discussion below.

Challenge Study With D-Fenfluramine

In this series of experiments, where d-fenfluramine was injected 30 minutes after the radiotracer, we did not observe pronounced effects as for the previous pretreatment studies (**Figure 3**). This was expected, given the slow dissociation rate of this radiotracer (Heusler et al., 2010), due to its high affinity for 5-HT$_{1A}$ receptors, combined with the short PET acquisition time of 90 min. Another mechanism that could contribute to the differences in absolute occupancy values between pretreatment and challenge studies would be a massive internalization of receptors after pretreatment studies, leading to a low density of

high affinity sites at the surface of neurons (Zimmer et al., 2004; Ginovart, 2005). However, this hypothesis seems unlikely because time activity curves displayed a slope inflection 10 min after serotonin release induced by d-fenfluramine in almost all regions of interest except the centrum semiovale. Although occupancy by 5-HT was lower when d-fenfluramine was administered 30 min after ^{18}F-F13640, it was significantly different from control scans in all regions of interest, with values ranging from 10% in the thalamus to 31% in the gray matter of cerebellum. Interestingly, the magnitude of the occupancy is in the same range of those calculated for 5-HT$_{1B}$ receptors with the partial agonist [^{11}C]AZ10419369, i.e., between 4 and 27% at 1 mg/kg of fenfluramine in three monkeys (Finnema et al., 2012) and also for the [^{11}C]CUMI-101 on 5HT$_{1A}$ receptors, i.e., 24% with 2.5 mg/kg fenfluramine in baboons (Milak et al., 2010). Accordingly, the voxel-based analysis detected significant decreases of [^{18}F]F13640 in many regions, including the dorsal raphe and in several serotonergic projection areas (precuneus, cingulate, parietal and occipital cortices, colliculi, and cerebellar cortex).

Changes of [^{18}F]F13640 Binding in Cerebellum

A pronounced sensitivity of [^{18}F]F13640 binding in the cerebellum to fenfluramine administration was observed in the PET experiments. This can be puzzling considering the high uptake of [^{18}F]F13640 in the cortical parts and the highest amplitude of effects in pretreatment and challenge paradigm. These *in vivo* data are also in discordance with our *in vitro* autoradiography results in the same region, i.e., a low level of binding which is not affected by serotonin displacement and not influenced by addition of Gpp(NH)p in buffer. However, for other regions, we observed the same range of decrease produced by uncoupling of receptors as described for the D2/D3 agonist [^{18}F]-5-OH-FPPAT, an average of 50% (Mukherjee et al., 2017). Classical 5-HT$_{1A}$ radiotracers also show low specific binding in the cerebellum (Mathis et al., 1994; Shiue et al., 1997). However, the present *in vivo* results must be compared with previous data revealing decreased [^{18}F]F13640 binding in the cerebellum after pre-administration of a 5-HT$_{1A}$ antagonist or agonist, indicating the existence of 5-HT$_{1A}$ receptors in this brain region (Vidal et al., 2018a). Furthermore, 5-HT release could occur in this region given that cat cerebellum contains 5-HT neuronal projections (Kitzman and Bishop, 1994; Leger et al., 2001). In this regard, 5-HT iontophoresis in cerebellar gray matter in cat induces strong inhibitory effects on local neurons – these are mediated by 5-HT$_{1A}$ receptors, highlighting the functional importance of cerebellar 5-HT$_{1A}$ receptors of this species (Kerr and Bishop, 1991). An autoradiographic study using a radiolabeled SSRI, [^{3}H]paroxetine, also indicates that 5-HT transporter expression occurs in the cat cerebellum, both in the granular layer and the dentate nucleus (Charnay et al., 1997). In this context of cerebellar heterogeneity of 5-HT$_{1A}$ receptor density, and strong effects of d-fenfluramine in the gray matter, we thus did not consider the cerebellar nuclei as a reference region. Instead, we identified a region in the anterior part of the white matter centrum semiovale that displayed consistently low signal in the three conditions and was less likely to be impacted by partial volume effects (**Figure 4**). This region was therefore used as reference, similarly to a previous study (Kudomi et al., 2013), for estimation of binding ratios and for the lp-ntPET modeling approach.

Kinetic Modeling of Serotonin Release

The kinetic modeling approach used in this study calculated that fenfluramine-induced serotonin release caused an increase of 10–30% of receptor occupancy by serotonin (**Figure 6**). We observed a delay of 45 min between d-fenfluramine administration and the maximal occupancy effect. Furthermore, we noticed that modeled curves of serotonin release were relatively close in the four cats. The variability observed is mainly driven by the maximal amplitude of each curve and corresponds to 8–15% across individuals, which can be considered as a low inter-subject variability and is in the same range as the variability obtained with binding ratios in the challenge study. Considering the variability of lp-ntPET model described in Irace et al. (2020), the results of discharge modeling in the article are very close between the four cats and could probably be reduced even more by using the robust b-ntPET algorithm presented by Irace et al. (2020). Finally, the kinetic modeling results suggest an apparent slow 5-HT release after d-fenfluramine injection, which is unexpected given its fast kinetics observed using microdialysis experiments. In fact, the slow washout of [^{18}F]F13640 seems to be responsible for this difference. Furthermore, results must be analyzed with caution because anesthesia is considered to change endogenous levels of 5-HT (Yokoyama et al., 2016) and numerous studies on conscious animals reveals differences in 5-HT levels or radiotracer binding (Zimmer et al., 2002; Udo de Haes et al., 2005; Yokoyama et al., 2016).

In the absence of microdialysis, the lp-ntPET model provides the first modeling of serotonin release induced by d-fenfluramine with a PET radiotracer of serotonin receptors. We proposed a lp-ntPET model which successfully discriminates control and challenge condition and confirms the hypothesis of a tracer displacement by a significant release of serotonin. The short acquisition time of 90 min appears as the major limitation of our study given the slow wash-out of the radiotracer (Vidal et al., 2018a). However, these results confirm that [^{18}F]F13640 binding is reversible, despite slow kinetics, by demonstrating its sensitivity to serotonin release. Further studies using [^{18}F]F13640 will need to be carried out using longer time scans to improve estimation of serotonin occupancy.

CONCLUSION

In conclusion, as compared with previous antagonist or partial agonist radiotracers, the present results demonstrate a high sensitivity of [^{18}F]F13640 to serotonin release induced by d-fenfluramine. Although we used a low dose of d-fenfluramine (1 mg/kg), a significant displacement of [^{18}F]F13640 was

observed for both pretreatment and challenge studies. These results support our initial hypothesis that an agonist PET tracer is better adapted to measure endogenous levels of serotonin than antagonist PET tracers. Indeed, while the agonist PET tracer, [^{18}F]F13640, binds only to G-protein-coupled 5-HT$_{1A}$ receptors, in the same manner as the endogenous neurotransmitter, antagonists binds to both G-protein-coupled and uncoupled receptors. Consequently, antagonist PET tracers appear less effective to detect changes in serotonin levels, especially when G-protein-coupled receptors constitute only a small proportion of the total receptor population (Shiue et al., 1997). Finally, the first kinetic modeling of serotonin release using [^{18}F]F13640 as radiotracer demonstrates the feasibility of evaluating 5-HT release in displacement experiments. The slow kinetics of our radiotracer indicate the necessity to perform longer acquisition times (or delayed PET scans) to ensure a better understanding of displacement or pretreatment studies, but also enable to perform displacement experiments without using a bolus followed by constant infusion administration. Overall, these results support the use of [^{18}F]F13640 to investigate changes in serotonin levels in humans, particularly in the context of experimental paradigms involving physiological (sleep/wake states) or pathological (neuropsychiatric pathologies) fluctuations of extracellular serotonin.

DATA AVAILABILITY STATEMENT

The original contributions presented in the study are included in the article, further inquiries can be directed to the corresponding author.

ETHICS STATEMENT

The animal study was reviewed and approved by the Celyne (CEEA-42), Lyon, France.

AUTHOR CONTRIBUTIONS

MC and BV carried out the experiments with PET imaging, performed the data analysis, participated in the study design, and co-wrote the manuscript. SF, FL, and CB carried out the experiments with PET imaging. TI and TB carried out the radiosynthesis of [^{18}F]F13640. JR, NC, IM, and ZI analyzed the PET data. AN-T provided precursor of [^{18}F]F13640 and reviewed the manuscript. LZ initiated the study, participated in its design, and reviewed the manuscript. All authors read and approved the final manuscript.

REFERENCES

Akimova, E., Lanzenberger, R., and Kasper, S. (2009). The serotonin-1A receptor in anxiety disorders. *Biol. Psychiatry* 66, 627–635. doi: 10.1016/j.biopsych.2009.03.012

Assié, M. B., and Koek, W. (1996). Possible in vivo 5-HT reuptake blocking properties of 8-OH-DPAT assessed by measuring hippocampal extracellular 5-HT using microdialysis in rats. *Br. J. Pharmacol.* 119, 845–850. doi: 10.1111/j.1476-5381.1996.tb15749.x

Aznavour, N., Rbah, L., Riad, M., Reilhac, A., Costes, N., Descarries, L., et al. (2006). A PET imaging study of 5-HT1A receptors in cat brain after acute and chronic fluoxetine treatment. *NeuroImage* 33, 834–842. doi: 10.1016/j.neuroimage.2006.08.012

Balcioglu, A., and Wurtman, R. J. (1998). Effects of fenfluramine and phentermine (fen-phen) on dopamine and serotonin release in rat striatum: in vivo microdialysis study in conscious animals. *Brain Res.* 813, 67–72. doi: 10.1016/s0006-8993(98)01003-8

Bantick, R. A., Rabiner, E. A., Hirani, E., de Vries, M. H., Hume, S. P., and Grasby, P. M. (2004). Occupancy of agonist drugs at the 5-HT1A receptor. *Neuropsychopharmacology* 29, 847–859. doi: 10.1038/sj.npp.1300390

Buhot, M. C. (1997). Serotonin receptors in cognitive behaviors. *Curr. Opin. Neurobiol.* 7, 243–254.

Charnay, Y., Léger, L., Vallet, P., Greggio, B., Hof, P. R., Jouvet, M., et al. (1997). Autoradiographic distribution of [3H]paroxetine binding sites in the cat brain. *Biogenic Amines* 13, 39–54.

Colom, M., Costes, N., Redouté, J., Dailler, F., Gobert, F., Le Bars, D., et al. (2020). 18F-F13640 PET imaging of functional receptors in humans. *Eur. J. Nucl. Med. Mol. Imaging* 47, 220–221. doi: 10.1007/s00259-019-04473-7

Colom, M., Vidal, B., and Zimmer, L. (2019). Is there a role for GPCR agonist radiotracers in PET neuroimaging? *Front. Mol. Neurosci.* 12:255. doi: 10.3389/fnmol.2019.00255

da Cunha-Bang, S., Ettrup, A., Mc Mahon, B., Skibsted, A. P., Schain, M., Lehel, S., et al. (2019). Measuring endogenous changes in serotonergic neurotransmission with [11C]Cimbi-36 positron emission tomography in humans. *Transl. Psychiatry* 9:134. doi: 10.1038/s41398-019-0468-8

Erritzoe, D., Ashok, A. H., Searle, G. E., Colasanti, A., Turton, S., Lewis, Y., et al. (2020). Serotonin release measured in the human brain: a PET study with [11C]CIMBI-36 and d-amphetamine challenge. *Neuropsychopharmacology* 45, 804–810. doi: 10.1038/s41386-019-0567-5

Finnema, S. J., Varrone, A., Hwang, T.-J., Halldin, C., and Farde, L. (2012). Confirmation of fenfluramine effect on 5-HT(1B) receptor binding of [(11)C]AZ10419369 using an equilibrium approach. *J. Cereb. Blood Flow Metab. Off. J. Int. Soc. Cereb. Blood Flow Metab.* 32, 685–695. doi: 10.1038/jcbfm.2011.172

Gardier, A. M., Trillat, A.-C., Malagié, I., and Jacquot, C. (1994). 8-OH-DPAT attenuates the dexfenfluramine-induced increase in extracellular serotonin: an in vivo dialysis study. *Eur. J. Pharmacol.* 265, 107–110. doi: 10.1016/0014-2999(94)90231-3

Ginovart, N. (2005). Imaging the dopamine system with in vivo [11C]raclopride displacement studies: understanding the true mechanism. *Mol. Imaging Biol. MIB Off. Publ. Acad. Mol. Imaging* 7, 45–52. doi: 10.1007/s11307-005-0932-0

Heusler, P., Palmier, C., Tardif, S., Bernois, S., Colpaert, F. C., and Cussac, D. (2010). [3H]-F13640, a novel, selective and high-efficacy serotonin 5-HT1A receptor agonist radioligand. *Naunyn Schmiedebergs Arch. Pharmacol.* 382, 321–330. doi: 10.1007/s00210-010-0551-4

Hume, S., Hirani, E., Opacka-Juffry, J., Myers, R., Townsend, C., Pike, V., et al. (2001). Effect of 5-HT on binding of [(11)C] WAY 100635 to 5-HT(IA) receptors in rat brain, assessed using in vivo microdialysis nd PET after fenfluramine. *Synapse* 41, 150–159. doi: 10.1002/syn.1069

Irace, Z., Mérida, I., Redouté, J., Fonteneau, C., Suaud-Chagny, M.-F., Brunelin, J., et al. (2020). Bayesian estimation of the ntPET model in single-scan competition PET studies. *Front. Physiol.* 11:498. doi: 10.3389/fphys.2020.00498

Jagoda, E. M., Lang, L., Tokugawa, J., Simmons, A., Ma, Y., Contoreggi, C., et al. (2006). Development of 5-HT1A receptor radioligands to determine receptor density and changes in endogenous 5-HT. *Synapse* 59, 330–341. doi: 10.1002/syn.20246

Jørgensen, L. M., Weikop, P., Villadsen, J., Visnapuu, T., Ettrup, A., Hansen, H. D., et al. (2017). Cerebral 5-HT release correlates with [11C]Cimbi36 PET measures of 5-HT2A receptor occupancy in the pig brain. *J. Cereb. Blood Flow Metab. Off. J. Int. Soc. Cereb. Blood Flow Metab.* 37, 425–434. doi: 10.1177/0271678X16629483

Kerr, C. W. H., and Bishop, G. A. (1991). Topographical organization in the origin of serotoninergic projections to different regions of the cat cerebellar cortex. *J. Comp. Neurol.* 304, 502–515. doi: 10.1002/cne.903040313

Kitzman, P. H., and Bishop, G. A. (1994). The origin of serotoninergic afferents to the cat's cerebellar nuclei. *J. Comp. Neurol.* 340, 541–550. doi: 10.1002/cne.903400407

Kristian Eide, P., Mjellem Joly, N., and Hole, K. (1990). The role of spinal cord 5-HT1A and 5-HT1B receptors in the modulation of a spinal nociceptive reflex. *Brain Res.* 536, 195–200. doi: 10.1016/0006-8993(90)90025-7

Kudomi, N., Hirano, Y., Koshino, K., Hayashi, T., Watabe, H., Fukushima, K., et al. (2013). Rapid quantitative *CBF* and *CMRO* $_2$ measurements from a single *PET* scan with sequential administration of dual ^{15} O-Labeled tracers. *J. Cereb. Blood Flow Metab.* 33, 440–448. doi: 10.1038/jcbfm.2012.188

Kyme, A. Z., Angelis, G. I., Eisenhuth, J., Fulton, R. R., Zhou, V., Hart, G., et al. (2019). Open-field PET: simultaneous brain functional imaging and behavioural response measurements in freely moving small animals. *NeuroImage* 188, 92–101. doi: 10.1016/j.neuroimage.2018.11.051

Lancelot, S., Costes, N., Lemoine, L., and Zimmer, L. (2010). Development and evaluation of a digital atlas for PET neuroimaging in domestic cat (*Felis catus*). *Eur. J. Nucl. Med. Mol. Imaging* 37, S387–S387.

Laruelle, M. (2000). Imaging synaptic neurotransmission with in vivo binding competition techniques: a critical review. *J. Cereb. Blood Flow Metab.* 20, 423–451.

Leger, L., Charnay, Y., Hof, P. R., Bouras, C., and Cespuglio, R. (2001). Anatomical distribution of serotonin-containing neurons and axons in the central nervous system of the cat. *J. Comp. Neurol.* 433, 157–182.

Lemoine, L., Becker, G., Vacher, B., Billard, T., Lancelot, S., Newman-Tancredi, A., et al. (2012). Radiosynthesis and preclinical evaluation of 18F-F13714 as a fluorinated 5-HT1A receptor agonist radioligand for PET neuroimaging. *J. Nucl. Med.* 53, 969–976. doi: 10.2967/jnumed.111.101212

Lemoine, L., Verdurand, M., Vacher, B., Blanc, E., Le Bars, D., Newman-Tancredi, A., et al. (2010). [18F]F15599, a novel 5-HT1A receptor agonist, as a radioligand for PET neuroimaging. *Eur. J. Nucl. Med. Mol. Imaging* 37, 594–605. doi: 10.1007/s00259-009-1274-y

Maćkowiak, M., Czyrak, A., and Wedzony, K. (2000). [The involvement of 5-HT1a serotonin receptors in the pathophysiology and pharmacotherapy of schizophrenia]. *Psychiatr. Pol.* 34, 607–621.

Mathis, C. A., Simpson, N. R., Mahmood, K., Kinahan, P. E., and Mintun, M. A. (1994). [11C]WAY 100635: a radioligand for imaging 5-HT1A receptors with positron emission tomography. *Life Sci.* 55, L403–L407. doi: 10.1016/0024-3205(94)00324-6

Merida, I., Olivier, F., Hammers, A., Redouté, J., Reilhac, A., Costes, N., et al. (2018). "Kinetic modelling for endogenous neurotransmitter discharge characterization using PET imaging: optimization of lp-ntPET," in *Proceedings of the 8th International Symposium of Functional Neuroreceptor Mapping of the Living Brain (NRM18)*, London.

Milak, M. S., DeLorenzo, C., Zanderigo, F., Prabhakaran, J., Kumar, J. S. D., Majo, V. J., et al. (2010). In vivo quantification of human serotonin 1A receptor using 11C-CUMI-101, an agonist PET radiotracer. *J. Nucl. Med.* 51, 1892–1900. doi: 10.2967/jnumed.110.076257

Miquel, M. C., Doucet, E., Riad, M., Adrien, J., Vergé, D., and Hamon, M. (1992). Effect of the selective lesion of serotoninergic neurons on the regional distribution of 5-HT1A receptor mRNA in the rat brain. *Brain Res. Mol. Brain Res.* 14, 357–362.

Mukherjee, J., Majji, D., Kaur, J., Constantinescu, C. C., Narayanan, T. K., Shi, B., et al. (2017). PET radiotracer development for imaging high-affinity state of dopamine D2 and D3 receptors: binding studies of fluorine-18 labeled aminotetralins in rodents: MUKHERJEE ET AL. *Synapse* 71:e21950. doi: 10.1002/syn.21950

Nénonéné, E. K., Radja, F., Carli, M., Grondin, L., and Reader, T. A. (1994). Heterogeneity of cortical and hippocampal 5-HT1A receptors: a reappraisal of homogenate binding with 8-[3H]hydroxydipropylaminotetralin. *J. Neurochem.* 62, 1822–1834. doi: 10.1046/j.1471-4159.1994.62051822.x

Nichols, D. E., and Nichols, C. D. (2008). Serotonin receptors. *Chem. Rev.* 108, 1614–1641.

Normandin, M. D., Schiffer, W. K., and Morris, E. D. (2012). A linear model for estimation of neurotransmitter response profiles from dynamic PET data. *NeuroImage* 59, 2689–2699. doi: 10.1016/j.neuroimage.2011.07.002

Paterson, L. M., Tyacke, R. J., Nutt, D. J., and Knudsen, G. M. (2010). Measuring endogenous 5-HT release by emission tomography: promises and pitfalls. *J. Cereb. Blood Flow Metab.* 30, 1682–1706. doi: 10.1038/jcbfm.2010.104

Pinborg, L. H., Feng, L., Haahr, M. E., Gillings, N., Dyssegaard, A., Madsen, J., et al. (2012). No change in [11C]CUMI-101 binding to 5-HT1A receptors after intravenous citalopram in human. *Synapse* 66, 880–884. doi: 10.1002/syn.21579

Portas, C. M., and McCarley, R. W. (1994). Behavioral state-related changes of extracellular serotonin concentration in the dorsal raphe nucleus: a microdialysis study in the freely moving cat. *Brain Res.* 648, 306–312. doi: 10.1016/0006-8993(94)91132-0

Radja, F., Laporte, A. M., Daval, G., Vergé, D., Gozlan, H., and Hamon, M. (1991). Autoradiography of serotonin receptor subtypes in the central nervous system. *Neurochem. Int.* 18, 1–15.

Riad, M., Garcia, S., Watkins, K. C., Jodoin, N., Doucet, E., Langlois, X., et al. (2000). Somatodendritic localization of 5-HT1A and preterminal axonal localization of 5-HT1B serotonin receptors in adult rat brain. *J. Comp. Neurol.* 417, 181–194.

Richardson-Jones, J. W., Craige, C. P., Guiard, B. P., Stephen, A., Metzger, K. L., Kung, H. F., et al. (2010). 5-HT1A autoreceptor levels determine vulnerability to stress and response to antidepressants. *Neuron* 65, 40–52. doi: 10.1016/j.neuron.2009.12.003

Sander, C. Y., Hooker, J. M., Catana, C., Normandin, M. D., Alpert, N. M., Knudsen, G. M., et al. (2013). Neurovascular coupling to D2/D3 dopamine receptor occupancy using simultaneous PET/functional MRI. *Proc. Natl. Acad. Sci. U.S.A.* 110, 11169–11174. doi: 10.1073/pnas.1220512110

Selvaraj, S., Turkheimer, F., Rosso, L., Faulkner, P., Mouchlianitis, E., Roiser, J. P., et al. (2012). Measuring endogenous changes in serotonergic neurotransmission in humans: a [11C]CUMI-101 PET challenge study. *Mol. Psychiatry* 17, 1254–1260. doi: 10.1038/mp.2012.78

Shimizu, S., and Ohno, Y. (2013). Improving the treatment of Parkinson's disease: a novel approach by modulating 5-HT(1A) receptors. *Aging Dis.* 4, 1–13.

Shiue, C. Y., Shiue, G. G., Mozley, P. D., Kung, M. P., Zhuang, Z. P., Kim, H. J., et al. (1997). P-[18F]-MPPF: a potential radioligand for PET studies of 5-HT1A receptors in humans. *Synapse* 25, 147–154.

Truchot, L., Costes, S. N., Zimmer, L., Laurent, B., Le Bars, D., Thomas-Anterion, C., et al. (2007). Up-regulation of hippocampal serotonin metabolism in mild cognitive impairment. *Neurology* 69, 1012–1017. doi: 10.1212/01.wnl.0000271377.52421.4a

Tyacke, R. J., and Nutt, D. J. (2015). Optimising PET approaches to measuring 5-HT release in human brain. *Synapse* 69, 505–511. doi: 10.1002/syn.21835

Udo de Haes, J. I., Cremers, T. I. F. H., Bosker, F.-J., Postema, F., Tiemersma-Wegman, T. D., and den Boer, J. A. (2005). Effect of increased serotonin levels on [18F]MPPF binding in rat brain: fenfluramine vs the combination of citalopram and ketanserin. *Neuropsychopharmacol. Off. Publ. Am. Coll. Neuropsychopharmacol.* 30, 1624–1631. doi: 10.1038/sj.npp.1300721

Udo de Haes, J. I., Harada, N., Elsinga, P. H., Maguire, R. P., and Tsukada, H. (2006). Effect of fenfluramine-induced increases in serotonin release on [18F]MPPF binding: a continuous infusion PET study in conscious monkeys. *Synapse* 59, 18–26. doi: 10.1002/syn.20209

Verge, D., Daval, G., Patey, A., Gozlan, H., el Mestikawy, S., and Hamon, M. (1985). Presynaptic 5-HT autoreceptors on serotonergic cell bodies and/or dendrites but not terminals are of the 5-HT1A subtype. *Eur. J. Pharmacol.* 113, 463–464. doi: 10.1016/0014-2999(85)90099-8

Vidal, B., Fieux, S., Colom, M., Billard, T., Bouillot, C., Barret, O., et al. (2018a). 18F-F13640 preclinical evaluation in rodent, cat and primate as a 5-HT1A receptor agonist for PET neuroimaging. *Brain Struct. Funct.* 223, 2973–2988. doi: 10.1007/s00429-018-1672-7

Vidal, B., Fieux, S., Redouté, J., Villien, M., Bonnefoi, F., Le Bars, D., et al. (2018b). In vivo biased agonism at 5-HT1A receptors: characterisation by simultaneous PET/MR imaging. *Neuropsychopharmacology* 43, 2310–2319. doi: 10.1038/s41386-018-0145-2

Yang, K.-C., Takano, A., Halldin, C., Farde, L., and Finnema, S. J. (2018). Serotonin concentration enhancers at clinically relevant doses reduce [11C]AZ10419369 binding to the 5-HT1B receptors in the nonhuman primate brain. *Transl. Psychiatry* 8:132. doi: 10.1038/s41398-018-0178-7

Yokoyama, C., Mawatari, A., Kawasaki, A., Takeda, C., Onoe, K., Doi, H., et al. (2016). Marmoset serotonin 5-HT $_{1A}$ receptor mapping with a biased agonist

PET Probe ^{18} F-F13714: comparison with an antagonist tracer ^{18} F-MPPF in awake and anesthetized states. *Int. J. Neuropsychopharmacol.* 19:yw079. doi: 10.1093/ijnp/pyw079

Zhang, Y., and Fox, G. B. (2012). PET imaging for receptor occupancy: meditations on calculation and simplification. *J. Biomed. Res.* 26, 69–76. doi: 10.1016/S1674-8301(12)60014-1

Zimmer, L., Mauger, G., Le Bars, D., Bonmarchand, G., Luxen, A., and Pujol, J.-F. (2002). Effect of endogenous serotonin on the binding of the 5-hT1A PET ligand 18F-MPPF in the rat hippocampus: kinetic beta measurements combined with microdialysis. *J. Neurochem.* 80, 278–286. doi: 10.1046/j.0022-3042.2001.00696.x

Zimmer, L., Rbah, L., Giacomelli, F., Le Bars, D., and Renaud, B. (2003). A reduced extracellular serotonin level increases the 5-HT1A PET ligand 18F-MPPF binding in the rat hippocampus. *J. Nucl. Med. Off. Publ. Soc. Nucl. Med.* 44, 1495–1501.

Zimmer, L., Riad, M., Rbah, L., Belkacem-Kahlouli, A., Le Bars, D., Renaud, B., et al. (2004). Toward brain imaging of serotonin 5-HT1A autoreceptor internalization. *NeuroImage* 22, 1421–1426. doi: 10.1016/j.neuroimage.2004.03.020

Conflict of Interest: AN-T is employed by Neurolixis.

The remaining authors declare that the research was conducted in the absence of any commercial or financial relationships that could be construed as a potential conflict of interest.

frontiers in Neuroscience

ORIGINAL RESEARCH
published: 18 March 2021
doi: 10.3389/fnins.2021.593723

^{18}F-FDG PET Combined With MR Spectroscopy Elucidates the Progressive Metabolic Cerebral Alterations After Blast-Induced Mild Traumatic Brain Injury in Rats

Yang Li[1,2,3†], Kaijun Liu[4†], Chang Li[2], Yu Guo[2], Jingqin Fang[2], Haipeng Tong[2], Yi Tang[1], Junfeng Zhang[2], Jinju Sun[1], Fangyang Jiao[1], Qianhui Zhang[5], Rongbing Jin[1,6], Kunlin Xiong[2,6*] and Xiao Chen[1,6*]*

[1] Department of Nuclear Medicine, Daping Hospital, Army Medical University, Chongqing, China, [2] Department of Radiology, Daping Hospital, Army Medical University, Chongqing, China, [3] Department of Medical Imaging, Air Force Hospital of Western Theater Command, Chengdu, China, [4] Department of Gastroenterology, Daping Hospital, Army Medical University, Chongqing, China, [5] Department of Foreign Language, Army Medical University, Chongqing, China, [6] Chongqing Clinical Research Center for Imaging and Nuclear Medicine, Chongqing, China

A majority of blast-induced mild traumatic brain injury (mTBI) patients experience persistent neurological dysfunction with no findings on conventional structural MR imaging. It is urgent to develop advanced imaging modalities to detect and understand the pathophysiology of blast-induced mTBI. Fluorine-18 fluorodeoxyglucose positron emission tomography (^{18}F-FDG PET) could detect neuronal function and activity of the injured brain, while MR spectroscopy provides complementary information and assesses metabolic irregularities following injury. This study aims to investigate the effectiveness of combining ^{18}F-FDG PET with MR spectroscopy to evaluate acute and subacute metabolic cerebral alterations caused by blast-induced mTBI. Thirty-two adult male Sprague–Dawley rats were exposed to a single blast (mTBI group) and 32 rats were not exposed to the blast (sham group), followed by ^{18}F-FDG PET, MRI, and histological evaluation at baseline, 1–3 h, 1 day, and 7 days post-injury in three separate cohorts. ^{18}F-FDG uptake showed a transient increase in the amygdala and somatosensory cortex, followed by a gradual return to baseline from day 1 to 7 days post-injury and a continuous rise in the motor cortex. In contrast, decreased ^{18}F-FDG uptake was seen in the midbrain structures (inferior and superior colliculus). Analysis of MR spectroscopy showed that inflammation marker myo-inositol (Ins), oxidative stress marker glutamine + glutamate (Glx), and hypoxia marker lactate (Lac) levels markedly elevated over time in the somatosensory cortex, while the major osmolyte taurine (Tau) level immediately increased at 1–3 h and 1 day, and then returned to sham level on 7 days post-injury, which could be due to the disruption of the blood–brain barrier. Increased ^{18}F-FDG uptake and elevated Ins and Glx levels over time were confirmed

OPEN ACCESS

Edited by:
Szilvia Anett Nagy, University of Pécs, Hungary

Reviewed by:
Arnold Tóth, University of Pécs, Hungary
Chuantao Zuo, Fudan University, China
Andre Obenaus, University of California, Irvine, United States

***Correspondence:**
Rongbing Jin
jinrb99@126.com
Kunlin Xiong
109948969@qq.com
Xiao Chen
xiaochen229@foxmail.com

† These authors have contributed equally to this work

Specialty section:
This article was submitted to Brain Imaging Methods, a section of the journal Frontiers in Neuroscience

Received: *11 August 2020*
Accepted: *19 February 2021*
Published: *18 March 2021*

Citation:
Li Y, Liu K, Li C, Guo Y, Fang J, Tong H, Tang Y, Zhang J, Sun J, Jiao F, Zhang Q, Jin R, Xiong K and Chen X (2021) ^{18}F-FDG PET Combined With MR Spectroscopy Elucidates the Progressive Metabolic Cerebral Alterations After Blast-Induced Mild Traumatic Brain Injury in Rats. Front. Neurosci. 15:593723. doi: 10.3389/fnins.2021.593723

by histology analysis which showed increased microglial activation and gliosis in the frontal cortex. These results suggest that ^{18}F-FDG PET and MR spectroscopy can be used together to reflect more comprehensive neuropathological alterations *in vivo*, which could improve our understanding of the complex alterations in the brain after blast-induced mTBI.

Keywords: blast injury, mild traumatic brain injury, positron emission tomography, fluorodeoxyglucose, magnetic resonance spectroscopy

INTRODUCTION

Blast-induced traumatic brain injury (TBI), the most common injury of modern warfare, has been receiving great interest worldwide recently (Benzinger et al., 2009). The nature of modern warfare and the frequent use of improvised explosive devices (IEDs) have led to increases in mild TBI (mTBI), which is defined as loss of consciousness lasting less than 30 min, an initial Glasgow Coma Score (GCS) of 13–15, and posttraumatic amnesia lasting less than 24 h (Bailes and Cantu, 2001; Belanger et al., 2007). Even though the acute symptoms of mTBI may be mild and transient, experimental and clinical studies have found metabolic, biochemical, and structural changes caused by mTBI. Mild TBI causes a complex pathophysiological cascade, including dramatic alterations in ionic homeostasis (Katayama et al., 1991), disruption of the blood–brain barrier (BBB) (Walls et al., 2016; Kuriakose et al., 2018), injury-induced neuroinflammation (Kokiko-Cochran and Godbout, 2018; Missault et al., 2019), and diffuse axonal injury (Ling et al., 2012; Venkatasubramanian et al., 2020). However, majority of mTBI patients experience neurological dysfunction with no findings on conventional clinical imaging methods, such as structural magnetic resonance imaging (MRI) or computed tomography (CT) (Le and Gean, 2009). Due to the difficulty of imaging assessment on mTBI patients, especially in the acute or subacute phase, there needs more emphasis on the development of advanced imaging modalities, so that the therapeutic management of mTBI patients can be improved.

Several advanced *in vivo* imaging techniques have been used to investigate TBI to better understand the temporal microstructural and functional changes following TBI, such as diffusion tensor imaging (DTI), functional MRI (fMRI), MR spectroscopy (MRS), positron emission tomography (PET), etc. (Croall et al., 2014; Zhuo et al., 2015; Harris et al., 2016; Jaiswal et al., 2019; Kulkarni et al., 2019; Venkatasubramanian et al., 2020). DTI has been widely used to investigate the microstructural responses after mTBI. Many different regions have been found to be affected, since DTI is highly sensitive to axonal damage related to mTBI (Mayer et al., 2010; Tang et al., 2017; Badea et al., 2018; Venkatasubramanian et al., 2020). In contrast to the structural information offered by DTI regarding brain integrity, some studies have explored functional and biochemical changes following brain injury using other imaging modalities. Fluorine-18 fluorodeoxyglucose PET (^{18}F-FDG PET) is a powerful imaging technique that can map regional cerebral metabolism patterns *in vivo*. Cerebral glucose metabolism significantly associates with neuronal function and activity of the injured brain (Garnett et al., 2001; Casey et al., 2008). Clinical and animal studies have shown that changes in glucose metabolism of the brain in hours to days following exposure to blast injury have been more complex than the chronic hypometabolism using ^{18}F-FDG PET (Stocker et al., 2014; Awwad et al., 2015; Meabon et al., 2016; Jaiswal et al., 2019). PET imaging provides exquisite sensitivity when compared with CT or MR imaging, but with reduced resolution. *In vivo* MRS provides complementary information and assesses metabolic irregularities following injury. Metabolites such as *N*-acetylaspartate (NAA), choline (Cho), and lactate (Lac), glutamate and glutamine (Glx), myo-inositol (Ins), and taurine (Tau) detected by ^{1}H MRS provide information related to brain injury, inflammation, ischemia, and mitochondrial dysfunction (Xu et al., 2011; Harris J.L. et al., 2012; Sajja et al., 2012; Zhuo et al., 2015). ^{18}F-FDG PET and MRS could be used to investigate the neuropathological changes after brain injury from different aspects. However, it is currently unclear if ^{18}F-FDG PET could be used synergistically with MRS to elucidate the acute pathological alterations in the brain and improve diagnostic and prognostic measures after blast-induced mTBI.

In this study, we aim to evaluate hyperacute, acute, and subacute metabolic cerebral alterations caused by blast-induced mTBI in rats *via* the combination of *in vivo* MRS and ^{18}F-FDG PET. Animals were exposed to a single blast overpressure wave, underwent MRS and ^{18}F-FDG PET, and sacrificed for histological analysis at baseline, 1–3 h post-injury (hyperacute phase), 1 day post-injury (acute phase), and 7 days post-injury (subacute phase). Combining these two imaging methods could reflect more comprehensive neuropathological alterations *in vivo* after blast-induced mTBI.

MATERIALS AND METHODS

Animals

Sixty-four adult male Sprague–Dawley rats (obtained from the Experimental Animal Center of Daping Hospital, Chongqing, China) weighing 200∼225 g were randomly assigned into two groups, namely the mTBI group (n = 32) and the sham group (n = 32). Throughout the experiment, rats were kept in a temperature- and humidity-controlled room under a 12-h light/12-h dark cycle with food and water except during ^{18}F-FDG uptake. All animal procedures used in this study were approved by the Administration of Affairs Concerning Experimental Animals Guideline of Army Medical University. The use of laboratory animals was in compliance with the guidelines

of National Institutes of Health. All animal experiments were approved by the Animal Use Subcommittee of Army Medical University.

Experimental Design

Figure 1A shows the experimental scheme for animals in this study. The study contained three cohorts of adult male Sprague–Dawley rats. The first cohort received blast-induced mTBI ($n = 6$) or sham ($n = 6$) and underwent PET/CT scans with ^{18}F-FDG prior to injury and at 1–3 h, 1 day, and 7 days post-injury. The second cohort received blast-induced mTBI ($n = 6$) or sham ($n = 6$) and underwent MRI scans including conventional structure imaging and MRS prior to injury and at 1–3 h, 1 day, and 7 days post-injury. The last cohort received blast-induced mTBI ($n = 20$) or sham ($n = 20$) and were sacrificed for Evans blue penetration assay and immunohistochemical analysis prior to injury and at 1–3 h, 1 day, and 7 days post-injury.

Blast-Induced mTBI Model

The bio-shock tube (BST-I) apparatus (**Figures 1B,C**) was used to produce blast injury as previously described (Ning et al., 2019). All rats were anesthetized in an induction chamber with 4–5% isoflurane in 100% oxygen for approximately 5 min. Then, the anesthetized rats in the mTBI group were placed into individual cages (one rat/cage) in the prone position with the left side facing the direction of the membrane during blast (**Figure 1D**). All cages were positioned at the same vertical plane to ensure equal pressure exposure and to prevent subsequent secondary or tertiary blast injuries. The BST-I apparatus generated two levels of lower-intensity blast waves. The values for the peak overpressure were 139.146 and 364.86 kPa, lasting 48.41 ms (**Figure 1E**). Following the blast, the rats were removed from the apparatus and placed in a supine position in a cage. Sham rats went through the same procedure of anesthesia and were placed in the BST-I apparatus without being exposed to the blast waves. The righting reflex time was recorded for both mTBI and sham rats.

PET/CT Imaging, Reconstruction, and Analysis

Rats were food-deprived 4∼6 h before ^{18}F-FDG injection. ^{18}F-FDG was injected intravenously *via* the tail vein to both mTBI and sham rats with the dose of 37 MBq/rat. After 40 min of uptake, static PET scan was performed for 30 min in list mode (350∼650 keV, 2.56 ns) using a small animal micro PET/CT scanner (Pingseng, Jiangsu, China). A three-bed CT scan was acquired in rat mode (60 kVp, 500 μA, exposure time 320 ms) following PET scans for anatomical localization, attenuation, and scatter corrections. The CT image matrix was 352 × 352 × 536 with a voxel size of 0.23 × 0.23 × 0.23 mm. The parameters for reconstruction were as follows: reconstruction algorithm = 3D-OSEM/MAP with 2 OSEM iterations and 18 MAP iterations; scatter, attenuation, and decay corrections applied; requested resolution = 0.5 mm; image matrix = 256 × 256 × 159; and voxel size = 0.39 × 0.39 × 0.80 mm. The intrinsic resolution of the PET scanner was approximately 1.4 mm full width at half maximum (FWHM) at the center of the field of view.

Processing and analysis of ^{18}F-FDG PET data was performed using PMOD software version 3.6 (PMOD Technologies, Ltd., Zurich, Switzerland) as previously described (Park et al., 2019). For volume of interest (VOI) analysis, the PET data were registered to the 58 regions in the W. Schiffer rat brain template and atlas by PMOD (**Supplementary Table 1**). The standard uptake value (SUV) in defined subregions of the rat brain was automatically applied to measure. This study evaluated 58 brain regions and the entire atlas was used for whole brain normalization as previously reported (Byrnes et al., 2014). The regional SUVw was calculated by dividing the standardized ^{18}F-FDG uptake value for the individual target region by that for the whole brain.

MR Imaging, Processing, and Analysis

MR imaging experiments were conducted before and at 1–3 h, 1 day, and 7 days after blast in the mTBI and sham groups. All MR imaging experiments were performed with 7 T animal scanner (Biospin70/20 USR, Bruker BioSpin, Ettlingen, Germany) equipped with a four-channel rat head transmitter/receiver coil. Rats were initially anesthetized in a box with 5% isoflurane in oxygen, then anesthesia was maintained by 2% isoflurane in oxygen during MR scanning. The respiration and heart rate were monitored throughout the experiment. Scanning sequences included T1-weighted imaging (Turbo-RARE, echo time/repetition time: 6.5 ms/800 ms, field of view: 30 × 30 mm, matrix: 256 × 256, slice thickness: 1 mm), T2-weighted imaging (Turbo-RARE, echo time/repetition time: 30 ms/3,000 ms, field of view: 30 × 30 mm, matrix: 256 × 256, slice thickness: 1 mm), and MRS (STEAM, echo time/repetition time: 3 ms/3.5 ms, a single 2 × 2 × 2 mm^3 voxel was located in the left somatosensory cortex region based on T2-weighted images). The MRS voxels were localized in the somatosensory cortex and hippocampus region of the rat brain. These regions were chosen because they were implicated in previous studies using other TBI models (Larson et al., 2011; Sajja et al., 2012; Awwad et al., 2015; Brabazon et al., 2017; Salberg et al., 2017; Tang et al., 2017). MRS data were analyzed by jMRUI software 5.2, and the method of parameterization implemented in jMRUI software was applied: advanced method for accurate, robust, and efficient spectral fitting (AMARES). The AMARES algorithm estimates the area under each peak based on the frequency and half-width of each peak (Vanhamme et al., 1997), and the relative levels of Ins, Tau, Cho, Glx, Glu, NAA, and Lac to creatine (Cr) were assessed. The Cr spectral intensity was used as reference as previously reported for relative quantitation because of its relatively stable concentration in the brain (Xu et al., 2011).

Evans Blue Penetration Assay

The permeability of the BBB was determined by measuring the penetration of Evans blue (Solarbio, Beijing, China) in the brain tissues of three rats in each group at each time point. Evans blue (2% in saline; 4 ml/kg body weight) was injected intravenously *via* the tail vein 1 h before measurement. The anesthetized rats were perfused transcardially with saline before sampling. Photos of the brains were taken with a digital camera. Each sample was

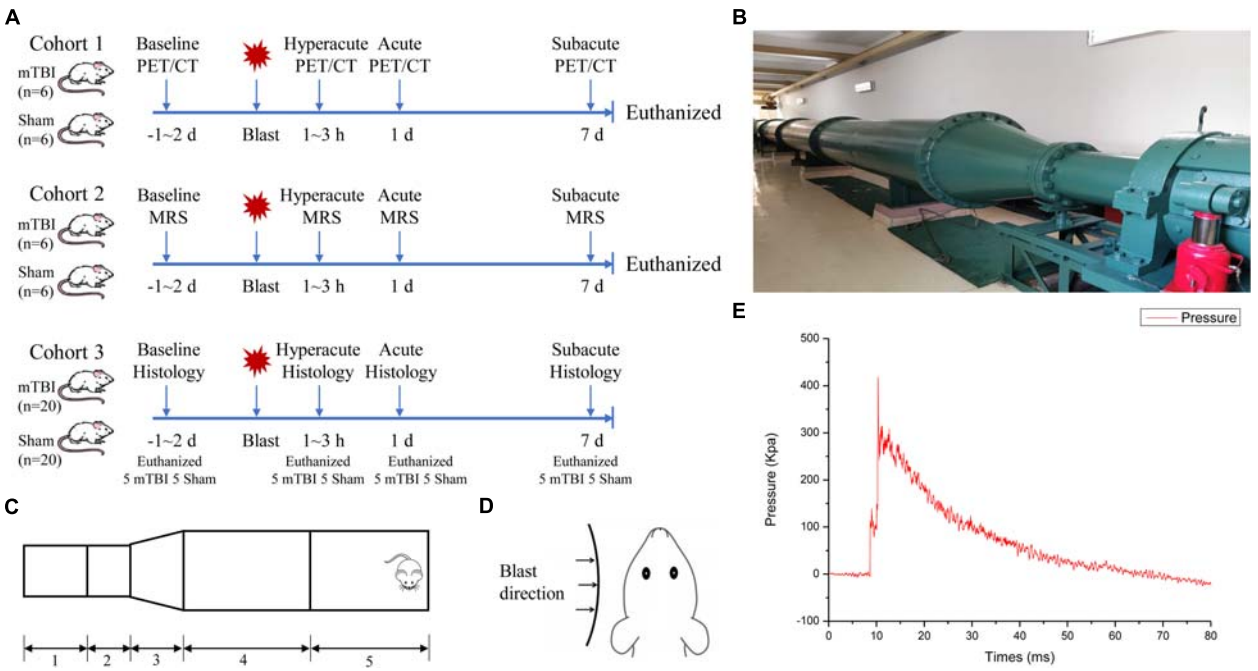

FIGURE 1 | Schematic drawing of the experimental protocol and bio-shock tubes (BST-I). **(A)** Overall experimental scheme for blast-induced mild traumatic brain injury (mTBI) and sham rats. **(B)** The diagram of the BST-I shock tube. **(C)** BST-I model: (1) driving section, (2) double-clamping diaphragm section, (3) conical section, (4) transition section, and (5) test section. **(D)** Blast was directed to the left side of all rats. **(E)** Representative blast waves from a single blast illustrating peak pressure values of 139.146 and 364.86 kPa, lasting 48.41 ms.

weighed and homogenized with 400 μl PBS, then precipitated by 60% trichloroacetic acid overnight. The sample was centrifuged for 30 min at 10,000 rpm. Absorption of the supernatant was measured at a wavelength of 620 nm with a plate reader. The extravasation of Evans blue was quantified as microgram/gram brain tissue with an Evans blue standardized curve.

Immunohistochemical Evaluation

For histological analysis of brain tissue, two rats in each group at each time point were euthanized, then perfused with 4% paraformaldehyde followed by saline. The entire brain was collected and fixed in 4% paraformaldehyde. After being fixed for over 48 h, the brain tissues were embedded in paraffin. Brain tissue was sectioned at 20 μm. Hematoxylin/eosin (H&E) staining on paraffin sections was histologically reviewed. For immunochemistry, Vectastain Elite ABC Kit (Vector Laboratories, Burlingame, CA, United States) and DAB Peroxidase Substrate Kit (Vector Laboratories, Burlingame, CA, United States) were used with primary antibodies, namely anti-rat Iba1 (ab178846, Abcam, Cambridge, MA, United States), anti-rat GFAP (ab7260, Abcam, Cambridge, MA, United States), and anti-rat NeuN (ab177487, Abcam, Cambridge, MA, United States), followed by biotinylated goat anti-rabbit and anti-mouse IgG that were used as secondary antibodies (Vector Laboratories, Burlingame, CA, United States). Images were then collected with an Olympus BX43 microscope (Olympus America, Center Valley, PA, United States). We examined entire sections at × 40 magnification to identify "hot spot" regions of protein expression within the frontal cortex and hippocampus, from which five hot spots were selected for imaging. Immunoreactivity of these proteins was evaluated using the mean optical density (IOD/area) of protein expressions at × 200 magnification field by Image-Pro Plus 6.0 (Media Cybernetics, Rockville, MD, United States).

Statistical Analysis

All data are presented as mean ± standard deviation (SD). For the PET, MRS, and immunohistochemical data, two-way analysis of variance (ANOVA) with repeated measures was used to analyze alterations in ^{18}F-FDG uptake, various neurometabolites, Evans blue, and immunohistochemical index (IOD/area values) over time. Individual comparisons at each time point or different groups were conducted with Sidak's multiple comparisons test. All statistical analyses were performed using GraphPad Prism 8 (GraphPad Software, San Diego, CA, United States). Two-tailed p values were calculated with the significance level at 0.05.

RESULTS

Trauma Induction

All rats survived the blast, without observable skull fracture and apnea. Both sham and mTBI groups had similar righting reflex time, with the average time of 296.2 ± 35.4 s for the sham group and 325.7 ± 40.2 s for the mTBI group. There were no significant differences in size and weight between these

two groups at any time points after the blast. Moreover, rats in neither group showed any visible sign of injury in the brain on T1- and T2-weighted images at any time points after the blast (**Supplementary Figure 1**).

^{18}F-FDG PET Detected Both Increased and Decreased Brain Metabolism in Multiple Regions After Blast-Induced mTBI

Among 58 brain regions, 10 VOIs were found significantly changed between sham and mTBI rats in ^{18}F-FDG uptake from baseline to day 7, including the bilateral amygdala ($F_{1,5}$ = 4.137, p = 0.0253), somatosensory cortex ($F_{1,5}$ = 13.43, p = 0.0145), motor cortex ($F_{1,5}$ = 7.479, p = 0.0410), colliculus inferior ($F_{1,5}$ = 38.77, p = 0.0016), and colliculus superior ($F_{1,5}$ = 16.82, p = 0.0093) (**Figure 2B** and **Supplementary Table 2**). As shown in **Supplementary Table 2**, the changes of ^{18}F-FDG uptake in bilateral VOIs were similar, so that we combined SUVw of the left and right VOIs as SUVw average to be compared at different time points. At 1–3 h post-injury, the amygdala (+ 5.97%, p = 0.0103) and somatosensory cortex (+ 6.82%, p = 0.0245) presented increased ^{18}F-FDG uptake in the mTBI group, compared with the sham group. Subsequently, ^{18}F-FDG uptake in the amygdala and somatosensory cortex gradually returned to baseline from 1 to 7 days post-injury in the mTBI group, with a significant difference in somatosensory cortex by 1 day (+ 6.12%, p = 0.0429) compared with the sham group (**Figures 2A,C,D**). ^{18}F-FDG uptake in the motor cortex increased in the mTBI group from 1 day (+ 3.60%, p = 0.0326) to 7 days post-injury (+ 3.41%, p = 0.0446) (**Figures 2A,E**). However, at 1–3 h post-injury, decreased ^{18}F-FDG uptake was observed in two midbrain structures, i.e., the inferior colliculus (-17.21%, $p < 0.0001$) and superior colliculus (-6.75%, p = 0.0094). Then, ^{18}F-FDG uptake in the superior colliculus and inferior colliculus gradually returned to baseline from 1 to 7 days post-injury in the mTBI group, with a significant difference in the inferior colliculus by 1 day (-12.43%, $p < 0.0001$) and 7 days (-7.68%, p = 0.0049) and in the superior colliculus by 1 day (-5.95%, p = 0.0230) compared with the sham group (**Figures 2A,F,G**).

MRS Revealed *in vivo* Dynamic Neurochemical Alterations in the Cortex Region After Blast-Induced mTBI

The MRS voxel was placed to the somatosensory cortex (**Figure 3A**) and hippocampus (**Supplementary Figure 2A**) of rat brain. High-quality spectra with narrow linewidths were generally obtained in this study (**Figure 3B** and **Supplementary Figure 2B**). For the somatosensory cortex, MRS revealed relative levels of glia marker Ins ($F_{1,5}$ = 54.49, p = 0.0007), oxidative stress and gliosis marker Glx ($F_{1,5}$ = 31.38, p = 0.0025), and hypoxic indicator Lac markedly elevated as early as 1–3 h and day 1 post-injury, together with day 7 (**Figures 3C–E**). The major osmolyte, the relative level of Tau ($F_{1,5}$ = 21.90, p = 0.0054), immediately increased as early as 1–3 h (+ 160.37%, $p < 0.0001$), continuously elevated by 1 day (+ 276.48%, $p < 0.0001$), but decreased to sham level on 7 days post-injury (+ 11.92%, p = 0.9444) (**Figure 3F**). The mTBI group showed a significant increased relative level of Cho on 7 days post-injury, compared with the sham group (+ 24.04%, p = 0.0366) (**Figure 3G**). No significant reduction in the relative level of NAA was found in the mTBI group, compared with the sham group at each time point ($F_{1,5}$ = 0.9721, p = 0.3694) (**Figure 3H**). However, no significant differences of these metabolites, namely Ins ($F_{1,5}$ = 3.218, p = 0.1328), Glx ($F_{1,5}$ = 2.068, p = 0.2099), Lac ($F_{1,5}$ = 1.860, p = 0.2308), Tau ($F_{1,5}$ = 0.03899, p = 0.8512), Cho ($F_{1,5}$ = 1.628, p = 0.2580), and NAA ($F_{1,5}$ = 0.7159, p = 0.4361), were observed in the hippocampus between the mTBI group and the sham group (**Supplementary Figures 2C–H**).

Blast-Induced mTBI and Immunohistochemical Markers of Inflammation, Injury, and Astrogliosis

To further corroborate the effect of the blast-induced mTBI on the frontal cortex and hippocampus shown in MRS and ^{18}F-FDG PET/CT examination, we employed histopathological analysis on brain tissue sections. Evans blue (EB) penetration assay showed significantly higher EB contents in mTBI rats at 1–3 h and 1 day after injury than those in the sham group (p = 0.0003, $p < 0.0001$, respectively), with no significant difference of EB contents between mTBI rats at 7 day and the sham group (p = 0.5252) (**Figures 4A,B**). This indicated that blast led to the disruption of the BBB immediately following injury to 1 day post-injury and recovered at 7 days post-injury. H&E staining showed no significant alteration in tissue composition of the frontal cortex (**Figure 5A**) and hippocampus (**Supplementary Figure 3A**) after blast at each time point. Furthermore, immunohistochemical staining for Iba 1, the microglia marker, revealed more Iba 1-positive cells in the frontal cortex of mTBI rats at each time point and elevated as the time went on ($p < 0.0001$), which was consistent with the findings of ^{18}F-FDG PET and Ins alterations in MRS (**Figures 5B,C**). Glial changes in the frontal cortex were also among the most marked after blast-induced mTBI. GFAP immunostaining for astrocytes demonstrated the same trend as Iba 1 in the mTBI group ($p < 0.0001$) (**Figures 5B,D**). However, no marked difference was found on NeuN expression, the neuron marker, in the frontal cortex between the mTBI group and the sham group at each time point post-injury (p = 0.1025) (**Figures 5B,E**). On the contrary, no significant difference was shown between the mTBI group and the sham group on the expressions of Iba 1 (p = 0.8591), GFAP (p = 0.5935), and NeuN (p = 0.7671) in the hippocampus (**Supplementary Figures 3B–E**).

DISCUSSION

To the best of our knowledge, this is the first *in vivo* study to apply a combination of ^{18}F-FDG PET and MRS to detect progressive changes of brain metabolism after blast-induced mTBI. We demonstrate early metabolic cerebral alterations following blast-induced mTBI, including hyperacute, acute, and subacute phases. Our current study reveals five main findings: (1) no visible brain injuries were observed on conventional T1- and T2-weighted imaging until 7 days following exposure to blast; (2) Ins, Glx,

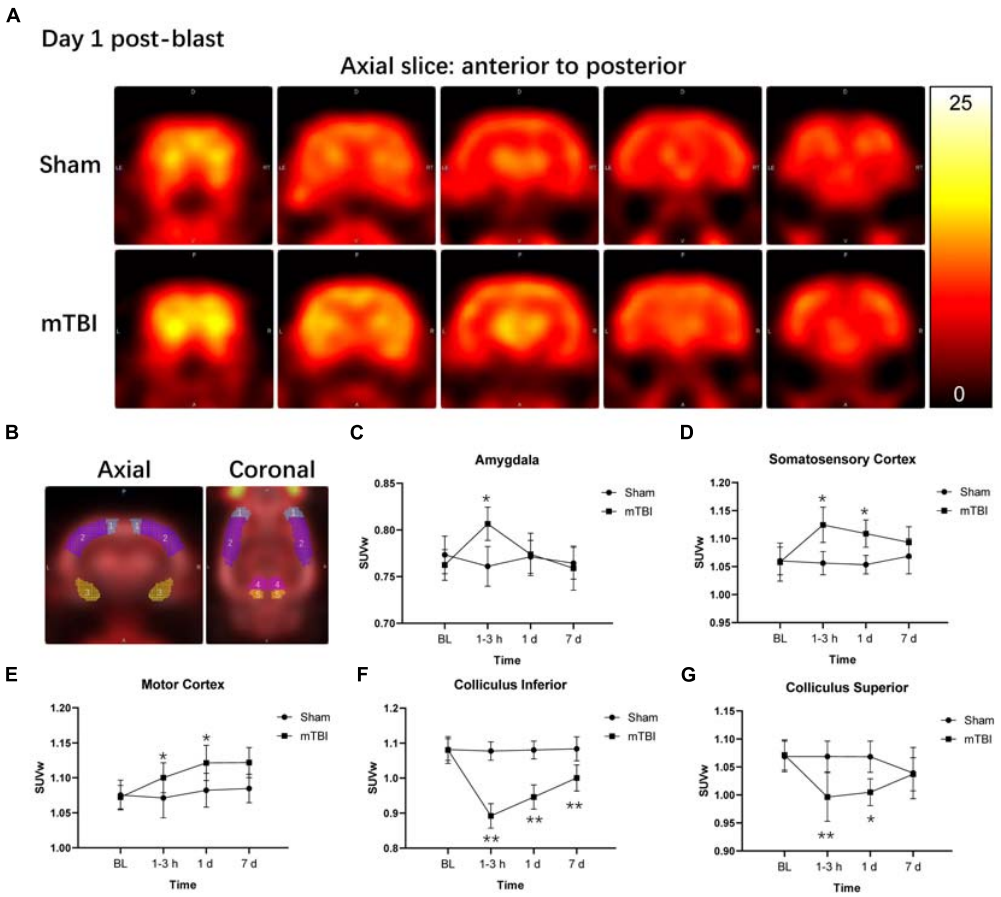

FIGURE 2 | Fluorine-18 fluorodeoxyglucose positron emission tomography (^{18}F-FDG PET) reveals both increased and decreased brain metabolism in multiple regions after blast-induced mTBI. **(A)** Representative axial ^{18}F-FDG PET images in the brain from anterior to posterior (left to right) of a sham (up) and a blast (bottom) rat on day 1 post-blast. In the corresponding PET images, yellow and black represent relative higher and lower values, respectively. **(B)** Volume-based analysis of ^{18}F-FDG uptake showing five regions with significant changes between sham and mTBI rats: (1) motor cortex, (2) somatosensory cortex, (3) amygdala, (4) colliculus superior, and (5) colliculus inferior. **(C–G)** Box plots show ^{18}F-FDG uptake at 1–3 h, 1 day, and 7 days post-injury in these five regions of mTBI and sham rats. Box and whisker plots display median, first and third quartiles, minimum, and maximum. $^{**}p < 0.01$ vs. the sham group; $^{*}p < 0.05$ vs. the sham group.

and Lac levels markedly elevated over time in the somatosensory cortex, while the Tau level immediately increased at 1–3 h and 1 day, and then returned to sham level on 7 days post-injury; (3) mTBI produced an acute increase in ^{18}F-FDG uptake in the amygdala, somatosensory cortex, and motor cortex, but decreases in the midbrain structures; (4) Evans blue penetration assay revealed that blast led to the disruption of the BBB immediately following injury to 1 day post-injury and recovered at 7 days post-injury; and (5) histological findings showed a significant elevated expression of inflammatory marker Iba 1 and gliosis marker GFAP over time in the frontal cortex.

Traditionally, physicians have relied on CT and MRI to identify intracranial bleeding, lesions, and skull fractures. However, many patients with mTBI suffer neural injury at a microscopic level. They have persistent neurological symptoms despite normal MRI and CT imaging (Delouche et al., 2016; Honce et al., 2016). This study showed no visible sign of lesions in the brain on T1- and T2-weighted images following exposure to blast, which is similar to the previous findings (Tang et al., 2017). Because of the sensitivity of ^{1}H MRS and ^{18}F-FDG PET to metabolic changes *in vivo*, we performed these techniques to track the dynamic changes of brain metabolism following blast-induced mTBI.

Ins is a glial marker, including the reactive gliosis or microglia infiltration, which has been recognized as a marker of inflammation (Ashwal et al., 2004). We observed increased Ins level in the somatosensory cortex from 1–3 h to 7 days post-injury, consistent with the inflammation and gliosis responding to injury. These findings were confirmed by the immunohistochemistry using Iba 1 and GFAP immunolabeling in this study. Oxidative stress produces rapid and excessive elevation of extracellular glutamate and then is taken up by astrocytes and forms glutamine *via* the glutamine synthase enzyme, which is tightly controlled by gliosis (Zhong et al., 2006; Maas et al., 2008; Petronilho et al., 2010). Glx, combined glutamate–glutamine, also markedly increased over time after blast in this study. Several studies have detected elevated Glu levels that persist for several hours following severe TBI in

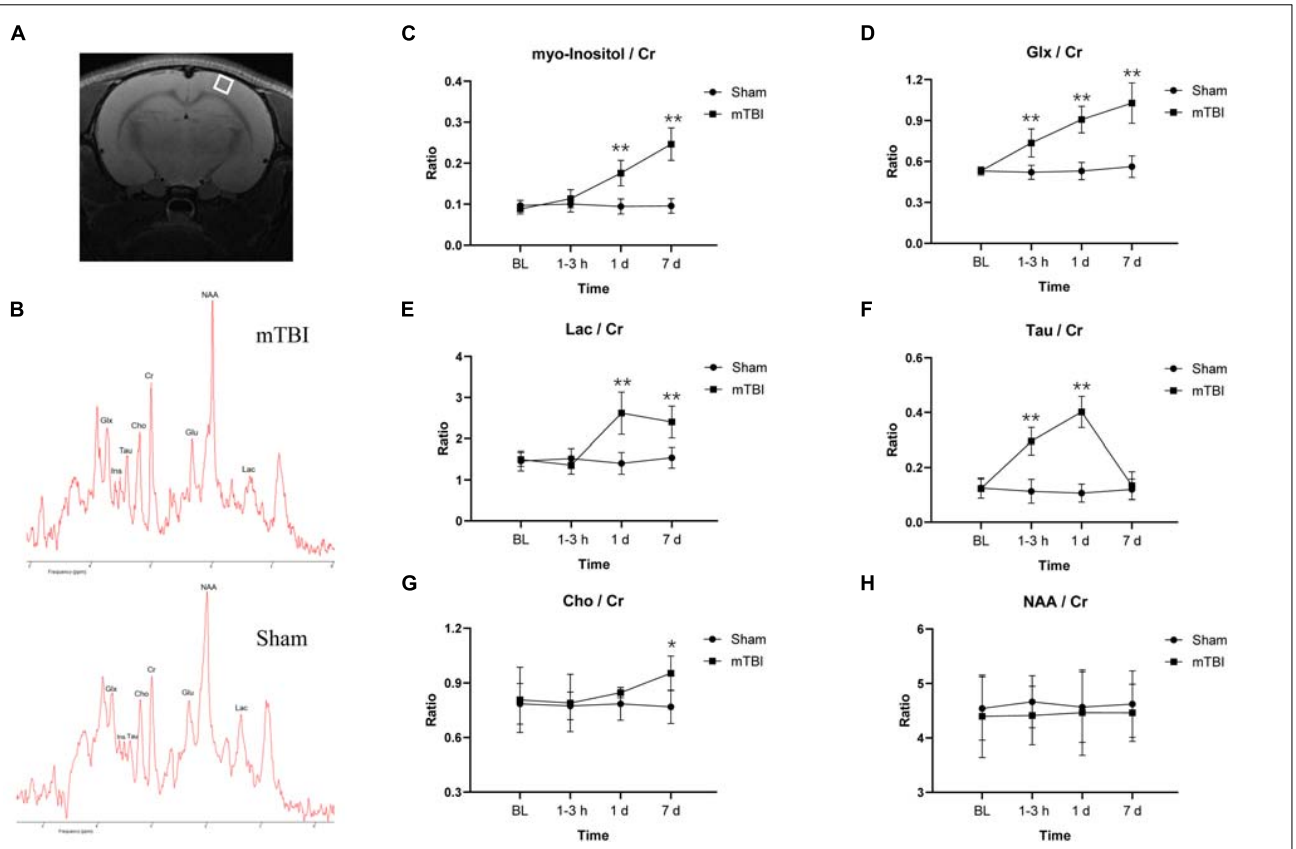

FIGURE 3 | Magnetic resonance spectroscopy (MRS) detects *in vivo* dynamic neurochemical alterations in the somatosensory cortex region after blast-induced mTBI. Placement of voxel in the somatosensory cortex region [white box **(A)**] with a representative spectrum (up: mTBI 1–3 h post-injury; bottom: sham) **(B)**. **(C–H)** Box plots show the relative levels of Ins, Glx, Lac, Tau, Cho, and NAA at 1–3 h, 1 day, and 7 days post-injury in somatosensory cortex of mTBI and sham rats. Box and whisker plots display median, first and third quartiles, minimum, and maximum. $^{**}p < 0.01$ vs. the sham group; $^{*}p < 0.05$ vs. the sham group. Ins, myo-inositol; Tau, taurine; Cho, choline; Glx, glutamine + glutamate; Glu, glutamate; NAA, *N*-acetylaspartate; Lac, lactate; Cr, creatine.

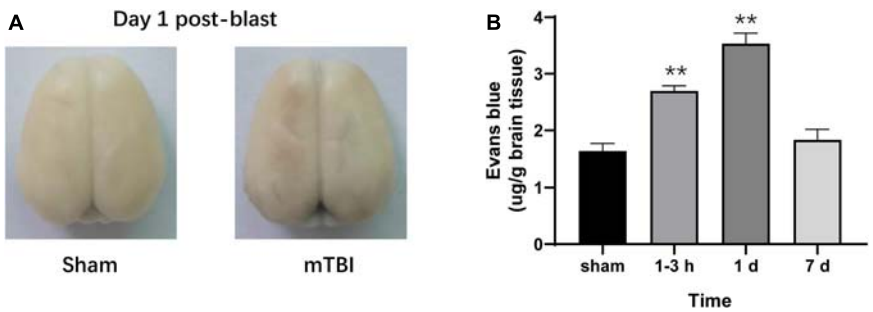

FIGURE 4 | Evans blue (EB) penetration assay reveals progressive alterations of the blood–brain barrier (BBB) in rats after blast-induced mTBI. **(A)** Representative EB dyeing images of a sham (left) and a blast (right) rat on day 1 post-blast. **(B)** EB content in brain tissue was also quantified and expressed as micrograms of EB per gram of brain tissue. $^{**}p < 0.001$ vs. the sham group.

humans and following mild to severe TBI in animal models (Singh et al., 2017), which agrees with our findings. Some other studies demonstrate that mitochondrial dysfunction caused by the very early stage of TBI may affect glutaminase activity leading to alterations of glutamate and glutamine (Xu et al., 2011). Lactate is the end product of anaerobic glycolysis and, therefore, a useful indicator of hypoxia/ischemic cellular condition. Lac level went up till 7 days post-injury, indicating hypoxia/ischemia and alternate metabolic pathways being likely activated in the somatosensory cortex after injury, which has also been reported in earlier studies on TBI (Makoroff et al., 2005; Dienel, 2012; Harris J.L. et al., 2012). Furthermore, Tau, a major osmolyte, immediately increased after trauma until 1 day post-injury, which may be due to the disruption of the BBB. In support of

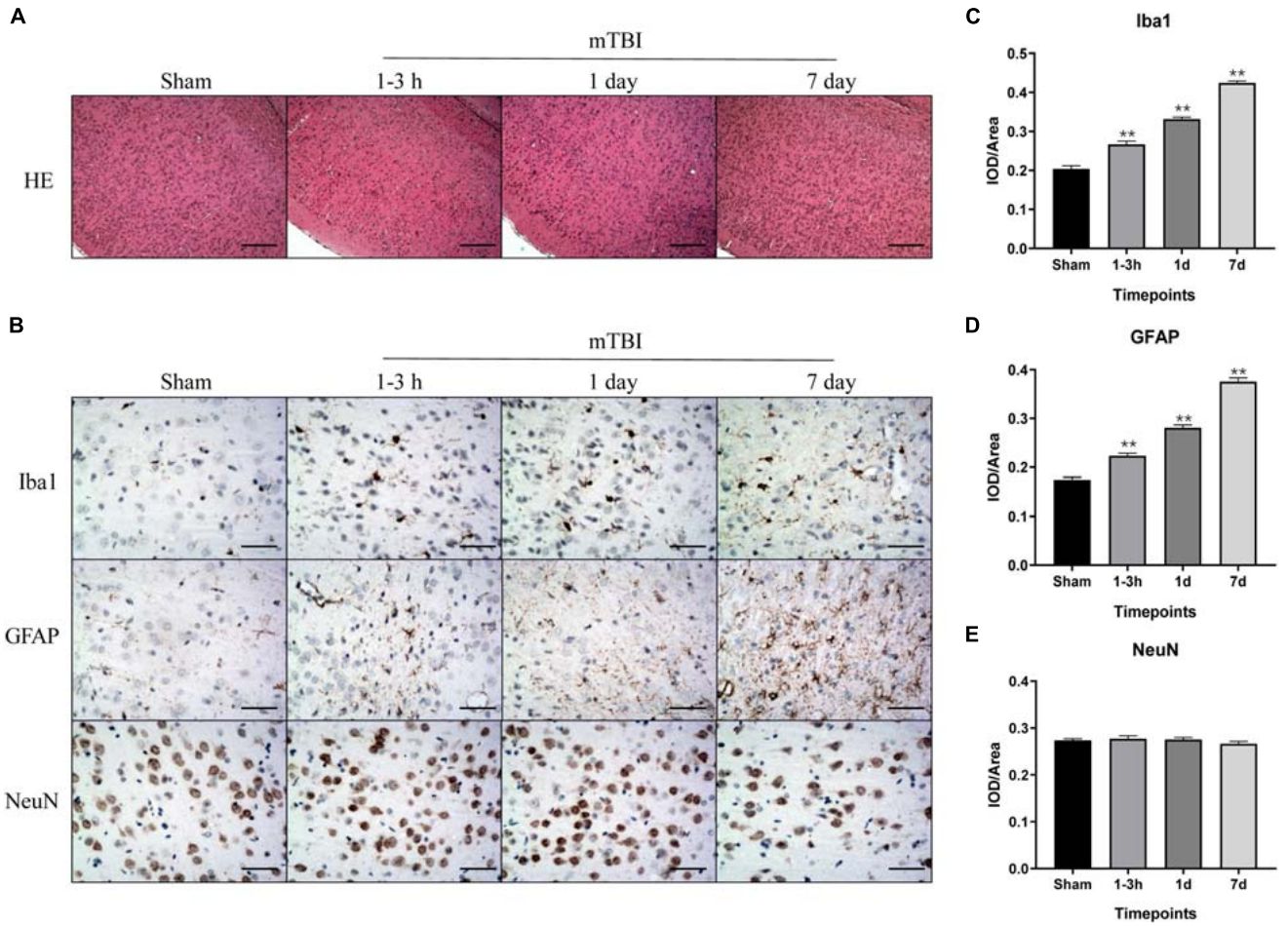

FIGURE 5 | Immunohistochemical analysis of inflammation, injury, and astrogliosis in the frontal cortex region after blast-induced mTBI. **(A)** H&E staining shows no obvious lesion after exposure to blast at each time point in mTBI rats. **(B)** Representative immunohistochemical staining for Iba 1, GFAP, and NeuN expression in the frontal cortex region is shown at each time point following injury in sham and mTBI rats. **(C–E)** Iba 1, GFAP, and NeuN expression levels were quantified. The scale bar denotes 250 μm in **(A)** and 50 μm in **(B)**. $^{**}p < 0.01$ vs. the sham group.

this idea, we performed Evans blue penetration assay to detect alteration of the BBB after injury, which revealed the disruption of the BBB immediately following injury to 1 day post-injury and recovered at 7 days post-injury. Moreover, recent studies have demonstrated that blast injury leads to the breakdown of the BBB immediately following injury with further increase in permeability continuing for several hours (Walls et al., 2016; Kuriakose et al., 2018). Interestingly, an elevated Cho level was only found on 7 days post-injury, which may be due to shearing of myelin and cellular membranes (Ross et al., 1998). The study of children with TBI showed significant increased Cho/Cr and decreased NAA/Cr in normal-appearing brain (Holshouser et al., 2005). However, no significant alterations were found in NAA level in our study. Immunohistochemistry showed that NeuN expression level did not change significantly over time, which confirmed the results of NAA in MRS.

Glucose is the major substrate for metabolism in the brain and has been studied extensively in non-blast TBI. Studies on non-blast TBI models reveal that metabolic alterations within the brain are dynamic and varied by regions depending on the severity of TBI, the model used, and the time of metabolic measurements (Richards et al., 2001; Casey et al., 2008; Harris N.G. et al., 2012; Prins et al., 2013). Few studies have detected changes in ^{18}F-FDG uptake following primary blast exposure in rodents. Increased ^{18}F-FDG uptake in the whole brain, especially regions associated with executive and vestibulomotor function, on 1 day post-injury was reported, and then resolved by 9 days following blast to head (Awwad et al., 2015). Jaiswal et al. (2019) examined ^{18}F-FDG uptake in the brain by VOI- and voxel-based analysis following a single blast. Like us, they observed an acute increase in ^{18}F-FDG uptake in the amygdala and somatosensory cortex and a decrease in multiple midbrain structures at 1–3 h following blast. Interestingly, in our current study, glucose metabolism in the motor cortex was also markedly elevated from 1 to 7 days post-injury, where increased Ins and Glx levels in MRS were observed. These temporal and regional changes in glucose metabolism following blast are due to inflammation and gliosis, which were confirmed by immunohistochemistry.

The hippocampus has been reported to be the common injured region. Previous studies have shown that the hippocampus was vulnerable to controlled cortical impact (CCI)-mediated neuronal death, occurring as early as 24 h post-injury and continuing for weeks after injury (Kabadi et al., 2012; Zhou et al., 2012; Loane et al., 2014). Rats undergoing lateral fluid percussion injury (FPI) showed markedly reduced FDG uptake in the hippocampus from 1 week after FPI to 6 months. However, in this study, no significant changes were found in the hippocampus on ^{18}F-FDG PET, MRS, and immunohistochemistry from the hyperacute phase to the subacute phase. Consistent with our study, Jaiswal et al. (2019) showed no significant difference between the blast-induced mTBI group and the sham group in the hippocampus on ^{18}F-FDG PET imaging at the acute and subacute stages. Walls et al. (2016) also showed no BBB damage and colocalized neuroinflammatory changes in the hippocampus from 4 h to several days post-injury in the blast-induced TBI model. These inconsistent results may be explained by different mTBI models and detected changes at different TBI stages. Further studies are needed to investigate alterations in the chronic phase and conduct other imaging modalities following blast-induced TBI.

In our study, ^{18}F-FDG PET imaging reflects neuronal function and activity of cells including neurons and glial cells/inflammatory cells. MRS provides complementary information and assesses metabolites following injury, which can reflect the pathophysiological condition of the brain after injury indirectly, such as inflammation, ischemia, hypoxia, etc. ^{18}F-FDG PET and MRS could be used to investigate neuropathological changes after brain injury from different aspects. Therefore, combining these two imaging methods could reflect more comprehensive neuropathological alterations *in vivo* after blast-induced mTBI. In addition, ^{18}F-FDG PET provides metabolic information of the whole brain after a single scanning, while MRS offers metabolic information of one specific region. Thus, this may provide us a diagnostic strategy that ^{18}F-FDG PET could firstly be performed on mTBI patients to find the abnormal regions and to define regions of interest for MRS, which may improve the diagnostic measures and therapeutic management after mTBI.

However, our study has limitations. First, the study design does not allow direct comparisons, since MRS and ^{18}F-FDG PET were performed in two different cohorts. Second, we did not assess behavioral outcome of these animals. Future work should combine comprehensive behavioral testing with *in vivo* findings. Third, a small number of animals were used in the histological analysis. Fourth, the corpus callosum was not contained in the 58 regions of the W. Schiffer rat brain template, resulting in no information of ^{18}F-FDG uptake in the corpus callosum. Previous studies have reported that the corpus callosum is more vulnerable to injury in non-blast TBI models (Brabazon et al., 2017). However, a characteristic pattern of blast-induced mTBI has not been identified. Thus, whether there are significant metabolic changes in the corpus callosum or not remains unknown. In future studies, other software should be used for PET image analysis, and DTI, sensitive to examining axonal injury, should also be performed to detect microstructural alterations after blast exposure.

CONCLUSION

In conclusion, we demonstrate for the first time that a combination of ^{18}F-FDG PET and MRS could detect progressive changes of brain metabolism after blast-induced mTBI in hyperacute, acute, and subacute post-injury period. Combining these two imaging methods could reflect more comprehensive neuropathological alterations *in vivo* after blast-induced mTBI. These findings offer useful information in understanding the pathophysiology of blast-induced mTBI, including inflammation, gliosis, hypoxia/ischemia, and BBB disruption.

DATA AVAILABILITY STATEMENT

The original contributions presented in the study are included in the article/**Supplementary Material**, further inquiries can be directed to the corresponding authors.

ETHICS STATEMENT

The animal study was reviewed and approved by the Animal Use Subcommittee of Army Medical University.

AUTHOR CONTRIBUTIONS

XC, RJ, and KX conceived and designed the study. YL and CL established the model. YL, YG, and JZ collected and analyzed the MRI and MRS data. YT produced the PET radioligand. JS and FJ conducted the PET measurements. XC and JF analyzed the FDG PET data. HT and KL conducted and analyzed the histology. XC and KL performed the statistics, figure preparation, and wrote the manuscript. QZ edited the manuscript. All authors revised the manuscript and read and approved the submitted version.

FUNDING

This work was supported by grants from the National Natural Science Foundation of China (81801672 and 81571889), the Natural Science Foundation of Chongqing (cstc2019jcyj-msxmX0123), Science and Technology Innovation Ability Enhancement Project of Army Medical University (2019XLC3054), Talent Innovation Ability Training Program of Daping Hospital (2019CXLCC010), and Chongqing Clinical Research Centre of Imaging and Nuclear Medicine (CSTC2015YFPT-gcjsyjzx0175).

SUPPLEMENTARY MATERIAL

The Supplementary Material for this article can be found online at: https://www.frontiersin.org/articles/10.3389/fnins.2021.593723/full#supplementary-material

REFERENCES

Ashwal, S., Holshouser, B., Tong, K., Serna, T., Osterdock, R., Gross, M., et al. (2004). Proton spectroscopy detected myoinositol in children with traumatic brain injury. *Pediatr. Res.* 56, 630–638. doi: 10.1203/01.PDR.0000139928.60530.7D

Awwad, H. O., Gonzalez, L. P., Tompkins, P., Lerner, M., Brackett, D. J., Awasthi, V., et al. (2015). Blast overpressure waves induce transient anxiety and regional changes in cerebral glucose metabolism and delayed hyperarousal in rats. *Front. Neurol.* 6:132. doi: 10.3389/fneur.2015.00132

Badea, A., Kamnaksh, A., Anderson, R. J., Calabrese, E., Long, J. B., and Agoston, D. V. (2018). Repeated mild blast exposure in young adult rats results in dynamic and persistent microstructural changes in the brain. *Neuroimage Clin.* 18, 60–73. doi: 10.1016/j.nicl.2018.01.007

Bailes, J. E., and Cantu, R. C. (2001). Head injury in athletes. *Neurosurgery* 48, 26–45. doi: 10.1097/00006123-200101000-00005 discussion 45-6.,

Belanger, H. G., Vanderploeg, R. D., Curtiss, G., and Warden, D. L. (2007). Recent neuroimaging techniques in mild traumatic brain injury. *J. Neuropsychiatry Clin. Neurosci.* 19, 5–20. doi: 10.1176/jnp.2007.19.1.5

Benzinger, T. L., Brody, D., Cardin, S., Curley, K. C., Mintun, M. A., Mun, S. K., et al. (2009). Blast-related brain injury: imaging for clinical and research applications: report of the 2008 st. Louis workshop. *J. Neurotrauma* 26, 2127–2144. doi: 10.1089/neu.2009-0885

Brabazon, F., Wilson, C. M., Shukla, D. K., Mathur, S., Jaiswal, S., Bermudez, S., et al. (2017). [(18)F]FDG-PET combined with MRI elucidates the pathophysiology of traumatic brain injury in rats. *J. Neurotrauma* 34, 1074–1085. doi: 10.1089/neu.2016.4540

Byrnes, K. R., Wilson, C. M., Brabazon, F., von Leden, R., Jurgens, J. S., Oakes, T. R., et al. (2014). FDG-PET imaging in mild traumatic brain injury: a critical review. *Front. Neuroenergetics* 5:13. doi: 10.3389/fnene.2013.00013

Casey, P. A., McKenna, M. C., Fiskum, G., Saraswati, M., and Robertson, C. L. (2008). Early and sustained alterations in cerebral metabolism after traumatic brain injury in immature rats. *J. Neurotrauma* 25, 603–614. doi: 10.1089/neu.2007.0481

Croall, I. D., Cowie, C. J., He, J., Peel, A., Wood, J., Aribisala, B. S., et al. (2014). White matter correlates of cognitive dysfunction after mild traumatic brain injury. *Neurology* 83, 494–501. doi: 10.1212/WNL.0000000000000666

Delouche, A., Attye, A., Heck, O., Grand, S., Kastler, A., Lamalle, L., et al. (2016). Diffusion MRI: pitfalls, literature review and future directions of research in mild traumatic brain injury. *Eur. J. Radiol.* 85, 25–30. doi: 10.1016/j.ejrad.2015.11.004

Dienel, G. A. (2012). Brain lactate metabolism: the discoveries and the controversies. *J. Cereb. Blood Flow Metab.* 32, 1107–1138. doi: 10.1038/jcbfm.2011.175

Garnett, M. R., Corkill, R. G., Blamire, A. M., Rajagopalan, B., Manners, D. N., Young, J. D., et al. (2001). Altered cellular metabolism following traumatic brain injury: a magnetic resonance spectroscopy study. *J. Neurotrauma* 18, 231–240. doi: 10.1089/08977150151070838

Harris, J. L., Yeh, H. W., Choi, I. Y., Lee, P., Berman, N. E., Swerdlow, R. H., et al. (2012). Altered neurochemical profile after traumatic brain injury: (1)H-MRS biomarkers of pathological mechanisms. *J. Cereb. Blood Flow Metab.* 32, 2122–2134. doi: 10.1038/jcbfm.2012.114

Harris, N. G., Mironova, Y. A., Chen, S. F., Richards, H. K., and Pickard, J. D. (2012). Preventing flow-metabolism uncoupling acutely reduces axonal injury after traumatic brain injury. *J. Neurotrauma* 29, 1469–1482. doi: 10.1089/neu.2011.2161

Harris, N. G., Verley, D. R., Gutman, B. A., Thompson, P. M., Yeh, H. J., and Brown, J. A. (2016). Disconnection and hyper-connectivity underlie reorganization after TBI: a rodent functional connectomic analysis. *Exp. Neurol.* 277, 124–138. doi: 10.1016/j.expneurol.2015.12.020

Holshouser, B. A., Tong, K. A., and Ashwal, S. (2005). Proton MR spectroscopic imaging depicts diffuse axonal injury in children with traumatic brain injury. *AJNR Am. J. Neuroradiol.* 26, 1276–1285.

Honce, J. M., Nyberg, E., Jones, I., and Nagae, L. (2016). Neuroimaging of Concussion. *Phys. Med. Rehabil. Clin. N. Am.* 27, 411–428. doi: 10.1016/j.pmr.2016.01.002

Jaiswal, S., Knutsen, A. K., Wilson, C. M., Fu, A. H., Tucker, L. B., Kim, Y., et al. (2019). Mild traumatic brain injury induced by primary blast overpressure produces dynamic regional changes in [(18)F]FDG uptake. *Brain Res.* 1723:146400. doi: 10.1016/j.brainres.2019.146400

Kabadi, S. V., Stoica, B. A., Loane, D. J., Byrnes, K. R., Hanscom, M., Cabatbat, R. M., et al. (2012). Cyclin D1 gene ablation confers neuroprotection in traumatic brain injury. *J. Neurotrauma* 29, 813–827. doi: 10.1089/neu.2011.1980

Katayama, Y., Kawamata, T., Tamura, T., Hovda, D. A., Becker, D. P., and Tsubokawa, T. (1991). Calcium-dependent glutamate release concomitant with massive potassium flux during cerebral ischemia in vivo. *Brain Res.* 558, 136–140. doi: 10.1016/0006-8993(91)90730-j

Kokiko-Cochran, O. N., and Godbout, J. P. (2018). The inflammatory continuum of traumatic brain injury and Alzheimer's Disease. *Front. Immunol.* 9:672. doi: 10.3389/fimmu.2018.00672

Kulkarni, P., Morrison, T. R., Cai, X., Iriah, S., Simon, N., Sabrick, J., et al. (2019). Neuroradiological changes following single or repetitive mild TBI. *Front. Syst. Neurosci.* 13:34. doi: 10.3389/fnsys.2019.00034

Kuriakose, M., Rama Rao, K. V., Younger, D., and Chandra, N. (2018). Temporal and spatial effects of blast overpressure on blood-brain barrier permeability in traumatic brain injury. *Sci. Rep.* 8:8681. doi: 10.1038/s41598-018-26813-7

Larson, M. J., Farrer, T. J., and Clayson, P. E. (2011). Cognitive control in mild traumatic brain injury: conflict monitoring and conflict adaptation. *Int. J. Psychophysiol.* 82, 69–78. doi: 10.1016/j.ijpsycho.2011.02.018

Le, T. H., and Gean, A. D. (2009). Neuroimaging of traumatic brain injury. *Mt. Sinai J. Med.* 76, 145–162. doi: 10.1002/msj.20102

Ling, J. M., Pena, A., Yeo, R. A., Merideth, F. L., Klimaj, S., Gasparovic, C., et al. (2012). Biomarkers of increased diffusion anisotropy in semi-acute mild traumatic brain injury: a longitudinal perspective. *Brain* 135, 1281–1292. doi: 10.1093/brain/aws073

Loane, D. J., Kumar, A., Stoica, B. A., Cabatbat, R., and Faden, A. I. (2014). Progressive neurodegeneration after experimental brain trauma: association with chronic microglial activation. *J. Neuropathol. Exp. Neurol.* 73, 14–29. doi: 10.1097/NEN.0000000000000021

Maas, A. I., Stocchetti, N., and Bullock, R. (2008). Moderate and severe traumatic brain injury in adults. *Lancet Neurol.* 7, 728–741. doi: 10.1016/S1474-4422(08)70164-9

Makoroff, K. L., Cecil, K. M., Care, M., and Ball, W. S. Jr. (2005). Elevated lactate as an early marker of brain injury in inflicted traumatic brain injury. *Pediatr. Radiol.* 35, 668–676. doi: 10.1007/s00247-005-1441-7

Mayer, A. R., Ling, J., Mannell, M. V., Gasparovic, C., Phillips, J. P., Doezema, D., et al. (2010). A prospective diffusion tensor imaging study in mild traumatic brain injury. *Neurology* 74, 643–650. doi: 10.1212/WNL.0b013e3181d0ccdd

Meabon, J. S., Huber, B. R., Cross, D. J., Richards, T. L., Minoshima, S., Pagulayan, K. F., et al. (2016). Repetitive blast exposure in mice and combat veterans causes persistent cerebellar dysfunction. *Sci. Transl. Med.* 8:321ra6. doi: 10.1126/scitranslmed.aaa9585

Missault, S., Anckaerts, C., Blockx, I., Deleye, S., Van Dam, D., Barriche, N., et al. (2019). Neuroimaging of subacute brain inflammation and microstructural changes predicts long-term functional outcome after experimental traumatic brain injury. *J. Neurotrauma* 36, 768–788. doi: 10.1089/neu.2018.5704

Ning, Y. L., Yang, N., Chen, X., Tian, H. K., Zhao, Z. A., Zhang, X. Z., et al. (2019). Caffeine attenuates brain injury but increases mortality induced by high-intensity blast wave exposure. *Toxicol. Lett.* 301, 90–97. doi: 10.1016/j.toxlet.2018.11.004

Park, J. H., Hong, J. H., Lee, S. W., Ji, H. D., Jung, J. A., Yoon, K. W., et al. (2019). The effect of chronic cerebral hypoperfusion on the pathology of Alzheimer's disease: a positron emission tomography study in rats. *Sci. Rep.* 9:14102. doi: 10.1038/s41598-019-50681-4

Petronilho, F., Feier, G., de Souza, B., Guglielmi, C., Constantino, L. S., Walz, R., et al. (2010). Oxidative stress in brain according to traumatic brain injury intensity. *J. Surg. Res.* 164, 316–320. doi: 10.1016/j.jss.2009.04.031

Prins, M. L., Alexander, D., Giza, C. C., and Hovda, D. A. (2013). Repeated mild traumatic brain injury: mechanisms of cerebral vulnerability. *J. Neurotrauma* 30, 30–38. doi: 10.1089/neu.2012.2399

Richards, H. K., Simac, S., Piechnik, S., and Pickard, J. D. (2001). Uncoupling of cerebral blood flow and metabolism after cerebral contusion in the rat. *J. Cereb. Blood Flow Metab.* 21, 779–781. doi: 10.1097/00004647-200107000-00002

Ross, B. D., Ernst, T., Kreis, R., Haseler, L. J., Bayer, S., Danielsen, E., et al. (1998). 1H MRS in acute traumatic brain injury. *J. Magn. Reson. Imaging* 8, 829–840. doi: 10.1002/jmri.1880080412

Sajja, V. S., Galloway, M. P., Ghoddoussi, F., Thiruthalinathan, D., Kepsel, A., Hay, K., et al. (2012). Blast-induced neurotrauma leads to neurochemical changes and neuronal degeneration in the rat hippocampus. *NMR Biomed.* 25, 1331–1339. doi: 10.1002/nbm.2805

Salberg, S., Yamakawa, G., Christensen, J., Kolb, B., and Mychasiuk, R. (2017). Assessment of a nutritional supplement containing resveratrol, prebiotic fiber, and omega-3 fatty acids for the prevention and treatment of mild traumatic brain injury in rats. *Neuroscience* 365, 146–157. doi: 10.1016/j.neuroscience.2017.09.053

Singh, K., Trivedi, R., Verma, A., D'Souza, M. M., Koundal, S., Rana, P., et al. (2017). Altered metabolites of the rat hippocampus after mild and moderate traumatic brain injury – a combined in vivo and in vitro (1) H-MRS study. *NMR Biomed.* 30:e3764. doi: 10.1002/nbm.3764

Stocker, R. P., Cieply, M. A., Paul, B., Khan, H., Henry, L., Kontos, A. P., et al. (2014). Combat-related blast exposure and traumatic brain injury influence brain glucose metabolism during REM sleep in military veterans. *Neuroimage* 99, 207–214. doi: 10.1016/j.neuroimage.2014.05.067

Tang, S., Xu, S., Fourney, W. L., Leiste, U. H., Proctor, J. L., Fiskum, G., et al. (2017). Central nervous system changes induced by underbody blast-induced hyperacceleration: an in vivo diffusion tensor imaging and magnetic resonance spectroscopy study. *J. Neurotrauma* 34, 1972–1980. doi: 10.1089/neu.2016.4650

Vanhamme, L., van den Boogaart, A., and Van Huffel, S. (1997). Improved method for accurate and efficient quantification of MRS data with use of prior knowledge. *J. Magn. Reson.* 129, 35–43. doi: 10.1006/jmre.1997.1244

Venkatasubramanian, P. N., Keni, P., Gastfield, R., Li, L., Aksenov, D., Sherman, S. A., et al. (2020). Diffusion tensor imaging detects acute and subacute changes in corpus callosum in blast-induced traumatic brain injury. *ASN Neuro* 12:1759091420922929. doi: 10.1177/1759091420922929

Walls, M. K., Race, N., Zheng, L., Vega-Alvarez, S. M., Acosta, G., Park, J., et al. (2016). Structural and biochemical abnormalities in the absence of acute deficits in mild primary blast-induced head trauma. *J. Neurosurg.* 124, 675–686. doi: 10.3171/2015.1.JNS141571

Xu, S., Zhuo, J., Racz, J., Shi, D., Roys, S., Fiskum, G., et al. (2011). Early microstructural and metabolic changes following controlled cortical impact injury in rat: a magnetic resonance imaging and spectroscopy study. *J. Neurotrauma* 28, 2091–2102. doi: 10.1089/neu.2010.1739

Zhong, C., Zhao, X., Van, K. C., Bzdega, T., Smyth, A., Zhou, J., et al. (2006). NAAG peptidase inhibitor increases dialysate NAAG and reduces glutamate, aspartate and GABA levels in the dorsal hippocampus following fluid percussion injury in the rat. *J. Neurochem.* 97, 1015–1025. doi: 10.1111/j.1471-4159.2006.03786.x

Zhou, H., Chen, L., Gao, X., Luo, B., and Chen, J. (2012). Moderate traumatic brain injury triggers rapid necrotic death of immature neurons in the hippocampus. *J. Neuropathol. Exp. Neurol.* 71, 348–359. doi: 10.1097/NEN.0b013e31824ea078

Zhuo, J., Keledjian, K., Xu, S., Pampori, A., Gerzanich, V., Simard, J. M., et al. (2015). Changes in diffusion kurtosis imaging and magnetic resonance spectroscopy in a direct cranial blast traumatic brain injury (dc-bTBI) model. *PLoS One* 10:e0136151. doi: 10.1371/journal.pone.0136151

Conflict of Interest: The reviewer CZ declared a past co-authorship with one of the author FJ to the handling editor.

The remaining authors declare that the research was conducted in the absence of any commercial or financial relationships that could be construed as a potential conflict of interest.

frontiers in Psychiatry

ORIGINAL RESEARCH
published: 26 March 2021
doi: 10.3389/fpsyt.2021.634299

Abnormal Large-Scale Network Activation Present in Bipolar Mania and Bipolar Depression Under Resting State

Can Zeng[1,2], *Brendan Ross*[3], *Zhimin Xue*[1,2], *Xiaojun Huang*[1,2], *Guowei Wu*[1,2], *Zhening Liu*[1,2], *Haojuan Tao*[1,2]* *and Weidan Pu*[4]*

[1] Department of Psychiatry, The Second Xiangya Hospital, Central South University, Changsha, China, [2] The China National Clinical Research Center for Mental Health Disorders, Changsha, China, [3] McGill Faculty of Medicine, Montreal, QC, Canada, [4] Medical Psychological Institute, The Second Xiangya Hospital, Central South University, Changsha, China

Introduction: Previous studies have primarily focused on the neuropathological mechanisms of the emotional circuit present in bipolar mania and bipolar depression. Recent studies applying resting-state functional magnetic resonance imaging (fMRI) have raise the possibility of examining brain-wide networks abnormality between the two oppositional emotion states, thus this study aimed to characterize the different functional architecture represented in mania and depression by employing group-independent component analysis (gICA).

Materials and Methods: Forty-one bipolar depressive patients, 20 bipolar manic patients, and 40 healthy controls (HCs) were recruited and received resting-state fMRI scans. Group-independent component analysis was applied to the brain network functional connectivity analysis. Then, we calculated the correlation between the value of between-group differences and clinical variables.

Results: Group-independent component analysis identified 15 components in all subjects, and ANOVA showed that functional connectivity (FC) differed significantly in the default mode network, central executive network, and frontoparietal network across the three groups. Further *post-hoc t*-tests showed a gradient descent of activity—depression > HC > mania—in all three networks, with the differences between depression and HCs, as well as between depression and mania, surviving after family wise error (FWE) correction. Moreover, central executive network and frontoparietal network activities were positively correlated with Hamilton depression rating scale (HAMD) scores and negatively correlated with Young manic rating scale (YMRS) scores.

Conclusions: Three brain networks heighten activity in depression, but not mania; and the discrepancy regions mainly located in prefrontal, which may imply that the differences in cognition and emotion between the two states is associated with top–down regulation in task-independent networks.

Keywords: bipolar mania, bipolar depression, group independent component analysis, resting state fMRI, brain image

OPEN ACCESS

Edited by:
Nicola Toschi,
University of Rome Tor Vergata, Italy

Reviewed by:
Zhifen Liu,
First Hospital of Shanxi Medical University, China
Gemma C. Monté-Rubio,
University of Barcelona, Spain

***Correspondence:**
Haojuan Tao
taohaojuan@163.com
Weidan Pu
weidanpu@csu.edu.cn

Specialty section:
This article was submitted to Neuroimaging and Stimulation, a section of the journal Frontiers in Psychiatry

Received: *10 December 2020*
Accepted: *16 February 2021*
Published: *26 March 2021*

Citation:
Zeng C, Ross B, Xue Z, Huang X, Wu G, Liu Z, Tao H and Pu W (2021) Abnormal Large-Scale Network Activation Present in Bipolar Mania and Bipolar Depression Under Resting State. Front. Psychiatry 12:634299. doi: 10.3389/fpsyt.2021.634299

INTRODUCTION

Bipolar disorder (BD) is a common severe psychiatric disorder with two opposite states, depression, and mania, which can occur in repeating or alternating episodes. Patients experiencing a manic episode are optimistic and show an increase in goal-directed activity (1), whereas those in a depressive episode are downhearted, pessimistic, and oriented toward internal thoughts (2–5), implying that different neuropathological underpinnings likely produce these overtly clinical distinctions. Thus, the identification of pathophysiologic biomarkers that differ between bipolar depression and bipolar manic can both inform dynamic change of BD and provide biological targets for the development of personalized treatments.

Previous studies have often performed emotional face-recognition tasks to examine the neuropathological mechanisms driving mania and depression (6–13), which have particularly involved a so-called "emotional circuit" that comprised the limbic structures (such as the amygdala, insula, anterior cingulate cortex) and prefrontal cortex including the medial prefrontal cortex (mPFC) and orbital frontal cortex (OFC) (14–18). Frontal hypofunction, for example, may provide a shared neural basis for mania and depression, and studies have consistently found decreased frontal activation or hypoconnectivity across mood states during tasks (11, 19–21), suggesting weakened top–down regulation. However, the amygdala, a key facet of emotional processing, exhibits inconsistent activation or functional connectivity (FC) that varies across the experimental paradigms and BD phases (7, 8, 11, 14, 22), with some studies finding increased amygdala activity, whereas others have found decreased activity. Research has suggested that the highs and lows of amygdala activity may be a state-dependent phenomenon caused by trait-like hypoactivation of regulatory frontal regions in BDs (9), but others have proposed that the amygdala fluctuations were affected by medication use or different emotional recognition tasks (e.g., sad, happy, fear face) (11).

These task-based functional magnetic resonance imaging (fMRI) studies have lent deep insight into the neuropathology of BD, particularly the role of an abnormal corticolimbic circuit; however, constrained by the limited emotion activation that one task can probe, our understanding of BD-related brain functional alteration remains fragmented. Fortunately, resting-state fMRI offers a unique opportunity to inspect the brain-wide functional architecture. To date, studies have characterized the neuropathology of manic or depressive states separately, but very few studies have used resting-state fMRI to examine differences or changes between the two states (1, 23–25). What should be noted is that these resting-state fMRI studies have mostly focused on circumscribed regions, such as the amygdala or striatal to mapping the abnormal brain function connectivity. Only one study examined the abnormal topographical balance between two specified networks (1). However, the brain cannot be fully understood by topographical characterization alone as it works as a complex system of interacting subsystems; therefore, mapping the whole brain large-scale networks may help to identify any difference in abnormality between mania and depression and thus will deepen our understanding of BD.

In this study, by applying a holistic brain-wide functional connectivity analysis of resting-state fMRI data, we aimed to investigate the different neural correlates of bipolar mania and depression in the resting state. This study compared the neuroimaging findings between bipolar mania, bipolar depression, and healthy controls (HCs) using the method of group-independent component analysis (gICA). Group-independent component analysis can separate independent "sources," mainly those in the spatial dimension that have been mixed, and as a result, it resists the skewing of results due to researchers' assumptions (26). Additionally, the relationship between the blood oxygen level-dependent (BOLD) signal of intrinsic networks (INs) and clinical scales, namely, the Hamilton Depressive Rating Scale (HAMD) and Young Mania Rating Scale (YMRS), was explored as well.

MATERIALS AND METHODS

Subjects

The patients including 41 bipolar depressive patients and 20 bipolar manic patients were recruited from outpatient and inpatient settings; most of the manic (18/20) and depressive subjects (31/41) were recruited from inpatient settings, whereas the remainder were outpatients. All patients were currently experiencing an episode and met the diagnostic criteria for the Structured Clinical Interview–Patient Version of the *Diagnostic and Statistical Manual of Mental Disorders, Fourth Edition* (SCID-I/P). Forty-two age- and sex-matched HCs were recruited from the community and met the diagnostic criteria of SCID Non-Patient confirming that neither them nor their first-degree relatives had any psychiatric disorders. The inclusion criteria for all the subjects were as follows: (a) aged 18–60 years, (b) right-handed, (c) received at least 9 years of education [due to the influence of education level on the brain function (27)]. And for the bipolar depressive patients, the HAMD score was $\geq$17, and YMRS score $\leq$6; and for bipolar manic patients, the YMRS score was $\geq$12, and HAMD score $\leq$7. Exclusion criteria included (a) other psychiatric disorder or significant physical illness, personality disorder, intellectual disability or substance dependence (except tobacco); (b) recent electric shock treatment; and (c) alcohol or benzodiazepines taken 24 h before the interview and fMRI.

All the patients were recruited at the Second Xiangya Hospital of Central South University, were provided information about the procedures, and signed the informed consent. The study was approved by the ethics committee of Xiangya.

Scan Acquisition and Data Preprocessing

All fMRI data were obtained using a Philips Gyroscan Achieva 3.0-T scanner (36 slices, repetition time = 2,000 ms, matrix = 64 × 64, echo time = 30 ms, flip angle = 90°, slice thickness = 4 mm, gap = 0 mm). Each subject was scanned 250 volumes, and the whole brain was effectively covered. When scanning, subjects were asked to close their eyes and remain calm without

excessive thinking. Head motion was strictly restricted; motion beyond 2.5 mm was discarded, and seven subjects' data were excluded for this reason. We also performed "scrubbing" to make sure that head-motion artifacts did not influence the observed effects. An assessment of head motion at each time point was computed as the frame-wise displacement (FD). Consistent with previous studies (28), any image with FD >0.5 was discarded and replaced with a linear interpolation. The mean absolute FD across the three groups did not differ significantly [mean HC: 0.145, (SD = 0.053), mean bipolar depression: 0.144 (SD = 0.079), mean bipolar mania: 0.181 (SD = 0.102)]. The data were preprocessed by DPARSF (29). The first 10 volumes were removed to allow scanner calibration and subjects' adaptation to the environment, and the remaining 240 volumes were processed by SPM8 (University College London, UK; http://www.fil.ion.ucl.ac.uk/spm). During preprocessing, the images were spatially normalized to a standard template (Montreal Neurological Institute) and resampled to 4 × 4 × 4-mm voxels, with standard parameters adopted throughout the preprocessing. Then, images were smoothed with an isotropic Gaussian kernel, the full-width at half maximum = 8 mm. Finally, the processed data were further temporally bandpass filtered (0.01–0.08 Hz) and linearly detrended to reduce the influence of low-frequency drifts and physiological high-frequency noise.

Independent Component Analysis

Spatial ICA was directed with resting-state fMRI data from all 103 participants using the Informix algorithm with the Group ICA of the fMRI Toolbox (GIFT) software (Medical Image Analysis Lab, University of New Mexico, Albuquerque, NM, USA; http://icatb.sourceforge.net/) (29); this exact model has also been used in our prior work (30–32). According to the regular minimum description length criteria tool, 35 spatial independent components (ICs) were determined. With principal component analysis, dimensions of the functional data were then reduced (26, 33), followed by an IC assessment by the Informix algorithm that generated spatial maps and time courses. Assessed ICs at the group level were then back-reconstructed for each participant established in principal component analysis compression and projection (26, 34), and each estimated component received subject-specific spatial maps and time courses. This specific back-reconstruction of the GIFT algorithm permits simultaneous analysis of all of the participants as part of a large ICA group matrix (34). Therefore, for each IC, the time courses of each component represented a pattern of synchronized brain activity, whose coherency pattern across voxels was represented in the related spatial map. And to exhibit voxels relevant to a particular IC, the intensity values were converted to z values in each map.

Identifying Resting State Networks

To identify valid resting state networks, the standard method of rejecting artifacts was adopted. First, an experienced researcher examined the network components visually to eliminate those clearly representing artifacts and then correlated spatially with a priori probabilistic gray-matter, white-matter, and cerebrospinal-fluid (CSF) templates using multiple regression in SPM8. Components having high association ($|\beta| > 2$) with CSF and white matter and low association ($|\beta| < 0.5$) with gray matter were removed (35). Finally, 20 components were removed as noise, and 15 valid components remained (see the Supplementary Materials **Figure 1S**). To make sure that only highly correlated brain regions were analyzed, we employed an explicit mask created by a voxel-wise one-sample t-test ($p < 0.05$ with family wise error (FWE) correction at voxel level).

Statistical Analysis

The SPM8 software was applied to the statistical analysis on fMRI data. After valid ICs were identified, by including the age as the covariate, one-way analysis of covariance (ACOVA) was performed with group as the control variable and BOLD signal of each IC as the observable variable to compare the FC differences among three groups, which is masked with the results from one-sample t-tests. An initial statistical threshold was set at $p < 0.05$ with FWE correction at the cluster level ($k > 40$) and uncorrected $p < 0.001$ at the voxel level. Further pairwise comparisons, including age as the covariate as well, were conducted using the mask involving the regions with significant differences in ACOVA. The statistical threshold for significance was also set at $p < 0.05$ with FWE correction at the cluster level ($k > 40$) and uncorrected $p < 0.001$ at the voxel level. By using REST (http://resting-fmri.sourceforge.net) (36), we extracted the BOLD signals of ICs exhibiting significant differences across the three groups with YMRS scores and HAMD scores using Pearson correlation ($p < 0.05$), including age as covariate. Considering bipolar depression and bipolar mania are two internally related and continuum-like states of one disorder, we merged two patient groups together to compute correlation.

RESULTS

Demographic and Clinical Characteristics

Demographic and clinical characteristics of the three groups are shown in **Table 1**. There is no significant difference in age, sex, age at illness onset, or illness duration across the three groups. Given that age produced marginal significance and antipsychotic use produced significant difference between patient groups, we included them as covariates in further analysis.

Distinct Regions From Intrinsic Networks

After performing one-way ANOVA analysis across the three groups for the remaining 15 valid ICs, three INs, including the DMN (IC7, IC33), frontoparietal network (FPN) (IC25), and central executive network (CEN) (IC26), showed significant differences (**Figure 1**). The locations with significant differences in each network were the left orbit inferior frontal gyrus for IC25 (**Figure 2**), right triangle inferior frontal gyrus for IC26, and the left frontal superior medial gyrus and right superior temporal for the DMN (IC7 and IC33), respectively (**Table 2**).

Further *post-hoc* testing found that the activity of these four regions showed a decline in activity trending across the three groups (depression > HC > mania). Except for the difference between the mania group and HC (at an uncorrected $p < 0.001$ level), differences of FC within four regions between depression

TABLE 1 | Subjects demographic and clinical characteristics.

	BD-D ($n = 41$)	BD-M ($n = 20$)	HC ($n = 42$)	$F/\chi^2/t$	P
Age, mean (SD) (years)	26.7(7.11)	28.1(8.13)	24.07(4.8)	2.793	0.066
Male	17	7	22	1.614	0.446
Female	24	13	20		
YMRS	1.95	23.7	—	−19.61**	0.00
HAMD	20.8	4.2	—	13.76**	0.00
Unmedicated (*n*)	7/41	4/20		0.078	0.519
Antipsychotics (*n*)	22/41	15/20		36.83**	0.00
Duration at onset (months)	55	73.8	—	2.335	0.316
Age at onset (years)	22.1	22.05	—	0.726	0.95

*BD-D, bipolar depression; BD-M, bipolar mania; HC, healthy control; YMRS, Young Manic Rating Scale; HAMD, Hamilton Depression Scale. *P < 0.05, **P < 0.01.*

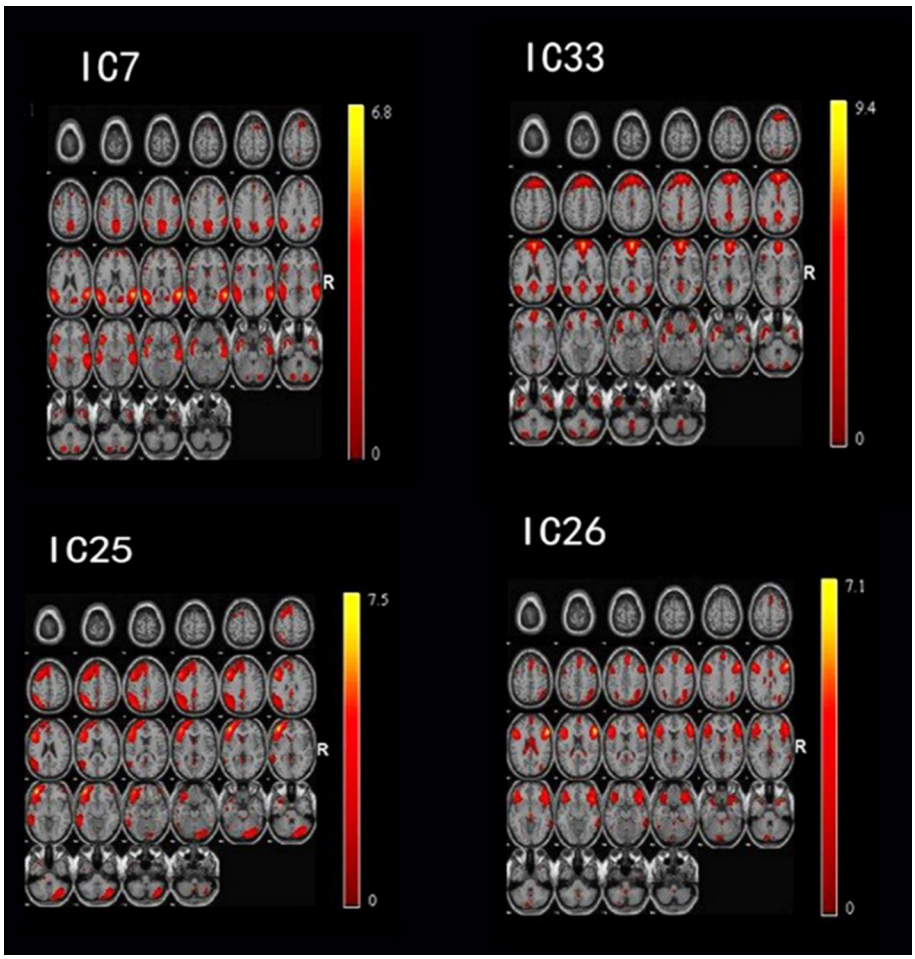

FIGURE 1 | By using the method of gICA, three intrinsic networks, including the default mode network (DMN) located at the IC7 and IC33, frontoparietal network (FPN) located at the IC25, and central executive network (CEN) located at the IC26, showed significant activity differences across healthy controls, bipolar depressive and bipolar manic patients.

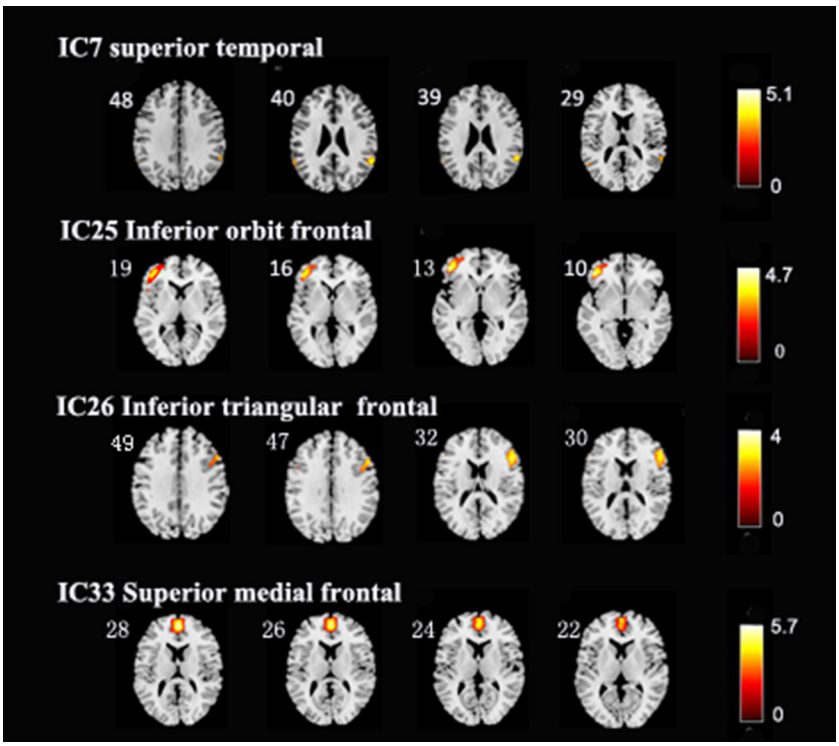

FIGURE 2 | In the three intrinsic networks, four regions, namely, inferior orbit frontal gyrus (L) in frontoparietal network (IC25), triangle inferior frontal gyrus(R) in central executive network (IC26), superior temporal (R), and frontal superior medial gyrus (L) in the default mode network (IC7, IC33) showed significant activity discrepancy across three groups (FWE, $p < 0.05$ corrected).

TABLE 2 | Distinct regions extracted from brain intrinsic networks.

IC	AAL region (L/R)	Voxel size	MNI coordinate (*x,y,z*)
IC7 (default mode network)	Superior temporal (R)	41	54, −51, 21
IC33 (default mode network)	Frontal superior medial gyrus (L)	80	−6, 45, 45
IC25 (frontoparietal network)	Orbit inferior frontal (L)	77	−45, 36, −15
IC26 (central executive network)	Triangle inferior frontal (R)	126	54, 24, 15

R, right, L, left; IC, independent component; MNI, Montreal Neurological Institute; AAL, anatomical automatic labeling.

TABLE 3 | *post-hoc* t-testing of the four brain regions.

Brain region	BD-D VS. BD-M	BD-D VS. HC
(IC25) orbit inferior frontal gyrus (L)	$t = 5.15$, $P_{FWE} = 0.011$*	$t = 4.61$, $P_{FWE} = 0.048$*
(IC26) triangle inferior frontal gyrus (R)	$t = 5.34$, $P_{FWE} = 0.003$**	$t = 4.91$, $P_{FWE} = 0.009$**
(IC33) frontal superior medial gyrus (L)	$t = 5.35$, $P_{FWE} = 0.005$**	$t = 4.55$, $P_{FWE} = 0.062$
(IC7) superior temporal (R)	$t = 4.72$, $P_{FWE} = 0.028$*	$t = 4.57$, $P_{FWE} = 0.035$*

*BD-D, bipolar depression, BD-M, bipolar mania, HC, healthy control; L, left; R, right. *P < 0.05, **P < 0.01.*

and HC, as well as between depression and mania, all survived after FWE correction ($p < 0.05$) (**Table 3**).

Correlation Between Intrinsic Networks and Clinical Features

Correlation analysis showed that the BOLD signal of the FPN has significant positive association with HAMD score ($r = 0.486$, $p < 0.01$) and significant negative correlation with YMRS ($r = -0.552$, $p < 0.01$). Similar correlation was found for CEN, positive association with HAMD score ($r = 0.535$, $p < 0.01$), and significant negative correlation with YMRS ($r = -0.578$, $p < 0.01$), but no significant correlation was found with the DMN.

DISCUSSION

This study aimed to explore the distinct alterations of large-scale brain networks between bipolar manic and depressive phases and found that there were three large-scale networks, including the

DMN, FPN, and CEN, presenting a gradient of declining activity from depression to mania, with higher activity in depression and lower activity in mania (depression > HC > mania). Further, the BOLD signal of the FPN and CEN both presented a positive correlation with HAMD, but a negative correlation with YMRS.

The DMN, including the mPFC, precuneus, posterior cingulate cortex, inferior parietal cortex, and hippocampus, has attracted extensive attention in this field (37, 38). This network is suggested to activate in the resting state and is involved in self-referential and introspective thought (39–41). Researchers had consistently found that it maintained hyperconnectivity in depressive patients (32, 42), but was inconsistently activated in mania, showing decreased connectivity or no significant difference (43, 44). Interestingly, this study found that the DMN, particularly the mPFC, displayed increased activity in bipolar depressive patients, but decreased in bipolar manic patients. The mPFC has been proposed to subserve attentional modulation on self-relevant information such as recalling autobiographical memory and episodic future thought related to oneself (45–47); therefore, a possible mechanism for the DMN being implicated in BD may be best explained by understanding from depression and mania, respectively. Patients in the depressive episode may be consumed by overly pessimistic thoughts about themselves in the past and future, which relates to hyperfunction of the DMN. In contrast, patients in the manic episode are easily drawn from their own attention to external environmental irrelevant stimuli instead of self-relevant stimuli, finally leading to the decreased activation of the DMN.

The FPN showed significantly greater activation discrepancy among the three groups. Earlier studies suggested that the FPN is associated with cognitive and executive control processes during goal-directed behavior (48–50), However, other studies also showed that the FP engages in self-referential tasks (i.e., recollecting one's past or imagining one's personal future), coupled with the DMN functioning as a mediator (51). Further, it has been documented that BD patients in depressive episodes often perform mental work to defensively ward off negative cognition about themselves (52), such as avoiding feelings of failure and uselessness; thus, overactivation of the FPN possibly serves a compensatory role in cognition for depressive patients. Anatomically, the OFC is a core region of the prefrontal cortex and is one of the regions most tightly connected with the amygdala and other subcortical limbic structures relevant to emotion (53, 54), implicating its role in emotion regulation. Numerous studies have shown that the metabolism, neurons, glial cell density, and gray matter volume of the OFC have significant alterations in major depressive disorder (MDD) (55–57). In particular, effective treatment for MDD often decreases the hyperfunction of OFC (58), suggesting that greater activation of the OFC may lead to excessive inhibition of emotion. In contrast, mania patients show decreased activation of the OFC or ventrolateral prefrontal (VLPFC) during the resting state (14, 59), which has been proposed to result in decreased inhibition of emotion in mania patients. Therefore, dysfunction of the OFC may lead to inappropriate emotional responses to changes in internal stimuli and environmental contexts (59), ultimately resulting in manic or depressive episodes.

The CEN also shows activation discrepancy across the three groups in the right triangular inferior frontal gyrus. The network is mainly composed of multiple prefrontal cortex regions and the lateral posterior cingulate cortex, which shows strong cooperative activation in a wide range of cognitively demanding tasks (60), actively participating in maintaining and managing information in working memory, solving rule-based problems, and making decisions in goal-directed behavior (61). Furthermore, some studies found that the CEN plays an important role in processing task-related information and suppressing the interference of irrelevant information (62). Deficits in these processes are characteristic of many major mental disorders and neurological disorders including BD, MDD, schizophrenia, and autism—they have all displayed dysfunction of the CEN (63, 64). In this network, we found that the triangular inferior frontal gyrus was abnormally activated in both states; thus, this region is suggested to be pertinent to reactive inhibition. Clinical studies from attention-deficit/hyperactivity disorder or substance-dependence patients with reactive inhibition deficits showed right inferior frontal cortex dysconnectivity during inhibitory tasks (64). Furthermore, a study also found that the degree of depression significantly correlated with the activation of the inferior frontal gyrus during a Go/No-Go task (65), suggesting that the inferior frontal gyrus affects the individual's level of cognitive inhibition in depression. Similar to the findings of OFC in the FPN relevant to the emotional suppression, this study also found increased IFG activation in depressive patients but decreased IFG activation in mania patients, suggesting the excessive cognition inhibition (such as memory deficit and lower thought speed) in depression and deficient cognition inhibition in mania (such as distractibility and racing thoughts). Consistent with this notion, our further partial correlation analysis found that greater activity in both FPN and CEN related to more severe depressive symptoms, whereas lower activity in two networks related to more severe manic symptoms.

Several limitations should be noted in the present study. First, medication may have been a confounding factor in our findings. Nearly all patients in the study were taking medications; mood stabilizers were used by most patients, and other medications (such as antidepressants, antipsychotics, and benzodiazepines) were also used according to patients' clinical performance. Future studies in drug-naive BD patients are warranted to verify the findings in our study. Second, the differences of the three networks between the bipolar mania patients and HCs did not survive after multiple corrections in our study, which may be due to the relatively small sample size of mania patients; thus, our findings on the decreased activity in three large-scale brain networks in mania patients should be replicated in future studies with larger sample size. Third, the study is a cross-sectional design, which limited us to explore the dynamic changes between depression and mania in BD patients, and further longitudinal studies with medical free patients are needed to clarify the dynamic transformation.

CONCLUSIONS

We compared whole-brain networks across bipolar depression and bipolar manic patients and HCs and by using the method of gICA, we found differences mainly in the core intrinsic brain networks across the DMN, FPN, and CEN. The discrepancy between bipolar mania and bipolar depression may be associated with top–down regulation in task-independent networks, which may underlie the differences in cognition and emotion between the two states.

DATA AVAILABILITY STATEMENT

The original contributions presented in the study are included in the article/**Supplementary Material**, further inquiries can be directed to the corresponding author/s.

ETHICS STATEMENT

The studies involving human participants were reviewed and approved by The ethics committee of Xiangya: beisha tang, huihuan tang, xiaoxia zuo, long mo, yuexiang lv, yixiong li, haihe jiang, jianping ning, shifang peng, meizuo zhong, yi shen, lu shen, yinglan li, wenen liu, runhua li, and tao yao. The patients/participants provided their written informed consent to participate in this study.

AUTHOR CONTRIBUTIONS

CZ wrote the main manuscript text, BR and ZL edited language, WP and ZX designed the experiments. XH and GW helped to analyzing data. HT revised the manuscript. All authors contributed to the article and approved the submitted version.

FUNDING

This study was supported by the China Precision Medicine Initiative (Grant Number: 2016YFC0906300), the National Natural Science Foundation of China (Grant Numbers: 81561168021, 81671335, 81701325, 81801353), and the Natural Science Foundation of Hunan Province, China (Grant Number: 2019JJ50848).

ACKNOWLEDGMENTS

We thank the BD patients who agreed to participate in this study, and thanks Ling Jing and OX very much for her help in revising the paper.

SUPPLEMENTARY MATERIAL

The Supplementary Material for this article can be found online at: https://www.frontiersin.org/articles/10.3389/fpsyt.2021.634299/full#supplementary-material

REFERENCES

1. Martino M, Magioncalda P, Huang Z, Conio B, Piaggio N, Duncan NW, et al. Contrasting variability patterns in the default mode and sensorimotor networks balance in bipolar depression and mania. *Proc Natl Acad Sci USA*. (2016) 113:201517558. doi: 10.1073/pnas.1517558113
2. Northoff G. Spatiotemporal psychopathology II: how does a psychopathology of the brain's resting state look like? Spatiotemporal approach and the history of psychopathology. *J Affect Disord*. (2015) 190:867. doi: 10.1016/j.jad.2015.05.008
3. Northoff G. Psychopathology and pathophysiology of the self in depression - neuropsychiatric hypothesis. *J Affect Disord*. (2007) 104:1–14. doi: 10.1016/j.jad.2007.02.012
4. Nolen-Hoeksema S, Wisco BE, Lyubomirsky S. Rethinking rumination. *Perspect Psychol Sci*. (2008) 3:400–24. doi: 10.1111/j.1745-6924.2008.00088.x
5. Northoff G. Spatiotemporal psychopathology I: no rest for the brain's resting state activity in depression? Spatiotemporal psychopathology of depressive symptoms. *J Affect Disord*. (2016) 190:854-66. doi: 10.1016/j.jad.2015.05.007
6. Marchand WR, Lee JN, Johnson S, Gale P, Thatcher J. Abnormal functional connectivity of the medial cortex in euthymic bipolar II disorder. *Progr Neuropsychopharmacol Biol Psychiatry*. (2014) 51:28–33. doi: 10.1016/j.pnpbp.2014.01.004
7. Perlman SB, Almeida JR, Kronhaus DM, Versace A, Labarbara EJ, Klein CR, et al. Amygdala activity and prefrontal cortex-amygdala effective connectivity to emerging emotional faces distinguish remitted and depressed mood states in bipolar disorder. *Bipolar Disord*. (2012) 14:162–74. doi: 10.1111/j.1399-5618.2012.00999.x
8. Radaelli D, Sferrazza PG, Vai B, Poletti S, Smeraldi E, Colombo C, et al. Fronto-limbic disconnection in bipolar disorder. *Eur Psychiatry*. (2015) 30:82–8. doi: 10.1016/j.eurpsy.2014.04.001
9. Hariri AR. The highs and lows of amygdala reactivity in bipolar disorders. *Amer J Psychiatry*. (2012) 169:780–3. doi: 10.1176/appi.ajp.2012.12050639
10. Cerullo MA, Fleck DE, Eliassen JC, Smith MS, Delbello MP, Adler CM, et al. A longitudinal functional connectivity analysis of the amygdala in bipolar I disorder across mood states. *Bipolar Disord*. (2012) 14:175–84. doi: 10.1111/j.1399-5618.2012.01002.x
11. Nathalie V, Rudie JD, Townsend JD, Salvatore T, Moody TD, Bookheimer SY, et al. Regional fMRI hypoactivation and altered functional connectivity during emotion processing in nonmedicated depressed patients with bipolar II disorder. *Am J Psychiatry*. (2012) 169:831–40. doi: 10.1176/appi.ajp.2012.11030349
12. Foland LC, Altshuler LL, Bookheimer SY, Naomi E, Jennifer T, Thompson PM. Evidence for deficient modulation of amygdala response by prefrontal cortex in bipolar mania. *Psychiatry Res Neuroimaging*. (2008) 162:27–37. doi: 10.1016/j.pscychresns.2007.04.007
13. Horacek J, Mikolas P, Tintera J, Novak T, Palenicek T, Brunovsky M, et al. Sad mood induction has an opposite effect on amygdala response to emotional stimuli in euthymic patients with bipolar disorder and healthy controls. *J Psychiatry Neurosci*. (2015) 40:134–42. doi: 10.1503/jpn.140044
14. Keri M, Schloesser RJ, Manji HK. Bipolar disorder: from genes to behavior pathways. *J Clin Investig*. (2009) 119:726–36. doi: 10.1172/JCI37703
15. Phillips ML, Swartz HA. A critical appraisal of neuroimaging studies of bipolar disorder: toward a new conceptualization of underlying neural circuitry and a road map for future research. *Amer J Psychiatry*. (2014) 171:829. doi: 10.1176/appi.ajp.2014.13081008
16. Strakowski SM, Delbello MP, Adler CM. The functional neuroanatomy of bipolar disorder: a review of neuroimaging findings. *Mol Psychiatry*. (2005) 10:105–16. doi: 10.1038/sj.mp.4001585
17. Vai B, Bertocchi C, Benedetti F. Cortico-limbic connectivity as a possible biomarker for bipolar disorder: where are we now? *Expert Rev Neurotherapeut*. (2019) 19:159–72. doi: 10.1080/14737175.2019.1562338

18. de Sá AS, Campos C, Rocha NB, Yuan TF, Paes F, Arias-Carrión O, et al. Neurobiology of bipolar disorder: abnormalities on cognitive and cortical functioning and biomarker levels. *CNS Neurol Disord Drug Targets*. (2016) 15:713–22. doi: 10.2174/1871527315666160321111359
19. Strakowski SM, Eliassen JC, Lamy M, Cerullo MA, Allendorfer JB, Madore M, et al. Functional magnetic resonance imaging brain activation in bipolar mania: evidence for disruption of the ventrolateral prefrontal-amygdala emotional pathway. *Biol Psychiatry*. (2011) 69:381–8. doi: 10.1016/j.biopsych.2010.09.019
20. Altshuler L, Bookheimer S, Townsend J, Proenza MA, Sabb F, Mintz J, et al. Regional brain changes in bipolar I depression: a functional magnetic resonance imaging study. *Bipolar Disord*. (2008) 10:708–17. doi: 10.1111/j.1399-5618.2008.00617.x
21. Townsend JD, Bookheimer SY, Foland-Ross LC, Moody TD, Eisenberger NI, Fischer JS, et al. Deficits in inferior frontal cortex activation in euthymic bipolar disorder patients during a response inhibition task. *Bipolar Disord*. (2012) 14:442–50. doi: 10.1111/j.1399-5618.2012.01020.x
22. Brady RO, Jr, Margolis A, Masters GA, Keshavan M, Öngür D. Bipolar mood state reflected in cortico-amygdala resting state connectivity: a cohort and longitudinal study. *J Affect Disord*. (2017) 217:205–9. doi: 10.1016/j.jad.2017.03.043
23. Altinay MI, Hulvershorn LA, Karne H, Beall EB, Anand A. Differential resting-state functional connectivity of striatal subregions in bipolar depression and hypomania. *Brain Connect*. (2016) 6:255–65. doi: 10.1089/brain.2015.0396
24. Li M, Huang C, Deng W, Ma X, Han Y, Wang Q, et al. Contrasting and convergent patterns of amygdala connectivity in mania and depression: a resting-state study. *J Affect Disord*. (2015) 173:53–8. doi: 10.1016/j.jad.2014.10.044
25. Spielberg JM, Beall EB, Hulvershorn LA, Altinay M, Karne H, Anand A. Resting state brain network disturbances related to hypomania and depression in medication-free bipolar disorder. *Neuropsychopharmacology*. (2016) 41:3016–24. doi: 10.1038/npp.2016.112
26. Calhoun VD, Adali T, Pearlson GD, Pekar JJ. A method for making group inferences from functional MRI data using independent component analysis. *Hum Brain Mapp*. (2001) 14:140–51. doi: 10.1002/hbm.1048
27. Jolles DD, Crone EA. Training the developing brain: a neurocognitive perspective. *Front Hum Neurosci*. (2012) 6:76. doi: 10.3389/fnhum.2012.00076
28. Power JD, Barnes KA, Snyder AZ, Schlaggar BL, Petersen SE. Spurious but systematic correlations in functional connectivity MRI networks arise from subject motion. *Neuroimage*. (2012) 59:2142–54. doi: 10.1016/j.neuroimage.2011.10.018
29. Yan CG, Zang YF. DPARSF: a MATLAB toolbox for "pipeline" data analysis of resting-state fMRI. *Front Syst Neurosci*. (2010) 4:13. doi: 10.3389/fnsys.2010.00013
30. Pu W, Luo Q, Jiang Y, Gao Y, Ming Q, Yao S. Alterations of brain functional architecture associated with psychopathic traits in male adolescents with conduct disorder. *Sci Rep*. (2017) 7:11349. doi: 10.1038/s41598-017-11775-z
31. Zhou L, Pu W, Wang J, Liu H, Wu G, Liu C, et al. Inefficient DMN suppression in schizophrenia patients with impaired cognitive function but not patients with preserved cognitive function. *Sci Rep*. (2016) 6:21657. doi: 10.1038/srep21657
32. Zhu X, Wang X, Xiao J, Liao J, Zhong M, Wang W, et al. Evidence of a dissociation pattern in resting-state default mode network connectivity in first-episode, treatment-naive major depression patients. *Biol Psychiatry*. (2012) 71:611–7. doi: 10.1016/j.biopsych.2011.10.035
33. Calhoun VD, Adali T, Pearlson GD, Pekar JJ. Spatial and temporal independent component analysis of functional MRI data containing a pair of task-related waveforms. *Hum Brain Mapp*. (2010) 13:43–53. doi: 10.1002/hbm.1024
34. Khadka S, Meda SA, Stevens MC, Glahn DC, Calhoun VD, Sweeney JA, et al. Is aberrant functional connectivity a psychosis endophenotype? A resting state functional magnetic resonance imaging study. *Biol Psychiatry*. (2013) 74:458–66. doi: 10.1016/j.biopsych.2013.04.024
35. Meda SA, Gill A, Stevens MC, Lorenzoni RP, Glahn DC, Calhoun VD, et al. Differences in resting-state functional magnetic resonance imaging functional network connectivity between schizophrenia and psychotic bipolar probands and their unaffected first-degree relatives. *Biol Psychiatry*. (2012) 71:881–9. doi: 10.1016/j.biopsych.2012.01.025
36. Song XW, Dong ZY, Long XY, Li SF, Zuo XN, Zhu CZ, et al. REST: a toolkit for resting-state functional magnetic resonance imaging data processing. *PLoS ONE*. (2011) 6:e25031. doi: 10.1371/journal.pone.0025031
37. Martino M, Magioncalda P, Saiote C, Conio B, Escelsior A, Rocchi G, et al. Abnormal functional–structural cingulum connectivity in mania: combined functional magnetic resonance imaging-diffusion tensor imaging investigation in different phases of bipolar disorder. *Acta Psychiatr Scand*. (2016) 134:339–49. doi: 10.1111/acps.12596
38. Ongur D, Lundy M, Greenhouse I, Shinn AK, Menon V, Cohen BM, et al. Default mode network abnormalities in bipolar disorder and schizophrenia. *Psychiatry Res*. (2010) 183:59–68. doi: 10.1016/j.pscychresns.2010.04.008
39. Mason MF, Norton MI, Horn JD, Van, Wegner DM, Grafton ST, C Neil M. Wandering minds: the default network and stimulus-independent thought. *Science*. (2007) 315:393–5. doi: 10.1126/science.1131295
40. Ralchle ME, Snyder AZ. A default mode of brain function: a brief history of an evolving idea. *Neuroimage*. (2007) 37:1083–90. doi: 10.1016/j.neuroimage.2007.02.041
41. Zhou HX, Chen X, Shen YQ, Li L, Chen NX, Zhu ZC, et al. Rumination and the default mode network: meta-analysis of brain imaging studies and implications for depression. *Neuroimage*. (2020) 206:116287. doi: 10.1016/j.neuroimage.2019.116287
42. Hamilton JP, Farmer M, Fogelman P, Gotlib IH. Depressive rumination, the default-mode network, and the dark matter of clinical neuroscience. *Biol Psychiatry*. (2015) 78:224–30. doi: 10.1016/j.biopsych.2015.02.020
43. Russo D, Martino M, Magioncalda P, Inglese M, Amore M, Northoff G. Opposing changes in the functional architecture of large-scale networks in bipolar mania and depression. *Schizophr Bull*. (2020). doi: 10.1093/schbul/sbaa004
44. Shao J, Dai Z, Zhu R, Wang X, Tao S, Bi K, et al. Early identification of bipolar from unipolar depression before manic episode: evidence from dynamic rfMRI. *Bipolar Disord*. (2019) 21:774–84. doi: 10.1111/bdi.12819
45. Macrae CN, Moran JM, Heatherton TF, Banfield JF, Kelley WM. Medial prefrontal activity predicts memory for self. *Cereb Cortex*. (2004) 14:647–54. doi: 10.1093/cercor/bhh025
46. Spreng RN, Mar RA, Kim AS. The common neural basis of autobiographical memory, prospection, navigation, theory of mind, and the default mode: a quantitative meta-analysis. *J Cogn Neurosci*. (2009) 21:489–510. doi: 10.1162/jocn.2008.21029
47. Szpunar KK, Chan JC, McDermott KB. Contextual processing in episodic future thought. *Cereb Cortex*. (2009) 19:1539–48. doi: 10.1093/cercor/bhn191
48. Marek S, Dosenbach NUF. The frontoparietal network: function, electrophysiology, and importance of individual precision mapping. *Dialog Clin Neurosci*. (2018) 20:133–40. doi: 10.31887/DCNS.2018.20.2/smarek
49. Seeley WW, Menon V, Schatzberg AF, Keller J, Glover GH, Kenna H, et al. Dissociable intrinsic connectivity networks for salience processing and executive control. *J Neurosci*. (2007) 27:2349–56. doi: 10.1523/JNEUROSCI.5587-06.2007
50. Dosenbach NU, Fair DA, Cohen AL, Schlaggar BL, Petersen SE. A dual-networks architecture of top-down control. *Trends Cogn Sci*. (2008) 12:99–105. doi: 10.1016/j.tics.2008.01.001
51. Spreng RN, Stevens WD, Chamberlain JP, Gilmore AW, Schacter DL. Default network activity, coupled with the frontoparietal control network, supports goal-directed cognition. *Neuroimage*. (2010) 53:303–17. doi: 10.1016/j.neuroimage.2010.06.016
52. Johnson S, Tran T. Bipolar disorder: what can psychotherapists learn from the cognitive research? *J Clin Psychol*. (2007) 63:425–32. doi: 10.1002/jclp.20361
53. Phillips ML, Ladouceur CD, Drevets WC. A neural model of voluntary and automatic emotion regulation: implications for understanding the pathophysiology and neurodevelopment of bipolar disorder. *Mol Psychiatry*. (2008) 13:829, 33–57. doi: 10.1038/mp.2008.82
54. Ongür D, Price JL. The organization of networks within the orbital and medial prefrontal cortex of rats, monkeys and humans. *Cereb Cortex*. (2000) 10:206. doi: 10.1093/cercor/10.3.206
55. Rajkowska G, Miguel-Hidalgo JJ, Wei J, Dilley G, Pittman SD, Meltzer HY, et al. Morphometric evidence for neuronal and glial prefrontal

cell pathology in major depression ∗. *Biol Psychiatry.* (1999) 45:1085–98. doi: 10.1016/S0006-3223(99)00041-4
56. Bremner JD, Innis RB, Salomon RM, Staib LH, Ng CK, Miller HL, et al. Positron emission tomography measurement of cerebral metabolic correlates of tryptophan depletion-induced depressive relapse. *Arch Gen Psychiatry.* (1997) 54:364–74. doi: 10.1001/archpsyc.1997.01830160092012
57. Bremner JD, Vythilingam M, Vermetten E, Nazeer A, Adil J, Khan S, et al. Reduced volume of orbitofrontal cortex in major depression. *Biol Psychiatry.* (2002) 51:273–9. doi: 10.1016/S0006-3223(01)01336-1
58. Drevets WC. Orbitofrontal cortex function and structure in depression. *Ann N Y Acad Sci.* (2007) 1121:499–527. doi: 10.1196/annals.1401.029
59. Brady Jr RO, Masters GA, Mathew IT, Margolis A, Cohen BM, Öngür D, et al. State dependent cortico-amygdala circuit dysfunction in bipolar disorder. *J Affect Disord.* (2016) 201:79–87. doi: 10.1016/j.jad.2016.04.052
60. Menon V. Large-scale brain networks and psychopathology: a unifying triple network model. *Trends Cogn Sci.* (2011) 15:483–506. doi: 10.1016/j.tics.2011.08.003
61. Koechlin E, Summerfield C. An information theoretical approach to prefrontal executive function. *Trends Cogn Sci.* (2007) 11:229–35. doi: 10.1016/j.tics.2007.04.005
62. Milham MP, Banich MT, Barad V. Competition for priority in processing increases prefrontal cortex's involvement in top-down control: an event-related fMRI study of the stroop task. *Brain Res Cogn Brain Res.* (2003) 17:212–22. doi: 10.1016/S0926-6410(03)00108-3
63. Brewin CR, Gregory JD, Lipton M, Burgess N. Intrusive images in psychological disorders: characteristics, neural mechanisms, and treatment implications. *Psychol Rev.* (2010) 117:210–32. doi: 10.1037/a0018113
64. Banich MT, Mackiewicz KL, Depue BE, Whitmer AJ, Miller GA, Heller W. Cognitive control mechanisms, emotion and memory: a neural perspective with implications for psychopathology. *Neurosci Biobehav Rev.* (2009) 33:613–30. doi: 10.1016/j.neubiorev.2008.09.010
65. Richard-Devantoy S, Ding Y, Lepage M, Turecki G, Jollant F. Cognitive inhibition in depression and suicidal behavior: a neuroimaging study. *Psychol Med.* (2016) 46:933–44. doi: 10.1017/S0033291715002421

Conflict of Interest: The authors declare that the research was conducted in the absence of any commercial or financial relationships that could be construed as a potential conflict of interest.

frontiers in Psychiatry

MINI REVIEW
published: 20 April 2021
doi: 10.3389/fpsyt.2021.634015

Neural Correlates of Mentalizing in Individuals With Clinical High Risk for Schizophrenia: ALE Meta-Analysis

Ksenija Vucurovic[1,2]*, *Stéphanie Caillies*[1] *and Arthur Kaladjian*[1,3]

[1] Laboratory Cognition, Santé, Société (C2S), Department of Psychology, University of Reims Champagne Ardenne, Reims, France, [2] Centre Rémois de Psychothérapie et Neuromodulation, Reims, France, [3] Pôle Universitaire de Psychiatrie, CHU de Reims, EPSM Marne, Reims, France

Psychotic disorder refers to a spectrum of disorders that have multiple etiologies, due to the complex interaction of biological and genetic vulnerability with familial and cultural factors. A clinical high risk (CHR) for schizophrenia is defined as the presence of brief, attenuated, or intermittent psychotic symptoms in non-schizophrenic individuals. The transition to schizophrenia appears significantly more frequent in this at-risk population than in the general population. Moreover, the ability to attribute mental states to others, known as mentalizing or theory of mind, and its neural correlates found in individuals with CHR are similar to those described in patients with schizophrenia. We have therefore explored neurofunctional correlates of mentalizing in individuals with CHR vs. healthy controls, in order to identify the differences in brain activation. A neural coordinate-based activation likelihood estimation meta-analysis of existing neuroimaging data revealed that three regions displayed decreased activation in individuals with CHR, compared with healthy controls: the right temporoparietal junction, the right middle temporal gyrus, and the left precuneus. These results, combined with those in the literature, further support the hypothesis that abnormal activation of posterior brain regions involved in mentalizing correlates with psychotic symptoms in help-seeking individuals.

Keywords: theory of mind, schizophrenia, psychosis proneness, fMRI, social cognition

OPEN ACCESS

Edited by:
Szilvia Anett Nagy,
University of Pécs, Hungary

Reviewed by:
Joseph Kambeitz,
Ludwig Maximilian University of Munich, Germany
Stijn Michielse,
Maastricht University, Netherlands

***Correspondence:**
Ksenija Vucurovic
kvucurovic@chu-reims.fr

Specialty section:
This article was submitted to Neuroimaging and Stimulation, a section of the journal Frontiers in Psychiatry

Received: *26 November 2020*
Accepted: *25 February 2021*
Published: *20 April 2021*

Citation:
Vucurovic K, Caillies S and Kaladjian A (2021) Neural Correlates of Mentalizing in Individuals With Clinical High Risk for Schizophrenia: ALE Meta-Analysis. Front. Psychiatry 12:634015. doi: 10.3389/fpsyt.2021.634015

INTRODUCTION

Schizophrenia, a severe psychotic disorder, is among the leading causes of long-term disability worldwide (1). Therefore, better understanding of schizophrenia's emergence and disability correlates is one of the major challenges for modern psychiatric practice. Retrospective research has shown that individuals who develop schizophrenia display subclinical symptoms years before disease onset (2). Accordingly, the concept of clinical high risk (CHR) or ultra-high risk for psychotic disorders has emerged in the prospective literature (3, 4), and early interventions have been offered to help-seeking individuals in order to decrease their rate of transition to schizophrenia.

CHR state diagnosis is recognized as a prodromal period before schizophrenia onset and as such it is included in the latest version of Diagnostic and Statistical Manuel 5th version as "attenuated psychotic syndrome" (5). CHR is characterized by attenuated psychotic symptoms, brief limited intermittent psychotic symptoms, or basic symptoms (6). "Attenuated psychotic symptoms" refers to delusions, hallucinations, disorganized speech, or other psychotic symptoms present in an

attenuated form. Reality testing is intact, but the symptoms are so frequent or severe that they cannot be ignored or discounted (7). Brief limited intermittent psychotic symptoms are frankly psychotic symptoms that do not last long enough for a diagnosis of schizophrenia to be made on the basis of current international criteria (8). Finally, basic symptoms are self-reported subtle, subclinical disturbances in stress tolerance and affective, cognitive, or perceptual drive, with full insight into their abnormal nature such that they motivate individuals to seek help (9, 10). Even though familial susceptibility to schizophrenia can be dissociated from CHR (11), it has been suggested that high genetic risk and functional decline are also diagnostic criteria for CHR (12).

It is thought that up to 20% of the general adult population have a psychotic-like experience (13). Nevertheless, individuals with CHR diagnostic criteria have a 16%−35% probability of developing a full-blown psychotic disorder within 2 years of CHR diagnosis (4, 14). Standardized validated instruments are used in clinical practice to identify individuals with CHR.

In schizophrenia, mentalizing is constantly impaired at both the behavioral and neurological levels (15, 16). Mentalizing (or theory of mind, ToM) is a social cognition process that confers on us the ability to attribute mental states to others and to further understand that these states may be different from ours (17). It enables individuals to make sense of social communication and interactions and to predict the social behavior of others (18). It has been suggested that the processes underlying mentalizing deficits are genetically influenced and may constitute an intermediate phenotype of schizophrenia (19–21). Consistent with this, both individuals with a high familial risk for schizophrenia (11) and those with CHR not only display poorer psychosocial functioning (22), but also perform more poorly on mentalizing tasks (23–27) and have abnormal brain activity compared with healthy controls (11, 28–34). For example, activation of the medial prefrontal cortex (mPFC) during a ToM task, specifically a false-belief task, has been found to be negatively correlated with social anhedonia and social functioning in CHR (35, 36), suggesting that the ToM processing impairment is related to relatively poor psychosocial functioning in this subclinical population.

The question now being asked is whether social cognition impairment is a marker of vulnerability to schizophrenia in individuals with CHR. Investigating the neural correlates of impaired mentalizing in CHR could make it possible to identify neuroimaging markers of psychotic disorders, which could then be added to the clinical criteria when screening at-risk individuals. This approach could help us identify useful targets for therapeutic interventions in psychosocial rehabilitation programs and, in turn, understand more fully the link between poor social cognitive functioning and the correlated brain network without a medication bias.

Even though several studies have already investigated the underlying ToM neural correlates in CHR, the small sample size of each study could lead to a lack of power. Reasoning that a meta-analysis of the existing neuroimaging data could help overcome this limitation, we carried out a systematic review of functional MRI studies of individuals with CHR, in order to examine which brain region activation in individual studies would keep robust association with TOM task resolution. We expected to find evidence of abnormal brain activation in core regions of the mentalizing brain previously shown as abnormally activated in schizophrenia during TOM task resolution, namely the bilateral temporoparietal junction (TPJ), left superior temporal sulcus, medial prefrontal cortex (mPFC), and precuneus.

METHODS AND MATERIALS

Literature Search and Selection

We searched the following databases: MEDLINE, PsycINFO, Embase, and Current Contents. Relevant references from the retrieved papers were added to our database. Only whole-brain studies published in English until December 2020 were eligible for the review. We used the following keywords: *at-risk mental states*, *ARMS*, *clinical high risk*, *CHR*, *ultra-high risk*, *UHR*, *psychosis*, *mentalizing*, *theory-of mind*, *perspective-taking*, *fMRI*, *PET*, and *brain*. Paper selection is detailed in the PRISMA figure (**Supplementary Material**). Our procedure adhered to the 10 simple rules of Muller et al. (37) for neuroimaging meta-analysis. The present meta-analysis was registered in PROSPERO (no. CRD42019135862).

The inclusion criteria were (1) whole-brain neuroimaging (reported in the MNI or Talairach atlas) to compare individuals with CHR and healthy controls, (2) BOLD contrasts between the experimental condition (mentalizing) and the control condition, (3) mentalizing paradigm (featuring cartoons, video, or audio material) requiring participants to attribute mental states (emotions, intentions, beliefs) to others, and (4) diagnosis of CHR using validated clinical instruments and criteria (38).

Exclusion criteria were (1) CHR diagnosis based solely on familial susceptibility to schizophrenia, (2) brain damage or neurological disorder, (3) absence of a control group, and (4) mentalizing paradigm requiring either the attribution of a mental state to the self or emotion recognition, for although these processes are close to mentalizing, they do not fully overlap with the attribution of mental states to others (35, 39–42).

Activation Likelihood Estimation Procedure

We submitted the neuroimaging data to a neural coordinate-based activation likelihood estimation (ALE) meta-analysis, using GingerALE version 2.3.6 (brainmap.org/ale) to run the ALE algorithm (43). We converted the coordinates from MNI space to the Talairach space using the *convert foci* option implemented in the GingerALE toolbox (44–46) and used the more conservative ALE method of Turkeltaub et al. (46) for the ALE calculation. We ran a cluster-level inference threshold correction algorithm (45), with $p < 0.001$ as the cluster-forming threshold and $p < 0.05$ for cluster-level inference. The cluster-level inference-corrected threshold set the minimum cluster volume such that only 5% of the simulated data's clusters exceeded this size. The minimum cluster size was 200 mm^3. We performed the ALE analysis for all foci for ToM contrasts extracted from studies that compared individuals with CHR and healthy controls (HC).

TABLE 1 | Activation clusters.

Cluster	Location (BA)	Talairach coordinates			ALE (×10^{-2})	Cluster size (mm^3)
		x	y	z		
HC>CHR						
1	Right supramarginal gyrus (40)	50	−44	30	1,99	960
2	Right middle temporal Gyrus (21)	59	−30	−10	1,77	560
3	Left precuneus (7)	−5	−56	42	1,77	560

BA, Brodmann Area; CHR, Clinical High Risk; HC, healthy controls; ALE, Activation Likelihood Estimation.
Centered cluster coordinates are reported.

RESULTS

The literature search yielded six studies (the research string is provided in **Supplementary Figure 1**), with seven experiments reporting 25 activation foci. Details about the studies we included, the paradigms they used, and the imaging characteristics are provided in **Table 1**. Two studies included individuals at familial high risk for schizophrenia (35, 47), but both studies focused on the clinical aspects of psychosis presented by the participants. Therefore, Marjoram et al. (47) compared individuals with high familial risk for schizophrenia with past or current attenuated psychotic symptoms with individuals with the comparable familial liability risk, but without those symptoms. Dodell-Feder et al. (35) included in their study the participants with both, familial liability to schizophrenia, and high scores on SIPS: Structured Interview for Prodromal Syndromes (**Table 1**). Therefore, the authors' consensus was that both studies meet typical CHR diagnostic criteria as defined by the field (48). A total of 91 individuals with CHR were compared with 110 HC. All the studies used fMRI. The ALE meta-analysis of the foci we extracted revealed decreased activation in the individuals with CHR, compared with HC, during mentalizing tasks in 1) a 960-mm^3 cluster extending from the right inferior parietal lobule (Talairach: $x = 46$, $y = -48$, $z = 26$; ALE = 0.02; Brodmann area, BA 40) to the right supramarginal gyrus (Talairach: $x = 54$, $y = -34$, $z = 34$; ALE = 0.02; BA 40) and overlapping with the right TPJ (rTPJ), 2) a 560-mm^3 cluster centered at $x = 59$, $y = -30$, $z = -10$ (Talairach) that covered the right middle temporal gyrus (MTG; BA 21), and 3) a 560-mm^3 cluster that extended from (−10, −58, 38) to (0, −50, 46), centered at (−5, −54, 42), and overlapped with the precuneus. Detailed results are provided in **Supplementary Table 1**. All the regions of decreased activation are shown in **Figure 1**, and the link to the NIFTI file is: https://www.dropbox.com/s/ixpt8g5ykljmy9w/TOM%20HCvsHRP_ALE_C05_1k.nii?dl=0.

No significant cluster of increased activation was found in the individuals with CHR compared with HC.

DISCUSSION

We investigated the neural correlates of mentalizing in a population with CHR by conducting a meta-analysis of the neuroimaging literature. Even though only a small number of studies were eligible for quantitative meta-analysis, we obtained a significant result with good statistical robustness for three brain regions, which appeared to be insufficiently activated in comparison with HC: right TPJ, right MTG (BA 21), and left precuneus. All three regions are critically involved in the processing of social cognitive information in neurotypical development (49).

Brain Function of Identified Areas

The right MTG (BA 21) was described as being involved in the processing of affective prosody in speech (50, 51), the auditory processing of complex sounds (52), visual memory function (53), and social cognition, particularly mentalizing during non-verbal tasks (54). The right TPJ is a highly integrative brain structure that enables high-order cognitive processing to take place. In social cognition, it is thought to be particularly involved in attention shift to unexpected stimuli and the attribution of intentions/beliefs to others (55). It has been suggested that the rTPJ can be divided into two functional domains: an anterior one involved in both ToM and attention and a posterior one that seems to be exclusively involved in ToM (55, 56). Disruption of the rTPJ impairs probabilistic belief updating (57). Finally, the precuneus is involved in a variety of cognitive processes, comprising the integration of environmental information and self-centered mental imagery strategies for its anterior portion (58), and episodic memory retrieval (58) and affective response to pain (59) for its posterior portion. The precuneus is reported to be involved in conscious information processing and closely connected to the mPFC, bilateral TPJ, and thalamus via the default mode network (60).

Our results are in line with volumetric studies of mentalizing in CHR that have found reduced gray-matter volume in the right superior temporal gyrus, left precuneus, left medial frontal gyrus, right middle frontal gyrus, bilateral parahippocampal/hippocampal regions and bilateral anterior cingulate, compared with HC (61). These authors further suggested that reduced gray-matter volume in the right inferior frontal gyrus and right superior temporal gyrus is predictive of the transition to psychotic disorder.

Comparison With Genetic Risk for Schizophrenia

The literature indicates that individuals with familial high risk (FHR) for schizophrenia exhibit decreased mPFC activation and increased activation of the right MTG and posterior

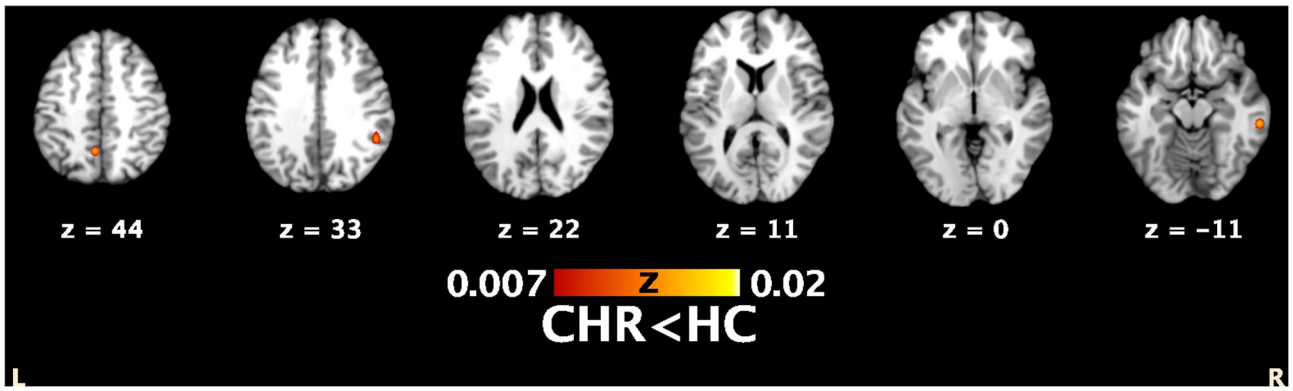

FIGURE 1 | Functional clusters from comparison analysis between mentalizing networks showing significant neurofunctional convergence of decreased activation in individuals with CHR vs. healthy controls in following brain structures (from left to right): the left precuneus, the right parieto-temporal junction and right middle temporal gyrus. Mask dimensions = 80 × 96 × 70; number of within-brain voxels = 226,657; number of foci = 25; number of experiments = 7; maximum ALE score = 0.02; threshold method = cluster-level inference; thresholding value = 0.05; thresholding permutations = 1,000; cluster-forming value = 0.001. Figure created using Mango (http://ric.uthscsa.edu/mango).

cingulate cortex during a mentalizing task (11). However, the results of fMRI studies comparing patients in acute psychosis and after recovery suggest that decreased mPFC activation is state-dependent (47, 62). In line with results observed in FHR, volumetric studies in schizophrenia have consistently described a positive correlation between ToM deficits and gray-matter reduction in the mPFC (63–68). In a large meta-analysis of ToM neural correlates, Schurz et al. (49) found that the mPFC is strongly activated in false-belief, strategic games, and trait judgment tasks and to a far lesser extent in social interactions, reading the mind in the eyes, and rational actions. The ventral mPFC is also described as being involved in processing explicit and implicit information about oneself and others in abstract and evaluative terms that enable individuals to understand complex psychological aspects of other people (69–72) or decouple mental states from their environment (73, 74). Barbey et al. (75) additionally claimed that the ventral mPFC specifically enables individuals to draw inferences about complex relations. It was therefore surprising not to find abnormal mPFC activation in our CHR meta-analysis. Even though some of the participants with CHR included in our meta-analysis had a genetic predisposition for schizophrenia, the major difference from relatives who were not affected by schizophrenia was the presence of attenuated psychotic symptoms, albeit at the subthreshold level. Consistently with this, Monhke et al. (11) demonstrated that activation of the right MTG and posterior cingulate cortex is correlated in FHR individuals with attenuated paranoid ideation. Abnormal mPFC activation during mentalizing tasks may therefore be an endophenotypic marker of schizophrenia related to genetic vulnerability (11), while abnormal activation of the temporoparietal cortex and precuneus may be related more to the psychopathology of psychotic disorders.

Comparison With Schizophrenia

Three recent coordinate-based meta-analyses explored brain activation during mentalizing tasks resolution in schizophrenia compared to healthy controls [(76), 73, 74]. Both (76), and Kronbichler et al. (77), used Seed-Based Mapping methodology and concordantly found spread abnormalities in brain activation patterns in the patients group. Both groups of authors reported decreased activation of the mPFC, left orbitofrontal cortex, medial parieto-occipital cortex, right premotor areas, cingulate and lingual gyri [(76), 73]. Interestingly, in both meta-analyses, different activation of the bilateral parieto-temporal junction was described, with decreased activation of posterior ventral portion and increased activation in the posterior dorsal portion in schizophrenia patients [(76), 73], suggesting abnormal brain functioning of this area of the brain in patients. Our team led the comparative neural-correlates-based meta-analysis of mentalizing and empathy in schizophrenia patients using ALE methodology. We found decreased left TPJ activation during mentalizing tasks and decreased right ventrolateral PFC activation during emotion attribution tasks (78). Those literature data compared with the results of this meta-analysis in CHR, suggest abnormal activation in brain regions related to mentalizing in both schizophrenia and CHR, with diverging activation patterns in the right TPJ. Moreover, in patients with schizophrenia, the rTPJ is functionally connected to the hippocampus, fusiform gyrus, and MTG during mental state inference (79). Pauly et al. (80) found a positive correlation between positive symptoms and activation of the parahippocampus that led them to suggest a possible increase in emotion-related responses as the disease progresses. The opposite pattern of rTPJ activation in schizophrenia and CHR may therefore be related to more severe psychopathology in schizophrenia and more particularly to a cognitive mechanism of over-attribution of mental states or over-generation of hypotheses, described as *hyper-ToM* (81). Chambon et al. (82) postulated that the physiopathological mechanism, whereby undue weight is given to prior expectations in schizophrenia with positive symptoms, stems from the abnormal encoding of prediction error signals in dopamine-rich brain areas (83).

LIMITATIONS AND CONCLUSION

Our study had several limitations. As our meta-analysis was based on the available literature, it may have been affected by the potential publication bias against null results. Furthermore, the tasks used to assess neural correlates during mentalizing may have had limited ecological validity. Although very few experiments were included in our meta-analysis, we explored more than 20 foci, which is the threshold suggested by different authors for meta-analysis validity (37, 84).

In conclusion, our findings suggest that individuals with CHR may not have some fully functional specialized neural correlates for inferring the mental states of others. We found decreased activation of posterior brain areas related to mentalizing in these individuals that may be related to their increasing psychopathology. Longitudinal studies should address the neurological markers that predict the transition to schizophrenia in this population.

AUTHOR CONTRIBUTIONS

KV, SC, and AK contributed to the study conception and design. KV realized the systematic review of literature, done the first selection of relevant articles, data collection, statistical analysis, and drafted manuscript preparation. SC and AK done the final selection of included articles and supervised the research. All authors reviewed the results and approved the final version of the manuscript.

FUNDING

This work was supported by the collaborative project between the University of Reims Champagne-Ardenne (URCA) and the University Hospital of Reims (CHU de Reims), called Projet Hospitalo-Universitaire (PHU), Social Cognition and Neurodevelopmental disorders (NDev-X), which was awarded to AK.

ACKNOWLEDGMENTS

We would like to thank Eric Fakra and Gilles Lafargue for their valuable comments on this research.

SUPPLEMENTARY MATERIAL

The Supplementary Material for this article can be found online at: https://www.frontiersin.org/articles/10.3389/fpsyt.2021.634015/full#supplementary-material

REFERENCES

1. Owen MJ, Sawa A, Mortensen PB. Schizophrenia. *Lancet.* (2016) 388:8697. doi: 10.1016/S0140-6736(15)01121-6
2. Klosterkötter J, Hellmich M, Steinmeyer EM, Schultze-Lutter F. Diagnosing schizophrenia in the initial prodromal phase. *Arch Gen Psychiatry.* (2001) 58:158164. doi: 10.1001/archpsyc.58.2.158
3. Miller TJ, McGlashan TH, Rosen JL, Somjee L, Markovich PJ, Stein K, et al. Prospective diagnosis of the initial prodrome for schizophrenia based on the Structured Interview for Prodromal Syndromes: preliminary evidence of interrater reliability and predictive validity. *Am J Psychiatry.* (2002) 159:863–5. doi: 10.1176/appi.ajp.159.5.863
4. Yung AR, Yuen HP, McGorry PD, Phillips LJ, Kelly D, Dell'Olio M, et al. Mapping the onset of psychosis: the Comprehensive Assessment of At-Risk Mental States. *Aust N Z J Psychiatry.* (2005) 39:964–71. doi: 10.1080/j.1440-1614.2005.01714.x
5. Fusar-Poli P, De Micheli A, Cappucciati M, Rutigliano G, Davies C, Ramella-Cravaro V, et al. Diagnostic and prognostic significance of DSM-5 attenuated psychosis syndrome in services for individuals at ultra high risk for psychosis. *Schizophr Bull.* (2018). 44:264–75. doi: 10.1093/schbul/sbx055
6. Dutt A, Tseng HH, Fonville L, Drakesmith M, Su L, Evans J, et al. Exploring neural dysfunction in 'clinical high risk' for psychosis: a quantitative review of fMRI studies. *J Psychiatr Res.* (2015) 61:122134. doi: 10.1016/j.jpsychires.2014.08.018
7. Yung AR, Nelson B. Young people at ultra high risk for psychosis: a research update. *Early Interv Psychiatry.* (2011) 5:5257. doi: 10.1111/j.1751-7893.2010.00241.x
8. McGlashan T, Walsh BC, Woods SW. *The Psychosis Risk Syndrome: Handbook for Diagnosis and Follow-up*. New York, NY: Oxford University Press (2010).
9. Schultze-Lutter F. Subjective symptoms of schizophrenia in research and the clinic: the basic symptom concept. *Schizophr Bull.* (2009) 35:58. doi: 10.1093/schbul/sbn139
10. Schultze-Lutter F, Ruhrmann S, Klosterkötter J. Early detection of psychosis -establishing a service for persons at risk. *Eur Psychiatry.* (2009) 24:110. doi: 10.1016/j.eurpsy.2008.08.004
11. Mohnke S, Erk S, Schnell K, Romanczuk-Seiferth N, Schmierer P, Romund L, et al. Theory of mind network activity is altered in subjects with familial liability for schizophrenia. *Soc Cogn Affect Neurosci.* (2015) 11:299307. doi: 10.1093/scan/nsv111
12. Andreou C, Borgwardt S. Structural and functional imaging markers for susceptibility to psychosis. *Mol Psychiatry.* (2020) 25:2773–85. doi: 10.1038/s41380-020-0679-7
13. Hanssen MS, Bijl RV, Vollebergh W, van Os J. Self-reported psychotic experiences in the general population: a valid screening tool for DSM-III-R psychotic disorders? *Acta Psychiatr Scand.* (2003) 107:369377. doi: 10.1034/j.1600-0447.2003.00058.x
14. Cannon TD. Brain biomarkers of vulnerability and progression to psychosis. *Schizophr Bull.* (2015) 42:S127–132. doi: 10.1093/schbul/sbv173
15. Green MF. Impact of cognitive and social cognitive impairment on functional outcomes in patients with schizophrenia. *J Clin Psychiatry.* (2016) 77(Suppl 2):811. doi: 10.4088/JCP.14074su1c.02
16. van Os J, Kapur S. Schizophrenia. *Lancet.* (2009) 374:635645. doi: 10.1016/S0140-6736(09)60995-8
17. Premack D, Woodruff G. Does the chimpanzee have a theory of mind? *Behav Brain Sci.* (1978) 1:515–26. doi: 10.1017/S0140525X00076512
18. Frith CD, Frith U. The neural basis of mentalizing. *Neuron.* (2006) 50:531534. doi: 10.1016/j.neuron.2006.05.001
19. Gottesman II, Gould TD. The endophenotype concept in psychiatry: etymology and strategic intentions. *Am J Psychiatry.* (2003) 160:636645. doi: 10.1176/appi.ajp.160.4.636
20. Meyer-Lindenberg A, Weinberger DR. Intermediate phenotypes and genetic mechanisms of psychiatric disorders. *Na Rev Neurosci.* (2006) 7:818827. doi: 10.1038/nrn1993
21. Walter H, Schnell K, Erk S, Arnold C, Kirsch P, Esslinger C, et al. Genetic risk for schizophrenia impacts Theory-of-Mind-related brain activation. *Mol Psychiatry.* (2011) 16:353. doi: 10.1038/mp.2011.25
22. Ventura J, Hellemann GS, Thames AD, Koellner V, Nuechterlein KH. Symptoms as mediators of the relationship between neurocognition and functional outcome in schizophrenia: a meta-analysis. *Schizophr Res.* (2009) 113:189199. doi: 10.1016/j.schres.2009.03.035
23. Koivukangas J, Björnholm L, Tervonen O, Miettunen J, Nordström T, Kiviniemi V, et al. White matter structure in young adults with familial risk for psychosis—the oulu brain and mind study. *Psychiatry Res.* (2015) 233:388393. doi: 10.1016/j.pscychresns.2015.06.015

24. Piskulic D, Liu L, Cadenhead KS, Cannon TD, Cornblatt BA, McGlashan TH, et al. Social cognition over time in individuals at clinical high risk for psychosis: findings from the NAPLS-2 cohort. *Schizophr Res.* (2016) 171:176181. doi: 10.1016/j.schres.2016.01.017
25. Stanford AD, Messinger J, Malaspina D, Corcoran CM. Theory of Mind in patients at clinical high risk for psychosis. *Schizophr Res.* (2011) 131:1117. doi: 10.1016/j.schres.2011.06.005
26. Versmissen D, Janssen I, Myin-Germeys I, Mengelers R, Campo JA, van Os J, et al. Evidence for a relationship between mentalising deficits and paranoia over the psychosis continuum. *Schizophr Res.* (2008) 99:103110. doi: 10.1016/j.schres.2007.09.024
27. Yong E, Barbato M, Penn DL, Keefe RS, Woods SW, Perkins DO, et al. Exploratory analysis of social cognition and neurocognition in individuals at clinical high risk for psychosis. *Psychiatry Res.* (2014) 218:3943. doi: 10.1016/j.psychres.2014.04.003
28. Brüne M, Ozgürdal S, Ansorge N, von Reventlow HG, Peters S, Nicolas V, et al. An fMRI study of "theory of mind" in at-risk states of psychosis: comparison with manifest schizophrenia and healthy controls. *Neuroimage.* (2011) 55:329337. doi: 10.1016/j.neuroimage.2010.12.018
29. Derntl B, Michel TM, Prempeh P, Backes V, Finkelmeyer A, Schneider F, et al. Empathy in individuals clinically at risk for psychosis: brain and behaviour. *Br J Psychiatry.* (2015) 207:407–13. doi: 10.1192/bjp.bp.114.159004
30. Goghari VM, Sanford N, Spilka MJ, Woodward TS. Task-related functional connectivity analysis of emotion discrimination in a family study of schizophrenia. *Schizophr Bull.* (2017) 43:1348–62. doi: 10.1093/schbul/sbx004
31. Ho KK, Lui SS, Hung KS, Wang Y, Li Z, Cheung EF, et al. Theory of mind impairments in patients with first-episode schizophrenia and their unaffected siblings. *Schizophr Res.* (2015) 166:18. doi: 10.1016/j.schres.2015.05.033
32. Modinos G, Renken R, Shamay-Tsoory SG, Ormel J, Aleman A. Neurobiological correlates of theory of mind in psychosis proneness. *Neuropsychologia.* (2010) 48:37153724. doi: 10.1016/j.neuropsychologia.2010.09.030
33. van der Meer L, Groenewold NA, Pijnenborg M, Aleman A. Psychosis-proneness and neural correlates of self-inhibition in theory of mind. *PLoS ONE.* (2013) 8:e67774. doi: 10.1371/journal.pone.0067774
34. Zhang T, Tang Y, Cui H, Lu X, Xu L, Liu X, et al. Theory of mind impairments in youth at clinical high risk of psychosis. *Psychiatry.* (2016) 79:4055. doi: 10.1080/00332747.2015.1123592
35. Dodell-Feder D, DeLisi LE, Hooker CI. Neural disruption to theory of mind predicts daily social functioning in individuals at familial high-risk for schizophrenia. *Soc Cogn Affect Neurosci.* (2014) 9:19141925. doi: 10.1093/scan/nst186
36. Glenthøj LB, Fagerlund B, Hjorthøj C, Jepsen JRM, Bak N, Kristensen TD, et al. Social cognition in patients at ultra-high risk for psychosis: what is the relation to social skills and functioning? *Schizophr Res Cogn.* (2016) 5:2127. doi: 10.1016/j.scog.2016.06.004
37. Müller VI, Cieslik EC, Laird AR, Fox PT, Radua J, Mataix-Cols D, et al. Ten simple rules for neuroimaging meta-analysis. *Neurosci Biobehav Rev.* (2018) 84:151–61. doi: 10.1016/j.neubiorev.2017.11.012
38. Fusar-Poli P. The Clinical High-Risk State for Psychosis (CHR-P), Version, I. *I Schizophr Bull.* (2017) 43:44–7. doi: 10.1093/schbul/sbw158
39. Fakra E, Jouve E, Guillaume F, Azorin JM, Blin O. Relation between facial affect recognition and configural face processing in antipsychotic-free schizophrenia. *Neuropsychology.* (2015) 29:197204. doi: 10.1037/neu0000136
40. Li H, Chan RC, McAlonan GM, Gong QY. Facial emotion processing in schizophrenia: a meta-analysis of functional neuroimaging data. *Schizophr Bull.* (2009) 36:10291039. doi: 10.1093/schbul/sbn190
41. Taylor SF, Kang J, Brege IS, Tso IF, Hosanagar A, Johnson TD. Meta-analysis of functional neuroimaging studies of emotion perception and experience in schizophrenia. *Biol Psychiatry.* (2012) 71:136145. doi: 10.1016/j.biopsych.2011.09.007
42. van Veluw SJ, Chance SA. Differentiating between self and others: an ALE meta-analysis of fMRI studies of self-recognition and theory of mind. *Brain Imaging Behav.* (2014) 8:24–38. doi: 10.1007/s11682-013-9266-8
43. Eickhoff SB, Laird AR, Fox PM, Lancaster JL, Fox PT. Implementation errors in the GingerALE software: description and recommendations. *Hum Brain Mapp.* (2017) 38:711. doi: 10.1002/hbm.23342
44. Eickhoff SB, Laird AR, Grefkes C, Wang LE, Zilles K, Fox PT. Coordinate-based activation likelihood estimation meta-analysis of neuroimaging data: a random-effects approach based on empirical estimates of spatial uncertainty. *Hum Brain Mapp.* (2009) 30:29072926. doi: 10.1002/hbm.20718
45. Eickhoff SB, Bzdok D, Laird AR, Kurth F, Fox PT. Activation likelihood estimation meta-analysis revisited. *Neuroimage.* (2012) 59:23492361. doi: 10.1016/j.neuroimage.2011.09.017
46. Turkeltaub PE, Eickhoff SB, Laird AR, Fox M, Wiener M, Fox P. Minimizing within-experiment and within-group effects in Activation Likelihood Estimation meta-analyses. *Hum Brain Mapp.* (2012) 33:113. doi: 10.1002/hbm.21186
47. Marjoram D, Job DE, Whalley HC, Gountouna VE, McIntosh AM, Simonotto E, et al. A visual joke fMRI investigation into theory of mind and enhanced risk of schizophrenia. *Neuroimage.* (2006) 31:18501858. doi: 10.1016/j.neuroimage.2006.02.011
48. Fusar-Poli P, Borgwardt S, Bechdolf A, Addington J, Riecher-Rössler A, Schultze-Lutter F, et al. The psychosis high-risk state: a comprehensive state-of-the-art review. *JAMA Psychiatry.* (2013) 70:107–20. doi: 10.1001/jamapsychiatry.2013.269
49. Schurz M, Radua J, Aichhorn M, Richlan F, Perner J. Fractionating theory of mind: a meta-analysis of functional brain imaging studies. *Neurosci Biobehav Rev.* (2014) 42:934. doi: 10.1016/j.neubiorev.2014.01.009
50. Ethofer T, Anders S, Erb M, Droll C, Royen L, Saur R, et al. Impact of voice on emotional judgment of faces: an event-related fMRI study. *Hum Brain Mapp.* (2006) 27:707714. doi: 10.1002/hbm.20212
51. Hesling I, Dilharreguy B, Clément S, Bordessoules M, Allard M. Cerebral mechanisms of prosodic sensory integration using low-frequency bands of connected speech. *Hum Brain Mapp.* (2005) 26:157169. doi: 10.1002/hbm.20147
52. Mirz F, Ovesen T, Ishizu K, Johannsen P, Madsen S, Gjedde A, et al. Stimulus-dependent central processing of auditory stimuli: a PET study. *Scand Audiol.* (1999) 28:161169. doi: 10.1080/010503999424734
53. Bonelli SB, Thompson PJ, Yogarajah M, Powell RH, Samson RS, McEvoy AW, et al. Memory reorganization following anterior temporal lobe resection: a longitudinal functional MRI study. *Brain.* (2013) 136:1889–900. doi: 10.1093/brain/awt105
54. Brunet E, Sarfati Y, Hardy-Baylé MC, Decety J. Abnormalities of brain function during a nonverbal theory of mind task in schizophrenia. *Neuropsychologia.* (2003) 41:15741582. doi: 10.1016/S0028-3932(03)00119-2
55. Krall SC, Volz LJ, Oberwelland E, Grefkes C, Fink GR, Konrad K. The right temporoparietal junction in attention and social interaction: a transcranial magnetic stimulation study. *Hum Brain Mapp.* (2016) 37:796807. doi: 10.1002/hbm.23068
56. Lee SM, McCarthy G. Functional heterogeneity and convergence in the right temporoparietal junction. *Cereb Cortex.* (2016) 26:11081116. doi: 10.1093/cercor/bhu292
57. Mengotti P, Dombert PL, Fink GR, Vossel S. Disruption of the right temporoparietal junction impairs probabilistic belief updating. *J Neurosci.* (2017) 37:54195428. doi: 10.1523/JNEUROSCI.3683-16.2017
58. Cavanna AE, Trimble MR. The precuneus: a review of its functional anatomy and behavioural correlates. *Brain.* (2006) 129:564583. doi: 10.1093/brain/awl004
59. Singer T, Seymour B, O'Doherty J, Kaube H, Dolan RJ, Frith CD. Empathy for pain involves the affective but not sensory components of pain. *Science.* (2004) 303:11571162. doi: 10.1126/science.1093535
60. Cunningham SI, Tomasi D, Volkow ND. Structural and functional connectivity of the precuneus and thalamus to the default mode network. *Hum Brain Mapp.* (2017) 38:938956. doi: 10.1002/hbm.23429
61. Fusar-Poli P, Howes OD, Allen P, Broome M, Valli I, Asselin MC, et al. Abnormal prefrontal activation directly related to pre-synaptic striatal dopamine dysfunction in people at clinical high risk for psychosis. *Mol Psychiatry.* (2011) 16:67–75. doi: 10.1038/mp.2009.108
62. Lee KH, Brown WH, Egleston PN, Green RD, Farrow TF, Hunter MD, et al. A functional magnetic resonance imaging study of social cognition in schizophrenia during an acute episode and after recovery. *Am J Psychiatry.* (2006) 163:19261933. doi: 10.1176/ajp.2006.163.11.1926

63. Haijma SV, Van Haren N, Cahn W, Koolschijn PC, Hulshoff Pol HE, Kahn RS. Brain volumes in schizophrenia: a meta-analysis in over 18 000 subjects. *Schizophr Bull.* (2013) 39:11291138. doi: 10.1093/schbul/sbs118
64. Herold R, Feldmann A, Simon M, Tényi T, Kövér F, Nagy F, et al. Regional gray matter reduction and theory of mind deficit in the early phase of schizophrenia: a voxel-based morphometric study. *Acta Psychiatr Scand.* (2009) 119:199–208. doi: 10.1111/j.1600-0447.2008.01297.x
65. Hirao K, Miyata J, Fujiwara H, Yamada M, Namiki C, Shimizu M, et al. Theory of mind and frontal lobe pathology in schizophrenia: a voxel-based morphometry study. *Schizophr Res.* (2008) 105:165174. doi: 10.1016/j.schres.2008.07.021
66. Hooker CI, Bruce L, Lincoln SH, Fisher M, Vinogradov S. Theory of mind skills are related to gray matter volume in the ventromedial prefrontal cortex in schizophrenia. *Biol Psychiatry.* (2011) 70:11691178. doi: 10.1016/j.biopsych.2011.07.027
67. Koelkebeck K, Hirao K, Miyata J, Kawada R, Saze T, Dannlowski U, et al. Impact of gray matter reductions on theory of mind abilities in patients with schizophrenia. *Soc Neurosci.* (2013) 8:631639. doi: 10.1080/17470919.2013.837094
68. Yamada M, Hirao K, Namiki C, Hanakawa T, Fukuyama H, Hayashi T, et al. Social cognition and frontal lobe pathology in schizophrenia: a voxel-based morphometric study. *Neuroimage.* (2007) 35:292298. doi: 10.1016/j.neuroimage.2006.10.046
69. Das P, Calhoun V, Malhi GS. Mentalizing in male schizophrenia patients is compromised by virtue of dysfunctional connectivity between task-positive and task-negative networks. *Schizophr Res.* (2012) 140:5158. doi: 10.1016/j.schres.2012.06.023
70. Forbes CE, Grafman J. The role of the human prefrontal cortex in social cognition and moral judgment. *Ann Rev Neurosci.* (2010) 33:299324. doi: 10.1146/annurev-neuro-060909-153230
71. Uddin LQ, Iacoboni M, Lange C, Keenan JP. The self and social cognition: the role of cortical midline structures and mirror neurons. *Trends Cogn Sci.* (2007) 11:153157. doi: 10.1016/j.tics.2007.01.001
72. Van Overwalle F. Social cognition and the brain: a meta-analysis. *Hum Brain Mapp.* (2009) 30:829858. doi: 10.1002/hbm.20547
73. Brunet-Gouet E, Decety J. Social brain dysfunctions in schizophrenia: a review of neuroimaging studies. *Psychiatry Res.* (2006) 148:7592. doi: 10.1016/j.pscychresns.2006.05.001
74. Walter H, Ciaramidaro A, Adenzato M, Vasic N, Ardito RB, Erk S, et al. Dysfunction of the social brain in schizophrenia is modulated by intention type: an fMRI study. *Soc Cogn Affect Neurosci.* (2009) 4:166176. doi: 10.1093/scan/nsn047
75. Barbey AK, Krueger F, Grafman J. An evolutionarily adaptive neural architecture for social reasoning. *Trends Neurosci.* (2009) 32:603610. doi: 10.1016/j.tins.2009.09.001
76. Jáni M, Kašpárek T. Emotion recognition and theory of mind in schizophrenia: a meta-analysis of neuroimaging studies. *World J Biol Psychiatry.* (2018) 19(sup3):S86–96. doi: 10.1080/15622975.2017.1324176
77. Kronbichler L, Tschernegg M, Martin AI, Schurz M, Kronbichler M. Abnormal brain activation during theory of mind tasks in schizophrenia: a meta-analysis. *Schizophr Bull.* (2017) 43:12401250. doi: 10.1093/schbul/sbx073
78. Vucurovic K, Caillies S, Kaladjian A. Neural correlates of theory of mind and empathy in schizophrenia: an activation likelihood estimation meta-analysis. *J Psychiatr Res.* (2020) 120:163–74. doi: 10.1016/j.jpsychires.2019.10.018
79. Bitsch F, Berger P, Nagels A, Falkenberg I, Straube B. Impaired right temporoparietal junction-hippocampus connectivity in schizophrenia and its relevance for generating representations of other minds. *Schizophr Bull.* (2018) 45:934–45. doi: 10.1093/schbul/sby132
80. Pauly KD, Kircher TT, Schneider F, Habel U. Me, myself and I: temporal dysfunctions during self-evaluation in patients with schizophrenia. *Soc Cogn Affect Neurosci.* (2014) 9:17791788. doi: 10.1093/scan/nst174
81. Abu-Akel A, Bailey AL. The possibility of different forms of theory of mind impairment in psychiatric and developmental disorders. *Psychol Med.* (2000) 30:735738. doi: 10.1017/S0033291799002123
82. Chambon V, Pacherie E, Barbalat G, Jacquet P, Franck N, Farrer C. Mentalizing under influence: abnormal dependence on prior expectations in patients with schizophrenia. *Brain.* (2011) 13:37283741. doi: 10.1093/brain/awr306
83. Gradin VB, Kumar P, Waiter G, Ahearn T, Stickle C, Milders M, et al. Expected value and prediction error abnormalities in depression and schizophrenia. *Brain.* (2011) 134(Pt 6):1751–64. doi: 10.1093/brain/awr059
84. Jardri R, Pouchet A, Pins D, Thomas P. Cortical activations during auditory verbal hallucinations in schizophrenia: a coordinate-based meta-analysis. *Am J Psychiatry.* (2011) 168:7381. doi: 10.1176/appi.ajp.2010.09101522

Conflict of Interest: The authors declare that the research was conducted in the absence of any commercial or financial relationships that could be construed as a potential conflict of interest.

frontiers in Psychiatry

BRIEF RESEARCH REPORT
published: 29 April 2021
doi: 10.3389/fpsyt.2021.664859

Abnormality of Resting-State Functional Connectivity in Major Depressive Disorder: A Study With Whole-Head Near-Infrared Spectroscopy

Eisuke Sakakibara[1]*, *Yoshihiro Satomura*[1], *Jun Matsuoka*[1], *Shinsuke Koike*[1,2,3,4,5], *Naohiro Okada*[1,2], *Hanako Sakurada*[1], *Mika Yamagishi*[1], *Norito Kawakami*[6] and *Kiyoto Kasai*[1,2,3,4]

[1] Department of Neuropsychiatry, Graduate School of Medicine, The University of Tokyo, Tokyo, Japan, [2] International Research Center for Neurointelligence (IRCN), The University of Tokyo Institutes for Advanced Study (UTIAS), The University of Tokyo, Tokyo, Japan, [3] University of Tokyo Institute for Diversity & Adaptation of Human Mind (UTIDAHM), Tokyo, Japan, [4] UTokyo Center for Integrative Science of Human Behavior (CiSHuB), Graduate School of Art and Sciences, The University of Tokyo, Tokyo, Japan, [5] Center for Evolutionary Cognitive Sciences, Graduate School of Arts and Sciences, The University of Tokyo, Tokyo, Japan, [6] Department of Mental Health, Graduate School of Medicine, The University of Tokyo, Tokyo, Japan

OPEN ACCESS

Edited by:
Szilvia Anett Nagy,
University of Pécs, Hungary

Reviewed by:
Xi-Nian Zuo,
Beijing Normal University, China
Hong Yang,
Zhejiang University, China

***Correspondence:**
Eisuke Sakakibara
sakakibara-tky@umin.ac.jp

Specialty section:
This article was submitted to Neuroimaging and Stimulation, a section of the journal Frontiers in Psychiatry

Received: *06 February 2021*
Accepted: *25 March 2021*
Published: *29 April 2021*

Citation:
Sakakibara E, Satomura Y, Matsuoka J, Koike S, Okada N, Sakurada H, Yamagishi M, Kawakami N and Kasai K (2021) Abnormality of Resting-State Functional Connectivity in Major Depressive Disorder: A Study With Whole-Head Near-Infrared Spectroscopy. Front. Psychiatry 12:664859. doi: 10.3389/fpsyt.2021.664859

Near-infrared spectroscopy (NIRS) is a functional neuroimaging modality that has advantages in clinical usage. Previous functional magnetic resonance imaging (fMRI) studies have found that the resting-state functional connectivity (RSFC) of the default mode network (DMN) is increased, while the RSFC of the cognitive control network (CCN) is reduced in patients with major depressive disorder (MDD) compared with healthy controls. This study tested whether the NIRS-based RSFC measurements can detect the abnormalities in RSFC that have been associated with MDD in previous fMRI studies. We measured 8 min of resting-state brain activity in 34 individuals with MDD and 78 age- and gender-matched healthy controls using a whole-head NIRS system. We applied a previously established partial correlation analysis for estimating RSFCs between the 17 cortical regions. We found that MDD patients had a lower RSFC between the left dorsolateral prefrontal cortex and the parietal lobe that comprise the CCN, and a higher RSFC between the right orbitofrontal cortex and ventrolateral prefrontal cortex, compared to those in healthy controls. The RSFC strength of the left CCN was negatively correlated with the severity of depressive symptoms and the dose of antipsychotic medication and positively correlated with the level of social functioning. The results of this study suggest that NIRS-based measurements of RSFCs have potential clinical applications.

Keywords: major depressive disorder, resting-state functional connectivity, near-infrared spectroscopy, cognitive control network, partial correlation analysis

INTRODUCTION

Near-infrared spectroscopy (NIRS) is a non-invasive and convenient neuroimaging technique that measures changes in the cortical blood oxygenation associated with neural activity. This has been widely used to study the cerebral function of various neuropsychiatric disorders (1). Among others, a meta-analysis of 14 studies found a significant reduction in the executive task-related elevation of blood oxygenation in individuals with MDD, even after their depressive

symptoms had remitted (2). The differences in blood oxygenation patterns during executive tasks in MDD, bipolar disorder, and schizophrenia have led to their clinical application for the differential diagnosis of psychiatric disorders in patients presenting with depressive symptoms (3).

The brain exhibits neural activity even at rest. Since the discovery of synchronous neural oscillatory activity between functionally-related brain regions, there has been a surge of research on resting-state functional connectivity (RSFC) (4). RSFC may provide clues on the mechanisms of functional integration in the brain and the neural substrate of neuropsychiatric disorders (5, 6).

Most previous studies on neuropsychiatric disorders, focusing on RSFC, have used functional magnetic resonance imaging (fMRI). Emotion regulation circuits comprising the cortex and limbic system were found dysfunctional in MDD (7). However, this dysfunction is not detected in NIRS because NIRS does not measure activities in deep brain regions. In contrast, recent studies have reported that the RSFC of the default mode network (DMN), comprising the medial prefrontal and posterior cingulate cortices, and bilateral parietal lobes, is increased, while the RSFC of the cognitive control network (CCN), comprising the frontal and parietal lobes, is reduced in patients with MDD compared with healthy controls (8, 9).

We have established the method for measuring RSFC between 17 cortical regions from NIRS blood oxygenation signals using partial correlation analysis, which has been demonstrated to reduce the influence of extracerebral blood flow (10). NIRS has certain advantages over fMRI in the clinical application of the RSFC measurement. First, NIRS has a higher temporal resolution (10 Hz) than fMRI (about 0.5 Hz); thus, it avoids the aliasing of cardiac or respiratory signals. Second, it is less expensive, convenient to set up, and more tolerant to motion artifacts than fMRI. Third, it can measure the cortical activity while the participant is sitting in a natural position in any ordinary room (10). The purpose of this study was to test whether the previously established NIRS-based RSFC measurements can detect the abnormalities in RSFCs of MDD patients, as reported in previous fMRI studies. Because these reports included the RSFC between superficial cerebral cortices, we hypothesized that the hyper- and hypoconnectivity of the DMN and CCN, respectively, in MDD patients can be detected by the NIRS-based RSFC measurement.

METHODS

Ethics

The study was performed following the Declaration of Helsinki and all participants provided written informed consent. This study was approved by The Research Ethics Committee of the Faculty of Medicine of the University of Tokyo (Approval no. 630, 3202, 3361). Written informed consent was obtained from the individual for the publication of any potentially identifiable images or data included in this article.

Participants

For the MDD group, a total of 71 individuals with depressive symptoms were recruited-−25 were admitted to the Department of Neuropsychiatry at the University of Tokyo Hospital between April 2015 and February 2020 for the assessment or treatment of depressive symptoms, and the remaining 46, who participated in the longitudinal study on the brain functional bases and changes in depressive psychiatric disorders, underwent RSFC measurements and clinical assessments (11). The inclusion criteria were current or past MDD defined by the Diagnostic and Statistical Manual Mental Disorders, 4th edition, through a structured clinical interview (12). The exclusion criteria were comorbid dysthymic disorder or substance-induced mood disorder, a history of coarse brain organic disease or epilepsy, alcohol dependence, use of illicit drugs at the time of the study, a childhood diagnosis of mental retardation or developmental disability, a history of loss of consciousness for more than 5 min, and an active physical illness that could present with psychiatric symptoms. Consequently, 51 individuals with current or past MDD were selected.

Of these 51 individuals, fifteen individuals who fell asleep during the NIRS measurements or reported sleepiness grades of 4 or more on the Stanford sleepiness scale (SSS, 0 [feeling active] to 7 [sleep onset]) were excluded from the analysis (13). Additionally, an automatic artifact detection algorithm was applied to the NIRS data, and two participants, for whom the cerebral region-averaged signals could not be estimated owing to excessive artifacts, were excluded (10). Following all the exclusions, we classified the remaining 34 participants as the MDD group. There were no significant differences in age, sex, and years of education between the 34 included and 37 excluded individuals in this study ($p > 0.15$).

For the healthy control (HC) group, 176 participants were recruited from the original pool of participants of the Japanese Study of Stratification, Health, Income, and Neighborhood (J-SHINE) survey, a population-representative survey in the metropolitan region of Tokyo (14). Of these 176 participants, 61 participants with psychiatric disorders detected using the Japanese version of the Composite International Diagnostic Interview or current use of psychotropic drugs were excluded (15, 16). Of these 115 participants, 35 participants who fell asleep during the measurements or were reported with 4 or more points on the SSS, and two participants whose cerebral region-averaged signals could not be estimated owing to excessive artifacts were excluded. The remaining 78 individuals were classified as the HC group.

The rate of participants who were excluded due to sleepiness or excessive artifacts was not significantly different between HC and MDD group (37/115 vs. 17/51, $p = 0.89$).

For both HC and MDD groups, the participants' age, sex, and years of education were assessed. Each participant's estimated (premorbid) intelligence quotient (eIQ) was assessed using the

Abbreviations: MDD, major depressive disorder; NIRS, near-infrared spectroscopy; fMRI, functional magnetic resonance imaging; RSFC, resting-state functional connectivity; DMN, default mode network; CCN, cognitive control network; HC, healthy control; eIQ, estimated (premorbid) intelligence quotient; SSS, Stanford sleepiness scale; HAMD, 17-item Hamilton rating scale for depression; CESD, Center for Epidemiologic Studies depression scale; GAF, global assessment of functioning; oxy-Hb, oxygenated hemoglobin; deoxy-Hb, deoxygenated hemoglobin; FDR, false discovery rate; DLPFC, dorsolateral prefrontal cortex; OFC, orbitofrontal cortex; VLPFC, ventrolateral prefrontal cortex.

25-item Japanese adult reading test (17, 18). Besides, we used the Center for Epidemiologic Studies depression scale (CESD) to evaluate the severity of the subjective depressive symptoms (19).

For the MDD group, a psychiatrist or clinical psychologist assessed the severity of the objective depressive symptoms using the 17-item Hamilton rating scale for depression (HAMD) (20). Social functioning was assessed using the global assessment of functioning (GAF) (21). We also calculated the imipramine equivalent for antidepressants, diazepam equivalent for anxiolytics, and chlorpromazine equivalent for antipsychotics, at the time of NIRS measurement (22).

NIRS Measurement

The measurement protocol was identical to our previous study (10). Participants were seated upright in a quiet room with eyes closed and instructed to stay awake. Changes in the relative concentrations of oxygenated hemoglobin (oxy-Hb) and deoxygenated hemoglobin (deoxy-Hb) were measured for 8 min using a whole-head NIRS arrangement (composed of two ETG-4000 machines from Hitachi, Tokyo, Japan). The system was composed of anterior and posterior thermoplastic shells (**Figures 1A,B**). The anterior shell contained 17 source and 16 detector probes. The posterior shell contained 12 source and 12 detector probes. The source and detector probes were placed alternately within the shells; this constituted 89 source-detector pairs (henceforth, channels), each distanced by 30 mm. Participants wore the probes such that the lowest probes were located on the planar surface defined by T3, Fpz, and T4, according to the international 10–20 system for electroencephalography (**Figure 1C**). This probe arrangement allowed the measurement of changes in oxy- and deoxy-Hb from the bilateral frontal, temporal, parietal, and occipital regions of the cortical surface (**Figure 1D**).

Data Preparation

Data were prepared using MATLAB R2020b (MathWorks, Inc., MA, USA). We applied the procedure previously established to estimate RSFCs between the predetermined 17 cerebral regions, for each oxy- and deoxy-Hb signal (10). Recapitulating the procedure, the signals containing significant artifacts were excluded using an automated algorithm. Then, the region-averaged signals for the 17 cerebral regions were calculated from the oxy- and deoxy-Hb signals acquired from 89 channels (**Figure 1D**). We used a Butterworth band-pass filter to extract the 0.009–0.08 Hz signal component. Finally, we defined the partial correlation coefficient of the signals from two given brain regions as the index of RSFC between the regions.

Statistical Analysis

Statistical analysis was performed using MATLAB R2020b and IBM SPSS Statistics 27 (IBM Inc., New York, USA). We examined whether there were significant differences in age, sex ratio, years of education, eIQ, and CESD scores between the MDD and HC groups. A chi-square test was used for the sex-ratio analysis, and unpaired two-sample *t*-tests were used for analyzing the other factors.

Statistical tests for the RSFC indices were performed by transforming the partial correlation coefficients into z-values using Fisher's z-transformation. Of the 136 brain region pairs, those with partial correlation coefficients of 0.1 or higher in the HC group were regarded as connected. For each connected pair, the difference in RSFCs between the MDD and HC groups was tested using the two-samples unpaired *t*-test.

Because this was a preliminary study, the significance level was set at 5% without any false discovery rate (FDR) correction. However, we also examined the significance of the differences after adjusting for FDR (23).

Besides, we tested the correlations between RSFCs and various clinical variables, including the HAMD, CESD, and GAF scores, and the amounts of imipramine equivalents of antidepressants, diazepam equivalents of anxiolytics, and chlorpromazine equivalents of antipsychotics taken by the participants, for each connected region-pair in the MDD group. The normality of the clinical variables was tested using the Shapiro-Wilk test; Pearson's and Spearman's rank correlation coefficients were obtained when the normality was not rejected and was rejected, respectively.

RESULTS

Demographic and Clinical Features of the MDD and HC Groups

The demographic and clinical features of the participants (34 and 78 in the MDD and HC groups, respectively) are shown in **Table 1**. There was no significant difference in age, sex ratio, years of education, and SSS between the MDD and HC groups ($p > 0.11$). In contrast, eIQ (112.0 vs. 107.5; Cohen's $d = 0.501$, 95% confidence intervals (CI) [0.092 0.908], $p = 0.02$) and CESD (20.0 vs. 8.1; Cohen's $d = 1.413$, 95% CI [0.937 1.882], $p < 0.001$) were significantly higher in the MDD than in the HC group. HAMD and GAF scores and medications used by the MDD participants are shown in **Table 1**. Twelve MDD participants were taking mood stabilizers (five used lithium, three lamotrigine, and eight valproate, with overlap).

Differences in RSFC Patterns Between the MDD and HC Groups

The RSFC patterns and *t*-tests results of the MDD and HC groups are shown in **Figure 2**. The MDD and HC groups had similar RSFC patterns. For oxy-Hb, the RSFC between the left dorsolateral prefrontal cortex (DLPFC) and parietal lobe was significantly lower in the MDD than in the HC group ($z = 0.038$ vs. 0.171; Cohen's $d = 0.583$, 95% CI [0.172 0.992], $p = 0.005$). The RSFC between the right orbitofrontal cortex (OFC) and ventrolateral prefrontal cortex (VLPFC) was significantly higher in the MDD than in the HC group ($z = 0.315$ vs. 0.202; Cohen's $d = 0.464$, 95% CI [0.055 0.870], $p = 0.03$). For deoxy-Hb, there were no region pairs with significant differences in RSFCs between the MDD and HC groups. In both oxy- and deoxy-Hb, the RSFCs between the bilateral parietal lobes did not differ significantly between the two groups. There was no brain

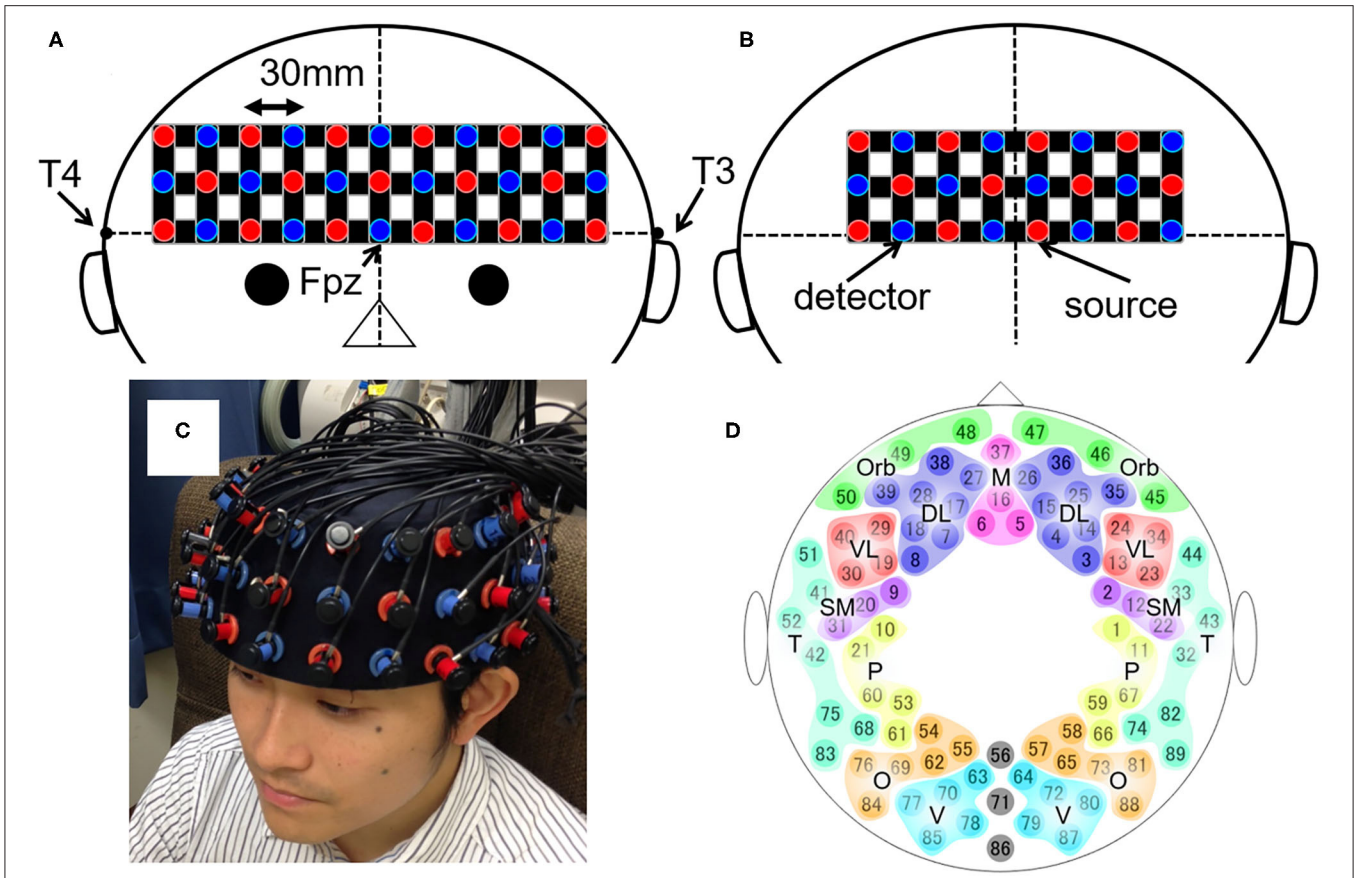

FIGURE 1 | The layout of the whole-head NIRS system and the 89 measuring points. **(A,B)** Schematic illustration of **(A)** the anterior and **(B)** the posterior shells of the whole-head NIRS arrangement. The red and blue circles depict the source and detector probes, respectively. The black horizontal line represents the planar surface defined by T3, Fpz, and T4 according to the international 10–20 system for electroencephalography. The black vertical line represents the midline. **(C)** The actual placement of the probes on the head. **(D)** Schematic illustration of the 89 measuring points and their categorization into 17 brain regions. DL, dorsolateral prefrontal cortex; M, medial prefrontal cortex; Orb, orbitofrontal cortex; VL, ventrolateral prefrontal cortex; SM, sensorimotor area; P, parietal lobe; T, temporal lobe; O, occipital lobe; V, visual area.

region pair in which the difference in RSFCs between the groups was significant after FDR correction.

The Correlation Between RSFCs and Clinical Variables in the MDD Group

The correlations between RSFCs obtained from oxy- and deoxy-Hb signals and various clinical variables in 34 MDD patients are shown in **Figure 3**. Pearson's correlation coefficients were calculated for CESD and GAF scores (normally distributed); Spearman's rank correlation coefficients were calculated for HAMD, antidepressant, antipsychotic, and anxiolytic doses (not normally distributed).

For oxy-Hb, the RSFC between the left DLPFC and parietal lobe was negatively correlated with CESD ($r = -0.405$, 95% CI [−0.676 −0.037], $p = 0.03$) and the antipsychotic dose ($\rho = -0.400$, 95% CI [−0.658 −0.058], $p = 0.02$), and positively correlated with GAF ($r = 0.452$, 95% CI [0.110 0.699], $p = 0.01$). The RSFC between the left and right DLPFCs was positively correlated with HAMD ($\rho = 0.541$, 95% CI [0.225 0.754], $p < 0.001$), CESD ($r = 0.619$, 95% CI [0.320 0.806], $p < 0.001$), and antipsychotic dose ($\rho = 0.473$, 95% CI [0.141 0.709], $p = 0.005$), and negatively correlated with GAF ($r = -0.720$, 95% CI [−0.858 −0.486], $p < 0.001$). Other positive correlations were found between HAMD and the RSFCs of the right sensorimotor cortex and the parietal lobe ($\rho = 0.356$, 95% CI [0.009 0.626], $p = 0.04$), GAF and the RSFCs of the left and right visual area ($r = 0.374$, 95% CI [0.016 0.647], $p = 0.04$), and GAF and the RSFCs of the right DLPFC and the medial prefrontal cortex ($r = 0.407$, 95% CI [0.054 0.669], $p = 0.03$). Correlation trends were inconsistent between the medications and the RSFCs of other brain region pairs. Correlations between the three clinical variables (HAMD, CESD, and GAF) and RSFCs of the left and right DLPFCs were significant following FDR correction.

For deoxy-Hb, HAMD correlated negatively with the RSFC between the left OFC and VLPFC ($\rho = -0.350$, 95% CI [−0.622 −0.002], $p = 0.04$) and positively with that between the left OFC and DLPFC ($\rho = 0.371$, 95% CI [0.026 0.637], $p = 0.03$). CESD correlated positively with the RSFC between the right VLPFC and sensorimotor area ($r = 0.410$, 95% CI [0.043 0.679], $p = 0.03$). GAF correlated negatively with the RSFC between the left

TABLE 1 | Demographic characteristics of participants.

	MDD		HC		Statistical values
	Mean	SD	Mean	SD	
Sex (m/f)	17/17		36/42		$\chi^2_{(1)} = 0.141$; $p = 0.71$
Age (years)	37.4	9.9	37.3	7.2	$t_{(110)} = 0.093$; $p = 0.93$
Education (years)	15.7	2.2	15.1	2	$t_{(101)} = 1.357$; $p = 0.18$
eIQ	112	8	107.5	9.3	$t_{(110)} = 2.440$; $p = 0.02$
CESD	20	14	8.1	5.2	$t^*_{(29.7)} = 4.391$; $p < 0.001$
SSS	2.74	0.51	2.54	0.73	$t^*_{(88.3)} = 1.631$; $p = 0.11$
HAMD	7.12	6.29			
GAF	57.4	16.4			
IMP	96.5	151.9			
CP	48.1	105.1			
DZP	4.9	8.7			

MDD, major depressive disorder; HC, healthy control; SD, standard deviation; m: male; f, female; eIQ, estimated (premorbid) intelligence quotient; SSS, Stanford sleepiness scale; HAMD, 17-item Hamilton rating scale for depression; CESD, Center for Epidemiologic Studies depression scale; GAF, global assessment of functioning; IMP, imipramine equivalent of antidepressant dosage; CP, chlorpromazine equivalent for antipsychotic dosage; DZP, diazepam equivalent for anxiolytic dosage.

**The degrees of freedom were adjusted for CESD and SSS because the equality of variances between the groups was rejected.*

and right DLPFCs ($r = -0.380$, 95% CI [−0.651 −0.023], $p = 0.04$) and that between the left OFC and DLPFC ($r = -0.489$, 95% CI [−0.722 −0.157], $p = 0.006$). The RSFC between the left DLPFC and parietal lobe correlated only with the antipsychotic dose ($\rho = -0.404$, 95% CI [−0.661 −0.062], $p = 0.02$). The correlation trends between medications (doses) and RSFCs of other brain region pairs were inconsistent. However, there was no brain region pair in which the RSFC significantly correlated with the clinical variables following FDR correction.

Analyses of Group Differences in RSFCs Between the Left DLPFC and Parietal Lobe

The RSFC between the left DLPFC and parietal lobe, which was significantly different between the MDD and HC groups, was correlated with the CESD, GAF, and antipsychotic medication dosage of the MDD group. Since GAF was not obtained for the HC group, we performed an analysis of covariance with the RSFC estimated from the oxy-Hb signals of the left DLPFC and parietal lobe as the dependent variable, the group (i.e., MDD or HC) as the fixed factor, and the CESD and dosage of antipsychotic medication as covariates. The results showed that after controlling for CESD and antipsychotic medication, the group differences in RSFCs between the left DLPFC and parietal lobe ceased to be significant, leaving the trend to be lower in the MDD than in the HC group [$F_{(1,102)} = 2.568$, partial $\eta^2 = 0.25$, $p = 0.11$].

DISCUSSION

Summary of Findings

This is the first study that utilized a whole-head NIRS system for elucidating RSFC abnormalities in MDD patients, applying the partial correlation analysis established previously. We found that the MDD group had a lower RSFC between the left DLPFC and parietal lobe and higher RSFC between the right OFC and VLPFC, compared to the HC group.

Furthermore, the RSFCs were correlated with various clinical variables in the MDD group. Particularly, the RSFC between the left DLPFC and parietal lobe, which was significantly lower in the MDD than in the HC group, was negatively correlated with the CESD and antipsychotic dose and was positively correlated with GAF. Besides, the RSFC between the left and right DLPFCs was positively correlated with the HAMD, CESD, and antipsychotic dose and negatively correlated with GAF.

Characteristic RSFC Patterns in MDD Patients

Mood disorders are psychiatric disorders characterized by mood dysregulation. Functional imaging studies in MDD have long focused on impairments in emotion regulation circuits, consisting of the limbic system and its connectivity with cortical regions (7, 24, 25). Recently, MDD has been associated with a variety of cognitive dysfunctions (26, 27), including, reduced psychomotor speed, memory, cognitive flexibility, and word fluency, as shown by a meta-analysis (28). Some of these cognitive impairments may persist even after symptomatic remission (29).

Other studies suggest that MDD patients have a reduced RSFC in the CCN and a stronger RSFC in the DMN, compared to those in healthy individuals (8, 9). A strong RSFC in the DMN causes the self-referential process of rumination, where negative thoughts, such as regret, self-loathing, hopelessness, or worry, repetitively occur in the individual (30).

In this study, the RSFC between the bilateral parietal lobes, which may reflect the DMN connectivity, did not differ between the two groups. In contrast, the RSFC between the left DLPFC and parietal lobe, which may reflect an impaired cognitive function, was weaker in the MDD than in the HC group.

Besides, the RSFC between the right OFC and VLPFC increased in MDD patients. A recent study on 282 MDD patients revealed that the RSFC between the right inferior frontal gyrus and other brain regions, including the OFC, was higher in MDD patients than in healthy individuals (31). In our study, the inferior frontal gyrus is classified as the VLPFC; therefore, our findings are in line with previous findings. The inferior frontal gyrus and OFC are activated when a subject successfully inhibits natural responses during the stop-signal task (32). Therefore, increased RSFC may be related to decreased motivation and excessive psychomotor inhibition found in MDD patients (31).

RSFC studies using NIRS are scarce. In a study that recruited 28 patients with mood disorders (i.e., bipolar disorder or MDD), the local RSFC among the right inferior frontal gyrus and the RSFC between the bilateral inferior frontal gyrus were significantly lower in the patients than in healthy controls (33). Another study that compared the prefrontal and parietal cortical activities of 49 individuals with late-life MDD and 51 non-depressive individuals during rest and trail making test showed reduced RSFC in the left frontopolar cortical network during the trail making test and increased RSFC in the left CCN at

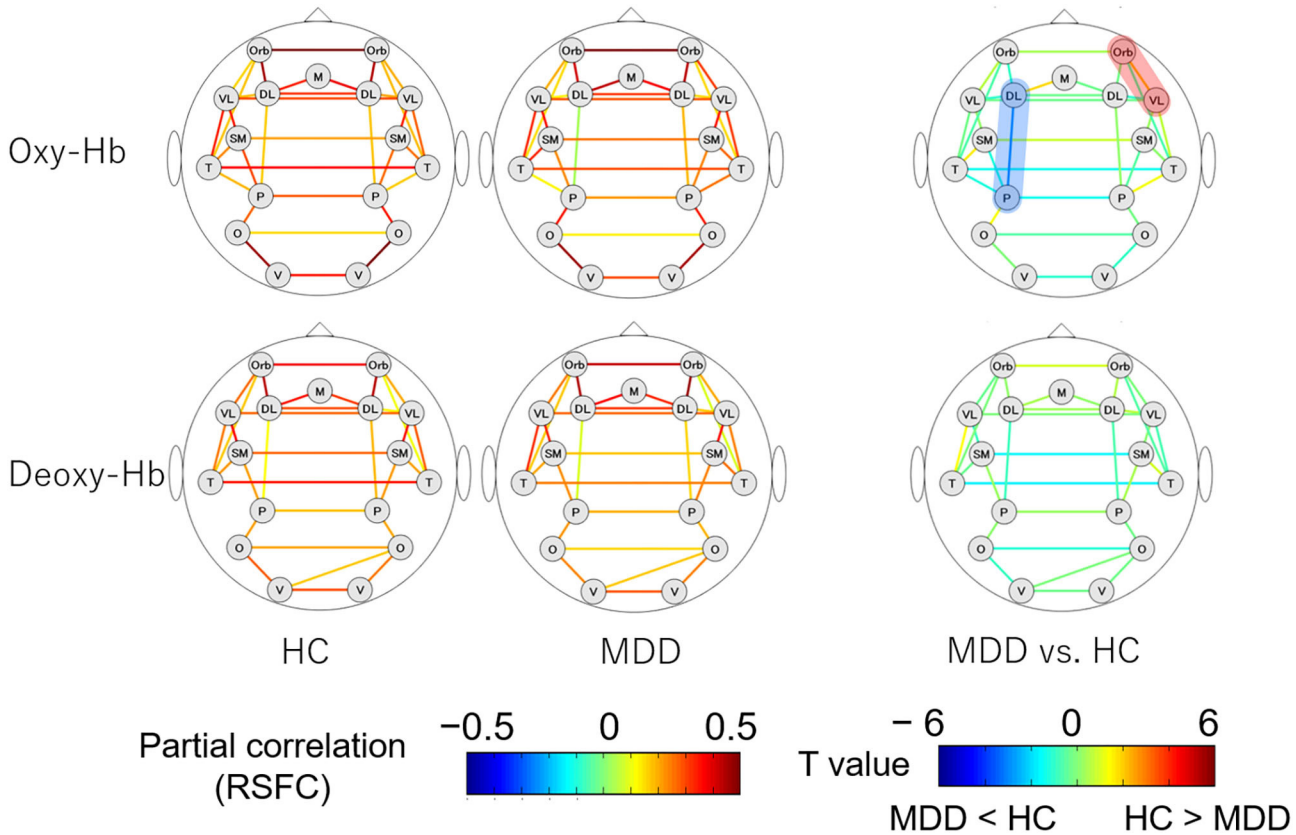

FIGURE 2 | RSFC patterns of the MDD and HC groups. The upper and lower rows show the RSFC patterns calculated from oxy- and deoxy-Hb signals, respectively. The figures on the left illustrate the RSFC patterns of the HC group and the figures in the middle illustrate the RSFC patterns of the MDD group. The figures on the right show the comparison of the strengths of RSFCs between the MDD and HC groups. The brain region pairs, where the strength of RSFC was significantly different between the groups are highlighted in red (MDD > HC) or blue (HC > MDD). MDD, major depressive disorder; RSFC, resting-state functional connectivity; HC, healthy control; oxy-Hb, oxygenated hemoglobin; deoxy-Hb, deoxygenated hemoglobin; DL, dorsolateral prefrontal cortex; M, medial prefrontal cortex; Orb, orbitofrontal cortex; VL, ventrolateral prefrontal cortex; SM, sensorimotor area; P, parietal lobe; T, temporal lobe; O, occipital lobe; V, visual area.

rest (34). In another study, the same research group recruited 60 MDD patients and 24 healthy individuals and discovered that the RSFC in the cortical part of the DMN was lower in MDD patients than in healthy individuals, and rumination was negatively correlated with the strength of RSFC in that region (35).

In the present study, the RSFC in the left CCN was low while that in the prefrontal regions was partially elevated in MDD patients. Although these results were consistent with previous fMRI studies on RSFC, they contradict the results obtained in previous NIRS studies on RSFC. These discrepancies may be attributed to differences in the arrangement of probes, ages of subjects, and the method of estimating the strength of RSFCs. Better consistency with previous fMRI studies could be explained by the usage of partial correlation coefficient as an index of RSFC because it reduces the influence of extracerebral blood flow than Pearson's correlation coefficient used in the previous NIRS studies.

State Dependence and Pharmacological Influence of RSFC

In our study, the RSFC of the left CCN was negatively correlated with CESD and positively correlated with GAF. Previous studies have examined correlations between various aspects of depressive symptoms and RSFCs (30). A recent meta-analysis, integrating data from 25 publications and 516 MDD patients, found that RSFCs of the CCN and DMN were not correlated with symptom severities (8). In contrast, a study that recruited individuals with subthreshold depressive symptoms reported that CESD scores were negatively correlated with the RSFC between DLPFC and the temporoparietal junction (36). Therefore, the correlation between the RSFC of the left CCN and severity of depressive symptoms in the present study may reflect the fact that this study included many remitters, and the reduced RSFC of the CCN was normalized by the remitters.

In the present study, the RSFC between bilateral DLPFCs was positively correlated with depressive symptoms and negatively correlated with GAF. These results are in agreement with a

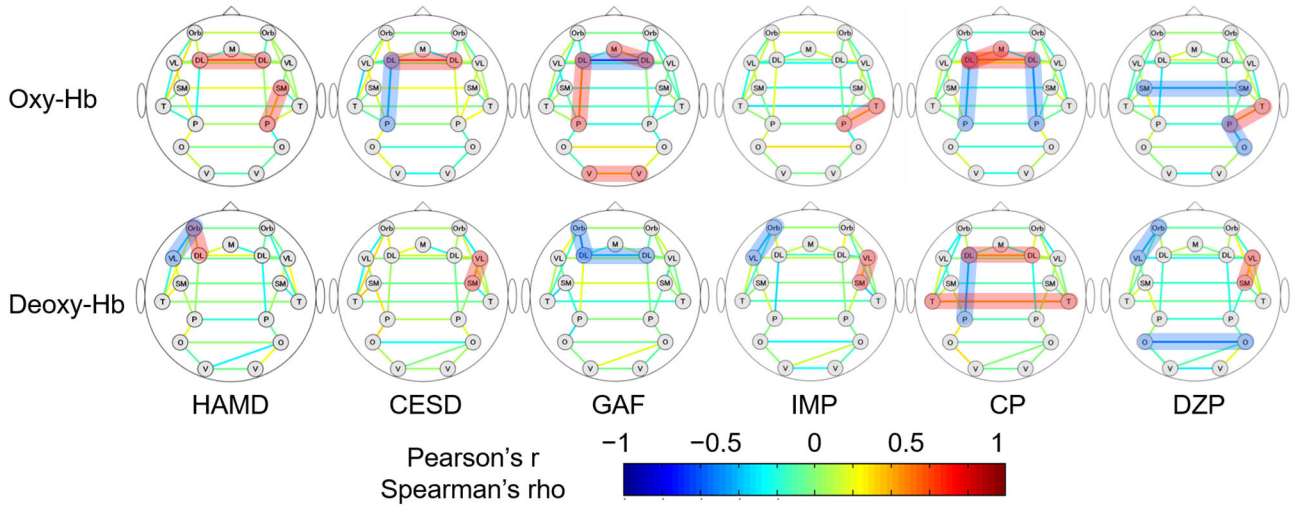

FIGURE 3 | The association between the strengths of RSFCs and clinical variables in MDD patients. The upper and lower rows show the RSFC patterns calculated from oxy- and deoxy-Hb signals, respectively. Pearson's correlation coefficients are depicted for CESD and GAF, while Spearman's rank correlation coefficients are depicted for the rest. The brain region pairs, where the correlation between the strengths of RSFCs and the clinical variables were significantly different between the groups are highlighted in red (positive correlation) or blue (negative correlation). HAMD, 17-item Hamilton rating scale for depression; CESD, Center for Epidemiologic Studies depression scale; GAF, global assessment of functioning; IMP, imipramine equivalent of antidepressant dosage; CP, chlorpromazine equivalent for antipsychotic dosage; DZP, diazepam equivalent for anxiolytic dosage; DL, dorsolateral prefrontal cortex; M, medial prefrontal cortex; Orb, orbitofrontal cortex; VL, ventrolateral prefrontal cortex; SM, sensorimotor area; P, parietal lobe; T, temporal lobe; O, occipital lobe; V, visual area.

previous report that stated that depressive symptoms and inter-hemispheric RSFC in the anterior subnetwork of the DMN were negatively correlated (37). In another study, researchers found that the RSFC between what they call "dorsal nexus," a part of the bilateral dorsomedial prefrontal cortex, and other brain regions, including, other prefrontal regions, the anterior and posterior cingulate cortex, and the precuneus, increased in MDD patients (38). They interpret this as a "hot-wiring" interconnect between DMN, CCN, and affective networks, which incubate various depressive symptoms. Therefore, the results in this study may indirectly reflect an increase in the RSFC between prefrontal regions mediated by the dorsal nexus.

In our study, the antidepressant medication dose did not correlate with the RSFC of the CCN, while the antipsychotic medication dose correlated negatively with the RSFC of the bilateral CCN and positively with the RSFC between the bilateral DLPFCs. In the aforementioned meta-analysis, antidepressants did not correlate with the RSFC of the CCN but normalized the hyperconnectivity in the DMN of MDD patients (9). A study that distinguished the anterior and posterior subnetworks of the DMN, where the posterior DMN subnetwork consisted of the bilateral precuneus and part of the parietal cortex, normalized the hyperconnectivity after antidepressant treatment (39).

Although the effects of antipsychotic medications on depressed patients have not been reported, antipsychotic medications in schizophrenia patients increased RSFCs between the striatum and anterior cingulate gyrus, DLPFC, hippocampus, and anterior insula, and decreased the RSFC between the striatum and parietal lobe, as psychotic symptoms improved. In another study, schizophrenia patients showed increased RSFCs in the right superior temporal gyrus, right medial frontal gyrus, and left superior frontal gyrus, and decreased RSFCs in the right posterior cingulate and precuneus of the DMN, after antipsychotic treatment (40). Besides, the patients exhibited decreased RSFCs in the right cerebellum anterior lobe and left insula in the salience network. The changes in RSFCs reported in these previous studies included brain regions that cannot be measured with NIRS. Furthermore, the previous studies compared the RSFCs before and after medication in the same subjects; this may be difficult to extrapolate for interpreting the variance among different subjects with different medications, as is the case in the present study. The results of this study suggest that psychotropic medications have substantial effects on RSFCs and different kinds of psychotropics have different influences.

Limitation of the Study

First, the differences in RSFCs between the HC and MDD groups and the correlations between RSFCs and clinical variables in the MDD group were not statistically significant after FDR correction, except for the association between clinical variables and the RSFC between the left and right DLPFCs. In addition, we performed a *post-hoc* sensitivity analysis using G*Power 3 (41). If we set $\alpha = 0.05$ and $\beta = 0.80$, the sample size of our study ($n = 34$ and 78) is estimated to have the power to detect the group difference with an effect size of 0.58 or more, a medium size effect. Therefore, smaller effect size differences may be undetected in our study. Furthermore, the importance of assessing the reliability

of measurement methods in neuroimage research has been indicated (42). However, there is no data on the reliability of the method used in this study. Therefore, the reproducibility of the results needs to be validated using larger datasets in the future, and the assessment of reliability of the method for estimating the strength of the RSFC used in this study should be clarified.

Second, in this study, the MDD patients were referred to the University of Tokyo Hospital, a tertiary care hospital, for the assessment of depressive symptoms that were refractory to treatment. The high percentage of patients taking antipsychotic medications and mood stabilizers, despite being diagnosed with MDD according to the Diagnostic and Statistical Manual Mental Disorders, indicates that the subjects in this study were not typical MDD patients. The study also included many patients from the longitudinal study, many of whom were already in the remission phase of their depressive symptoms. Besides, this study suggests that antipsychotic medications have various effects on RSFCs. Therefore, the RSFC characteristics and their correlations with clinical variables in the MDD group are likely to be influenced by antipsychotic medications. Therefore, careful consideration is required when the study results are extrapolated to a more typical depressed group, who are non-medicated or solely taking antidepressants.

SUMMARY

The present study used a whole-head NIRS system to elucidate RSFC patterns characteristic of MDD. Compared with the HC group, MDD patients had a lower RSFC between the left DLPFC and parietal lobe, which may constitute the CCN. The RSFC in the CCN was negatively correlated with the severity of depressive symptoms and dosage of antipsychotic medication and positively correlated with the level of functioning. Therefore, these might reflect an individual's depressive status rather than the trait predisposing to depression. This study confirms that abnormalities in RSFC patterns in major depressive disorders, as identified by previous fMRI studies, can be partially detected by measuring the resting-state brain activities using NIRS. Combining the convenience of measuring the brain activity using NIRS and the ease of performing resting-state measurements (no requirement for cognitive tasks), NIRS-based measurements of RSFCs have potential clinical applications. Therefore, further studies validating the result of our findings and those of the NIRS-based RSFC measurements in other psychiatric disorders are warranted.

DATA AVAILABILITY STATEMENT

The datasets analyzed during the current study are not publicly available due to ethical considerations in this study but are available from the corresponding author on reasonable request, with the approval of the Research Ethics Committee of the Faculty of Medicine of the University of Tokyo.

ETHICS STATEMENT

The studies involving human participants were reviewed and approved by The Research Ethics Committee of the Faculty of Medicine of the University of Tokyo (Approval No. 630, 3202, 3361). The patients/participants provided their written informed consent to participate in this study.

AUTHOR CONTRIBUTIONS

YS, NK, and KK designed the study. Data were collected by ES, YS, JM, MY, HS, and NK. ES analyzed and interpreted the data with intellectual input from YS, JM, SK, NO, HS, MY, and KK. ES wrote the manuscript, which was revised by YS, SK, and KK. All the authors have approved the final manuscript.

FUNDING

This study was supported by JSPS KAKENHI [Grant Nos. 20H03596 (KK), 20K16642 (YS), and 20K16665 (ES)], the Brain Mapping by Integrated Neurotechnologies for Disease Studies (Brain/MINDS) from Japan Agency for Medical Research and Development, AMED under Grant No. JP20dm0207069, and the Grants-in-Aid for Scientific Research on Innovative Areas by MEXT, Japan: Elucidation of social stratification mechanism and control over health inequality in contemporary Japan: New interdisciplinary area of social and health sciences project [Grant No. 21119003 to NK]. This study was also supported by the University of Tokyo Center for Integrative Science of Human Behavior (CiSHuB) and the International Research Center for Neurointelligence (IRCN) at the University of Tokyo Institutes for Advanced Study (UTIAS). The funders had no role in the study design, data collection and analysis, publication decision, or manuscript preparation.

ACKNOWLEDGMENTS

We thank Hideki Hashimoto for providing the data from J-SHINE studies. We also thank all the participants of the study and the staff who helped with the psychiatric assessment.

REFERENCES

1. Boas DA, Elwell CE, Ferrari M, Taga G. Twenty years of functional near-infrared spectroscopy: introduction for the special issue. *Neuroimage*. (2014) 85 Pt 1:1–5. doi: 10.1016/j.neuroimage.2013.11.033
2. Zhang H, Dong W, Dang W, Quan W, Tian J, Chen R, et al. Near-infrared spectroscopy for examination of prefrontal activation during cognitive tasks in patients with major depressive disorder: a meta-analysis of observational studies. *Psychiatry Clin Neurosci*. (2015) 69:22–33. doi: 10.1111/pcn.12209
3. Takizawa R, Fukuda M, Kawasaki S, Kasai K, Mimura M, Pu S, et al. Neuroimaging-aided differential diagnosis of the depressive state. *Neuroimage*. (2014) 85(Pt 1):498–507. doi: 10.1016/j.neuroimage.2013.05.126

4. Biswal B, Yetkin FZ, Haughton VM, Hyde JS. Functional connectivity in the motor cortex of resting human brain using echo-planar MRI. *Magn Reson Med*. (1995) 34:537–41. doi: 10.1002/mrm.1910340409
5. Greicius M. Resting-state functional connectivity in neuropsychiatric disorders. *Curr Opin Neurol*. (2008) 21:424–30. doi: 10.1097/WCO.0b013e328306f2c5
6. van den Heuvel MP, Hulshoff Pol HE. Exploring the brain network: a review on resting-state fMRI functional connectivity. *Eur Neuropsychopharmacol*. (2010) 20:519–34. doi: 10.1016/j.euroneuro.2010.03.008
7. Anand A, Li Y, Wang Y, Wu J, Gao S, Bukhari L, et al. Activity and connectivity of brain mood regulating circuit in depression: a functional magnetic resonance study. *Biol Psychiatr*. (2005) 57:1079–88. doi: 10.1016/j.biopsych.2005.02.021
8. Kaiser RH, Andrews-Hanna JR, Wager TD, Pizzagalli DA. Large-scale network dysfunction in major depressive disorder: a meta-analysis of resting-state functional connectivity. *JAMA Psychiatr*. (2015) 72:603–11. doi: 10.1001/jamapsychiatry.2015.0071
9. Alexopoulos GS, Hoptman MJ, Kanellopoulos D, Murphy CF, Lim KO, Gunning FM. Functional connectivity in the cognitive control network and the default mode network in late-life depression. *J Affect Disord*. (2012) 139:56–65. doi: 10.1016/j.jad.2011.12.002
10. Sakakibara E, Homae F, Kawasaki S, Nishimura Y, Takizawa R, Koike S, et al. Detection of resting state functional connectivity using partial correlation analysis: a study using multi-distance and whole-head probe near-infrared spectroscopy. *Neuroimage*. (2016) 142:590–601. doi: 10.1016/j.neuroimage.2016.08.011
11. Satomura Y, Sakakibara E, Takizawa R, Koike S, Nishimura Y, Sakurada H, et al. Severity-dependent and -independent brain regions of major depressive disorder: a long-term longitudinal near-infrared spectroscopy study. *J Affect Disord*. (2019) 243:249–54. doi: 10.1016/j.jad.2018.09.029
12. First MB, Spitzer RL, Gibbon M, Williams JBW. *User's Guide for the Structured Clinical Interview for DSM-IV Axis I Disorders SCID-I: Clinician Version*. Washington, DC: American Psychiatric Publishing (1997).
13. Hoddes E, Zarcone V, Smythe H, Phillips R, Dement WC. Quantification of sleepiness: a new approach. *Psychophysiology*. (1973) 10:431–6. doi: 10.1111/j.1469-8986.1973.tb00801.x
14. Takada M, Kondo N, Hashimoto H, J-SHINE Data Management Committee. Japanese study on stratification, health, income, and neighborhood: study protocol and profiles of participants. *J Epidemiol*. (2014) 24:334–44. doi: 10.2188/jea.JE20130084
15. Kawakami N, Takeshima T, Ono Y, Uda H, Hata Y, Nakane Y, et al. Twelve-month prevalence, severity, and treatment of common mental disorders in communities in Japan: preliminary finding from the World Mental Health Japan Survey 2002-2003. *Psychiatr Clin Neurosci*. (2005) 59:441–52. doi: 10.1111/j.1440-1819.2005.01397.x
16. Kessler RC, Ustün TB. The World Mental Health (WMH) Survey Initiative Version of the World Health Organization (WHO) Composite International Diagnostic Interview (CIDI). *Int J Methods Psychiatr Res*. (2004) 13:93–121. doi: 10.1002/mpr.168
17. Matsuoka K, Kim Y. *Japanese Adult Reading Test*. Tokyo: Shinko-Igaku publishers (2006).
18. Matsuoka K, Uno M, Kasai K, Koyama K, Kim Y. Estimation of premorbid IQ in individuals with Alzheimer's disease using Japanese ideographic script (Kanji) compound words: Japanese version of National Adult Reading Test. *Psychiatry Clin Neurosci*. (2006) 60:332–9. doi: 10.1111/j.1440-1819.2006.01510.x
19. Wada K, Tanaka K, Theriault G, Satoh T, Mimura M, Miyaoka H, et al. Validity of the Center for epidemiologic studies depression scale as a screening instrument of major depressive disorder among Japanese workers. *Am J Ind Med*. (2007) 50:8–12. doi: 10.1002/ajim.20403
20. Hamilton M. A rating scale for depression. *J Neurol Neurosurg Psychiatr*. (1960) 23:56–62. doi: 10.1136/jnnp.23.1.56
21. American Psychiatric Association. *Diagnostic and Statistical Manual of Mental Disorders: DSM-IV-TR*. 4th ed. Washington, DC (2000).
22. Inada T, Inagaki A. Psychotropic dose equivalence in Japan. *Psychiatry Clin Neurosci*. (2015) 69:440–7. doi: 10.1111/pcn.12275
23. Singh AK, Dan I. Exploring the false discovery rate in multichannel NIRS. *Neuroimage*. (2006) 33:542–9. doi: 10.1016/j.neuroimage.2006.06.047
24. Anand A, Li Y, Wang Y, Gardner K, Lowe MJ. Reciprocal effects of antidepressant treatment on activity and connectivity of the mood regulating circuit: an FMRI study. *J Neuropsychiatry Clin Neurosci*. (2007) 19:274–82. doi: 10.1176/jnp.2007.19.3.274
25. Anand A, Li Y, Wang Y, Lowe MJ, Dzemidzic M. Resting state corticolimbic connectivity abnormalities in unmedicated bipolar disorder and unipolar depression. *Psychiatry Res*. (2009) 171:189–98. doi: 10.1016/j.pscychresns.2008.03.012
26. Austin MP, Mitchell P, Goodwin GM. Cognitive deficits in depression: possible implications for functional neuropathology. *Br J Psychiatr*. (2001) 178:200–6. doi: 10.1192/bjp.178.3.200
27. Martínez-Arán A, Vieta E, Reinares M, Colom F, Torrent C, Sánchez-Moreno J, et al. Cognitive function across manic or hypomanic, depressed, and euthymic states in bipolar disorder. *Am J Psychiatr*. (2004) 161:262–70. doi: 10.1176/appi.ajp.161.2.262
28. Lee RSC, Hermens DF, Porter MA, Redoblado-Hodge MA. A meta-analysis of cognitive deficits in first-episode major depressive disorder. *J Affect Disord*. (2012) 140:113–24. doi: 10.1016/j.jad.2011.10.023
29. Hasselbalch BJ, Knorr U, Kessing LV. Cognitive impairment in the remitted state of unipolar depressive disorder: a systematic review. *J Affect Disord*. (2011) 134:20–31. doi: 10.1016/j.jad.2010.11.011
30. Brakowski J, Spinelli S, Dörig N, Bosch OG, Manoliu A, Holtforth MG, et al. Resting state brain network function in major depression – depression symptomatology, antidepressant treatment effects, future research. *J Psychiatr Res*. (2017) 92:147–59. doi: 10.1016/j.jpsychires.2017.04.007
31. Rolls ET, Cheng W, Du J, Wei D, Qiu J, Dai D, et al. Functional connectivity of the right inferior frontal gyrus and orbitofrontal cortex in depression. *Soc Cogn Affect Neurosci*. (2020) 15:75–86. doi: 10.1093/scan/nsaa014
32. Deng W, Rolls ET, Ji X, Robbins TW, Banaschewski T, Bokde ALW, et al. Separate neural systems for behavioral change and for emotional responses to failure during behavioral inhibition. *Hum Brain Mapp*. (2017) 38:3527–37. doi: 10.1002/hbm.23607
33. Zhu H, Xu J, Li J, Peng H, Cai T, Li X, et al. Decreased functional connectivity and disrupted neural network in the prefrontal cortex of affective disorders: a resting-state fNIRS study. *J Affect Disord*. (2017) 221:132–44. doi: 10.1016/j.jad.2017.06.024
34. Rosenbaum D, Hagen K, Deppermann S, Kroczek AM, Haeussinger FB, Heinzel S, et al. State-dependent altered connectivity in late-life depression: a functional near-infrared spectroscopy study. *Neurobiol Aging*. (2016) 39:57–68. doi: 10.1016/j.neurobiolaging.2015.11.022
35. Rosenbaum D, Haipt A, Fuhr K, Haeussinger FB, Metzger FG, Nuerk HC, et al. Aberrant functional connectivity in depression as an index of state and trait rumination. *Sci Rep*. (2017) 7:2174. doi: 10.1038/s41598-017-02277-z
36. Hwang JW, Egorova N, Yang XQ, Zhang WY, Chen J, Yang XY, et al. Subthreshold depression is associated with impaired resting-state functional connectivity of the cognitive control network. *Transl Psychiatr*. (2015) 5:e683. doi: 10.1038/tp.2015.174
37. Lai C-H, Wu Y-T. Decreased inter-hemispheric connectivity in anterior sub-network of default mode network and cerebellum: significant findings in major depressive disorder. *Int J Neuropsychopharmacol*. (2014) 17:1935–42. doi: 10.1017/S1461145714000947
38. Sheline YI, Price JL, Yan Z, Mintun MA. Resting-state functional MRI in depression unmasks increased connectivity between networks via the dorsal nexus. *Proc Natl Acad Sci USA*. (2010) 107:11020–5. doi: 10.1073/pnas.1000446107
39. Li B, Liu L, Friston KJ, Shen H, Wang L, Zeng LL, et al. A treatment-resistant default mode subnetwork in major depression. *Biol Psychiatr*. (2013) 74:48–54. doi: 10.1016/j.biopsych.2012.11.007
40. Wang Y, Tang W, Fan X, Zhang J, Geng D, Jiang K, et al. Resting-state functional connectivity changes within the default mode network and the salience network after antipsychotic treatment in early-phase schizophrenia. *Neuropsychiatr Dis Treat*. (2017) 13:397–406. doi: 10.2147/NDT.S123598
41. Faul F, Erdfelder E, Lang A-G, Buchner A. G*Power 3: a flexible statistical power analysis program for the social, behavioral, and biomedical sciences. *Behav Res Methods*. (2007) 39:175–91. doi: 10.3758/BF03193146

42. Zuo X-N, Xu T, Milham MP. Harnessing reliability for neuroscience research. *Nat Hum Behav*. (2019) 3:768–771. doi: 10.1038/s41562-019-0655-x

Conflict of Interest: The authors declare that the research was conducted in the absence of any commercial or financial relationships that could be construed as a potential conflict of interest.

frontiers in Psychiatry

ORIGINAL RESEARCH
published: 08 June 2021
doi: 10.3389/fpsyt.2021.674568

Gray Matter Abnormalities of Orbitofrontal Cortex and Striatum in Drug-Naïve Adult Patients With Obsessive-Compulsive Disorder

Zhang Bowen[1†], *Tan Changlian*[2†], *Liu Qian*[1], *Peng Wanrong*[3], *Yang Huihui*[3], *Liu Zhaoxia*[3], *Li Feng*[1], *Liu Jinyu*[1], *Zhu Xiongzhao*[3,4] *and Zhong Mingtian*[1*]

[1] Guangdong Key Laboratory of Mental Health and Cognitive Science, Center for Studies of Psychological Application, School of Psychology, South China Normal University, Guangzhou, China, [2] Department of Radiology, Second Xiangya Hospital, Central South University, Changsha, China, [3] Medical Psychological Center, The Second Xiangya Hospital, Central South University, Changsha, China, [4] Medical Psychological Institute, Central South University, Changsha, China

OPEN ACCESS

Edited by:
Boldizsar Czeh,
University of Pécs, Hungary

Reviewed by:
Hao Yan,
Peking University, China
Zhiqiang Sha,
Max Planck Institute for Psycholinguistics, Netherlands
Zhen Wang,
Shanghai Jiao Tong University, China

***Correspondence:**
Zhong Mingtian
ztomorrow@126.com

[†]These authors have contributed equally to this work and share first authorship

Specialty section:
This article was submitted to Neuroimaging and Stimulation, a section of the journal Frontiers in Psychiatry

Received: 05 March 2021
Accepted: 14 May 2021
Published: 08 June 2021

Citation:
Bowen Z, Changlian T, Qian L, Wanrong P, Huihui Y, Zhaoxia L, Feng L, Jinyu L, Xiongzhao Z and Mingtian Z (2021) Gray Matter Abnormalities of Orbitofrontal Cortex and Striatum in Drug-Naïve Adult Patients With Obsessive-Compulsive Disorder. Front. Psychiatry 12:674568. doi: 10.3389/fpsyt.2021.674568

Objective: This study examined whether obsessive-compulsive disorder (OCD) patients have gray matter abnormalities in regions related to executive function, and whether such abnormalities are associated with impaired executive function.

Methods: Multiple scales were administered to 27 first-episode drug-naïve OCD patients and 29 healthy controls. Comprehensive brain morphometric indicators of orbitofrontal cortex (OFC) and three striatum areas (caudate, putamen, and pallidum) were determined. Hemisphere lateralization index was calculated for each region of interest. Correlations between lateralization index and psychological variables were examined in OCD group.

Results: The OCD group had greater local gyrification index for the right OFC and greater gray matter volumes of the bilateral putamen and left pallidum than healthy controls. They also had weaker left hemisphere superiority for local gyrification index of the OFC and gray matter volume of the putamen, but stronger left hemisphere superiority for gray matter volume of the pallidum. Patients' lateralization index for local gyrification index of the OFC correlated negatively with Yale-Brown Obsessive Compulsive Scale and Dysexecutive Questionnaire scores, respectively.

Conclusion: Structural abnormalities of the bilateral putamen, left pallidum, and right OFC may underlie OCD pathology. Abnormal lateralization in OCD may contribute to the onset of obsessive-compulsive symptoms and impaired executive function.

Keywords: orbitofrontal cortex, striatum, local gyrification index, lateralization index, executive function

INTRODUCTION

Obsessive-compulsive disorder (OCD) is a severe and potentially disabling mental disorder that is associated with neurodevelopmental risk factors (1). Commonly, OCD patients suffer from various types of cognitive impairment (2), such as altered flexibility (3), inhibition (4), and decision-making (5, 6).

There has been a growth in research efforts focused on the pathological mechanism of OCD (1, 7, 8). High-resolution brain magnetic resonance imaging (MRI) techniques investigating the cerebral changes associated with OCD and the pathological mechanism underlying OCD have revealed structural and functional abnormalities (1, 7, 8). Functional hyperactivity in the cortical-striatal-thalamic-cortical (CSTC) pathway has been suggested to underlie the manifestations of OCD (9, 10). A previous connectionism study indicated that functional alterations in the CSTC pathway were associated with structural alterations affecting connectivity between the orbitofrontal cortex (OFC) and the striatum (11, 12). Structural MRI studies have also revealed anatomical abnormalities of the OFC (13–15), striatum (16–18), and anterior cingulate cortex (ACC) (19), thalamus, hippocampus (1), and occipital cortex (20).

The CSTC pathway, a putative pathological loop of OCD (21, 22), is a multi-synaptic neuronal circuit that connects the cortex, striatum, and thalamus. It mediates important psychological functions, including movement selection and execution, behavioral initiation, habit formation, and reward. Oscillations and synchronous activity in CSTC pathway brain regions are important for the execution of habitual actions (9). Thus, synaptic dysfunction in the CSTC loop in OCD may underlie the repetitive involuntary movements associated with the disorder (10).

Research examining OCD has been focused on the OFC and striatum, which have been related to decision-making, emotion control, and cognition (7, 15, 23). Multiple studies have found an altered gray matter volume (GMV) of the OFC in OCD patients, though the direction and location of the alteration have been variable (13, 14, 24). Christian reported OCD had an greater GMV of the left OFC than healthy controls (HCs) (14), whereas van den Heuvel found a reduced GMV of the left OFC (25). Additionally, Radua et al. reported that OCD had a smaller surface area (SA) of the right OFC (17). Fouche et al. and Shin et al. both reported reduced cortical thickness (CT) of the left OFC and right inferior frontal cortex (8, 26).

The striatum consists of the caudate nucleus, putamen, and pallidum. Various structural alterations of the striatum have been found in OCD studies (15, 21, 24, 27). Some have reported greater GMVs of the caudate nucleus in OCD (16, 17), whereas others found reduced GMVs of the caudate nucleus and putamen in OCD (18, 28) and an inverse correlation between striatal GMV and OCD symptom severity (28). A meta-analysis also indicated that adult patients with OCD had significantly larger pallidum volumes compared with controls (1).

The aforementioned inconsistencies could be due to multiple factors. Firstly, cohort heterogeneity, such as depressive comorbidity, treatment, age of onset, disease course, and symptom severity, may contribute to the disparate findings. Secondly, although there may be atypical lateralization among psychiatric patients (29), most OCD studies have not accounted for lateralization. Thirdly, noise may be introduced by different researchers employing different methodological paradigms, such as focusing on a priori regions of interest (ROIs) vs. whole brain analysis, the use of voxel-based vs. surface-based morphometric analyses, and the use of different morphometric indicators.

Commonly, structural MRI studies of OCD have examined GMV, SA, and CT. Meanwhile, there remains little information regarding cortical folding in OCD. GMV is determined by both SA and CT, parameters that are influenced by different developmental factors. Cortical SA increases with cortical folding during the later stages of fetal development and CT changes dynamically across the lifespan as a consequence of development and disease (30). The differing developmental trajectories of these properties is likely to be reflected in the morphometric indicator findings associated with them.

Most studies that have examined cortical folding in OCD have focused on the ACC (19), prefrontal cortex (31), and occipital cortex (20). Wobrock found that OCD patients had hypogyrification of the left prefrontal cortex compared with HCs and pointed out that it might be a structural correlate of OCD-related impairments in executive function (EF) (31). Rus et al. found hypogyrification of rostral middle frontal regions as well as a positive association of age of onset with average local gyrification index (LGI) of the right hemisphere, including the insula, rostral middle frontal cortex, and lateral OFC (32). Venkatasubramanian found inverse correlations between OCD patients' Yale-Brown Obsessive Compulsive Scale (Y-BOCS) compulsion and insight scores with LGI values obtained for the right OFC and left medial OFC, respectively (33). Cortical folding is an indicator of early neurodevelopment, and OCD has been associated with early neurodevelopmental abnormalities (33). Thus far, there have been few studies focused on OFC folding in OCD patients.

Lateralization of cortical and subcortical structure abnormalities have been described in some patients with neuropsychiatric diagnoses (34, 35). Although few studies have focused on brain lateralization in OCD patients directly, some studies have provided hints of possible abnormal lateralization patterns in OCD. For example, Chen found that patients with OCD showed weaker connectivity between left caudate nucleus and thalamus compared with controls, which was also correlated with the duration of OCD (22). Hu et al. found that a greater GMV of the left putamen was most prominent in samples with higher percentages of medicated adult OCD patients (27). Lazaro observed that treatment of OCD patients was associated with a greater GMV of the right striatum (24). These studies suggest that OCD may be related to left hemisphere-lateralized brain alterations.

EF impairments, such as executive inhibition, transformation, refreshment, and working memory impairments, represent the core features of OCD (23, 36, 37). Neuroimaging researches suggested that EF impairments in OCD were related to malfunction of CSTC loop (37–39), and excessive activation of the OFC and striatum might be the most prominent findings in OCD patients (37, 40, 41). The OFC is strongly involved in the process of response inhibition, planning and problem solving, therefore, its dysfunction might result in corresponding EF impairment (40–42). While the striatum collects, modulates and integrates cortical information for EF, its dysfunction might impair EF, such as inhibition and decision making (43). However, the relationship between lateralized OFC/striatum differences

and the clinical manifestations of OCD, especially impaired EF, is lacking.

This study aimed to test the hypothesis that impaired executive function in OCD patients is related to gray matter abnormalities, including cortical folding and hemispherical lateralization, in regions related with executive function, with OFC and striatum as ROIs.

MATERIALS AND METHODS

Subjects

Twenty-seven drug-naïve young OCD patients participated in this study. All patients were recruited from outpatient clinics affiliated with the Second Xiangya Hospital of Central South University in Changsha, Hunan, China. The diagnoses of OCD and axis I psychiatric comorbidities were established independently by two highly-experienced psychiatrists based on the Structured Clinical Interview for DSM-IV. The inclusion criteria were: (1) ≥18 years old; (2) ≥9 years of formal education; (3) compliance with OCD diagnostic criteria in the DSM-IV; (4) first-episode and drug-naïve status; (5) no past or current other axis I diagnosis.

Twenty-nine age-matched community population participants were recruited to form the HC group. HCs were evaluated independently by two highly-experienced psychiatrists to rule out any axis I/II psychiatric disorders based on the Structured Clinical Interview for DSM-IV. The inclusion criteria were: (1) ≥18 years old; (2) ≥9 years of formal education; (3) axis I/II psychiatric disorders ruled out.

The exclusion criteria for all participants were: (1) a history of major medical or neurological problems (e.g., hypothyroidism, seizure disorder, or brain injury); (2) MRI contraindication; (3) taking drugs that affect cognitive function or related treatment; (4) being pregnant, lactating, or preparing for pregnancy; (5) inability to cooperate with the MRI procedure.

The study was conducted in accord with the Declaration of Helsinki and approved by Ethics Committee of the Second Xiangya Hospital of Central South University. All subjects provided written informed consent after receiving a full explanation of the purpose and procedures of the study.

Self-Report Instruments

At the time of recruitment, participants completed the Chinese versions of several psychological assessments, including the self-reported Beck Depression Inventory (BDI), the State-Trait Anxiety Inventory (STAI), and Dysexecutive Questionnaire (DEQ). Patients with OCD also completed the Y-BOCS. The BDI and STAI were used to assess depression and anxiety levels, respectively (44). The DEQ was applied to detect executive dysfunction (45). The Y-BOCS was used to assess the severity and symptom profile of obsessive-compulsive disorder (46). All of the scales used in this study have been shown to have good reliability and validity (44, 47–49), see **Supplementary Material** for details.

MRI Data Acquisition

Imaging data were acquired on a Siemens Skyra 3-T magnetic resonance scanner at the Second Xiangya Hospital of Central South University. We collected three-dimensional T1-weighted magnetization-prepared rapid gradient echo sagittal images (50), with the follow parameters: 176 slices, 1,900-ms repetition time, 2.01-ms echo time, 1.00-mm slice thickness, 1.00-mm^3 voxel size, 9° flip angle, 900-ms inversion time, 256-mm field of view, and 256 × 256 matrix (51).

Image Processing

Image data were processed by surface-based, multi-step, and semi-automated morphometric analyses. The FreeSurfer image analysis software suite was used to generate a cortical surface representations (composed of a mesh of triangles) for measurement of GMV, SA, and CT and determination of LGI values at each vertex. Preprocessing steps included visual inspection of data for motion artifacts, transformation to Talairach space, intensity normalization for correction of magnetic field inhomogeneities, and removal of non-brain tissues. For volumetric data, FreeSurfer classified cortical structures automatically. The analysis was enhanced by reference to the ROIs defined anatomically from the 2009 Destrieux Atlas during FreeSurfer segmentation (52).

The ROIs used in this study were the OFC and striatum (**Figure 1**). The following four morphometric parameters (per vertex) were extracted with FreeSurfer: GMV in cortex, SA (of pial surfaces), CT (the distance between white matter and pial surfaces), and LGI. LGI was calculated to evaluate the cortical folding pattern and utilized in the context of the FreeSurfer analysis suite. The original gyrification index was obtained by the following four steps: (1) three-dimensional reconstruction of pial cortical surface; (2) delineation of the outer hull that tightly warps the pial surface; (3) computation of LGI for each outer-surface vertex; and (4) propagation of LGI values from the outer

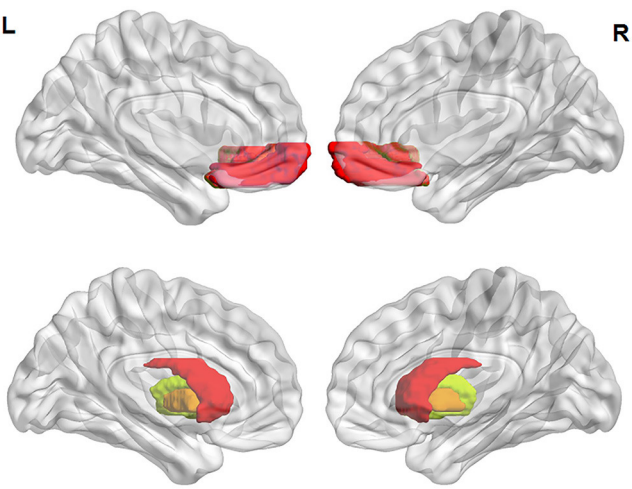

FIGURE 1 | ROI locations. The ROIs defined as in the 2009 Destrieux Atlas. Pseudocolored areas show pial surface representations of the OFC (above) and volume representations of the striatum (below), wherein red shows the caudate nucleus, yellow shows the putamen, and orange shows the pallidum. ROI, region of interest; L, left; R, right.

surface mesh to the pial surface mesh to produce a cortical map of LGIs (53).

Statistical Analyses

Surface-based group analyses were performed with FreeSurfer's general linear model tools. Prior to group comparison, each participant's data were resampled into a common anatomical space. Surface-based measurements of GMV, SA, CT, and LGI for all subjects were smoothed with 5-mm full-width at half-maximum Gaussian kernels. After defining the OFC and striatum as ROIs in volume space, we transformed each spherical ROI volume into an area (cluster) ROI in the surface space and measured the mean GMV, SA, CT, and LGI of each cluster ROI for each subject.

Differences in demographic and clinical characteristics between the OCD and HC groups were detected by two-sample *t*-tests or chi-squared test in SPSS software (version 22.0; Chicago, IL). Linear correlation of ROI variables with Y-BOCS and DEQ scores were assessed by Pearson correlation analysis. Regional GMV, SA, CT, and LGI data were subjected to analysis of repeated measurement variance with covariates (ANCOVAs), with hemisphere (left or right) as a within-subject factor, group as a between-subjects factor, and intracranial volume as a covariate. Main effects and interactions were evaluated with Greenhouse-Geisser corrected degrees of freedom and had a significance criterion of $p < 0.05$ before *post hoc* pairwise contrasts.

Laterality Index (LI) was calculated for each subject, see **Supplementary Materials**. Mean LI values are reported for each group with standard deviations (SDs). Shapiro-Wilk test was used to verify the normality of LI (54), which were shown in **Supplementary Table 1**. For the LI of putamen and pallidum were non-normal data ($ps < 0.05$), two sample *t* test and permutation test ($N = 10{,}000$) were applied to examine the regional LI differences between OCD group and HC group, respectively (55). Two-tailed partial correlation analyses between LI and psychological variables were performed with intracranial volume as the control variable. Effect size η^2 and Cohen's *d* values were indicated where appropriate (56, 57).

RESULTS

Demographic and Clinical Data

The characteristics of the subjects in each group are summarized in **Table 1**. All subjects were right handed and there were no significant group differences in age, sex, or intracranial volume (all $p > 0.05$). The OCD group had significantly higher BDI, STAI-S, STAI-T, and DEQ scores than the HC group.

Morphometrics of the OFC and Striatum

Mean regional GMV, SA, CT, and LGI values obtained for the OFC and GMV for the three substructures of the striatum are reported for the left hemisphere and right hemisphere in **Table 2**.

GMV

For GMV of the OFC, there was no significant group difference [$F_{(1, 53)} = 1.44, p = 0.24$], no main effect of hemisphere [$F_{(1, 53)} = 3.95, p = 0.052$], and no significant group' hemisphere interaction [$F_{(1, 53)} = 1.15, p = 0.29$]. For GMV of the caudate nucleus, there

TABLE 1 | Demographic and psychological variables of subjects by group.

Parameter	OCD (*N* = 27), Mean (SD)	HC (*N* = 29), Mean(SD)	Statistic (t†X†)	*p*§	Cohen's d
Age, years	21.04 (5.42)	22.83 (2.22)	−1.60	0.12	-
Sex, male/female	14/13	12/17	0.62	0.43	-
Education, years	13.07 (3.13)	14.31 (3.04)	−1.55	0.12	-
Disease duration, mos.	34.11 (48.00)	-	-	-	-
Psychometrics					
BDI	17.48 (9.54)	6.59 (5.32)	5.23****	<0.001	1.41
STAI-S	54.59 (11.09)	36.66 (9.26)	6.59****	<0.001	1.77
STAI-T	55.74 (7.69)	39.66 (9.25)	7.05****	<0.001	1.89
DEQ Total	30.67 (12.91)	22.34 (11.59)	2.54*	0.014	0.68
Inhibition	8.70 (5.04)	6.41 (3.77)	1.94	0.058	-
Intentionality	10.33 (4.81)	7.69 (3.84)	2.28*	0.027	0.61
Executive memory	4.04 (2.68)	2.14 (1.66)	3.16***	0.003	0.85
Positive affect	4.67 (1.88)	3.41 (2.34)	2.199*	0.032	0.59
Negative affect	2.93 (1.71)	2.69 (1.73)	0.51	0.61	-
Y-BOCS total	30.63 (5.50)	-	-	-	-
Y-BOCS-CS	13.81 (4.57)	-	-	-	-
Y-BOCS-OS	16.81 (2.47)	-	-	-	-
Intracranial volume(ml)	1672.58 (132.41)	1605.55 (191.08)	1.52	0.14	-

*OCD, obsessive-compulsive disorder; HC, healthy control; SD, standard deviation; BDI, Beck Depression Inventory; STAI-S, Spielberger State-Trait Anxiety Inventory-State Form; STAI-T, Spielberger State-Trait Anxiety Inventory-Trait Form; DEQ, Dysexecutive Questionnaire; Y-BOCS, Yale-Brown Obsessive Compulsive Scale; Y-BOCS-CS, Y-BOCS compulsion score; Y-BOCS-OS, Y-BOCS obsession score. Data are given as mean (standard deviation) unless otherwise indicated. † Independent sample t-test. ‡ Chi-square test. § 2-tailed, significance at p = 0.05; *p < 0.05; ***p < 0.005; ****p < 0.001.*

TABLE 2 | Means(SDs) of gray matter structural metrics for each group in each ROI and comparison of LI values between OCD and HC.

ROI	Variable	OCD(*N* = 27)			HC(*N* = 29)			Statistic ($t^{\dagger}$)	$p^{\dagger}$	Cohen's d
		Left	Right	LI	Left	Right	LI			
OFC	GMV	1279.56 (231.97)	1219.74 (273.44)	2.75 (11.41)	1242.28 (224.05)	1081.76 (219.19)	7.08 (9.94)	−1.513	0.136	-
	SA	292.63 (53.85)	283.89 (53.59)	1.50 (11.41)	295.24 (47.38)	264.41 (51.72)	5.68 (10.37)	−1.438	0.156	-
	CT	3.01 (0.13)	3.02 (0.24)	−0.05 (4.81)	2.93 (0.22)	2.96 (0.23)	−0.52 (3.77)	−0.493	0.624	-
	LGI	2.46 (0.16)	2.47 (0.21)	−1.04 (6.19)	2.49 (0.17)	2.33 (0.24)	5.39 (4.44)	−3.034	0.004***	−0.81
Caudate	GMV	3949.34 (441.15)	3993.88 (412.88)	−0.59 (1.83)	3729.26 (419.28)	3769.53 (462.65)	−0.47 (1.95)	−0.235	0.815	-
Putamen	GMV	6038.81 (744.77)	6172.68 (687.78)	−1.38 (1.50)	5533.98 (796.54)	5557.87 (530.99)	0.35 (3.69)	-	0.007*	−0.61
Pallidum	GMV	2270.45 (188.53)	2158.69 (183.99)	2.53 (2.55)	2144.01 (217.29)	2115.27 (280.16)	0.79 (3.63)	-	0.019*	0.55

SD, standard deviation; ROI, region of interest; LI values, laterality index values; OCD, obsessive-compulsive disorder; HC, healthy control; OFC, orbitalfrontal cortex; GMV, gray matter volume; SA, surface area; CT, cortical thickness; LGI, Local Gyrification Index. GMV and SA values are corrected for intracranial volume. GMV reported in mm^3, SA in mm^2, and CT in mm.

*†Independent sample t-test of LIs between two groups. ‡2-tailed, significance at $p = 0.05$; *$p < 0.05$; ***$p < 0.005$.*

was no significant group difference [$F_{(1, 53)} = 1.55$, $p = 0.22$], no significant main effect of hemisphere [$F_{(1, 53)} = 0.01$, $p = 0.91$], and no significant group' hemisphere interaction [$F_{(1, 53)} = 0.007$, $p = 0.93$]. For GMV of the pallidum, we observed a main effect of hemisphere [$F_{(1, 53)} = 6.88$, $p = 0.01$, $\eta^2 = 0.12$] and a significant group' hemisphere interaction [$F_{(1, 53)} = 6.61$, $p = 0.01$, $\eta^2 = 0.11$], but no main effect of group [$F_{(1, 53)} = 0.33$, $p = 0.57$]. Simple effect analysis showed that differences between the left and right pallidum were significant for the OCD group [$p < 0.001$, $d = 0.60$], but not for the HC group ($p = 0.46$). Relative to the HC group, the OCD group had a greater left pallidum GMV ($p = 0.02$; $d = 0.62$) but no significant difference in GMV for the right pallidum ($p = 0.50$), see **Figure 2**.

For the putamen, there were main effects of group [$F_{(1, 53)} = 8.54$, $p = 0.005$, $\eta^2 = 0.14$] and hemisphere [$F_{(1, 53)} = 20.68$, $p < 0.001$, $\eta^2 = 0.28$], as well as a significant group' hemisphere interaction [$F_{(1, 53)} = 5.03$, $p = 0.03$, $\eta^2 = 0.09$]. Simple effects analysis showed that the differences between left and right putamen were significant in the OCD group ($p = 0.001$, $d = 0.19$), but not the HC group ($p = 0.39$). The OCD group had greater GMVs in both the left putamen ($p = 0.02$; $d = 0.65$) and right putamen ($p = 0.001$; $d = 1.00$) than the HC group (**Figure 2**).

SA and CT

There were no main effects on OFC SA of group [$F_{(1, 53)} = 0.06$, $p = 0.81$] or hemisphere [$F_{(1, 53)} = 3.44$, $p = 0.07$], and no significant group' hemisphere interaction [$F_{(1, 53)} = 1.04$, $p = 0.31$]. Likewise, we did not obtain significant main effects on OFC CT of group [$F_{(1, 53)} = 2.39$, $p = 0.13$] or hemisphere [$F_{(1, 53)} = 0.37$, $p = 0.55$], nor a group' hemisphere interaction [$F_{(1, 53)} = 0.27$, $p = 0.61$].

Gyrification

For LGI of the OFC, we obtained a main effect of hemisphere [$F_{(1, 53)} = 4.04$, $p = 0.05$, $\eta^2 = 0.07$] and a significant group × hemisphere [$F_{(1,53)} = 4.37$, $p = 0.04$, $\eta^2 = 0.08$], but no main effect of group [$F_{(1, 53)} = 2.07$, $p = 0.16$]. Simple effects analysis showed significant differences between the left and right OFC for the HC group ($p = 0.007$; $d = 0.05$), but not for the OCD group ($p = 0.96$). Compared to HCs, the OCD group had a larger LGI for the right OFC ($p = 0.03$; $d = 0.69$) but not for the left OFC ($p = 0.60$), see **Figure 2**.

Laterality

LI of putamen and pallidum were non-normal data ($ps < 0.05$), see **Supplementary Table 1**. Mean LI values obtained for the OFC and the three substructures of the striatum are reported in **Table 2** with their SDs and statistical values. Notably, we obtained significantly different LI values between the OCD group and HC group for GMVs of the pallidum and the putamen, as well as for LGIs of the OFC.

Partial Correlation of LI and Psychological Variables

DEQ scores correlated negatively with LI values obtained for the LGI of the OFC, including DEQ total score ($r = -0.34$, $p = 0.01$)

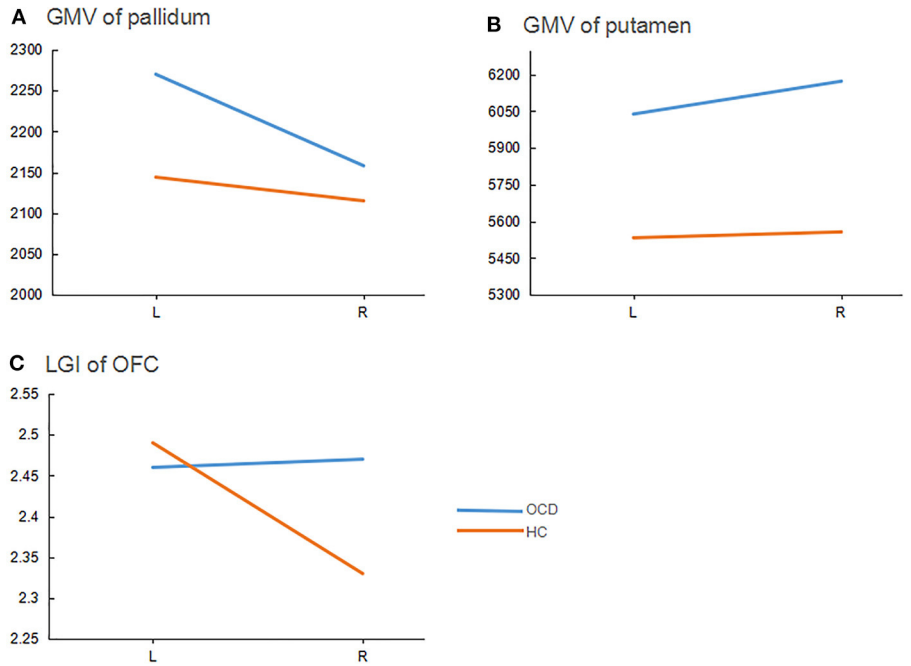

FIGURE 2 | Group-hemisphere interactions of morphometric indicators for each ROI. ROI, region of interest; GMV, gray matter volume (mm^3); OFC, orbitalfrontal cortex; L, left; R, right; LGI, local gyrification index. OCD, obsessive-compulsive disorder patients; HC, healthy controls.

as well as executive memory ($r = -0.33$, $p = 0.01$), inhibition ($r = -0.35$, $p = 0.008$), positive affect ($r = -0.27$, $p = 0.049$), and negative affect ($r = -0.26$, $p = 0.05$) subscale scores. YBOCS scores correlated negatively with LI values obtained for the LGI of OFC ($r = -0.40$, $p = 0.04$).

Effect Sizes of Group and Hemisphere Differences

Effect sizes for group differences in each ROI are reported in **Figure 3** (for significant interactions), and effect sizes for differences between the left and right hemispheres within each group are presented in **Figure 3**. The most significant group difference was observed for GMVs of the right putamen ($d = 1$, OCD vs. HC). The most significant hemisphere difference was observed for LGIs of the OFC in the HC group (Cohen's $d = 0.82$, left vs. right).

DISCUSSION

In this study, we found that, relative to HCs, first-episode drug-naive young OCD patients had greater GMVs of the left pallidum and bilateral putamen, as well as an greater LGI of the right OFC, consistent with the view that OCD patients have a structurally abnormal OFC and striatum (1, 11, 12, 36). We also found that, relative to HCs, OCD patients had weaker left hemisphere LGI superiority of the OFC and GMV superiority of the putamen, as well as stronger left hemisphere GMV superiority of the pallidum. In the OCD group, LIs of OFC LGI correlated negatively with Y-BOCS scores and DEQ scores, respectively.

We found that OCD patients had a larger left pallidal GMV than HCs. A meta-analysis indicated that adult OCD patients had larger pallidal volumes than age-matched controls (1). Similarly, our study found OCD patients had larger GMVs of the bilateral putamen than HCs. Shape analysis revealed that the segmented putamen was larger than normal in OCD patients, while a voxel based morphometry study indicated that OCD patients had larger right putamen volumes than normal (1). Variability of subcortical structural alteration results in OCD may be due to different analysis methods, limited statistical power, and clinical heterogeneity with respect to patient profile and developmental stage (33).

Although OFC abnormalities have been widely reported in OCD, the results have been inconsistent (13, 17, 28), and few studies have studied cortical folding of the OFC directly. Relative to other indicators, cortical folding reflects earlier neurodevelopmental processes, and some mental disorders have been linked with abnormalities in cortical folding (58). Thus, analyzing it in OCD may reveal potential neurodevelopmental risk factors of OCD, such as CSTC loop abnormalities (37). The present findings of greater LGIs of OFC in OCD patients are consistent with the possibility that abnormal cortical folding may play an important role in the pathogenesis of OCD.

We also found that LI values obtained for the GMVs of the pallidum and putamen and for LGIs of the OFC differed between the OCD and HC groups. Hemispheric asymmetry is a basic feature of the brain that is, like cortical folding, an indicator of early neurodevelopment (59, 60). Goldberg found that heteromodal inferoparietal and lateral prefrontal cortices

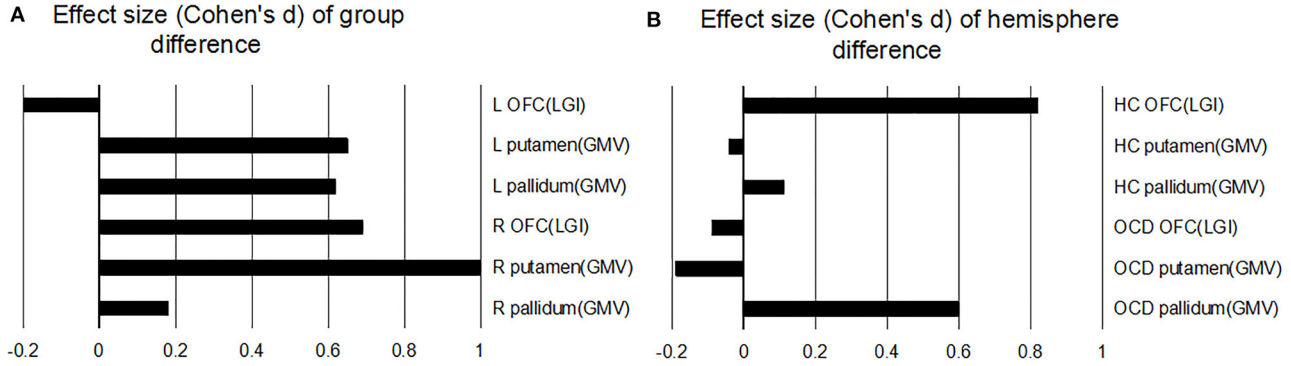

FIGURE 3 | Effect sizes. Effect sizes, as represented by Cohen's d values, are shown for **(A)** group differences (OCD vs. HC) within each ROI in each hemisphere and for **(B)** hemisphere differences [left (L) vs. right (R)] in each group of each ROI. OCD, OCD patients; HC, healthy controls; GMV, gray matter volume.

are more extensive in the right than in the left hemisphere, whereas heteromodal mesial and orbital prefrontal and cingulate cortices are more extensive in the left than in the right hemisphere (61). Impaired early neurodevelopment including abnormalities in brain lateralization may be etiological factors of some neurobehavioral disorders (59), such as autism spectrum disorder (62). Although the possibility that atypical lateralization may be involved in OCD, there is little direct information on the matter.

In this study, we found a significant group differences in LI values of LGIs for the OFC, wherein OCD patients had a less dominant left-side superiority than HCs, with HCs showing the typical relative enlargement of the left OFC over the right. The OFC is critical for salience-driven decision-making guided by internal states, motivations, and needs (59). The left OFC is closely related to speech and logic, whereas the right OFC has been closely related to emotional experience (59). Reduced left lateralization of the OFC in OCD patients suggests that their logical functions may be weakened while their emotional experiences may be enhanced, a supposition that fits with the OCD clinical characteristics of unnecessary repetitive behaviors and emotional distress (DSM-5, 2013).

The OCD group also had weakened left-side dominance of the putamen with respect to GMVs. The putamen controls autonomic movements. In the general population, the putamen is more dominant in the left hemisphere than in the right, and putamen injury can disrupt autonomic nervous system functions (59). Depression severity has been associated with the GMV of the left putamen (63). The bilaterally reduced putamen with weakened left dominance in OCD patients reported here may underlie, at least in part, the compulsive behavior and depression seen in OCD patients.

The pallidum, which plays an important role in regulation of body movement, typically, shows left-hemisphere dominance (59). Pathological changes affecting the pallidum may result in increased muscle tone, decreased movement, and resting tremor. Moreover, diagnoses involving a compromised the pallidum are often associated with obsessive-compulsive symptoms. Hence, the present findings of a greater GMV of the left pallidum in OCD patients and enhancement of left pallidal dominance, relative to HCs, are consistent with the repetitive behaviors characteristic of OCD and thus suggest that these alterations could underlie compulsive behaviors in OCD patients.

It is noteworthy that our LI values correlated with psychological variables, namely Y-BOCS and DEQ scores, in the OCD group. Previously, Tang found that the GMV of the left anterior insula correlated positively with Y-BOCS scores, while the GMV of the right dorsolateral prefrontal cortex correlated negatively with Y-BOCS scores (64). However, to the best of our knowledge, the relationship OFC LGI lateralization and OCD clinical characteristics had not been examined previously. The present correlation analyses indicated that OCD patients with higher Y-BOCS obsession scores tended to have less dominant left side superiority. Y-BOCS scores in OCD patients have been reported previously to correlate negatively with GMVs of the bilateral OFC (65). Our results further suggest that OCD symptom severity may be associated with abnormal lateralization LGI patterns in the OFC.

LI values of the LGI for the OFC were also inversely correlated with DEQ total and subscale scores in OCD patients. Hence, OCD patients with weaker left OFC dominance tended to exhibit greater executive dysfunction. Burgess and colleagues found that right dorsolateral prefrontal gyrus damage was associated with impairments in the ability to make plans, whereas left superior frontal gyrus damage was associated with impairments in the ability to follow plans and rules (66). Our results suggest that impaired EF in OCD patients might be related to abnormal LGI lateralization of the OFC, consistent with a neurodevelopmental etiology of OCD (33).

This study had some limitations. First, being a cross-sectional rather than a longitudinal study, it could not answer the question of whether observed asymmetries were genetically determined (innate) or consequent to the development of OCD symptoms. Follow-up studies are needed to clarify the causality direction between brain abnormalities and OCD symptoms. Second, only gray matter abnormalities and their relationships with executive dysfunction metrics were analyzed. Task-related fMRI studies may reveal specific indicators of impaired EF in

OCD. Finally, the relatively small sample size may limit the generalizability of the findings. Studies with multiple comparison correction being conducted in larger sample sizes are needed to reduce the type I error and examine the repeatability of our results.

Our study found that drug-naïve adult patients with OCD indeed have abnormalities in cortical folding and lateralization patterns, which provided further evidences that OCD is an early neurodevelopmental disorder. This finding also suggested that the abnormalities of cortical folding and lateralization patterns in OFC and striatum may be biomarkers to early identify obsessive-compulsive disorder. The Follow-up studies are needed to provide more evidences.

DATA AVAILABILITY STATEMENT

The data that support the findings of this study are available from the corresponding author upon reasonable request.

ETHICS STATEMENT

The studies involving human participants were reviewed and approved by Ethics Committee of the Second Xiangya Hospital of Central South University. The patients/participants provided their written informed consent to participate in this study.

AUTHOR CONTRIBUTIONS

All authors contributed to the study conception and design. Material preparation, data analyses were performed by ZB and TC. Data collection were performed by LQ, PW, YH, LZ, LF, and LJ. The first draft of the manuscript was written by ZB. TC, LQ, and ZM revised the manuscript and all authors commented on previous versions of the manuscript. All authors read and approved the final manuscript.

FUNDING

This study was supported by grant from the National Natural Science Foundation of China (Grant No. 31871112).

ACKNOWLEDGMENTS

The authors are grateful to the all the subjects for their participation.

SUPPLEMENTARY MATERIAL

The Supplementary Material for this article can be found online at: https://www.frontiersin.org/articles/10.3389/fpsyt.2021.674568/full#supplementary-material

REFERENCES

1. Boedhoe PSW, Schmaal L, Abe Y, Ameis SH, Arnold PD, Batistuzzo MC, et al. Distinct subcortical volume alterations in pediatric and adult OCD: a worldwide meta- and mega-analysis. *Am J Psychiatry*. (2017) 174:60–70. doi: 10.1176/appi.ajp.2016.16020201
2. Benzina N, Mallet L, Burguière E, N'Diaye K, Pelissolo A. Cognitive dysfunction in obsessive-compulsive disorder. *Curr Psychiatry Rep*. (2016) 18:80. doi: 10.1007/s11920-016-0720-3
3. Gruner P, Pittenger C. Cognitive inflexibility in obsessive-compulsive disorder. *Neuroscience*. (2017) 345:243–55. doi: 10.1016/j.neuroscience.2016.07.030
4. Bari A, Robbins TW. Inhibition and impulsivity: behavioral and neural basis of response control. *Prog Neurobiol*. (2013) 108:44–79. doi: 10.1016/j.pneurobio.2013.06.005
5. Hiebert NM, Lawrence MR, Ganjavi H, Watling M, Owen AM, Seergobin KN, et al. Striatum-mediated deficits in stimulus-response learning and decision-making in OCD. *Front Psychiatry*. (2020) 11:13. doi: 10.3389/fpsyt.2020.00013
6. *Diagnostic and Statistical Manual of Mental Disorders (DSM-5®)*. Washington, DC: American Psychiatric Pub (2013).
7. Fan J, Zhong M, Zhu X, Gan J, Liu W, Niu C, et al. Resting-state functional connectivity between right anterior insula and right orbital frontal cortex correlate with insight level in obsessive-compulsive disorder. *NeuroImage Clin*. (2017) 15:1–7. doi: 10.1016/j.nicl.2017.04.002
8. Fouche JP, Du Plessis S, Hattingh C, Roos A, Lochner C, Soriano-Mas C, et al. Cortical thickness in obsessive-compulsive disorder: multisite mega-analysis of 780 brain scans from six centres. *Br J Psychiatry*. (2017) 210:67–74. doi: 10.1192/bjp.bp.115.164020
9. Rădulescu A, Herron J, Kennedy C, Scimemi A. Global and local excitation and inhibition shape the dynamics of the cortico-striatal-thalamo-cortical pathway. *Sci Rep*. (2017) 7:7608. doi: 10.1038/s41598-017-07527-8
10. Ting JT FG. Neural circuitry dysfunction through mouse genetics. *Curr Opin Neurobiol*. (2012) 21:842–48. doi: 10.1016/j.conb.2011.04.010
11. Reess TJ, Rus OG, Schmidt R, De Reus MA, Zaudig M, Wagner G, et al. Connectomics-based structural network alterations in obsessive-compulsive disorder. *Transl Psychiatry*. (2016) 6:e882. doi: 10.1038/tp.2016.163
12. Nakamae T, Sakai Y, Abe Y, Nishida S, Fukui K, Yamada K, et al. Altered fronto-striatal fiber topography and connectivity in obsessive-compulsive disorder. *PLoS ONE*. (2014) 9:112075. doi: 10.1371/journal.pone.0112075
13. Togao O, Yoshiura T, Nakao T, Nabeyama M, Sanematsu H, Nakagawa A, et al. Regional gray and white matter volume abnormalities in obsessive-compulsive disorder: a voxel-based morphometry study. *Psychiatry Res-Neuroimaging*. (2010) 184:29–37. doi: 10.1016/j.pscychresns.2010.06.011
14. Christian CJ, Lencz T, Robinson DG, Burdick KE, Ashtari M, Malhotra AK, et.al. Gray matter structural alterations in obsessive-compulsive disorder: relationship to neuropsychological functions. *Psychiatry Res*. (2008) 164:123–31. doi: 10.1016/j.pscychresns.2008.03.005
15. Loes Gabriëls BN. Deep brain stimulation in the ventral capsule/ventral striatum for the treatment of obsessive-compulsive disorder: role of the bed nucleus of the stria terminalis. In D. Denys, M. Feenstra, R. Schuurman, editors. *Deep Brain Stimulation*. Berlin; Heidelberg: Springer. (2012). p. 35–41. doi: 10.1007/978-3-642-30991-5_4
16. Peng ZW, Lui SSY, Cheung EFC, Jin Z, Miao GD, Jing J, et al. Brain structural abnormalities in obsessive-compulsive disorder: converging evidence from white matter and grey matter. *Asian J Psychiatry*. (2012) 5:290–96. doi: 10.1016/j.ajp.2012.07.004
17. Radua J, Mataix-Cols D. Voxel-wise meta-analysis of grey matter changes in obsessive-compulsive disorder. *Br J Psychiatr*. (2009) 195:393–402. doi: 10.1192/bjp.bp.108.055046
18. Tang W, Zhu Q, Gong X, Zhu C, Wang Y, Chen S. Cortico-striato-thalamo-cortical circuit abnormalities in obsessive-compulsive disorder: a voxel-based morphometric and fMRI study of the whole brain. *Behav Brain Res*. (2016) 313:17–22. doi: 10.1016/j.bbr.2016.07.004
19. Shim G, Jung WH, Choi JS, Jung MH, Jang JH, Park JY, et al. Reduced cortical folding of the anterior cingulate cortex in obsessive-compulsive disorder. *J Psychiatry Neurosci*. (2009) 34:443–49.

20. Fan Q, Palaniyappan L, Tan L, Wang J, Wang X, Li C, et al. Surface anatomical profile of the cerebral cortex in obsessive-compulsive disorder: a study of cortical thickness, folding and surface area. *Psychol Med.* (2013) 43:1081–91. doi: 10.1017/S0033291712001845
21. Jung WH, Yücel M, Yun JY, Yoon YB, Cho KIK, Parkes L, et al. Altered functional network architecture in orbitofronto-striato-thalamic circuit of unmedicated patients with obsessive-compulsive disorder. *Hum Brain Mapp.* (2017) 38:109–19. doi: 10.1002/hbm.23347
22. Chen Y, Juhás M, Greenshaw AJ, Hu Q, Meng X, Cui H, et al. Abnormal resting-state functional connectivity of the left caudate nucleus in obsessive-compulsive disorder. *Neurosci Lett.* (2016) 623:57–62. doi: 10.1016/j.neulet.2016.04.030
23. Gremel CM, Costa RM. Orbitofrontal and striatal circuits dynamically encode the shift between goal-directed and habitual actions. *Nat Commun.* (2013) 4:2264. doi: 10.1038/ncomms3264
24. Lázaro L, Bargalló N, Castro-Fornieles J, Falcón C, Andrés S, Calvo R, et al. Brain changes in children and adolescents with obsessive-compulsive disorder before and after treatment: a voxel-based morphometric MRI study. *Psychiatry Res.* (2009) 172:140–46. doi: 10.1016/j.pscychresns.2008.12.007
25. Van Den Heuvel OA, Remijnse PL, Mataix-Cols D, Vrenken H, Groenewegen HJ, Uylings HBM, et al. The major symptom dimensions of obsessive-compulsive disorder are mediated by partially distinct neural systems. *Brain.* (2009) 132:853–68. doi: 10.1093/brain/awn267
26. Shin YW, So YY, Jun KL, Tae HH, Kyung JL, Jong ML, et al. Cortical thinning in obsessive compulsive disorder. *Hum Brain Mapp.* (2007) 28:1128–35. doi: 10.1002/hbm.20338
27. Hu X, Du M, Chen L, Li L, Zhou M, Zhang L, et al. Meta-analytic investigations of common and distinct grey matter alterations in youths and adults with obsessive-compulsive disorder. *Neurosci Biobehav Rev.* (2017) 78:91–103. doi: 10.1016/j.neubiorev.2017.04.012
28. Szeszko PR, Christian C, MacMaster F, Lencz T, Mirza Y, Taormina SP, et al. Gray matter structural alterations in psychotropic drug-naive pediatric obsessive-compulsive disorder: an optimized voxel-based morphometry study. *Am J Psychiatry.* (2008) 165:1299–307. doi: 10.1176/appi.ajp.2008.08010033
29. Wu T, Hou Y, Hallett M, Zhang J, Chan P. Lateralization of brain activity pattern during unilateral movement in Parkinson's disease. *Hum Brain Mapp.* (2015) 36:1878–91. doi: 10.1002/hbm.22743
30. Kapellou O, Counsell SJ, Kennea N, Dyet L, Saeed N, Stark J, et al. Abnormal cortical development after premature birth shown by altered allometric scaling of brain growth. *PLoS Med.* (2006) 3:1382–90. doi: 10.1371/journal.pmed.0030265
31. Wobrock T, Gruber O, McIntosh AM, Kraft S, Klinghardt A, Scherk H, et al. Reduced prefrontal gyrification in obsessive-compulsive disorder. *Eur Arch Psychiatry Clin Neurosci.* (2010) 260:455–64. doi: 10.1007/s00406-009-0096-z
32. Rus OG, Reess TJ, Wagner G, Zaudig M, Zimmer C, Koch K. Hypogyrification in obsessive-compulsive disorder. *Psychol Med.* (2017) 47:1053–61. doi: 10.1017/S0033291716003202
33. Venkatasubramanian G, Zutshi A, Jindal S, Srikanth SG, Kovoor JME, Kumar JK, et al. Comprehensive evaluation of cortical structure abnormalities in drug-naïve, adult patients with obsessive-compulsive disorder: a surface-based morphometry study. *J Psychiatr Res.* (2012) 46:1161–68. doi: 10.1016/j.jpsychires.2012.06.003
34. Zhang S, Hu S, Chao HH, Li C shan R. Hemispheric lateralization of resting-state functional connectivity of the ventral striatum: an exploratory study. *Brain Struct Funct.* (2017) 222:2573–83. doi: 10.1007/s00429-016-1358-y
35. Kong XZ, Boedhoe PSW, Abe Y, Alonso P, Ameis SH, Arnold PD, et al. Mapping cortical and subcortical asymmetry in obsessive-compulsive disorder: findings from the ENIGMA consortium. *Biol Psychiatry.* (2020) 87:1022–34. doi: 10.1016/j.biopsych.2019.04.022
36. Wood J, Ahmari SE. A framework for understanding the emerging role of corticolimbic-ventral striatal networks in OCD-associated repetitive behaviors. *Front Syst Neurosci.* (2015) 9:1–22. doi: 10.3389/fnsys.2015.00171
37. Morein-Zamir S, Voon V, Dodds CM, Sule A, Van Niekerk J, Sahakian BJ, et al. Divergent subcortical activity for distinct executive functions: stopping and shifting in obsessive compulsive disorder. *Psychol Med.* (2016) 46:829–40. doi: 10.1017/S0033291715002330
38. Xing X, Jin L, Li Q, Yang Q, Han H, Xu C, et al. Modeling essential connections in obsessive–compulsive disorder patients using functional MRI. *Brain Behav.* (2020) 10:e01499. doi: 10.1002/brb3.1499
39. Ullrich M, Weber M, Post AM, Popp S, Grein J, Zechner M, et al. OCD-like behavior is caused by dysfunction of thalamo-amygdala circuits and upregulated TrkB/ERK-MAPK signaling as a result of SPRED2 deficiency. *Mol Psychiatr.* (2018) 23:444–58. doi: 10.1038/mp.2016.232
40. Vriend C, de Wit SJ, Remijnse PL, van Balkom AJLM, Veltman DJ, van den Heuvel OA. Switch the itch: a naturalistic follow-up study on the neural correlates of cognitive flexibility in obsessive-compulsive disorder. *Psychiatry Res.* (2013) 213:31–8. doi: 10.1016/j.pscychresns.2012.12.006
41. Maltby N, Tolin DF, Worhunsky P, O'Keefe TM, Kiehl KA. Dysfunctional action monitoring hyperactivates frontal-striatal circuits in obsessive-compulsive disorder: an event-related fMRI study. *Neuroimage.* (2005) 24:495–503. doi: 10.1016/j.neuroimage.2004.08.041
42. Rubia K, Lee F, Cleare AJ, Tunstall N, Fu CHY, Brammer M, et al. Tryptophan depletion reduces right inferior prefrontal activation during response inhibition in fast, event-related fMRI. *Psychopharmacology.* (2005) 179:791–803. doi: 10.1007/s00213-004-2116-z
43. Breiding MJ. The striatum's role in executing rational and irrational economic behaviors. *Neuroscientist.* (2019) 25:475–90. doi: 10.1177/1073858418824256
44. Osman A, Downs WR, Barrios FX, Kopper BA, Gutierrez PM, Chiros CE. Factor structure and psychometric characteristics of the Beck Depression Inventory-II. *J Psychopathol Behav Assess.* (1997) 19:359–76. doi: 10.1007/BF02229026
45. Burgess PW, Alderman N, Evans J, Emslie H, Wilson BA. The ecological validity of tests of executive function. *J Int Neuropsychol Soc.* (1998) 4:547–58. doi: 10.1017/S1355617798466037
46. Goodman WK, Price LH, Rasmussen SA, Mazure C, Fleischmann RL, Hill CL, et al. The Yale-Brown obsessive compulsive scale: I. development, use, and reliability. *Arch Gen Psychiatry.* (1989) 46:1006–11. doi: 10.1001/archpsyc.1989.01810110048007
47. Guillén-Riquelme A, Buela-Casal G. Meta-analysis of group comparison and meta-analysis of reliability generalization of the State-Trait Anxiety Inventory Questionnaire (STAI). *Rev Esp Salud Publica.* (2014) 88:101–12. doi: 10.4321/S1135-57272014000100007
48. Shaw S, Oei TPS, Sawang S. Psychometric validation of the dysexecutive questionnaire (DEX). *Psychol Assess.* (2015) 27:138–47. doi: 10.1037/a0038195
49. Anholt GE, van Oppen P, Cath DC, Smit JH, den Boer JA, Verbraak MJPM, et al. The yale-brown obsessive-compulsive scale: Factor structure of a large sample. *Front Psychiatry.* (2010) 1:1–7. doi: 10.3389/fpsyt.2010.00018
50. Wang J, He L, Zheng H, Lu ZL. Optimizing the magnetization-prepared rapid gradient-Echo (MP-RAGE) sequence. *PLoS ONE.* (2014) 9:96899. doi: 10.1371/journal.pone.0096899
51. Fan J, Liu W, Xia J, Li S, Gao F, Zhu J, et al. Childhood trauma is associated with elevated anhedonia and altered core reward circuitry in major depression patients and controls. *Hum Brain Mapp.* (2020) 286–97. doi: 10.1002/hbm.25222
52. Destrieux C, Fischl B, Dale A, Halgren E. Automatic parcellation of human cortical gyri and sulci using standard anatomical nomenclature. *Neuroimage.* (2010) 53:1–15. doi: 10.1016/j.neuroimage.2010.06.010
53. Schaer M, Bach Cuadra M, Tamarit L, Lazeyras F, Eliez S, Thiran JP. A Surface-based approach to quantify local cortical gyrification. *IEEE Trans Med Imaging.* (2008) 27:161–70. doi: 10.1109/TMI.2007.903576
54. Vetter TR. Fundamentals of research data and variables: the devil is in the details. *Anesth Anal.* (2017) 125:1375–80. doi: 10.1213/ANE.0000000000002370
55. Phipson B, Smyth GK. Permutation P-values should never be zero: calculating exact P-values when permutations are randomly drawn. *Stat Appl Genet Mol Biol.* (2010) 9:39. doi: 10.2202/1544-6115.1585
56. Cohen J. A power primer. *Psychol Bull.* (1992) 112:155–9. doi: 10.1037/0033-2909.112.1.155
57. Norouzian R, Plonsky L. Eta- and partial eta-squared in L2 research: a cautionary review and guide to more appropriate usage. *Second Lang Res.* (2018) 34:257–71. doi: 10.1177/0267658316684904

58. Vogeley K, Schneider-Axmann T, Pfeiffer U, Tepest R, Bayer TA, Bogerts B, et al. Disturbed gyrification of the prefrontal region in male schizophrenic patients: a morphometric postmortem study. *Am J Psychiatry*. (2000) 157:34–9. doi: 10.1176/ajp.157.1.34
59. Kang X, Herron TJ, Ettlinger M, Woods DL. Hemispheric asymmetries in cortical and subcortical anatomy. *Laterality*. (2015) 20:658–84. doi: 10.1080/1357650X.2015.1032975
60. Henson R, Shallice T, Dolan R. Neuroimaging evidence for dissociable forms of repetition priming. *Science*. (2000) 287:1269–72. doi: 10.1126/science.287.5456.1269
61. Goldberg E, Roediger D, Kucukboyaci NE, Carlson C, Devinsky O, Kuzniecky R, et al. Hemispheric asymmetries of cortical volume in the human brain. *Cortex*. (2013) 49:200–10. doi: 10.1016/j.cortex.2011.11.002
62. Boddaert N, Chabane N, Gervais H, Good CD, Bourgeois M, Plumet MH, et al. Superior temporal sulcus anatomical abnormalities in childhood autism: a voxel-based morphometry MRI study. *Neuroimage*. (2004) 23:364–69. doi: 10.1016/j.neuroimage.2004.06.016
63. Du M, Liu J, Chen Z, Huang X, Li J, Kuang W, et al. Brain grey matter volume alterations in late-life depression. *J Psychiatry Neurosci*. (2014) 39:397–406. doi: 10.1503/jpn.130275
64. Tang W, Huang X, Li B, Jiang X, Li F, Xu J, et al. Structural brain abnormalities correlate with clinical features in patients with drug-naïve OCD: a DARTEL-enhanced voxel-based morphometry study. *Behav Brain Res*. (2015) 294:72–80. doi: 10.1016/j.bbr.2015.07.061
65. Jayarajan RN, Agarwal SM, Viswanath B, Kalmady SV, Venkatasubramanian G, Srinath S, et al. A voxel based morphometry study of brain gray matter volumes in juvenile obsessive compulsive disorder. *J Can Acad Child Adolesc Psychiatr*. (2015) 24:84.
66. Burgess PW, Veitch E, De Lacy Costello A, Shallice T. The cognitive and neuroanatomical correlates of multitasking. *Neuropsychologia*. (2000) 38:848–63. doi: 10.1016/S0028-3932(99)00134-7

Conflict of Interest: The authors declare that the research was conducted in the absence of any commercial or financial relationships that could be construed as a potential conflict of interest.

frontiers in Neuroscience

ORIGINAL RESEARCH
published: 16 August 2021
doi: 10.3389/fnins.2021.678144

[^{18}F]PBR146 and [^{18}F]DPA-714 *in vivo* Imaging of Neuroinflammation in Chronic Hepatic Encephalopathy Rats

Xiang Kong[1], Song Luo[1], Yun Fei Wang[1], Gui Fen Yang[2], Guang Ming Lu[1] and Long Jiang Zhang[1]**

[1] Department of Diagnostic Radiology, Jinling Hospital, Medical School of Nanjing University, Nanjing, China, [2] Department of Nuclear Medicine, Jinling Hospital, Medical School of Nanjing University, Nanjing, China

Neuroinflammation is an important pathogenesis of hepatic encephalopathy (HE). The upregulation of translocator protein (TSPO) during neuroinflammation provides an imaging molecular target to evaluate the severity of neuroinflammation in chronic HE rats. [18F]DPA-714 and [18F]PBR146 targeting TSPO are often used for neuroinflammation imaging. This study performed bile duct ligation (BDL) in rats to simulate chronic HE model, tested the behavioral experiments, and conducted [18F]PBR146 and [18F]DPA-714 micro-PET/CT scans followed analyzing the average %ID/g values of the whole brain, brain regions and main organs of subjects. After sacrifice the rats, the blood plasma samples were taken for blood biochemical indexes and plasma inflammatory factor levels examination, the liver and brain specimens were obtained for pathological analysis. The BDL rats showed chronic liver failure with defects in cognition, motor coordination ability and mental state. [18F]PBR146 and [18F]DPA-714 micro-PET/CT imaging results were similar in whole brain of BDL group and Sham group. Besides, some regional brain areas in BDL rats were found abnormal uptakes mainly located in basal ganglia area, auditory cortex, motor cortex, cingulate gyrus, somatosensory cortex, hippocampus, thalamus, midbrain, and medulla oblongata, and these regions also correlated with behavioral alterations. In conclusion, both [18F]PBR146 and [18F]DPA-714 had the similar imaging effects in hepatic encephalopathy models could quantitatively evaluate neuroinflammation load and distribution. The difference brain regions with higher uptake values of radiotracers in BDL rats were correlated with behavioral alterations

Keywords: hepatic encephalopathy, positron emission tomography, neuroinflammation, translocator protein, cognition

OPEN ACCESS

Edited by:
Boldizsar Czeh, University of Pécs, Hungary

Reviewed by:
Cristina Barca, Universität Münster, Germany
Amanda Brown, Johns Hopkins University, United States

****Correspondence:***
Guang Ming Lu
cjr.luguangming@vip.163.com
Long Jiang Zhang
kevinzhlj@163.com

Specialty section:
This article was submitted to Brain Imaging Methods, a section of the journal Frontiers in Neuroscience

Received: *09 March 2021*
Accepted: *28 July 2021*
Published: *16 August 2021*

Citation:
Kong X, Luo S, Wang YF, Yang GF, Lu GM and Zhang LJ (2021) [^{18}F]PBR146 and [^{18}F]DPA-714 in vivo Imaging of Neuroinflammation in Chronic Hepatic Encephalopathy Rats. Front. Neurosci. 15:678144. doi: 10.3389/fnins.2021.678144

INTRODUCTION

Hepatic encephalopathy (HE) is a serious complication characterized by advanced liver failure and a spectrum of neuropsychiatric impairments ranging from minimal HE to delirium or coma, which are correlated with a poor prognosis (Bajaj, 2018; Kerbert and Jalan, 2020). Systemic inflammation and hyperammonemia attributed to acute and chronic liver failure induce neuroinflammation and

brain dysfunction (Butterworth, 2013). Since HE is often accompanied by multiple organ failure and high mortality, this has resulted in little progress in the drug treatment of HE. However, neuroinflammation may offer pathophysiological insight into the underlying mechanisms of cognitive alterations during the development of HE (Bass et al., 2010).

In particular, bile duct ligation (BDL) can induce biliary cirrhosis with hyperammonemia and jaundice after more than 28 days post-surgery, which has provided researchers with an experimental rat model of chronic HE (Butterworth et al., 2009). The translocator protein (TSPO), previously known as peripheral-type benzodiazepine receptor (PBR), was originally identified in peripheral organs and is expressed at low concentrations in healthy brain parenchyma. The upregulation of TSPO occurs when microglia are activated during neuroinflammation, which has 10 min at 50 min to serve as a clinical biomarker for neuroinflammation in neurological diseases (Rupprecht et al., 2009; Setiawan et al., 2015; Jaipuria et al., 2017). Radiolabeled ligands targeting TSPO for positron emission tomography (PET) help visualize the distribution of TSPO *in vivo* in order to detect activated microglia in the brain. Furthermore, they have been considered a novel biomarker for neuroinflammation, and more than 40 TSPO compounds labeled with [^{11}C] or [^{18}F] have been identified over the past two decades (Alam et al., 2017).

Previously, [^{18}F]DPA-714 and [^{11}C]PK11195 imaging has been performed in acute and chronic HE rat models. Studies demonstrated that [^{18}F]DPA-714 may be a more suitable agent in HE experimental models (Kong et al., 2016; Luo et al., 2018). Another radiotracer [^{18}F]PBR146 (N,N-diethyl-2-(2-(4-(3-[^{18}F] fluoropropoxy)phenyl)-5,7-dimethylpyrazolo[1,5-a]pyrimidin-3 -yl)acetamide) was proposed in 2007 and was found to have high *in vitro* affinity and selectivity for PBR (Fookes et al., 2008). While [^{18}F]PBR146 has not been applied to a HE rat model, we performed [^{18}F]PBR146 and [^{18}F]DPA-714 micro-PET/CT imaging in a chronic HE rat model with high levels of neuroinflammation. We hope that the [^{18}F]PBR146 might have the same imaging effect for chronic HE as [^{18}F]DPA-714. We also performed behavioral assessments, biochemical indexes measurements, inflammatory factor level examination, and pathological analysis to determine the relationships among neuroinflammation, cognitive function, and systemic inflammation in BDL rats.

MATERIALS AND METHODS

Animal Model

A total of 20 male (excluding the effects of estrogenic hormones) Sprague-Dawley rats (160–190 g) were used with the permission of the local animal experimental ethics committee. Experimental protocols were conducted in accordance with the guidelines for laboratory animal care and use following the ARRIVE guideline. The rats were freely fed commercial rat food and water sterilized by ^{60}Co. Controlled conditions were maintained at 18–22°C, 40–60% relative humidity, and a noise level of < 60 dB at a 12 h (h)/12 h day/night cycle. All subjects were randomized into two groups: sham group ($n = 8$) or BDL group ($n = 12$). The sample size was determined by considering the mortality rate according to previous studies (Kong et al., 2016; Luo et al., 2018). Details regarding the BDL procedure are described in the **Supplementary Materials**. Sham group rats were handled similarly except for the bile duct ligation and abscission (Rodrigo et al., 2010; Kong et al., 2016).

Behavioral Studies

The behavioral studies involved the rotarod test, beam walking test, and motor activity experiment performed 2–3 days prior to the micro-PET scans. The tests were performed to evaluate motor coordination, tolerance, locomotor activity, and vertical activity of the rats (Jover et al., 2006; Rodrigo et al., 2010; Agusti et al., 2011; Kong et al., 2016). Detailed procedures are described in the **Supplementary Materials**.

Radiosynthesis of Ligands, Micro-PET/CT Scans, and Image Processing

Both [^{18}F]PBR146 and [^{18}F]DPA-714 can be applied as PET radioligands for TSPO imaging. [^{18}F]PBR146 and [^{18}F]DPA-714 were synthesized as previously described (Fookes et al., 2008; Lavisse et al., 2015; Kong et al., 2016; Luo et al., 2018). Procedures for the synthesis of [^{18}F]DPA-714 and [^{18}F]PBR146 are provided in the **Supplementary Materials**. BDL and sham rats were housed in the same conditions for more than 28 days (Butterworth et al., 2009). Micro-PET/CT scans were implemented using an Inveon small animal scanner (Siemens Preclinical Solution) after completion of the behavior studies.

Rats were fixed in the prone position after anesthetization by isoflurane inhalation (induction: 3%, thereafter: 2–2.5%) in oxygen. Radioactive tracers were injected intravenously into the lateral tail vein. PET data were acquired first by CT data acquisition. PET acquisitions were obtained by scanning for 10 min at 50 min post-radiotracer injection, followed by CT scanning for ∼6–10 min to allow for coregistration of radiotracer uptake with tissues. PET setting parameters were as follows: slice thickness = 0.78 mm, matrix size = 128 × 128, field of view (FOV) = 4 cm × 4 cm, and energy levels of acquisition = ∼350–650 keV (default) (Kong et al., 2016). CT setting parameters were as follows: current = 500 A, voltage = 50 kV, and exposure time = 500 ms (Cochran et al., 2017). Micro-PET/CT scans with [^{18}F]PBR146 and [^{18}F]DPA-714 were performed for two consecutive days.

Image reconstruction was performed using the Inveon Research Workplace (IRW 3.0, Siemens). PET and CT images were coregistered for correct alignment in three dimensions. Global brain and some organs (e.g., lungs, heart, liver, and kidneys) were drawn on the images for the region of interest (ROI) for quantification. The quantified radioactivity uptake of each ROI was presented as the percent injected dose per gram (%ID/g), calculated by dividing tissue radioactivity with injected dose (assuming the tissue density is 1 g/mL). In addition, regional brain uptake of the radiotracer was evaluated using PMOD software (version 3.7, PMOD Technologies LTD, Zurich,

Switzerland). PET images were manually fused with the T2-MRI template after coregistration with CT images. The software then drew 58 ROIs of the brain on the PET images with reference to the MR imaging-based atlas, which yielded corresponding radioactivity concentration values. This processing avoided the effects of peripheral vessels and tissues, which show higher tracer distribution (Cochran et al., 2017; Jiang et al., 2019).

Biochemical, Histopathological, and Immunohistochemical Characterizations

Rats were anesthetized to collect canthus blood (1–2 mL) into procoagulant tubes in the morning, one day prior to micro-PET/CT scans. Blood samples were centrifugalized at 3,000 × g for 10 min (min) at 4°C, and the supernatant was collected and transferred to the local hospital within 2 h for venous blood ammonia measurement. The day after micro-PET/CT scans, blood samples from the heart cavity (5–10 mL) were collected from each rat after deep anesthetization by 10% chloral hydrate. Determination of liver and renal function indicators were conducted in a clinical laboratory. These biochemical indicators from plasma included total bilirubin, direct bilirubin, indirect bilirubin, total protein, albumin, globulin, alanine aminotransferase (ALT), aspartate aminotransferase (AST), alkaline phosphatase, total cholesterol, high-density lipoprotein cholesterol (HDL-C), low-density lipoprotein cholesterol (LDL-C), urea, creatinine, and uric acid (Nanjing Jiancheng Bioengineering Institute, Jiangsu, China). Finally, 5-hydroxytryptamine (5-HT), interferon-γ (IFN-γ), interleukin 1β (IL-1β), IL-6, IL-10, and tumor necrosis factor alpha (TNF-α) were analyzed from plasma samples using enzyme-linked immune sorbent assay (ELISA) kits (Nanjing Jiancheng Bioengineering Institute, Jiangsu, China).

After blood samples were collected, all rats were transcardially perfused with 100–150 mL of saline, followed by 150 mL of phosphate buffered saline (PBS, pH = 7.4) for 20–30 min. The liver, brain, jejunum, ileum, and colon specimens were removed, fixed in 10% buffered formaldehyde, paraffin-embedded, and sliced. The specimens were stained with hematoxylin-eosin (H&E) as previously described (Kong et al., 2016; Luo et al., 2018). In addition, microglia were stained by performing immunohistochemistry of glial fibrillary acidic protein (GFAP, 1:800) and ionized calcium binding adaptor molecule-1 (IBA-1, 1:500) (Wuhan servicebio technology CO.,LTD, Hubei, China) (Dickens et al., 2014; Israel et al., 2016). All histopathological and immunohistochemical slices were scanned using a pathological section scanner. Morphological analysis and cell counts were performed using CaseViewer 1.4 and ImageJ software.

Statistical Analysis

Data analysis was performed using SPSS 20.0 statistical software (SPSS Inc, Chicago, IL, United States). The normality of continuous variables was confirmed by performing a Shapiro-Wilk test. The normally distributed quantitative variables were expressed as mean ± standard deviation (SD), and the median and interquartile range (IQR) were calculated for non-normally distributed data. Independent-sample t-tests and Mann-Whitney tests were performed for sham and BDL group comparisons when appropriate (Kong et al., 2016; Luo et al., 2018). The relationship between behavioral data and radiotracer uptake values in the rat brains was investigated using Spearman's rank correlation test. P-values of <0.05 were deemed statistically significant.

RESULTS

Weight, Behavioral Studies, and Biochemical Results

All eight rats in the sham group were alive during the whole experiment, while four rats in the BDL group died due to a biliary fistula or an anesthesia accident. Weights of the sham group rats were significantly higher than the BDL group rats from the first day after operation to the end of the experiment (**Supplementary Figure 1**). Results of the rotarod test, beam walking test, and motor activity were significantly different between the sham and BDL groups ($P < 0.05$, **Table 1**), indicating that BDL rats developed significant impairments in coordination, tolerance, and motor activity. Serum ammonia levels in the BDL group (39.43 ± 7.91 μmol/L) were higher than those in the sham group (29.88 ± 4.22 μmol/L, $P = 0.026$). Plasma bilirubin, albumin, globulin, ALT, and AST levels in the BDL group were significantly higher than those in the sham group ($P < 0.01$, **Table 1**).

There were significant differences between the two groups regarding plasma total cholesterol, HDL-C, and LDL-C levels ($P < 0.01$, **Table 1**). Plasma urea and uric acid levels showed significant differences between the sham and BDL groups ($P = 0.032$ and $P = 0.002$, respectively), while plasma creatinine levels showed no significant differences between groups ($P = 0.442$, **Table 1**). Plasma 5-HT, IFN-γ, IL-1β, IL-6, IL-10, and TNF-α levels in the BDL group were significantly higher than those in the sham group ($P < 0.01$, **Table 1**). These biochemical measurements indicate liver impairments in the rats who underwent BDL.

Micro-PET/CT Results

[^{18}F]DPA-714 and [^{18}F]PBR146 micro-PET/CT imaging was conducted on two consecutive days. Although the mean injected radioactivity of [^{18}F]DPA-714 (279.3 ± 16.7 μci) and [^{18}F]PBR146 (245.9 ± 19.2 μci) showed significant differences ($P < 0.001$), the injected radioactivities of [^{18}F]DPA-714 and [^{18}F]PBR146 in the sham group (270.9 ± 13.9 and 235.7 ± 19.4 μci, respectively) were not significantly different from the BDL group (286.5 ± 16.4 and 256.1 ± 13.4 μci; $P = 0.094$ and $P = 0.060$, respectively). All six rats in the sham group were subject to [^{18}F]DPA-714 and [^{18}F]PBR146 micro-PET/CT imaging. Seven rats in the BDL group were subject to [^{18}F]DPA-714 micro-PET/CT imaging, while [^{18}F]PBR146 micro-PET/CT scanning was conducted successfully on six BDL group rats, except that one rat died due to an anesthesia accident.

The average%ID/g values in the global brain of [^{18}F]DPA-714 and [^{18}F]PBR146 in the BDL rats were higher than those in the sham rats ($P < 0.001$, **Figures 1A,B** and **Supplementary Table 1**). There were significant differences in [^{18}F]DPA-714 and [^{18}F]PBR146 uptake values of the lung, liver, and kidney

TABLE 1 | Comparisons of behavioral, biochemical, and histopathological measurements between sham and BDL rats.

Parameters	Sham group	BDL group	*P*
Time on the rotarod (s)	94.7 ± 21.4	73.5 ± 15.3	0.044*
Beam walking			
Cross time (s)	10.9 ± 3.5	22.0 ± 12.1	0.025*
Fault numbers (IQR), n §	1.0 (0, 2.0)	3.5 (1.5, 5.5)	0.010*
Motor activity			
Crossovers, n	9.1 ± 5.1	4.1 ± 3.1	0.026*
Rearings (IQR), n §	28.0 (12.0, 40.0)	11.0 (8.3, 15.5)	0.015*
Biochemical measurements			
Serum ammonia (μmol/L)	29.88 ± 4.22	39.43 ± 7.91	0.026*
Total bilirubin (μmol/L, IQR) §	2.20 (1.70, 2.50)	111.50 (92.48, 136.95)	0.001**
Direct bilirubin (μmol/L, IQR) §	1.40 (1.00, 1.60)	108.00 (91.45, 131.20)	0.001**
Indirect bilirubin (μmol/L, IQR) §	0.50 (0.30, 1.10)	4.25 (1.25, 5.75)	0.036*
Total protein (g/L)	65.61 ± 3.48	64.68 ± 7.95	0.778
Albumin (g/L)	30.47 ± 2.45	20.93 ± 4.05	< 0.001***
Globulin (g/L)	35.14 ± 1.77	43.75 ± 5.68	0.002**
ALT (U/L)	38.71 ± 6.80	90.00 ± 33.51	0.003**
AST (U/L, IQR)§	66.50 (60.50, 74.25)	289.50 (209.00, 462.25)	0.002**
Alkaline phosphatase (U/L)	2.33 ± 0.82	16.38 ± 7.76	0.001**
Total cholesterol (μmol/L, IQR) §	2.00 (1.75, 2.05)	4.92 (3.65, 5.85)	0.001**
HDL-C (μmol/L)	0.84 ± 0.07	0.47 ± 0.23	0.001**
LDL-C (μmol/L, IQR) §	0.18 (0.18, 0.20)	1.61 (1.20, 2.50)	0.001**
Urea (μmol/L, IQR) §	6.10 (5.70, 6.40)	4.95 (3.65, 5.85)	0.032*
Creatinine (μmol/L)	22.63 ± 3.53	24.83 ± 6.52	0.442
Uric acid (μmol/L)	19.43 ± 7.44	42.88 ± 13.86	0.002**
5-HT (pg/mL)	245.11 ± 23.13	481.90 ± 17.06	< 0.001***
IFN-γ (pg/mL)	1049.34 ± 136.37	1980.77 ± 152.95	< 0.001***
IL-1β (pg/mL)	26.82 ± 2.68	42.56 ± 2.22	< 0.001***
IL-6 (pg/mL)	57.13 ± 6.84	135.14 ± 13.94	< 0.001***
IL-10 (pg/mL)	56.48 ± 3.05	107.77 ± 9.07	< 0.001***
TNF-α (pg/mL)	192.48 ± 43.73	326.93 ± 76.68	0.007**
No. of microglia (cells/mm^2)†	29.70 ± 2.68	35.07 ± 1.97	0.006**

Non-normally distributed values are represented as the IQR, and other values are represented as the mean ± standard deviation from at least four rats in each group for the behavioral studies and from at least five rats in each group for the biochemical measurements.

**P < 0.05, **P < 0.01, and ***P < 0.001 were regarded as statistically significant.*

BDL, bile duct ligation; IQR, interquartile range; ALT, alanine aminotransferase; AST, aspartate aminotransferase; HDL-C, high-density lipoprotein cholesterol; LDL-C, low-density lipoprotein cholesterol; 5-HT, 5-hydroxytryptamine; IFN-γ, interferon-γ; IL-1β, interleukin 1β; IL-6, interleukin 6; IL-10, interleukin 10; TNF-α, tumor necrosis factor alpha.

§ *A non-parametric test (Mann-Whitney test) was performed for between-group comparisons.*

† *IBA-1 positive microglia cells were counted in the basal ganglia.*

between the BDL and sham groups ($P < 0.05$), while there were no significant differences in the myocardium ($P > 0.05$, **Figures 1A,B** and **Supplementary Table 1**). Comparison results grouped by [^{18}F]DPA-714 and [^{18}F]PBR146 are shown in **Table 2**. Most organs showed no significant differences ($P > 0.05$), except that the livers of sham rats showed statistical differences between the two groups ($P < 0.001$, **Table 2**).

The comparison of [^{18}F]DPA-714 and [^{18}F]PBR146 uptake values in regional brain areas showed consistent results (**Supplementary Tables 2**, **3**). Significant differences among brain regions between the sham and BDL groups were mainly located in the basal ganglia, cingulate cortex, auditory cortex, motor cortex, somatosensory cortex, hippocampus, thalamus, midbrain, and medulla ($P < 0.05$, **Figure 2**). The average%ID/g values of the BDL group were higher than the sham group in the brain regions without statistical differences ($P > 0.05$, **Supplementary Tables 2**, **3**).

Histopathological and Immunohistochemical Characterizations

Liver weights in the sham group (17.87 ± 1.76 g) were significantly lower than the BDL group (24.71 ± 6.44 g, $P = 0.048$), suggesting that the livers of rats in the BDL group showed compensatory hyperplasia. Liver H&E staining in the sham group showed normal hepatic structure, while staining in the BDL group revealed biliary cirrhosis with destroyed hepatic cords, expanded bile ducts, and inflammatory infiltration. Additionally, the jejunum, ileum, and colon tissues

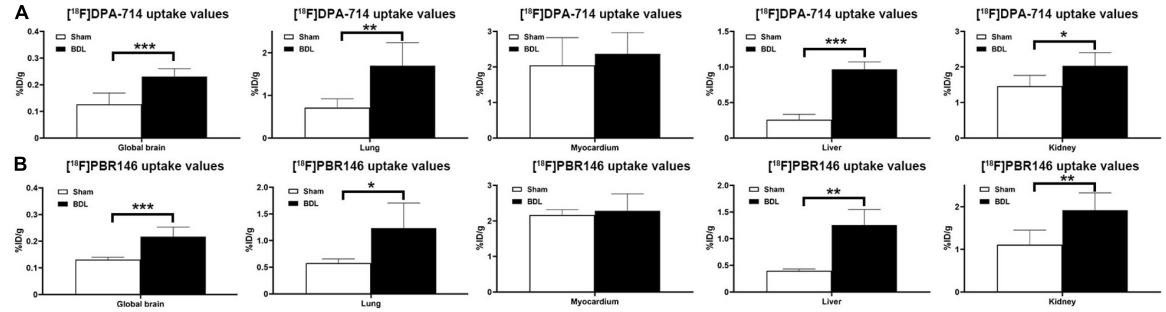

FIGURE 1 | Histograms of uptake values in global brains and organs of sham and BDL rats. The [^{18}F]DPA-714 uptake values in global brain and several organs **(A)** similar to that of [^{18}F]PBR146 uptake values, **(B)** global brain, and most organs showed significantly differences between Sham and BDL rats except myocardium. BDL = bile duct ligation; *$P < 0.05$, **$P < 0.01$, and ***$P < 0.001$.

showed normal intestinal structures in the sham and BDL groups (**Figure 3**). Brain tissue after H&E staining showed no significant differences between the sham group and BDL group, while histopathological changes were observed during GFAP and IBA-1 immunohistochemical analysis of brain microglia. In particular, microglial cells in the sham rats showed ramified shapes (resting microglia), while they showed amoeboid shapes (activated microglia) in the BDL rats (**Figure 3**). The sham group showed significantly lower amounts of IBA-1 immune reactive microglia in the basal ganglia than BDL rats ($P = 0.006$, **Table 1**).

Relationship Between Behavioral Results and Micro-PET/CT Results

Duration of time spent on the rotarod and number of crossovers during the motor activity test showed no correlation with [^{18}F]DPA-714 uptake values ($P > 0.05$), while the beam crossing time showed a positive correlation with [^{18}F]DPA-714 uptake values in the global brain ($r = 0.571$, $P = 0.042$), including structures such as the bilateral accumbens, striatum, auditory cortex, cingulate cortex, insular cortex, medial prefrontal cortex, orbitofrontal cortex, visual cortex, olfactory, right amygdala, motor cortex, retrosplenial cortex, hippocampus anterodorsal, hippocampus posterior, hypothalamus, and colliculus superior ($P < 0.05$, **Supplementary Table 4**).

Beam walking cross time showed no correlation with [^{18}F]PBR146 uptake values, and the behavioral results showed no correlation with [^{18}F]PBR146 uptake values in the global brain ($P > 0.05$, **Supplementary Table 5**). Duration of time spent on the rotarod showed a negative correlation with [^{18}F]PBR146 uptake values in the bilateral auditory cortex, cingulate cortex, entorhinal cortex, motor cortex, hypothalamus, left accumbens, medial prefrontal cortex, retrosplenial cortex, hippocampus antero dorsal, right amygdala, frontal association cortex, somatosensory cortex, hippocampus posterior, and olfactory ($P < 0.05$, **Supplementary Table 5**). The number of crossovers during the motor activity test showed a negative correlation with [^{18}F]PBR146 uptake values in the bilateral entorhinal cortex, insular cortex, olfactory, left amygdala, hypothalamus, and right accumbens ($P < 0.05$, **Supplementary Table 5**).

TABLE 2 | Comparison of [^{18}F]DPA-714 and [^{18}F]PBR146 uptake values (%ID/g) in global brains and organs between sham and BDL rats.

Groups	[^{18}F]DPA-714	[^{18}F]PBR146	*P*
Sham group			
Global brain	0.127 ± 0.042	0.131 ± 0.009	0.800
Lung	0.715 ± 0.207	0.580 ± 0.076	0.165
Myocardium	2.047 ± 0.778	2.167 ± 0.151	0.719
Liver	0.259 ± 0.075	0.397 ± 0.036	0.002**
Kidney	1.460 ± 0.305	1.109 ± 0.342	0.125
BDL group			
Global brain	0.231 ± 0.029	0.217 ± 0.036	0.450
Lung	1.697 ± 0.542	1.234 ± 0.470	0.132
Myocardium	2.371 ± 0.596	2.283 ± 0.479	0.777
Liver	0.967 ± 0.105	1.256 ± 0.293	0.061
Kidney	2.033 ± 0.372	1.917 ± 0.407	0.616

***P < 0.01 was regarded as statistically significant. BDL = bile duct ligation.*

DISCUSSION

The pathogenesis of HE has received increased attention in neuroinflammation research in recent years, which has provided new insight into non-invasive imaging methods for HE monitoring (Butterworth, 2013; Alam et al., 2017). Higher TSPO expression in activated microglia during neuroinflammation provides a novel target for radiotracers in PET imaging in order to identify neuroinflammation in various central nervous system diseases (Alam et al., 2017). In the present study, [^{18}F]PBR146 and [^{18}F]DPA-714 uptake values were measured in the brains and organs of rats modeling chronic HE compared to control model rats. It was found that both [^{18}F]DPA-714 and [^{18}F]PBR146 uptake values were useful for neuroinflammation imaging in BDL rats. Abnormal brain regions were associated with cognitive impairment, suggesting that neuroinflammation is involved in the disease progression of HE.

The International Society on Hepatic Encephalopathy and Nitrogen Metabolism recommended BDL as the experimental rat model of chronic HE, which induces biliary cirrhosis with

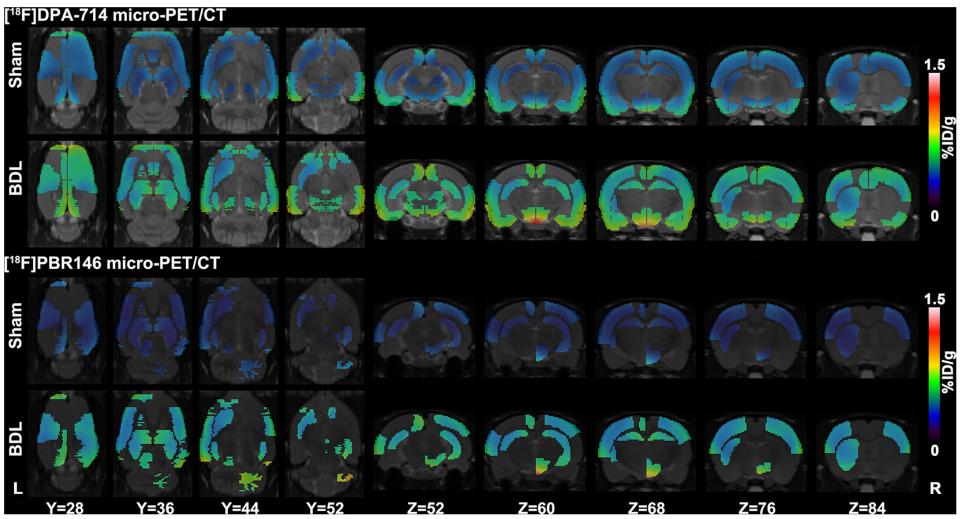

FIGURE 2 | Representative [^{18}F]DPA-714 and [^{18}F]PBR146 micro-PET/CT images of sham and BDL rats. Brain regions, including the basal ganglia, cingulate cortex, auditory cortex, motor cortex, somatosensory cortex, hippocampus, thalamus, midbrain, and medulla, showed significant differences in average%ID/g values between the sham and BDL groups. The [^{18}F]DPA-714 and [^{18}F]PBR146 micro-PET/CT showed consistent results in these regions. BDL = bile duct ligation; L = left; R = right.

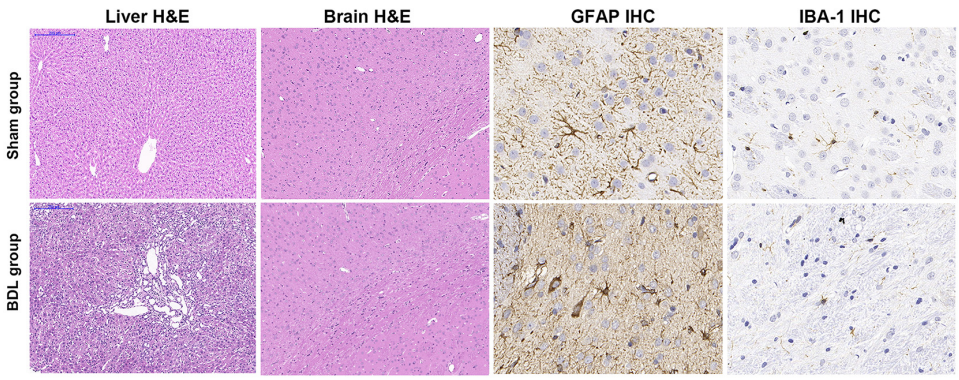

FIGURE 3 | Representative H&E staining and IHC findings in sham and BDL rats. Liver H&E staining (100 × magnification) showed normal hepatic histology in the sham group. Staining in the BDL group showed destroyed hepatic cords, expanded bile duct, and inflammatory infiltration. H&E staining (100×) of brain tissue showed no significant differences between the sham and BDL groups. GFAP IHC micrographs of microglia in the basal ganglia were similar to IBA-1 IHC findings (400×). Microglial cells in the sham rats showed ramified shapes (resting microglia), while microglial cells in the BDL rats showed amoeboid shapes (activated microglia) in the basal ganglia. H&E = hematoxylin-eosin; IHC = immunohistochemistry; BDL = bile duct ligation; GFAP = glial fibrillary acidic protein; IBA–1 = ionized calcium-binding adapter molecule 1.

hyperammonemia and jaundice after more than 28 days post-surgery (Butterworth et al., 2009). The mortality of BDL rats in this study was 33% (4/12), mainly due to liver failure with infection. The serum ammonia level of BDL rats was significantly higher than that of Sham rats, and the liver function, such as bilirubin levels, ALT, and AST levels, were significantly increased in BDL rats. The renal function indicators also showed differences between the two groups, but these alterations were slight compared with liver injury in BDL rats. Liver tissue H&E staining results also showed chronic liver injury, and the chronic HE BDL rats showed decreased motor activity and coordination deficits in behavioral tests. Previous studies reported that [^{18}F]DPA-714 shows greater promise for modeling acute or chronic HE (Kong et al., 2016; Luo et al., 2018). The peripheral organs uptake values were similar between [^{18}F]DPA-714 and [^{18}F]PBR146, all radiotracers uptake values in the lungs, liver, and kidneys of the BDL group were higher than those in the sham group, and plasma inflammatory factors were also significantly increased in BDL rats, suggesting that the initial systemic inflammatory response syndrome because of cytokine storm was related to end-stage liver failure and might serve as a prerequisite for neuroinflammation in chronic HE (Kong et al., 2016; Sarin and Choudhury, 2018). It is noteworthy that the [^{18}F]PBR146 uptake values in the liver were significantly higher than [18F]DPA-714, this might suggest that [^{18}F]PBR146 could be further applied widely in chronic liver failure animal models, requiring more

studies in the future. [^{18}F]PBR146 was first reported by Fookes et al. (2008), but it has not yet been applied to HE models. However, it was found that [^{18}F]PBR146 was not inferior to [^{18}F]DPA-714 regarding its neuroinflammation imaging ability in chronic HE rats. The uptake values in the liver and global brain were significantly different between the BDL and sham rats in this study.

In addition, the regional brain area results were similar between [^{18}F]PBR146 and [^{18}F]DPA-714 micro-PET/CT imaging in structures including the basal ganglia, cingulate cortex, auditory cortex, motor cortex, somatosensory cortex, and hippocampus. The brain regions with statistical significance were inconsistent between the two radiotracers, which might be because of the statistical errors in the controlled range. Agusti et al. (2014) found that [^{3}H]-PK11195 uptake by the striatum, frontal cortex, parietal cortex, thalamus, and hippocampus were statistically increased in a minimal HE rat model due to portacaval shunt compared to sham rats, which was consistent with this study. These results were also similar to another previous study (Kong et al., 2016). It was found that [^{18}F]DPA-714 uptake values in the global brain were positively correlated with beam walking cross time and that [^{18}F]DPA-714 uptake values in regional brain areas (in this case, the basal ganglia, cingulate cortex, auditory cortex, motor cortex, somatosensory cortex, and hippocampus) were positively correlated with beam walking cross time. However, beam cross time showed no correlation with [^{18}F]PBR146 uptake values. It was found that the duration of time on the rotarod and the number of crossovers during the motor activity test showed a negative correlation with [^{18}F]PBR146 uptake values in the basal ganglia, cingulate cortex, entorhinal cortex, motor cortex, somatosensory cortex, and hippocampus.

The basal ganglia are associated with motor, cognitive, and affective functions (Bostan and Strick, 2018). The cingulate cortex is associated with rewards to actions involved in emotion (Rolls, 2019). The auditory cortex is essential for analyzing the identity and behavioral importance of tones paired with emotional events (Concina et al., 2019). The hippocampal-entorhinal circuits are crucial to episodic memory and require the encoding of time and binding to events (Tsao et al., 2018). Finally, the motor cortex is important for motor skill learning (Papale and Hooks, 2018). [^{18}F]DPA-714 and [^{18}F]PBR146 uptake values in these brain regions showed correlations with behavioral alterations, suggesting that neuroinflammation may contribute to cognitive dysfunction in a rat model of chronic HE (Kong et al., 2016).

This study has some limitations that need to be considered. First, the sample size of each group may have influenced the accuracy of statistical results. Second, the behavioral studies mainly evaluated motor and emotional parameters; thus, the learning abilities of the rats should be examined in a further investigation (i.e., by performing a water maze or Y maze test). Third, the study lacked TSPO immunohistochemistry staining, immunofluorescent staining, and autoradiography to exclude potential imaging affected factors. Fourth, indicators of TSPO quantification and suitable analytical models to explain either radiotracer uptake values in the brain or behavior or biochemical examination results. Fifth, further studies are needed to investigate the effects of different treatments on chronic HE.

In conclusion, both [^{18}F]PBR146 and [^{18}F]DPA-714 can be used for TSPO imaging of chronic HE in rats. These two radiotracers may help quantitatively evaluate the neuroinflammation load and distribution of different brain regions correlated with partial behavioral alterations. Thus, [^{18}F]PBR146 and [^{18}F]DPA-714 may non-invasively monitor neuroinflammation, which will be useful in future investigations of treatment efficacy in neuroinflammation of BDL-induced chronic HE.

DATA AVAILABILITY STATEMENT

The raw data supporting the conclusions of this article will be made available by the authors, without undue reservation.

ETHICS STATEMENT

The animal study was reviewed and approved by The Animal Experimental Ethics Committee of Jinling Hospital, Medical School of Nanjing University.

AUTHOR CONTRIBUTIONS

GL and LZ conceived and designed the study. XK, YW, and SL contributed to the literatures search. XK and GY completed the experiment and the writing and revision of this manuscript. All authors approved it for publication.

FUNDING

This work was supported by grants from National Natural Science Foundation of China (Grant Nos. 81322020, 81230032, and 81171313 to LZ, 81401468 to GY, and 81601486 to SL) and the program B for Outstanding Ph.D. candidate of Nanjing University (No. 201801B055 to XK).

ACKNOWLEDGMENTS

We would like to thank Zhi Hong Xu, Xia Bin Chen, Bo Hua Xu, Li Jia Lu, Ming Zhao, and Xiao Fei Yin from Jiangsu Huayi Technology Co., Ltd., for their core facility and excellent technical assistance, and Xiao Xiao Qu and Cai Hua Li from Shanghai Tianhao Biotechnology Co., Ltd., for their technical assistance of microbiota analysis.

SUPPLEMENTARY MATERIAL

The Supplementary Material for this article can be found online at: https://www.frontiersin.org/articles/10.3389/fnins.2021.678144/full#supplementary-material

REFERENCES

Agusti, A., Cauli, O., Rodrigo, R., Llansola, M., Hernández-Rabaza, V., and Felipo, V. (2011). p38 MAP kinase is a therapeutic target for hepatic encephalopathy in rats with portacaval shunts. *Gut* 60, 1572–1579. doi: 10.1136/gut.2010.236083

Agusti, A., Dziedzic, J. L., Hernandez-Rabaza, V., Guilarte, T. R., and Felipo, V. (2014). Rats with minimal hepatic encephalopathy due to portacaval shunt show differential increase of translocator protein (18 kDa) binding in different brain areas, which is not affected by chronic MAP-kinase p38 inhibition. *Metab. Brain Dis.* 29, 955–963. doi: 10.1007/s11011-013-9461-8

Alam, M. M., Lee, J., and Lee, S. Y. (2017). Recent progress in the development of TSPO PET ligands for neuroinflammation imaging in neurological diseases. *Nucl. Med. Mol. Imaging* 51, 283–296. doi: 10.1007/s13139-017-0475-8

Bajaj, J. S. (2018). Hepatic encephalopathy: classification and treatment. *J. Hepatol.* 68, 838–839. doi: 10.1016/j.jhep.2017.11.005

Bass, N. M., Mullen, K. D., Sanyal, A., Poordad, F., Neff, G., Leevy, C. B., et al. (2010). Rifaximin treatment in hepatic encephalopathy. *N. Engl. J. Med.* 362, 1071–1081. doi: 10.1056/NEJMoa0907893

Bostan, A. C., and Strick, P. L. (2018). The basal ganglia and the cerebellum: nodes in an integrated network. *Nat. Rev. Neurosci.* 19, 338–350. doi: 10.1038/s41583-018-0002-7

Butterworth, R. F. (2013). The liver-brain axis in liver failure: neuroinflammation and encephalopathy. *Nat. Rev. Gastroenterol. Hepatol.* 10, 522–528. doi: 10.1038/nrgastro.2013.99

Butterworth, R. F., Norenberg, M. D., Felipo, V., Ferenci, P., Albrecht, J., Blei, A. T., et al. (2009). Experimental models of hepatic encephalopathy: ISHEN guidelines. *Liver Int.* 29, 783–788. doi: 10.1111/j.1478-3231.2009.02034.x

Cochran, B. J., Ryder, W. J., Parmar, A., Klaeser, K., Reilhac, A., Angelis, G. I., et al. (2017). Determining glucose metabolism kinetics using 18F-FDG micro-PET/CT. *J. Vis. Exp.* 123:55184. doi: 10.3791/55184

Concina, G., Renna, A., Grosso, A., and Sacchetti, B. (2019). The auditory cortex and the emotional valence of sounds. *Neurosci. Biobehav. Rev.* 98, 256–264. doi: 10.1016/j.neubiorev.2019.01.018

Dickens, A. M., Vainio, S., Marjamäki, P., Johansson, J., Lehtiniemi, P., Rokka, J., et al. (2014). Detection of microglial activation in an acute model of neuroinflammation using PET and radiotracers 11C-(R)-PK11195 and 18F-GE-180. *J. Nucl. Med.* 55, 466–472. doi: 10.2967/jnumed.113.125625

Fookes, C. J., Pham, T. Q., Mattner, F., Greguric, I., Loc'h, C., Liu, X., et al. (2008). Synthesis and biological evaluation of substituted [18F]imidazo[1,2-a]pyridines and [18F]pyrazolo[1,5-a]pyrimidines for the study of the peripheral benzodiazepine receptor using positron emission tomography. *J. Med. Chem.* 51, 3700–3712. doi: 10.1021/jm7014556

Israel, I., Ohsiek, A., Al-Momani, E., Albert-Weissenberger, C., Stetter, C., Mencl, S., et al. (2016). Combined [(18)F]DPA-714 micro-positron emission tomography and autoradiography imaging of microglia activation after closed head injury in mice. *J. Neuroinflammation* 13:140. doi: 10.1186/s12974-016-0604-9

Jaipuria, G., Leonov, A., Giller, K., Vasa, S. K., Jaremko, Ł, Jaremko, M., et al. (2017). Cholesterol-mediated allosteric regulation of the mitochondrial translocator protein structure. *Nat. Commun.* 8:14893. doi: 10.1038/ncomms14893

Jiang, D., Lu, X., Li, Z., Rydberg, N., Zuo, C., Peng, F., et al. (2019). Increased vesicular monoamine transporter 2 (VMAT2) and dopamine transporter (DAT) expression in adolescent brain development: a longitudinal micro-PET/CT study in rodent. *Front. Neurosci.* 12:1052. doi: 10.3389/fnins.2018.01052

Jover, R., Rodrigo, R., Felipo, V., Insausti, R., Sáez-Valero, J., García-Ayllón, M. S., et al. (2006). Brain edema and inflammatory activation in bile duct ligated rats with diet-induced hyperammonemia: a model of hepatic encephalopathy in cirrhosis. *Hepatology* 43, 1257–1266. doi: 10.1002/hep.21180

Kerbert, A. J. C., and Jalan, R. (2020). Recent advances in understanding and managing hepatic encephalopathy in chronic liver disease. *F1000Res* 9:F1000 Faculty Rev–312. doi: 10.12688/f1000research.22183.1

Kong, X., Luo, S., Wu, J. R., Wu, S., De Cecco, C. N., Schoepf, U. J., et al. (2016). 18F-DPA-714 PET imaging for detecting neuroinflammation in rats with chronic hepatic encephalopathy. *Theranostics* 6, 1220–1231. doi: 10.7150/thno.15362

Lavisse, S., Inoue, K., Jan, C., Peyronneau, M. A., Petit, F., Goutal, S., et al. (2015). [18F]DPA-714 PET imaging of translocator protein TSPO (18 kDa) in the normal and excitotoxically-lesioned nonhuman primate brain. *Eur. J. Nucl. Med. Mol. Imaging* 42, 478–494. doi: 10.1007/s00259-014-2962-9

Luo, S., Kong, X., Wu, J. R., Wang, C. Y., Tian, Y., Zheng, G., et al. (2018). Neuroinflammation in acute hepatic encephalopathy rats: imaging and therapeutic effectiveness evaluation using 11C-PK11195 and 18F-DPA-714 micro-positron emission tomography. *Metab. Brain Dis.* 33, 1733–1742. doi: 10.1007/s11011-018-0282-7

Papale, A. E., and Hooks, B. M. (2018). Circuit changes in motor cortex during motor skill learning. *Neuroscience* 368, 283–297. doi: 10.1016/j.neuroscience.2017.09.010

Rodrigo, R., Cauli, O., Gomez-Pinedo, U., Agusti, A., Hernandez-Rabaza, V., Garcia-Verdugo, J. M., et al. (2010). Hyperammonemia induces neuroinflammation that contributes to cognitive impairment in rats with hepatic encephalopathy. *Gastroenterology* 139, 675–684. doi: 10.1053/j.gastro.2010.03.040

Rolls, E. T. (2019). The cingulate cortex and limbic systems for emotion, action, and memory. *Brain Struct. Funct.* 224, 3001–3018. doi: 10.1007/s00429-019-01945-2

Rupprecht, R., Rammes, G., Eser, D., Baghai, T. C., Schüle, C., Nothdurfter, C., et al. (2009). Translocator protein (18 kD) as target for anxiolytics without benzodiazepine-like side effects. *Science* 325, 490–493. doi: 10.1126/science.1175055

Sarin, S. K., and Choudhury, A. (2018). Management of acute-on-chronic liver failure: an algorithmic approach. *Hepatol. Int.* 12, 402–416. doi: 10.1007/s12072-018-9887-5

Setiawan, E., Wilson, A. A., Mizrahi, R., Rusjan, P. M., Miler, L., Rajkowska, G., et al. (2015). Role of translocator protein density, a marker of neuroinflammation, in the brain during major depressive episodes. *JAMA Psychiatry* 72, 268–275. doi: 10.1001/jamapsychiatry.2014.2427

Tsao, A., Sugar, J., Lu, L., Wang, C., Knierim, J. J., Moser, M. B., et al. (2018). Integrating time from experience in the lateral entorhinal cortex. *Nature* 561, 57–62. doi: 10.1038/s41586-018-0459-6

Conflict of Interest: The authors declare that the research was conducted in the absence of any commercial or financial relationships that could be construed as a potential conflict of interest.

frontiers in Neurology

ORIGINAL RESEARCH
published: 27 October 2021
doi: 10.3389/fneur.2021.607476

Comparing Brain Functional Activities in Patients With Blepharospasm and Dry Eye Disease Measured With Resting-State fMRI

Changqiang Feng[1†], Wenyan Jiang[1†], Yousheng Xiao[1], Yang Liu[1], Lulu Pang[1], Meilan Liang[1], Jingqun Tang[1], Yulin Lu[1], Jing Wei[2], Wenmei Li[3], Yiwu Lei[3], Wenbin Guo[4] and Shuguang Luo[1*]*

[1] Department of Neurology, The First Affiliated Hospital of Guangxi Medical University, Nanning, China, [2] Department of Comprehensive Internal Medicine, Guangxi Medical University Affiliated Tumor Hospital, Nanning, China, [3] Department of Radiology, The First Affiliated Hospital of Guangxi Medical University, Nanning, China, [4] Department of Psychiatry, National Clinical Research Center for Mental Disorders, The Second Xiangya Hospital of Central South University, Changsha, China

OPEN ACCESS

Edited by:
Boldizsar Czeh,
University of Pécs, Hungary

Reviewed by:
Manxiu Ma,
Virginia Tech Carilion, United States
Gina Ferrazzano,
Sapienza University of Rome, Italy

***Correspondence:**
Wenbin Guo
guowenbin76@csu.edu.cn
Shuguang Luo
robert58243@sohu.com

[†]These authors have contributed equally to this work

Specialty section:
This article was submitted to Applied Neuroimaging, a section of the journal Frontiers in Neurology

Received: 26 September 2020
Accepted: 24 September 2021
Published: 27 October 2021

Citation:
Feng C, Jiang W, Xiao Y, Liu Y, Pang L, Liang M, Tang J, Lu Y, Wei J, Li W, Lei Y, Guo W and Luo S (2021) Comparing Brain Functional Activities in Patients With Blepharospasm and Dry Eye Disease Measured With Resting-State fMRI. Front. Neurol. 12:607476. doi: 10.3389/fneur.2021.607476

Background: Blepharospasm (BSP) and dry eye disease (DED) are clinically common diseases characterized by an increased blinking rate. A sustained eyelid muscle activity may alter the cortical sensorimotor concordance and lead to secondary functional changes. This study aimed to explore the central mechanism of BSP by assessing brain functional differences between the two groups and comparing them with healthy controls.

Methods: In this study, 25 patients with BSP, 22 patients with DED, and 23 healthy controls underwent resting-state functional magnetic resonance imaging (fMRI) scan. The amplitude of low-frequency fluctuations (ALFF) was applied to analyze the imaging data.

Results: Analysis of covariance (ANCOVA) revealed widespread differences in ALFF across the three groups. In comparison with healthy controls, patients with BSP showed abnormal ALFF in the sensorimotor integration related-brain regions, including the bilateral supplementary motor area (SMA), left cerebellar Crus I, left fusiform gyrus, bilateral superior medial prefrontal cortex (MPFC), and right superior frontal gyrus (SFG). In comparison with patients with DED, patients with BSP exhibited a significantly increased ALFF in the left cerebellar Crus I and left SMA. ALFF in the left fusiform gyrus/cerebellar Crus I was positively correlated with symptomatic severity of BSP.

Conclusions: Our results reveal that the distinctive changes in the brain function in patients with BSP are different from those in patients with DED and healthy controls. The results further emphasize the primary role of sensorimotor integration in the pathophysiology of BSP.

Keywords: blepharospasm, dry eye disease, functional magnetic resonance imaging, amplitude of low-frequency fluctuations, sensorimotor integration

INTRODUCTION

Characterized by excessive involuntary spasms of the orbicularis oculi, blepharospasm (BSP) is now recognized as a common form of adult-onset focal dystonia (1, 2). As disease progresses, it may result in difficulty in opening the eyes or even functional blindness, which causes functional disability in work and daily life and decreases quality of life (3–5). Though the symptomatology of this disease is well-defined, its pathophysiology remains unclear. In addition, the onset of BSP is insidious and mainly characterized by atypical symptoms such as increasing blinking and photophobia in early stages (6). These early symptoms of patients with BSP are very similar to the manifestations of dry eye disease (DED), which is considered a peripheral disease associated with tear hyperosmolarity and ocular surface inflammation (7). Typical manifestations of DED include photophobia, burning sensation, dryness of the eyes, and visual impairment. These unpleasant sensations in DED often initiated secondary increased blink rate. This might be a result of increased reflex non-spasmodic closure of the eyelids to the sensory symptoms other than the involuntary orbicularis oculi spasms in BSP. It is usually difficult to differentiate BSP in early stages from DED merely according to clinical symptoms. Differences in neural activity between the two diseases remain unclear, and sustained muscular activity might alter the cortical sensory-motor concordance directly or indirectly, leading to secondary structural or functional changes that are almost indistinguishable from the underlying pathophysiological characteristics of BSP. It is necessary to identify the potential central effects of peripheral sensory feedback.

Although BSP was initially believed to be a disease of the basal ganglia, neuroimaging evidence suggested that it involved the anatomy and function of several brain regions (8, 9). Promising neuroimaging techniques have provided new methods for analyzing changes in brain function and structure, thereby expanding the focus of traditional research. Structurally, voxel-based morphometry analysis has shown an increased gray matter density in the cingulate gyrus, primary sensorimotor cortex, and right middle frontal gyrus, indicating that multiple regions contribute to the development of BSP (10, 11). Functionally, many fMRI trials on BSP have revealed abnormal regional spontaneous brain activities and altered functional connectivity in sensorimotor structures, including the basal ganglia, SMA, cerebellum, primary sensorimotor cortex, and visual areas (12–16). These studies have demonstrated that local microstructural and functional abnormalities in multiple regions may be associated with BSP, thus bringing forward the viewpoint that BSP might be a network disorder (17). However, these functional and structural changes in BSP are unable to definitely divide into primary or secondary. Whether imaging abnormalities in these areas are characteristic spontaneous changes in BSP or secondary central effects caused by an increased blinking rate should be further investigated. Moreover, little is known about brain activity alterations in DED with commonly recognized peripheral mechanisms. Both disease situations present with similar clinical manifestations, especially increased blinking. To improve the understanding of spasmodic conditions, specific functional changes of BSP should be distinguished from possible confounding effects through dialectical comparative analysis. Therefore, DED may be used as controls to investigate the neural mechanisms of BSP.

In early studies about BSP, an activation paradigm evoked by simple motor tasks was used. However, different abnormalities have shown in the task-based fMRI studies during different task performance (18–20). The lack of a unified stimulus paradigm may make it difficult to support each other across the existent task-based studies. Besides, individual differences may activate the unrelated brain regions during performing the motor task. In contrast to task-based fMRI, increasing attention has been paid to resting-state fMRI (rs-fMRI), a promising neuroimaging technique that can examine brain neurophysiological processes without the requirement of specific task execution based on the fluctuation of the blood-oxygen-level dependent signal. The technique can avoid the potential limitations of task-based fMRI and contributes to further understanding of abnormalities of neural activity. As an effective analytical method of rs-fMRI technique, amplitude of low-frequency fluctuations (ALFF) is widely utilized to identify functional changes in brain regions at rest (21–24). In the present study, we used the ALFF method to explore the different types of alterations in the spontaneous regional brain activity among patients with BSP, patients with DED, and healthy controls. We also examined correlations between abnormal ALFF and clinical variables in patients with BSP. We hypothesized that ALFF alterations in BSP would be distinguishable from those in patients with DED and healthy subjects.

METHODS AND MATERIALS

Participants

All participants in the present study volunteered to take part in the study and signed a written consent after they were informed of the research process. The study received ethics approval by the Ethics Committee of the First Affiliated Hospital of Guangxi Medical University. Patients with BSP and DED were treated at the Department of Neurology in the First Affiliated Hospital of Guangxi Medical University from October 2017 to October 2019.

Patients With BSP

Inclusion criteria: (1) blepharospasm in accordance with clinical diagnostic criteria (25); (2) no organic changes in conventional head MRI; (3) no other serious neurological or mental diseases; (4) not received botulinum toxin treatment or any medication for dystonia or mental illness within 3 months before enrollment; and (5) right-handedness. Exclusion criteria: (1) abnormal intracranial lesions found *via* MRI; (2) dry eye, eyelid aphasia, or severe systemic diseases, such as hepatolenticular degeneration; (3) previous history of neurological and mental diseases; and (4) inability to cooperate with or contraindicate MRI examination.

Patients With DED

Inclusion criteria: (1) conform to the diagnostic criteria in accordance with the *TFOS DEWS II Definition and Classification*

Report (26); (2) no accompany blepharospasm; (3) not received botulinum toxin, and without any drugs for dystonia or mental illness within 3 months before enrollment; and (4) right-handedness. Exclusion criteria: (1) orbital organic lesions confirmed by orbital CT examination; (2) head and facial trauma or operation history and neuropsychiatric system diseases; (3) abnormal intracranial lesions found through imaging examination; and (4) inability to cooperate with or unsuitable for MRI examination.

Healthy Controls

Healthy adults from the local community were recruited as healthy controls and matched with age and education with subjects with BSP and patients with DED. Inclusion criteria: (1) no neurological and mental system diseases; (2) no abnormality in ophthalmology and nervous system examination; (3) no abnormality in head imaging examination; and (4) right-handedness.

Resting-State fMRI Images Acquisition

Images were collected by the same skilled technician using a Siemens 3T MR scanner in the First Affiliated Hospital of Guangxi Medical University. All subjects were given head retainers and earplugs to minimize head movement and machine noise. During scanning, all participants were required to relax and minimize head and body movement as much as possible, while staying awake with eyes closed. An echo-planar imaging sequence was used to acquire resting-state fMRI images with the following parameters: repetition time/echo time = 2,000 ms/30 ms, matrix size = 64 × 64, slices number = 30, flip angle = 90°, field of view = 24 cm, gap = 0.4 mm, slice thickness = 4 mm, and 250 volumes (500 s).

Clinical information, including age, gender, illness duration (except healthy control groups), education level, and BSP symptomatic severity, were collected. The symptom severity of patients with BSP was assessed by professional neurologists utilizing the Jankovic Rating Scale (JRS) (27). In addition, patients with BSP were assessed in terms of their depression and anxiety symptoms by using, respectively, the self-rating depression scale (SDS) and self-rating anxiety scale (SAS).

Data Preprocessing

Data Processing Assistant for Resting-State fMRI (DPARSF) software package based on MatlabR2012b platform was used to perform data preprocessing. First, images of the first 10 time points were eliminated, and the remaining 240 images were retained for analysis. Time layer and head motion were corrected to eliminate data whose head movement horizontal displacement was >2 mm and rotation was >2°. Next, the images were spatially normalized to the Montreal Neurological Institute (MNI) EPI template and resampled to 3 mm × 3 mm × 3 mm in the statistical parameter map software (SPM12, http://www.fil.ion.ucl.ac.uk/spm). Afterward, the processed image was spatially smoothened with a 4 mm full width at half maximum Gaussian kernel. Finally, linear drifts removal and temporal band-pass filtering (0.01–0.08 Hz) were conducted on all smoothed images to remove the influence of low-frequency drift and high-frequency respiratory and cardiac noise.

ALFF Analysis

The REST (http://resting-fmri.sourceforge.net) software was used to analyze ALFF (28). ALFF is the sum of the low-frequency spectral amplitudes across 0.01–0.08 Hz. First, the time series of each voxel was transformed to the frequency domain by utilizing a fast Fourier transform and the power spectrum was obtained. Then, the square root of each frequency on the power spectrum was calculated, and the mean square root across 0.01–0.08 Hz at each voxel was taken as the ALFF (29). For data standardization, the ALFF of each voxel was divided by the global mean ALFF value.

Statistical Analysis

Demographic data, such as gender, age, and education level, were statistically analyzed using IBM SPSS 23.0 software. Analyses of variance (ANOVA) were conducted to compare age and education level across the three groups, and gender differences were compared *via* a chi-square test. A two-sample *t*-test was used to compare illness duration between the BSP group and the DED group. The threshold of above tests was set at $p < 0.05$ that indicated statistically significant differences.

ANCOVA was performed to compare the ALFF images across three groups with the REST software. Subsequently, *post-hoc t*-tests were carried out to examine ALFF differences between each pair of groups. Age, gender, and education were used as covariates to reduce their potential impact. The significance threshold was corrected to $p < 0.05$ for multiple comparisons using Gaussian random field (GRF) theory (voxel significance: $p < 0.001$, cluster significance: $p < 0.05$).

The mean ALFF values were extracted from abnormal brain regions showing significant differences in BSP group

TABLE 1 | Demographic information and clinical profile of the participants.

Variables	BSP ($n = 25$)	DED ($n = 22$)	Healthy controls ($n = 23$)	*p*-value
Gender (male/female)	8/17	8/14	4/19	0.332[a]
Age (years)	49.68 ± 8.41	51.82 ± 8.68	49.69 ± 6.51	0.583[b]
Education (years)	10.32 ± 2.30	10.23 ± 3.42	9.78 ± 2.59	0.746[b]
Illness duration (months)	11.64 ± 9.01	21.77 ± 17.30		0.019[c]
Symptom severity	2.64 ± 0.81			
SAS	42.52 ± 10.18			
SDA	48.51 ± 8.86			

BSP, blepharospasm; DED, dry eye disease; SAS, Self-rating anxiety scale; SDS, Self-rating depression scale. [a]The p-value for sex distribution was obtained by a chi-square test. [b]The p-values were obtained by analyses of variance. [c]The P-values were obtained by a two-sample t-test.

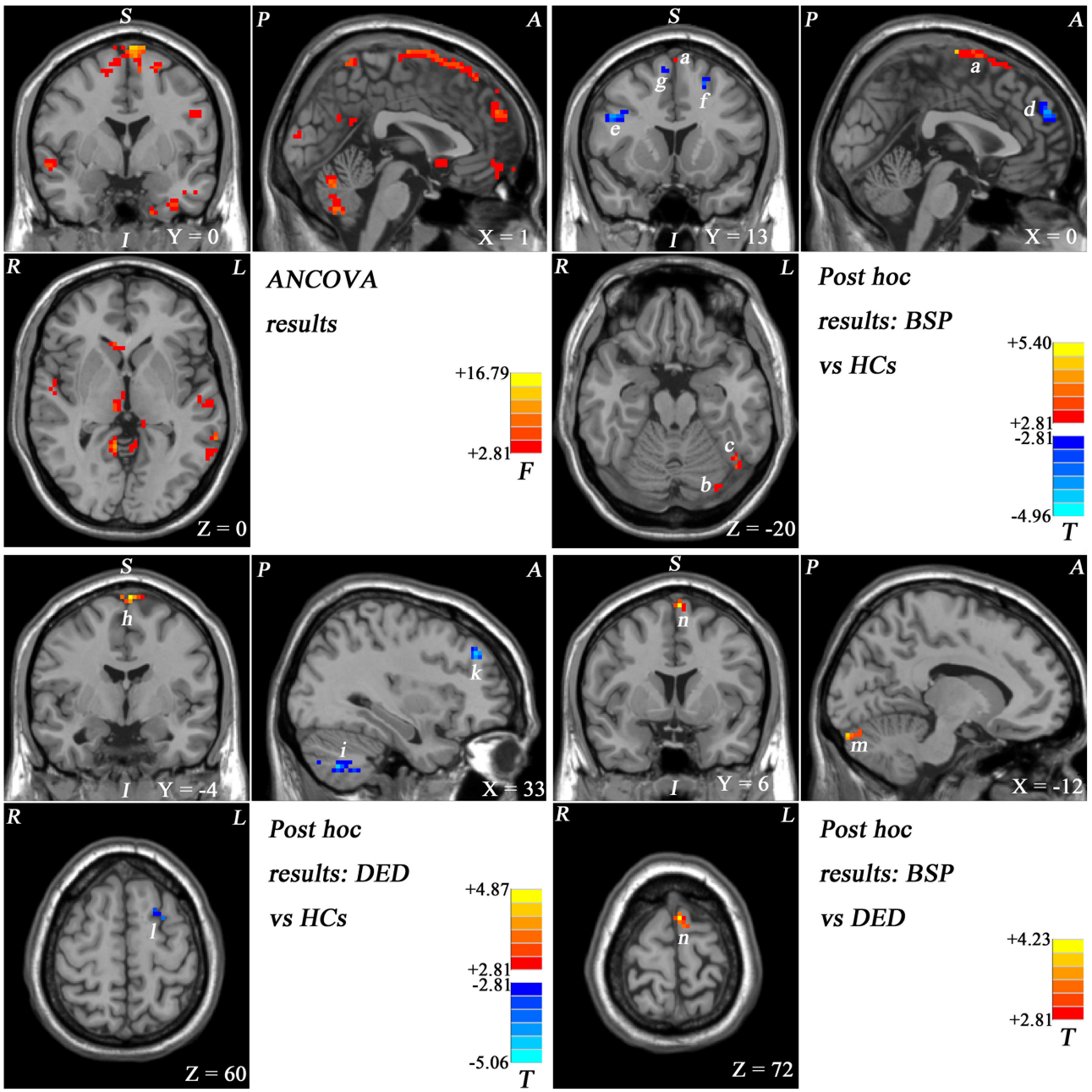

FIGURE 1 | Statistical maps showing ALFF values differences in different brain regions across studied groups. Red and blue represent higher and lower ALFF, respectively. The color bars indicate the *F*-values from the ANOVA analyses and the *T*-values from *post-hoc* analysis between each pair of groups. (a) Bilateral SMA, (b) left cerebellar crus I, (c) left fusiform gyrus/cerebellar crus I, (d) bilateral superior MPFC, (e) right inferior frontal gyrus, (f) left middle frontal gyrus, (g) right superior frontal gyrus, (h) bilateral SMA, (i) right cerebellar VIII/VIIb, (k) right middle frontal gyrus, (l) left middle frontal gyrus, (m) left cerebellar crus I, and (n) left SMA.

and DED group by between-group comparisons for further correlation analysis.

Pearson correlation or Spearman correlation analyses were performed to examine the association of ALFF values and clinical variables in patients with BSP and patients with DED when apposite. Significance level was set at $p < 0.05$ (corrected for Bonferroni correction).

RESULTS

Demographics and Clinical Information

A total of 70 participants were included in the study: 25 patients with BSP, 22 patients with DED, and 23 healthy controls. Demographics and clinical characteristics of these participants are shown in **Table 1**. There was no significant difference in

TABLE 2 | Regions with abnormal ALFF in the patients.

Cluster location	Peak (MNI)			Number of voxels	*T*-value[a]
	x	*y*	*z*		
BSP vs. controls					
Bilateral SMA	−3	−12	78	119	5.3996
Left cerebellar crus I	−33	−81	−24	46	4.2125
Left fusiform gyrus/cerebellar crus I	−45	−63	−18	25	5.1248
Bilateral superior MPFC	3	57	30	35	−4.4314
Right inferior frontal gyrus	48	15	27	37	−4.9554
Left middle frontal gyrus	−24	9	51	23	−4.1464
Right superior frontal gyrus	6	18	57	59	−4.8495
DED vs. controls					
Bilateral SMA	−3	−3	78	45	4.8692
Right cerebellar VIII/VIIb	18	−69	−51	128	−5.0609
Left cerebellar VIII/VIIb	−18	−72	−42	172	−4.4160
Right middle frontal gyrus	33	39	36	21	−4.6227
Left middle frontal gyrus	−27	6	60	26	−3.5618
BSP vs. DED					
Left cerebellar crus I	−12	−93	−24	27	3.9253
Left SMA	−3	6	72	25	4.2264

MNI, Montreal Neurological Institute; ALFF, amplitude of low-frequency fluctuations; MPFC, medial prefrontal cortex; ACC, anterior cingulate cortex; SMA, supplementary motor area.

[a]*A positive/negative T-value represents increased/decreased ALFF.*

age and education level across the three groups. Moreover, we observed that 20 patients of BSP (80.00%) exhibited sensory tricks, a characteristic feature in primary dystonia. That is, stimulus such as touching the cheeks and wearing glasses could temporarily alleviate the symptom of eyelid spasms.

Group Differences in ALFF

As shown in **Figure 1** and **Supplementary Figure 1**, the ALFF values were significantly different in the frontal and cerebellar regions across the three groups by ANCOVA.

Patients with BSP showed increased ALFF in the bilateral SMA, left cerebellar Crus I, and left fusiform gyrus/cerebellar Crus I and decreased ALFF in the superior part of the bilateral MPFC, right SFG, left middle frontal gyrus, and right inferior frontal gyrus compared with healthy controls (**Figure 1**; **Supplementary Figure 2**; **Table 2**).

Patients with DED exhibited increased ALFF in the bilateral SMA and decreased ALFF in the bilateral cerebellar VIII/VIIb, left middle frontal gyrus, and right middle frontal gyrus compared with that of healthy controls (**Figure 1**; **Supplementary Figure 3**; **Table 2**).

Compared with patients with DED, patients with BSP showed significantly increased ALFF in the left SMA and left cerebellar Crus I (**Figure 1**; **Supplementary Figure 4**; **Table 2**).

Correlation Analysis

A significantly positive correlation was observed between ALFF values in the left fusiform gyrus/cerebellar Crus I and symptomatic severity ($r = 0.444$, $p = 0.026$) in patients with BSP by using a Spearman correlation analysis (**Figure 2**). No significant correlation was revealed between abnormal ALFF and other clinical variables of patients with BSP. No correlation between abnormal ALFF and clinical variables was observed in the subjects with DED.

DISCUSSION

The present study was the first to explore functional changes in brain regions of patients with BSP, patients with DED, and healthy controls by measuring ALFF of fMRI signals at rest. Abnormal ALFF values were located in the sensorimotor integration related brain regions in patients with BSP, including the bilateral SMA, left cerebellar Crus I, left fusiform gyrus, bilateral superior MPFC, and right SFG compared with healthy controls. Patients with BSP exhibited significantly increased ALFF in the left cerebellar Crus I and the left SMA compared with patients with DED. In addition, ALFF in the left fusiform gyrus/cerebellar Crus I was positively correlated with the symptomatic severity of BSP.

Dystonia was previously described as a movement disorder resulting from basal ganglion dysfunction, but this description has been remarkably revised, and the role of sensorimotor integration in the pathophysiology of dystonia has been gradually recognized (30–33). In general, sensorimotor integration refers to all processes that sensory information is used to plan and carry out volitional movements, and the sensory counterparts of each implemented movement (34). Indeed, patients with dystonia exhibit not only motor symptoms but also some sensory field disorders, including abnormalities in sensory and perceptual functions (35–38). For example, patients with BSP often complain to have photophobia and other ocular discomforts, and neck pain is frequently associated with cervical dystonia (39, 40). In addition, a well-known clinical feature of dystonia is the sensory trick that can alleviate dystonic symptoms in some ways (41–44). Similarly, touching certain areas of the face, wearing colored glasses, or singing can relieve the spasm symptom in patients with BSP (45, 46). In our study, 20 patients of BSP (80.00%) presented with sensory tricks, which might be the adjustment of motor output through the modification of sensory input. Sensorimotor integration is a complex neural activity involving multiple brain regions and circuits, most of which are component parts of the sensorimotor network (SMN) (47). This network mainly involves action execution and sensory processing, and the SMA is one of the key nodes (48). The SMA receives signals from the basal ganglia and cerebellum and then delivers them to primary motor cortex to coordinate motion execution instructions and participate in sensorimotor integration (36, 49, 50). Many structural and functional MRI studies on dystonia, including BSP, have usually revealed abnormalities in the SMA, and animal models of dystonia have shown overexcitability and increased proprioceptive input in the SMA (51–54). In our study, high ALFF was observed in the bilateral SMA in patients with BSP and patients with DED, and this result might be caused

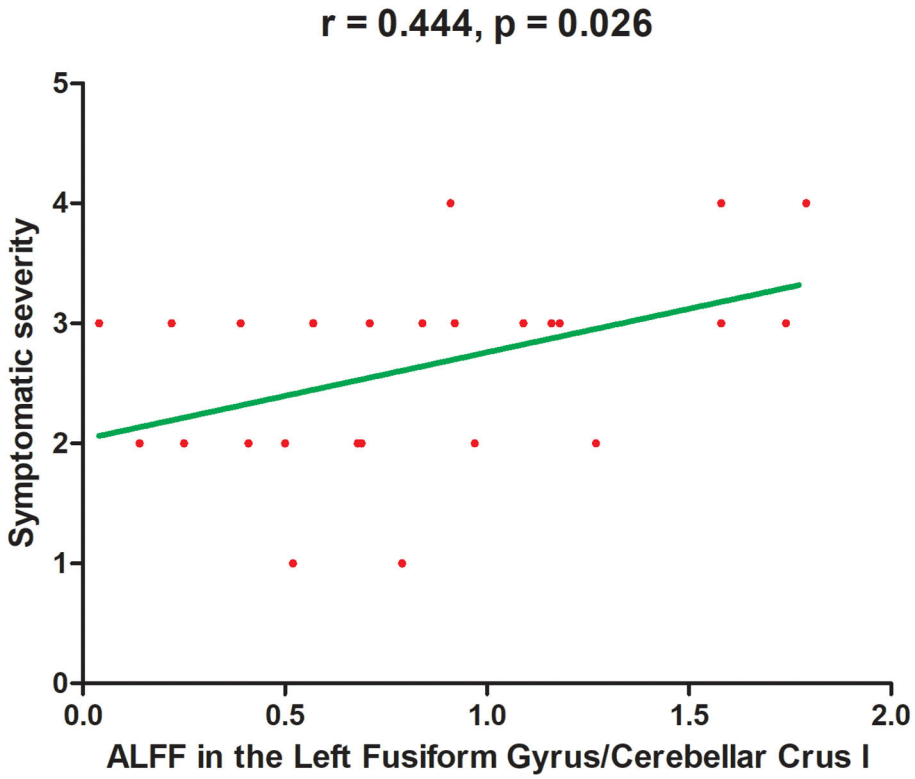

FIGURE 2 | A significantly positive correlation between symptomatic severity and ALFF values in the left fusiform gyrus/cerebellar crus I in patients with BSP. ALFF, amplitude of low-frequency fluctuations. *X*-axis represents ALFF *z*-score. *Y*-axis represents symptomatic severity.

by some interference from peripheral paresthesia components. However, patients with BSP exhibited increased ALFF in the left SMA compared with patients with DED, indicating that this region might be a primary change in BSP. Speculatively, the present observation of increased ALFF in the left SMA may reflect the possibility that abnormal motor information from SMA to primary motor cortex results in improper motor outflow, creating involuntary closure of the orbicularis oculi that characterizes BSP.

The function of the cerebellum in motion control and coordination has been traditionally accepted, and further research evidence has emphasized the critical role of the cerebellum in the pathophysiology of dystonia (55, 56). For instance, diffusion tensor imaging studies have demonstrated abnormal integrity of cerebellar-thalamo-cortical fiber tracts in isolated focal dystonia phenotypes and decreased fractional anisotropy in the right cerebellum of patients with cervical dystonia (57, 58). Similarly, we found increased ALFF in the left cerebellar Crus I in patients with BSP compared with healthy controls and patients with DED. In addition, no correlation was seen between the increased ALFF in the left cerebellar crus I and JRS scores or symptomatic severity in BSP patients, suggesting that the abnormal ALFF values in the left cerebellar crus I might be independent of the illness duration and disease severity. The cerebellum receives fibers from the brainstem cerebellar pathway and projects them to the sensorimotor cortex through the cerebellar Crus I/II to modulate muscular tone and coordinate muscle groups (59, 60). In addition, separate cortico–cerebellar circuits can engage visual–spatial processing and response to the visual stimulus, supporting the assumption that the cerebellum is also involved in vision modulation (61). There is increased ALFF in the left cerebellar Crus I of patients with BSP, suggesting that the cerebellum might be another key node that received abnormal visual sensation and muscle tension caused by persistent eye spasm. As a consequence, it becomes hyperactive to regulate abnormal movement through sensorimotor integration process. Therefore, alterations in the left cerebellar Crus I might be distinctive in BSP, and an increased cerebellar neuronal activity might induce subsequent adaptive activities in motor systems. Traditional deep brain stimulation (DBS) and TMS therapeutic targets such as the globus pallidus interma and subthalamic nucleus of dystonia have expanded to the cerebellum in certain types of dystonia (62, 63). Cerebellum could be a potential target for in-depth exploration of intervention strategies in BSP.

Interestingly, our results showed an increased ALFF in the left fusiform gyrus and a positive correlation between ALFF in this region and symptomatic severity in patients with BSP. As part of the primary visual network, the fusiform gyrus is an important link in the human ventral visual information processing pathway that processes color information

and facial expression perception (64, 65). A wide range of cognitive deficits are found in patients with BSP; among them, visuospatial function is the most frequently affected area (66). The characteristics of this visuospatial function abnormality was mutually supported by our results, which might be distinctive visual network changes secondary to aberrant visual input caused by eyelid spasms. Moreover, visual areas are widely connected to the basal ganglia and other motor areas. Thus, ALFF alterations in the left fusiform gyrus might result in visual-motor integration dysfunction, a form of sensorimotor integration. The positive correlation between ALFF in the left fusiform gyrus and symptomatic severity of BSP might represent an adaptive role or reaction to abnormal visual information.

We also found decreased ALFF in the bilateral superior MPFC and right SFG in patients with BSP. The MPFC and SFG are core components of the brain's default mode network (DMN), which is commonly recognized to be involved in cognitive functions and emotional processes (67). Our previous study in patients with BSP revealed an enhanced homotopic coordination in the inferior temporal gyrus and posterior cingulate cortex within the DMN (15). These abnormalities indicated distinct differences within the DMN in patients with BSP. One possibility is that these changes within the DMN might be related to nonmotor symptoms, such as anxiety, depression, and cognitive impairments, in patients with BSP; and these changes occur more frequently in patients with BSP than that in healthy controls (9). Although our results showed no significant difference in SAS/SDS scores between patients with BSP and healthy controls, it still raises a possibility that our patients might have subclinical emotional and cognitive impairments. A widely accepted viewpoint proposed that the MPFC is a high-level nervous center located at the top of the information processing stream, which flexibly map sensory signals to motor actions and achieve an adaptive choice behavior (68–70). It can be seen that the MPFC plays a role in sensorimotor integration. Moreover, MPFC has been thought to involve higher-level cognitive functions related to voluntary action, including formation of movement plans and choice of executive actions (71, 72). Likewise, the SFG is connected to the critical nodes of the motor-related network, including the precentral gyrus, caudate nucleus and thalamus (73). In this regard, the DMN might partly contribute to motor regulation apart from non-motor symptoms in BSP through functional connectivity.

In addition to small sample size, some limitations should be noted in this study. First, the potential dystonic activity of the eyelids during fMRI scanning should be considered although all subjects denied this phenomenon. Second, we were unable to detect the potential dysfunction of connections across different brain regions of patients with BSP because the ALFF measurements do not reflect the integration of the brain function activity at a network level. Furthermore, it should be noted that the application of head retainers and earplugs during images acquisition might induce sensory tricks, thus disturbing the "resting-state" to some extent.

CONCLUSION

Despite the limitations, the design of combining patients with BSP and patients with DED may be a feasible option to distinguish the secondary central effects of the sustained muscle activity in neuroimaging studies on BSP. In conclusion, our results reveal that the distinctive changes in the brain function of patients with BSP are different from those in patients with DED and healthy controls. The results further emphasize the primary role of sensorimotor integration in the pathophysiology of BSP.

DATA AVAILABILITY STATEMENT

The raw data supporting the conclusions of this article will be made available by the authors, without undue reservation.

ETHICS STATEMENT

The studies involving human participants were reviewed and approved by the Ethics Committee of the First Affiliated Hospital of Guangxi Medical University. The patients/participants provided their written informed consent to participate in this study.

AUTHOR CONTRIBUTIONS

SL, WG, CF, and WJ made substantial contributions to the conception of the work. YiL and WL did the acquisition of data. YX, YaL, YuL, JT, JW, LP, and ML analyzed the data. CF and WJ wrote the main manuscript text. All authors reviewed and approved the manuscript.

FUNDING

This study was supported by grants from the National Natural Science Foundation of China (Grant No. 81771447), National Key R&D Program of China (Grant No. 2016YFC1307100), Guangxi Appropriate Technology for Medical and Health Research Development Project (Grant No. S2020028), and Incubation Project of Research Team (Grant No. MINKEFY202108).

ACKNOWLEDGMENTS

We are grateful to all the foundations mentioned above and all the participants in the study.

SUPPLEMENTARY MATERIAL

The Supplementary Material for this article can be found online at: https://www.frontiersin.org/articles/10.3389/fneur.2021.607476/full#supplementary-material

REFERENCES

1. Hallett M. Blepharospasm: recent advances. *Neurology.* (2002) 59:1306–12. doi: 10.1212/01.WNL.0000027361.73814.0E
2. Peckham EL, Lopez G, Shamim EA, Richardson SP, Sanku S, Malkani R, et al. Clinical features of patients with blepharospasm: a report of 240 patients. *Eur J Neurol.* (2011) 18:382–6. doi: 10.1111/j.1468-1331.2010.03161.x
3. Jinnah HA, Berardelli A, Comella C, Defazio G, Delong MR, Factor S, et al. The focal dystonias: current views and challenges for future research. *Mov Disord.* (2013) 28:926–43. doi: 10.1002/mds.25567
4. Defazio G, Conte A, Gigante AF, Ferrazzano G, Pellicciari R, Dagostino S, et al. Clinical heterogeneity in patients with idiopathic blepharospasm: a cluster analysis. *Parkinsonism Relat Disord.* (2017) 40:64–8. doi: 10.1016/j.parkreldis.2017.04.014
5. Ferrazzano G, Conte A, Gigante A, Defazio G, Berardelli A, Fabbrini G. Disease progression in blepharospasm: a 5-year longitudinal study. *Eur J Neurol.* (2019) 26:268–73. doi: 10.1111/ene.13832
6. Defazio G, Abbruzzese G, Aniello MS, Di Fede R, Esposito M, Fabbrini G, et al. Eye symptoms in relatives of patients with primary adult-onset dystonia. *Mov Disord.* (2012) 27:305–7. doi: 10.1002/mds.24026
7. Shimazaki J. Definition and diagnostic criteria of dry eye disease: historical overview and future directions. *Invest Ophthalmol Vis Sci.* (2018) 59:DES7–DES12. doi: 10.1167/iovs.17-23475
8. Kranz G, Shamim EA, Lin PT, Kranz GS, Voller B, Hallett M. Blepharospasm and the modulation of cortical excitability in primary and secondary motor areas. *Neurology.* (2009) 73:2031–6. doi: 10.1212/WNL.0b013e3181c5b42d
9. Valls-Sole J, Defazio G. Blepharospasm: update on epidemiology, clinical aspects, and pathophysiology. *Front Neurol.* (2016) 7:45. doi: 10.3389/fneur.2016.00045
10. Martino D, Di Giorgio A, D'Ambrosio E, Popolizio T, Macerollo A, Livrea P, et al. Cortical gray matter changes in primary blepharospasm: a voxel-based morphometry study. *Mov Disord.* (2011) 26:1907–12. doi: 10.1002/mds.23724
11. Suzuki Y, Kiyosawa M, Wakakura M, Mochizuki M, Ishii K. Gray matter density increase in the primary sensorimotor cortex in long-term essential blepharospasm. *Neuroimage.* (2011) 56:1–7. doi: 10.1016/j.neuroimage.2011.01.081
12. Battistella G, Termsarasab P, Ramdhani RA, Fuertinger S, Simonyan KJCC. Isolated focal dystonia as a disorder of large-scale functional networks. *Cereb Cortex.* (2015) 27:1203–15. doi: 10.1093/cercor/bhv313
13. Huang XF, Zhu MR, Shan P, Pei CH, Liang ZH, Zhou HL, et al. Multiple neural networks malfunction in primary blepharospasm: an independent components analysis. *Front Hum Neurosci.* (2017) 11:235. doi: 10.3389/fnhum.2017.00235
14. Jochim A, Li Y, Gora-Stahlberg G, Mantel T, Berndt M, Castrop F, et al. Altered functional connectivity in blepharospasm/orofacial dystonia. *Brain Behav.* (2018) 8:e00894. doi: 10.1002/brb3.894
15. Wei J, Wei S, Yang R, Yang L, Yin Q, Li H, et al. Voxel-mirrored homotopic connectivity of resting-state functional magnetic resonance imaging in blepharospasm. *Front Psychol.* (2018) 9:1620. doi: 10.3389/fpsyg.2018.01620
16. Jiang WY, Lan Y, Cen CY, Liu Y, Feng CQ, Lei YW, et al. Abnormal spontaneous neural activity of brain regions in patients with primary blepharospasm at rest. *J Neurol Sci.* (2019) 403:44–9. doi: 10.1016/j.jns.2019.06.002
17. Defazio G, Hallett M, Jinnah HA, Conte A, Berardelli A. Blepharospasm 40 years later. *Mov Disord.* (2017) 32:498–509. doi: 10.1002/mds.26934
18. Baker RS, Andersen AH, Morecraft RJ, Smith CD. A functional magnetic resonance imaging study in patients with benign essential blepharospasm. *J Neuroophthalmol.* (2003) 23:11–5. doi: 10.1097/00041327-200303000-00003
19. Schmidt KE, Linden DE, Goebel R, Zanella FE, Lanfermann H, Zubcov AA. Striatal activation during blepharospasm revealed by fMRI. *Neurology.* (2003) 60:1738–43. doi: 10.1212/01.WNL.0000063306.67984.8C
20. Biswal BB. Resting state fMRI: a personal history. *Neuroimage.* (2012) 62:938–44. doi: 10.1016/j.neuroimage.2012.01.090
21. Hoptman MJ, Zuo XN, Butler PD, Javitt DC, D'Angelo D, Mauro CJ, et al. Amplitude of low-frequency oscillations in schizophrenia: a resting state fMRI study. *Schizophr Res.* (2010) 117:13–20. doi: 10.1016/j.schres.2009.09.030
22. Zhang Y, Zhu C, Chen H, Duan X, Lu F, Li M, et al. Frequency-dependent alterations in the amplitude of low-frequency fluctuations in social anxiety disorder. *J Affect Disord.* (2015) 174:329–35. doi: 10.1016/j.jad.2014.12.001
23. Li H, Guo W, Liu F, Chen J, Su Q, Zhang Z, et al. Enhanced baseline activity in the left ventromedial putamen predicts individual treatment response in drug-naive, first-episode schizophrenia: results from two independent study samples. *EBioMedicine.* (2019) 46:248–55. doi: 10.1016/j.ebiom.2019.07.022
24. Su Q, Yu M, Liu F, Zhang Z, Lei M, Jiang Y, et al. Frequency-specific alterations of the frontal-cerebellar circuit in first-episode, drug-naive somatization disorder. *J Affect Disord.* (2021) 280(Pt A):319–25. doi: 10.1016/j.jad.2020.11.090
25. Defazio G, Hallett M, Jinnah HA, Berardelli A. Development and validation of a clinical guideline for diagnosing blepharospasm. *Neurology.* (2013) 81:236–40. doi: 10.1212/WNL.0b013e31829bfdf6
26. Craig JP, Nichols KK, Akpek EK, Caffery B, Dua HS, Joo CK, et al. TFOS DEWS II definition and classification report. *Ocul Surf.* (2017) 15:276–83. doi: 10.1016/j.jtos.2017.05.008
27. Joseph J, Christopher K, Susanne G, Roman G, George CJMD. Relationship between various clinical outcome assessments in patients with blepharospasm. *Mov Disord.* (2009) 24:407–13. doi: 10.1002/mds.22368
28. Song XW, Dong ZY, Long XY, Li SF, Zuo XN, Zhu CZ, et al. REST: a toolkit for resting-state functional magnetic resonance imaging data processing. *PLoS One.* (2011) 6:e25031. doi: 10.1371/journal.pone.0025031
29. Zang YF, He Y, Zhu CZ, Cao QJ, Sui MQ, Liang M, et al. Altered baseline brain activity in children with ADHD revealed by resting-state functional MRI. *Brain Dev.* (2007) 29:83–91. doi: 10.1016/j.braindev.2006.07.002
30. Obermann M, Yaldizli O, De Greiff A, Lachenmayer ML, Buhl AR, Tumczak F, et al. Morphometric changes of sensorimotor structures in focal dystonia. *Mov Disord.* (2007) 22:1117–23. doi: 10.1002/mds.21495
31. Tinazzi M, Fiorio M, Fiaschi A, Rothwell JC, Bhatia KP. Sensory functions in dystonia: insights from behavioral studies. *Mov Disord.* (2009) 24:1427–36. doi: 10.1002/mds.22490
32. Patel N, Jankovic J, Hallett M. Sensory aspects of movement disorders. *Lancet Neurol.* (2014) 13:100–12. doi: 10.1016/S1474-4422(13)70213-8
33. Zittel S, Helmich RC, Demiralay C, Munchau A, Baumer T. Normalization of sensorimotor integration by repetitive transcranial magnetic stimulation in cervical dystonia. *J Neurol.* (2015) 262:1883–9. doi: 10.1007/s00415-015-7789-1
34. Avanzino L, Tinazzi M, Ionta S, Fiorio M. Sensory-motor integration in focal dystonia. *Neuropsychologia.* (2015) 79(Pt B):288–300. doi: 10.1016/j.neuropsychologia.2015.07.008
35. Stamelou M, Edwards MJ, Hallett M, Bhatia KP. The non-motor syndrome of primary dystonia: clinical and pathophysiological implications. *Brain.* (2012) 135(Pt 6):1668–81. doi: 10.1093/brain/awr224
36. Perruchoud D, Murray MM, Lefebvre J, Ionta S. Focal dystonia and the Sensory-Motor Integrative Loop for Enacting (SMILE). *Front Hum Neurosci.* (2014) 8:458. doi: 10.3389/fnhum.2014.00458
37. Yang J, Shao N, Song W, Wei Q, Ou R, Wu Y, et al. Nonmotor symptoms in primary adult-onset cervical dystonia and blepharospasm. *Brain Behav.* (2017) 7:e00592. doi: 10.1002/brb3.592
38. Ferrazzano G, Berardelli I, Conte A, Baione V, Concolato C, Belvisi D, et al. Motor and non-motor symptoms in blepharospasm: clinical and pathophysiological implications. *J Neurol.* (2019) 266:2780–5. doi: 10.1007/s00415-019-09484-w
39. Conte A, Berardelli I, Ferrazzano G, Pasquini M, Berardelli A, Fabbrini G. Non-motor symptoms in patients with adult-onset focal dystonia: sensory and psychiatric disturbances. *Parkinsonism Relat Disord.* (2016) 22(Suppl. 1):S111–S4. doi: 10.1016/j.parkreldis.2015.09.001
40. Byun YS, Kim SE, Paik JS, Yang SW. Increased pupillary constriction velocity in benign essential blepharospasm associated with photophobia. *PLoS One.* (2019) 14:e0217924. doi: 10.1371/journal.pone.0217924
41. Naumann M, Magyar-Lehmann S, Reiners K, Erbguth F, Leenders KL. Sensory tricks in cervical dystonia: perceptual dysbalance of parietal cortex modulates frontal motor programming. *Ann Neurol.* (2000) 47:322–8. doi: 10.1002/1531-8249(200003)47:3<322::AID-ANA7>3.0.CO;2-E

42. Amadio S, Houdayer E, Bianchi F, Tesfaghebriel Tekle H, Urban IP, Butera C, et al. Sensory tricks and brain excitability in cervical dystonia: a transcranial magnetic stimulation study. *Mov Disord.* (2014) 29:1185–8. doi: 10.1002/mds.25888
43. Patel N, Hanfelt J, Marsh L, Jankovic J, members of the Dystonia Coalition. Alleviating manoeuvres (sensory tricks) in cervical dystonia. *J Neurol Neurosurg Psychiatry.* (2014) 85:882–4. doi: 10.1136/jnnp-2013-307316
44. Ramos VF, Karp BI, Hallett M. Tricks in dystonia: ordering the complexity. *J Neurol Neurosurg Psychiatry.* (2014) 85:987–93. doi: 10.1136/jnnp-2013-306971
45. Martino D, Liuzzi D, Macerollo A, Aniello MS, Livrea P, Defazio G. The phenomenology of the geste antagoniste in primary blepharospasm and cervical dystonia. *Mov Disord.* (2010) 25:407–12. doi: 10.1002/mds.23011
46. Ferrazzano G, Conte A, Belvisi D, Fabbrini A, Baione V, Berardelli A, et al. Writing, reading, and speaking in blepharospasm. *J Neurol.* (2019) 266:1136–40. doi: 10.1007/s00415-019-09243-x
47. Delnooz CC, Pasman JW, Beckmann CF, van de Warrenburg BP. Altered striatal and pallidal connectivity in cervical dystonia. *Brain Struct Funct.* (2015) 220:513–23. doi: 10.1007/s00429-013-0671-y
48. Smith SM, Fox PT, Miller KL, Glahn DC, Fox PM, Mackay CE, et al. Correspondence of the brain's functional architecture during activation and rest. *Proc Natl Acad Sci U S A.* (2009) 106:13040–5. doi: 10.1073/pnas.0905267106
49. Carbonnell L, Hasbroucq T, Grapperon J, Vidal F. Response selection and motor areas: a behavioural and electrophysiological study. *Clin Neurophysiol.* (2004) 115:2164–74. doi: 10.1016/j.clinph.2004.04.012
50. Gross J, Pollok B, Dirks M, Timmermann L, Butz M, Schnitzler A. Task-dependent oscillations during unimanual and bimanual movements in the human primary motor cortex and SMA studied with magnetoencephalography. *Neuroimage.* (2005) 26:91–8. doi: 10.1016/j.neuroimage.2005.01.025
51. Cuny E, Ghorayeb I, Guehl D, Escola L, Bioulac B, Burbaud PJN, et al. Sensory motor mismatch within the supplementary motor area in the dystonic monkey. *Neurobiol Dis.* (2008) 30:151–61. doi: 10.1016/j.nbd.2007.12.011
52. Opavsky R, Hlustik P, Otruba P, Kanovsky P. Sensorimotor network in cervical dystonia and the effect of botulinum toxin treatment: a functional MRI study. *J Neurol Sci.* (2011) 306:71–5. doi: 10.1016/j.jns.2011.03.040
53. Mantel T, Meindl T, Li Y, Jochim A, Gora-Stahlberg G, Kraenbring J, et al. Network-specific resting-state connectivity changes in the premotor-parietal axis in writer's cramp. *Neuroimage Clin.* (2018) 17:137–44. doi: 10.1016/j.nicl.2017.10.001
54. Jiang W, Lei Y, Wei J, Yang L, Wei S, Yin Q, et al. Alterations of interhemispheric functional connectivity and degree centrality in cervical dystonia: a resting-state fMRI study. *Neural Plast.* (2019) 2019:7349894. doi: 10.1155/2019/7349894
55. Filip P, Gallea C, Lehericy S, Bertasi E, Popa T, Marecek R, et al. Disruption in cerebellar and basal ganglia networks during a visuospatial task in cervical dystonia. *Mov Disord.* (2017) 32:757–68. doi: 10.1002/mds.26930
56. Shakkottai VG, Batla A, Bhatia K, Dauer WT, Dresel C, Niethammer M, et al. Current opinions and areas of consensus on the role of the cerebellum in dystonia. *Cerebellum.* (2017) 16:577–94. doi: 10.1007/s12311-016-0825-6
57. Teo JT, van de Warrenburg BP, Schneider SA, Rothwell JC, Bhatia KP. Neurophysiological evidence for cerebellar dysfunction in primary focal dystonia. *J Neurol Neurosurg Psychiatry.* (2009) 80:80–3. doi: 10.1136/jnnp.2008.144626
58. Berman BD, Honce JM, Shelton E, Sillau SH, Nagae LM. Isolated focal dystonia phenotypes are associated with distinct patterns of altered microstructure. *Neuroimage Clin.* (2018) 19:805–12. doi: 10.1016/j.nicl.2018.06.004
59. Buckner RL. The cerebellum and cognitive function: 25 years of insight from anatomy and neuroimaging. *Neuron.* (2013) 80:807–15. doi: 10.1016/j.neuron.2013.10.044
60. Witter L, De Zeeuw CI. Regional functionality of the cerebellum. *Curr Opin Neurobiol.* (2015) 33:150–5. doi: 10.1016/j.conb.2015.03.017
61. Brissenden JA, Tobyne SM, Osher DE, Levin EJ, Halko MA, Somers DC. Topographic cortico-cerebellar networks revealed by visual attention and working memory. *Curr Biol.* (2018) 28:3364–72.e3365. doi: 10.1016/j.cub.2018.08.059
62. Koch G, Porcacchia P, Ponzo V, Carrillo F, Caceres-Redondo MT, Brusa L, et al. Effects of two weeks of cerebellar theta burst stimulation in cervical dystonia patients. *Brain Stimul.* (2014) 7:564–72. doi: 10.1016/j.brs.2014.05.002
63. Bradnam LV, Graetz LJ, McDonnell MN, Ridding MC. Anodal transcranial direct current stimulation to the cerebellum improves handwriting and cyclic drawing kinematics in focal hand dystonia. *Front Hum Neurosci.* (2015) 9:286. doi: 10.3389/fnhum.2015.00286
64. Radua J, Phillips ML, Russell T, Lawrence N, Marshall N, Kalidindi S, et al. Neural response to specific components of fearful faces in healthy and schizophrenic adults. *Neuroimage.* (2010) 49:939–46. doi: 10.1016/j.neuroimage.2009.08.030
65. Muller VI, Hohner Y, Eickhoff SB. Influence of task instructions and stimuli on the neural network of face processing: an ALE meta-analysis. *Cortex.* (2018) 103:240–55. doi: 10.1016/j.cortex.2018.03.011
66. Yang J, Song W, Wei Q, Ou R, Cao B, Liu W, et al. Screening for cognitive impairments in primary blepharospasm. *PLoS One.* (2016) 11:e0160867. doi: 10.1371/journal.pone.0160867
67. Marsland AL, Kuan DC, Sheu LK, Krajina K, Kraynak TE, Manuck SB, et al. Systemic inflammation and resting state connectivity of the default mode network. *Brain Behav Immun.* (2017) 62:162–70. doi: 10.1016/j.bbi.2017.01.013
68. Gusnard DA, Akbudak E, Shulman GL, Raichle ME. Medial prefrontal cortex and self-referential mental activity: relation to a default mode of brain function. *Proc Natl Acad Sci U S A.* (2001) 98:4259–64. doi: 10.1073/pnas.071043098
69. Euston DR, Gruber AJ, McNaughton BL. The role of medial prefrontal cortex in memory and decision making. *Neuron.* (2012) 76:1057–70. doi: 10.1016/j.neuron.2012.12.002
70. Duncan NW, Hayes DJ, Wiebking C, Tiret B, Pietruska K, Chen DQ, et al. Negative childhood experiences alter a prefrontal-insular-motor cortical network in healthy adults: a preliminary multimodal rsfMRI-fMRI-MRS-dMRI study. *Hum Brain Mapp.* (2015) 36:4622–37. doi: 10.1002/hbm.22941
71. Rushworth MF. Intention, choice, and the medial frontal cortex. *Ann N Y Acad Sci.* (2008) 1124:181–207. doi: 10.1196/annals.1440.014
72. Phillips HN, Cope TE, Hughes LE, Zhang J, Rowe JB. Monitoring the past and choosing the future: the prefrontal cortical influences on voluntary action. *Sci Rep.* (2018) 8:7247. doi: 10.1038/s41598-018-25127-y
73. du Boisgueheneuc F, Levy R, Volle E, Seassau M, Duffau H, Kinkingnehun S, et al. Functions of the left superior frontal gyrus in humans: a lesion study. *Brain.* (2006) 129(Pt 12):3315–28. doi: 10.1093/brain/awl244

Conflict of Interest: The authors declare that the research was conducted in the absence of any commercial or financial relationships that could be construed as a potential conflict of interest.

Advantages of publishing in Frontiers

OPEN ACCESS
Articles are free to read for greatest visibility and readership

FAST PUBLICATION
Around 90 days from submission to decision

HIGH QUALITY PEER-REVIEW
Rigorous, collaborative, and constructive peer-review

TRANSPARENT PEER-REVIEW
Editors and reviewers acknowledged by name on published articles

Frontiers
Avenue du Tribunal-Fédéral 34
1005 Lausanne | Switzerland

Visit us: www.frontiersin.org
Contact us: frontiersin.org/about/contact

REPRODUCIBILITY OF RESEARCH
Support open data and methods to enhance research reproducibility

DIGITAL PUBLISHING
Articles designed for optimal readership across devices

FOLLOW US
@frontiersin

IMPACT METRICS
Advanced article metrics track visibility across digital media

EXTENSIVE PROMOTION
Marketing and promotion of impactful research

LOOP RESEARCH NETWORK
Our network increases your article's readership